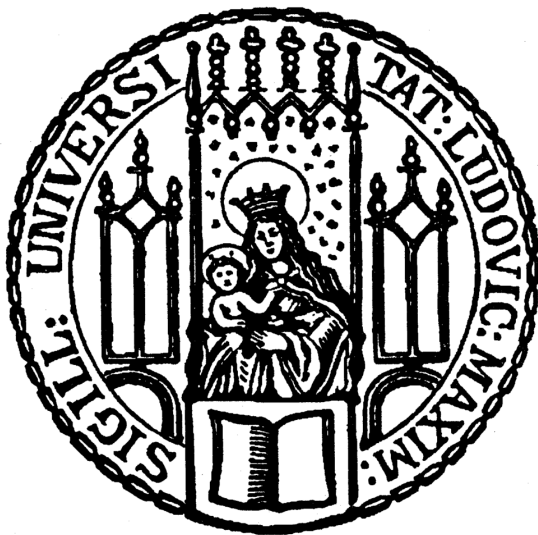


SIMULATING MAGNETIC FIELDS IN GALAXY CLUSTERS

Ph.D. Thesis in Astronomy

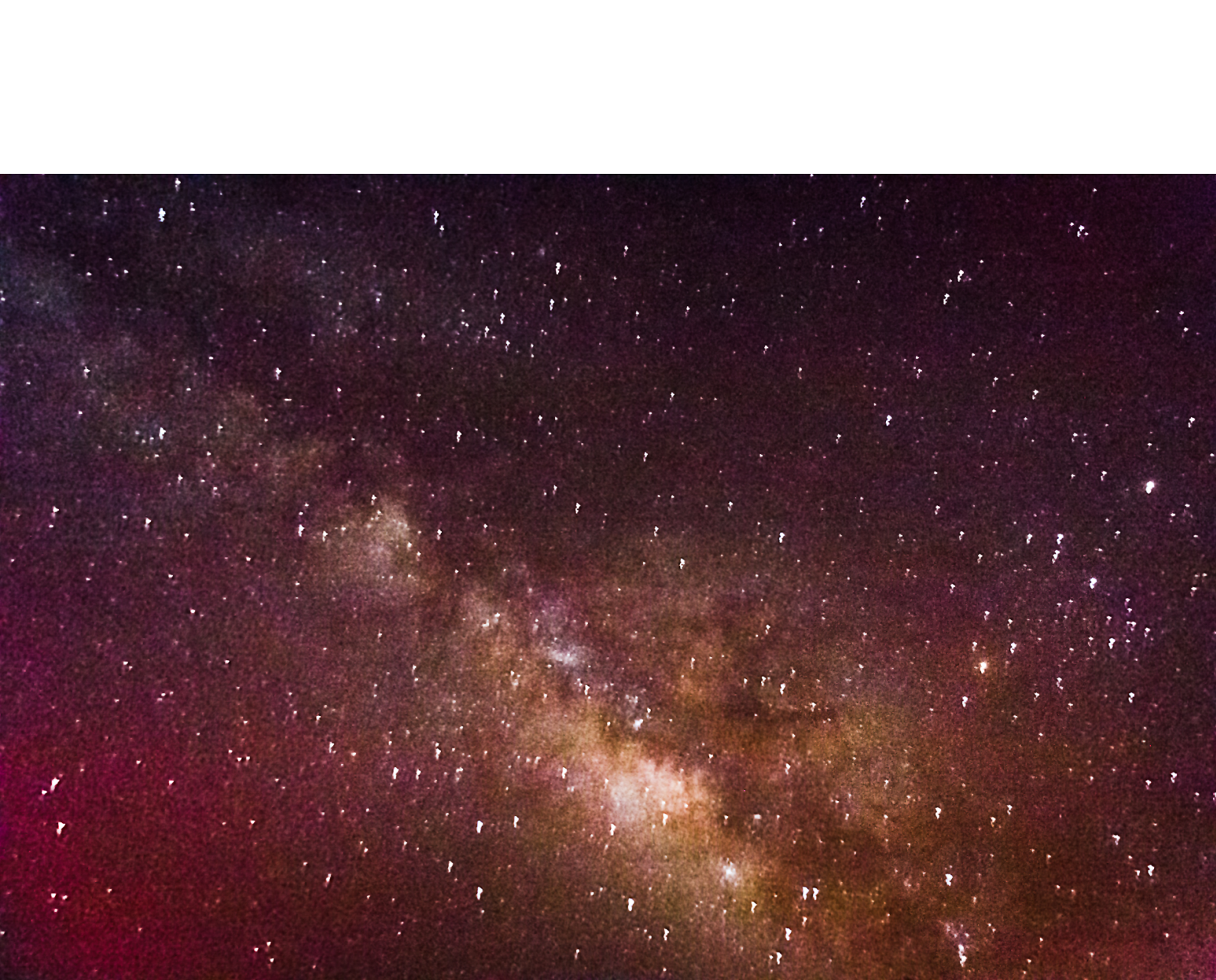
at the Faculty of Physics
of the Ludwig-Maximilians-Universität München



submitted by

Alexander Arth
from Munich, Germany

Munich, March 16th, 2018



Milky Way above the open volcano Kīlauea on Hawaii.

First evaluator: Prof. Dr. Harald Lesch
Second evaluator: PD Dr. Klaus Dolag

Date of the oral exam: April 24th, 2018

Zusammenfassung

Der Weltraum - unendliche Weiten.

– Star Trek

Seit der Antike betrachten wir den nächtlichen Himmel, fasziniert von den Sternen und der Weite des Universums. Der starke Einfluss dieser Faszination resultierte z.B. in der Geburt der Science Fiction. Die vielleicht älteste Geschichte ist der sumerische “Epos des Gilgamesh” 2000 Jahre vor Christus. Trotz des immensen Fortschritts, Menschen und Technik in das All zu bringen, sind wir hierbei nach wie vor auf unsere Umgebung im Sonnensystem begrenzt. Unsere Vorstellungskraft erforscht jedoch das ganze Universum mittels echter Wissenschaft und Forschung: Astronomie und Astrophysik.

Moderne Computer erlauben es uns, unser Verständnis über Prozesse im Universum voranzutreiben. Rechenkapazitäten sind soweit gestiegen, dass wir endlich in der Lage sind, die Hypothesen zu testen, die Astrophysiker im Laufe des letzten Jahrhunderts aufgestellt haben. Wir sind an einem Punkt angelangt, an dem weiterer Fortschritt meist dadurch limitiert ist, wie gut wir unsere grundlegenden numerischen Beschreibungen verbessern und Software optimieren können. Im ersten Teil dieser Dissertation geben wir einen Eindruck darüber, was bereits dahingehend erreicht wurde, das Universum zu beobachten, zu simulieren und zu verstehen. Wir legen den Fokus auf kosmische Magnetfelder in Galaxien und Galaxienhaufen und werfen offene Fragen auf. Von Kapitel IV an präsentieren wir den Hauptteil dieser Arbeit, der sich mit Verbesserungen und Erweiterungen unserer numerischen Werkzeuge, Simulationen von Galaxien und Galaxienhaufen mit verbesserter numerischer Genauigkeit und neuen Modellen beschäftigt und betten diesen in den großen Kontext der Arbeit ein.

Nach [Naab and Ostriker, 2017](#) können wir die Aufgabe, astrophysikalische Objekte zu simulieren, in vier Aspekte aufteilen:

1. **Wissen über physikalische Prozesse:** Bevor wir etwas simulieren können, müssen wir wissen, welche physikalischen Prozesse eine Rolle spielen und verstehen, wie diese vonstatten gehen, um sie korrekt modellieren zu können. Das reicht von bekannteren wie Hydrodynamik und Gravitation bis hin zu hochkomplexen wie Sternentstehung, Kühlungsprozesse und der Behandlung von schwarzen Löchern. Wir geben einen knappen Überblick über die Entstehungsgeschichte des Universums und aktuelle Beobachtungen, vorwiegend von Galaxien und Galaxienhaufen in Kapitel I. Wir fahren mit Beobachtungsmethoden, um kosmische Magnetfelder zu untersuchen, fort und geben eine theoretische Beschreibung der Magneto-Hydrodynamik in Kapitel II. Weitere Modellierung physikalischer Prozesse spielt eine Rolle in der restlichen Dissertation.

2. **Anfangsbedingungen:** Wir benötigen eine exakte Beschreibung der Anfangsbedingungen jegliches Systems, welches wir simulieren wollen. Sei es ein/e isolierte Galaxie/Galaxienhaufen die wir direkt aufsetzen, oder eine kosmologische Box mittels eines Dichtefelds, das wir aus Beobachtungen des kosmischen Mikrowellenhintergrunds erlangen. Außerdem müssen wir diese mathematische Beschreibung korrekt in ein Format umsetzen, welches der Simulationscode verstehen kann. Hohe Qualität ist hier von Nöten, da jegliche Fehler durch die Simulation propagieren und die Ergebnisse negativ beeinflussen. Dies ist keine leichte Aufgabe, derer wir uns in Kapitel IV widmen. Dort präsentieren wir einen neuartigen Code, der beliebige Dichtefunktionen für Smoothed Particle Hydrodynamics (SPH) umsetzen kann, um u.a. Code Tests generieren zu können.
3. **Rechenwerkzeuge:** Von einer numerisch stabilen Diskretisierung, über die Validierung von Testergebnissen bis zu Parallelisierung und Optimierung eines Codes, sodass er riesige Aufgaben mit guter Auflösung bewältigen kann - all das gehört zu dieser Kategorie. Sowohl durch verbesserte Werkzeuge als auch steigende Anforderungen wird dies immer wichtiger und zeitaufwändiger. In Kapitel III fassen wir übliche Techniken zusammen, die in astrophysikalischen Codes verwendet werden. In Kapitel V präsentieren wir neueste Verbesserungen des GADGET Codes und werten ausführliche Tests seiner numerischen Eigenschaften aus. Da Rechenkapazität exponentiell wächst, werden immer mehr Daten generiert und die Nachbearbeitung kann zu einer extrem schwierigen Aufgabe werden. In Kapitel VII beschreiben wir deshalb eine neuartige Computerbibliothek, die es ermöglicht, riesige Datenmengen mit C++ Code automatisch zu verwalten. In Kapitel VI behandeln wir die Interpretation von SPH Daten, indem wir eine verbesserte Transformationsmethode auf ein reguläres Gitter mit ausgezeichneten Erhaltungseigenschaften aufzeigen. Außerdem präsentieren wir zwei neuartige Codes, die diese Methode mit ausführlichen Nachbearbeitungsroutinen implementieren die wir durchwegs verwenden.
4. **Vergleiche mit Beobachtungen:** Nach dem Simulieren müssen die Ergebnisse analysiert und mit unserer besten Informationsquelle, den Beobachtungen, verglichen werden. In Kapitel VIII präsentieren wir eine neuartige SPH Implementierung und den deutlichen Einfluss von anisotroper Wärmeleitung in Galaxienhaufen bezüglich deren Entstehung, mit sowohl kalten Zentren, als auch solchen mit etwa konstanter Temperatur. Wir geben einen Eindruck eines kürzlich gestarteten Galaxienhaufen Code-Vergleichsprojektes in Kapitel IX. Dessen Grundlage sind neue Simulationen von über dreihundert Galaxienhaufen mit verschiedensten numerischen Codes. Weiterhin untersuchen wir in Kapitel X, in wie weit Magnetfelder Ausflüsse von Scheibengalaxien verursachen können, indem sie senkrecht zur Scheibenebene aufbrechen und zeigen außerdem den Einfluss auf unter anderem die Sternentstehungsrate. Dazu simulieren wir mehrere isolierte Galaxien in einem vergleichsweise heißen Gashalo. Im Anschluss vergleichen wir in Kapitel XI kürzlich veröffentlichte Beobachtungen bezüglich abfallender galaktischer Rotationskurven bei Rotverschiebung $z \sim 2$ mit Galaxien aus den MAGNETICUM Simulationen. Daraus resultiert, dass die Beobachtungen mit dem üblichen Λ CDM Modell reproduziert werden können und diesem nicht widersprechen. Wir schließen in Kapitel XII mit generellen Schlussbemerkungen sowie Ideen, was als nächstes folgen könnte.

Abstract

Space - the final frontier.

– Star Trek

Since ancient times people gaze into the night's sky, fascinated by the stars and the vastness of the universe. This fascination has expressed a great influence onto not only our modern culture. It has given rise to science fiction in various forms. Maybe the oldest tale is the Sumerian “Epic of Gilgamesh” which dates back to 2000 BC. Although great progress has been made in terms of actually bringing humans into space we are still limited to our nearest proximity in our solar system. That which lets the mind explore the universe is not only science fiction but also actual science and research, Astronomy and Astrophysics.

Modern computers allow us to further our understanding of processes in the universe. Computing power has grown so much in an accelerated fashion, that we are finally able to actually test the hypotheses made by astrophysicists over the last century. We have come to a point where further progress is actually mostly limited by our capacity of improving the fundamental numerical prescriptions and optimising our software. In the first part of this thesis we aspire to give a glance on what modern Astrophysics has achieved so far, in observing, simulating and understanding the universe with more detailed focus onto cosmic magnetic fields in galaxies and galaxy clusters and pose some open questions. From chapter IV on, we present the main fruits of this PhD project, improving and extending our numerical tool kit and simulating galaxies and galaxy clusters with increased numerical accuracy and modelling, and embed them into the bigger context of this work.

Following [Naab and Ostriker, 2017](#) we can break down the task of simulating astrophysical objects into four required aspects:

1. **Knowledge of physical processes:** Before we can simulate the evolution of anything we need to know which physical processes actually play a role and understand their workings in order to model them properly. This goes from the basic ones like hydrodynamics and gravity to more complex ones like star formation, radiative cooling and the treatment of black holes. We give a brief overview over the universe's formation history and present observations of mainly galaxies and galaxy clusters in chapter I. We continue with observational methods to investigate cosmic magnetic fields and assess the required theoretical description of magneto-hydrodynamics in chapter II. Further modelling of physical processes plays a role throughout the whole thesis.
2. **Initial conditions:** We need to know an exact description of initial conditions for the system we want to simulate, be it an isolated galaxy or galaxy cluster which we directly

set up or a cosmological box using a density seed field provided by observations of the Cosmic Microwave Background. Additionally, we need to properly translate this mathematical description into a format which the simulation code can understand. High quality is very important here, since any error will propagate through the simulation and can flaw the whole result. This is not an easy task that we tackle in chapter [IV](#). We describe a novel code to set up arbitrary density models for Smoothed Particle Hydrodynamics (SPH) which turned out to be required especially to be able to properly generate tests for our actual simulation code.

3. **Computational tools:** From a numerically stable discretisation of the physical models over proper validation of the results in test problems to parallelisation and optimisation of the code so that it can actually handle huge problems with good resolution, all this belongs in the category of computational tools. As we improve our tools and demands alike this becomes an increasingly important and especially time consuming topic. In chapter [III](#) we review common techniques used in astrophysical codes. In chapter [V](#) we present recent state of the art improvements of the GADGET code and carry out extensive tests of its numerical properties. As computing power grows exponentially, more data are generated and post processing can become a really difficult task. In chapter [VII](#) we describe a novel library to automatically handle the management of huge amounts of data in any C++ code in order to approach this issue. In chapter [VI](#) we handle the interpretation of SPH data by proposing an improved transformation method onto a regular grid with excellent conservation properties. Additionally, we present two novel codes employing this method amongst extensive post processing toolkits which we used everywhere throughout this work.
4. **Test against observations:** Finally, after actually carrying out simulations, they can be analysed and tested against our best source of knowledge: observational data. In chapter [VIII](#) we present a novel SPH implementation and the significant impact of anisotropic thermal conduction in galaxy clusters regarding the formation of both cool-core and non-cool-core clusters. We give some insight into a recently started galaxy cluster code comparison project in chapter [IX](#) whose backbone is the re-simulation of over three hundred galaxy cluster regions with different numerical codes. Furthermore, we investigate how magnetic fields can drive outflows from disk galaxies in chapter [X](#) by breaking up perpendicular to the disk plane and show how this affects e.g. the star formation rate in the galaxy using state of the art simulations of isolated disk galaxies sitting in a hot gas halo. Afterwards, we compare some recent observations of declining galactic rotation curves at redshift $z \sim 2$ to galaxies produced in the MAGNETICUM simulations in chapter [XI](#). We conclude that the observations can be well reproduced with a standard Λ CDM cosmology and do not contradict it. Finally, we give some general conclusion remarks and outlook ideas how to proceed from this point on in chapter [XII](#).

Contents

I	Superlatives in the universe: Galaxies and Galaxy Clusters	1
I-1	Cosmological evolution of the universe: The Λ CDM model	1
I-2	Zooming out: Observing the small and the big	7
II	The elephant in the room: Magnetic Fields	17
II-1	Important processes and observation methods	17
II-1.1	Synchrotron radiation	17
II-1.2	Inverse Compton effect	24
II-1.3	Dust Polarisation	26
II-1.4	Zeeman effect and Goldreich-Kylafis effect	26
II-1.5	Examples for novel approaches	30
II-2	Magnetic fields in simulations: Analytic prelude	35
II-2.1	Pure Hydrodynamics	35
II-2.2	Ideal MHD approximation	39
II-2.3	Importance of non ideal MHD	41
II-2.4	Overview of magnetic field (simulation) history	45
III	Simulation techniques: Euler or Lagrange?	49
III-1	The history and necessity of simulations	49
III-2	Commonly used and established techniques	50
III-2.1	Volume discretisation	51
III-2.2	Mass discretisation	54
III-3	SPH formalism in details	55
III-3.1	Density approximation and kernel theory	56
III-3.2	(Magneto-) Hydrodynamics	62
III-4	Modern approaches: Everything we need from now?	65
III-4.1	Hybrid approaches: Moving mesh and Meshless	65
III-4.2	Look around: Modified versions of SPH	70
III-4.3	Code diversity through modern astrophysical codes	72
III-5	Additional physics beyond MHD	74
III-5.1	Understanding the gravity of Newton vs Einstein	75
III-5.2	Additional models as subgrid approach	79
III-6	Goals of this work and into the future	79

IV	Initial conditions generation: Difficulties of SPH	83
IV-0	Abstract	83
IV-1	Introduction	84
IV-2	Overview of IC generation	84
IV-2.1	Requirements and degrees of freedom	84
IV-2.2	Particle placement	85
IV-2.3	Variable density modifications	87
IV-3	Code description	87
IV-3.1	WVT relaxation	87
IV-3.2	Initial state	89
IV-3.3	Additional redistribution	90
IV-4	Test Problems for crucial features	91
IV-4.1	Constant density	93
IV-4.2	Variable density	94
IV-4.3	Additional redistribution	101
IV-4.4	Convergence of the iteration process	102
IV-4.5	Convergence with variable amount of particles	103
IV-5	Applications	106
IV-5.1	Code testing: (Magneto-) Hydrodynamics	106
IV-5.2	Binary star formation	108
IV-5.3	Isolated galaxy cluster	108
IV-5.4	Reading in an initial setup: Image processing	112
IV-6	Code usage	112
IV-6.1	Requirements and compilation	112
IV-6.2	Parameters and running the application	113
IV-7	Summary and Conclusions	114
V	A modern SPH scheme: Handling numerics properly	117
V-0	Abstract	117
V-1	Introduction	118
V-2	A new SPH implementation	120
V-2.1	Original code platform	120
V-2.2	Kernel functions and density estimate	120
V-2.3	Equation of motion	123
V-2.4	Artificial viscosity	123
V-2.5	Artificial conductivity with gravity correction	126
V-2.6	Particle wake-up and time-step limiter	128
V-3	Hydrodynamical tests without gravity	129
V-3.1	Sod shock tube	129
V-3.2	Sedov blast	130
V-3.3	Keplerian ring	130
V-3.4	Cold blob test	135
V-3.5	Kelvin-Helmholtz instability	139
V-3.6	Decaying Subsonic Turbulence	139

V-4	Hydrodynamical tests with gravity	146
V-4.1	Hydrostatic sphere	146
V-4.2	Evrard collapse	147
V-4.3	Zel'dovich pancake	149
V-5	Astrophysical applications	150
V-5.1	Idealized galaxy formation	152
V-5.2	Santa Barbara Cluster	154
V-6	Summary and conclusions	157
VI	Understanding SPH data: Transformation to a grid	163
VI-0	Abstract	163
VI-1	Introduction	164
VI-2	SPH principles	165
VI-3	SPH to Grid: Different Methods	166
VI-3.1	Particle-Mesh and Window Functions	166
VI-3.2	SPH Kernel Methods	167
VI-4	Comparison by Examples	173
VI-4.1	The dataset	174
VI-4.2	Conservation properties	176
VI-4.3	Power-spectra	181
VI-5	Analysis packages	182
VI-5.1	Pygad	182
VI-5.2	SPHMapper	183
VI-6	Conclusion	183
VII	Analysing big data: The Rambrain library	185
VII-0	Abstract	185
VII-1	Introduction	186
VII-2	Common strategies to avoid out-of-memory errors	187
VII-3	Interfacing Rambrain	190
VII-3.1	Basic usage	190
VII-3.2	Advanced usage	192
VII-3.3	Design considerations for user code	194
VII-4	Architecture and Design	195
VII-4.1	Swapping Strategy	195
VII-4.2	Preemptive element swap-in and decay	197
VII-4.3	Swap file usage	198
VII-4.4	Asynchronous I/O and Direct Memory Access	199
VII-4.5	Compatibility to multithreading	201
VII-5	Results and Discussion	203
VII-5.1	Library overhead without swapping	203
VII-5.2	Matrix operations	205
VII-5.3	Asynchronous I/O and preemptive reading/writing	206
VII-5.4	Constant vs Non-Constant	207

VII-5.5	Comparison with native OS swapping	208
VII-5.6	Real world application: Difference imaging	209
VII-6	Conclusions And Outlook	211
VII-7	Acknowledgements	212
VIII	Anisotropic thermal conduction in SPH: Influence of magnetic fields	213
VIII-0	Abstract	213
VIII-1	Introduction	214
VIII-2	Phenomenology of thermal conduction	216
VIII-2.1	Review of isotropic thermal conduction	216
VIII-2.2	Description of anisotropic conduction	218
VIII-2.3	The anisotropic conduction equation	221
VIII-3	Numerical implementation	222
VIII-3.1	A fully consistent derivation	222
VIII-3.2	Ensuring the 2nd law of thermodynamics	224
VIII-3.3	Discretising the hall term	225
VIII-3.4	Solving the differential equation	226
VIII-4	Tests for the new code	228
VIII-4.1	Temperature step problem	229
VIII-4.2	Smooth temperature distribution	235
VIII-4.3	Hot gas sphere	236
VIII-4.4	Temperature step with perpendicular Conduction	237
VIII-4.5	Summary of test results	239
VIII-5	Application to galaxy clusters	241
VIII-5.1	The effects of different conduction prescriptions	242
VIII-5.2	The magnetic field structure in the simulated clusters	252
VIII-6	Summary and Conclusions	257
VIII-A	Solving the Taylor approximation for the second order term	259
VIII-B	Analytic solution for the temperature step problem	262
VIII-C	Temperature step with vacuum boundaries	263
IX	Galaxy cluster code comparison: The 300	265
IX-1	The MultiDark parent simulation	265
IX-2	Zoom simulations	266
IX-3	nIFTy: What has been achieved so far	268
IX-4	The Three Hundred	271
X	Magnetic driven winds: Break up of a galaxy	273
X-0	Abstract	273
X-1	Introduction	274
X-2	Simulation Method	275
X-2.1	Kernel function and density estimate	276
X-2.2	SPH and SPMHD formulation	276
X-2.3	Advanced SPH Methods	277

X-2.4	Cooling, Star formation and Supernova Seeding	278
X-3	Initial conditions	278
X-3.1	Dark matter halo	279
X-3.2	Bulge, stellar and gaseous disk	279
X-3.3	Initial values for the multi phase model of star formation	280
X-3.4	Circumgalactic medium	282
X-3.5	Combination of the galactic disk with the CGM	284
X-4	Results	285
X-4.1	Morphology of the galactic disk and the magnetic field	285
X-4.2	Star formation rate within the different models	288
X-4.3	Amplification of the magnetic field	290
X-4.4	Interaction between the galactic disk and the CGM	293
X-4.5	Magnetic driven outflows	293
X-4.6	Magnetic field structure	295
X-4.7	Divergence Cleaning	300
X-5	Conclusions	301
XI	Rotation curves of galaxies in Magneticum: Supporting ΛCDM	303
XI-0	Abstract	303
XI-1	Introduction	304
XI-2	The Simulations	304
XI-3	Sample of Galaxies	306
XI-4	Rotation Curves at $z = 2$	307
XI-5	DM Fractions	309
XI-6	Surface Density, Dispersion and Theoretical Rotation Curve	310
XI-7	Discussion and Conclusions	310
XII	Conclusions and Outlook: The Answer to the ultimate question of life, the universe and everything?	313
Bibliography	317
List of Figures	362
List of Tables	366
Acknowledgements	369

Chapter I

Superlatives in the universe: Galaxies and Galaxy Clusters

By three methods we may lean wisdom: First by reflection, which is noblest; Second by imitation, which is easiest; and third by experience, which is bitterest.

– Confucius

Astronomy is one of the oldest yet one of the most modern sciences. It dates back to the ancient high cultures of Babylon, Egypt, China and the Maya and Inka thousands of years BC being utilised for navigation, time measurements, the introduction of a calendar and religious purposes.¹ The beginning of modern astronomy can be set at around 1500 AD with exceptional scientists like Copernicus, Brahe, Kepler, Galilei and slightly later Newton. The progress has always been limited by our ability to observe the sky and to develop methods to understand the taken data. A big leap has been made with Fraunhofer and Herschel in the 1800s. The second half of the 19th century can be set as the birth of astrophysics as spectral analyses and photometry became common methods. From that on the field has split up multiple times into different sub parts as we know them now, from planetary and stellar physics to cosmology. In this chapter we aim to give a brief overview over the evolution of the universe as far as we understand it and introduce the relevant basics for this work.

I-1 Cosmological evolution of the universe: The Λ CDM model

To formulate a cosmological model to describe the evolution of the universe we need two important ingredients. First, the cosmological principle which occurs first qualitatively in Newton's *Philosophiae Naturalis Principia Mathematica* (Newton, 1687):

At each epoch, the universe presents the same aspect from every point, except for local irregularities.

In strict terms it means that at each time t the universe is homogeneous and isotropic on large scales. Second, we need Weyls postulate (Weyl, 1926):

¹For further details see e.g. [Herrmann, Bukor, and Bukor, 1973](#).

The particles of the substratum lie in space-time on a congruence of time-like geodesics diverging from a point in the finite or infinite past.

Galaxies move like fundamental particles in a fluid on unique geodesics with a unique velocity of the order of the speed of light c . Locally movement deviates from this geodesic motion randomly with a comparatively very small velocity. To analyse a universe which obeys these two use the Friedmann-Lemaître-Robertson-Walker (FLRW) metric.² A metric gives a way to measure distance, for example in flat space and Cartesian coordinates

$$ds^2 = g_{ij}dx^i dx^j = dx^2 + dy^2 + dz^2. \quad (\text{I-1})$$

the metric tensor $g_{ij} = \delta_{ij}$ is the unity matrix. For the FLRW metric in a four dimensional space-time we have

$$ds^2 = c^2 dt^2 - a(t)^2 K^2 \left(\frac{dx^2}{1 - kx^2} + x^2 d\Omega^2 \right) \quad (\text{I-2})$$

with the sign of the curvature $k = \pm 1; 0$, $x = r/K$, r the distance of the comoving observer, K the radius of curvature (absolute value), $a(t)$ the scale factor of the universe at time t and

$$d\Omega^2 = d\Theta^2 + \sin^2 \Theta d\Phi^2. \quad (\text{I-3})$$

This metric only covers large scales. Everything happening on “small” scales in this context lies beyond. This includes all identifiable objects, even galaxy clusters.

The main equation we get from general relativity is the Einstein equation which, including a cosmological constant Λ , is given by:

$$G_{\alpha\beta} = 8\pi G T_{\alpha\beta} + \Lambda g_{\alpha\beta} \quad (\text{I-4})$$

with the Einstein tensor $G_{\alpha\beta}$ which depends only on the metric tensor, the energy-impulse tensor $T_{\alpha\beta}$, the gravitational constant G , the metric tensor $g_{\alpha\beta}$. Using the FLRW metric and a general fluid energy-impulse tensor we obtain the Friedmann equations which describe the evolution of the universe

$$\frac{\dot{a}^2}{a^2} + \frac{K}{a^2} = \frac{8\pi G}{3}\rho + \frac{\Lambda}{3} \quad (\text{I-5})$$

$$\frac{\ddot{a}}{a} = -\frac{4\pi G}{3}(\rho + 3p) + \frac{\Lambda}{3} \quad (\text{I-6})$$

with the density ρ and the pressure p containing contributions from baryonic and dark matter and radiation. As we mention dark matter and a cosmological constant it is important to note that throughout this thesis we assume the commonly most accepted and simplest cosmological model compatible with observational data called Λ CDM where CDM stands for “cold dark matter”. The cosmological constant is usually identified with the presence of dark energy required in the energy budget for an accelerated expansion. Dark matter poses a possibility to explain

²We do not consider alternative models for gravity in this work and limit ourselves to the successful theory of Einstein's general relativity.

for example observed rotation curves from disk galaxies which behave as if more mass was present in the outskirts than is visible, ergo a dark matter halo. A similar observation can be made with galaxy clusters. The idea for dark matter has first come up about 85 years ago with [Oort, 1932](#); [Zwicky, 1933](#). Galactic rotation curves will become important later this thesis in chapter [XI](#) where we follow up with simulation results consistent with Λ CDM onto state of the art observations of galaxies, finding declining rotation curves and low dark matter fractions at redshift $z \sim 2$. Since the exact composition and origin of neither dark matter nor dark energy is known several candidates and ideas have been discussed over the last decades and alternative approaches to circumvent them have come up. An example being “Modified Newtonian Dynamics” (MOND) which, however, also brings its own problems and lacking explanations along. For a discussion see e.g. [Bertone and Hooper, 2016](#). Also so called warm or even hot dark matter has been discussed. This relates to a certain degree of interaction, dark matter particles may experience besides the obvious gravitational one. Hot dark matter on its own has been already ruled out by simulations ([White, Frenk, and Davis, 1983](#)) and by observations of the cosmic microwave background (CMB) of the COBE satellite ([Wright et al., 1992](#)), but weakly interacting warm dark matter or mixtures of hot and cold dark matter are still an open possibility (see e.g. [Lopez-Honorez et al., 2017](#), for a recent review paper on the topic). We will not go into further details about these and commit ourselves fully to the Λ CDM model.

As we have four main contributors to the total energy budget of the universe, (non-) baryonic matter, radiation and dark energy, it is a straight forward hypothesis that each of them might have had varying significance during the evolution of the cosmos so far. Following [Fließbach, 2006](#) we rewrite equation [I-5](#) to

$$\dot{a}^2 - \frac{K_r}{a^2} - \frac{K_m}{a} - \frac{1}{3}\Lambda R^2 = -K \quad (\text{I-7})$$

by splitting up the density part into a matter and radiation contribution and rewriting them to

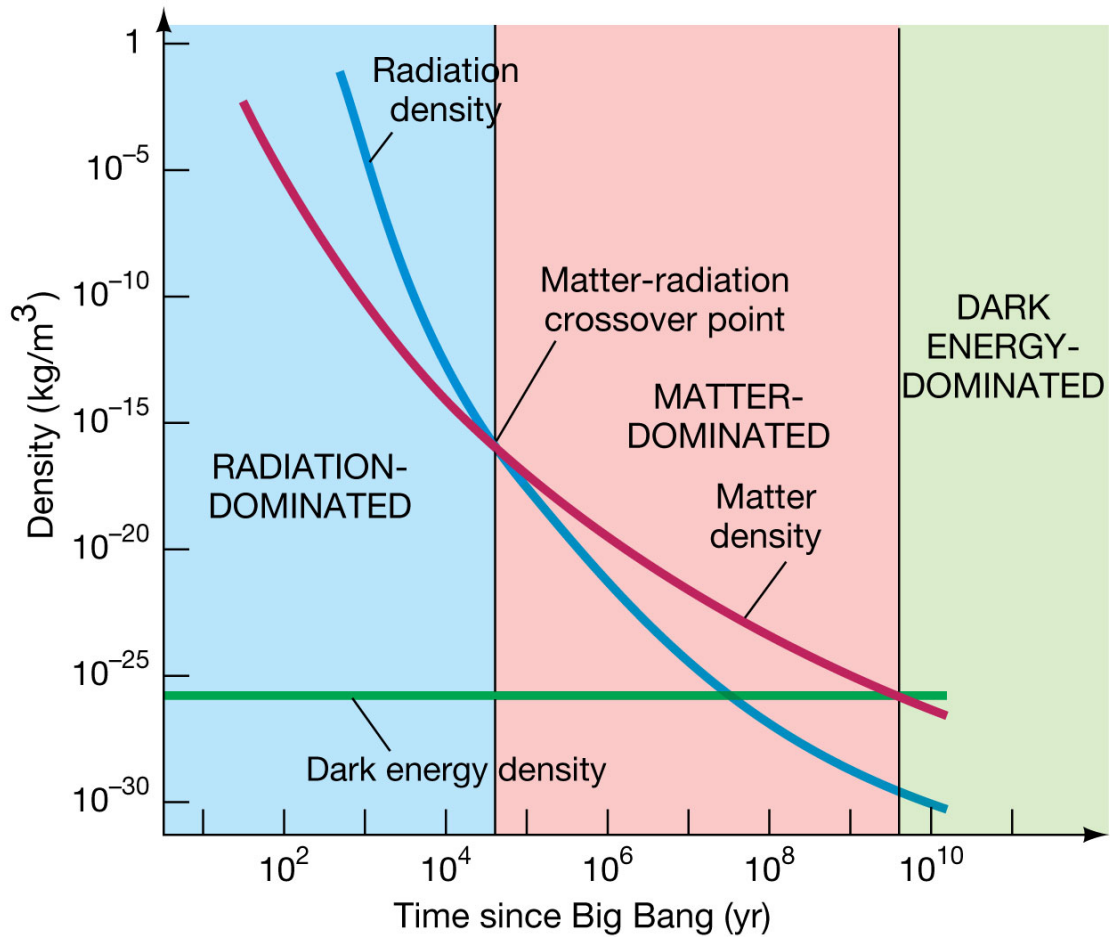
$$K_r = \frac{8\pi G}{3c^2} \rho_r a^4 = \text{const} \quad (\text{I-8})$$

$$K_m = \frac{8\pi G}{3c^2} \rho_m a^3 = \text{const.} \quad (\text{I-9})$$

The different scalings with scalefactor a come from the pressure term which is added onto the density when calculating the conservation $\rho_r \dot{a} = 0$. The pressure is equal to zero for dust only and proportional to the density for radiation. Next we assume that the total curvature of the universe is negligibly small (we will back this up by observations shortly), meaning $K = 0$. Analysing each term’s different proportionality to a in equation [I-7](#), we see directly that we can differentiate three different eras in time where this term dominates the other two:

$$\dot{a}^2 \sim \begin{cases} K_r/a^2 & \text{for } 0 < t < t_1 \\ K_m/a & \text{for } t_1 < t < t_2 \\ \Lambda a^2/3 & \text{for } t_2 < t \end{cases} \quad (\text{I-10})$$

In figure [I.1](#) we illustrate the different scalings and the rough crossover times. According to this model we are presently in the last of the three eras dominated by the cosmological constant



©2011 Pearson Education, Inc.

Figure I.1: Energy density evolution over time split up into the three different contributions: mass, radiation and dark energy (cosmological constant). Coloured are the three different eras of domination, one per component. ©Pearson Education.

leading to an accelerated expansion. The current composition of energy densities is showcased in figure I.2 with data taken from the latest Planck satellite paper (Planck, 2016b). The energy density in radiation is so small, that it is not even visible in this diagram ($\Omega_r \sim 10^{-5}$) and we additionally split up matter into baryonic (Ω_b) and dark matter (Ω_{dm}). These are defined as the ratio of the respective energy density with respect to the critical density of the universe

$$\Omega = \frac{\rho}{\rho_c} = \frac{\rho \cdot 8\pi G}{3H^2} \quad (I-11)$$

which is the density for the universe to be completely flat which we see to be given by these observational data to a very good degree. H is the Hubble function given by

$$H = \frac{\dot{a}}{a} \quad (I-12)$$

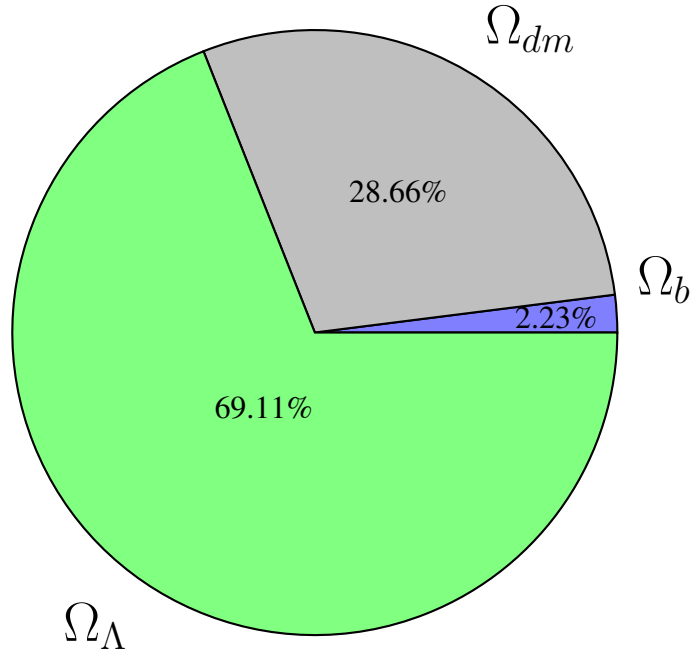


Figure I.2: Current energy budget of the universe. Values taken from [Planck, 2016b](#).

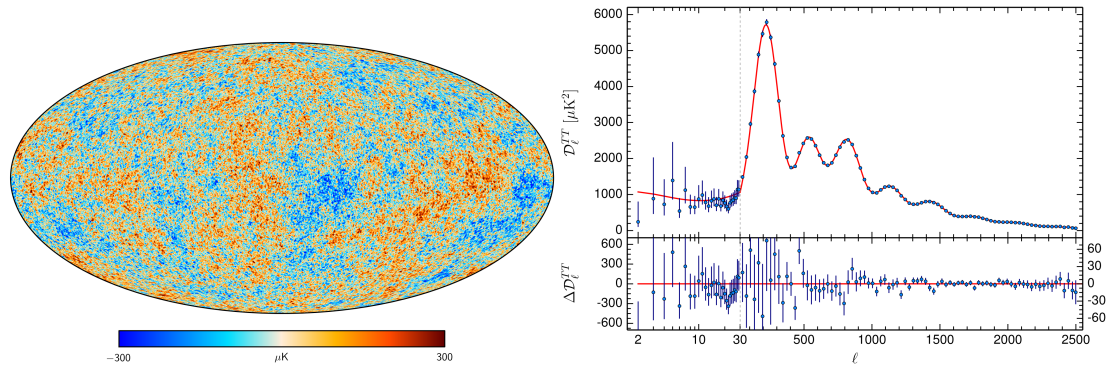


Figure I.3: Left: CMB temperature deviations from the mean temperature over the full sky observed by the Planck satellite. Taken from [Planck, 2016a](#). Right: TT-mode of the CMB spectrum (temperature angular power spectrum) also measured with the Planck. Taken from [Planck, 2016b](#).

It's value at present time is typically called the Hubble constant $H_0 = 67.74 \pm 0.46$ according to [Planck, 2016b](#).

The Planck satellite has been launched in 2009 with it's main task being to give more accurate measurements of cosmological parameters over the course of over four years mission time. For a Planck mission overview see [Planck, 2016a](#). In [Planck, 2016b](#) the latest measurements in conjunction with other methods can be found. With this task it follows predecessors like COBE or WMAP. The increased resolution in comparison to these is really noteworthy and is reflected for example in it's all sky measurements of the CMB as shown in figure I.3. Observing the cosmic microwave background corrected for all the foreground sources properly is an extraordinary achievement since it allows us to look as far back into the history of the universe as possible directly with radiation dating back to when the universe was about only $3.8 \cdot 10^5$ years old and matter decoupled from radiation. Before this so called era of recombination the universe was small enough for the densities being so large that everything was optically thick. Matter was hot enough to exist only in a Plasma state and Photons would be absorbed, re-emitted and scattered with such large cross sections that they could never reach an observer. After reaching a certain size everything cooled down enough to actually form neutral atoms and let photons decouple and travel rather freely. These photons are what we observe today as the CMB as they have been redshifted quite drastically from the optical/infrared to the microwave spectrum. The different peaks of the CMB temperature spectrum (right panel of figure I.3) are related for example to the curvature of the universe as well as the mean density and the density perturbations at the time of photon decoupling. A sketch of the universe's evolution is shown in figure I.4.

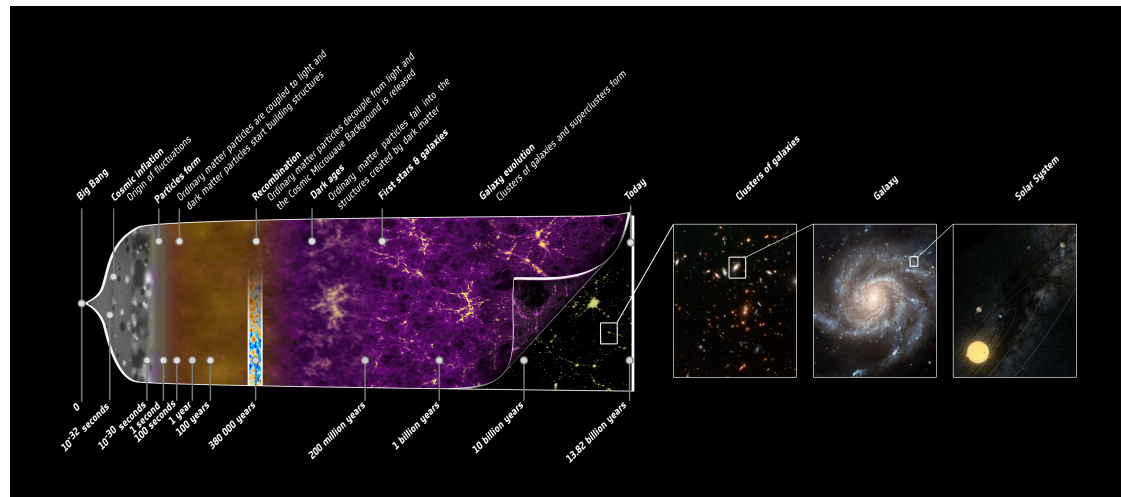


Figure I.4: Different stages of the universe's evolution emphasizing especially the very early times following the Big Bang model. Taken from https://www.nasa.gov/mission_pages/planck/multimedia/pia16876b.html.

I-2 Zooming out: Observing the small and the big

Leaving the early universe behind us, the term “structure formation” covers most of what happens during 99% of the universe’s lifetime. In a world with uniform density, as we have assumed it last section, no structures would form since the gravitational forces completely balance each other. Luckily for us there have been small perturbations in the density field which acted as seeds for clumping of matter. The imprint of these perturbations is visible in the CMB.

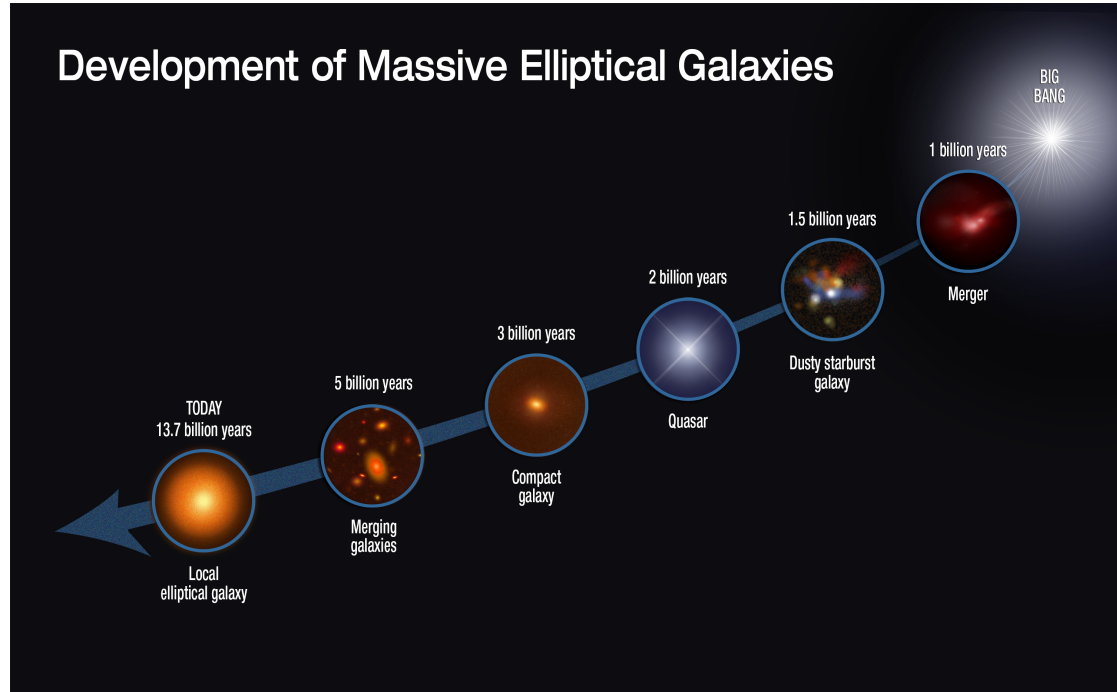


Figure I.5: Bottom-up evolution resulting in an elliptical galaxy. Starting with clumping of material to form star clusters, a first galaxy, an active galactic nucleus and then merging with possible multiple other galaxies to form the resulting elliptical. Taken from <https://www.nasa.gov/jpl/spitzer/galaxies-20140129>.

There are two possible extreme scenarios how the structures we observe could have formed: either “bottom-up” starting with small objects which merge together to bigger ones or “top-down” where the biggest structures formed first and then small ones inside later. Today we favour the former one as depicted exemplary on the basis of an elliptical galaxy in figure I.5. Matter starts clumping and cools. As soon as the gravitational forces overcome the internal pressure a first star is born. Due to the nature of the density perturbations multiple stars are formed in a close proximity to each other and form star clusters and then the first galaxy. Due to the large amount of gas present a lot of huge stars are formed and rather quickly die out, enriching the surrounding medium with higher order elements. Everything beyond Helium is typically called a metal in astrophysical jargon. These first stars are still a big mystery to us, because we lack any direct observation so far. When these stars explode in supernovae neutron stars and stellar

black holes are the typical results. Additionally, due to high concentration of matter close to the centre even a galactic black hole might form. Similar to stars forming close to each other also galaxies typically form in a close proximity forming a galaxy group or cluster. In these regions it is highly probable that galaxies experience many close encounters with other galaxies and merge together. We distinguish between minor and major mergers according to the mass proportion of both partners. Typically a galaxy can experience tens and hundreds of minor merges or a few major ones until the resulting object becomes an elliptical galaxy. For an extensive discussion of the details of structure formation we refer to textbooks like [Mo, Van den Bosch, and White, 2010](#).

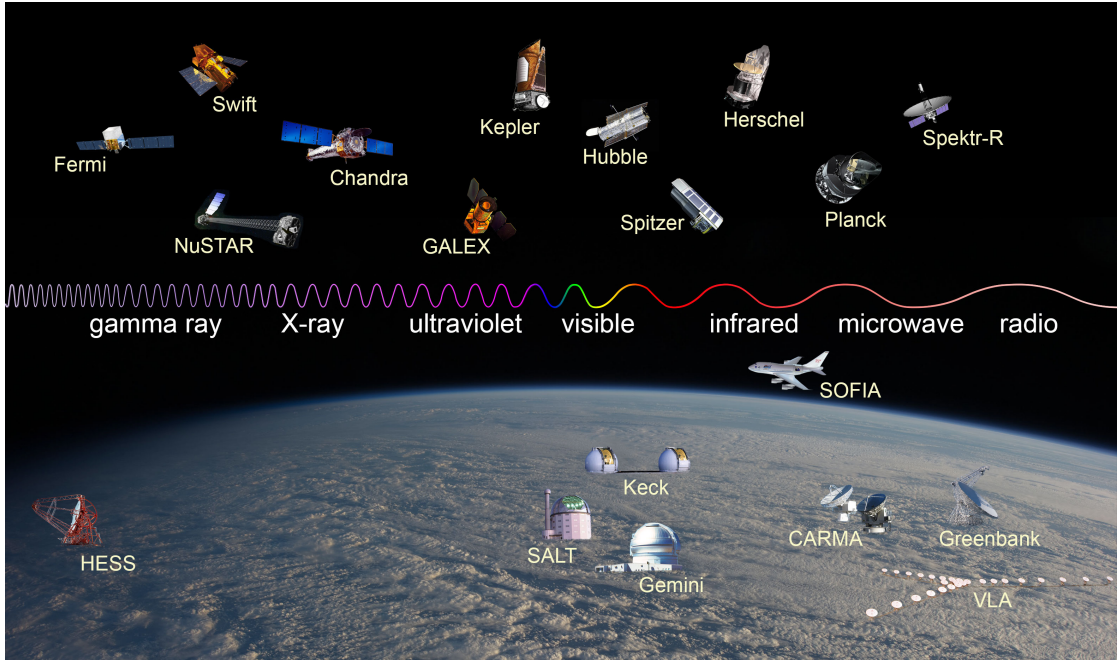


Figure I.6: Some of the recent observatories tied to the wavelength regime they observe in. Taken from https://imagine.gsfc.nasa.gov/science/toolbox/emspectrum_observatories1.html.

We have learned so much about how structures in the universe evolved by the combination of theoretical models, simulations and observations to (de-) confirm them. In figure I.6 we show some of the recent telescopes both earth-bound and spaceborne which are used to observe the sky over a huge portion of the electromagnetic spectrum from radio frequencies over visible light to high energy X-ray and γ -ray radiation. All of them are equipped with different instruments which are sensitive to different waveband channels and serve various purposes. Some directly take pictures of a portion of the sky while others rely on interferometry to increase their resolution manifold. Some of the telescopes do not operate from earth's surface but from a satellite in an orbit around earth. Although much more complicated and especially costly to design, construction and maintenance it is helpful decreasing sources of error in most waveband and crucial in the high energy ones due to earth's atmosphere which does a great job absorbing radiation

especially efficient from UV up to higher energies.

With help of figure I.7 we take a quick journey through the universe from small to large objects beyond our solar system starting top left with Eta Carinae (1,2) which is one of the most luminous systems in our galaxy, the Milky Way. Most of these images are observed in different wavebands and composed together in different colours. We see a rapidly expanding cloud of dust which absorbs light from a central and very massive binary star system and re-emits it in the optical and infrared.³ Next is M16 (3), the Eagle nebula with the so called pillars of creation. The name originates from the impressive gas and dust columns visible in the optical spectrum which are the birthplace of many stars. Although star formation seems to decline already, indicated by most stars sitting outside of the pillars, we can observe many young stars in the X-ray which allows us to look behind gas and dust effectively. The point sources in this image are coloured from red over green to blue to indicate the energy band in the X-ray spectrum from low to high.⁴ Sticking to the proximity of individual stars we have next IC443 called the Jellyfish Nebula (4). It is a remnant of a supernova type II about $5000ly$ away from earth. A supernova type II is created when a massive star runs out of fuel and starts collapsing. The centre forms a dense core, typically a neutron star and the outer layers collapse onto it, giving it the name core-collapse supernova. Due to the immense compression further fusion processes ignite and the system explodes, carrying the outer shells with it in the explosion which then form such a remnant. The zoom region in the top right features a rotating neutron star, a pulsar, called J0617. We see typical X-ray winds emitted from the pulsar in blue overlayed on top of the optical data.⁵ Skipping star clusters, both open and globular clusters, we go directly to what we talked about already: a spiral galaxy. M51 (5) or also called the Whirlpool galaxy is a disk galaxy about $7.1Mpc$ away which stands almost perfectly face on towards earth allowing us to thoroughly observe it. Therefore, it is probably one of the best observed galaxies ever. The name whirlpool originates from the nicely visible spiral arms and hundreds of point like X-ray sources in them. The latter are mostly binary systems of compact stars and a black hole. Material from the compact companion is accelerated towards the black hole and thereby heated up which leads to the observed X-ray emission. The diffuse X-ray emission visible in purple on top of the optical image is probably emitted from gas heated by supernovae. Additionally, this system allows us to gain insight about galactic mergers as M51 and a small companion encounter each other in the top left of the image, triggering waves of star formation in the process.⁶ Sticking to galaxies next up we have Stephan's Quintet (6) which is a compact group of five interacting galaxies. The image consists of four bands of optical data showing the galaxies themselves and a curved light blue region in the centre of X-ray emission probably due to shock heating because of the pass through of NGC7318b through the group's centre. This is a beautiful case for studying the complex interaction of several galaxies and showcases their evolution from X-ray faint spirals

³Credits: Wide Field Credits: Optical: DSS, Infrared: NASA/JPL-Caltech <http://chandra.harvard.edu/photo/2014/etacar/more.html>

⁴Credits X-ray: NASA/CXC/U.Colorado/Linsky et al.; Optical: NASA/ESA/STScI/ASU/J.Hester & P.Scowen. <http://chandra.harvard.edu/photo/2007/m16/>

⁵Credits Wide Field Optical: Focal Pointe Observatory/B.Franke, Inset: X-ray: NASA/CXC/MSFC/D.Swartz et al, Inset: Optical: DSS, SARA <http://chandra.harvard.edu/photo/2015/ic443/>

⁶Credits: X-ray: NASA/CXC/Wesleyan Univ./R.Kilgard, et al; Optical: NASA/STScI <http://chandra.harvard.edu/photo/2014/m51/>



Figure I.7: Collage of different observations ranging from star forming regions to galaxy clusters. Starting top left following the green spiral these are Eta Carinae first in the infrared then in the optical band, M 16, IC 443, M 51, Stephans quintet, Arp 148, Centre of the Perseus cluster, Hydra A, Abell 1689, El Gordo cluster. Taken from <http://chandra.harvard.edu> and <http://hubblesite.org>, individual credits in text.

to bright ellipticals.⁷ Another interesting interaction of two galaxies is Arp148 (7), also called Mayall’s object. It is the result of a previous encounter of two galaxies which resulted in a ring shaped main galaxy and a long tailed companion.⁸

Next we go to a bigger class of objects and present the central region of the Perseus galaxy cluster (8) in three different wavebands: X-ray in blue, optical in pink and radio in red. The size of this image is about $2.8 \cdot 10^5 ly$ per side while the visible part of such a cluster in total is typically a few Mpc in diameter⁹ and contains about $10^{15} M_\odot$ in mass. Galaxy clusters are among the most interesting objects to study in the whole universe as they connect the physics of very small scales, like the studies of nuclei and plasmas, to those of the largest scales in the universe by being excellent probes for cosmology. This makes them a perfect class of objects to probe our understanding of nature. Perseus is a very well studied galaxy cluster because we nicely see the hot intra cluster medium (ICM) in the X-ray component, as it is extremely hot plasma ($T \sim 10^8 K$) and cools constantly. It is a very prominent example for cooling flows, hot gas which cools and thereby falls towards the centre of the cluster. It has been a long-standing problem, because that we can still observe the gas cool means that it is still hot although it calculating cooling rates suggest that it should have cooled done quite significantly already. Typical cooling times are computed to be even less than $1Gyr$. Several different approaches to solve this issue have been proposed, typically on the basis of a heating mechanism which offsets the cooling. Heating from a central AGN is a favoured process. For a nice review we refer to [Borgani and Kravtsov, 2009](#). Also the significance of thermal conduction as a transport process is heavily discussed. Over the decades of studies the paradigm has changed and nowadays we rather classify clusters as (non-) cool core, depending on their central temperature profile, metal distribution and surface brightness (see e.g. [Tornatore et al., 2007](#)). From a simulation point of view the bimodality of (non-) cool core clusters is very interesting because different numerical approaches until just recently had a lot of difficulties to reproduce it properly and actually agree with each other (see e.g. [Power, Read, and Hobbs, 2014](#)). The treatment of AGN feedback also plays a crucial role in this discussion ([Rasia et al., 2015](#); [Barai et al., 2016](#)). We further investigate the topic of thermal conduction and cool core clusters explicitly in chapter [VIII](#) where we present an implementation of conduction in the presence of magnetic fields and it’s impact onto galaxy cluster simulations.

Another interesting feature which has been found in Perseus is related to excess emission of $E = h\nu \sim 3.5 keV$ X-ray photons observed by XMM-Newton and Chandra. It seems to be unclear where these really originate from and recent papers even suggest models of “luminous dark matter” particles being responsible for these observations. It may also result from the instrument itself, because although XMM-Netwon and Chandra both see this excess emission, the third telescope Hitomi does not ([Conlon et al., 2017](#)).¹⁰ We follow up with the Hydra A cluster (9) with a

⁷Credits: X-ray (NASA/CXC/CfA/E.O’Sullivan); Optical (Canada-France-Hawaii-Telescope/Coelum) <http://chandra.harvard.edu/photo/2009/stephq/>

⁸Credits: NASA, ESA, the Hubble Heritage (STScI/AURA)-ESA/Hubble Collaboration, and A. Evans (University of Virginia, Charlottesville/NRAO/Stony Brook University); http://hubblesite.org/image/2309/news_release/2008-16

⁹ $1Mpc \approx 3.3 \cdot 10^6 ly$.

¹⁰Credits: X-ray: NASA/CXO/Oxford University/J. Conlon et al. Radio: NRAO/AUI/NSF/Univ. of Montreal/Gendron-Marsolais et al. Optical: NASA/ESA/IoA/A. Fabian et al.; DSS <http://chandra>.

bright X-ray component in blue, radio jets emitted from a central AGN in pink and optical data to see stars in yellow. It is a very nice example to study the behaviour of active galactic nuclei. The outbursts apparently create cavities in the hot gas indicated by radio emission being strong in holes of the diffuse X-ray emission.¹¹ Next comes the $2.3 \cdot 10^9 ly$ away Abell1689 cluster (10) which shows a high merging activity of it's galaxies. Despite that it's appearance is quite smooth in the X-ray (purple coloured). It shows arcs and distortions of galaxies from gravitational lensing effects and is a very fitting object to study mass discrepancies between derivations using the X-ray emissions and lensing. Estimating masses of galaxy clusters is an important task on the way to learn more about them but unfortunately it is not very easy. Typically one even needs to assume the cluster to be in hydrostatic equilibrium which is, however, not always a good approximation. For a recent discussion we refer to [Biffi et al., 2016](#).¹² Last, we have El Gordo (11) which is a collision between two galaxy clusters. It is the most massive, hottest and X-ray brightest system measured at it's distance of $\approx 7 \cdot 10^9 ly$ and beyond. Blue coloured is the X-ray emission, stars are shown in the optical mostly infrared due to the cosmological redshift. It's unusually bright and blue central galaxy is probably the result of a merger of both original BCGs (brightest cluster galaxies). Mass measurements are in line with other galaxy clusters and reveal that only a few percent of the mass lies in stars while the hot ICM is the main contributor to the visible matter in such a cluster (typically about 15% of the total mass).¹³

Even beyond galaxy cluster merges in terms of energy come so called γ -ray bursts, which are the most high energetic radiation events observable in the universe and originate possibly from extremely high mass stars exploding in a hypernova. In terms of size beyond galaxy clusters come so called super clusters. Regions in space where we can identify groups of galaxy clusters closely together. Zooming even further out we reach a view of the cosmic web, along whose threads all these structures sit with huge void regions in between.

It becomes clear that we can dissect any of these objects into their different components by looking at it in different wavebands. A more detailed example is given in figure I.8 for M51, our closest neighbouring galaxy Andromeda. In radio emissions we see gas in the outskirts of the galaxy. Infrared highlights the dust between spiral arms. The visible regime is the one we are most suited to. It shows all the stars in the galaxy, from young and blue ones in the spiral arms to old and red ones in the central galactic bulge. Hot stars are emphasized in the ultraviolet bands and sit typically along the edges of spiral arms. Finally in the X-ray we see the most energetic regions near the centre, typically connected to a central black hole. In Andromeda's centre we also see a huge number of old stars and with them come supernovae and possible many stellar black holes which can cause X-ray radiation as mentioned earlier.

Investigating the radio observations closer, especially studying polarisation reveals galactic magnetic fields which are aligned pretty well with the spiral arms of the galaxy as shown in figure

harvard.edu/photo/2017/dark/

¹¹Credits: X-ray: NASA/CXC/U.Waterloo/C.Kirkpatrick et al.; Radio: NSF/NRAO/VLA; Optical: Canada-France-Hawaii-Telescope/DSS <http://chandra.harvard.edu/photo/2009/hydra/>

¹²Credits: X-ray: NASA/CXC/MIT/E.-H Peng et al; Optical: NASA/STScI; <http://chandra.harvard.edu/photo/2008/a1689/>

¹³Credits: X-ray: NASA/CXC/Rutgers/J.Hughes et al, Optical: ESO/VLT/Pontificia Universidad Catolica de Chile/L.Infante & SOAR (MSU/NOAO/UNC/CNPq-Brazil)/Rutgers/F.Menanteau, IR: NASA/JPL/Rutgers/F.Menanteau <http://chandra.harvard.edu/photo/2012/elgordo/>

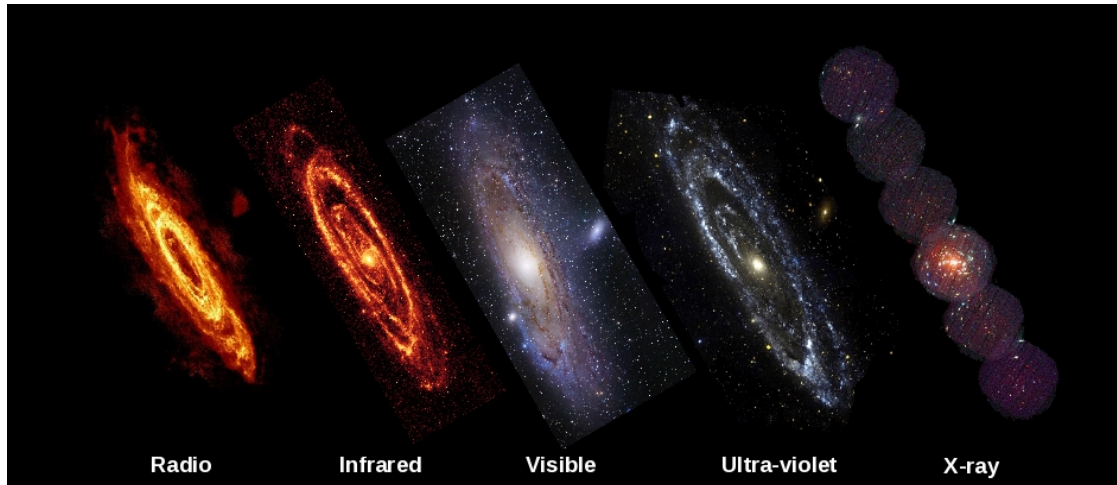


Figure I.8: M51 (Andromeda galaxy) observed in multiple wavelengths from radio to X-ray. Image credits: Radio: WSRT/R. Braun; Infrared: NASA/Spitzer/K. Gordon; Visible: Robert Gendler; Ultraviolet: NASA/GALEX; X-ray: ESA/XMM/W. Pietsch. Taken from <http://planck.cf.ac.uk/science/mm-wave-astronomy>.

I.9. Cosmic magnetic fields are actually pretty common. The first detections have been made when Galilei and fellow scientists in the early 1600s studied dark spots at the surface of our sun. Stellar magnetic fields are strongly tied to the movement of plasma at the surface of the sun and influence heat transfer, leading to these colder dark spots.

Then there are galactic magnetic fields of the order of several μG as in M51 (Beck, 2016) and of course also in our Milky Way as just recently again shown by Planck (see figure I.10). A exciting topic to study is the evolution of galactic magnetic fields and how they contribute to the overall dynamics of such a galaxy. For example outflows from galaxies have recently been in the focus of the galactic simulation community because of their relation towards suppression of the overall star formation rate which has been typically way to high in simulations. Outflows then again can be related to magnetic fields breaking up and forming channels for movement perpendicularly to the plane of a disk galaxy, as we investigate later in chapter X.

Magnetic fields are also especially interesting to study in galaxy clusters. We have already seen two types of radio emission: the radio halo around the centre of the Perseus cluster and the AGN jets emitted in Hydra A. The former is one of three types of diffuse radio emission observed at 1.4GHz related to the ICM which are in the focus of research over the last decades: Radio haloes, mini haloes and relics. Following e.g. the review of Feretti et al., 2012 and looking at figure I.11 we can give some basic insight into these object classes. In this image we see the Coma galaxy cluster which contains both a radio halo and a relic which are additionally even connected by a bridge of low brightness radio emission because their origin might be actually related. A previous merging event which have rise to the radio halo might have been also the source of the shock fronts responsible for the relic. Radio haloes are typically centred in a cluster and spherical while relics are far more outside and often appear in pairs on opposite sites of the cluster due to their believed origin related to shock fronts giving them a curved structure. Furthermore,

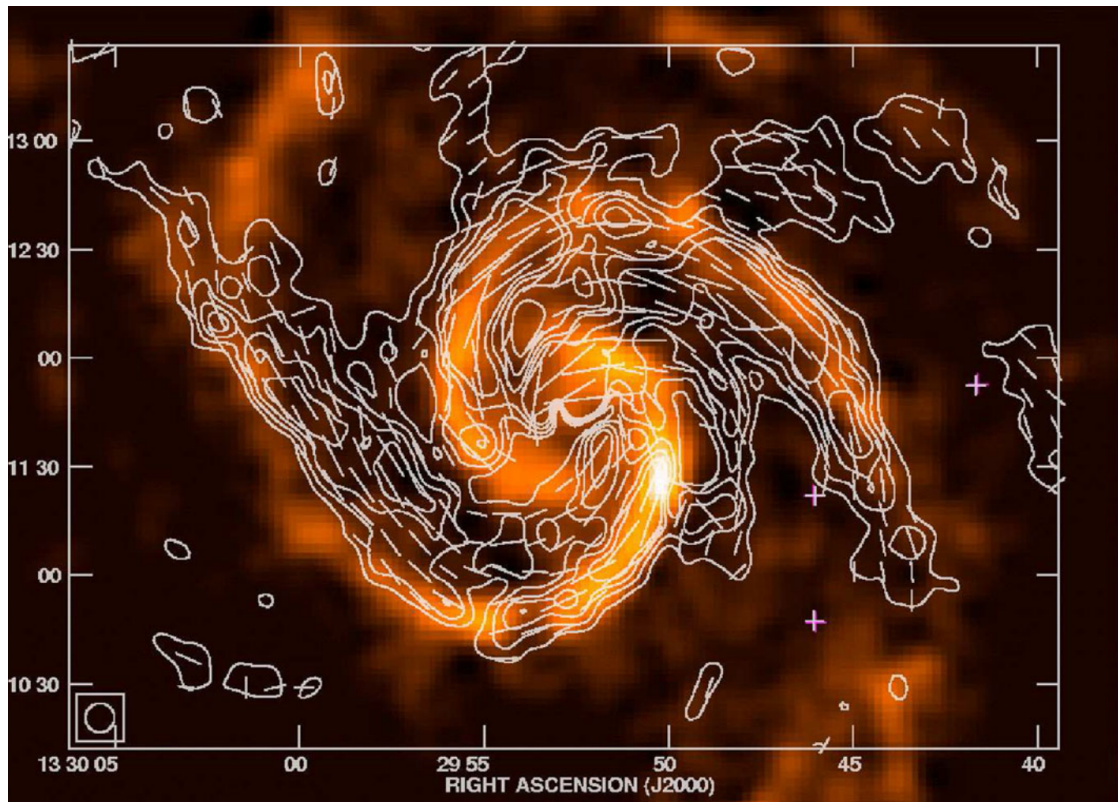


Figure I.9: Polarized radio emission (contours) and B-vectors of M 51, combined from observations at 6 cm wavelength with the VLA and Effelsberg telescopes at 8 resolution (from Fletcher et al. 2011). The background colour image shows the CO line emission from molecular gas (from Helfer et al. 2003). Taken from [Beck, 2016](#).

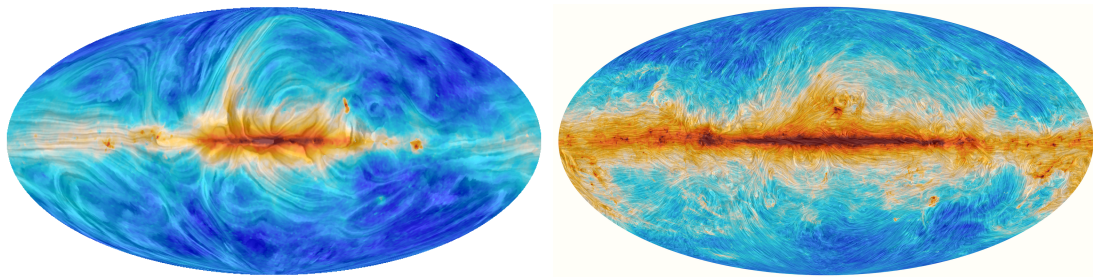


Figure I.10: Left: 30GHz synchrotron emission observed by Planck. Right: 353GHz dust emission observation by Planck. Both rotated by 90° to indicate magnetic field structures in the sky. See later sections [II-1.1](#) and [II-1.3](#). Both taken from [Planck, 2016a](#).

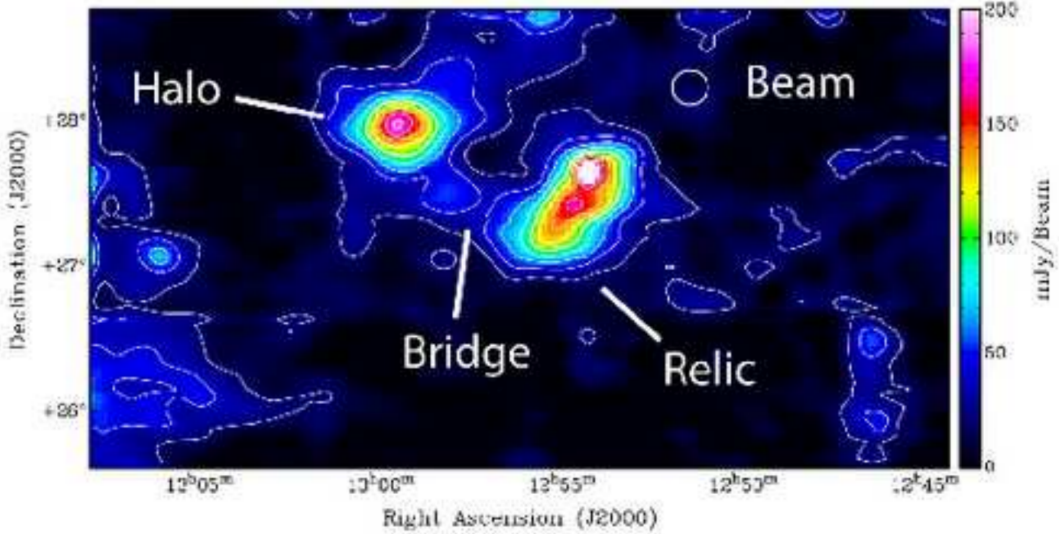


Figure I.11: Polarized radio emission in the Coma galaxy cluster after subtracting the bright background source Coma A. Left is the radio halo Coma C around the centre of the cluster, right is the relic 2153+275 both connected by a diffuse radio emission bridge. The beam size of $14.25' \times 13'$ is indicated in the top right. Taken from [Brown and Rudnick, 2011](#).

haloes have hardly any net polarisation (only a few percent) while relics show polarisations of about 30% which makes it possible to distinguish them even despite projection effects. Both classes are typically of similar low surface brightness ($\sim 1 - 0.1 \mu\text{Jy arcsec}^{-2}$), have a steep spectrum and large size ($\gtrsim 1 \text{ Mpc}$) while mini haloes are obviously much smaller. They are typically connected to a powerful radio galaxy and also inhabit a relatively central region in the cluster. Radio haloes additionally show a correlation between emitted radio power and X-ray luminosity of their host cluster which enforces the idea that their origin must be connected to the ICM ([Roettiger, Stone, and Burns, 1999](#); [Kale et al., 2013](#); [Kale et al., 2015](#); [Brunetti and Lazarian, 2011](#)).

These diffusive radio emission signatures hint to the presence of μG magnetic fields tangled on sizes of about 20 kpc ([Schlickeiser, Sievers, and Thiermann, 1987](#)) and a population of relativistic electrons which emit this non-thermal radiation. Typically these can carry Lorentz factors of $\gamma \ll 1000$ but occur only in number densities of about 10^{-10} cm^{-3} which is very small compared to an average ICM density of 10^{-3} cm^{-3} . The energy density budget contributed amounts then typically to less than one percent but that does not mean that these relativistic electrons and magnetic fields are not important for the evolution of such a cluster as we will see later when investigating the impact of magnetic fields onto thermal conduction in clusters in chapter [VIII](#). Their effect on small scales has to be modelled correctly and can definitely have a visible net impact.

But where do these magnetic fields actually originate from? Since the induction equation which describes the evolution of magnetic fields does not generate a new field out of nothing some kind of seed field is required. The presence of so called primordial magnetic fields has been discussed

for quite a while now and multiple models for e.g. homogeneous or stochastical background fields have been developed. [Planck, 2016c](#) test multiple possible origins and observational constraints which give consistent results with maximal primordial fields of $\sim nG$ levels which is sufficient as simulations show (see chapter [X](#) where we compare simulations with different magnetic seeding mechanisms). For recent reviews of this topic see for example [Ryu et al., 2012](#); [Widrow et al., 2012](#). The amplification of magnetic fields from weak primordial ones to what we observe in the universe is much better understood already, see e.g. [Dormy and Soward, 2007](#).

In order to improve our understanding of the impact of magnetic fields and small scale processes we first need to assess some basic requirements to do so. During the next two chapters we review different observation techniques regarding the detection of magnetic fields in order to understand how they might be coupled to their surroundings and which physics we need to understand. We follow up with a theoretical description of magneto-hydrodynamics, the tool set in order to solve the evolution equations for gas in galaxies and galaxy clusters. As these become quite complicated it is necessary to resort to numerical simulations. For that purpose we review common techniques and modern variations and alternatives which have come up and compare their advantages and disadvantages to understand what is required from there on to proceed properly.

Chapter II

The elephant in the room: Magnetic Fields

No law or ordinance is mightier than understanding.

– Plato

As we have shown in our overview in the last chapter many fascinating phenomena in the universe are related to the existence of cosmic magnetic fields. Nevertheless, especially theorists like to neglect them in their calculations or simulations in order to keep their life simpler. Thus, magnetic fields are often called the elephant in the room (see figure II.1). This chapter is supposed to give a broad overview over both observational techniques to gain information about cosmic magnetic fields (section II-1) as well as a theoretical description of the equations which we will treat numerically later on (section II-2).

II-1 Important processes and observation methods

We investigate observationally relevant processes involving magnetic fields and the corresponding observational methods and tracers with the goal to learn as much as possible about cosmic magnetic fields. The goal of these techniques may, however, differ slightly. Some convey information about magnetic field strengths, some about the field lines' structures. Some tell us about the line of sight component some rather about the perpendicular component. Also the applicability of these approaches to astrophysical objects may differ, depending on several factors like size, distance or degree of ionisation with additional individual limitations coming into play. Therefore, it is important to keep the whole picture in mind because the final answer might always lie in a combination of all that follows. We start with commonly known and well established practices and then peak into the territory of novel approaches which are still under development.

II-1.1 Synchrotron radiation

Synchrotron emission from relativistic charged particles (typical electrons) is probably the most direct tracer of magnetic fields possible. The basic process behind it is that charged particles



Figure II.1: Illustration for the importance of magnetic fields in the universe as the elephant in the room. Flyer logo for magnetic fields summer school Tenerife, Spain. Taken from <http://www.iac.es/winterschool/2013/>.

in the presence of magnetic fields are subject to the Lorentz force $\vec{F}_L = q\vec{v}/c \times \vec{B}$. They do not experience any force parallel to the magnetic field, only perpendicular to it and thus spiral around the magnetic field lines (in the non-relativistic limit) with the gyro frequency

$$\omega = \frac{eB}{m_e c}. \quad (\text{II-1})$$

For relativistic velocities the Lorentz factor γ has to be multiplied onto the denominator. The radius of the circular motion is called the gyro radius or Larmor radius¹:

$$r_g = \frac{m_e c v_{\perp}}{e B}. \quad (\text{II-2})$$

¹Named after Joseph Larmor.

The emitted power is given by the Larmor formula:

$$P = \frac{2}{3} \frac{e^2 a^2}{c^3}, \quad (\text{II-3})$$

with the acceleration in the relativistic case becoming

$$a^2 = \gamma^4 \left(\gamma^2 a_{\parallel}^2 + a_{\perp}^2 \right) \quad (\text{II-4})$$

with the Lorentz factor

$$\gamma = \frac{1}{\sqrt{1 - \beta^2}} = \frac{1}{\sqrt{1 - \left(\frac{v}{c}\right)^2}}. \quad (\text{II-5})$$

As already mentioned, $a_{\parallel} = 0$ and a_{\perp} comes from the Lorentz force. This leads to

$$P = \frac{2e^4}{3m^2 c^3} B^2 \gamma^2 \beta^2 \sin^2 \theta \quad (\text{II-6})$$

with the pitch angle θ between velocity and magnetic field. Using the classical electron radius

$$r_{ce} = \frac{e^2}{m_e c^2}, \quad (\text{II-7})$$

the Thomson scattering cross section

$$\sigma_T = \frac{8\pi r_{ce}^2}{3} \quad (\text{II-8})$$

and further substituting the magnetic pressure²

$$p_B = \frac{B^2}{8\pi} \quad (\text{II-9})$$

we get in total

$$P = 2\sigma_T c p_B \gamma^2 \beta^2 \sin^2 \theta. \quad (\text{II-10})$$

Averaging over all angles then gives

$$P = \frac{4}{3} \sigma_T c p_B \gamma^2 \beta^2. \quad (\text{II-11})$$

For further insight into the exact calculations we refer for example to [Ghisellini, 2013](#). As the total emitted power directly depends on the magnetic field strength it serves as an excellent tracer as we will argue in a bit from an observational point of view.

Before that we quickly show, how the synchrotron spectrum directly results from the (single) electron having a relativistic velocity. In figure [II.2](#) we show, what happens to if we vary the velocity v from very small values to those close to the speed of light. In the first case, photons are emitted isotropically forwards and backwards, indicated by the blue emission lobes in the left column. The detected electric field is then sinusoidal, the spectrum contains only one frequency.

²Or energy density, depending on the point of view.

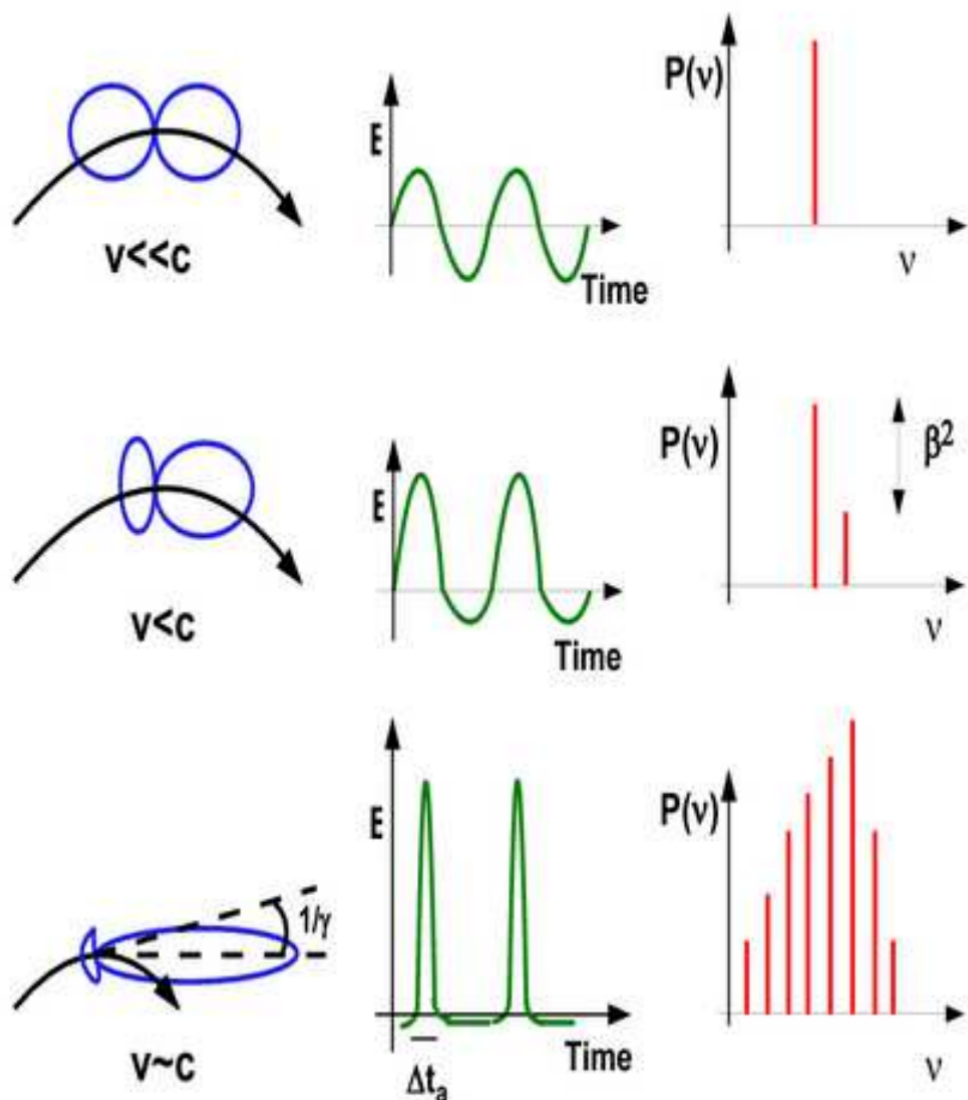


Figure II.2: Illustration of relativistic beaming and it's effects onto the spectrum. Taken from [Ghisellini, 2013](#).

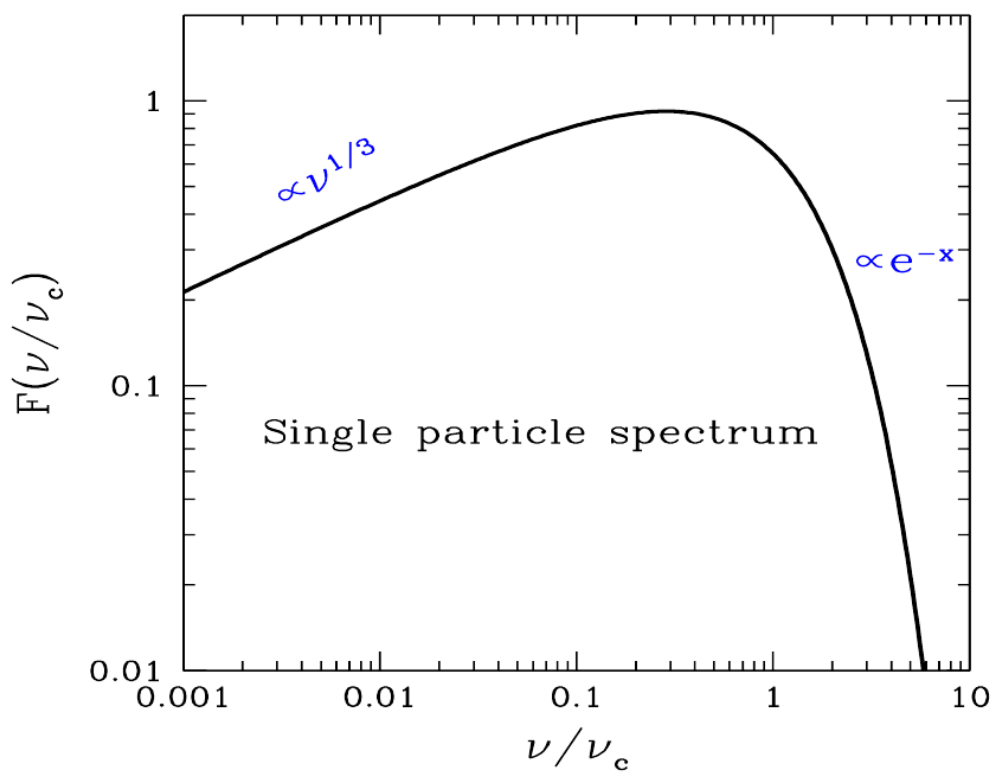


Figure II.3: Synchrotron spectrum of a single electron. The frequency ν is normalised to the peak frequency of the inverse Compton effect spectrum ν_c . Taken from [Ghisellini, 2013](#).

Increasing v makes the emission more asymmetric because relativity becomes important. This effect is called relativistic beaming. Higher order harmonics are added to the electric field and the spectrum becomes broader. The typical spectrum is again plotted in figure II.3.

To elaborate how we can infer information about the 3D magnetic field from these considerations we follow [Dormy and Soward, 2007](#). As already mentioned, the magnetic field strength can be estimated from the synchrotron intensity. What we have not considered so far is polarisation. Linear polarised light which travels through an ionised medium undergoes a rotation of its polarisation angle due to the Faraday effect. Three quantities depicted as integrals over the line of sight are then useful to observer: the total intensity I , the polarised intensity P and the Faraday rotation measure RM :

$$I \propto \int_{l.o.s.} n_{cr} B_{\perp}^2 dz \quad (II-12)$$

$$P \propto \int_{l.o.s.} n_{cr} \langle B \rangle_{\perp}^2 dz \quad (II-13)$$

$$RM \propto \int_{l.o.s.} n_e B_{\parallel}^2 dz, \quad (II-14)$$

with the magnetic field split up into a large scale regular component $\langle \vec{B} \rangle$ and a small scale random one \vec{b} , the number densities of relativistic cosmic ray electrons n_{cr} and of thermal electrons n_e . A positive rotation measure corresponds to magnetic field lines pointing towards the observer and vice versa. The degree of polarisation is given by

$$p = \frac{P}{I}. \quad (II-15)$$

The angle equals to

$$\Delta\beta = RM \cdot \lambda^2 \propto n_e B_z^2 \Delta z \lambda^2. \quad (II-16)$$

Informations about the integrated thermal electron density can be retrieved via the dispersion measure

$$DM = \int_{l.o.s.} n_e dz \quad (II-17)$$

or using a theoretical model as for example a beta model for a galaxy cluster:

$$n_e(r) = n_0 \left(1 + \frac{r^2}{r_c^2} \right)^{-3\beta/2}. \quad (II-18)$$

RM as well as DM can be derived theoretically from the dispersion relation

$$n = \frac{ck}{\omega} = \sqrt{1 - \frac{\omega_p^2}{\omega^2 \pm \omega \cdot \omega_g}} \quad (II-19)$$

with the gyro frequency ω_g and the plasma frequency

$$\omega_p = \sqrt{\frac{4\pi n_e e^2}{m_e}} \quad (\text{II-20})$$

by calculating the phase velocity $v_{ph} = \omega/k$ and the group velocity $v_{gr} = \partial\omega/\partial k$ respectively. In the Milky Way light from pulsars is used to obtain these data, therefore the obtained information depends highly on the knowledge of the distance to the respective pulsar and of the nature of the line of sight gas. Combining both dispersion and rotation measure leads to the line of sight component of the magnetic field:

$$B_{\parallel} \propto \frac{RM}{DM}, \quad (\text{II-21})$$

using equations II-14 and II-17. The quality of this estimate depends on the nature of a statistical correlation between fluctuations in the magnetic field and the thermal electron density, leading to factors of a few in error (Beck et al., 2003). For further reference see, amongst others, Padoan et al., 2001; Ostriker, 2002; Crutcher, 2012.

Using these measurements a lot of data regarding the magnetic field strengths in the Milky Way and external galaxies has been collected (see e.g. Ruzmaikin, Shukurov, and Sokoloff, 1988; Beck et al., 1996; Beck, 2000; Beck, 2001). Typically galaxies contain magnetic fields of the order of $10\mu Gs$ according to Beck, 2000 and a typical polarisation at short radio wavelengths of $p \sim 10 - 20\%$ according to Dormy and Soward, 2007. The latter leads to ordered magnetic field components of $\langle B \rangle / B \sim 0.4 - 0.5$ as a lower limit which makes equation II-21 in general usable. Magnetic field strengths inferred from rotation measures seem to be systematically lower than those from synchrotron intensity (see e.g. Beck et al., 2003). For a discussion of these differences see e.g. Dormy and Soward, 2007.

In figure II.4 we show an illustration of the observed light's path subject to Faraday rotation. Typically light from a distant radio galaxy or a pulsar which travels through the magnetic field of a galaxy cluster is used to infer information about said cluster field. In order to properly probe the whole cluster many of these observations are actually required which poses maybe the biggest difficulty of the process. Therefore, the better the sensitivity and resolution of a telescope, the more individual sources can be observed and the more information can be extracted. State of the art is only about $1 - 3$ sources per deg^2 . Especially the Square Kilometre Array (SKA) is the white hope to further these analyses bringing that number up to estimated 300 sources per deg^2 with SKA1 and 5000 per deg^2 sources with SKA2. Due to resolution limits only very large objects, typically galaxies and mostly galaxy clusters, have been observed with Faraday rotation so far (Clarke, 2004). An example for such an observation of an extended object, in this case Hydra A, is shown in figure II.5. Smaller objects like molecular clouds are typically beyond these limits. Things are further complicated in these regimes due to a lower degree of ionisation and small path lengths (Crutcher, 2012), however the SKA is expected to also shed light onto them (Strong, Dickinson, and Murphy, 2014) and also the Very Large Array (VLA) can be effectively utilised for that (Betti et al., 2017).

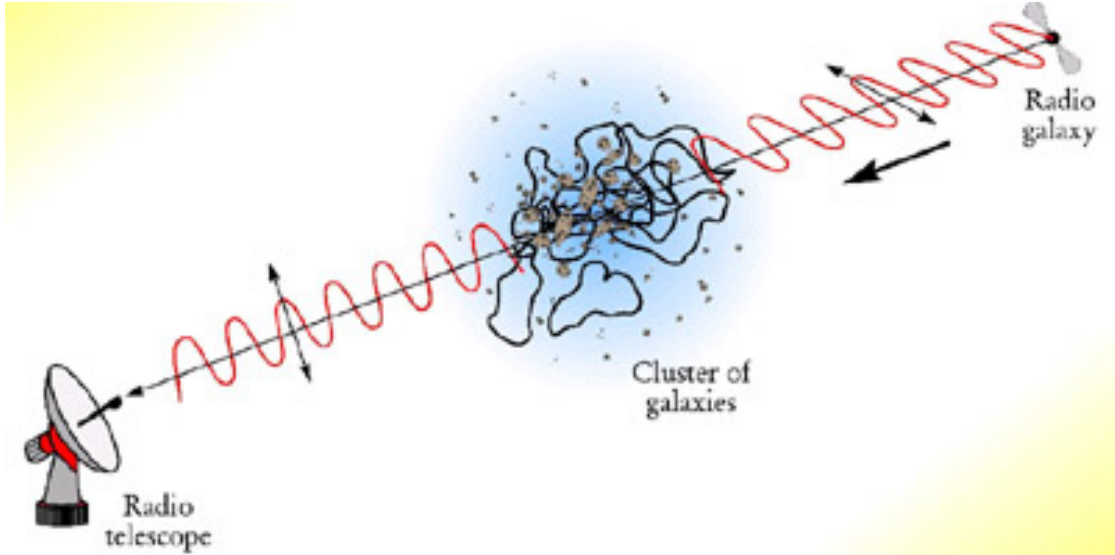


Figure II.4: Illustration of the detection process of the Faraday rotation measure. Taken from <https://www.skatelescope.org/magnetism/>.

II-1.2 Inverse Compton effect

A process that also plays a role when talking about the effects of relativistic electrons is the inverse Compton effect: high energy electrons scatter with lower energy photons and increase the energy of said photons drastically. As an example consider electrons with gamma factors of $\gamma \sim 1000$ which carry an energy of $E = \gamma m_e c^2 \sim 0.5 \text{ GeV}$. If such an electron conveys just a portion of it's energy to a CMB photon ($E_{CMB} \sim 6.6 \cdot 10^4 \text{ eV}$) it boosts up it's frequency to X-ray ($E_{X-ray} \sim 1 - 100 \text{ keV}$) or even γ -ray radiation levels. This radiation can be observed and combined with synchrotron radiation of the same electrons to again infer information about the magnetic field strength. To illustrate this we write down the fraction of the power from synchrotron emission and inverse Compton which translates into the fractions of the respective source energy densities u :

$$\frac{P_s}{P_{ic}} = \frac{u_B}{u_{cmb}} = \frac{B^2}{8\pi} \Big/ \frac{4\sigma T^4}{c} \quad (\text{II-22})$$

with σ the Stefan-Boltzmann constant and the CMB temperature depending on the redshift z

$$T = T_0 \cdot (1 + z). \quad (\text{II-23})$$

The numerator is the energy density of a magnetic field equal to the magnetic pressure. The denominator resembles the Stefan-Boltzmann law and results from integrating the black body spectrum over all frequencies:

$$u_{cmb} = \frac{8\pi h}{c^3} \int_0^{\infty} d\nu \frac{\nu^3}{\exp\left(\frac{h\nu}{k_B T}\right) - 1}. \quad (\text{II-24})$$

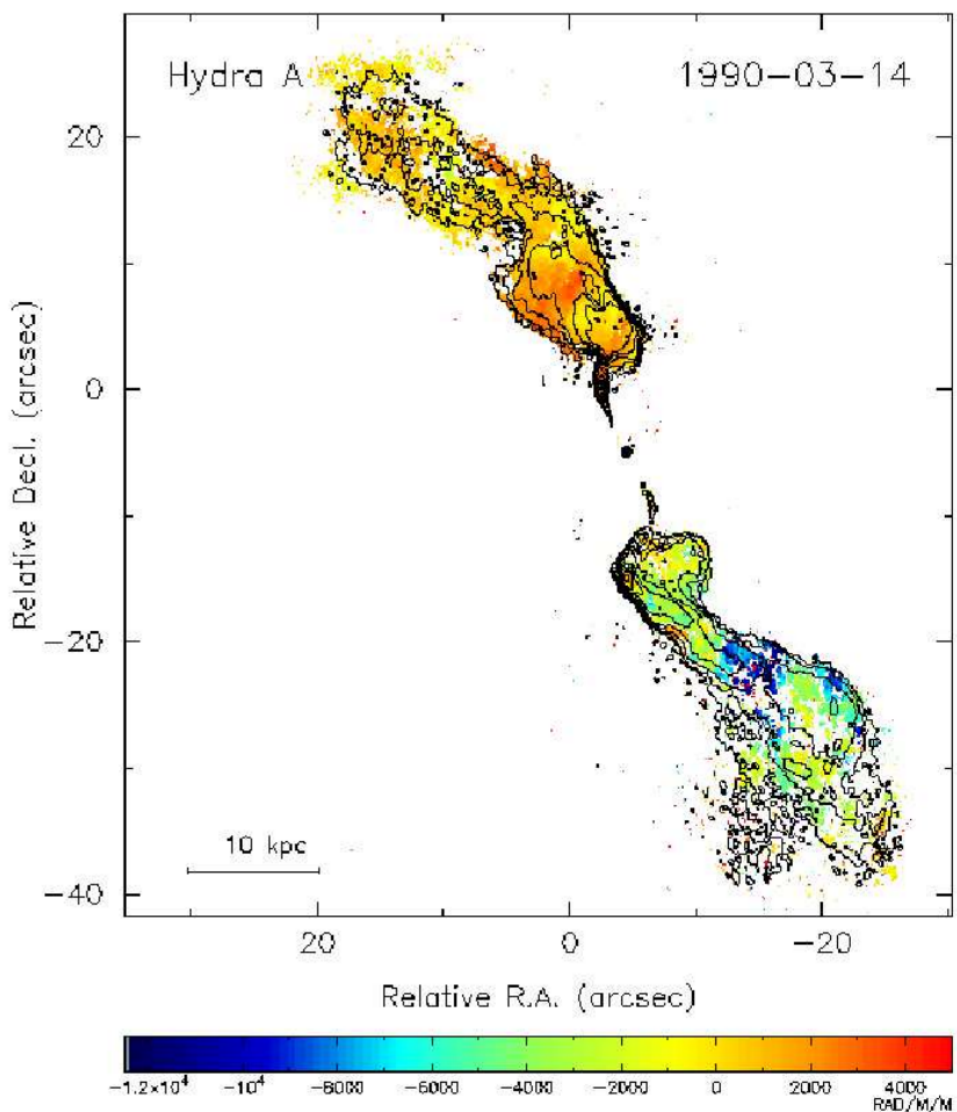


Figure II.5: Faraday rotation map of Hydra A overlayed over total intensity in colours. Taken from [Clarke, 2004](#).

Both powers on the left hand side as well as the CMB temperature can be measured, leaving the magnetic field as the remaining unknown quantity which can then be determined. For more details about inverse Compton radiation and the resulting spectrum see e.g. [Felten and Morrison, 1966](#).

II-1.3 Dust Polarisation

Following [Crutcher, 2012](#) dust polarisation measurements both due to absorption and emission are very suitable tools to infer properties of the magnetic field morphology in the interstellar medium (ISM). Since it highly depends on the alignment of dust grains it becomes clear that the required resolution actually limits the applicability to targets further away quite a strongly. [Hoang and Lazarian, 2008](#) state, that the maximum polarised emission of dust grains is perpendicular to the magnetic field component in the plane of the sky. The degree of alignment is, however, highly dependent on the grain size. Typically emissions in the mm and sub-mm bands corresponding to molecular clumps are used. The result is then the direction of the magnetic field vectors in the plane of the sky, modulo a 180° ambiguity. An example for a resulting polarisation map is shown in figure [II.6](#). The vector field shown in this observation is very smooth, making the inferred magnetic field vectors likely representative of a larger scale, ordered component of the field on top of which a turbulent more random component may also exist. That is backed up by the fact that dust emission is typically optically thin which leads to the whole line of sight being probed by this analyse and therefore most probably rather averaged results ([Crutcher, 2012](#)).

In addition to these absorption features, dust grains are also visible in linear polarised emission through thermal radiation. The first successful measurements date back to observations of M42 in 1982 ([Cudlip et al., 1982](#)). Observations have been made with single dish telescopes as well as interferometers like the Submillimeter Array.

II-1.4 Zeeman effect and Goldreich-Kylafis effect

An important physical effect for measuring magnetic fields is the so called Zeeman effect, which has been detected by Pieter Zeeman in 1897 ([Zeeman, 1897](#)) and awarded the physics Nobel price in 1902. It states that spectral lines are split into several components in the presence of a magnetic field with a small shift in frequency $\Delta\nu \ll \nu$ due to the coupling of the electron magnetic dipole to the background field. In terms of quantum mechanics this means splitting up an energy level into several fine structure levels related to the magnetic quantum number m_l . The magnetic quantum number can take on values symmetric around zero with the maximum given by the azimuthal quantum number and therefore the principal quantum number. Due to selection rules, the magnetic quantum number in any transition may only change by

$$\Delta m_l = 0, \pm 1 \tag{II-25}$$

for given l . Consequently, a singlet line subject to the Zeeman effect splits up into three individual lines, symmetrically around the original one. $\Delta m_l = 0$ is called the π line with $\nu = \nu_0$, the others are the so called σ lines with $\nu = \nu_0 \pm \Delta\nu$. We follow [Crutcher, 2012](#) to give a brief overview over the Zeeman effect's application onto astrophysics.

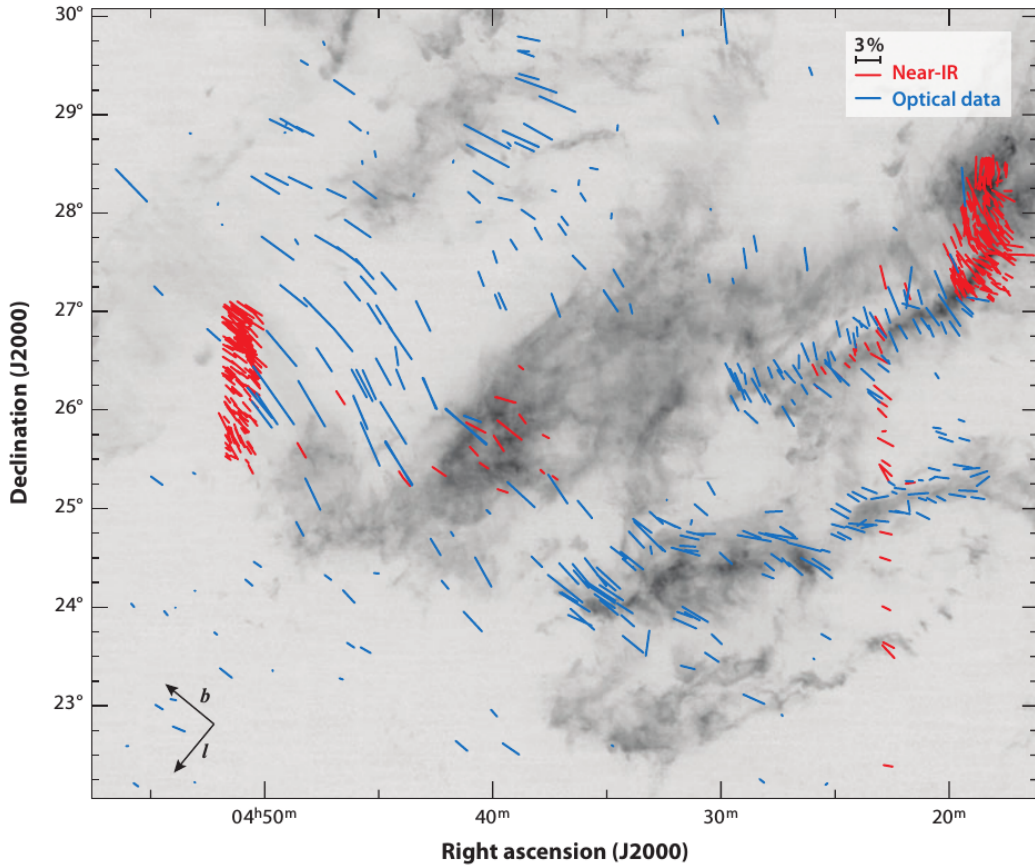


Figure II.6: Dust polarisation measurements indicating the magnetic field directions in the Taurus dark-cloud complex superimposed on a ^{13}CO map (black background). The coloured lines depict the magnetic field directions taken perpendicular to the measured polarisation as indicated by the two vectors bottom left. The line length scales with the degree of net polarisation. Taken from [Chapman et al., 2011](#) and modified by [Crutcher, 2012](#).

As the Zeeman effect depends on the magnetic dipole moment of an electron, not every molecule is well suited for detection of Zeeman splitting.³ We can write down the change in frequency as

$$\Delta\nu = \pm Z \left| \vec{B} \right| \quad (\text{II-26})$$

with Z depending on the spectral transition. To get a feeling for the small magnitude of this effect, a maximum Z can be inferred from the Bohr magneton as⁴

$$Z \lesssim Z_{BM} = \frac{e}{4\pi mc} = 1,4 \frac{\text{Hz}}{\mu\text{G}} \quad (\text{II-27})$$

which results in an upper limit of only one Hertz in a typical μG environment. Representative detections have been made using the HI 21cm absorption line (first detection by [Verschuur, 1968](#) looking at the Cassiopeia A supernova remnant), OH absorption (observing the molecular cloud NGC 2024 [Crutcher and Kazes, 1983](#)) and CN (e.g. [Crutcher and M., 1999](#)). For example the 21 cm line corresponds to

$$\nu = 1.4\text{GHz} \approx 10^9 \cdot \Delta\nu \cdot \frac{B}{1\mu\text{G}} \quad (\text{II-28})$$

Therefore, a really good spectral resolution is required to actually measure Zeeman splitting even for good tracer molecules, limiting the method to relatively close targets like interstellar clouds. Nevertheless, whenever applicable it poses an excellent method because it can allow to reconstruct the total magnetic field: The π component is linear polarised and its strength is proportional to the magnetic field strength in the plane of the sky parallel to \vec{B} , while the sigma components are elliptically polarised. The elliptical polarisation comes due to a linear component in the plane of the sky perpendicular to \vec{B} and a circular component proportional to the magnetic field strength along the line of sight. Additionally, the direction of circular polarisation even gives us the sign of the line of sky magnetic field component ([Crutcher et al., 1993](#)). Applicability of the whole method is of course also limited by magnetic field variations along the line of sight.

An extensive discussion of the result from Zeeman observations in molecular clouds can be found in [Crutcher and M., 1999](#), where magnetic fields have been found as a dynamically very important component of the energy density budget. Additionally, hints towards the importance of ambipolar diffusion for star formation are given. We will pick up the topic of non ideal MHD effects later in section [II-2.3](#). We present typical results from observing molecular clouds taken from [Crutcher, 2012](#) in figure [II.7](#).

This can be further expanded to higher densities and smaller scales by applying Zeeman measurements to Masers⁵, typically using molecules like OH, H₂O and CH₃OH. Masers also allow to extend these measurements to some extent to large scale galactic magnetic fields. This has been attempted for the Milky Way already in 1960, albeit unsuccessful in the beginning, by [Galt, Slater, and Shuter, 1960](#) and later e.g. by [Reid and Silverstein, 1990](#). [Reid and Silverstein, 1990](#)

³Depending on the respective molecule being paramagnetic.

⁴Please note that the formula given by [Crutcher, 2012](#) contains an extra factor h and actually leads to an energy difference.

⁵Microwave Amplification by Stimulated Emission of Radiation, therefore the analogue of a laser emitting coherent electromagnetic waves in the microwave band.

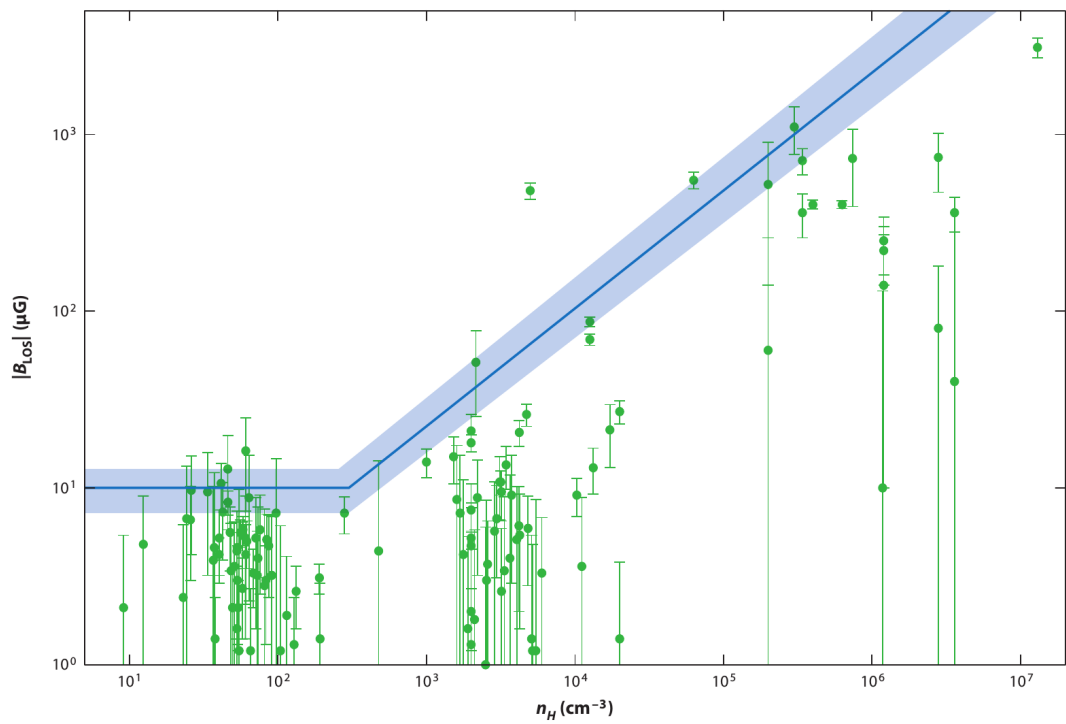


Figure II.7: Observational results of diffuse and molecular cloud Zeeman measurements plotting the line of sight magnetic field strength against the number density (green). Additionally the inferred total magnetic field strength using a Bayesian model is plotted (blue). Figure taken from [Crutcher, 2012](#).

note, that the line of sight magnetic field direction should be mostly preserved through contraction from interstellar densities ($n \sim 10^{-3} \text{ cm}^{-3}$), giant molecular clouds ($n \sim 10^3 \text{ cm}^{-3}$) to OH maser regions ($n \sim 10^7 \text{ cm}^{-3}$) close to young massive stars during collapse. Recent surveys observing masers in the Milky Way include the Methanol Multibeam survey (MMB, Caswell et al., 2010; Caswell et al., 2011; Green et al., 2010; Green et al., 2012), the MAGMO survey using the Australia Telescope Compact Array (Wilson et al., 2011) and GASKAP (Dickey et al., 2013).

For further reading we refer to the recently written PhD thesis of Robishaw, 2008 who states some collected insight onto the question of success of Zeeman measurements. Although the method theoretically gives information about all properties of the observed magnetic field, especially on galactic scales observations are unfortunately more dominated by negative results than positive ones.

An extension of this discussion is the so called “Goldreich-Kylafis effect” which we will not discuss in detail. Goldreich and Kylafis, 1981; Kylafis and D., 1983; Deguchi and Watson, 1984 have shown, that linear polarisation can be observed also in non-maser lines. The basic idea behind this is, that an (external but also internal) anisotropic radiation field excites the Zeeman split levels non-symmetrically. We already discussed the different polarisation properties of the π and σ transitions. If the transitions now occur non isotropically a net linear polarisation can be observed. Although first attempts to actually detect the GK effect were not successful (Wannier, Scoville, and Barvainis, 1983), positive detections in star envelopes and molecular clouds have been achieved since then (see e.g. Glenn et al., 1997; Greaves et al., 1999).

II-1.5 Examples for novel approaches

Having outlined the most known and well established techniques for magnetic field observations we follow up with a quick overview over rather recent newcomers to the field or methods which are still actively refined in recent work.

Chandrasekhar-Fermi method

The Chandrasekhar-Fermi method (hereafter C-F method, Chandrasekhar and Fermi, 1953) is commonly used to determine the intensity of magnetic fields in the plane of sky when the variations of polarisation direction and velocity dispersion are both known (Ostriker, Stone, and Gammie, 2001; Falceta-Gonçalves, Lazarian, and Kowal, 2008; Houde et al., 2009; Novak, Dotson, and Li, 2009; González-Casanova and Lazarian, 2017). The basic idea behind the C-F method is, that under the assumption of a flux frozen field turbulent motion leads to irregular magnetic fields on top of a general mean field. Chandrasekhar and Fermi, 1953 further assume turbulence to be isotropic and incompressible and equipartition between turbulent and magnetic energy. The magnetic field value is then given by

$$|\vec{B}_{POS}| = \sqrt{4\pi\rho} \frac{\delta v}{\delta\phi} \quad (\text{II-29})$$

with δv being the one dimensional velocity dispersion and $\delta\phi$ the polarisation angle dispersion. This method contains several potential sources of error. For example not all of the structure

of a potentially tangled magnetic field along the line of sight might be captured, leading to a reduced $\delta\phi$. [Ostriker, Stone, and Gammie, 2001](#) have presented some work tackling this issue. [Falceta-Gonçalves, Lazarian, and Kowal, 2008](#) also present an improved version using the two-point correlation function of polarisation angles with resulting uncertainties of lower than 20%. Furthermore, also [Cho and Yoo, 2016](#) and many more show additional modifications of the C-F method which we will not investigate in any more details here. More references can for example be found in the review of [Crutcher, 2012](#).

Spectral line width

[Houde et al., 2000](#) suggested an idea to gain information about magnetic fields from spectral line widths. Due to the restriction of a charged particle's movement perpendicular to magnetic field lines, meaning it following a gyration motion, its mean perpendicular velocity can become on average negligibly small. That has a direct impact onto the width of observed spectral lines, decreasing it for charged particles in contrast to a neutral ones. To compare the change in line width one has to observe two particle species located in the same region, as for example HCN and HCO⁺ and can from that infer the presence of a sufficiently large magnetic field. Further extensions to the method have been for example carried out by [Li and Houde, 2008](#) who also take the turbulent velocity dispersion into account. According to [Crutcher, 2012](#) the technique is promising but still not fully proven to be working.

Density structures: HI Fibers and more

[Clark, Peek, and Putman, 2014](#) present a novel approach to determine the direction of magnetic fields in the ISM using neutral hydrogen (HI) observations and the so called “Rolling Hough transform” (RHT). This technique is used to determine linear structures in a huge data set as a modification of the original Hough transform ([Hough V and Paul C., 1962](#)). For a review of the original method and its applicability in image processing see [Illingworth and Kittler, 1988](#). The modified version of [Clark, Peek, and Putman, 2014](#) does not only assign a binary value to each pixel of the data map but rather a probability for that pixel to be part of a coherent linear structure. They use observation data from the GALFA-HI survey ([Peek et al., 2011](#)) and the GASS survey ([McClure-Griffiths et al., 2009](#)) and additional single target observations to demonstrate a correlation between the orientation of HI fibres⁶ and starlight polarisation and magnetic fields, depending on resolution. That supports the common idea, that magnetic fields should in general follow density structures. [Clark, Peek, and Putman, 2014](#) further use the RHT result to slightly modify the CF-method, achieving qualitatively the same result as with the classical approach.

These results are further backed up by simulation results presented by [Soler et al., 2013](#). They show several simulations of molecular clouds with varying parameters and use the Histogram of Relative Orientations (HRO) technique ([Leonardis, Bischof, and Pinz, 2006](#)) to identify density structures in two as well as three dimensions which are then mostly correlated to their simulated magnetic fields.

⁶I.e. elongated HI structures.

Velocity gradients

A novel technique presented by (González-Casanova and Lazarian, 2017; Yuen and Lazarian, 2017) depends on velocity gradients as tracer of magnetic fields. According to Goldreich and Srigar, 1995; Lazarian and Vishniac, 1999; Cho and Vishniac, 2000; Cho, Lazarian, and Vishniac, 2002 turbulent eddies in a strongly magnetised turbulent medium show rotation related to the magnetic field lines. As elongated eddies contain largest velocity gradients perpendicular to their long axes and the magnetic field lines are preferentially parallel to these axes for sub-Alfvénic turbulence it follows that the local magnetic field should be mostly perpendicular to velocity gradients. Alternatively density gradients could be used, however Beresnyak, Lazarian, and Cho, 2005; Kowal, Lazarian, and Beresnyak, 2007 have shown that especially at high Mach numbers turbulence is better traced by velocity than density.

Since velocity gradients can be observed via spectroscopy using Doppler shifted lines this provides a suitable tracer for the direction of magnetic field lines whenever these assumptions hold, as for example in the ISM. This utilises the analysis of the normalised and non-normalised velocity centroids $C(\vec{x})$ and $S(\vec{x})$ (Munch and Wheelon, 1958; Kleiner and Dickman, 1985; O 'dell and Castañeda, 1987; Miesch, Scalo, and Bally, 1999). Assuming that the intensity $I(\vec{x})$ is proportional to the column-density⁷, they are given by

$$S(\vec{x}) = \int_{l.o.s.} v_z \rho \, dz \quad (\text{II-30})$$

$$I(\vec{x}) = \int_{l.o.s.} \rho \, dz \quad (\text{II-31})$$

$$C(\vec{x}) = \frac{S(\vec{x})}{I(\vec{x})}. \quad (\text{II-32})$$

The projected data is distributed on a Cartesian grid. For each cell they use the neighbourhood in a certain radius to calculate the direction in which the gradient is largest:

$$\nabla^U(\vec{x}) = \max \left\{ \frac{|U(\vec{x}) - U(\vec{x}' - \vec{x})|}{\vec{x}'} \right\} \quad (\text{II-33})$$

for $U = S$ or C and \vec{x}' being the centre of the neighbouring cell. The search radius is dependent on the available data resolution and a value of 7 – 10 cells is suggested by the authors. The bigger the neighbouring region, the more discrete options for the resulting direction are possible. A quick sketch in figure II.8 illustrates this graphically for $r = 1$ which results in only four possible directions.

The value of the velocity gradient is only required for the calculation of the maximum, but in the end only the direction

$$\Omega^U(\vec{x}) = \vec{x}' - \vec{x} \quad (\text{II-34})$$

⁷The density integrated along the line of sight.

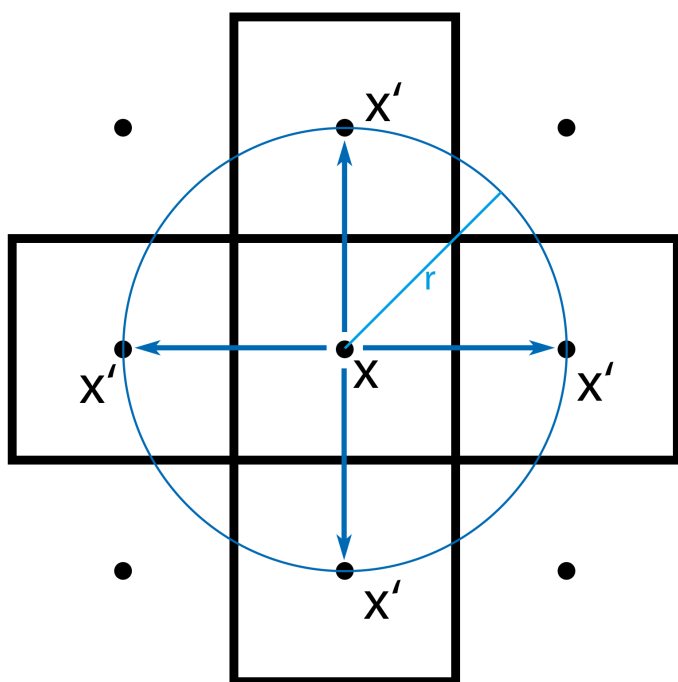


Figure II.8: A schematic illustrating the calculation of velocity gradients as in [González-Casanova and Lazarian, 2017](#) with search radius $r = 1$ resulting in four possible directions. Extending to $r = 2$ leads to 8 directions of the gradient, including the diagonals.

counts, since

$$\vec{B} \perp \Omega^U(\vec{x}). \quad (\text{II-35})$$

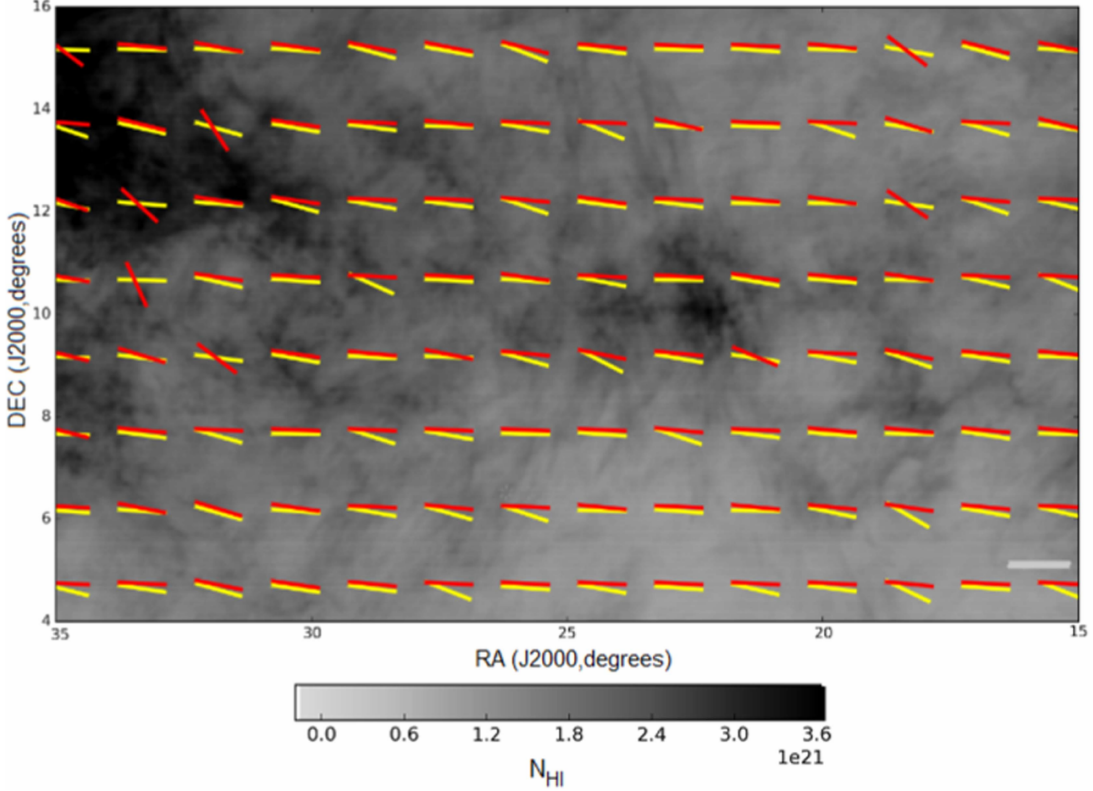


Figure II.9: Magnetic field directions obtained via the velocity gradient technique using GALFA HI data (yellow lines) compared to measurements of polarisation with PLANCK (red) on top of HI column density presenting very good agreement. Taken from [Yuen and Lazarian, 2017](#).

Using simulations of a turbulent box [González-Casanova and Lazarian, 2017](#) show how well this method performs and come to the conclusion that both the normalised and non-normalised centroids give similar results, both better than using only the density centroid. [Yuen and Lazarian, 2017](#) then apply the method to GALFA HI data and compare the resulting magnetic field directions to polarization measures using PLANCK, resulting in broadly very good agreement (see figure II.9).

Furthermore, a modification of the C-F method by using gradients of velocity centroids instead of the polarization angle dispersion is proposed, removing the requirement for dust polarization data. However, a correction factor has to be introduced which might depend on the strength of turbulence, self gravity and other environmental properties.

This leads directly to the strongest limitation of this method. This study depends highly on the relationship between velocity gradients and magnetic field lines studied in a non self-gravitating

turbulent environment. If self gravity becomes important, this relation is likely to change and is still subject to ongoing research.

II-2 Magnetic fields in simulations: Analytic prelude

II-2.1 Pure Hydrodynamics

Justification for Hydrodynamics

In order to simulate astrophysical environments like galaxies or galaxy clusters we solve the equations of hydrodynamics. To be able to do that, the gas needs to be highly collisional meaning that the mean free path is small with respect to the system size. [Spitzer, 1956](#) gives an approximation for the electron mean free path as

$$\lambda_e \approx 22.5 \left(\frac{T_e}{10^8 K} \right)^2 \left(\frac{n_e}{10^{-3} cm^{-3}} \right)^{-1} kpc. \quad (\text{II-36})$$

This formula treats a system only with averaged properties, neglecting any substructure in which the mean free path would be smaller anyway. Looking at the most extreme case, the hot and diffuse intra cluster medium (ICM), the electron mean free path is of the order of tens of kpc, which is certainly not small enough to justify the usage of hydrodynamics. However, we have to keep in mind the turbulent, tangled magnetic fields present in these environments. Therefore, the movement of charged particles like electrons is rather determined by their gyroradius given by

$$r_{g,e} = \frac{m_e c v}{e B} \quad (\text{II-37})$$

or the typical length scale on which magnetic fields change

$$\frac{|\vec{B}|}{\nabla \cdot \vec{B}}. \quad (\text{II-38})$$

Assuming again a typical cluster environment with a velocity of $v = 1000 km/s$ and a magnetic field strength of $B = 1 \mu G$ we get a gyroradius of $r_e = 57 km$ which is about 16 orders of magnitude smaller than the mean free path and definitely small enough to allow to treat the ICM as a highly compressible fluid.

Furthermore, for example [Lazarian and Desiati, 2010](#); [Brunetti and Lazarian, 2011](#) argue, that the collisionality of the ICM is actually underestimated when only considering Coulomb collisions. Because it is fully ionised and therefore in a plasma state corresponding plasma instabilities should naturally occur in the presence of turbulence and further decrease the mean free path (see also [Lazarian and Beresnyak, 2006](#); [Schekochihin and Cowley, 2006](#)). Since a tangled magnetic field is exactly the result of turbulent motion and plasma instabilities this line of argumentation is basically the same. We revisit the calculation of the actual degree of ionisation of a gas depending on temperature and density in section [II-2.3](#).

Following up on this argumentation, we can make a quick random walk experiment. We take a homogeneous sphere of radius $R = 3 Mpc$ of temperature $T = 10^8 K$ and density

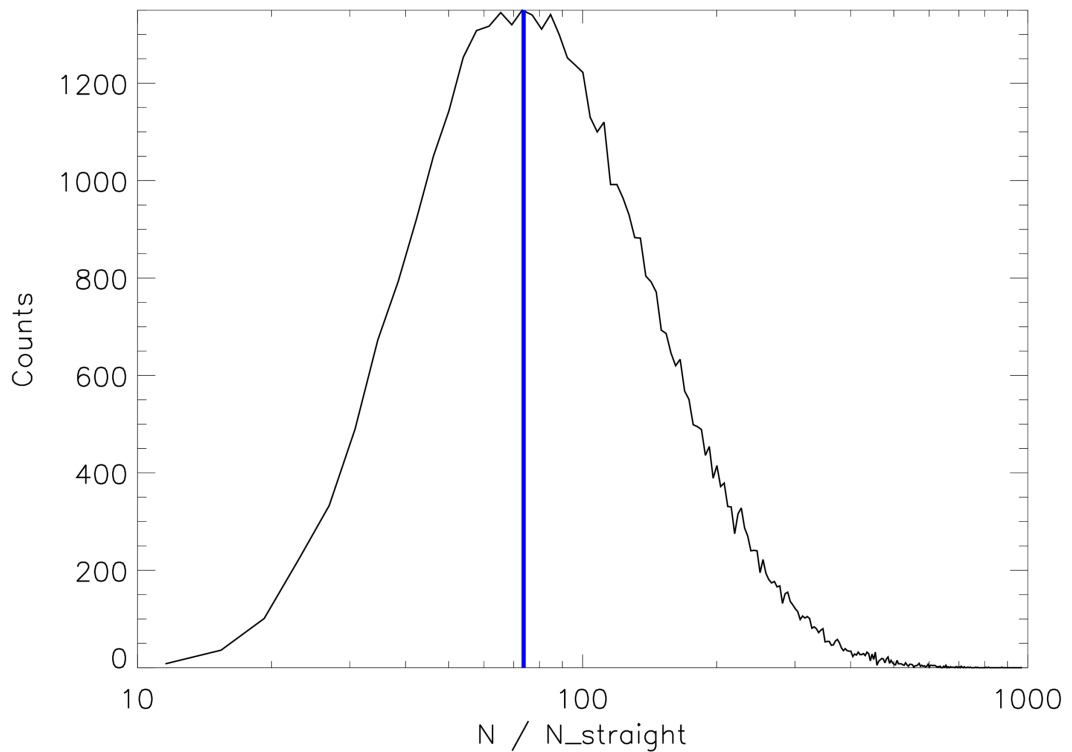


Figure II.10: Number of scatterings compared to a straight fly outwards, calculated using a random walk from the centre of an artificial galaxy cluster outwards. The blue line denotes the maximum value of a Gaussian fit at $N/N_{\text{straight}} \approx 74$. The asymmetric look regarding smoothness and scattering comes from using linear bins on a logarithmic scale.

$n = 10^{-3} \text{ cm}^{-3}$ and put a test particle into the centre of this sphere. We assume that the particle undergoes a collision every $\lambda_e = 22.5 \text{ kpc}$ as given by equation II-36 which scatters the particle in a random angle α . We continue this random walk until the particle leaves the sphere and note the number of collision N_c it experiences. We compare that to the number of scattering events in the case of a straight fly through N_{straight} . This process is repeated a significant number of times in order to generate proper statistics. We plot the result after $5 \cdot 10^4$ test particles in figure II-10. Fitting the histogram to a Gaussian gives a factor of ~ 74 more scatterings than for a straight path.

The equations of Hydrodynamics

To derive the basic equations of hydrodynamics in Lagrangian form, following [Landau and Lifschitz, 2007](#); [Teyssier, 2015](#), we start by considering an enclosed volume V . The total force onto the boundaries of that volume given through all the pressure p onto the boundaries dA is

$$\vec{F} = - \oint_{\partial V} p \, d\vec{A} = - \int_V \vec{\nabla} p \, dV \quad (\text{II-39})$$

using the Gauss's theorem. The integrand can be understood as the force acting per unit volume. According to Newton's second law we then get the equations of motion

$$\rho \frac{d\vec{v}}{dt} = -\vec{\nabla} p \quad (\text{II-40})$$

with the macroscopic⁸ gas velocity \vec{v} and density ρ . These three equations are called Euler equations. Note, that the total time derivative operator has to be taken as the Lagrangian derivative

$$\frac{d}{dt} = \frac{\partial}{\partial t} + \vec{v} \cdot \vec{\nabla}. \quad (\text{II-41})$$

Other forces acting, like gravity, can then be simply added to the right hand side of equation II-40. Next we have a look at the conservation of mass. All the mass flowing outside a volume V per time can be associated with a mass change rate:

$$\oint_{\partial V} \rho \vec{v} \, dA = \frac{\partial}{\partial t} \int_V \rho \, dV. \quad (\text{II-42})$$

Using again Gauss's theorem leads to

$$\int_V \left(\frac{\partial \rho}{\partial t} + \vec{\nabla} \cdot (\rho \vec{v}) \right) \, dV = 0 \quad (\text{II-43})$$

which must hold for any Volume V . Therefore, we get the continuity equation (i.e. conservation of mass):

$$\frac{\partial \rho}{\partial t} + \vec{\nabla} \cdot (\rho \vec{v}) = 0 \quad (\text{II-44})$$

⁸Not to be confused with the velocity of the gas particles but rather the velocity of the whole flow.

Additionally we need the first of thermodynamics to describe the evolution of the gas' internal energy U (or rather of the specific internal energy u), ergo energy conservation:

$$dU = m \cdot du = -p \cdot dV \quad (\text{II-45})$$

and describe the rate of change of the fluid volume using the velocity divergence

$$\frac{1}{V} \frac{dV}{dt} = \vec{\nabla} \cdot \vec{v}. \quad (\text{II-46})$$

Combining these two equations leads to

$$\rho \frac{du}{dt} = -p \vec{\nabla} \cdot \vec{v} \quad (\text{II-47})$$

Furthermore, we can assume the system to behave adiabatically which results in the introduction of a constant entropy

$$\frac{ds}{dt} = 0. \quad (\text{II-48})$$

Alternatively we can rewrite the conservation equations and equations of motion into their Eulerian form, which reveals their conservative properties even better:

$$\frac{\partial \rho \vec{v}}{\partial t} + \vec{\nabla} \cdot (\rho \vec{v} \otimes \vec{v} + p \mathbf{1}) = 0 \quad (\text{II-49})$$

$$\frac{\partial \rho}{\partial t} + \vec{\nabla} \cdot (\rho \vec{v}) = 0 \quad (\text{II-50})$$

$$\frac{\partial E}{\partial t} + \vec{\nabla} \cdot (\vec{v} (E + p)) = 0 \quad (\text{II-51})$$

with the fluid energy density

$$E = \rho u + \frac{1}{2} \rho |\vec{v}|^2. \quad (\text{II-52})$$

In the Lagrangian formulation before we considered an individually moving fluid element while the Eulerian formulation is based on the description of scalar and vector fields. Both describe the same system using this different though process. In addition to these equations we need an equation of state, as for example for an ideal gas given by

$$p = (\gamma - 1) \rho u \quad (\text{II-53})$$

with the adiabatic index γ . In addition to these we have to add non-ideal and higher order effects if they play a relevant role in the system we study. These include for example a treatment of physical viscosity, requiring to solve the Navier-Stokes equations instead of the Euler equations, and thermal conduction as studied in chapter [VIII](#) of this thesis.

We finish this section with some quick calculations regarding the importance of physical viscosity and the connection to turbulence following [Shu, 1991](#). The Euler equations we presented derive directly from the lowest order approximation of the Boltzmann equation, while the next

order leads to the Navier-Stokes equations. We get an additional term Ψ on the right side of the energy conservation equation (equation II-51) of the form:

$$\Psi = \pi_{ik} \frac{\partial v_i}{\partial x_k}, \quad (\text{II-54})$$

which is the rate of viscous dissipation of energy. Also the equations of motion get an extra term $\sim \vec{\nabla} \pi$ decelerating the motion. Microscopically we can understand viscosity as the exchange of particles between different regions across a shear flow which leads to a frictional flow. We can then define the so called shear viscosity coefficient as

$$\mu = \frac{5}{8} \frac{\sqrt{\pi m k_B T}}{\sigma} \sim \frac{mv_T}{\sigma} \quad (\text{II-55})$$

depending on the thermal velocity v_T and the cross section σ . By comparing the gradients of the energy density of the flow and of the viscous term we can further identify the dimensionless Reynolds number

$$\frac{\partial (\rho v_i v_k) / \partial x_k}{\partial \pi_{ik} / \partial x_k} \sim \frac{\rho v^2 / L}{\mu v / L^2} = \frac{vL}{\nu} =: Re \quad (\text{II-56})$$

using the typical flow velocity v , the typical length scale L and the kinematic viscosity

$$\nu = \frac{\mu}{\rho} = v_T \cdot \lambda. \quad (\text{II-57})$$

For a thermal flow of $v \sim v_T$ we get

$$Re = \frac{vL}{v_T \lambda} \sim \frac{L}{\lambda} \quad (\text{II-58})$$

which we already calculated to be in general much bigger than one. The Reynolds number is a measurement of the degree of turbulence in a system, as it depends on the fraction of the typical flow velocity to the thermal velocity. Furthermore, viscous forces are not dominant in turbulent environments, as $Re \propto \mu^{-1}$. Further comparisons, including conductivity follow later this chapter in section II-2.3. The question whether we need to treat hydrodynamics relativistically instead of classically as we wrote down the equations here will be answered in more detail later in section III-5 where we discuss that issue for gravity. In case of hydrodynamics not only the fluid velocities have to be much smaller than the speed of light but also the velocities of all microscopical particles out of which the fluid consists of. In short, for simulations of galaxy or galaxy cluster formation the answer to the question if we need to solve the relativistic equations of hydrodynamics is a clear “No”.

II-2.2 Ideal MHD approximation

In order to derive the equations of magnetohydrodynamics, we modify the hydrodynamics equations by adding contributions of the magnetic field and introduce the evolution equation for magnetic fields, the induction equation. For further calculations we require Maxwell's equations:

$$\text{Gauss' law :} \quad \vec{\nabla} \cdot \vec{E} = 4\pi \rho_q \quad (\text{II-59})$$

$$\text{Magnetic monopoles: } \vec{\nabla} \cdot \vec{B} = 0 \quad (\text{II-60})$$

$$\text{Faraday's law: } \vec{\nabla} \times \vec{E} = -\frac{1}{c} \frac{\partial \vec{B}}{\partial t} \quad (\text{II-61})$$

$$\text{Ampère's law: } \vec{\nabla} \times \vec{B} = \frac{1}{c} \left(4\pi \vec{j} + \frac{\partial \vec{E}}{\partial t} \right) \quad (\text{II-62})$$

with the electric field \vec{E} , the magnetic field \vec{B} , the charge density ρ_q and the current density \vec{j} . We start by modifying equation II-40 which in the presence of magnetic fields looks like

$$\rho \frac{d\vec{v}}{dt} = -\vec{\nabla} p + \vec{j} \times \vec{B} \quad (\text{II-63})$$

due to the Lorentz force. Assuming that we can neglect displacement currents, $\frac{\partial \vec{E}}{\partial t}$ becomes zero and we can rewrite the equation using equations II-60, II-62 as

$$\rho \frac{d\vec{v}}{dt} = -\vec{\nabla} p + \frac{c}{4\pi} (\vec{\nabla} \times \vec{B}) \times \vec{B} \quad (\text{II-64})$$

$$= -\vec{\nabla} p + \frac{c}{4\pi} \left[(\vec{B} \cdot \vec{\nabla}) \vec{B} - \frac{1}{2} \vec{\nabla} |\vec{B}|^2 \right]. \quad (\text{II-65})$$

The right hand side now consists (in that order) of the thermal pressure, the magnetic tension, which works towards straight magnetic field lines, and the magnetic pressure. Furthermore, we modify Faraday's law of induction (equation II-61) by combining Ohm's law with a general Lorentz transformation:

$$\vec{j} = \sigma \vec{E}' \quad (\text{II-66})$$

$$\frac{1}{\sigma} \vec{j} = \vec{E} + \frac{1}{c} \vec{v} \times \vec{B} \quad (\text{II-67})$$

Assuming perfect conductivity we get

$$\vec{E} = -\frac{1}{c} \vec{v} \times \vec{B} \quad (\text{II-68})$$

and therefore the resulting induction equation for MHD as

$$\frac{\partial \vec{B}}{\partial t} = \vec{\nabla} \times (\vec{v} \times \vec{B}). \quad (\text{II-69})$$

Corresponding, the ideal MHD equations in Eulerian form (following Teyssier, 2015) are given by

$$\frac{\partial \rho \vec{v}}{\partial t} + \vec{\nabla} \cdot (\rho \vec{v} \otimes \vec{v} + p \mathbb{1} - \vec{B} \otimes \vec{B}) = 0 \quad (\text{II-70})$$

$$\frac{\partial \rho}{\partial t} + \vec{\nabla} \cdot (\rho \vec{v}) = 0 \quad (\text{II-71})$$

$$\frac{\partial E}{\partial t} + \vec{\nabla} \cdot (\vec{v} (E_{MHD} + p_{MHD}) - \vec{B} (\vec{B} \cdot \vec{v})) = 0 \quad (\text{II-72})$$

with the total energy density and pressure

$$E_{MHD} = E_{HD} + \frac{1}{2} \vec{B} \cdot \vec{B} = \rho u + \frac{1}{2} \rho |\vec{v}|^2 + \frac{1}{2} \vec{B} \cdot \vec{B} \quad (\text{II-73})$$

$$p_{MHD} = p_{HD} + \frac{1}{2} \vec{B} \cdot \vec{B} = (\gamma - 1) \rho u + \frac{1}{2} \vec{B} \cdot \vec{B} \quad (\text{II-74})$$

II-2.3 Importance of non ideal MHD

So far we have only considered ideal MHD. In this section we want to briefly elaborate on non-ideal MHD effects and their importance for astrophysical simulations. So far we assumed total ionisation of the gas we treat using the equations of magneto-hydrodynamics. Later this section we come back to calculations of ionisation degrees, but for the moment we drop this assumption. Partial ionisation gives rise to the three main non-ideal MHD effects:

1. **Ohmic resistivity:** Drift between electrons and ions / neutral particles where none of the charged particles are dynamically tied to the magnetic field; Ions and electrons frequently collide with neutrals over one electron gyration time
2. **Hall effect:** Drift between electrons and ions with electrons being tied to the magnetic field; Ions are collisionally coupled to neutral gas
3. **Ambipolar diffusion:** Drift between ions and neutral particles with both electrons and ions being tied to the magnetic field

The importance of either these effects varies respectively, depending mainly on the gas density and the magnetic field strength. Recently the importance of these non-ideal MHD effects has been noted by several authors in the field of protoplanetary disks where they are a proposed solution for the so called magnetic braking catastrophe - the inability of numerical simulations to produce rotationally supported Keplerian disks in the presence of typical magnetic field strengths as observed in molecular clouds (see e.g. [Wurster, Price, and Bate, 2016](#), and references therein). Non ideal MHD effects may actually play an important role there, as low ionisation fractions in molecular clouds have actually been calculated already by [Mestel and Spitzer, 1956](#).

Following [Wurster, Price, and Bate, 2016](#), the three effects manifest as an additional term on the right hand side of the induction equation, as

$$\frac{\partial \vec{B}}{\partial t} \bigg|_{\text{Resistivity}} = -\vec{\nabla} \times \left(\eta_R \left(\vec{\nabla} \times \vec{B} \right) \right) \quad (\text{II-75})$$

$$\frac{\partial \vec{B}}{\partial t} \bigg|_{\text{Hall}} = -\vec{\nabla} \times \left(\eta_H \left(\vec{\nabla} \times \vec{B} \right) \times \hat{B} \right) \quad (\text{II-76})$$

$$\frac{\partial \vec{B}}{\partial t} \bigg|_{\text{Ambipolar}} = -\vec{\nabla} \times \left(\eta_A \left(\left(\vec{\nabla} \times \vec{B} \right) \times \hat{B} \right) \times \hat{B} \right). \quad (\text{II-77})$$

The three resistivity coefficients η_i are given by [Wardle and Mark, 2007](#) and further depend on the conductivities of the different particle species.

In order to evaluate the importance of non-ideal MHD effects for general astrophysical simulations, we follow the calculations of [Balbus and Henri, 2008](#) regarding the so called Prandtl number. This quantity is named after the German engineer Ludwig Prandtl, who contributed a lot of knowledge and research to the field of fluid dynamics. The Prandtl number is defined as the relation of viscosity to conductivity of a fluid:

$$P_m = \frac{\nu_{visc}}{\nu_M} = \frac{Re_m}{Re_h} \quad (\text{II-78})$$

In our case it can be written as the viscous diffusivity ν_{visc} divided by the magnetic diffusivity ν_M or as the inverse fraction of the related Reynolds numbers. Depending on the order of magnitude of this dimensionless quantity we can judge upon the importance of non-ideal MHD effects, as they are following diffusion equations. Assuming a fully ionised plasma consisting of 90% hydrogen and 10% helium and following [Spitzer, 1962](#) we can estimate the two diffusivities as

$$\nu_{visc} \approx \frac{10^{-15} \cdot T[K]^{5/2}}{\rho[g/cm^3] \cdot \ln \Lambda_{H-H}} \text{ cm}^2 \text{ s}^{-1} \quad (\text{II-79})$$

$$\nu_M \approx \frac{10^{12} \cdot \ln \Lambda_{e-H}}{T[K]^{3/2}} \text{ cm}^2 \text{ s}^{-1} \quad (\text{II-80})$$

with ρ the density and $\ln \Lambda$ the Coulomb logarithm for scattering either of protons by protons or protons by electrons. Therefore, we get

$$P_m \approx 10^{-27} \cdot \frac{T[K]^4}{\rho[g/cm^3] \cdot \ln \Lambda_{H-H} \ln \Lambda_{e-H}}. \quad (\text{II-81})$$

Using our assumptions on the gas composition we can calculate the mean molecular weight as

$$\mu = \frac{1 + 4 \cdot Y_{He}}{2 + 3 \cdot Y_{He}} \cdot m_p \approx 0.5 m_p \quad (\text{II-82})$$

using

$$Y_{He} = \frac{1 - X_H}{4 \cdot X_H} \approx 0.03 \quad (\text{II-83})$$

with X_H the hydrogen and Y_{He} the helium fraction of the gas. Using

$$\rho = \mu \cdot n_H \quad (\text{II-84})$$

and assuming an approximate value of 40 for the product of coulomb logarithms we get

$$P_m \approx 10^{-5} \frac{T[K]^4}{n_H[\text{cm}^{-3}]} \quad (\text{II-85})$$

In table [II.1](#) we present approximative values for different astrophysical environments. Even if the assumptions have been very crude, we get a feeling for the order of magnitude. If the Prandtl

System	$\langle T \rangle [K]$	$\langle n_H \rangle [cm^{-3}]$	$\langle P_m \rangle$
Galaxy cluster ICM	10^8	10^{-3}	10^{30}
H-II Clouds	10^4	10^3	10^8
H-I Clouds	10^2	10^2	10^1
Molecular Clouds	10^1	10^4	10^{-5}

Table II.1: Prandtl numbers estimated for different astrophysical systems.

number is way bigger than one we can conclude, that non-ideal MHD effects will most probably not have a big influence in the respective system due to magnetic fields being dynamically unimportant. They are most probably only important in rather cold and dense systems, like star formation regions but not in the hot gas in galaxies and galaxy clusters.

Additionally, as mentioned in the beginning of the section, we take a look at calculating the degree of ionisation of a gas. For that we consider the Saha-Boltzmann equation and for simplicity assume a pure Hydrogen gas:

$$\frac{n_e^2}{n - n_e} = \frac{2}{\lambda_{tdB}^3} \frac{g_1}{g_0} \exp\left(-\frac{13.6eV}{k_B T}\right) =: A(T), \quad (\text{II-86})$$

with the thermal deBroglie wavelength

$$\lambda_{tdB} = \sqrt{\frac{h^2}{2\pi m_e k_B T}} = 7,5 \cdot 10^{-6} \left(\frac{T}{1K}\right)^{-1/2} cm \quad (\text{II-87})$$

and the factor

$$\frac{g_1}{g_0} = \frac{1}{2} \quad (\text{II-88})$$

which are the statistical weights to account for the degrees of freedom. g_0 relates to the neutral Hydrogen and follows

$$g_n = 2(n+1)^2 \quad (\text{II-89})$$

while g_1 relates to the proton which results just in $g_1 = 1$ and does not follow that equation. We solve the equation for the ionisation fraction

$$\frac{n_e}{n} = \frac{1}{2} \cdot \left[-\frac{A(T)}{n} + \sqrt{\frac{A(T)^2}{n^2} + 4 \cdot \frac{A(T)}{n}} \right] = \frac{A(T)}{2n} \cdot \left[-1 + \sqrt{1 + 4 \frac{n}{A(T)}} \right]. \quad (\text{II-90})$$

For large values of $A(T)/n$ this breaks down, as the quadratic term dominates over the linear one so much, that the numerator in total becomes zero. To solve that issue we can Taylor expand the square root until the second order and get

$$\lim_{T \rightarrow \infty} \frac{n_e}{n} \approx 1 - \frac{n}{4A(T)} \quad (\text{II-91})$$

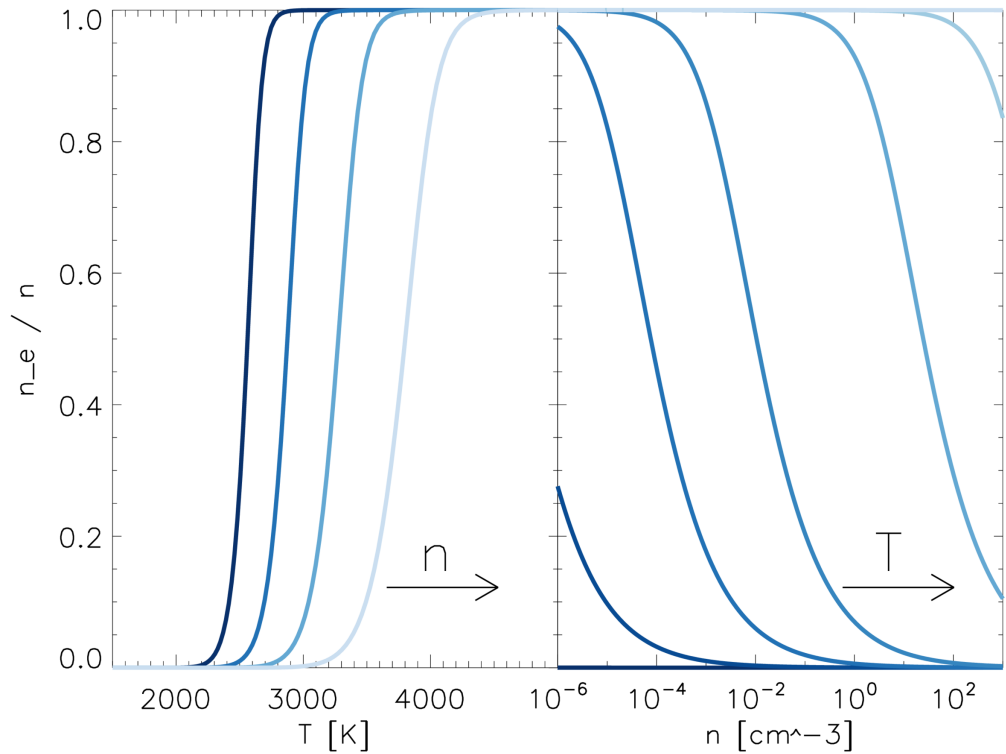


Figure II.11: Ionisation fraction due to the Saha equation for a pure Hydrogen gas at different temperatures and densities.

Left: $n \in \{10^{-6}, 10^{-3}, 1, 10^3\} \text{ cm}^{-3}$ from dark to light blue.

Right: $T \in \{2 \cdot 10^3, 2.5 \cdot 10^3, 2.75 \cdot 10^3, 3 \cdot 10^3, 3.5 \cdot 10^3, 4 \cdot 10^3, 5 \cdot 10^3\} \text{ K}$ from dark to light blue.

As shown in figure II.11, we see that in simulations of galaxies and galaxy clusters we mostly treat fully ionised plasma. The temperature dependence is way stronger than the density dependence. For the whole relevant density regime and even beyond that ionisation quickly changes from 0% to 100% due to a small temperature change, having fully ionised gas already at a few thousand Kelvin. Of course these results change when we drop the assumption of pure Hydrogen gas for a more realistic approach, however the basic conclusion stays intact.

Summing up, Ohmic resistivity, the Hall effect and ambipolar diffusion are only important for systems like molecular clouds, as recent papers like [Gressel et al., 2015](#); [Hennebelle et al., 2016](#); [Wurster, Price, and Bate, 2016](#) show, but play a very negligible role in simulations of galaxies and galaxy clusters. Therefore, we will neglect them in the work presented from here on.

II-2.4 Overview of magnetic field (simulation) history

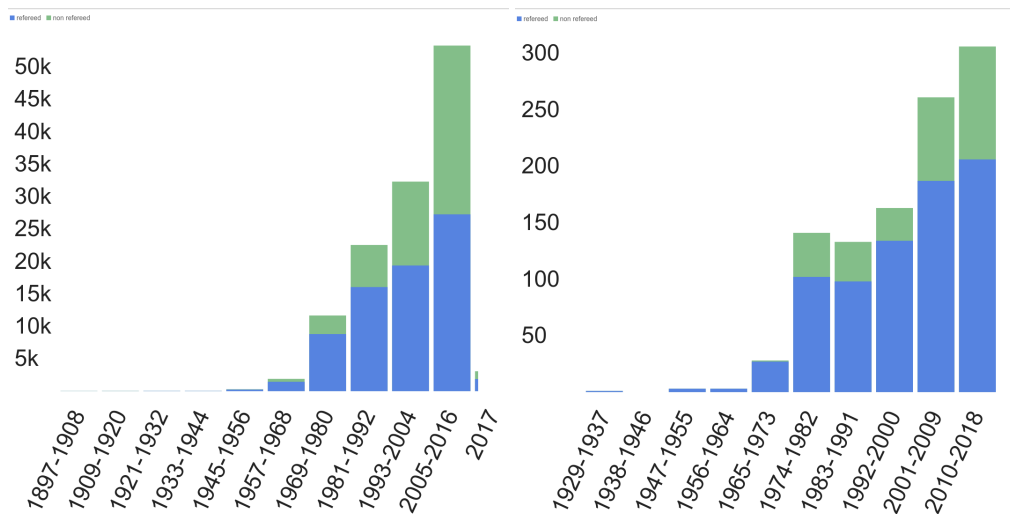


Figure II.12: Paper statistics with “magnetic field” w/o (left) and w/ (right) “numeric” in the abstract. Blue are the refereed publications, green contain also the non-refereed ones.

To conclude this discussion of magnetic fields we want to give a quick glance back in history using basic paper statistics. We use the Astrophysics Data System (ADS, see <http://adsabs.harvard.edu/>) to retrieve these data about recorded astrophysical publications. In figure II.12 we plot a histogram of publications over time which contain the words “magnetic field” in their abstract in the left panel. Please keep in mind that the further we go back, the less complete these records are. We start at the end of the 19th century, since extragalactic magnetic fields (after those of our sun) have been peaking interest even beyond that. For example [Alfvén, 1937](#) presenting work about cosmic rays and their connection to magnetic fields, [Fermi, 1949](#) reporting of μGs magnetic fields or [Hall, 1949](#) writing about observations of polarised starlight. We see a major trend of massively increased amounts of literature appearing in the second half of the 20th century. Of course that trend is not because of sudden popularity of magnetic fields but traces the increased amounts of publications per year in general. Nevertheless, with about

5000 publications per year magnetic fields have definitely earned a spot of importance. In the right panel we combine this analysis with the additional term “numeric”. The absolute numbers of publications decrease drastically. This is only a very crude and incomplete analysis but the fact that computing power needed to drastically increase before we could even think about treating magnetic fields in conjunction with for example structure formation simulations is well mirrored in this graph.

For completeness we do the same analysis only for abstracts containing “numeric” and plot the results in figure II.13. The top panel shows the full view since the first publication listed. The bottom panels show zoomed in regions of this plot with rescaled axes. Again we can see the rise in amounts of publication, now even more accelerated by the rise in computing power and the availability of computers. With this single word alone in the abstract, we have reached the point of about 35000 publications per year and rising. Considering about 15 pages as an average that would leave somebody only one minute per page to read all these papers until the year is over without any break, reading 24 hours a day, 7 days a week.

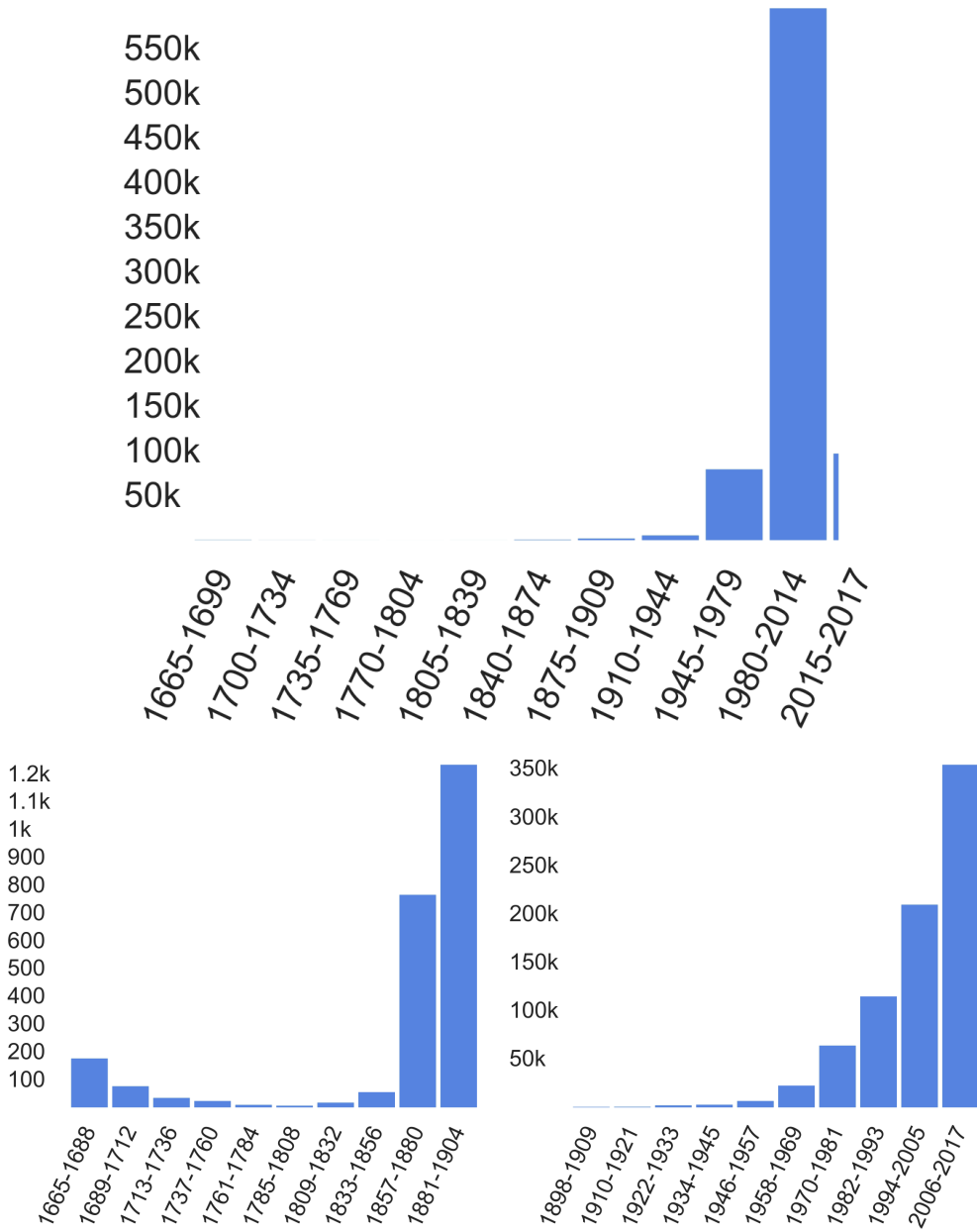


Figure II.13: Paper statistics with “numeric” in the abstract.

Chapter III

Simulation techniques: Euler or Lagrange?

In the midst of chaos, there is also opportunity

– Sun Tzu, *The Art of War*

Having described a picture of modern observational astronomy focused on magnetic fields we now come to its counterpart: numerical astrophysics which gives us the tool set to understand the underlying physical processes of what we can observe. In this chapter we give a quick introduction into the field of astrophysical simulations (section III-1), review the common types of techniques which are employed to solve the equations of (magneto-) hydrodynamics (section III-2) and describe the basics of the Smoothed Particle Hydrodynamics method and show, how the governing equations can be implemented (section III-3). After this overview we briefly mention modern hybrid approaches and some possible modifications of the standard methods (section III-4). We follow up by discussing how this plays together with an implementation of gravity on the one hand and models for complex processes like star formation on the other hand (section III-5) and conclude with a projection into the rest of this thesis and the possible future of computational astrophysics (III-6).

III-1 The history and necessity of simulations

The simulation community has grown a lot since the first astrophysical simulation conducted by [Holmberg, 1941](#). Due to the difficulty of integrating the gravitational forces in a complex system, instead of mass point tracers for the simulation of a disk galaxy [Holmberg, 1941](#) took light bulbs and put them onto a distortable frame. Exploiting the analogy of light intensity to gravity, both following a r^{-2} -law, he measured all accelerations at a certain point in time using photocells and galvanometers. Then he integrated the equation of motion for a small time step dt by moving all light bulbs according to these accelerations and started over. With this brilliant idea he could simulate the formation of spiral arms in a disk galaxy for the first time and even way before the introduction of a computer. The first NBody code to solve gravitational interaction directly was developed forty years later by [Hockney and Eastwood, 1981](#).

Nowadays things have become much easier for us, utilising the exponentially growing computing power, our capabilities to evaluate the interplay of complex numerical models in huge details has become our daily task. By this development it may seem that simulation codes are sometimes extended and improved just for the sake of improvement without any specific scientific goal in mind. Scientific in this case meaning regarding the field of physics and not computer science, where this would be exactly the goal to reach without any doubt. The easiest reply to this apprehension is the big picture itself. Like mathematics, the numerical side of, for example, computational astrophysics could become a mere tool set which is developed to answer questions coming up in the future and thereby allowing progress for the sake of itself. While this might be a valid approach for the future it actually sacrifices what is both the biggest advantage and difficulty right now: the close coupling between science goals and developing numerical ways to achieve them.

Now let us take a step back and think about why we actually require simulations nowadays. Trying to model the universe has been a long-standing desire and even before the invention of computers, people actually applied similar methods manually. On first glance one would say, that the alternative to simulations is posed by analytic calculations to solve the coupled systems of equations which we plug into our simulation codes. However, this is not really an alternative but actually integrates directly into a combined concept by posing as the direct predecessor of numerical modelling. Analytic derivations drive us so far that we can actually define the system of coupled equations we want to solve up until the point where the complexity rises to the point where we require the assistance of computer based calculations. Therefore, computer simulations are not to be seen as a replacement of traditional calculations but rather as an extension to what we can evaluate.

The advantages of simulations are easy to spot. They allow us to model all kind of physical processes from gravity and fluid dynamics to star formation and the interplay of matter and radiation. The list can be endlessly expanded to almost every field of science and we are only limited by the knowledge we acquired so far. Instead of just static images of the celestial objects we desire to study, simulations provide us with the opportunity to actually study their formation and evolution over huge periods of time, much longer than the lifespan of humanity. But this leads directly to the biggest drawback. What we can observe is actually part of nature but what simulations show us is just the result from a combination of numerical models. Even if we assume that we put all the important processes inside our simulation codes all models only present an approximation to how astrophysicists think, these processes work. All implementations are flawed by their approximate nature and in addition to numerical inaccuracy of calculations, errors can accumulate and combine to drastically different results just from minor changes. Therefore, we want to review some of the most common simulation techniques in today's astrophysical community in the next sections and give some insight in the individual capabilities, advantages and disadvantages.

III-2 Commonly used and established techniques

We start with a quick discussion of two commonly used strategies to handle the equations of (magneto-) hydrodynamics for astrophysical simulations: volume discretising *Grid* codes and

the mass discretisation approach posed by *Smoothed Particle Hydrodynamics* (SPH). Of course there exist also other techniques, modern ones as we will present afterwards and also ones which have been around for quite some time as for example the *Particle In Cell* (PIC) method. PIC simulations go back to the 1950s and 1960s, when (Buneman, 1959; Dawson, 1960; Dawson, 1962; Morse, 1969) applied this method to simulations of plasma physics. As the name already states the basic idea behind this approach is, to simulate the behaviour of (maybe few) particles, like electrons, in a volume discretised medium.

III-2.1 Volume discretisation

One of the main classes of astrophysical codes come with a volume discretised scheme. In this section we give a brief review of the basics leading to classical grid codes following Teyssier, 2015.

A volume discretisation is basically partitioning up the simulation space into grid cells. In principle these cells may be of any shape. The most fundamental being a Cartesian grid with equally sized, cubic cells. This consequently introduces predominant directions in space which may be totally arbitrary but nevertheless influence the result at least slightly. To formulate the equations of hydrodynamics (see section II-2.1) on a grid we use the Eulerian form of the Euler equations and then typically follow a finite volume approach. All relevant variables describing the (magneto-hydrodynamical) state are assigned to each cell. To evolve the system in time fluxes across cell faces are calculated and integrated. We distinguish between flow variables, which may be discontinuous, and flux functions, which appear in a divergence operator and must be continuous over cell boundaries.

Solving the conservations laws with propagating waves is a well known problem typically solved with a Godunov method (Godunov, 1959; Toro, 2009) which provides a solution through cell averaged conservative variables U as

$$\frac{\vec{U}_i^{n+1} - \vec{U}_i^n}{\Delta t} = -\frac{1}{V_i} \int_{S_i} \tilde{F} \cdot \vec{n} \, dS \quad (\text{III-1})$$

with the face's normal vector \vec{n} and the time averaged flux

$$\tilde{F} = \frac{1}{\Delta t} \int_{t^n}^{t^{n+1}} \vec{F} dt. \quad (\text{III-2})$$

Here i is the cell index and n denotes the iteration step, meaning the point in time. This can be used to generate a numerical scheme at any order of accuracy for any mesh geometry (Harten, Lax, and Leer, 1983). First order results in a piecewise constant, second order in a piecewise linear formulation and so on. The first order accurate scheme is well known as the so called Riemann problem which allows due to self similarity properties to straight forwardly calculate the flux functions. The Riemann problem is very well studied and multiple solvers have been presented and utilised over the years. We can primarily distinguish between exact and approximate Riemann solvers. As the name says, the former solves the Riemann problem directly which, however, is computationally very expensive. Therefore, usually approximate solvers are used.

They converge towards the correct result and the iteration process can be terminated after much less computation time when reaching the desired level of accuracy. For a review of different Riemann solvers we refer to [Toro, 2009](#). [Teyssier, 2015](#) mention the Lax-Friedrich flux function ([LeVeque, 1992](#)) as the simplest one. For that, the flux function between left state L and right one R is given by

$$F(\vec{U}_L, \vec{U}_R) = \frac{\vec{F}_R + \vec{F}_L}{2} - \frac{S_{max}}{2} (\vec{U}_R - \vec{U}_L) \quad (\text{III-3})$$

with S_{max} being the maximal wave speed in both cells. To make this better understandable

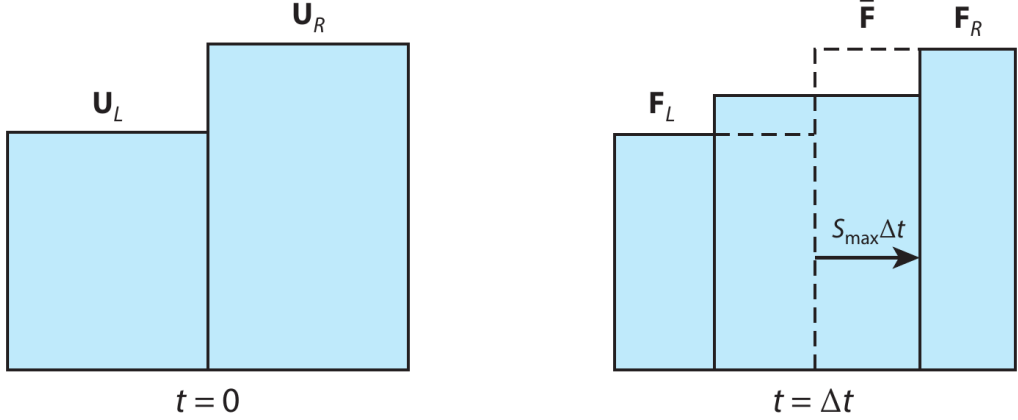


Figure III.1: Illustration of the one dimensional Riemann problem. Taken from [Teyssier, 2015](#).

we show a schematic for the one dimensional Riemann problem in Figure III.1. The left panel shows the initial state at $t = 0$, with the two states $\vec{U}_L \neq \vec{U}_R$. The right panel shows the fluxes between cells and illustrates how the maximum wave speed and the time step correspond to the cell size. On first glance one could say that the first term of equation III-3 should be already sufficient since it depicts the average of the left and right fluxes and is a second order accurate approximation of the flux through the cells' touching faces. The second term is introduced due to an additional problematic we have not mentioned yet. While it helps to make the numerical solution actually stable, it is typically associated with numerical diffusion proportional in strength to the cell size. It is clearly of numerical origin and unphysical. This has been a long standing problem for grid codes and reducing this diffusion component is an important task in order to improve the accuracy of any such code. For example higher order schemes help to reduce this numerical diffusion. This includes for example transitioning from a finite volume approach to a finite element one which is much harder to construct ([Zienkiewicz, 1971](#)) or going even further to a discontinuous Galerkin method ([Cockburn and Shu, 1998](#)). An alternative approach is to stick with a finite volume scheme but increase the amount of neighbouring cells taken into account. These higher order schemes lose the self similarity of the Riemann problem which makes solving them much more time consuming. Typical approaches are a predictor-corrector scheme, a Runge-Kutta solver or a high order Taylor expansion scheme ([Suresh and Huynh,](#)

1997; Titarev and Toro, 2002).

An important addition typically employed are so called slope limiters. They ensure positivity as well as smoothness of the solutions and thereby work towards suppressing oscillatory perturbation effects. Again there is quite a variety of slope limiters around, which can be considered (Hubbard, 1999).

When applying these methods to astrophysical problems they are confronted with a highly compressible medium with discontinuities and singularities in the important variables describing the state of the fluid. Studies show, that high order methods are for these kind of challenges typically less efficient than low order methods with higher resolution and therefore comparable computation cost. As a result typically second order schemes are used in the astrophysical community. To preserve Galilean invariance with grid codes is very hard but otherwise results are sensitive to the presence of bulk velocities Tasker et al., 2008, e.g. when simulating multiple galaxies which move relatively with very large velocities even faster than the sound speed of the dense ISM. This leads to not necessarily wrong results but such dependent on frame of reference which still not desirable.

Solving the equations of magneto-hydrodynamics poses an additional challenge on top of hydrodynamics alone. The most crucial problem all numerical approaches (not only grid codes) have to face, is the well known requirement that

$$\nabla \cdot \vec{B} = 0 \quad (\text{III-4})$$

down to numerical resolution. Since this can almost never been enforced strongly without violating any other equation but spurious monopoles can quickly lead to instabilities one typically has to settle for a trade off. Traditionally some kind of “divergence cleaning” is applied, which means that any occurring $\nabla \cdot \vec{B}$ sources are artificially removed from the magnetic field vectors. This can be done for basically any numerical scheme. A classical divergence cleaning scheme is for example given by Brackbill and Barnes, 1980:

$$\Delta\phi = \nabla \cdot \vec{B}^{old} \quad (\text{III-5})$$

$$\vec{B}^{new} = \vec{B}^{old} - \nabla\phi \quad (\text{III-6})$$

The physically incorrect magnetic field is taken, the potential leading to monopoles is calculated and it's gradient is used to calculate a monopole free, new magnetic field. More advanced approaches might also try to do that in a way which tries to conserve the magnetic energy. Nevertheless, a divergence cleaning approach is not ideal. Magnetic monopoles can still appear briefly and solving Poisson's equation (equation III-5) is rather expensive and should be avoided if possible. Additionally, higher order schemes actually need several cleaning steps (Crockett et al., 2005). A more advanced approach is for example Powell's eight-wave scheme (Powell et al., 1999) which directly accounts for monopoles but is again not strictly conservative any more.

Finally we want to address a typical issue with classical grid codes: their lack of adaptivity. If a fixed grid is used this determines the resolution achieved from the beginning of the simulation on. More resolution means a lot more grid cells and therefore an extreme increase in computing power. To solve this issue, different approaches have come up. The most well established is

probably “Adaptive Mesh Refinement” (AMR). The inherent idea is easy to understand. If we can identify regions in the simulation regime where a higher resolution is desired, for example due to high densities or velocities at that point, the corresponding grid cells are taken and divided up into smaller sub cells. This (de-) refinement is typically done using factors of two. This kind of discontinuous refinement can, however, lead to subtle errors. Small scale processes might be resolved a bit too late, delaying their evolution slightly leading to all kind of secondary effects. The implementation of an AMR scheme in a numerically stable way with low errors is highly non trivial due to the very complex resulting mesh geometry. Although it is not cheap to build such a refined grid and to keep all the structural information in memory it helps a lot to allow high resolution simulations with moderate computational cost. AMR has already been introduced by [Berger and Oliger, 1984](#); [Berger and Colella, 1989](#) in general fluid dynamics and by [Klein, McKee, and Colella, 1994](#) in astrophysics. Later it has been adapted to self gravitating cosmological flows in the code ENZO by [Bryan et al., 1995](#) which leads to difficulties with changing gravitational softening due to the refinement strategy. Moreover, self gravity itself can also be a problem for Eulerian codes, due to emerging problems conserving the total energy ([Mueller and Steinmetz, 1995](#); [Springel, 2010a](#)). [O’Shea et al., 2005](#); [Heitmann et al., 2008](#) have shown that even state-of-the-art AMR codes (at that time) had problems solving gravity as well as high precision N-body codes without meshes fine grained to an extremely resource wasting level.

Alternatively to refinement of Cartesian grids people developed algorithms for deformable Lagrangian meshes in order to let adaptivity enter directly in the mesh geometry on a more basic level ([Gnedin, 1995](#); [Pen, 1998](#)). Unfortunately mesh deformations tend to become very extreme especially in the presence of shear flows and numerical errors build up quite a lot. Furthermore, Cartesian meshes allow for more cancellation of terms in high order schemes than irregular grids ([Calhoun and LeVeque, 2000](#)). This has ultimately lead to the idea of a Moving Mesh (see e.g. [Springel, 2010b](#)), which we will come back to later in section [III-4](#).

III-2.2 Mass discretisation

In contrast to a volume discretisation scheme, we can also take the mass as our most basic discretised variable. That has the advantage, that we have a natural feeling for what happens, as we are used to think in terms of particles. The most important point has to be made right here in the beginning, when defining proper nomenclature. Typically one actually calls these mass elements particles for simplicity. However, they may, but in general do not, correspond to actual particles but rather to moving fluid parcels. That is for example the case in Smoothed Particle Hydrodynamics.

To derive the proper equations for our system, we simply use the Lagrangian form of the Euler equations as derived in section [II-2.1](#) and discretise these. A proper derivation of the resulting SPH equations follow later in section [III-3](#).

We already discussed some of the advantages and disadvantages of grid based methods, so how does a mass discretised method like SPH fit into that picture? While a grid code requires the definition of a fixed spatial domain, particles can in principle move arbitrarily in some (extendible) simulation space. Therefore, it is easier to treat phenomena like outflows without the need to cut at some point and let mass leave the simulation. Although on first glance better, mass leaving a

simulation might actually be desirable if it can be assumed that it will never flow back anyway and computing time can be saved that way. It all depends on the individual situation.

What we can straight forwardly infer from the concept of particles moving with the flow, is adaptivity of resolution. Adaptive mesh refinement is a rather complicated addition to grid codes but particle schemes do not require such a modification. High spatial resolution is required where densities are big and therefore, where a lot of mass is concentrated. That corresponds directly to an over-abundance of particles which in return represents higher resolution. That is probably the best and most important feature of a particle based scheme, because this adaptivity comes totally for free. Moreover, it explains why SPH is widely used in cosmological simulations of galaxies and galaxy clusters, where we have huge ranges of densities which we try to resolve. Furthermore, mass discretised codes are easily able to couple together, as for example an N-Body code for solving gravity and an SPH code for hydrodynamics. We come back to solving gravity in more detail later in section III-5.1. Let us just note here, that actually the first astrophysical simulations coupling self gravity and hydrodynamics have been carried out using SPH ([Efstathiou and Eastwood, 1981](#); [Evraud, 1988](#); [Hernquist and Katz, 1989](#)).

Coming back to the governing equations of (magneto-) hydrodynamics, although they are used in Lagrangian form conservation properties still hold. Further, conservation of angular momentum is given for free in a spherical symmetric particle scheme like SPH, while it is more complicated in a method based on a Cartesian grid. The same goes for Galilean invariance due to the absence of principal axes in the discretisation.

But there are also drawbacks with particle based methods, as for example the detection and treatment of shock fronts. A volume discretisation code which works on the basis of solving the Riemann problem at each cell boundary is exactly built to properly resolve shock fronts i.e. jumps at interfaces while Particle codes can not even clearly define these boundaries and therefore not give as sharp solutions at sudden discontinuities. Dissipation in sub sonic turbulence can be understood easier in grid codes, because the cell geometry gives a natural dissipation length, which is very hard to come by in a Lagrangian code. Classical SPH has a lot of further problems like proper fluid mixing which combined with the mentioned issues with shocks requires the introduction of an artificial viscosity and conductivity component. One can mitigate these problems by changing to a different form of SPH by alternating which hydrodynamical variables we discretise as the base quantities, but that only shifts the issues to other fluid variables. However, many advancements have been made over the past decade in order to improve on all these problems and provide modern astrophysical codes with a proper hydrodynamics scheme. More details on these improvements are shown later in chapter [V](#) where we describe the current state of our version of the GADGET code.

III-3 SPH formalism in details

Having described the main differences, advantages and disadvantages of both volume and mass discretised schemes we will now go into some more details of the SPH method, as it is used during the course of this thesis. The origin of SPH can be tracked back to [Lucy, 1977](#); [Gingold and Monaghan, 1977](#). During these 41 years the method has undergone drastic changes to overcome its flaws and further refine its accuracy in solving not only astrophysical problems.

Some changes are considered mandatory nowadays in the astrophysical community, some are rather side tracks of the main consensus. We go into further details about the state of the art later in chapter V and concentrate here on the basics required to understand what comes later in this thesis. When we say that SPH is not only used in astrophysics, then where is it actually relevant besides that? In Principle it can be applied anywhere, where equations of hydrodynamics have to be solved and even beyond that. It has become a very popular method in the game and movie industry, since even badly resolved simulations look very convincing to the bare eye due to the inherent smoothness of the method. Examples are for example (Spoiler alert) Gollum falling into the lava of Mount Doom at the end of “Lord of the Rings: Return of the King” (Monaghan, 2011) or various types of fluids to be experienced in “Alice: Madness Returns” (Coombes, 2011). For further reading see also Gourlay, 2013. Also other branches of sciences have picked up the method, from simulations of tsunamis (Wei et al., 2015) and earthquakes (Chen and Qiu, 2013) up to engineering simulations of turbines, wind canals or dams (Marongiu and Parkinson, 2006; Xu, 2016). These efforts have also led to the publication of open source codes like DualSPHysics (Crespo et al., 2015). We will take a look into developments of the SPH method especially outside the astrophysical community in section III-4.2.

For explaining the basic concepts and equations of SPH we use the Lagrangian formulation of the (magneto-) hydrodynamical equations derived earlier in chapter II and follow along the excellent review papers of Springel, 2010b; Price, 2012b; Somerville and Davé, 2015. Therefore, we will not give a full derivation of classical SPH and its transition towards what is typically used nowadays but start right away with a formulation of SPH derived from the fluid Lagrangian

$$L = \int \rho \left(\frac{\vec{v}^2}{2} - u \right) dV \quad (\text{III-7})$$

for inviscid ideal gas (Eckart, 1960).

III-3.1 Density approximation and kernel theory

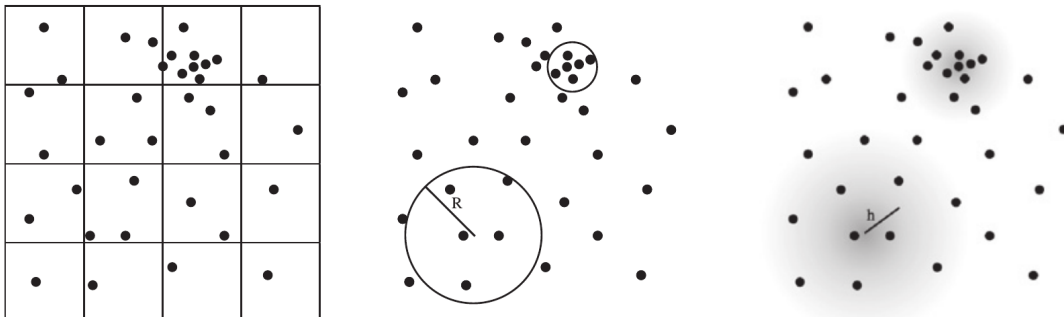


Figure III.2: Illustration of three approaches to calculate the density from mass elements. Taken from Price, 2012b.

But before we can write down the equations describing our hydrodynamical system in SPH formalism we need to define the basics required for this method. As we discretise mass elements tracing the fluid the most straight forward quantity to start with is density. One can think of several possibilities on how to calculate the density at each point in space \vec{r} from a distribution of mass points. Three of them are shown in figure III.2. The left panel depicts the easiest approach. We lay out a fixed Cartesian grid over the volume and in each cell the density is given by sum of all mass elements inside the cell divided by the volume. The question is, would we gain anything from this approach instead of just working with a grid right away? Probably not. The second approach we show is to take a spherical region of influence around each particle in which the density is again calculated as sum of all masses divided by the spherical volume. This has the advantage of Galilean invariance leading to the conservation of angular momentum and allows us to evaluate each position by drawing a sphere around it. In addition, it provides us with the possibility of adaptivity if the radius of the sphere is calculated individually for each particle to keep for example the mass in each sphere constant leading to shorter radii in regions with larger clustering of mass elements (assuming equal mass elements). The third option in the right panel adds another improvement on top of the second method which is shown by the grey shaded region. Masses are not simply summed up any more, they are rather weighted inversely by their distance to the sphere centre. The idea behind this, that the closer a particle sits to the evaluation spot \vec{r} , the more important it's contribution should be. This is the general basis of the Smoothed Particle Hydrodynamics approach. The density can then be expressed like

$$\rho(\vec{r}) = \sum_j^{N_{ngb}} m_j W(|\vec{r} - \vec{r}_j|, h) \quad (\text{III-8})$$

with W the weighting or so called kernel function with a smoothing radius (or length) h and N_{ngb} the number of neighbouring particles. A quick dimensional analysis reveals the unit of W to be an inverse volume. In order to find a good candidate for the kernel function we can list a few basic requirements it should fulfil:

- Positivity
- Monotonically decreasing to weight closer mass elements more than those further away
- Smoothness of derivatives
- Dependency only on the absolute distance and a smoothing length
- Flat central region to reduce impact of small dislocations
- Normalised to unity when integrated over the volume
- Finite in order to decrease computational cost.

A natural choice fulfilling all of the above except the last one is the Gaussian. However, since it never truncates in principle all particles have to be taken into account as neighbours, even if their contributions become very small which leads to an unnecessary high computational cost.

A typical approach is then to truncate a Gaussian artificially, violating the smoothness of derivatives at maximum radius. Alternative approaches try to mimic the form of the Gaussian using polynomials as for example the well established spline functions which are generated from a Fourier transform (Schoenberg, 1973; Monaghan and Lattanzio, 1985). Other popular choices are for example Core-Triangle or High Order Core-Triangle (HOCT) kernels (Read, Hayfield, and Agertz, 2010) or the Wendland functions (Dehnen and Aly, 2012). These try to solve two known issues with SPH: The so called tensile or clumping instability (first described by Swegle, Hicks, and Attaway, 1995) and the pairing instability. Although both instabilities show the same symptoms, particles unphysically clumping together, they emerge due to different reasons. While the tensile instability appears due to a (originally kernel independent) effective negative pressure, the pairing instability comes from a negative Fourier transform of the kernel function (Dehnen and Aly, 2012). The HOCT kernels try to help mitigate the tensile instability by introducing a constant central core to the kernel gradient, resulting in a constant force term in the centre to prevent this clumping sacrificing monotonicity in the very central region. Different approaches instead of a peaked kernel are for example an artificial steepened first derivative of the kernel (Steinmetz, 1996) or an artificial pressure term (Monaghan, 2000). While the tensile instability is very well observed in idealised test cases it is, however, hardly seen in reality due to dynamics overshadowing the effect (Springel, 2010b). The pairing instability is really a direct result from the kernel itself, actually adding another requirement to the list above: a positive Fourier transform. Therefore, Dehnen and Aly, 2012 propose the Wendland functions which adhere to this demand. The pairing instability typically arises when the kernel sizes are chosen too big or correspondingly a large neighbour number is desired. Classical kernels limit the amount of neighbours drastically by this instability, but not so the Wendland functions.

All of the mentioned state of the art kernel functions come in different orders. Higher order kernels are computationally slightly more expensive due to additional terms but approximate a Gaussian better than lower order ones leading to possibly better convergence. Nevertheless, choosing a moderate kernel order is usually advisable since higher order kernels can induce additional instabilities (Wendland, 2017).

A further well known error arising is the so called kernel bias which originates in the contribution of the central particle (see e.g. Whitworth, 1995). Taking a perfectly uniform density distribution and calculating the density with different kernels and varying neighbour numbers reveals that sometimes the density actually under- or overestimated as shown in figure III.3. This figure, taken from Dehnen and Aly, 2012, illustrates the degree of bias in the density calculating for varying types of initial configurations (like lattice, glass, etc), kernel functions and neighbour numbers, which can even reach the percent level for small number of neighbours. Even sub-percent levels of errors are bad, since they immediately translate into every other fluid variable and calculation and may over time flaw any simulation result. All these initial distributions plotted are not fully random but adhere to some internal structure. The topic of proper initial conditions is very complex and we come back to it later in chapter IV. Only for a totally random distribution evaluating the density at a position where no particle sits would not result in such a density error (Silverman, 1986), while at a particle position the self contribution ($W(0, h)$) results in an overestimate. A quasi random distribution can then result in any kind of error, even none for some special cases as we can see at about 32 or 64 neighbours for the cubic spline

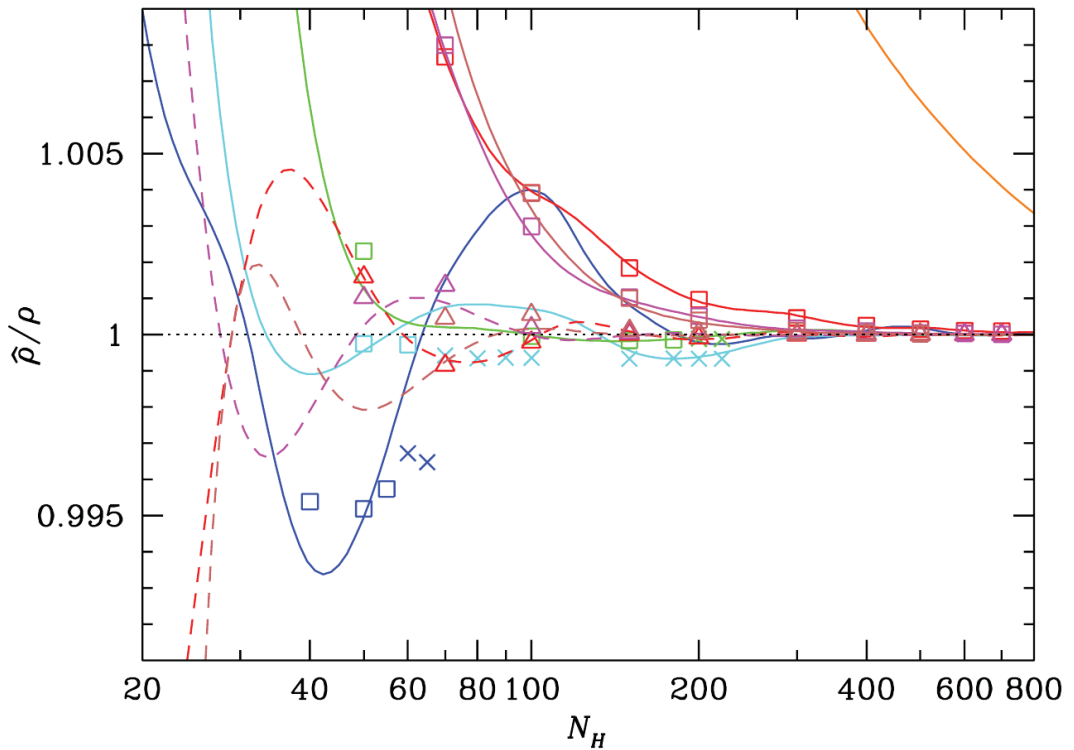


Figure III.3: Density calculated with different initial conditions (symbols) and different kernels (colours) for the same uniform density illustrating the kernel bias. Plotted is the number of particles inside the kernel (neighbour number) against the density calculated via SPH divided by the actual density. Taken from [Dehnen and Aly, 2012](#).

(blue). Due to the oscillatory nature of this error for spline kernels it is very hard to find a computationally cheap correction for all neighbour numbers, which is why these sweet spots have become very popular choices. The HOCT4 kernel (plotted in orange) shows the biggest error which is very well understandable due to its central shape. The Wendland kernels (different orders plotted in tones of red), as focused on by [Dehnen and Aly, 2012](#), show a moderate level of bias which decreases monotonically with neighbour number. On the one hand this suggests to use quite large neighbour numbers to mitigate this error and on the other hand it makes it rather straight forward to find a fit simple fit function to correct for the bias for all relevant numbers of neighbours. This is required for a code like GADGET, where we input a desired mean number of neighbours which can, however, fluctuate quite drastically between individual particles. During the course of a Bachelor's thesis we have investigated the kernel bias and confirmed the results of [Dehnen and Aly, 2012](#).

Summing up, in Gadget we typically use the WendlandC4 or C6 kernel with a few hundreds of neighbours in three dimensions, as shown later in chapter [V](#).

Now that we have investigated the fundamentals of SPH we can proceed to show how we can actually write down any equation in SPH formalism starting with the following identity for an arbitrary variable A :

$$A(\vec{r}) = \int A(\vec{r}') \delta(\vec{r} - \vec{r}') d\vec{r}'. \quad (\text{III-9})$$

Next, we replace the delta function with the kernel and split up the integral into the mean value and error terms. The mean value of A expanded by a factor $1 = \rho(\vec{r}') / \rho(\vec{r})$ then looks like

$$\langle A(\vec{r}) \rangle = \int \frac{A(\vec{r}')}{\rho(\vec{r}')} W(|\vec{r} - \vec{r}'|, h) \rho(\vec{r}') d\vec{r}' \quad (\text{III-10})$$

$$\approx \sum_j^{N_{ngb}} m_j \frac{A_j}{\rho_j} W(|\vec{r} - \vec{r}_j|, h). \quad (\text{III-11})$$

Consequently we can express the quantity A of particle i as

$$A_i \approx \sum_j^{N_{ngb}} m_j \frac{A_j}{\rho_j} W_{ij}(h_i) \quad (\text{III-12})$$

introducing a shortened version to write down a kernel function

$$W_{ij}(h_i) = W(|\vec{r}_i - \vec{r}_j|, h_i), \quad (\text{III-13})$$

which is symmetric under exchange of particle index. A similar derivation can be made for derivatives of A which results in:

$$\mathcal{D} A_i \approx \sum_j^{N_{ngb}} m_j \frac{A_j}{\rho_j} \mathcal{D} W_{ij}(h_i) \quad (\text{III-14})$$

for any spatial derivative operator e.g. $\mathcal{D} = \vec{\nabla}_k = \frac{\partial}{\partial \vec{r}_k}$ or even the unity operator. This is consistent with equation III-8 as the density of a particle i as

$$\rho_i = \sum_j^{N_{ngb}} m_j W_{ij} (h_i) \quad (\text{III-15})$$

which can be considered the probably most fundamental equation of traditional SPH. For variable smoothing lengths this equation has to be solved in conjunction with

$$h_i = h(\vec{r}_i) = \eta \left(\frac{m_i}{\rho_i} \right)^{1/d} \quad (\text{III-16})$$

with d the number of spatial dimensions considered and η a constant factor depending on the relation between kernel support radius and smoothing length (see e.g. [Dehnen and Aly, 2012](#)). Constant smoothing lengths instead make it easier derive some equations and prove properties of the algorithm (as we will see in the next section) but without this adaptivity SPH loses its most important benefit. Properly considering also variations of smoothing lengths and the continuity equation (equation II-44) leads to the full time and spatial derivatives of the density as follows:

$$\frac{d\rho_i}{dt} = \frac{1}{\Omega_i} \sum_j^{N_{ngb}} m_j (\vec{v}_i - \vec{v}_j) \cdot \vec{\nabla}_i W_{ij} (h_i) \quad (\text{III-17})$$

$$\vec{\nabla}_i \rho_j = \frac{1}{\Omega_j} \sum_k^{N_{ngb}} m_k \nabla_i W_{jk} (h_j) (\delta_{ij} - \delta_{ik}) \quad (\text{III-18})$$

with a term depending on variations of h :

$$\Omega_i = 1 - \frac{\partial h_i}{\partial \rho_i} \sum_j^{N_{ngb}} m_j \frac{\partial W_{ij} (h_i)}{\partial h_i}. \quad (\text{III-19})$$

We will not go into a full analysis of errors in SPH, as it is done in the mentioned review articles, but close with a quick remark derivatives. So far there is still some degree of ambiguity present in the formulation of SPH we have presented up until now. This can be exploited to improve the correctness of discretisations. For example calculating the gradient of a quantity A_i as given by equation III-14 can be expanded into error terms. Subtracting the 0th order term results in

$$\vec{\nabla} A_i \approx \sum_j^{N_{ngb}} \frac{m_j}{\rho_j} (A_j - A_i) \vec{\nabla}_i W_{ij} \quad (\text{III-20})$$

which gives a much better estimate and can be interpreted as

$$\vec{\nabla} A \approx \langle \vec{\nabla} A \rangle - A \langle \vec{\nabla} 1 \rangle \quad (\text{III-21})$$

and applying equation III-14. Similar corrections can be carried out in different cases. Also the straight forward definition of a second order derivative is numerically very problematic but a much better derivative operator can be actually found. This will become important in chapter [VIII](#) where we present the implementation of thermal conduction in the presence of magnetic fields in SPH.

III-3.2 (Magneto-) Hydrodynamics

Having outlined the basics of the SPH method we can proceed by transforming the equations of magnetohydrodynamics into the formalism. Starting with the fluid Lagrangian (equation III-7) and applying the least action principle results in the Euler-Lagrange equations of our system which give us the equations derived earlier in section II-2. For further reference regarding an implementation of the more general Navier-Stokes equation in SPH see for example [Liu and Liu, 2003](#). We get the equations of motion

$$\frac{d\vec{v}_i}{dt} = - \sum_j m_j \left(\frac{p_i}{\Omega_i \rho_i^2} \vec{\nabla}_i W_{ij} (h_i) + \frac{p_j}{\Omega_j \rho_j^2} \vec{\nabla}_i W_{ij} (h_j) \right). \quad (\text{III-22})$$

For constant smoothing lengths Ω becomes 1 and this simplifies to

$$\frac{d\vec{v}_i}{dt} = - \sum_j m_j \left(\frac{p_i}{\rho_i^2} + \frac{p_j}{\rho_j^2} \right) \vec{\nabla}_i W_{ij}. \quad (\text{III-23})$$

We see directly the conservation of linear momentum by calculating

$$\frac{d}{dt} \sum_i m_i \vec{v}_i = \sum_i m_i \frac{d\vec{v}_i}{dt} = 0 \quad (\text{III-24})$$

because of the antisymmetry of the kernel gradient with respect to permutation of the particle index:¹

$$\sum_{ij} \vec{\nabla}_i W_{ij} = - \sum_{ij} \vec{\nabla}_j W_{ij} = 0. \quad (\text{III-25})$$

Geometrically speaking for a particle pair i, j we look down the gradient from one particle but up the gradient if we switch perspective to the other particle. The same argument holds also for conservation of angular momentum when looking at

$$\sum_i m_i \vec{r}_i \times \frac{d\vec{v}_i}{dt} = 0. \quad (\text{III-26})$$

These conservational properties correspond directly to invariance under translation and rotation as generally known from Noether's theorem.

Next up is the energy equation which can be derived for either the specific internal energy, the total specific energy or, as typically favoured, a function of the entropy² $A(S)$ (see also [Ryu et al., 1993; Springel and Hernquist, 2002](#)):

$$A(S) = \frac{P}{\rho^\gamma} = (\gamma - 1) \frac{u}{\rho^{\gamma-1}}. \quad (\text{III-27})$$

It is related to the thermodynamic entropy as given by

$$S = N \cdot \frac{3}{2} k_B \left[\ln \left(\frac{mA}{N} \right) + \ln \left(\frac{2\pi m^{5/3}}{h^2} \right) + \frac{5}{3} \right] \quad (\text{III-28})$$

¹Remember that the kernel itself is symmetric, so it all comes down to the gradient.

²Often just called entropy for simplicity.

with the number of atoms N . The change of specific internal energy is given by

$$\frac{du_i}{dt} = \frac{p_i}{\rho_i^2} \frac{d\rho_i}{dt} = \frac{p_i}{\Omega_i \rho_i^2} \sum_j m_j (\vec{v}_i - \vec{v}_j) \cdot \vec{\nabla}_i W_{ij} (h_i) \quad (\text{III-29})$$

using the time derivative of the density from equation III-17. With this we can confirm energy conservation by calculating

$$\frac{dE_i}{dt} = \sum_i m_i \frac{de_i}{dt} = \sum_i m_i \left(\vec{v}_i \cdot \frac{d\vec{v}_i}{dt} + \frac{du_i}{dt} \right) = 0 \quad (\text{III-30})$$

which holds due to the same antisymmetry argument as before.

Now we can extend this to MHD. The first implementation of magnetic forces in SPH has been performed by [Gingold and Monaghan, 1977](#) while the first full MHD implementation was presented by [Phillips and Monaghan, 1985](#). As in chapter II we add the magnetic pressure to all the terms containing the hydrodynamical pressure and additionally transform the induction equation which then looks like

$$\frac{d}{dt} \left(\frac{\vec{B}_i}{\rho_i} \right) = - \sum_j m_j (\vec{v}_i - \vec{v}_j) \frac{\vec{B}_i}{\Omega_i \rho_i^2} \cdot \vec{\nabla}_i W_{ij} (h_i). \quad (\text{III-31})$$

The equations of motion (equation III-22) component wise transforms to

$$\frac{dv_i^a}{dt} = \sum_j m_j \left(\frac{S_i^{ab}}{\Omega_i \rho_i^2} \nabla_i^b W_{ij} (h_i) + \frac{S_j^{ab}}{\Omega_j \rho_j^2} \nabla_i^b W_{ij} (h_j) \right) \quad (\text{III-32})$$

using Einstein's sum convention over index b and introducing the MHD stress tensor (in cgs units)

$$S^{ab} \equiv - \left(P + \frac{1}{8\pi} \vec{B}^2 \right) \delta^{ab} + \frac{1}{4\pi} B^a B^b. \quad (\text{III-33})$$

The total specific energy

$$e = \frac{1}{2} v^2 + u + \frac{1}{8\pi} \frac{B^2}{\rho} \quad (\text{III-34})$$

changes accordingly to

$$\frac{de_i}{dt} = \sum_j m_j \left(\frac{S_i^{ab}}{\Omega_i \rho_i^2} v_j^a \nabla_i^b W_{ij} (h_i) + \frac{S_j^{ab}}{\Omega_j \rho_j^2} v_i^a \nabla_i^b W_{ij} (h_j) \right). \quad (\text{III-35})$$

Similar to grid codes SPH also requires a divergence cleaning mechanism, to keep the magnetic fields source free. [Price, 2012b](#) give an extensive review over different types of cleaning methods, which we will not cover here. We just want to mention that carrying out divergence cleaning in the context of a cosmological simulation is an additional challenge on top.

As already mentioned in section III-2.2 there are some flaws SPH brings along and solutions for them, which we need to talk about. The Euler equations natively produce shocks and contact

discontinuities (Landau and Lifschitz, 2007) leading to Rankine-Hugoniot jump conditions at the shock front where the entropy is always increased. Therefore, we need some kind of treatment of viscosity - be it physical or artificial - to dissipate kinetic energy into heat and thereby producing the required entropy. Additionally comes the introduction of an artificial conductivity term to improve fluid mixing and an artificial dissipation of magnetic energy similar to viscosity but for MHD shocks resembling a resistivity term. An in depth analysis of the state of the art formulations of the artificial hydrodynamics terms is given later in chapter V.

However, these are not the only options to circumvent these issues. What we have presented so far is known as the “Density-Entropy” formulation of SPH (assuming we evolve A and not actually u or e , which would then be called “Density-Energy” formulation). An alternative has come up and become also quite popular, called the “Pressure-Entropy” formulation. Instead of a smooth density it evolves the pressure, keeping it smooth and therefore circumventing the artificial surface tension otherwise leading to issues with the pressure (Ritchie and Thomas, 2001; Read, Hayfield, and Agertz, 2010; Saitoh and Makino, 2013; Hopkins, 2013; Hu et al., 2014). For a derivation of the evolution equations for these different formulations in comparison see e.g. Hopkins, 2013. While this apparently solves the issue it actually just shifts it somewhere else: the density. It is highly application dependent which formulation is then actually the most desirable. For example in constant pressure and variable density fluid mixing tests a pressure instead of density formulation is superior and vice versa. In real applications the, although significant, impact of these different approaches can be totally hidden by the effects of all the different physical models part of a complex astrophysical code.

As we typically treat classical fluids ($v \ll c$), we do not present an implementation of relativistic hydrodynamics into SPH here but refer the interested reader to Springel, 2010b and references therein.

Finally, we have not talked about how to actually evolve the presented equations in time. It has become state of the art to assign individual time steps for each particle, typically in a power of two hierarchy (Hernquist and Katz, 1989) using a standard Courant criterion to calculate Δt

$$\Delta t_i = C \cdot \frac{h_i}{v_i^{sig}} \quad (\text{III-36})$$

depending on a dimensionless parameter C , the smoothing length h_i and the signal velocity v_i^{sig} which may be equal to the sound speed or the Alfvén speed of the fluid. This incorporates well small time steps due to both high densities and fast fluid flows.

In general symplectic integration schemes (Hairer, Wanner, and Lubich, 2002; Springel, 2005a) such as Leapfrog are most common and desired because they are time reversible and therefore do not violate energy conservation. However, to construct a high order symplectic scheme is quite challenging and carrying it out is time consuming. Springel, 2010b argues that since simulations typically contain not only (magneto-) hydrodynamics but also a lot of other problems, they are nevertheless typically not time reversible any more, even if a symplectic integrator is chosen. Therefore, it is not most important to stick to a symplectic integrator but maybe go to a more standard high order scheme like Runge-Kutta or a predictor-corrector method.

III-4 Modern approaches: Everything we need from now?

Grid and SPH codes are well established in the astrophysical simulation community. People have made great efforts to come around their flaws and thereby modern hybrid approaches have arisen and celebrated their débüt in astrophysics during the past decade. In this section we present the key thoughts behind the two main competitors of “classical” codes: “Moving Mesh” and “Meshless Finite Mass / Volume” and give some insight into the question if these approaches could (and should) replace classical Eulerian and SPH codes completely. Additionally we present a quick survey over modified versions of SPH which have been developed not only for astrophysics and close with an overview over the current code landscape.

III-4.1 Hybrid approaches: Moving mesh and Meshless

We already briefly touched the idea of a Lagrangian, deformable mesh back in section III-2.1 but came to the conclusion that this becomes problematically very quickly because of mesh distortions for example in strong shear flows (Vilar, Maire, and Abgrall, 2014). In rotating flows the mesh can even tangle itself. The moving mesh concept follows this approach directly but circumvents these distortions in a clever way. For this description we follow Springel, 2010a who describes the concept as it is applied in the AREPO code.

The main idea is to combine the ability of Eulerian codes to treat shocks with very high accuracy and the inherent adaptivity of a Lagrangian approach without the diffusivity of a classical grid code. Whitehurst, 1995 presented as one of the first a hydrodynamical code utilising Voronoi tessellation to circumvent this problem. Gnedin, 1995; Pen, 1998 tried to approach the mesh distortions using a remeshing algorithm whenever they become to large, which is very challenging, computationally expensive and adds numerical diffusion. The generic term for these types of codes is “arbitrary Lagrangian-Eulerian” in short ALE. Inspired by these predecessors Springel, 2010a construct their code based upon a Voronoi mesh constructed from a set of mass points instead of a classical Cartesian one. The density of each cell is given by the particle mass divided by the Voronoi cell’s volume, following Hess et al., 2010. Due to the mathematical properties of the Voronoi tessellation deformations are prevented by a frequently changing mesh topology which also circumvents the need for a mesh refinement technique to gain better mass resolution. A Voronoi tessellation of space for a given set of points is defined such, that each cell contains all the volume closer to the corresponding point than to all other points. Therefore, we get polyhedra in three dimensions whose faces are equidistant to the original points. An illustration for better understanding of this concept (in two dimensions) is shown in the left panel of figure III.4. with S_{max} being the maximal wave speed in both cells.

For practical reasons we can compute the Delaunay triangulation instead of the Voronoi tessellation since they are topologically dual to each other. In the picture of a Delaunay triangulation the set of points gives the vertices of triangles (in two dimensions) defined uniquely such that the circumcircle around each triangle contains no other mesh generating point. In three dimensions we have tetrahedra instead of triangles and spheres instead of circles correspondingly. This is depicted in the middle panel of figure III.4. The mid points of the Delaunay triangles form the vertices of the Voronoi cells and for each line an orthogonal face is corresponding as shown in the right panel. Constructing these kind of meshes is a well known task and literature con-

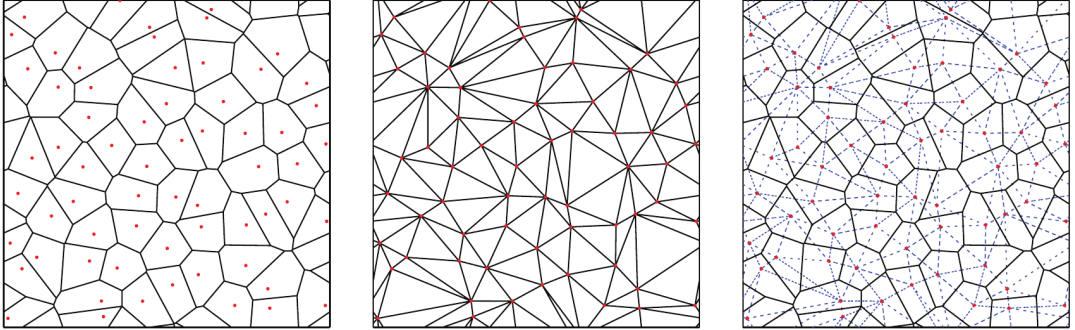


Figure III.4: Illustration of a 2D Voronoi grid (left), the corresponding Delaunay triangulation (middle) and both overlayed with each other (right). Taken from [Springel, 2010a](#).

tains multiple different algorithms to approach that. [Springel, 2010a](#) chose the “incremental insertion” ([Bowyer, 1981](#); [Watson, 1981](#)) which is among the fastest of these algorithms and allows to compute the grid without prior knowledge of the amount of mesh generating points which helps to formulate it in a well parallelisable way. We present a sketch guiding through the different steps of this approach in figure III.5. The basic idea behind it is, to take an existing triangulation, add an additional point and split the triangle in which it sits into three. Then for each triangle the circumcircle is tested and edges are flipped until all triangles pass the test.

Having constructed the mesh associated with a set of mass points a Godunov type method can be used to solve the Riemann problem across each face. [Springel, 2010a](#) use a MUSCL-Hancock scheme as basis for their work ([Leer, 1984](#)). Also slope limiters, as discussed earlier, come into play here. The choice of slope limiter poses a trade-off between numerical dissipation of the scheme and emerging post-shock oscillations. Since the mesh is not a Cartesian one, operators can not be split along the principal axes but a more complex vector based calculation has to be carried out. Galilean invariance of the scheme is possible by tying the mesh movement (due to movement of the underlying mass points) to the fluid motion (which is not a general requirement for ALE schemes). This does not strictly guarantee that all cell faces also move with exactly with the fluid motion, resulting still in mass flux between cells, albeit rather small. Therefore, one can describe the scheme probably best as quasi Lagrangian. In order to avoid noisiness for example in poorly resolved, cold flows, the same entropic function as in SPH is used in AREPO and added as an additionally conserved quantity using

$$\frac{\partial}{\partial t} (\rho A) + \vec{\nabla} \cdot (\rho A \vec{v}) = 0, \quad (\text{III-37})$$

which is fully consistent with the fluid description of the Euler equations and just serves as an additional tool to control conservation of entropy instead of conservation of energy.

[Springel, 2010a](#) further present a possible algorithm to make the cells more honeycomb like if their aspect ratios start to rise to much in order to suppress numerical instabilities. They use Lloyd’s method ([Lloyd, 1982](#)) which moves a mesh generating point to the centre of mass of it’s cell. Then the mesh is reconstructed and the process can be repeated until the result looks sufficiently regular again. However, they note that to avoid instabilities the order of reconstruc-

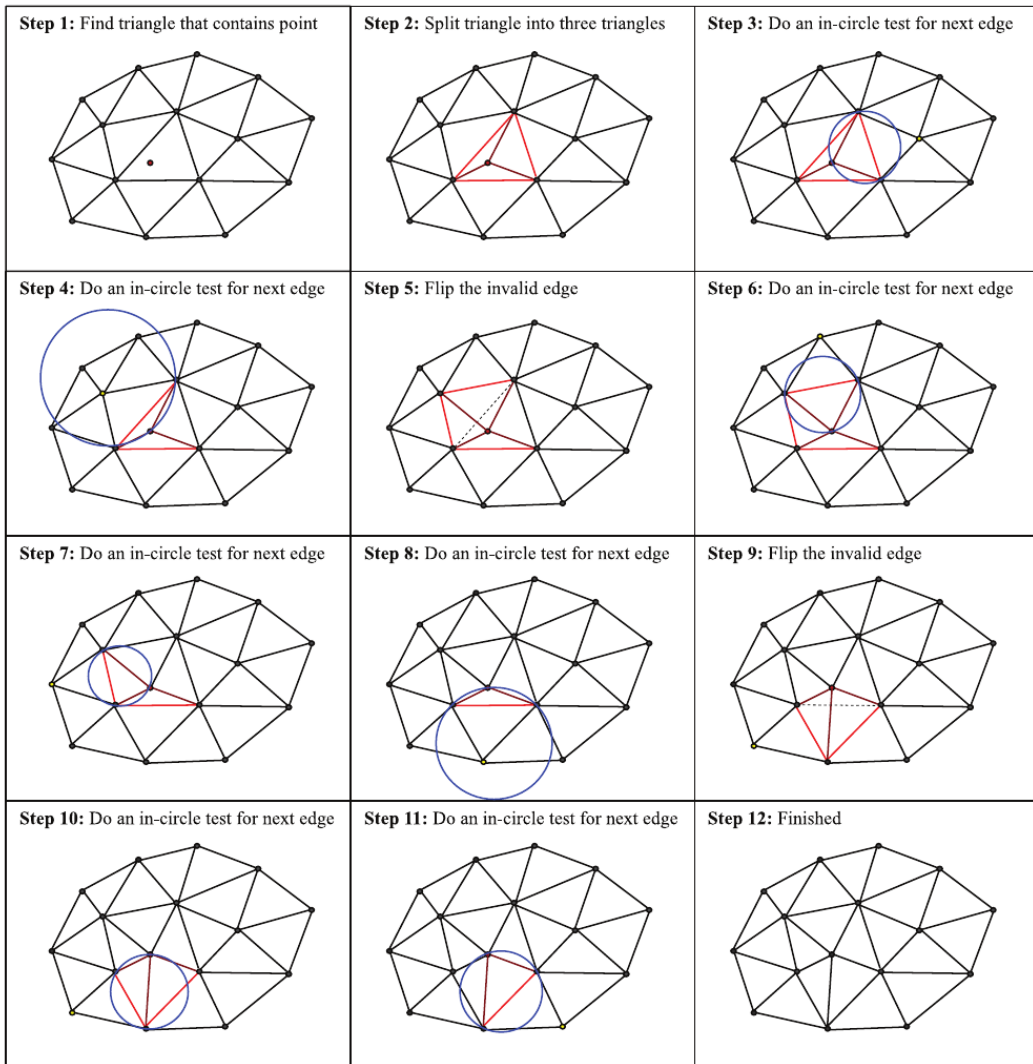


Figure III.5: Illustration of the point insertion algorithm to construct a Delaunay triangulation. Taken from [Springel, 2010a](#).

tion needs to be reduced near fluid discontinuities. Additionally, they talk about adaptively (de-) refining the mesh. While this is not required in order to keep a approximately fixed mass in each cell, other reasons may exist to increase resolution at any point. For example the volume of each cell needs to be limited to properly resolve small scale processes and to keep neighbouring cells of similar size. This means splitting and joining of cells, which is more challenging than typical AMR since the mesh geometry might need to be adjusted completely afterwards.

Coupling self gravity to the hydrodynamical scheme is very important for astrophysical set ups and moving mesh codes inherit a great simplicity from their Lagrangian nature and is therefore not subject to the issues AMR codes experience. Other physics models can be in principle adapted from other grid codes due to the similarity of their approach to solve equations across faces.

Finally, a moving mesh code provides the user with a rather easy treatment of boundaries using special cells which could be kept fixed. Nevertheless, one has to be careful since big differences in cell sizes also at the boundaries can result in a notable reduction of accuracy.

Standard fluid tests reveal a very nice performance of the moving mesh code AREPO, for example outperforming SPH at shocks and AMR codes at contact discontinuities. To judge on results means also to consider the amount of computing time required to achieve them, as they are mostly also dependent on the chosen resolution. At the state of the paper [Springel, 2010a](#) reports similar but slightly less efficiency than the version of GADGET-3 at that time.

The second popular ALE approach we want to discuss here is called the meshless approach. From the general method two derivations have become popular lately: “Meshless Finite Volume” (MFV) and “Meshless Finite Mass” (MFM). Originally introduced by [Lanson and Vila, 2008a](#); [Lanson and Vila, 2008b](#); [Gaburov and Nitadori, 2011](#) the two state of the art astrophysical codes GIZMO and GANDALF contain these methods and the according papers of [Hopkins, 2015](#) and [Hubber, Rosotti, and Booth, 2017](#) present extensive comparisons with traditional and state of the art SPH as well as grid and moving mesh codes’ performances. As MFM and MFV belong to the class of ALE methods they automatically share a lot of the advantages with the Moving Mesh approach, as we listed them earlier this section. Therefore, we limit this description to the required minimum to understand what it is about and refer to the excellent papers mentioned for further reading.

The derivation of the governing equations starts similar to the moving mesh technique with the Euler equations in a moving frame. Except for some mathematical details the main difference of this approach is how the volume is partitioned. Instead of a Voronoi mesh the volume is partitioned around particles using a weighting function similar to an SPH kernel. The fraction of the volume $d^v \vec{x}$ of a particle i is then given by

$$\Psi_i(\vec{x}) = \frac{1}{\omega(\vec{x})} W(\vec{x} - \vec{x}_i, h(\vec{x})) \quad (\text{III-38})$$

with the appropriate normalisation

$$\omega(\vec{x}) = \sum_j W(\vec{x} - \vec{x}_j, h(\vec{x})). \quad (\text{III-39})$$

This means that at each location \vec{x} $\Psi_i(\vec{x})$ determines the degree of how much this spot is associated with particle i . Due to typical kernel-like properties of the weighting function this is

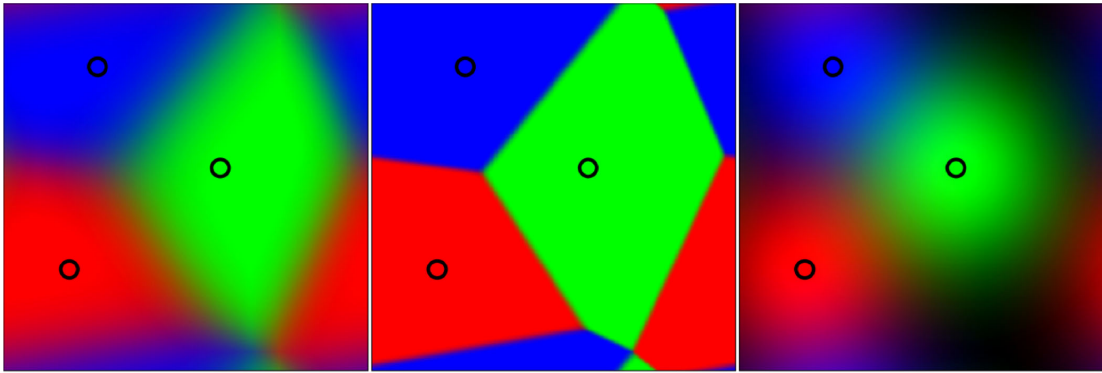


Figure III.6: Illustration of the cell/particle volumes in MFM/MFV, moving mesh, and SPH. Taken from [Hopkins, 2015](#).

a smooth transition between the realm of one particle and another with a mixedly influenced region in between. An illustration depicting this behaviour in comparison to a Voronoi mesh and an SPH partitioning is shown in figure III.6. We see that MFM/MFV can be understood as some sort of middle ground between the latter two, incorporating the bisection of space between two particles overlayed with an SPH like smoothing indicating that the moving mesh method can be considered a special case just without the smoothing (except for some implementation dependent, subtle differences maybe). [Hopkins, 2015](#) explicitly stresses that MFM and MFV are not a form of SPH despite the similarities.

[Hopkins, 2015](#) and [Hubber, Rosotti, and Booth, 2017](#) both apply again a MUSCL-Hancock scheme and use a Riemann solver as discussed before. [Hopkins, 2015](#) proposes a different gradient estimator with higher accuracy as described by [Mocz, Vogelsberger, and Hernquist, 2014](#) which employs a direct SPH gradient estimator as fall-back, if the condition number of the corresponding matrix which has to be inverted is not good enough. The latter is supposed to happen only in rare cases though. As before, the particles used as building blocks for the discretisation could be kept fixed but are ideally moved alongside the fluid to get rid of bulk motion effects and automatically gain Lagrangian adaptivity.

Besides even higher order schemes being possible, MFM and MFV have become popular approaches of choice. But what is actually the difference between these two? As indicated by the respective names, the treatment of volumes and masses differ. Assuming movement of particles with the fluid bulk motion, the faces between particles can be considered stationary in this moving frame and a classical Riemann problem can be solved across those faces. That is called the MFV method. However, except for the bulk motion of the fluid there are usually quite huge fluctuations present which lead to cell distortions in the other schemes. A different assumption is, to let the Lagrangian volume actually distort such that the mass inside is conserved leading to the MFM method. In this picture there remains residual motion of the face which has to be considered in the Riemann problem. In total, one of the schemes keeps the cells' volumes fixed and allows mass flux between cells while the other one rather keeps the mass fixed and let's the volumes change. For a smooth flow it is clear, that both methods must become exactly identical (up to second order accuracy).

Both the GIZMO and GANDALF paper present extensive test suited comparing the capabilities of their codes to properly solve idealised hydrodynamical test problems towards codes utilising SPH, AMR or even moving mesh. We review these slightly when presenting the proficiency of our modernised version of GADGET later in chapter V. Just for a quick overview we want to mention that the meshless approaches produce similarly good results as the moving mesh compared to well known issues with SPH and AMR. While in SPH modern codes typically employ high order kernels and several hundreds of neighbours, the meshless approach works at least equally well with only 32 neighbours for a similar computational cost.³ Meaning that, while maybe not necessary at the moment, increasing the neighbour number here will let the computational cost rise a lot, way beyond that of SPH with the same neighbour number. Furthermore, MFM and MFV differ slightly in the quality of their results and it depends on the type of test which one ultimately performs better. MFM has the advantage of better particle tracking, due to conserved particle mass, better angular momentum conservation and less noise than MFV which comes for the cost of a slightly more diffusive algorithm capturing discontinuities less sharply. In total, MFM seems to be somewhat preferable for typical astrophysical applications. [Hopkins, 2015](#) does not show the results from both methods for each tests and reading [Hubber, Rosotti, and Booth, 2017](#) carefully might reveal why. Although the results in general are really great, there are still errors left which are in some cases definitely notable and need to be addressed. Differences between meshless and moving mesh are the most subtle and need to undergo careful investigation. A key point is however, that due to the SPH like smoothing discontinuities will be never as sharp as in any grid code without smoothing, just by construction. That said, the main point left is to state that while SPH and classical finite volume is well studied, these new hybrid approaches also need some time to be understood thoroughly and be fine tuned to the problems at hand despite producing very nice results in standardised tests already.

As a quick side note, since magnetic fields are important to us. GIZMO has since it's first release been extended by a description of non-ideal MHD (see e.g. [Hopkins and Raives, 2016](#)) utilising the constrained transport scheme of [Evans and Hawley, 1988](#); [Mocz, Vogelsberger, and Hernquist, 2014](#) to control potentially upcoming magnetic field divergence terms. Without the constrained transport scheme this type of code which is optimised to minimise numerical diffusion in combination with the employed Powell 8-wave approach tends to produce very long lasting monopoles. This has not been such a big issue in classical grid codes, as diffusion tends to damp the occurrence of these non-physical monopoles ([Tóth and Gábor, 2000](#); [Pakmor and Springel, 2013](#)).

III-4.2 Look around: Modified versions of SPH

Outside the realm of astrophysics there exists a big community which also utilises SPH and brought forward it's own take onto the problems the numerical discretisation brings with it and that is engineering. Although the physical problems approached are quite different to what we do in our simulations, for example a dam break or calculation of flows in turbines, SPH is also quite suited there. Due to the nature of these tasks, other problems arise. Where we simulate typically very diffuse and compressible gases with open boundaries, at least weakly or even in-

³32 being one of the sweet spots where the kernel bias becomes very small, see section III-3.1.

compressible fluids like water and their interaction with solid objects and boundaries play a role, which brings a whole new set of challenges with it. Nevertheless, a Lagrangian code is naturally well suited for the interaction with free surfaces which is why it is commonly employed as the basis for such simulations. In comparison to SPH in astrophysics which started with [Lucy, 1977](#); [Gingold and Monaghan, 1977](#) these applications are even younger, with the first publications appearing only 25 years ago with [Liberky et al., 1993](#); [Randles and Libersky, 1996](#). And in the last two decades SPH for these applications has evolved as much as it did in the astrophysical community. Since our own community has grown so large, we often lack an overview of what other people in completely unrelated science areas develop, even if they evolve from the same basis. Therefore, we aim to give a quick overview of some of the different flavours of SPH that have emerged and show, that sometimes the similarity to our own research is remarkable with only a common taxonomy missing.

[Liu and Liu, 2003](#) give an overview over different flavours of the SPH method, including *Adaptive SPH* (ASPH), also called *Discontinuous SPH* which has been first presented by [Shapiro et al., 1996](#); [Owen et al., 1998](#). The adaptivity of this approach lies in a modification of the kernel function which is replaced by an anisotropic matrix and, therefore, can handle density anisotropies below the level of one kernel size. Consequently, instead of one smoothing length per particle they carry an anisotropic smoothing tensor. The success of this approach is rather limited in the astrophysical community, where we rather tend to increase the number of resolution elements, it can have promising effects for particles interacting with fixed boundaries. Amongst others, [Yu and Turk, 2013](#); [Wang et al., 2016](#) present algorithmic descriptions and e.g. [Fang et al., 2017](#) writes about the idea of inverse kernels, which is related. [Spreng et al., 2017](#) also call their method *Adaptive SPH*, which approaches boundary problems with a different approach by introducing an additional refinement technique. Based on the consistency order matrix SPH particles can be splitted or merged together to generate additional resolution where required even in constant density problems.

An approach similar to the idea of inverse kernels, is the *Reproducing Kernel Particle Method* (RKPM) by [Liu et al., 1995](#), which is described as “similar to SPH but without the tensile instability”, using correction functions for boundary effects. It can be formulated based on a Fourier transformation and reminds of the definitions of the typical spline kernel functions ([Schoenberg, 1973](#); [Monaghan and Lattanzio, 1985](#)). The idea behind the RKPM is basically, to modify the kernel function in order to gain a higher order correctness of discretised estimates. Furthermore, it can be implemented into a Galerkin finite elements formulation, which has the advantage of being a standardised formulation with a lot of research and experience already present. RPKM is still actively developed further, see e.g. [Imin, Iminjan, and Halik, 2017](#) for a detailed description of the method and bridging the gap back to anisotropy in kernel functions and boundary interactions. For further reading about a Galerkin formulation of SPH see also for example [Cueto-Felgueroso et al., 2004](#).

As mentioned, naming of the different modifications and distinguishing them can be an issue. There is for example *Symmetric SPH* (SSPH), which itself is an over-class of classical SPH, RKPM, *Modified SPH* (MSPH) and *Moving Least Squares* (MLS), and *Corrected SPH* (CSPH). The names suggest differences but in the core these methods target the same problems and are sometimes of similar nature. For further reading about these, see e.g. [Dilts, 2000](#); [Fernández-](#)

[Méndez, Bonet, and Huerta, 2005](#); [Batra and Zhang, 2007](#); [Zhang and Batra, 2009](#) and references therein.

Exploring in a different direction is for example so called δ –SPH, which is applied to weakly compressible fluids and features an additional (physical or artificial) diffusive term in the continuity equation ([Molteni and Colagrossi, 2009](#); [Antuono, Colagrossi, and Marrone, 2012](#)).

SPH-ALE is another interesting topic which reminds of the moving mesh and meshless methods we discussed in section [III-4.1](#). The basic idea behind this is, to solve a Riemann problem between each neighbouring particle pair, therefore the method is also known as *Riemann SPH*. That allows the SPH formalism to be coupled with a finite volume code. [Vila, 1999](#) present such an approach and discuss how the merged result can look like. In the astrophysical community basically the same approach has been discussed under the name *Godunov SPH* as originally presented by [Inutsuka, 1994](#). [Murante et al., 2011](#) discuss an implementation of this approach into the GADGET-3 code and show it's performance in several test cases. The main advantage gained, is a better treatment of shock fronts and contact discontinuities, the latter getting rid of the so called pressure blip, without the need for artificial viscosity. Although on first glance the Riemann solver is computationally rather expensive, an approximate solver can mitigate this but the main downside is the choice of kernel. As they present an implementation for a Gaussian kernel, neighbour numbers become very large which makes this approach very hard to utilise properly. Also [Kumar et al., 2013](#) present an implementation using a truncated Gaussian.

III-4.3 Code diversity through modern astrophysical codes

Now that we have thoroughly investigated the typical numerical techniques used in astrophysics and extensions which have come up beyond that, the obvious question “Which one is the best?” stands dominantly in the middle of the room.⁴ Looking at the huge range of scales astrophysics covers, from star forming regions to galaxy clusters, from dense to ultra diffuse gas, from just a few Kelvins of temperature up to 10^8 Kelvin it is easily understandable that there can not be just one answer to that question. It has to be at least modified to “Which one is the best for the specific problem we want to solve right now?”. With the vast range of different problems and approaches we can take, a huge landscape of astrophysical codes has emerged and we can just note a subset of all these listed in table [III.1](#).

We have given insight not only into how these different approaches basically work but also described the advantages of each method and it's drawbacks which people have tried to mitigate over the years. The performance of each method and thereby of each of these codes has been properly measured using standardised hydrodynamical tests for which have a basic understanding of what should happen. These cover the treatment of shocks and contact discontinuities, fluid mixing, the development of instabilities and stability of hydrostatic setups. While all these tests assess the performance of the underlying (magneto-) hydrodynamical scheme from a computer science point of view they are already a few steps ahead from general code testing which is unfortunately rarely done in an automatic fashion in the astrophysical community. Some modern codes like GANDALF ([Hubber, Rosotti, and Booth, 2017](#)) stand out as good examples. These standard hydro tests maybe simple enough to properly grasp the quality of the numerical results

⁴On top of the magnetic elephant.

Mesh based codes	
AREPO	Springel, 2010a
ART	Kravtsov, Klypin, and Khokhlov, 1997
ATHENA	Stone et al., 2008
ENZO	Bryan et al., 2014
FLASH	Fryxell et al., 2000
NIRVANA	Ziegler and Udo, 1998; Ziegler, 2005
PLUTO	Mignone et al., 2007
RAMSES	Teyssier, 2002; Fromang, Hennebelle, and Teyssier, 2006
ZEUS	Stone and Norman, 1992a; Stone and Norman, 1992b
SPH codes	
GADGET	Springel, 2005a
GASOLINE	Wadsley, Stadel, and Quinn, 2004
MAGMA	Rosswog and Price, 2007
PHANTOM	Price et al., 2017
SEREN	Hubber et al., 2011
SWIFT	Gonnet et al., 2013
Multiple solvers	
GANDALF	Hubber, Rosotti, and Booth, 2017
GIZMO	Hopkins, 2015; Hopkins, 2017

Table III.1: Incomplete list of popular astrophysical hydrodynamics codes grouped by the type of code and sorted alphabetically.

and the correct result may be even calculable analytically but two important notes have to be taken here when interpreting the results.

First of all an important factor has to be taken into account and that is the quality of the initial conditions used for these tests. Depending on the type of code it is highly non trivial to set up a proper starting configuration which exactly resembles a given model with low numerical noise. While this is rather straight forward for (at least stationary) grids, particle type methods are much more difficult. Especially if we want to compare the performance of a grid and a SPH code where we need different initial conditions we need to take good care that they are of equally high quality. The topic of initial conditions is of course not only important for testing but also for setting up simulations for the problems we want to actually solve. We will come back to this topic later in chapter IV where we present a novel code to set up particle configurations following any given density model.

The second remark does not directly affect a test's result but rather targets the importance of these results. Although the vast comparisons of hydrodynamical solvers have shown notable differences in practise there is something which may cause even bigger effects. Namely all the different physics modules we employ in addition to pure (magneto-) hydrodynamics, like a prescription for star formation, feedback, metal diffusion, AGNs and many more. We have not touched these extensions so far - but will do so in the next section - since hydrodynamics alone is not even that simple to solve as we have seen. At this point one can at best take a middle

ground between two extreme positions. One stating that the underlying numerical description of a code affects everything which is implemented and that any code which does not even treat hydrodynamics properly could or rather should never be used for a proper scientific analysis of even more complex processes. The other extreme would be to say that the differences in hydrodynamical solvers are still very small compared to, and can be completely shadowed by, different physical prescriptions of other processes and therefore work has to go into modelling these processes rather than squeezing out the last bit of accuracy from the underlying solver in test cases which never occur isolated from other effects anyway. Extensive code comparison projects also on a higher abstraction level have been carried out over the decades, like the famous Santa Barbara galaxy cluster comparison where all the different codes showed drastically differences for the results of an isolated galaxy cluster simulation even without radiative processes involved (Frenk et al., 1999; Agertz et al., 2007; Tasker et al., 2008; Mitchell et al., 2009). The performance of our modernised version of GADGET regarding this cluster simulation is presented in chapter V. Later there came for example the Aquila project with simulations of Milky Way like disk galaxies (Scannapieco et al., 2012) and just recently another extensive comparison project has been launched starting under the name NIFTY which has now evolved into a comparison of about 300 re-simulated galaxy clusters from a big cosmological box called “The Threehundred”. We will come back to this project later in chapter IX.

In the end both positions have their valid points and it is best to keep both of them in mind and find a good way to satisfy both. Modern approaches like moving mesh and MFM might be the future of astrophysical simulation codes and slowly replace classical SPH and fixed mesh codes but at the present time there is still a lot more work to be done to properly understand their behaviour in all the vast ranges of applications. And they are most probably also not the end of the line, as there are always issues to solve and errors to decrease. Actually, the diversity of so many different codes is not even something bad because it really gives us the opportunity to simulate some problem with different approaches and then compare the results and maybe learn from that which results are rather of numerical origin than of the physical modelling employed. When we reach a point where all the different codes give us the same answer it is maybe much more believable than just using one code’s result which makes the mentioned comparison projects extremely beneficial. As we see for example later in chapter V and compare the Santa Barbara cluster result to Springel, 2010a this kind of convergence actually happens which is very exciting. Summing up, classical grid codes and SPH are definitely not dead and it is still worth further improving them pursuing ambitious science goals.

III-5 Additional physics beyond MHD

Of course not everything can be answered with (magneto-) hydrodynamics alone. Before adding advanced models for processes like star formation or radiative cooling there stands something even more important: the gravitational forces via an external potential and self gravity between all fluid elements. Actually it is even more important than hydrodynamics in order to properly reproduce structure formation in the universe. While it may seem simple compared to everything we talked so far, it is definitely not. And without a proper treatment of gravity all the effort can go to waste. Therefore, big simulation projects typically start with a dark matter only box, where

only gravity plays a role. The publicly most well known and successful although not biggest dark matter only simulation is probably the Millennium simulation (Springel et al., 2005). See e.g. Frenk and White, 2012 for review of the state DM simulations are in. The next two subsections will give some overview over treatment of gravity and additional physics.

III-5.1 Understanding the gravity of Newton vs Einstein

Cosmological simulations already contain a big hint in their labelling: “cosmological”. Simulations like Magneticum (Dolag et al. in prep.), Illustris (Vogelsberger et al., 2014) or Eagle (Schaye et al., 2015) treat the evolution of a big cosmological volume starting at very high redshift up until present time. In order to properly run these simulations it offers quite a lot of benefit, to treat all variables in a co-moving way in order to factor out the expansion of the universe properly. The next logical step then would be to assume, that we can no longer treat gravity classically but need to resort to a general relativistic treatment. That might be true, depending on the target of what is simulated. For the mentioned cosmological boxes, however, it only plays a very minor role as linear structure growth is the same in both Newtonian and relativistic gravity and because non linear structure growth induces only velocities much smaller than the speed of light (Frenk and White, 2012). Chisari and Zaldarriaga, 2011 also show that Newtonian dynamics actually solves dynamics correctly even on large scales. They give a recipe how to judge on that comparing general relativistic results and the Newtonian limit.

Nevertheless, a more accurate treatment might be relevant in the future. To quantitatively judge on the importance of a relativistic approach we have to assert the following necessary conditions:

1. To be able to neglect even special relativistic effects, all velocities have to be much smaller than the speed of light: $v_i \ll c$.
2. In Newtonian physics the forces of gravity work instantaneously while in general relativity the signal velocity is the speed of which gravitational waves travel with: the speed of light c . In order to neglect that we require the typical dynamical timescales to be much bigger than the time for gravity to operate: $t_{dyn} \gg t_{light \ crossing}$.
3. In general relativity matter equals to deformation of space-time. To neglect that, the curvature caused by all the fluid elements’ masses has to be negligible.

From observations and analysing simulations we know that velocities are typically small compared to the speed of light. This depends on what we actually look at, but for galaxy formation (or a similar topic) it is definitely the case and the first condition is fulfilled.

Instantaneous gravity

The velocity of gravitational waves plays a bigger role, the larger the volume we want to simulate is. A typical example would be a $b = 1Gpc$ sized box with a central halo forming a galaxy cluster with $r = 2Mpc$. We do the analysis at redshift $z = 0$ since the physical volume is then largest and we do not have to convert between comoving and physical variables. The typical dynamical timescale can be estimated by the free fall time:

$$t_{ff} \sim \frac{r}{v} \approx 20Gyr \quad (\text{III-40})$$

for a typical velocity of 100km/s . Sound waves travel with velocities even up to a factor 10 faster, decreasing this time by an order of magnitude. Now, calculating the time a gravitational wave travels from one side of the box to the other takes

$$t_{box} = \frac{b}{c} \approx 3\text{Gyr} \quad (\text{III-41})$$

which is actually of comparable magnitude. However, considering only where gravitational forces are strong we can decrease the travel length from the whole box size down to something similar to the galaxy cluster's size, where most of the mass will end up:

$$t_{gc} = \frac{2 \cdot r}{c} \approx 10\text{Myr.} \quad (\text{III-42})$$

That is now several orders of magnitude smaller and the posed criterion can be considered fulfilled up to some degree of error.

Curvature due to matter overdensities

In order to judge upon the effects of the simulated matter onto space-time we have two possibilities. For one, we need to consider Einstein's equation (equation I-4). Curvature is depicted by the Riemann tensor or by reduction of dimensions the Ricci tensor and scalar. To prove that space-time is sufficiently flat we have to consider an appropriate energy-momentum tensor for matter and radiation in the region of interest and show that the Ricci scalar is appropriately small. However, this requires some very complex calculations and a scale with which we can we can actually judge the resulting value.

The alternative approach is much simpler but gives a very satisfying result. It is based on the assumption that the radius of the space-time curvature induced by any object can be at most as large as the size of the object itself. Furthermore, if the radius curvature is much larger than the Schwarzschild radius of said object, it does not play a significant role:

$$r_K \gtrsim r \gg r_s. \quad (\text{III-43})$$

The Schwarzschild radius is given by

$$r_s = \frac{2mG}{c^2}. \quad (\text{III-44})$$

For our sample galaxy cluster with $r = 2\text{Mpc}$ we can assume a mass of $m = 10^{15} M_\odot$ which leads to $r_s = 9.6 \cdot 10^{-5} \text{Mpc}$ which fulfills the inequality. The same calculation can be done for a sample Milky Way type galaxy with $r = 30\text{kpc}$ and $m = 10^{12} M_\odot$ and therefore $r_s = 9.6 \cdot 10^{-5} \text{kpc}$. Just to give a counterexample, neutron stars are so condensed that their size comes close to their Schwarzschild radius and the inequality is not fulfilled any more.

Approaches to treat Newtonian gravity

Most of the hydrodynamics codes listed in table III.1 contain a coupled gravity solver in order to follow self gravity of the fluid. The unification of SPH and a tree based gravity solver (which

we explain in a bit) for example goes back to the code TreeSPH (Hernquist and Katz, 1989). Besides them there also exist pure gravity solvers like NBODY6 (Aarseth, 2003) or STARLAB/kira (Portegies Zwart et al., 2001). Here we will discuss some of the most popular approaches how to actually incorporate gravitational forces into such a code.

To add Newtonian self gravity to the equations of hydrodynamics we add the gravitational potential Φ as source term on the right hand side (rhs) of equations II-49

$$\text{rhs} = -\rho \vec{\nabla} \Phi \quad (\text{III-45})$$

and II-51

$$\text{rhs} = -\rho \vec{v} \cdot \vec{\nabla} \Phi \quad (\text{III-46})$$

or the Lagrangian equations respectively. Φ comes from Poisson's equation:

$$\Delta \Phi = 4\pi G \rho. \quad (\text{III-47})$$

Instead of calculating the potential we can also directly work with gravitational forces and apply them to the accelerations. There are several different approaches we can take and we discuss a few popular choices in this section.

The most straight forward choice, especially in a particle picture, is the direct sum. This means to evaluate the gravitational force between each particle pair and apply it to both particles. The advantage of this approach is the extreme accuracy we can reach with it unfortunately for an immense cost of an algorithm scaling with $\mathcal{O}(N^2)$, N being the amount of particles, which is typically not feasible. However one has to note that the amount of particles is always much less than the amount of real physical particles in the simulated domain, which makes even this direct approach rather a Monte Carlo method than a totally correct computation.

Due to the bad scaling with particle number of the direct sum approach, typically a so called tree code is used as for example in the popular form of the Barnes-Hut tree (Barnes and Hut, 1986) which is implemented in GADGET. The basic idea behind that is, to partition the simulation space in a hierarchical tree structure. For example an oct-tree divides each cell into 8 sub cells in three dimensions up until some criterion after which a tree node is considered a leaf and not further divided. Typically the criterion is chosen such, that only a few particles are left in the cell. Alternatively the height can be kept fixed using empty cells for easier parallelisation as shown by Nabors et al., 1994. Alternatives to an oct-tree are for example a binary kD-tree (Stadel, 2001) or a structure based on nearest-neighbour pairings (Jernigan and Porter, 1989). However, an oct-tree has proven it self as very effective since it keeps cell aspect ratios small, reducing the magnitude of high order multipoles. Furthermore, it can be directly used for neighbour searching in case it is coupled to for example an SPH code as in GADGET which is very beneficial since the tree has to be built only once per time step. It can be directly coupled to space partitioning using a space filling curve which also helps efforts for parallelisation. To calculate the gravitational forces regarding one particle the tree is traversed and if a cell is far enough away and/or small enough then the force is evaluated with respect to the whole cell instead of all the particles inside it. A multipole expansion can be carried out with the monopole assuming all particles inside a cell sitting approximately at the cell's centre which is typically sufficient. This saves a lot of interactions compared to the direct sum and it scales only with $\mathcal{O}(N \log(N))$

which makes the method much faster and still pretty accurate depending on the exact opening criterion, which is typically formulated as a critical angle, for the evaluation. [Springel, 2005a](#) presents an adaptive criterion based on the mass M inside a node of size l at distance r as

$$\frac{GM}{r^2} \left(\frac{l}{r} \right)^2 \leq \alpha |\vec{a}| \quad (\text{III-48})$$

with the total acceleration $|\vec{a}|$ saved from the last time step and a numerical factor α . Using such a criterion, the typical force error can be kept approximately constant over the whole simulation domain.

Another hierarchical algorithm is the Fast Multipole method (FMM, see e.g. [Cheng, Greengard, and Rokhlin, 1999](#)), as implemented in the FMB code, and a hybrid approach presented by [Dehnen, 2000](#); [Dehnen, 2002](#), as implemented in falcON. FMM decomposes the interactions into a directly computed near field part and a far field part for which a multipole expansion into spherical harmonics up to an accuracy order P is carried out. The scaling is then of the order $\mathcal{O}(N)$ which is very quick for large particle numbers but becomes very slow for high desired accuracy. It is also implemented typically using an oct-tree structure, which has to be traversed only two times: Once upwards to build the multipole expansions always using those previously calculated for sub cells and once downwards calculating the local expansion of each cell using the multipole expansions. The good scaling comes from the ability to keep interactions on a cell-cell level instead of particle-cell. Dehnen's hybrid approach combines the Barnes-Hut tree with the FMM method in a clever but more complicated way assuming that the required precision is anyway limited due to gravitational softening. Gravitational softening means to apply always a minimum distance between each particle pair to prevent extremely large forces (or even singularities in case of the same location) which would require very small time integration steps. Since the degree of softening amounts basically to a resolution limit ideas have come up to vary it in a spatially adaptive way ([Price and Monaghan, 2007](#)).

As a quick side-note, [Fortin, Athanassoula, and Lambert, 2011](#) reviewed these hierarchical approaches and assessed accuracy as well as scaling in serial as well as parallel execution. The important conclusion for us at this point is, that for a large number of neighbours and amount of processes in parallel the BH-tree in GADGET is definitely the best choice. Looking into [Springel, 2005a](#) reveals that there is even more to it, since it can be coupled to a further method which goes away from the idea of a hierarchical solver but comes back to the formulation of a gravitational potential: The Particle-Mesh (PM) approach, Tree-PM in the coupled version (see also [Xu, 1995](#); [Bode, Ostriker, and Xu, 2000](#); [Bagla, 2002](#); [Bagla and Ray, 2003](#)). The idea behind the particle mesh is that the gravitational potential is split in Fourier space into a short range and a long range part. The short range part is solved in real space and is in the coupled method taken over using the Tree while the long range part uses a mesh based Fourier method. This is also a very common approach, since libraries such as FFTW offer a well tested, good scaling and fast interface. While this is a very quick and accurate way to compute the gravitational forces, the drawback lies in the fact that there is one whole tree for the full simulation domain. As the amount of particles grow this tree becomes very large, requiring a huge chunk of memory just to save the structure on each compute node. This will at some point become an important bottleneck which lies not to far in the future. Especially due to the recent efforts

to build hybrid CPU/GPU codes which solve gravity (and of course other parts) on the GPU. Examples are the upcoming GADGET4 and OPENGADGET.

III-5.2 Additional models as subgrid approach

So far we have discussed the treatment of gravity and magnetohydrodynamics. With this knowledge we can reproduce structure formation and start to simulate astrophysical objects. However, there are still very important key ingredients missing in our prescription of the universe including star formation, stellar feedback, supernovae, chemistry as in treatment of heavy elements, radiative cooling, formation and feedback from black holes and many more. All these have to be modelled, if deemed necessary, in a way that they work properly at the given resolution level and resemble what we think to know about how the underlying processes act. And that is already the crux here: resolution. Assuming an SPH simulation in which we have modelled a fluid using mass tracers but we never resolve it down to the level where one tracer particle equals an actual physical particle. The same comes into play here on several different levels. For example we want to simulate the evolution of a whole galaxy cluster with all the hundreds of galaxies inside. In order to form stars the external pressure needs to be large enough on a gas cloud so that it can collapse. But we can not even resolve these gas clouds in a crude way let alone sample them well enough to formulate such a criterion properly. Also the time it takes for the cloud to collapse and a star to form is so much smaller than the typical time steps applied, that is also falls through time-wise and not only spatial resolution. What astrophysicists do in such a case is called subgrid model. We try to find a, typically statistical, prescription which mimics the effect of such a process as star formation on a much coarser level. But this comes with a price: The model can be plainly wrong. Or it might be correct statistically but a similar model with the same statistical output can handle details so much differently that the outcome differs quite a lot. Additionally, each model typically requires some parameters which need to be set such that the outcome looks realistically. Sometimes model parameters correspond directly to some physical process and can be constrained well by observations. Otherwise it can become quite arbitrary how to set them properly. The resulting danger is that people can tune their parameters such that they basically get out what they put in - which in return lets us learn absolutely nothing about the correctness of the employed model. Sometimes it is very hard to distinguish which results are actually biased in such a way and which are not. For overview of these models and challenges with respect to galaxy formation in a cosmological context see e.g. [Somerville and Davé, 2015](#). The detailed models used during this work will be referenced in the respective chapters.

III-6 Goals of this work and into the future

Having outlined the different approaches we take to simulate astrophysical objects and their formation and evolution, it has become clear that this is indeed a very difficult endeavour. It is not only about understanding the physics required but also the computer science behind all these different methods and codes. One needs to keep some balance between the two since neither can not work without the other. And as computing power rises we try to increase resolution and accuracy both in order to be able to really cover all the necessary processes properly. Figure [III.7](#)

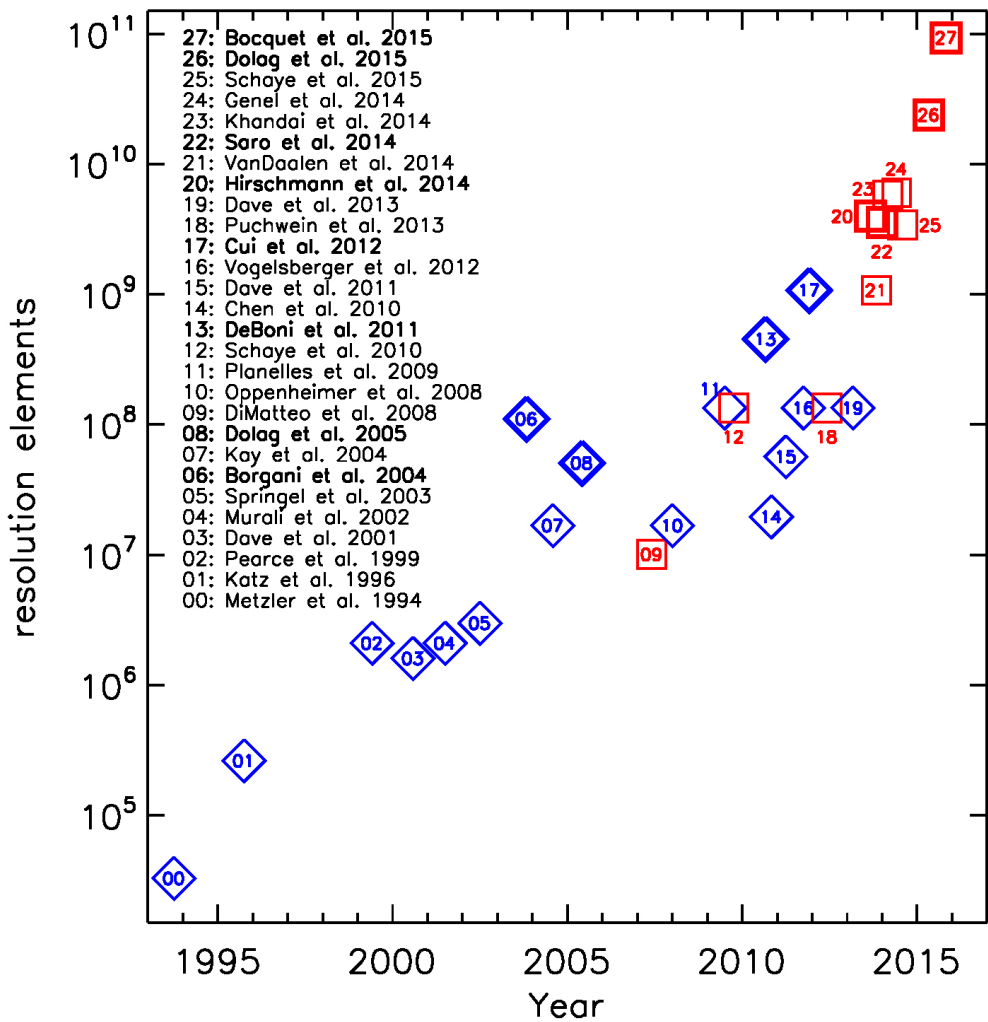


Figure III.7: Moore's law as number of resolution elements over time. Taken from <http://magneticum.org/simulations.html>

shows Moore's law for the number of resolution elements in huge astrophysical simulations over time. Originally stating that the number of transistors in an integrated circuit doubles each year it also shows this exponential growth in this related matter.

In order to make this growth possible we need to solve all the problems arising due to the increased number of resolution elements and/or accuracy. This means generating equally high quality initial conditions (chapter [IV](#)), improving our SPH scheme to mitigate the discussed weak points and testing it properly (chapter [V](#)), properly analysing the resulting particle based data by translating it to a volume discretised picture (chapter [VI](#)) and finding ways to actually handle these huge amounts of data (chapter [VII](#)). Only then can we proceed to learn more about astrophysical processes like the influence of anisotropic thermal conduction in galaxy clusters (chapter [VIII](#)), starting with a new generation of a code comparison project studying galaxy clusters (chapter [IX](#)), studying magnetically driven winds (chapter [X](#)) and rotation curves (chapter [XI](#)) in disk galaxies.

Chapter IV

Initial conditions generation: Difficulties of SPH

Everything of importance has been said before by someone who did not discover it.

– Alfred North Whitehead

As laid out earlier the first ingredients of any simulation are proper initial conditions. They come with two important aspects: First, a good model describing the initial state properly, like a density field $\rho(\vec{r})$, a temperature field $T(\vec{r})$, a velocity field $\vec{v}(\vec{r})$ and so on. This model might describe for example a rotation disk galaxy in hydrodynamic equilibrium or contain the information from cosmological density perturbations in order to study structure formation. Second, these scalar and vector fields must be properly translated into a form which the code at hand can understand. For volume discretising codes this is fairly straight forward, as the functions can be directly evaluated at whatever sampling point. Mass discretisation schemes like SPH, which we use throughout this work, are much more difficult to satisfy because the fields need to be translated properly onto tracer particles. Not only the properties these particles carry are important but also their locations. One could eliminate the dependency on location by aligning them on some kind of grid but even that becomes non-trivial in the presence of density gradients. This chapter revolves around a novel (and future open source) code which tackles this problem and is supposed to generate any initial conditions by just supplying the describing scalar and vector fields alongside some general parameters like the number of particles. It is based on the paper draft of Arth, Donnert, Steinwandel, Halbesma, Pütz, Hubber and Dolag in prep. whose publication will be pursued in the near future.

IV-0 Abstract

We present a novel application to generate glass-like initial conditions for Smoothed Particle Hydrodynamics following arbitrary density models based on the work shown in [Donnert, 2014](#). We enhance an algorithm presented by [Diehl et al., 2012](#) based on a weighted Voronoi tessellation and combine it with improved initial configurations and an additional particle reshuffling scheme. We show our application's ability to sample different kinds of density features and to converge properly towards the given model density as well as a glass-like particle configuration.

We analyse convergence with iterations as well as with varying particle number. Additionally, we demonstrate the versatility of the implemented algorithms by providing an extensive test suite for standard (magneto-) hydrodynamics tests as well as a few common astrophysical applications. We indicate the potential to bridge further between observational astronomy and simulations as well as applicability to other fields of science by advanced features such as describing a density model using gridded data for example from an image file instead of an analytic model.

IV-1 Introduction

With rising computing power simulations have become an integral part of modern astrophysics over the last few decades. In the past years people have traversed more and more from theoretical calculations with pen and paper to complex computer driven computations. These range from high precision simulations of idealised systems on various scales, as for example [Bate, Tricco, and Price, 2013](#); [Pakmor and Springel, 2013](#); [Bonafede et al., 2011](#), to large cosmological boxes which model a significant portion of the visible universe (e.g. [Hirschmann et al., 2014](#); [Vogelsberger et al., 2014](#); [Schaye et al., 2015](#)). Several numerical techniques have been developed, refined and compared in order to improve the tools to widen our understanding of the physical processes which take place in the universe.

What they all have in common is the prerequisite of some sort of initial conditions for their simulations. These may be physically motivated as in the examples given above or simply pose the means to test the behaviour of one's code with an analytically understood problem. Not only a proper definition of the physical key quantities in these initial conditions is important, but also their numerical representation. Often simulations try to analyse physical processes with extremely small effects which can be easily hidden by noise produced from bad initial conditions. Depending on the kind of numerical code chosen this might be a nearly trivial task or rather complicated. The former being the case e.g. for a standard fixed volume discretisation scheme and the latter, as in the focus of this paper, for example a mass discretisation scheme such as Smoothed Particle Hydrodynamics (SPH) ([Lucy, 1977](#); [Gingold and Monaghan, 1977](#)) or Meshless Finite Mass / Volume ([Gaburov and Nitadori, 2011](#); [Hopkins, 2015](#)). In this paper we present an open source code which can generate relaxed initial conditions for SPH given any arbitrary physical description of initial conditions based on the work of [Donnert, 2014](#). We start by defining the actual task in section [IV-2](#), followed by a description of the presented algorithms in section [IV-3](#). In section [IV-4](#) we show the performance of our implementation measured by way of several test problems and finally present a few applications in section [IV-5](#) before closing with describing the actual usage of the application in section [IV-6](#).

IV-2 Overview of IC generation

IV-2.1 Requirements and degrees of freedom

Initial conditions contain a complete physical description of all physical quantities as a function of position inside the simulation volume, such as the density $\rho(\vec{r})$, internal energy $u(\vec{r})$ and

the velocity $\vec{v}(\vec{r})$. This mathematical description can be translated into a volume discretisation in a straight forward way, just by evaluating the functions at the discretisation points. For a mass discretisation scheme this is not easy because mass sampling particles have to be placed somewhere in the simulation volume in such a way, that the physical quantities calculated from the ensemble resemble the mathematical description given. It directly follows, that the most important quantity is the density, since it results from the placement of mass tracers. The other quantities then fall into place and need not to be discussed further.

The density in SPH for a particle i is calculated via a sum over the nearest neighbours of the mass times the kernel function:

$$\rho_i = \sum_j^{\#NGBs} m_j W(|\vec{r}_i - \vec{r}_j|, h_i) \quad (\text{IV-1})$$

The kernel function depends on the distance between both particles i and j and the smoothing length h_i . As standard kernel in our implementation and all tests presented in this paper we chose the Wendland C6 kernel function with 295 neighbours in three dimensions, following [Dehnen and Aly, 2012](#). Since this is the only SPH specific type of equation we need for this paper, we refer the interested reader to [Price, 2012b](#) for a recent review of the SPH method.

To reach a certain model density one can chose to use either constant or variable mass particles. While the latter makes it possible to choose a universally ideal particle placement by adjusting the masses to fit the density, it is very disadvantageous. A significant contrast in particle masses leads to either a large variance in the amount of neighbours inside a kernel and to high computational cost in low density regions or even to numerical instabilities. [Monaghan and Price, 2006](#) have shown, that one can not reach a low energy state with variable mass SPH particles with the classical SPH method.¹ Therefore, we restrict ourselves to constant mass SPH particles.

IV-2.2 Particle placement

Even for the ideal case of a constant density there exist several common approaches for particle placement. These include for example random positions, lattice configurations and so called glass files.

The former, while being very easy to implement, have the inherent flaw of poison noise which translates directly into the density estimate. In the left panel of figure [IV.1](#) we present a two dimensional, random particle distribution, which reveals an irregular structure full of holes and clumps. Furthermore, particles are more likely to be closer to each other than the mean particle distance, than further away, which introduces an additional anisotropy onto the density noise.

Lattice configurations come in different flavours, for example based on a cubic unit cell (cP, bcc or fcc) or in hexagonal configuration (hcp, see for example [Kotarba et al., 2011](#)). The advantage of these configurations is their regularity which results in an easy equilibrium configuration. However, effects known from grid codes are introduced, like the introduction of principle axes which may lead to orientation dependent results.

Finally, in a glass file particles are distributed in a similar fashion as molecules in a physical

¹There exist modern hybrid methods for which this is not necessarily the case, like the MFV method presented in [Hopkins, 2015](#).

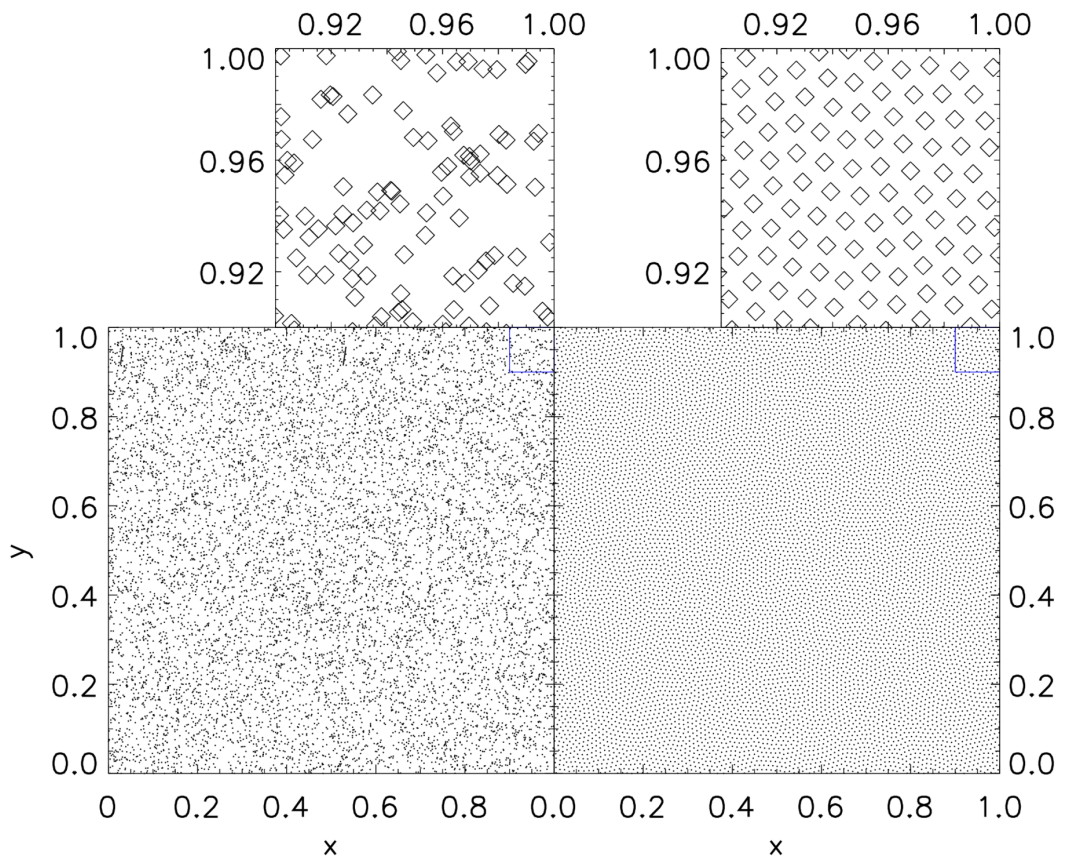


Figure IV.1: 2D particle placement for a constant density model with 10^4 particles. Left: Random distribution; Right: Glass distribution

glass. It defines a hydrostatic equilibrium condition for the system and therefore poses a low energy state. Particles are distributed non-regularly, however, with a very confined distribution of inter particle distances which helps to reduce noise (White, 1994). This can be seen in the right panel of figure IV.1.

IV-2.3 Variable density modifications

The random positions can be easily adjusted to follow a different density distribution than the uniform one and we will later exploit this in section IV-3.2. However, the aforementioned sampling error remains. Therefore, we rule out this method.² Lattices and glass files can not be easily translated to a variable density. The homogeneous setup has to be stretched and compressed to follow the underlying density model. This process is already not straight forward and in addition it results in a loss of regularity for the lattice and usually a less relaxed ensemble in the glass case. Nevertheless, stretching of uniform distributions is still commonly applied in the community (Price and Monaghan, 2005). We refer to Diehl et al., 2012 for a comparison of different approaches.

For example the initial conditions generation used for the novel SPH/N-body code Gandalf (Hubber and Rosotti, 2016; Hubber, Rosotti, and Booth, 2017) relaxes a set of particles towards a density model and a glass distribution simultaneously by applying two forces between particle pairs, one for each target property. The algorithm we present in this paper works similar at its core and we proceed by describing our approach in the next section.

IV-3 Code description

Our implementation is based on the method presented in Diehl et al., 2012, called Weighted Voronoi Tessellation (WVT) and aims to produce relaxed, low energy glass files for any arbitrary, given physical model. In the following subsections we will first describe the core parts of the algorithm, clarify typically arising issues and present a quick study on how to improve the convergence by choosing the best possible starting configuration.

IV-3.1 WVT relaxation

As shown by Diehl et al., 2012 the original algorithm is based on a Voronoi tessellation, hence the name WVT, however we do not need to implement the actual tessellation. A short pseudo code describing the main routine is given in listing IV.1. The relevant parts of the relaxation algorithm are wrapped inside a generic SPH code which calculates densities and smoothing lengths for the current particle configuration. In each relaxation step a neighbour sum in classical SPH fashion is executed and for each particle pair a force is calculated to push the particles apart. The force is weighted with both the target smoothing length and the distance of both particles in order to converge to the given density model as well as a glass-like structure. In addition, a scaling factor for the movement of particles is set, depending on the mean inter-particle distance. The goal is to find the sweet spot for the magnitude of particle pushes between

²However, random sampling will still pose as a valid starting state for our approach.

Listing IV.1: Algorithm in pseudo code

```

1 Initial particle placement
2 Do Until converged:
3   Calculate Density, Smoothing Lengths
4   For each particle loop over neighbours:
5     Distance vector between particle pair
6     Weight with expected smoothing & kernel
7     Push particles apart
8   Check convergence criteria
9   Set other quantities at particle positions

```

wasting computing time through small steps and the possibility of overshooting. The net particle displacement of particle i due to particle j is then given by

$$\Delta \vec{r}_i = \text{const} \cdot h_{ij}^m \cdot W(|\vec{r}_{ij}|, h_{ij}^m) \cdot \frac{\vec{r}_{ij}}{|\vec{r}_{ij}|} \quad (\text{IV-2})$$

with the expected model smoothing length

$$h_i^m = h^m(\vec{r}_i) = \left(\frac{N_{NGB} \cdot m}{\frac{4}{3}\pi \rho^m(\vec{r}_i)} \right)^{1/3}, \quad (\text{IV-3})$$

which is normalised such that it equals to

$$h_i^m = \left(\frac{1}{\frac{4}{3}\pi} \cdot \frac{\rho^m(\vec{r}_i)}{\sum_j \rho^m(\vec{r}_j)} \right)^{1/3}. \quad (\text{IV-4})$$

Furthermore, it enters in symmetrised form depending on both particles i and j :

$$h_{ij}^m = \frac{(h_i + h_j)}{2}. \quad (\text{IV-5})$$

There are two main changes made compared to the algorithm proposed by [Diehl et al., 2012](#): First, instead of an arbitrary weighting function which declines with distance we employ the most natural choice and use the kernel function from the surrounding SPH code, following [Donnert, 2014](#). Second, we switch the multiplicative factor of h_i^m for it's symmetrised version. While this may seem more intuitive it has not been done for a clear reason. Consider an ideal distribution of particles which exactly follows the model density. Then, the algorithm should not move particles, meaning $\Delta \vec{r}_i = 0 \forall i$. In a simplified picture the push from a neighbour on one side and one on the opposing side should cancel each other out. However, that is not the case any more in with the symmetrised version. But, the use case for our code is to start with an imperfect particle distribution and iterate towards the desired solution. Tests show, that we never reach the exact model solution globally anyway and that the symmetrised version gives much better convergence towards it and lower resulting density errors. Whether we employ the

arithmetic or geometric mean for the symmetrisation does not make any notable difference, so we keep the arithmetic one.

Furthermore, since the algorithm is formulated locally, on neighbouring particle pairs, it can in principle get stuck in a local energy minimum. However, under the condition that the density structures are well resolved (meaning kernels are not large enough to smooth them out), convergence is generally not an issue. Its properties are thoroughly analysed in section IV-4. On the other hand detecting convergence poses a difficult task. Typical criteria formulated on the average and the maximum density error have proven to be inapt since computation time can be easily wasted without the majority of particles moving any more. Therefore we employ a more pragmatic criterion to stop the relaxation as soon as most particles are moved less than a small fraction of inter-particle distance. In addition, we put an upper limit onto the maximum number of iterations to prevent getting stuck and wasting computing time.

IV-3.2 Initial state

The rate of convergence is drastically influenced by the initial state of the particle distribution. Therefore we compare a few different approaches:

- Uniform random distribution
- Von Neumann rejection sampling
- Statistical model along a space filling curve

The simplest approach for an initial setup is just a random arrangement of particles with positions drawn from a uniform distribution. As already discussed in section IV-2.2 this itself does not pose a very good density estimate but can still serve as a valid starting point for relaxation. Due to the distance dependence in our algorithm the most crucial flaw of a random distribution, namely holes and clumps of particles, are dissolved quite rapidly.

In cases where the density model varies clearly from a uniform density one can improve the initial state quite a lot with a small amount of effort by changing the random number distribution to the density function itself. This ensures that the particle density already follows the model much better without changing any other properties. This is known as Von Neumann rejection sampling (Von Neumann, 1951) and is basically a Monte Carlo integration method. While the rejection can sometimes be costly for extremely heterogeneous distributions, the computational effort is still negligible compared to the relaxation afterwards.

Despite the noise due to particle placement, people still use random distributions in certain cases. For example when the numerical noise is quickly overshadowed by any physical process or noise this can be the case without introducing a large error.

We experimented with a different approach where we iterate along a space filling curve through the simulation volume³ and for each cell compute the probability to place a particle there. This requires a space filling curve which is much finer grained than the amount of particles to distribute, so that this statistical approach is valid. One can easily prove that a probability of the

³We chose a Peano curve (Peano, 1890)

Listing IV.2: Additional redistribution in pseudo code

```

1 Calculate max amount and probes
2 dependent on iteration
3
4 While redistributed particles < max amount
5 and probes < max probes
6
7   Draw untouched random particle  $i$ 
8   increase probes until accepted for movement
9    $\forall i$  tested increment probes
10
11  Draw random particle  $j$ 
12  until accepted as destination
13
14  Random position  $x$  with  $|x - x_j| < 0.3h_j$ 
15  Move  $i$  to position  $x$ 
16  Mark  $i$  as touched

```

form

$$P = V_{Cell} \cdot \frac{\rho(\vec{r}_{Cell})}{m_{Particle}} \quad (\text{IV-6})$$

is properly normalised such that in the limit of very small cells the right amount of particles is chosen:

$$\lim_{V \rightarrow 0} \sum P = \int dV \frac{\rho(\vec{r})}{m_{Particle}} = N_{Particle}. \quad (\text{IV-7})$$

While this approach is possibly faster than the rejection sampling in practise it never generates the exact amount of particles desired.

If a particle is put in a Peano cell it can either be positioned in the cell centre, where the density was evaluated, or for a more mixed result again placed at a random position inside the cell. The former guarantees a minimum distance of particles while the latter forms a less ordered result. It turns out, that the statistical nature of this approach leads to a very similar result as the rejection sampling just without guaranteeing a certain particle number.

In summary, we therefore prefer the rejection sampling and while the application offers all three of these possibilities, we carry out all following tests using only this Monte Carlo approach.

IV-3.3 Additional redistribution

While the WVT algorithm allows us to converge against both a given density model and a glass distribution of particles it turns out that it can not reach any model density perfectly. It will always converge asymptotically towards the given constraints and settle in a low energy state. Since the algorithm operates only locally using a kernel weighting a global force term might help and also change convergence properties. Therefore, we include the possibility for an additional

global particle redistribution step in our code, which is carried out every few (typically of the order of five) relaxation steps.

The basic idea behind this approach is, that particles from regions with $\rho > \rho_{\text{model}}$ are taken and directly moved into regions with $\rho < \rho_{\text{model}}$. We design an algorithm which is similar to the well known Metropolis algorithm (Metropolis et al., 1953) with the relative density error serving as the energy analogue. On top of that we put an upper limit to the amount of particles sampled, so that less particles are redistributed the closer we come to the model solution. We present corresponding pseudo code in listing IV.2. We randomly select particles to be moved and particles which we can use as tracers of an under dense region. Then we place the respective particles into the close proximity of these region by drawing a random position with maximum distance of 0.3 of the kernel support radius. To accept a particle i for redistribution we check if a random number r_i fulfils

$$r_i \in [0, 1] < \text{erf} \left(\frac{\rho_i - \rho^m(\vec{x}_i)}{\rho^m(\vec{x}_i)} \right). \quad (\text{IV-8})$$

Similarly a particle j is viable as destination if another random number r_j fulfils

$$r_j \in [0, 1] < \frac{\rho^m(\vec{x}_j) - \rho_j}{\rho^m(\vec{x}_j)}. \quad (\text{IV-9})$$

This ensures that particles with large density errors are preferred and that more particles are probed the closer the density comes to the model. We limit ourselves to a percentage of the particles in order to preserve the overall density profile and allow us to omit density calculations in between this process. Otherwise the computational cost would be to high for the method to be feasible. The maximum number of particles to be redistributed and to be probed is given by run-time parameters. In order to assist convergence we also let both percentages decay exponentially over time. For example we start at 1% of particles and decay down to 0.1% of particles until a certain iteration step. Between each redistribution we carry out several relaxation iterations to smooth out the distribution. At some point we stop the redistribution and only let the relaxation run. The impact of this additional algorithm is investigated in section IV-4.3.

IV-4 Test Problems for crucial features

We present how the algorithm behaves in a typical use case. While it is fairly straight forward to measure the accuracy of the resulting density distribution, the “glassiness” is less easy to judge on, using properties of the particle distribution. We start with a quick analysis of generated constant density distributions and then go one step further to our actual application of variable density models. All test cases are carried out in 3D with periodic boundaries, if not mentioned otherwise. In order to save computation time we generally set up non-cubic boxes. We run all tests for maximal 1024 iterations but terminate in general earlier when reaching a quasi steady state. The additional redistribution of particles is switched off, we demonstrate the effect of this tweak afterwards.

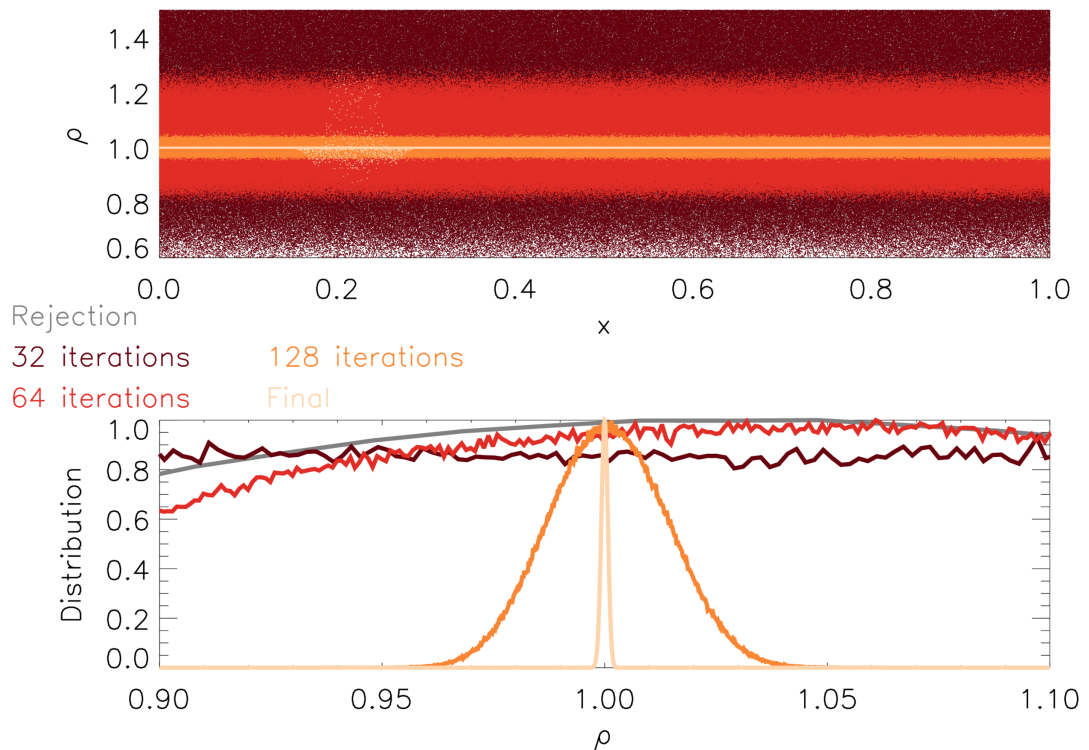


Figure IV.2: Density evolution of a 3D constant density model starting from a random distribution with 10^6 particles. Top: Density ρ against one coordinate of the position x . Bottom: Distribution of density values.

IV-4.1 Constant density

We start with the simplest case and show how the density evolves for a constant density model during relaxation in figure IV.2. The top plot shows the density values of all SPH particles after different number of relaxation steps while the lower plot presents the according distribution of density values zoomed onto a $\pm 10\%$ region of density values. We start with the typical Poisson noise of the order of $\pm 50\%$ around the target value, visible in the top plot of figure IV.2, and quickly damp down to a reasonable agreement with the density model. One can clearly see the asymptotic behaviour of the convergence until the algorithm stops after 389 iterations.

To analyse the quality of the particle distribution, an analysis similar to figure IV.1 can reveal the emerging patterns only in an obscured way due to the integrated third dimension. Furthermore, it lacks the power of a proper quantitative analysis with a parameter to measure the quality. A better judgement can be made by looking at the distribution of nearest neighbour distances (figure IV.3) and the radial distance autocorrelation function⁴ (figure IV.4).

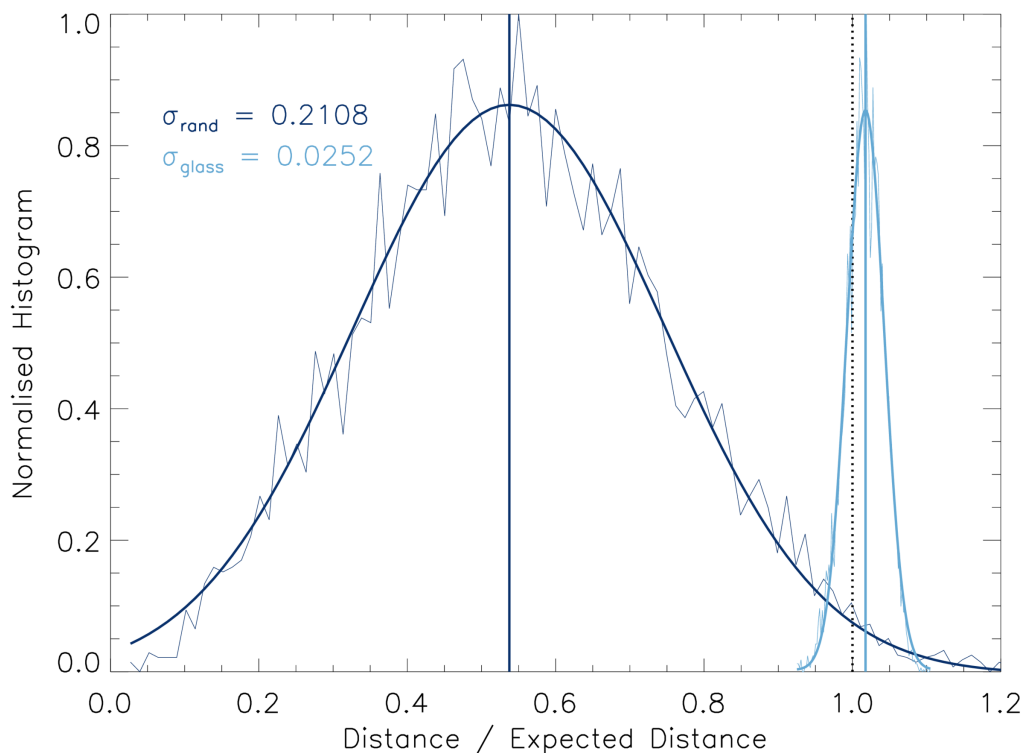


Figure IV.3: Histogram of nearest neighbour distances for a 3D constant density model for random placement and a glass distribution. The expected distance by which the x-axis is normalised is calculated by dividing the whole box volume up equally onto all particles.

We compare these two measurements for a random distribution and a relaxed glass distribution

⁴Or just “radial distribution function” in the field of molecular dynamics.

for a 3D constant density model with only 10^4 particles in a periodic box to prevent running into memory issues in our analysis script. We scale the distance by the expected distance calculated from a perfect distribution of the volume in the periodic box using

$$d = (V_p)^{1.0/3.0} = (V/N_p)^{1.0/3.0} \quad (\text{IV-10})$$

with V the volume of the whole box and N_p the particle number. Note that while this is the optimal distribution of volume onto all particles it does not present a feasible configuration. Even in best close packing of spheres, there is still about 22.2% of the volume lost (Muder, 1988). This is reached by a proper hcp lattice and depicts the asymptotic target for a well relaxed glass distribution. The distributions in figure IV.3 can be fitted by a Gaussian. The deviation of the mean value from the expected mean and the width of the fit can be taken as a measurement of quality of the distribution. Since particles tend to clump in a random distribution, the whole distribution shifts to smaller distances. The width is dominated by the Poisson noise seen in the density distribution of figure IV.2. While smaller distances are in principal desirable, this plot completely obscures that when particles clump some also spread to far from each other. Therefore, we have to not only consider the next neighbours but better analyse the whole distribution of particles using the autocorrelation function. It gives us even more insight into how well our particle distribution resembles a physical glass. We bin the distances of all particle pairs and divide each resulting value by

$$\text{Norm} = \frac{V_{\text{bin}} \cdot \langle \rho \rangle \cdot N_p}{m}, \quad (\text{IV-11})$$

with V_{bin} the bin's spherical shell volume, $\langle \rho \rangle$ the mean density in the bin, N_p the particle number and m the particle mass as presented in Frenkel and Smit, 2001.

We analyse these data by creating a histogram of the distribution (figure IV.4) which we do not further normalise or stretch in any way. The results from the different approaches can be compared to a Lennard-Jones fluid model as presented for example in Frenkel and Smit, 2001. Two criteria of quality are the height of the first peak and the behaviour on large scales. First of all a glass is characterised by a main peak height of 2.85 according to the Hansen-Verlet criterion (Hansen and Verlet, 1969) which characterises the transition from a liquid to a frozen state, demonstrating that our glass is indeed well relaxed. Also the peak's location is important. Since the first peak is mainly dominated by next neighbours we did this comparison already in figure IV.3. While the random sample damps down pretty quickly to a fairly constant distribution of values, we see damped wave like behaviour for our glass distribution around a central value of about one, as expected. The zoom onto large scales in the lower panel of figure IV.4 especially shows, that this extends out properly until the maximum distances given by half of the box' size, showing that the glass distribution we produce is of high quality.

IV-4.2 Variable density

Transitioning to variable density models, the next test consists of two plateaus connected with linear slopes. Here we examine the behaviour of our implementation with respect to linear gradients and kinks in the density function. In figure IV.5 we present the evolution of the resulting

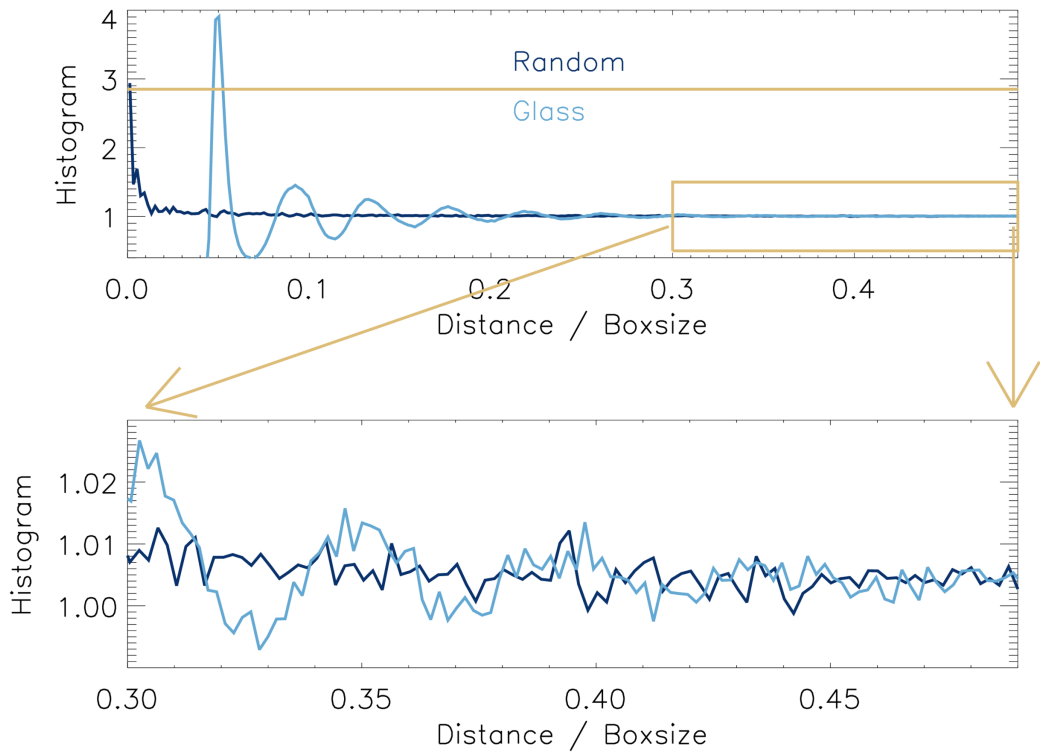


Figure IV.4: Auto correlation function for a 3D constant density model for random placement and a glass distribution including a zoom onto the large distances in the lower panel. The horizontal line marks the Hansen-Verlet criterion for a proper glass.

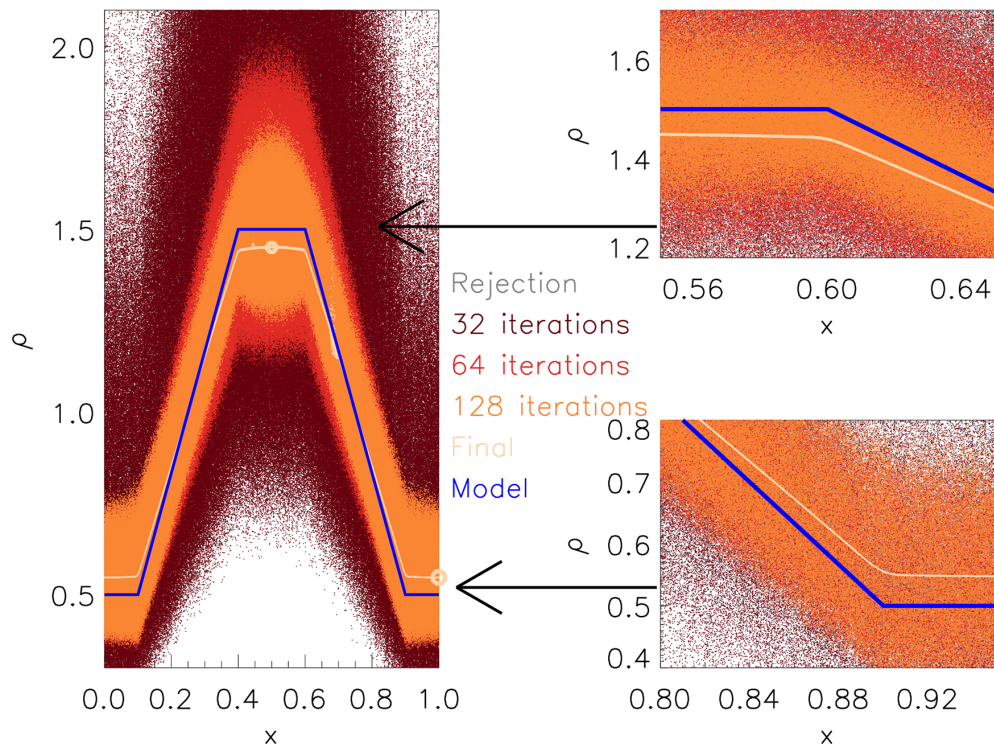


Figure IV.5: Evolution of a plateau density function with 10^6 particles. The right two plots present zooms of two kink regions in the profile.

density profile along with the analytic model. In addition to the overall profile, we also show zooms onto one upper and one lower kink of the distribution. The analytic model is given by

$$\rho(x) = \begin{cases} 0.5, & \text{for } x < 0.1 \\ 0.5 + (x - 0.1)/0.3 & \text{for } 0.1 < x < 0.4 \\ 1.5 & \text{for } 0.4 < x < 0.6 \\ 1.5 - (x - 0.6)/0.3 & \text{for } 0.6 < x < 0.9 \\ 0.5 & \text{for } x > 0.9. \end{cases} \quad (\text{IV-12})$$

Again the scatter reduces quite rapidly and we converge towards the model density. As the scatter decreases, the density flattens marginally with respect to the actual maxima and minima of the given density function. Therefore, a low energy state and following the proper density model seem to be slightly exclusive. Since the extremal values are not fully resolved, the gradients are marginally shallower than imposed. Also the constant density parts are not totally flat but show a slight curvature which is expected due to the influence of their surroundings. SPH can not produce any sharp edges by construction, only up to the resolution level given by the kernel size. We overplot two circles in both the high and low density region in order to give an idea of the size of the respective kernels in these regions to show that the model is well resolved with 10^6 particles. In the end, after 851 iterations steps, we reach a steady solution with a very low degree of scatter which deviates from the analytic solution by a few percent and shows slight curvature in the plateau and smoothed out kinks which, however, sit at the expected x -values.

Next, we look at a smoother density model to investigate the error in maxima / minima further without the introduction of sharp edges or linear gradients. We set the density model according to

$$\rho(x) = 1 + \frac{1}{2} \cdot \sin(2\pi x) \quad (\text{IV-13})$$

and plot the resulting density evolution in figure IV.6. Due to the smooth nature of this test it already converges after 412 iterations. When reducing the scatter to a very low degree the density function again slightly deviates from the model at the maxima and minima, proving that this is not an effect of non-smooth density definitions. The lower panel shows the resulting relative density error compared to the imposed model for all plotted steps. Although slightly asymmetric the error being of the order of a few percent is definitely satisfactory.

Finally we investigate our algorithm's behaviour when confronted with sudden density jumps. We set the target density to

$$\rho(x) = \frac{1}{2} + 2 \cdot \left(x \bmod \frac{1}{2} \right) \quad (\text{IV-14})$$

and plot the result in figure IV.7. While we can observe slightly more scatter here than in the previous tests, indicating that the final state (992 iterations) is probably less converged due to the presence of the prominent density discontinuity, the very nice thing to see is that the jump itself is very well resolved. Already after 32 iterations hardly any particles populate intermediate densities between the high and the low state, except for some scatter of course. Also the resulting density error is in the same regime as before. Thereby, we conclude that our implementation is able to reproduce all kind of density models within the boundaries of SPH itself and the imposed

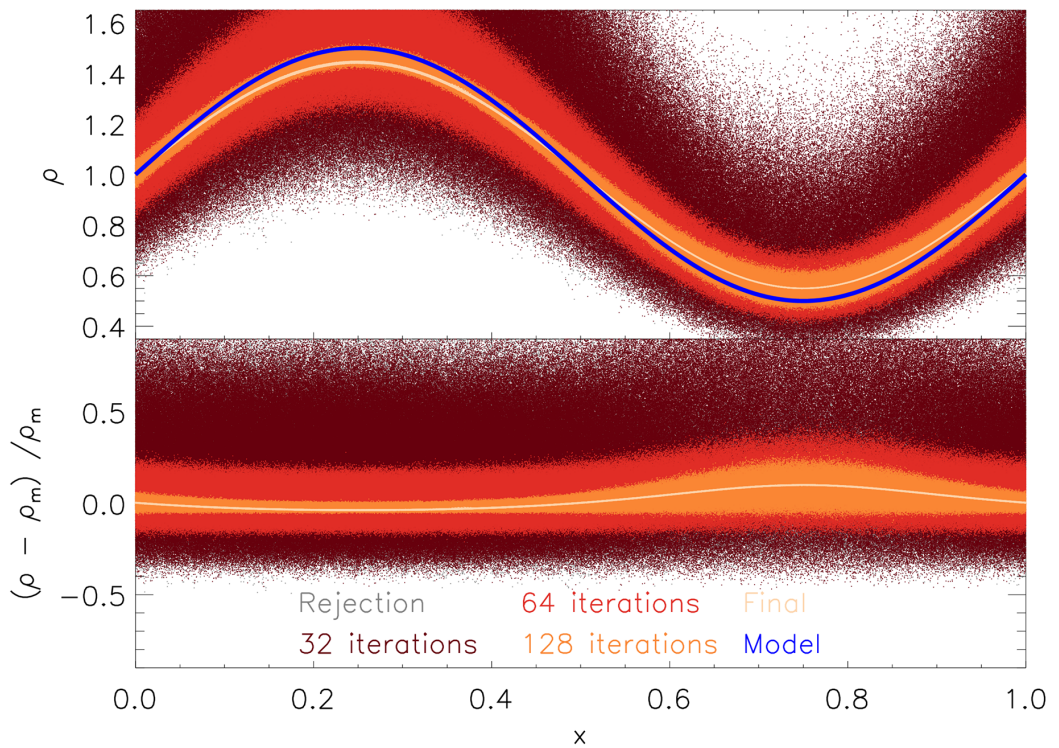


Figure IV.6: Evolution of a sine wave density function with 10^6 particles. Density distribution in the top panel, relative density error in the lower one.

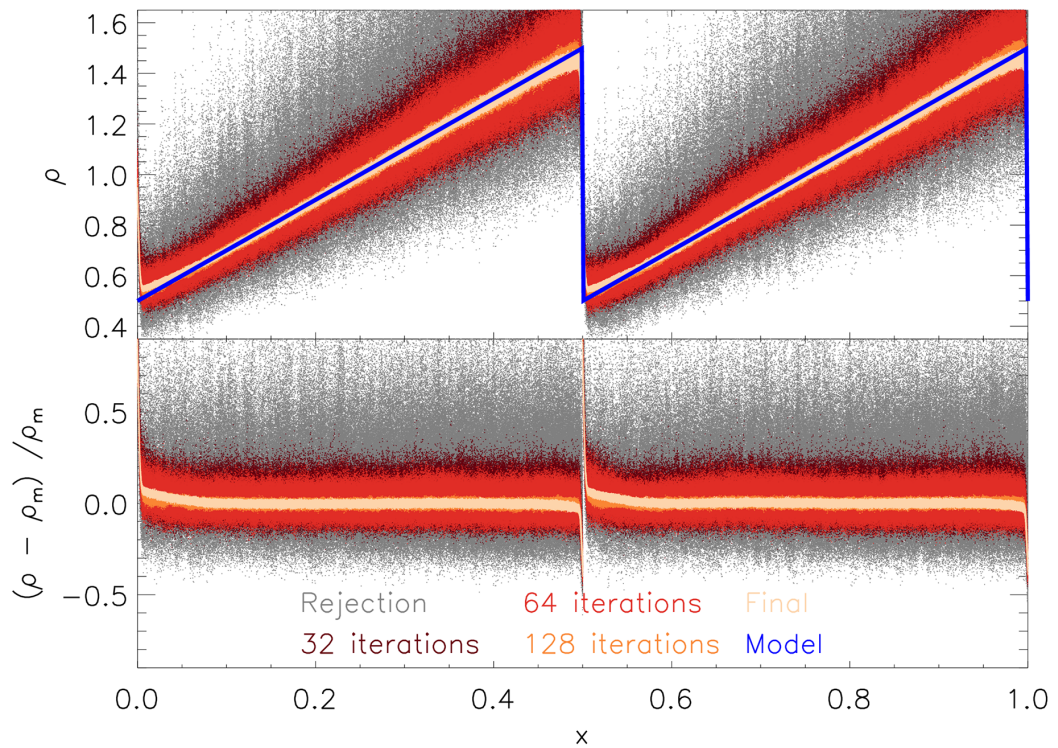


Figure IV.7: Evolution of a sawtooth density function with 10^6 particles. Density distribution in the top panel, relative density error in the lower one.

resolution. Only density models which contain regions with $\rho = 0$ may pose a strong challenge and require some fine tuning in our current neighbour finding routine.

Now, we look again at the quality of the produced glasses. If density variations can be de-

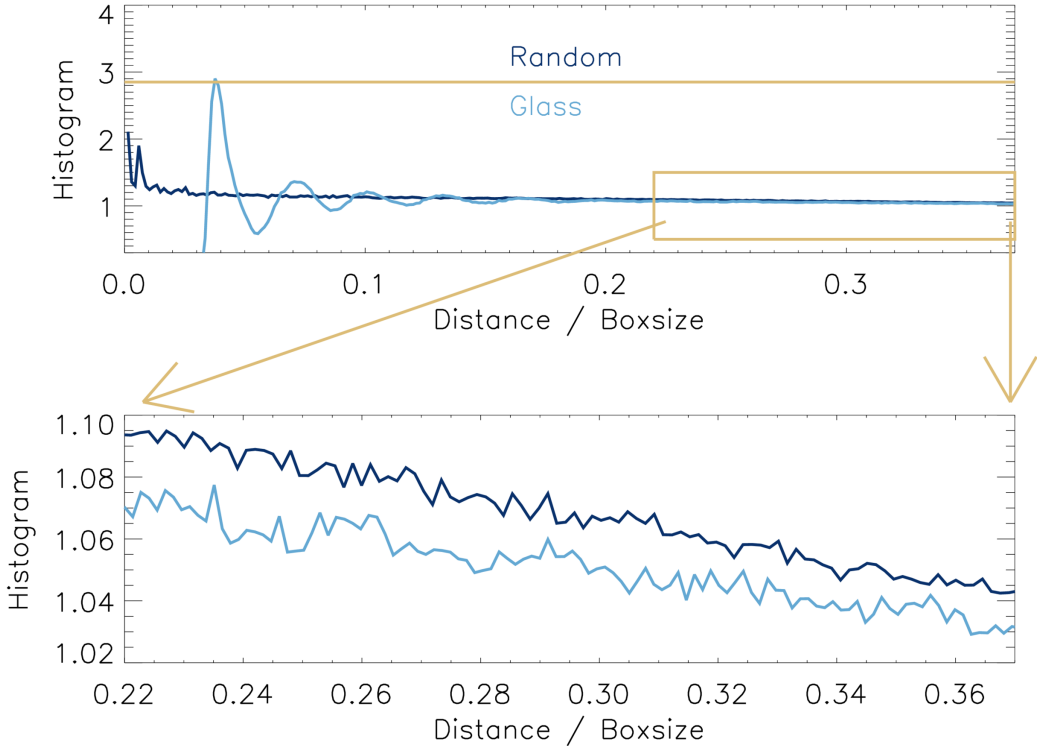


Figure IV.8: Auto correlation function for a sine wave density model for random placement and a glass distribution including a zoom onto the large distances in the lower panel. The horizontal line marks the Hansen-Verlet criterion.

scribed as small perturbations we can approximate the distribution as constant and apply the same analysis. Also regularity of the density function helps to keep a clear picture. Since the tests presented in this section fulfil these conditions slightly, we plot again the autocorrelation function for 10^4 particles distributed according to the sine wave model density. While the mean density is still at the same level as in section IV-4.1, this introduces higher and lower density regions. High density regions contain more particles than the average. This leads to a shift in the distribution to smaller distances, especially noticeable at the main peak. We still see the damped wave pattern as before, however, the dampening is stronger now. Furthermore, we notice that the distribution overall declines slightly when going to large scales. We have to truncate this plot at smaller scales since we divide the distances by the box size in x direction while the y and z direction are slightly smaller here to save computing time.

Summing up, we can judge via this method, that our 3D particle distributions actually form good glass configurations. Unfortunately, we can not execute a more quantitative analysis and have to

note, that density variations overshadow for example the wave features of the autocorrelation at large scales.

IV-4.3 Additional redistribution

Now we investigate the effects of our additionally proposed particle redistribution scheme (section IV-3.3). We start to probe ten percent and to redistribute at maximum one percent of all particles. We carry out this algorithm every 5 iterations until we reach the 512th iteration step and let the percentages decay exponentially to go down a factor of ten until the end. We carry out all three presented variable density tests with this setup and compare to the results presented in section IV-4.2.

The sine wave density shows a bit larger scatter until the redistribution is switched off and the end results improves by a very small amount. However, it requires about double the amount of iterations to converge that far, because until the 512th step we basically disturb the distribution all the time. This can be mitigated by adjusting the parameters initially chosen. The sawtooth shows only minimal effects, only that the density at the discontinuity becomes a bit sharper and less round. Since the plateau density shows the biggest effect, we plot the result in figure IV.9.

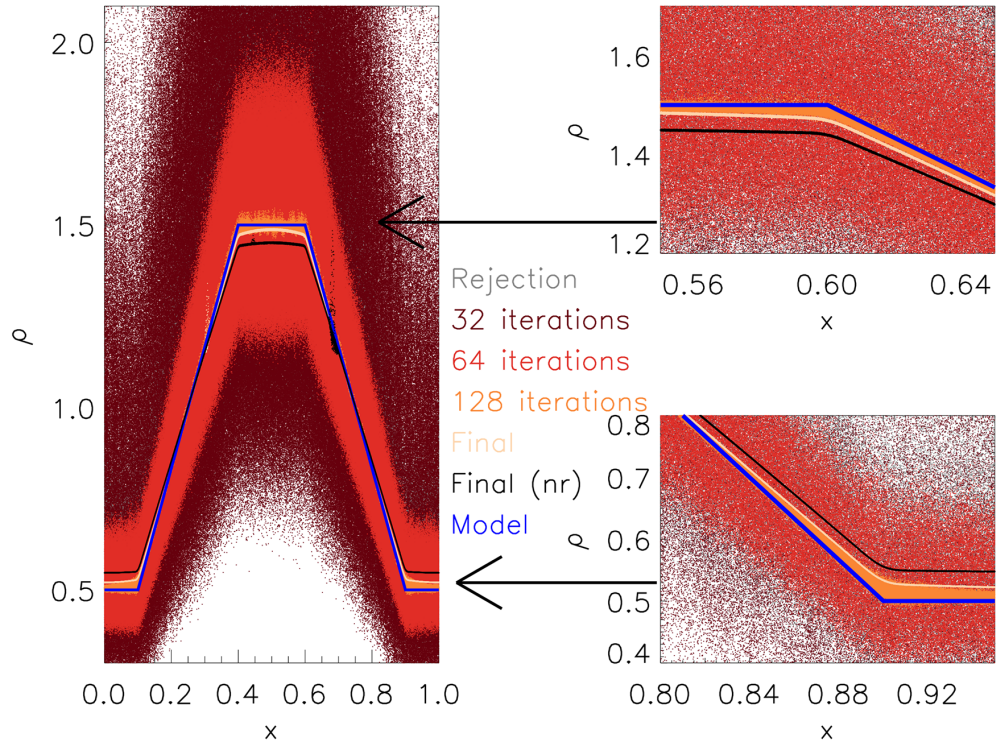


Figure IV.9: Comparison w/ (colours) and w/o (black) redistribution in the plateau test with 10^6 particles.

The colours indicate the same iteration steps as before in figure IV.5 for better comparison and we include the final result from before as a black line. As can be clearly seen, it settles much closer to the actual model density here but not without a cost. In this case the amount of iterations it takes to converge is actually about the same, but due to the additional disturbance the plateau comes out less straight than before. In the end, it is highly problem dependent how much the redistribution algorithm affects the resulting density distribution but it does so always in a positive manner.

IV-4.4 Convergence of the iteration process

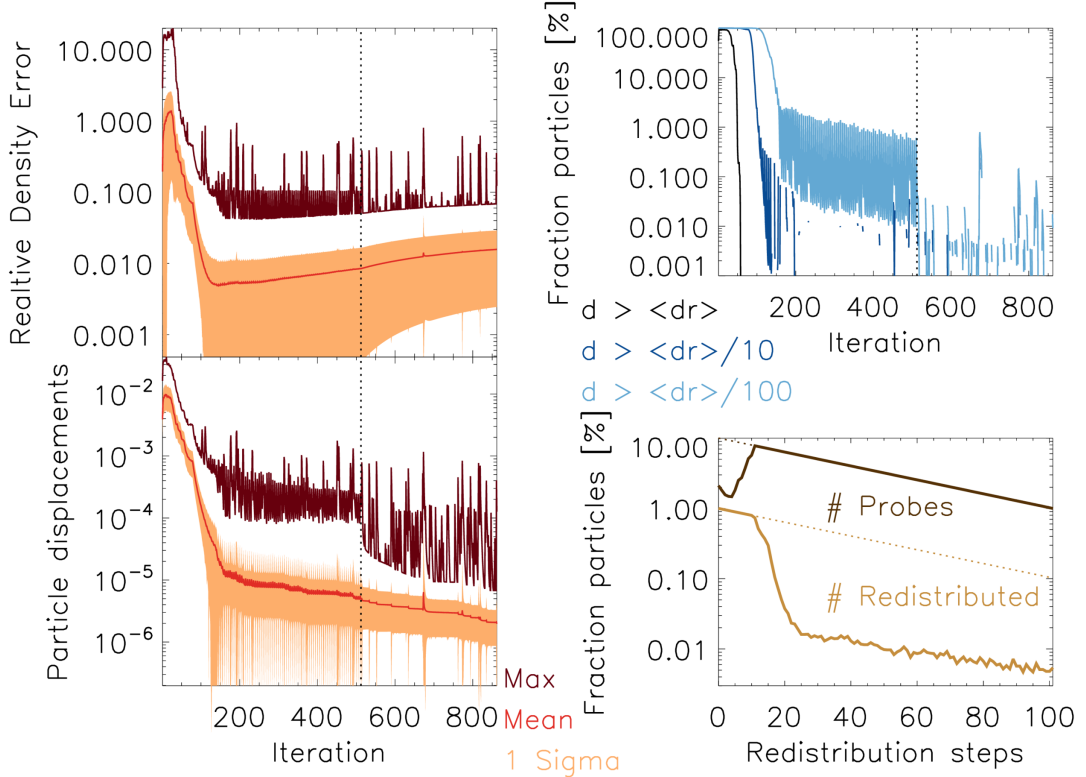


Figure IV.10: We carry out the plateau & gradients test with 10^6 particles. Top left panel: Min, mean and max density errors; Top right panel: Fractions of particles moved farther than 1, 0.1 and 0.01 of the local mean particle separation; Bottom left panel: Min, mean and max displacements calculated; Bottom right panel: Particles probed and actually redistributed; All plotted over the course of all 862 iterations.

We choose the test shown in the last subsection, with the density plateau and linear gradients carried out with 10^6 particles and the redistribution algorithm in place to have a more detailed look onto the iteration process. Each iteration we write out some statistics on the global density error, the movement of all particles in the last step and the degree of particle displacements. We

plot the results in figure IV.10. In the beginning large particle displacements due to large density errors take place. These damp down rather quickly and with them very large displacements fade away. At about 50 iterations, the maximum density error has gone down to a few percent while the mean error is even a factor 10 smaller. As the errors decline a periodic pattern emerges which actually increases errors and resulting movement frequently. The errors decays down quickly again before the next jump happens. This is the imprint of our particle redistribution scheme, which removes particles from local overdensities and puts them into underdense regions. It locally destroys the particle ordering and thus worsens the density correctness at first. We see, that the algorithm actually recovers very quickly from this kind of perturbation. Nevertheless, we hinder convergence of particle movement while this redistribution part is operational and we can not see the improvements in the final density correctness shown earlier properly in this plot. Looking at the bottom right panel reveals that the algorithm operates as designed. The amount of probes necessary quickly reach the allowed maximum and the amount of particles actually touched declines drastically down to 10^{-4} and then follows the imposed decay. We mark the spot where this part of the code is shut off in the plots by a dotted vertical line, illustrating that the high frequency periodic imprint stops immediately. We do not improve on the density error any more but rather sacrifice density correctness slightly for a better glass distribution and therefore less scatter in the density. The net particle pushes decrease as the distribution relaxes and movement damps down quickly. One can clearly see, that the net particle movement is well suited for an abortion criterion since it experiences the quickest change and directly indicates a steady state.

IV-4.5 Convergence with variable amount of particles

To investigate our implementation's performance for variable number of particles we plot the density for the plateau test case with 10^4 , 10^5 and 10^6 particles next to each other in figure IV.11, zooming onto the top plateau. In all three runs we adjust the parameters such, that the initial degree of particle movement is of the same order to have a fair comparison. While the random sampling produces very similar results we see that the particle distribution develops differently in all three runs. The lower resolution runs converge much quicker than the higher resolution one due to our algorithm working locally on neighbouring particles. The plateau comes closer to the imposed model with increasing resolution but shows more curvature as we have seen before. We can distinguish effects of the whole algorithm and of the inherent kernel smoothing. The latter becomes the most apparent in the lowest resolution, where we see stronger curvature at the position of the kinks. Finally, the resulting scatter in all three runs is of the same order.

To investigate the behaviour of convergence with iterations and changing amount of particles quantitatively, we present the L1-error of all of our three standard tests in three different resolution steps in figure IV.12. The L1 error is defined in e.g. [Hopkins, 2015](#) as

$$L1 = \frac{\sum_i |\rho_i - \rho_m|}{N_p} \quad (\text{IV-15})$$

All tests have been carried out again with a similar degree of movement in the initial setup and without the redistribution algorithm. Since the L1 error is a global measurement we only see the globally most prominent evolution as it happens in the beginning when transitioning from

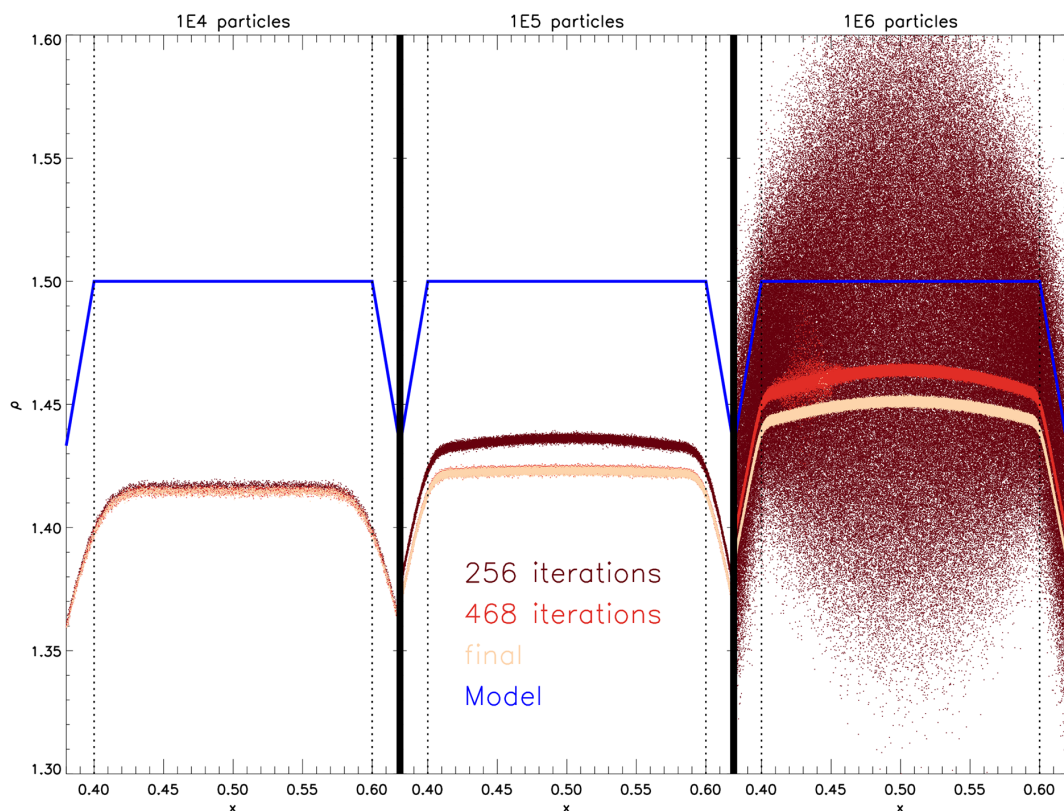


Figure IV.11: Zoom of the plateau test with 10^4 (left), 10^5 (middle) and 10^6 particles (right).

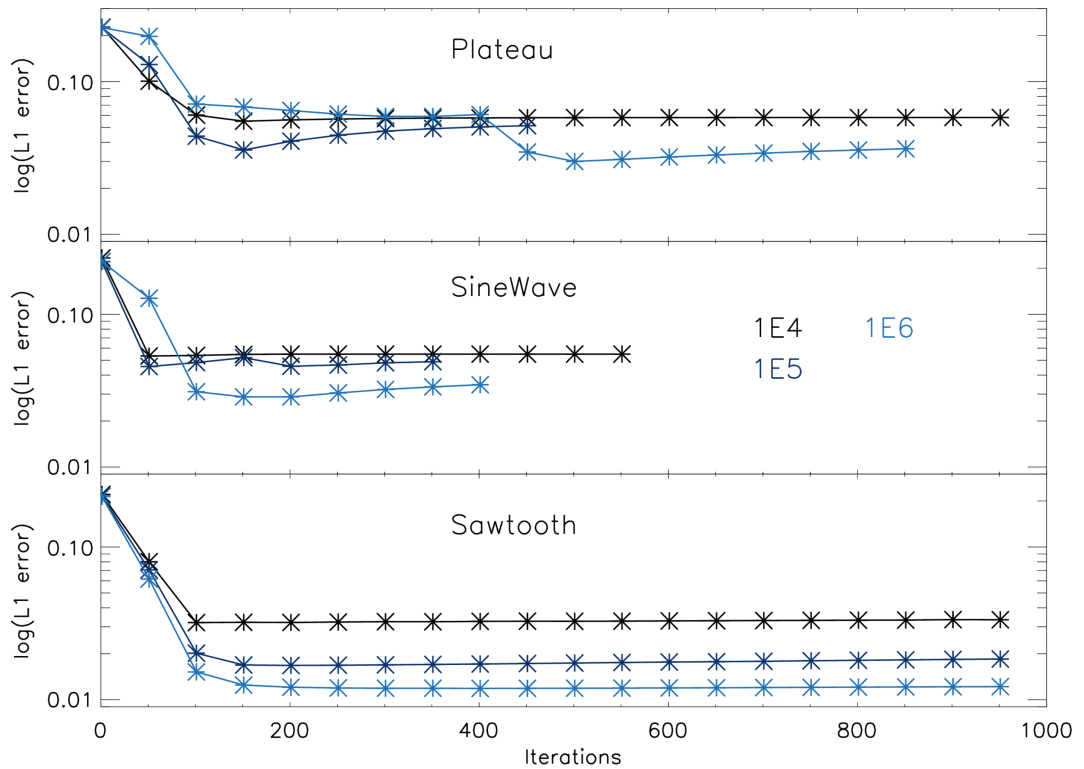


Figure IV.12: L1 error plotted after different iteration counts for all tests and different particle numbers. Top: Plateau with gradients; Middle: Sine Wave; Bottom: Sawtooth

a random distribution towards one which actually shows the features of the imposed density model. After about 100 steps the evolution becomes in general so slow, that we can hardly see a change. Nevertheless, as expected we see a clear improvement of the L1 error when increasing the particle number. According to the argumentation of [Hopkins, 2015](#) the L1-error can not become better than $10^{-2} - 10^{-3}$ in classical SPH due to the E_0 gradient error of particle disorder ([Read, Hayfield, and Agertz, 2010](#)), which poses a lower bound for convergence with particle number anyway. Nevertheless, we are still dominated by the fact that creating a good glass distribution hinders us from actually coming this close to the desired density model.

IV-5 Applications

In this section we demonstrate typical use cases in astrophysics from standard code tests to studies of astrophysical objects.

IV-5.1 Code testing: (Magneto-) Hydrodynamics

Development of a SPH code requires extensive testing of the implementation's ability to solve the (magneto-) hydrodynamical equations. Thus, every code release paper needs to prove the capability of succeeding in standard (magneto-) hydrodynamical benchmark tests. This has been presented for many common astrophysical codes over the last decade. See for example [Springel, 2005b](#), [Dolag and Stasyszyn, 2009](#), [Hu et al., 2014](#) and [Beck et al., 2016](#) for GADGET-2/3, [Springel, 2010a](#) for AREPO, [Hopkins, 2015](#) and [Hopkins and Raives, 2016](#) for GIZMO and [Hubber, Rosotti, and Booth, 2017](#) for GANDALF.

A very important part in the construction of a test suite is the generation of high quality initial conditions to ensure that the SPH code solves the equations of hydrodynamics coming from a well defined initial state with a low degree of noise. Since the method we present in this paper is capable of sampling arbitrary density profiles, we provide implementations of such common benchmark tests listed in table IV.1, alongside references for the implemented models. As one of the more complex examples of this collection we present the so called Zel'dovich Pancake ([Zeldovich, 1970](#)). We use the same initial configuration, which has been presented in [Beck et al., 2016](#). We start with the comoving position

$$x(q, z) = q - \frac{1 + z_c \sin(kq)}{1 + z} \frac{\sin(kq)}{k}, \quad (\text{IV-16})$$

with the wavenumber of the perturbation $k = 2\pi/\lambda$ and the unperturbed coordinate q , as well as the collapse redshift $z_c = 1$. The density profile is then given via

$$\rho(x, z) = \frac{\rho_0}{1 - \frac{1+z_c}{1+z} \cos(kq)}, \quad (\text{IV-17})$$

with the initial density ρ_0 . We use a Box with 64 Mpc side length and sample the density profile with 10^6 gas particles. The Zel'dovich Pancake is an important test problem for both numerical hydrodynamics and numerical integration in a comoving frame where time t is replaced with the Hubble-function $H(t)$. The resulting initial conditions are shown in figure IV.13. The quality of the initial conditions is very well in line with our previous results.

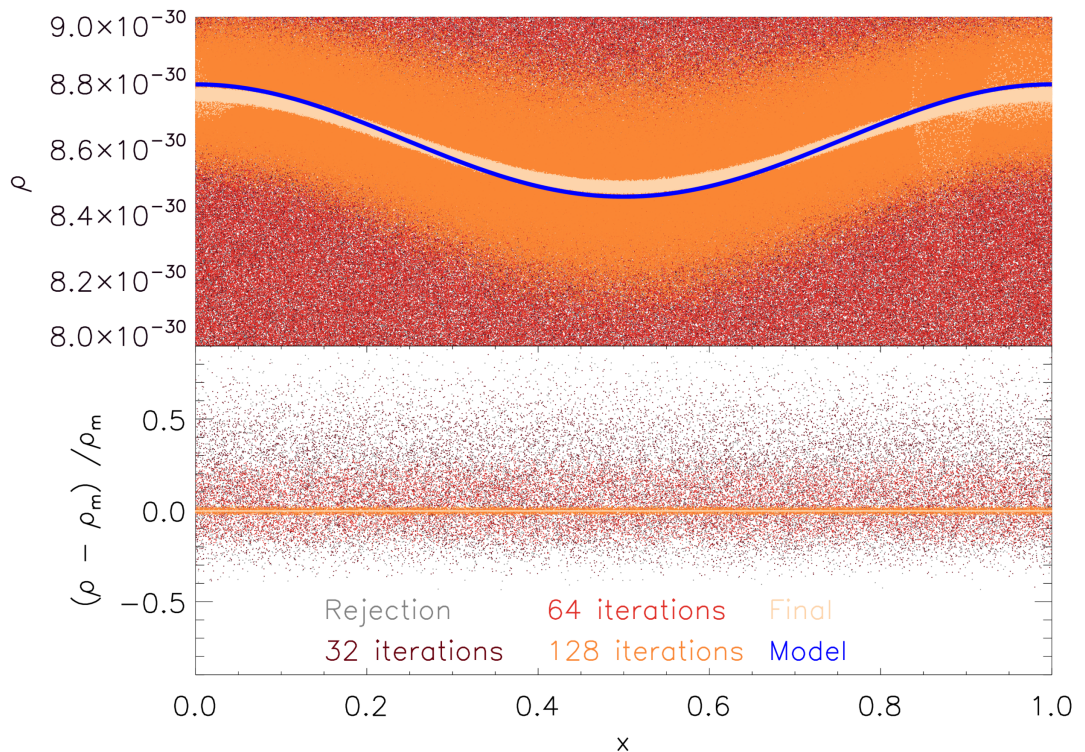


Figure IV.13: Zel'dovich pancake initial conditions with 10^6 particles.

Classical Hydrodynamic Tests	
Sod-Shock tube	Sod, 1978
Sedov blast wave	Hu et al., 2016
Kelvin-Helmholtz Instability	McNally, Lyra, and Passy, 2012
Keplerian Ring	Maddison, Murray, and Monaghan, 1996
Cold Blob	Agertz et al., 2007
Hydrostatic Sphere	Springel, 2005b
Evrard Collapse	Evrard, 1988
Zel'dovich Pancake	Zeldovich, 1970
Box-Test	Hess et al., 2010
Gresho-Vortex	Gresho and Chan, 1990
Classical Magneto-hydrodynamic Tests	
Ryu-Jones Shock tube	Ryu, Jones, and Frank, 1995
Fast-Rotor	Balsara and Spicer, 1999
Strong-Blast	Hopkins and Raives, 2016
Orszag-Tang-Vortex	Hopkins and Raives, 2016
Linear Alfvén Wave	Stone et al., 2008
Rayleigh-Taylor-Instability	Abel, 2011

Table IV.1: Hydrodynamic and magneto-hydrodynamics test cases, implemented in the code.

IV-5.2 Binary star formation

In this section, we present the initial conditions for the Boss and Bodenheimer test case (Boss and Bodenheimer, 1979) to simulate the formation of a binary system of stars. We follow the implementation presented in Springel, 2005b with the density profile

$$\rho = \rho_0[1 + 0.1 \cos(2\varphi)], \quad (\text{IV-18})$$

using a central density $\rho_0 = 3.82 \cdot 10^{-18} \text{ g/cm}^3$. Furthermore, we set up a sphere of radius $R = 5 \cdot 10^{16} \text{ cm}$, a total mass of $1M_\odot$, speed of sound $c_s = 1.66 \cdot 10^4 \text{ cm/s}$ and a solid body rotation of $\omega = 7.2 \cdot 10^{-13} \text{ 1/s}$, as of Burkert and Bodenheimer, 1993. In figure IV.14 we show the rendered density profile in x-y plane with the perturbation in direction of φ which matches the model very well.

IV-5.3 Isolated galaxy cluster

The baryonic content of clusters of galaxies, in general, follows a beta model profile (e.g. Cavaliere and Fusco-Femiano, 1978), given by

$$\rho_{\text{gas}}(r) = \rho_0 \left[1 + (r/r_c)^2\right]^{-3\beta/2}, \quad (\text{IV-19})$$

where the density within the core radius r_c is constant and decays as a power-law outside the core. Donnert, (2014) set up initial conditions for idealised binary merger simulations in the proprietary code TOYCLUSTER, further improved by Donnert et al., (2017b) by adding WVT

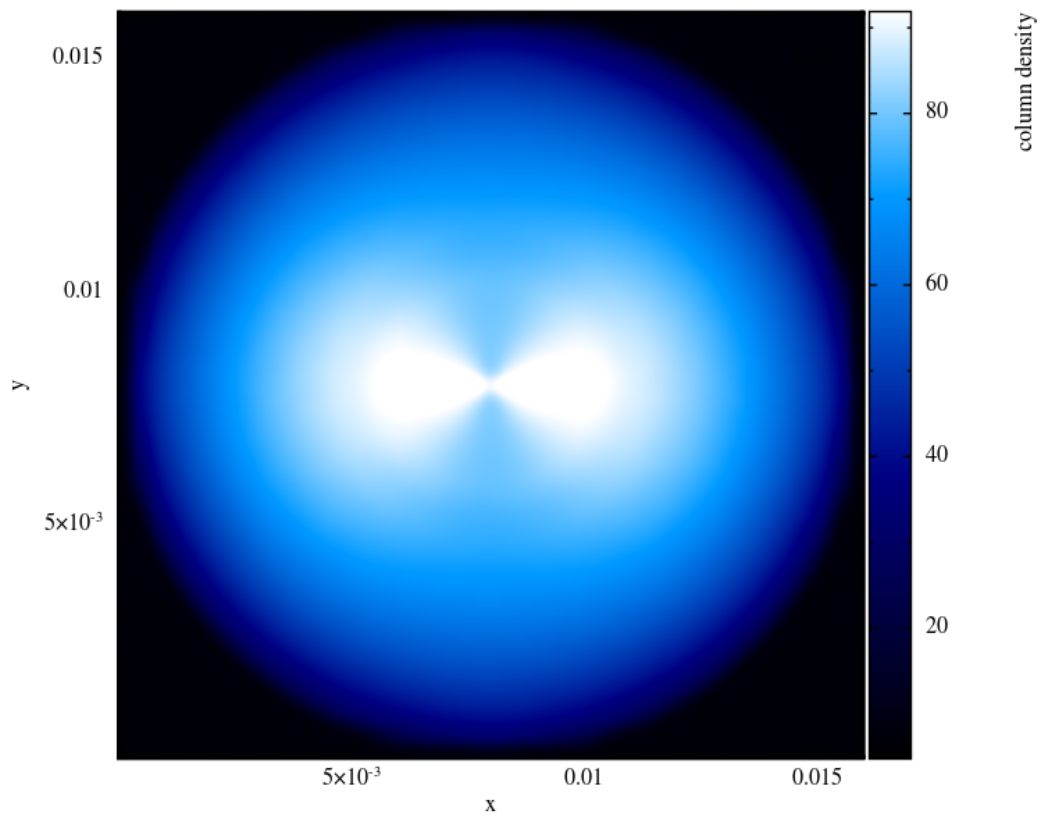


Figure IV.14: Integrated density of the Boss-Bodenheimer test case for binary star formation in the x-y-plane with 10^6 particles.

relaxation. For simplicity, here we ignore the dark matter halo of the cluster as well as the temperature structure. The ‘cluster’ is set up with general parameters $\rho_0 = 10^{-26} \text{ g/cm}^{-3}$, $r_c = 20 \text{ kpc}$, and $\beta = 2/3$ which could resemble a cool-core cluster of galaxies. We sample the density profile using 10^6 SPH particles.

We show the resulting density in figure IV.15 at 32, 64, 128 and 1024 iterations, where we hit

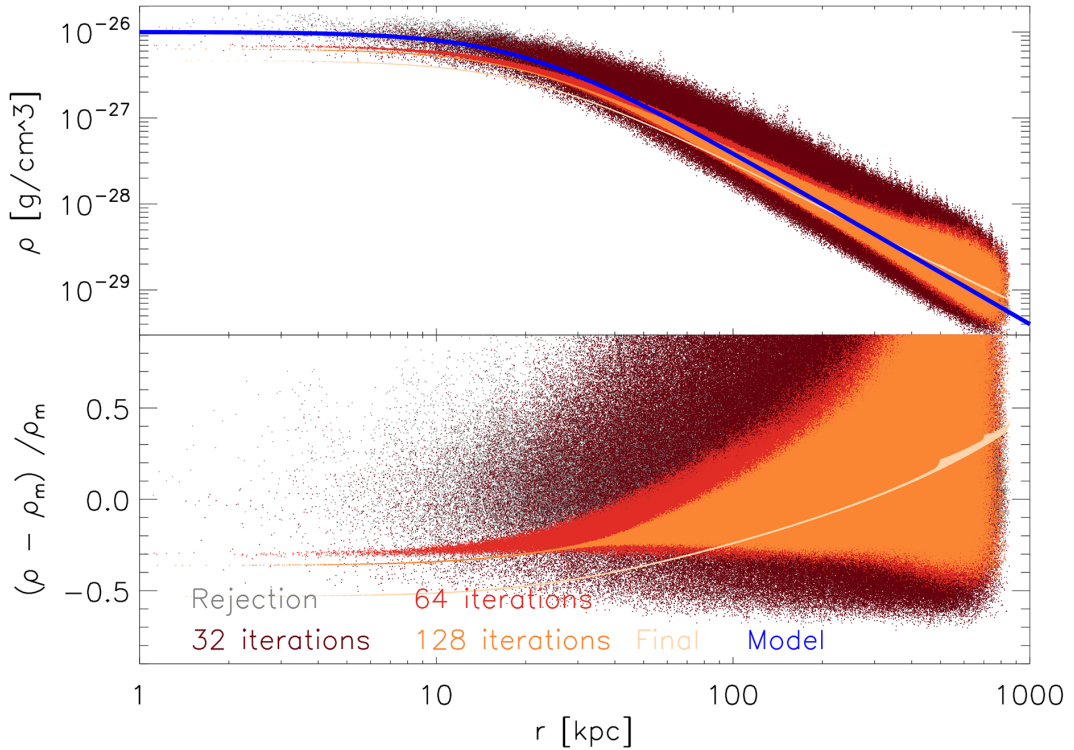


Figure IV.15: Beta profile for an isolated galaxy cluster with 10^6 particles.

the maximum number of iterations and the algorithm terminated. This happens due to the large range of more than three orders of magnitudes in density which we try to sample with only 10^6 particles. In the low density region we can not properly resolve the gradient any more because the SPH kernels become very large, leading to a locally large spread in the density distribution early on which it relaxes away nicely. Furthermore, this results in quite big density errors in the low density regions of the resulting distribution. Judging these errors relatively to the mean density they are, however, quite small. Consequently, since the particle masses are calculated from the mean density, this overdensity directly leads to an underdensity in the central regime. Nevertheless our results are consistent with [Donnert, 2014](#), who successfully uses similar initial conditions for actual simulations of galaxy cluster mergers.

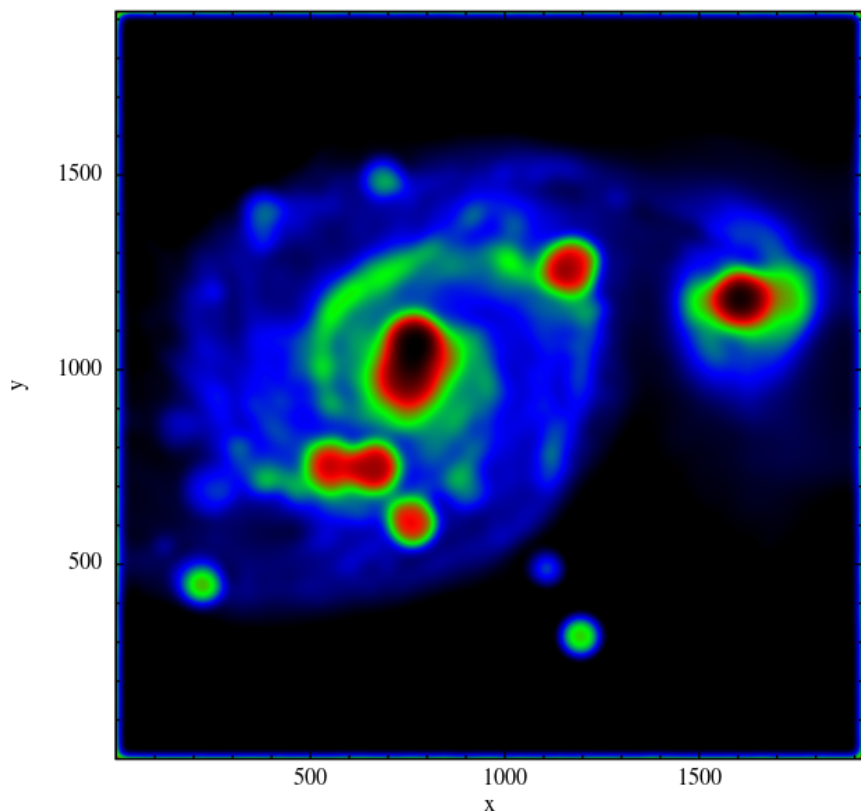


Figure IV.16: Example for initial conditions sampled according to a read image of the whirlpool galaxy M51a and it's companion M51b with 10^6 particles.

IV-5.4 Reading in an initial setup: Image processing

Finally, we present a special feature of our application which allows us to read in a given set of three dimensional gridded data for the definition of a model density, instead of providing a hard coded analytic solution. An example where we directly used the brightness scale of an image utilising our built in png reading routine is shown in figure IV.16. The goal of astrophysical simulations is always the comparison to observations in order to learn more about the processes in the universe. Mostly only statistical comparisons can be made because it is extremely difficult to simulate an observed object exactly in all its details. This feature might actually help here, taking in an observational image in order to model the underlying matter distribution. The implementation is currently being expanded to take in proper 3D data which might be for example de-projected from observational images. Other applications outside of astrophysics can be found, where one might for example build a CAD model of a 3D distribution see e.g. [Dauch et al., 2017](#).

IV-6 Code usage

In this final section we talk briefly about the actual usage of our application. It can be downloaded from github ([Donnert et al., 2017a](#)) and will be made publicly available under the GPL license with the release of this paper. The current code version described here is v2.1. This section is split into two parts: First, we state the compilation requirements. Second, we show the currently required parameters and describe how to actually run the application successfully.

IV-6.1 Requirements and compilation

The code is written in OpenMP parallel C with the C99 standard and requires the gsl and gslcblas libraries. If the png reader shall be used, libpng is necessary in addition. There are no special requirements regarding the choice of compiler or any known issues with optimisation flags.

For compilation we provide two identical approaches, a direct Makefile or, as required by some

Option	Default	Description
SAVE_WVT_STEPS	ON	Write out a snapshot after each relaxation iteration
SPH_CUBIC_SPLINE	OFF	Switch from Wendland C6 kernel to cubic spline
SPH_WC2	OFF	Switch from Wendland C6 kernel to Wendland C2
REJECTION_SAMPLING	ON	Use rejection sampling for initial particle distribution
PEANO_SAMPLING	OFF	Use a Peano curve for the initial particle distribution
EAT_PNG	ON	Compile with png reading support
TWO_DIM	OFF	Switch from 3D to 2D, ignoring z coordinates
BRUTE_FORCE_NGB	OFF	Instead of a tree use a brute force neighbour finder (mainly used for debugging purposes)
OUTPUT_DIAGNOSTICS	ON	Output additional diagnostics to file each iteration

Table IV.2: Compilation options with default values and description.

IDEs, a CMake file which then generates an own Makefile. Both approaches provide the possibility to adjust the compilation by setting some options which are translated into preprocessor defines. An overview is given in table [IV.2](#).

IV-6.2 Parameters and running the application

Parameter	Default	Description
Npart	100000	Amount of particles to distribute
Maxiter	512	Maximum iterations of relaxation
MpsFraction	1.0	Scaling parameter for the particle displacements
StepReduction	0.95	Factor to reduce step sizes in case of overshooting
LimitMps	-1	Abort if particles moved farther than the local mean particle separation below this percentage
LimitMps10	-1	Abort if particles moved farther than one tenth of the local mean particle separation below this percentage
LimitMps100	-1	Abort if particles moved farther than one hundredth of the local mean particle separation below this percentage
LimitMps1000	-1	Abort if particles moved farther than one thousandth of the local mean particle separation below this percentage
MoveFractionMin	0.001	Fraction of particles to redistribute maximally after the decay
MoveFractionMax	0.01	Fraction of particles to redistribute maximally initially
ProbesFraction	0.1	Fraction of particles to be probed for redistribution initially
RedistributionFrequency	5	How many relaxation steps are executed between two steps of redistribution
LastMoveStep	256	Exponential decay of the redistribution amount until this iteration, afterwards shutoff
Problem_Flag	0	Main flag to chose the initial conditions model (full list in ics.par)
Problem_Subflag	0	Sub flag to chose the initial conditions model (full list in ics.par)
PNG_Filename	pic.png	Which png to read in, if the respective Flag and Subflag have been chosen

Table IV.3: Runtime parameters with example values and descriptions.

In order to run the application, one has to provide a parameter file by path. The main code directory contains already a sample parameter file called “ics.par”. It lists all provided runtime configuration options to adjust the main algorithms of the code and chose the respective initial conditions model. A list of parameters including standard values and short explanations are given in table [IV.3](#).

Besides these parameters one can change the behaviour of the OpenMP parallelisation by setting the usual environment variables to appropriate values, like `OMP_NUM_THREADS`.

IV-7 Summary and Conclusions

In this paper we presented a novel application to generate arbitrary initial conditions for SPH with a glass-like particle structure. The applied algorithms are based on a combination of weighted Voronoi tessellation (Diehl et al., 2012), density aware random sampling (Von Neumann, 1951; Peano, 1890) and an additional reshuffling of particles (Metropolis et al., 1953). We showed an overview of common methods to solve this task and illustrated the challenges that come along. We ran several test problems with different density features, like linear and non-linear gradients, kinks and jumps, and investigated thoroughly how our implementation performs when confronted with them. We found that our algorithms converge reasonably well towards the given density models while also iterating towards a glass structure, which we analysed in 3D using a radial distance distribution function. We showed, that converging towards the correct density and a glass distribution at the same time is extremely difficult, since both tasks slightly contradict each other. Particles have to be pushed apart from each other in order to remove clumps and holes in the particle distribution, but this results in particles being moved out of high density regions resulting in lower density maxima and consequently also higher minima. Therefore, one has to settle for an application dependent trade-off. We also analysed the convergence of our algorithms with variable particle number and see desired behaviour.

Our application also inhibits a suite of various sets of initial conditions, including many standard test problems for (magneto-) hydrodynamics and the ability to produce idealised setups for a galaxy cluster (as in Donnert, 2014). These tests are frequently required for code development of SPH codes and often the ability to judge the quality of a code was limited by poor initial conditions.

We also presented a special feature which allows the code to sample a density model according to a png image instead of an analytic model. This might be useful to bridge observations and simulations further, since it can lead to the ability to simulate observed objects better. For that more development has to be done, though.

Finally, we also presented the actual usage of our application, including a short description of all options and parameters which can be set at the moment (v2.1). The source code resides on github (Donnert et al., 2017a) and will be made publicly available with the release of this paper. More development will go into the project, in order to provide more features and further improve the usability. This includes for example support for more read in / write out formats, extending the possible choices of SPH kernels, expanding the 2D image reader eventually to 3D and even improvements on the core algorithms themselves. One idea to reduce the density errors in the converged result is for example, to encapsulate the existing algorithms in another loop which gradually adjusts the density model slightly by changing the amplitudes of extremal values. This could be done for example by a machine learning approach. We feel, that the goal, to write a flexible and versatile tool applicable for all kinds of problems has been reached and the next stage of development can then begin. Any feedback and contributions via github are

welcome.

Acknowledgements

The authors would like to thank their colleague's Martin Zintl and Stefan Heigl for useful discussions. This product includes software developed by Greg Roelofs and contributors for the book, "PNG: The Definitive Guide" published by O'Reilly and Associated. AA, US and KD are using SuperMuc of the Leibniz-Rechenzentrum via project 'pr86re'.

Chapter V

A modern SPH scheme: Handling numerics properly

Mathematics is a game played according to certain simple rules with meaningless marks on paper.

– David Hilbert

In this chapter we demonstrate recent improvements for our SPH solver. In chapter III we presented the basics of the SPH method including common advantages and flaws it has inherently. These improvements are designed to overcome these limitations in such a way that no additional errors are imposed and that the resulting scheme is numerically stable and well behaved. We demonstrate how our implementation into GADGET-3 performs in comparison to a classical SPH implementation in various hydrodynamical test cases. The content of this chapter has been published in [Beck et al., 2016](#) in a slightly modified manner.

V-0 Abstract

We present an implementation of smoothed particle hydrodynamics (SPH) with improved accuracy for simulations of galaxies and the large-scale structure. In particular, we implement and test a vast majority of SPH improvement in the developer version of GADGET-3. We use the Wendland kernel functions, a particle wake-up time-step limiting mechanism and a time-dependent scheme for artificial viscosity including high-order gradient computation and shear flow limiter. Additionally, we include a novel prescription for time-dependent artificial conduction, which corrects for gravitationally induced pressure gradients and improves the SPH performance in capturing the development of gas-dynamical instabilities.

We extensively test our new implementation in a wide range of hydrodynamical standard tests including weak and strong shocks as well as shear flows, turbulent spectra, gas mixing, hydrostatic equilibria and self-gravitating gas clouds. We jointly employ all modifications; however, when necessary we study the performance of individual code modules. We approximate hydrodynamical states more accurately and with significantly less noise than standard GADGET-SPH. Furthermore, the new implementation promotes the mixing of entropy between different fluid phases, also within cosmological simulations.

Finally, we study the performance of the hydrodynamical solver in the context of radiative galaxy formation and non-radiative galaxy cluster formation. We find galactic disks to be colder and more extended and galaxy clusters showing entropy cores instead of steadily declining entropy profiles. In summary, we demonstrate that our improved SPH implementation overcomes most of the undesirable limitations of standard GADGET-SPH, thus becoming the core of an efficient code for large cosmological simulations.

V-1 Introduction

Smoothed particle hydrodynamics (SPH) is a commonly employed numerical method in astrophysics. It solves the fluid equations (Landau and Lifschitz, 2007) in a Lagrangian mass-discretised fashion, which ensures Galilean invariance and conservation of mass, momentum, angular momentum, energy and entropy. It was pioneered by Gingold and Monaghan, 1977 and Lucy, 1977 and has since then become one of the cornerstones of computational astrophysics. The discretisation of mass automatically adapts spatial resolution by removing the constraint of handling geometry explicitly. It also easily couples to N-Body schemes for calculation of gravitational forces (Hernquist and Katz, 1989). An excessive amount of papers and literature about SPH has been produced over the past decades. We point out the latest reviews by Ross-woog, 2009, Springel, 2010a, Monaghan, 2012 and Price, 2012b for the basic concepts and e.g. Ritchie and Thomas, 2001 for an extension to multi-phase fluids and Rosswog et al., 2014 for a special-relativistic adaption. As every numerical method, SPH comes with its own set of benefits and pitfalls, which we address in this paper.

The inability of traditional SPH methods to treat contact discontinuities and to mix different fluid phases is a long-standing problem (Agertz et al., 2007; Wadsley, Veeravalli, and Couchman, 2008). It leads to a completely numerical spurious surface tension at the discontinuities preventing particle movements. Consequently, it results in a failure of these formulations of SPH to resolve fluid instabilities such as the Kelvin-Helmholtz or Rayleigh-Taylor instabilities (see e.g. Junk et al., 2010; Valcke et al., 2010; McNally, Lyra, and Passy, 2012; Puri and Ramachandran, 2013). In applications to cosmic structure formation it causes entropy profiles to diverge towards the centres of dark matter haloes, at variance with Eulerian codes that predict entropy plateaus to build up (Frenk et al., 1999; Wadsley, Veeravalli, and Couchman, 2008; Planelles and Quilis, 2009; Vazza, 2011; Power, Read, and Hobbs, 2014; Biffi and Valdarnini, 2015; Rasia et al., 2015). This difference is due to the lack of mixing in simple SPH, which makes low-entropy gas in merging substructures sink toward the centre of the main structure. Many modifications have been proposed to overcome this problem. For example, Wadsley, Veeravalli, and Couchman, 2008 propose a mixing solution, which resolves the differences in the entropy profiles of dark matter haloes between Eulerian and SPH codes (Frenk et al., 1999). Further cosmological applications have been performed by Shen, Wadsley, and Stinson, 2010. Firstly, the equation of motion (EoM) can be re-formulated from a standard 'density' approach into a 'pressure' based approach (Saitoh and Makino, 2013; Hopkins, 2013). While the 'pressure' formulation correctly treats contact discontinuities, it leads to increased noise at strong shocks. Secondly, considerable effort has been made to unite grid-based solvers for the fluid equations with the Lagrangian nature of SPH. Eulerian Godunov methods (see e.g. Cha, Inutsuka, and Nayakshin, 2010; Springel,

2010b; Murante et al., 2011) and their coupling to Lagrangian methods is a promising alternative. Connecting a Lagrangian moving-mesh with grid-based solvers (Springel, 2010b) or mesh-free approaches (Hopkins, 2015; Hopkins and Raives, 2016) represent more advanced approaches. Thirdly, artificially modelled conduction (AC) of internal energy can be employed to overcome the mixing problem. Most modern SPH codes include AC of some sort to diffuse entropy (Read and Hayfield, 2012) or energy (Price, 2008) across particles. The use of AC has to be taken carefully and it is only desirable at contact discontinuities in traditional 'density' SPH and at shocks in modern 'pressure' SPH. The application of AC in other regions can have catastrophic impact on the fluid dynamics and can smear out gravitationally established pressure gradients, thus leading to totally numerically induced transport of internal energy (Valdarnini, 2012).

Next, traditional SPH has difficulties treating subsonic turbulence as it experiences a high effective viscosity, which limits the inertial range (see e.g. Bauer and Springel, 2012). Thus, traditional SPH cannot achieve high Reynolds' numbers compared to, for example, Eulerian methods. This high effective viscosity is a function of resolution, but no general solution has yet been proposed to resolve this issue in general. For the correct capturing of shocks numerically motivated artificial viscosity (AV) is commonly employed. It smooths the particle velocity distribution and gives order to the fluid sampling. However, AV is only desired at the shock and the fluid should be inviscid otherwise. Too much AV smears out physical motions and damps subsonic and turbulent motions in isolated tests (Bauer and Springel, 2012) as well as in cosmological simulations (Dolag et al., 2005b). Therefore, several different implementations of AV reduction are proposed (Morris and Monaghan, 1997; Cullen and Dehnen, 2010). They are all based around a proper shock detection method and a time-dependent viscosity decay scheme. Application of such advanced schemes give better results in the description of fluid motions (Dolag et al., 2005b; Price, 2012a).

Finally, it might seem easy to simply reduce the quantitative errors by increasing the number of neighbours, which contribute to the local density and force estimators. However, the standard weighting functions of SPH respond differently to an increase of smoothing neighbours and can possibly become unstable to the pairing instability (Schüssler and Schmitt, 1981; Price, 2012b). Therefore, recently, alternative kernel functions immune against this instability are proposed for better fluid sampling and convergence (Read, Hayfield, and Agertz, 2010; Dehnen and Aly, 2012). The advantage of flexible geometry of SPH comes with difficulties in creating well-defined initial conditions or sampling analytical profiles, where we use either glass set-ups (White et al., 1996) or Weighted Voronoi-Tessellations (Diehl et al., 2012).

To overcome the named disadvantages we implement a large set of improvements for SPH into the developer version of the cosmological N-Body / SPH simulation code GADGET-3 (Springel, Yoshida, and White, 2001; Springel, 2005b). We include a time-step limiter for strong shocks, a time-dependent viscosity scheme for subsonic turbulence, a high-order gradient estimator and shear flow limiter for shearing motions, an improved kernel function for convergence and a time-dependent artificial conduction scheme to promote fluid mixing. We discuss the accuracy and the performance of our new scheme in hydrodynamical standard test problems, within quiet and violent environments as well as in idealized simulations of galaxy and galaxy cluster formation, in which our new scheme is applied to reasonable astrophysical problems.

The paper is organised as follows. The improved implementation of hydrodynamics is presented in Section 2. In Section 3 we validate our SPH algorithms in a set of hydrodynamical standard tests and we proceed to standard tests with gravity in Section 4. We continue in Section 5 with Idealized applications to the evolution of an isolated disk galaxy and a forming galaxy cluster. We summarise our developments and code performance in Section 6.

V-2 A new SPH implementation

We start with a presentation of the main equations corresponding to a ‘standard’ and our ‘new’ formalism of GADGET-SPH. The formalism of SPH is already well described by a large number of reviews (see e.g. [Price, 2012b](#)). We refer to the ‘standard’ version of SPH as the implementation within the GADGET-3 code without our modifications. We point out our modifications and discuss the kernel function, the EoM, the particle wake-up scheme and the time-dependent AV and AC.

V-2.1 Original code platform

We implement our SPH modifications into the developer version of the cosmological N-Body/SPH code GADGET-3 ([Springel, Yoshida, and White, 2001](#); [Springel, 2005b](#)). We evolve entropy as the thermodynamical variable ([Springel and Hernquist, 2002](#)) and use the prescriptions for radiative cooling, supernova feedback and star formation following [Springel and Hernquist, 2003](#). In the following sections we compare two different SPH schemes (see also table V.1), which are distinguished as follows. The ‘standard’ implementation corresponds to the developer version of GADGET-3 without our modifications ([Springel, 2005b](#)). The ‘new’ implementation includes all the SPH improvements presented in this section. In principle, we always use the entire new scheme and we also employ the same set of all numerical parameters throughout our entire simulation test suite. Thus, unless otherwise stated, we do not tune individual standard tests or astrophysical applications. However, if necessary we sometimes switch off some of the modifications to analyse their individual and isolated impact on several of the test problems.

V-2.2 Kernel functions and density estimate

Foremost, there is the question in a Lagrangian method how to derive fluid field quantities from a given set of point masses. In particular, the estimation of the gas density is crucial as many further equations rely on it. We employ the standard estimator of SPH and calculate the density $\rho(\mathbf{x}_i) = \rho_i$ of an individual particle i at the position \mathbf{x}_i by summing the contributions of N_i neighbouring particles j within a smoothing radius $h(\mathbf{x}_i)$ at a distance x_{ij} in a mass-weighted (m_j) and distance-weighted ($W_{ij}(x_{ij}, h_i)$) fashion

$$\rho_i = \sum_j m_j W_{ij}(x_{ij}, h_i). \quad (\text{V-1})$$

	Standard	New	
Density estimator	Traditional	Bias-corrected	Dehnen and Aly, 2012
Kernel function	Cubic spline	Wendland C ⁴	Dehnen and Aly, 2012
Neighbours (3D)	64	200	Dehnen and Aly, 2012
Equation of motion	Density-Entropy	Density-Entropy	Springel and Hernquist, 2002
Grad- h terms	Yes	Yes	Springel and Hernquist, 2002
Velocity gradients	Low-order	High-order	Price, 2012b; Hu et al., 2014
Artificial viscosity	Constant	Adaptive (locally)	Dolag et al., 2005b; Cullen and Dehnen, 2010
Balsara limiter	Low-order	High-order	Introduction, 1995; Cullen and Dehnen, 2010; Price, 2012b
Artificial conduction	No	Adaptive (locally)	Wadsley, Veeravalli, and Couchman, 2008; Price, 2008
Hydrostatic correction	No	Adaptive (locally)	Price, 2008; Valdarnini, 2012
Particle wake-up	No	yes ($f_w = 3$)	Saitoh and Makino, 2009; Pakmor, 2010; Pakmor et al., 2012

Table V.1: Comparison of the ‘standard’ (column 2) and ‘new’ (column 3) SPH implementations in the GADGET code. Furthermore, we give some references (column 4) for extended descriptions and discussions.

Simultaneously, the smoothing length h_i is a function of density

$$h(\mathbf{x}_i) = \eta \left(\frac{m_i}{\rho_i} \right)^{1/3}, \quad (\text{V-2})$$

where η defines the ratio of smoothing length to the mean distance between particles. Equations (V-1) and (V-2) roughly ensure constant mass resolution throughout the simulation and have to be solved in parallel. This mimics the evolution of spheres of the same mass $4/3\pi h_i^3 \rho_i = N_i m_i$ but with varying number of neighbours. The number of neighbours varies across space and time with an increase or decrease of smoothing length and local quality of fluid sampling by the point masses. The weighting function is commonly chosen to decrease monotonically with distance, yield smooth derivatives, is symmetric with respect to $x_{ij} = x_{ji}$ and has a flat central portion. A historical choice (Monaghan and Lattanzio, 1985) of kernel function

$$W_{ij}(x_{ij}, h_i) = w(q)/h_i^3, \quad (\text{V-3})$$

is the cubic B-spline function with $q = x_{ij}/h_i$ and

$$w(q) = \frac{8}{\pi} \begin{cases} 1 - 6q^2 + 6q^3 & 0 \leq q \leq \frac{1}{2} \\ 2(1 - q)^3 & \frac{1}{2} \leq q \leq 1 \\ 0 & 1 \leq q \end{cases}, \quad (\text{V-4})$$

which we commonly employ with a choice of 64 neighbours in three dimensions. However, this traditional kernel function is subject to the pairing (or clumping) instability when the number of neighbours is too large (see Price, 2012b). An alternative choice to achieve better numerical convergence is necessary and an entire new family of kernels is needed. In a kernel stability analysis Dehnen and Aly, 2012 show that the Wendland kernel functions are a much better choice. We choose the Wendland C^4 (WC4) kernel with 200 neighbours in three dimensions as our smoothing function without the pairing instability problem. The functional form of the C^4 is given by

$$w(q) = \frac{495}{32\pi} (1 - q)^6 (1 + 6q + \frac{35}{3}q^2). \quad (\text{V-5})$$

For values of $q > 1$ it is set to $w(q) = 0$. The Wendland functions require similar computational effort as the cubic spline kernel but nevertheless, the total computational time increases due to larger number of neighbours. Therefore, we do not employ the higher-order C^6 functions because of the required 295 neighbours. In summary, the total computational cost of the density and hydrodynamical force calculation increases by a factor of about two in comparison to a cubic spline with 64 neighbours. However, a better estimate of the kernel will result in a more accurate density estimate and improved gradient estimators. These estimators are the cornerstones of the SPH formalism and determine the accuracy and convergence rate in all our test simulations.

V-2.3 Equation of motion

The EoM for a system of point masses are derived (see e.g. [Price, 2012b](#)) from a discretised version of the fluid Lagrangian

$$L = \sum_i m_i \left[\frac{1}{2} v_i^2 - u_i \right], \quad (\text{V-6})$$

where v denotes velocities and u internal energy of individual particles. The Lagrangian nature of SPH, when complemented with a symplectic time integration scheme, automatically conserves mass, momentum, angular momentum, energy and entropy. We use the standard kick-drift-kick Leapfrog time integration of GADGET ([Springel, 2005b](#)). The EoM then follows from the principle of least action, where the spatial derivative of internal energy comes (if constant entropy is assumed) from the first law of thermodynamics $dU = -PdV$. We choose a volume element depending on density ($V = m/\rho$) and an adiabatic equation of state for the pressure $P = A\rho^\gamma$, which is defined individually for every particle. We integrate entropy A as the thermodynamical variable of choice and thus employ what is commonly called 'density-entropy' SPH.

The EoM in the 'density-entropy' (for a derivation see [Springel and Hernquist, 2002](#)) for the hydrodynamical force part of an individual particle reads

$$\frac{d\mathbf{v}_i}{dt} \Big|_{\text{hyd}} = - \sum_j m_j \left[f_i^{\text{co}} \frac{P_i}{\rho_i^2} \nabla_i W_{ij}(h_i) + f_j^{\text{co}} \frac{P_j}{\rho_j^2} \nabla_i W_{ij}(h_j) \right], \quad (\text{V-7})$$

where the factor f^{co} is a correction factor, which accounts for the mutual co-dependence of smoothing length $h(\rho)$ and density $\rho(h)$ and their corresponding derivatives. Its functional form is given by

$$f_i^{\text{co}} = \left[1 + \frac{h_i}{3\rho_i} \frac{\partial \rho_i}{\partial h_i} \right]^{-1}. \quad (\text{V-8})$$

Equation (V-7) leads to a non-vanishing force at contact discontinuities even when pressure is constant. This is the artificial 'surface tension' of SPH, which suppresses particle movement across contact discontinuities. In the following sections, we present our equations in notation of internal energy u , which is related to the entropic function $A = (\gamma - 1)u/\rho^{\gamma-1}$.

V-2.4 Artificial viscosity

Smoothing of jumps

By construction, SPH solves the ideal Euler equation and no dissipative terms are included but those are necessary to describe discontinuities correctly. In highly dynamical regions (e.g. in shocks) fast particles commonly penetrate into regions of resting particles causing unwanted particle disorder and oscillations in the sampling of the fluid. However, SPH already contains an intrinsic remeshing force but to re-establish particle order and capture shocks properly an

additional dissipative term in velocity is needed. This AV aims to remove post-shock oscillations and noise and helps to smooth the velocity field (see [Monaghan and Gingold, 1983](#)). We include AV in an energy conserving way with a contribution to the EoM of the form

$$\frac{d\mathbf{v}_i}{dt} \Big|_{\text{visc}} = \frac{1}{2} \sum_j \frac{m_j}{\rho_{ij}} (\mathbf{v}_j - \mathbf{v}_i) \alpha_{ij}^v f_{ij}^{\text{shear}} v_{ij}^{\text{sig},v} \bar{F}_{ij}, \quad (\text{V-9})$$

and with a contribution to the energy equation of the form

$$\frac{du_i}{dt} \Big|_{\text{visc}} = -\frac{1}{2} \sum_j \frac{m_j}{\rho_{ij}} (\mathbf{v}_j - \mathbf{v}_i)^2 \alpha_{ij}^v f_{ij}^{\text{shear}} v_{ij}^{\text{sig},v} \bar{F}_{ij}, \quad (\text{V-10})$$

where the symmetrised variables represent $\rho_{ij} = (\rho_i + \rho_j)/2$ for the density, $\alpha_{ij}^v = (\alpha_i^v + \alpha_j^v)/2$ as a numerical coefficient to include AV (see below) and $f_{ij}^{\text{shear}} = (f_i^{\text{shear}} + f_j^{\text{shear}})/2$ as the [Introduction, 1995](#) shear flow limiter (see Section 2.3.2 below), which aims to ensure the application of AV only in strong shocks (high velocity divergence) and not in rotating or shearing flows (high velocity curl). Furthermore, in the above equation $\bar{F}_{ij} = (F_{ij}(h_i) + F_{ij}(h_j))/2$ is the symmetrised scalar part of the kernel gradient terms $\nabla_i W_{ij}(h_i) = F_{ij} \mathbf{r}_{ij}/r_{ij}$, which are used to linearly interpolate the second-order Laplacian derivative in the velocity field diffusion equation. The pairwise signal velocity $v_{ij}^{\text{sig},v}$ (first introduced by [Monaghan, 1997](#), and already used in GADGET-2) determines the strength of AV and directly includes a quantitative measure of particle disorder

$$v_{ij}^{\text{sig},v} = c_i^s + c_j^s - \beta \mu_{ij}, \quad (\text{V-11})$$

where c^s is the sound speed of the particles and $\mu_{ij} = \mathbf{v}_{ij} \cdot \mathbf{x}_{ij}/x_{ij}$ with a commonly chosen pre-factor of $\beta = 3$. AV is only applied between approaching pairs of particles (i.e. $\mu_{ij} < 0$) and otherwise switched off. The local signal velocity v_i^{sig} (also used by the time-step criterion, see Section [V – 2.6](#)) represents the maximum value of $v_{ij}^{\text{sig},v}$ between all particle pairs ij within the entire smoothing sphere of particle i .

The calculation of the viscosity coefficient α_i^v is based on an approach developed by [Cullen and Dehnen, 2010](#) but modified for more efficient computation as follows. The presence of a shock is indicated via computation of velocity divergence contributions across the entire smoothing length by

$$R_i = \frac{1}{\rho_i} \sum_j \text{sign}(\nabla \cdot \mathbf{v})_j m_j W_{ij}, \quad (\text{V-12})$$

where a shock corresponds to $R_i \approx -1$. In principle, an accurate calculation of R_i for every particle requires the previous computation of $(\nabla \cdot \mathbf{v})_i$ for every particle. Therefore, an extra SPH summation loop added between the calculation of density (where velocity divergence can also be calculated) and hydro forces would be necessary. For computational reasons we use the velocity divergence calculated in the previous time-step. Furthermore, a convergent flow is

also indicated by a high velocity divergence but that condition does not distinguish between pre-shock and post-shock regions. Therefore, we employ the time derivative of velocity divergence to determine a directional shock indicator

$$A_i = \xi_i \max(0, -(\dot{\nabla} \cdot \mathbf{v})_i), \quad (\text{V-13})$$

which is able to distinguish between pre-shock and post-shock regions. We calculate $(\dot{\nabla} \cdot \mathbf{v})_i$ via interpolation between the current and the previous time-step (as suggested by [Cullen and Dehnen, 2010](#)) in the time interval Δt_i .

Subsequently, we use the shock indicator R_i to determine the ratio ξ_i of strength of shock and strength of shear in quadratic form via

$$\xi_i = \frac{|2(1 - R_i)^4(\nabla \cdot \mathbf{v})_i|^2}{|2(1 - R_i)^4(\nabla \cdot \mathbf{v})_i|^2 + |\nabla \times \mathbf{v}|_i^2}, \quad (\text{V-14})$$

which is proposed by [Cullen and Dehnen, 2010](#) as an additional limiting factor for AV in equation [\(V-13\)](#) and was experimentally determined. Now, for every particle we can define and set the target value $\alpha_i^{\text{loc},v}$ of AV with the help of the directional shock indicator to

$$\alpha_i^{\text{loc},v} = \alpha_{\max} \frac{h_i^2 A_i}{h_i^2 A_i + (v_i^{\text{sig}})^2}. \quad (\text{V-15})$$

In the case, where the viscosity coefficient α_i^v is smaller than $\alpha_i^{\text{loc},v}$, we set the coefficient to $\alpha_i^{\text{loc},v}$. Otherwise, we let it decay with time according to

$$\dot{\alpha}_i^v = (\alpha_i^{\text{loc},v} - \alpha_i^v) \frac{v_i^{\text{sig}}}{\ell h_i}, \quad (\text{V-16})$$

which we integrate in time together with the hydrodynamical quantities. The constant ℓ specifies the decay length and in our test problems we find a numerical value of $\ell = 4.0$ to give reasonable results.

Gradient estimators

We use the [Introduction, 1995](#) form of the shear viscosity limiter

$$f_i^{\text{shear}} = \frac{|\nabla \cdot \mathbf{v}|_i}{|\nabla \cdot \mathbf{v}|_i + |\nabla \times \mathbf{v}|_i + \sigma_i}, \quad (\text{V-17})$$

with $\sigma_i = 0.0001 c_i^s / h_i$ for numerical stability reasons. At this point, the question arises how to calculate the divergence and vorticity. The common curl estimator of SPH reads

$$(\nabla \times \mathbf{v})_i = -\frac{1}{\rho_i} \sum_j m_j (\mathbf{v}_j - \mathbf{v}_i) \times \nabla_i W_{ij}, \quad (\text{V-18})$$

which takes the lowest order error term into account. Since higher-order error terms are neglected, this formation performs very poorly in the regime of strong shear flows. Therefore, we resort to a higher-order calculation scheme of the velocity gradient matrix (see similar approaches by [Cullen and Dehnen, 2010](#); [Price, 2012b](#); [Hu et al., 2014](#)). We follow the approach presented in [Price, 2012b](#) for the computation of the gradient matrix. We expand \mathbf{v}_j for every vector component k in a Taylor-series around i with

$$v_j^k = v_i^k + (\partial_\delta v_i^k)(\mathbf{x}_j - \mathbf{x}_i)^\delta + O(h^2). \quad (\text{V-19})$$

Inserting equation (V-19) into equation (V-18) yields an easy solution for the linear term $\partial_\delta v_i^k$ and the velocity gradient matrix by solving the following system of equations:

$$\chi^{\alpha\beta} = \sum_j m_j (\mathbf{x}_j - \mathbf{x}_i)^\alpha \nabla_i^\beta W_{ij}, \quad (\text{V-20})$$

$$\chi^{\alpha\beta} \frac{\partial v_i^k}{\partial \mathbf{x}^\alpha} = \sum_j m_j (\mathbf{v}_j - \mathbf{v}_i)^k \nabla_i^\beta W_{ij}, \quad (\text{V-21})$$

which requires a matrix inversion for $\chi^{\alpha\beta}$. Conveniently, the estimator is also independent of density and thus, can be calculated in the same computational loop along with densities. Subsequently, the updated estimates of velocity divergence and curl are calculated directly from the full velocity gradient matrix via

$$(\nabla \cdot \mathbf{v})_i = \frac{\partial v_i^\alpha}{\partial \mathbf{x}^\alpha}, \quad (\text{V-22})$$

$$(\nabla \times \mathbf{v})_i^\delta = \epsilon_{\alpha\beta\delta} \frac{\partial v_i^\beta}{\partial \mathbf{x}^\alpha}. \quad (\text{V-23})$$

In our test problems we find the low-order estimator of velocity divergence to give already satisfying results (see also appendix A2 in [Schaye et al., 2015](#)). In contrast, the low-order estimator of velocity curl performs very poorly and we obtain significantly improved results with the high-order curl estimator of equation (V-23). The high-order estimators are not restricted to the AV scheme but they also enter various other modules of the code, where their precise calculation is required. For example, this additionally greatly improves the approximation of fluid vorticity written into the simulation snapshots.

V-2.5 Artificial conductivity with gravity correction

Smoothing of jumps

We move on to address the mixing problem in SPH by introducing a kernel-scale exchange term for internal energy transport. We include AC for purely numerical reasons to treat discontinuities in the internal energy (similar to the capturing of velocity jumps by AV), which arise from our 'density-entropy' formulation of SPH. We note that a 'pressure-entropy' formulation of the EoM is also able to address the mixing problem but it also requires the presence of AC in order to

smooth noise in internal energy behind shocks (Hopkins, 2013; Hu et al., 2014). Thus, in either flavour of SPH the inclusion of AC is recommended and many different formulations of the AC diffusion equation have been investigated so far. Although their precise details vary across the literature, they all ensure conservation of internal energy within the kernel. Price, 2008, Price, 2012b and Valdarnini, 2012 propose the diffusion of internal energy, while Read and Hayfield, 2012 propose the diffusion of entropy. Wadsley, Veeravalli, and Couchman, 2008 propose a first mixing formulation to resolve the differences in entropy profiles within cosmological comparison simulations (Frenk et al., 1999) between grid and SPH codes. The diffusion coefficient is approximately proportional to $\alpha^c v_{ij}^{\text{sig},c} x_{ij}$ and the numerical coefficient α^c is commonly treated as constant through space and time. We adapt the formulation of a spatially varying coefficient of Tricco and Price, 2013 and additionally calculate a limiter depending on the local hydrodynamical and gravitational states. We compute the gradient of internal energy as

$$(\nabla u)_i = \frac{1}{\rho_i} \sum_j m_j (u_j - u_i) \nabla_i W_{ij} \quad (\text{V-24})$$

and approximate the AC coefficient

$$\alpha_i^c = \frac{h_i}{3} \frac{|\nabla u|_i}{|u_i|} \quad (\text{V-25})$$

as a measure of noise of internal energy sampling on kernel scale. The time evolution (i.e. spatially varying SPH discretisation of the second-order diffusion equation) of the internal energy for each particle and its neighbours is then given by

$$\frac{du_i}{dt} \Big|_{\text{cond}} = \sum_j \frac{m_j}{\rho_{ij}} (u_j - u_i) \alpha_{ij}^c v_{ij}^{\text{sig},c} \bar{F}_{ij}, \quad (\text{V-26})$$

where we employ the choice of Price, 2008 for signal velocity depending on the pressure gradient of the form

$$v_{ij}^{\text{sig},c} = \sqrt{\frac{|P_i - P_j|}{\rho_{ij}}} \quad (\text{V-27})$$

and $\alpha_{ij}^c = (\alpha_i^c + \alpha_j^c)/2$ is the symmetrised conduction coefficient, which are individually limited to the interval $[0, 1]$. In the literature several other forms of AC (see e.g. Wadsley, Veeravalli, and Couchman, 2008; Valdarnini, 2012) or approaches to the mixing problem (see e.g. Hopkins, 2013) have been proposed.

Gravity limiter

We note that the amount of AC applied depends on the gradients of internal energy and of pressure. In the case that the thermal pressure gradient is determined by gravitational forces (i.e. hydrostatic equilibrium) this method would incorrectly lead to unwanted conduction. In the following, we determine the contribution of hydrostatic equilibrium to the total thermal pressure

gradient and present a method to limit the amount of conduction. Firstly, for every individual active particle, we project the gravitational force \mathbf{F}^g onto the hydrodynamical force \mathbf{F}_i^h and calculate the partial force \mathbf{F}_i^p of \mathbf{F}_i^h , which is balanced by \mathbf{F}_i^g to

$$\mathbf{F}_i^p = \frac{(\mathbf{F}_i^g \cdot \mathbf{F}_i^h)}{|\mathbf{F}_i^h|^2} \mathbf{F}_i^h. \quad (\text{V-28})$$

The sign of \mathbf{F}_i^p depends on the spatial orientation of the force vectors. Secondly, we subtract/add the partial force \mathbf{F}_i^p from/to the hydrodynamical force \mathbf{F}_i^h and obtain \mathbf{F}_i^c , which we call the gravitationally adjusted hydrodynamical force

$$\mathbf{F}_i^c = \mathbf{F}_i^h + \mathbf{F}_i^p \quad (\text{V-29})$$

and which we use to determine a limitation factor δ_i^c for AC

$$\delta_i^c = \left(\frac{(\mathbf{F}_i^c \cdot \mathbf{F}_i^h)}{|\mathbf{F}_i^h|^2} \right)^q. \quad (\text{V-30})$$

The limiter ensures that AC is only applied to the part of \mathbf{F}_i^h which is not balanced by \mathbf{F}_i^g . The exponent q represents a scaling for the aggressivity of the gravity correction. We limit our correction factor to the interval $[0, 1]$ and directly multiply it onto the individual AC coefficients α_i^c . The limiter performs only as well as the hydrodynamical scheme is able to resolve hydrostatic equilibrium (in the ideal case the angle between force vectors is 180°). However, in SPH simulations small-scale noise is present at all times within the kernel and thus also in the force vector angles. The exponent q (applied after the boundary verification) can then be understood to account for the noise in the particle distribution and mimics an opening angle of force vectors. After extensive studies and performing a variety of test problems, we settle with $q = 5$. The limiter returns zero in the case no hydrodynamical forces are present and one in the case, where no gravitational forces are present. We are aware that in the presence of strong pressure gradients and rotational forces our approach only marginally limits the amount of AC applied. However, we did not encounter major problems in our simulations performed with the ‘new’ scheme so far. Therefore, we assume this issue to be not too important at the present state.

V-2.6 Particle wake-up and time-step limiter

GADGET employs individual time-steps for all of the particles to increase computational efficiency. Thus, the particle population is split into a set of active particles, whose hydrodynamical properties are integrated in the current time-step and a set of inactive particles, which reside on larger time-steps. These individual time-steps are computed from the local thermodynamical properties of each particle. However, the splitting between active and inactive computational regions creates problems, where both sets of particles are overlapping. In the case of a rapid gain in velocity or entropy an active particle can penetrate into a region of inactive particles. The inactive particles do not notice the sudden presence of the highly dynamical particle and therefore large gradients in the time-steps and unphysical results can occur. As a treatment we adopt

a time-step limiting particle wake-up scheme as proposed and implemented in the GADGET-3 code by [Pakmor, 2010](#) and [Pakmor et al., 2012](#) with the help of K. Dolag. It is similar to the time-step limiting scheme described by [Durier and Dalla Vecchia, 2012](#) and can be considered an extension of the [Saitoh and Makino, 2009](#) mechanism. Furthermore, our limiter compares signal velocities instead of time-steps and accounts for incorrect extrapolations. For every active particle, in every time-step, the individual time-steps themselves are re-computed according to

$$\Delta t_i = \frac{Ch_i}{v_i^{\text{sig}}}, \quad (\text{V-31})$$

where C is the Courant factor and v_i^{sig} the maximum signal velocity (see Section [V-2.4](#)). For the calculation of the time-step the maximum of the signal velocity computed between the active particle i and all its neighbour particles j within the entire kernel is used. GADGET employs a check during the hydrodynamical force computation for large differences in signal velocities (see equation [\(V-11\)](#)) within the kernel by evaluating

$$v_{ij}^{\text{sig}} > f_w v_j^{\text{sig}}, \quad (\text{V-32})$$

with a tolerance factor f_w corresponding to a wake-up triggering criterion, which captures sudden changes in the pairwise signal velocity. From our hydrodynamical standard tests we find $f_w = 3$ to give reasonable results. Additionally, the fluid quantities of the recently woken-up particles could have already been predicted half a time-step into the future. Therefore, the incorrect extrapolation is removed and the contribution from the real time-step added. These corrections are performed for all particles for which the time-steps are adapted.

V-3 Hydrodynamical tests without gravity

We evaluate the performance and accuracy of the two different SPH implementations with a first set of standard problems. These first test problems are purely hydrodynamical and do not include gravity or more advanced physics, yet. Throughout all the test problems we use an adiabatic index of $\gamma = 5/3$, the same set of numerical parameters (see Section 2) and we do not specifically tune individual test problems.

V-3.1 Sod shock tube

We consider the Sod shock tube problem ([Sod, 1978](#)) to study the SPH behaviour in a simple weak shock test. We set up 630000 particles of equal masses using a relaxed glass file in a three-dimensional periodic box with dimensions $\Delta x = 140$, $\Delta y = 1$ and $\Delta z = 1$. On the left half side of the computational domain ($x < 70$) we initialize 560000 particles with a density of $\rho_L = 1.0$ and a pressure of $P_L = 1.0$. On the right half side of the computational domain ($x > 70$) we initialize 70000 particles with a density of $\rho_R = 0.125$ and a pressure of $P_R = 0.1$. Figure [V.1](#) shows the results of the test problem at time $t = 5.0$. In general, both SPH schemes agree fairly well with a reference solution (green line) obtained with the ATHENA code ([Stone et al., 2008](#)) but we note the following differences. In the ‘standard’ scheme (blue dots), the

discontinuity in internal energy results in a 'blip' of pressure (see figure V.2) and energy, which corresponds to the artificial spurious surface tension of SPH. The issue of the 'blip' has been discussed for a long time (see e.g. [Monaghan, 1992](#)). In the 'new' scheme (red dots), AC promotes mixing, resolves the discontinuity, regularizes the pressure and provides a treatment of the 'blip'. A closer look at individual particles (see figure V.3) shows that the pure noise in velocity of particles behind the shock front is lower, which is a direct result of the improved prescription of AV. However, reducing the viscosity gives rise to post-shock ringing. Additionally, the change of kernel function improves the sampling quality of the fluid and yields a smoother estimation of density. At last, the time-step limiter is of little importance due to the weak shock in this test. However, as seen in figure V.2 the 'blip' is not completely removed and this is where some residual surface tension shows up.

V-3.2 Sedov blast

We consider the Sedov blast problem ([Sedov, 1959](#)) to study the SPH behaviour in a simple ultrasonic strong shock test. We set up 130^3 particles of equal masses using a relaxed glass file in a three-dimensional periodic box with dimensions $\Delta x = \Delta y = \Delta z = 6$ kpc. In the entire computational domain we initialize the particles with a density of $1.24 \times 10^6 M_\odot$ kpc $^{-3}$ and one Kelvin as temperature. At the centre of the box we point-like distribute the energy $E = 6.78 \times 10^{53}$ erg to mimic a supernova explosion among the nearest 102 particles.

Figure V.4 shows thin slices through the centre of the simulation box and figure V.5 the corresponding particle distribution at time $t = 0.03$. Furthermore, we perform the 'standard' scheme test also with the time-step limiter ($f_w = 8000$) because of the very strong shock (Mach $\gg 100$) of the blast and otherwise any comparison will fail. Without the limiter, shocked particles penetrate into quiescent regions causing a highly distorted fluid sampling, which results in an incorrect solution leading to an incorrect propagation of the shock front (see discussions in [Saitoh and Makino, 2009](#); [Durier and Dalla Vecchia, 2012](#)) and corresponding smoothing. The entire 'new scheme' reproduces the analytical solution (black line) very well, with the 'standard' run (green dots) totally failing, and the 'new' run (red dots) capturing the position, density and temperature of the shock fairly well. In addition, we show a partially improved 'standard' run (blue dots), where we enabled the time-step limiter but nothing else. This run also yields reasonable good results in this test, but as we see later comes short in other tests. We see that the 'new' scheme yields a smooth distribution of particles within the central region and therefore a well-resolved, but smoothed due to AC, temperature solution.

V-3.3 Keplerian ring

We consider the Keplerian ring problem ([Cartwright, Stamatellos, and Whitworth, 2009](#); [Cullen and Dehnen, 2010](#)) to study the SPH behaviour in a simple rotating and shearing test problem. We set up 20000 particles of equal masses sampling a two-dimensional ring with a Gaussian surface density profile with a peak at radius $R = 15.0$ kpc and a standard deviation of $\sigma = 2.0$ kpc. For numerical reasons we initialize the distribution in concentric shifted circles and not in a random fashion ([Cartwright, Stamatellos, and Whitworth, 2009](#)). We set the particles on Keplerian orbits around a central $10^9 M_\odot$ point mass with a rotation period of $t = 2\pi$. We

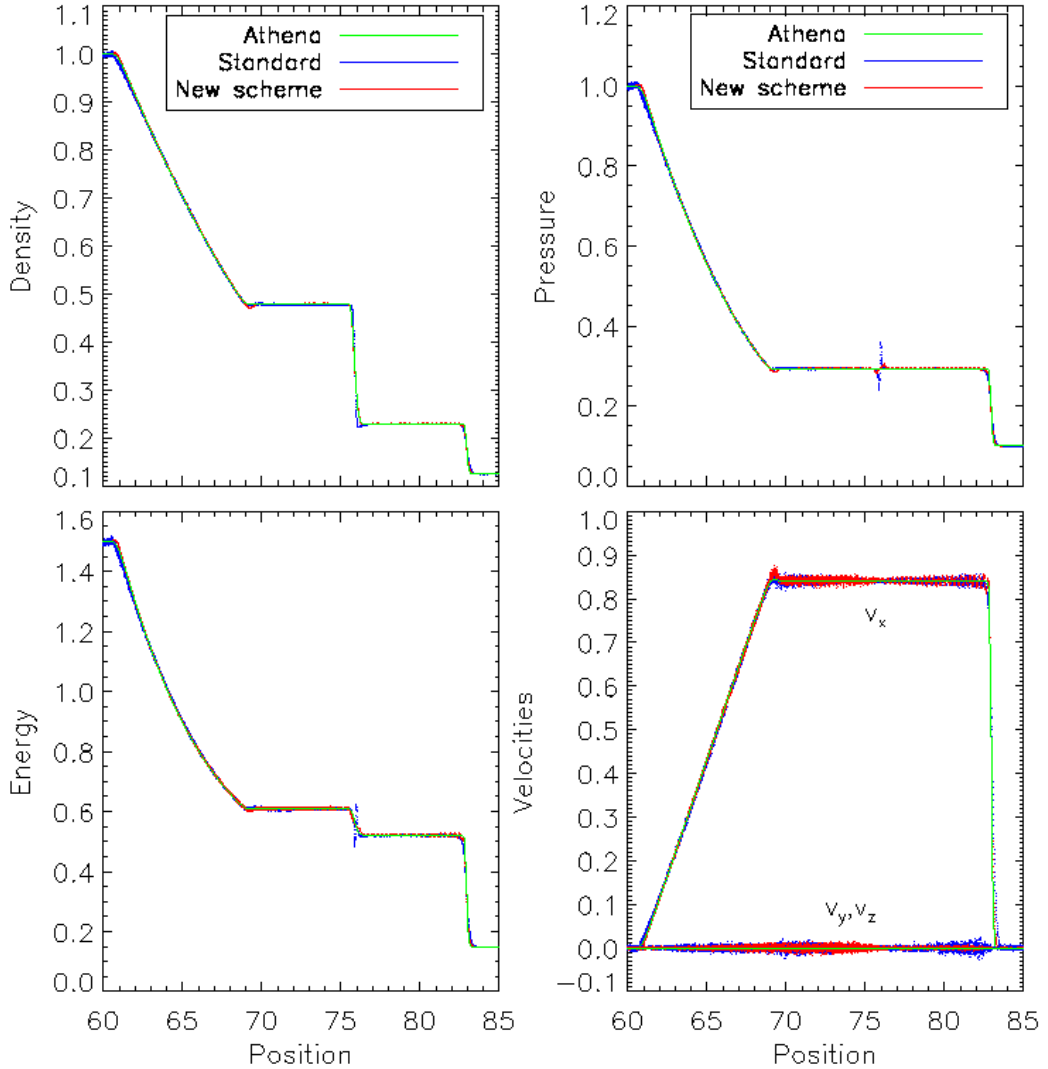


Figure V.1: Sod shock tube. We show the spatial distribution of particles (every 10_{th} particle is plotted) for density, thermal pressure, total energy and velocities at time $t = 5.0$. Both SPH schemes capture the shock well but with differences as follows. The ‘new’ scheme converges better in the density estimate and the presence of AC nearly removes the pressure blip at the contact discontinuity.

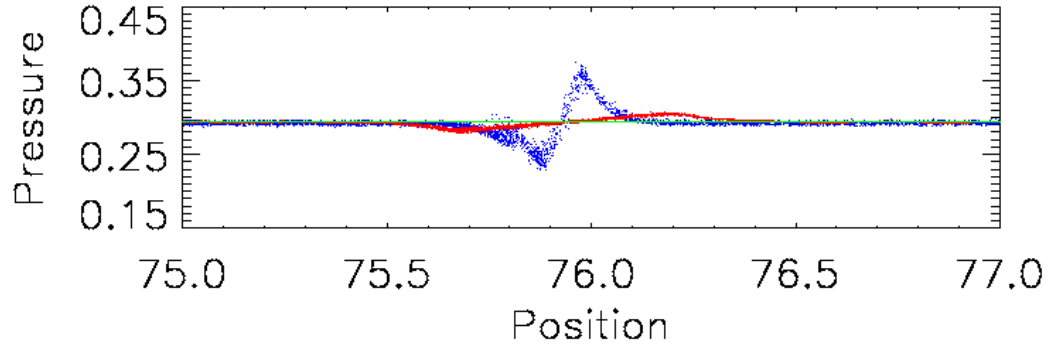


Figure V.2: Sod shock tube. We show a zoom-in on the pressure blip (see figure V.1, upper right panel) at time $t = 5.0$. Only a small residual of surface tension is left.

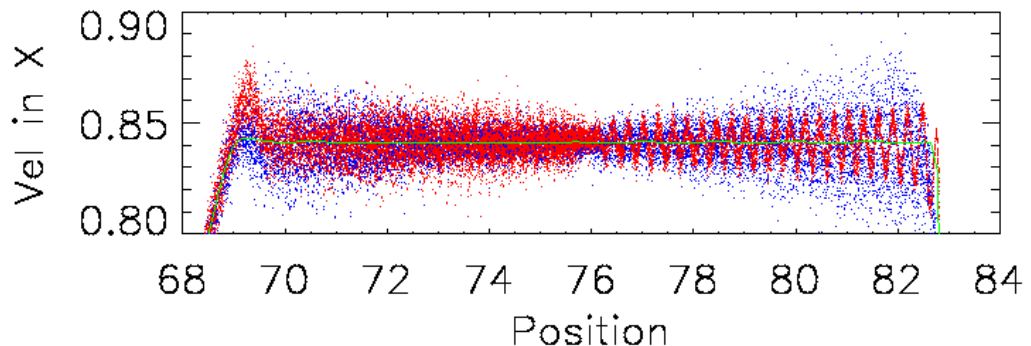


Figure V.3: Sod shock tube. We show a zoom-in on velocity in x -direction (see figure V.1, bottom right panel) at time $t = 5.0$. Besides some post-shock ringing, the post-shock noise is smaller with the 'new' scheme.

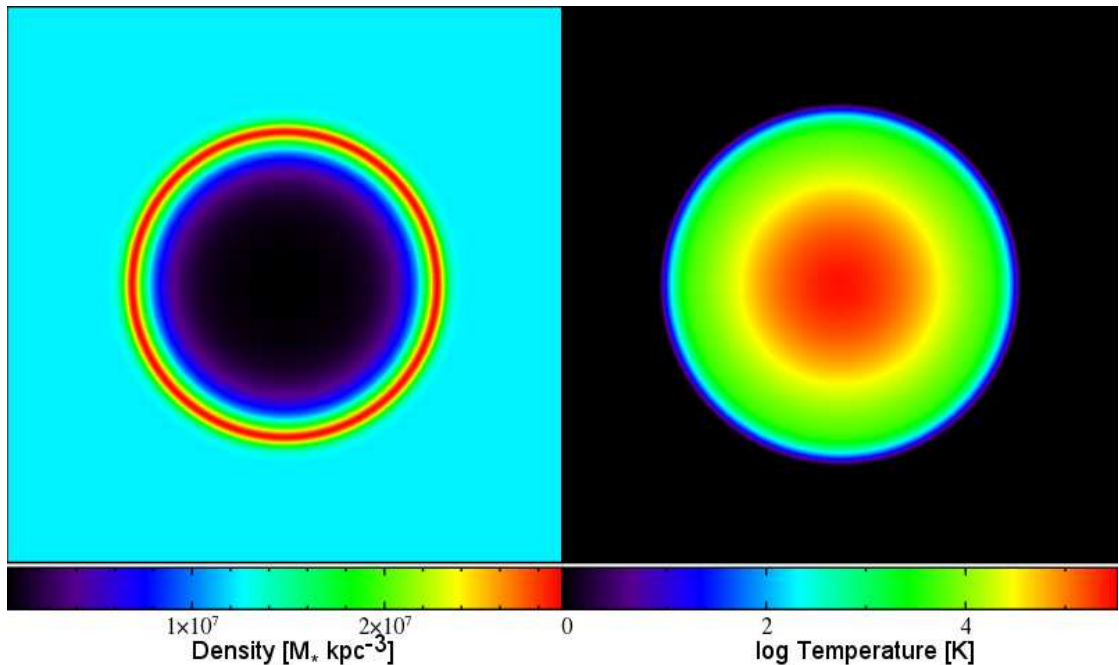


Figure V.4: Sedov blast wave. We show thin slices through the centre of the computational volume at time $t = 0.03$ of the test performed with the ‘new’ scheme. The shock front is clearly visible in the gas density (left panel) as well as the temperature (right panel).

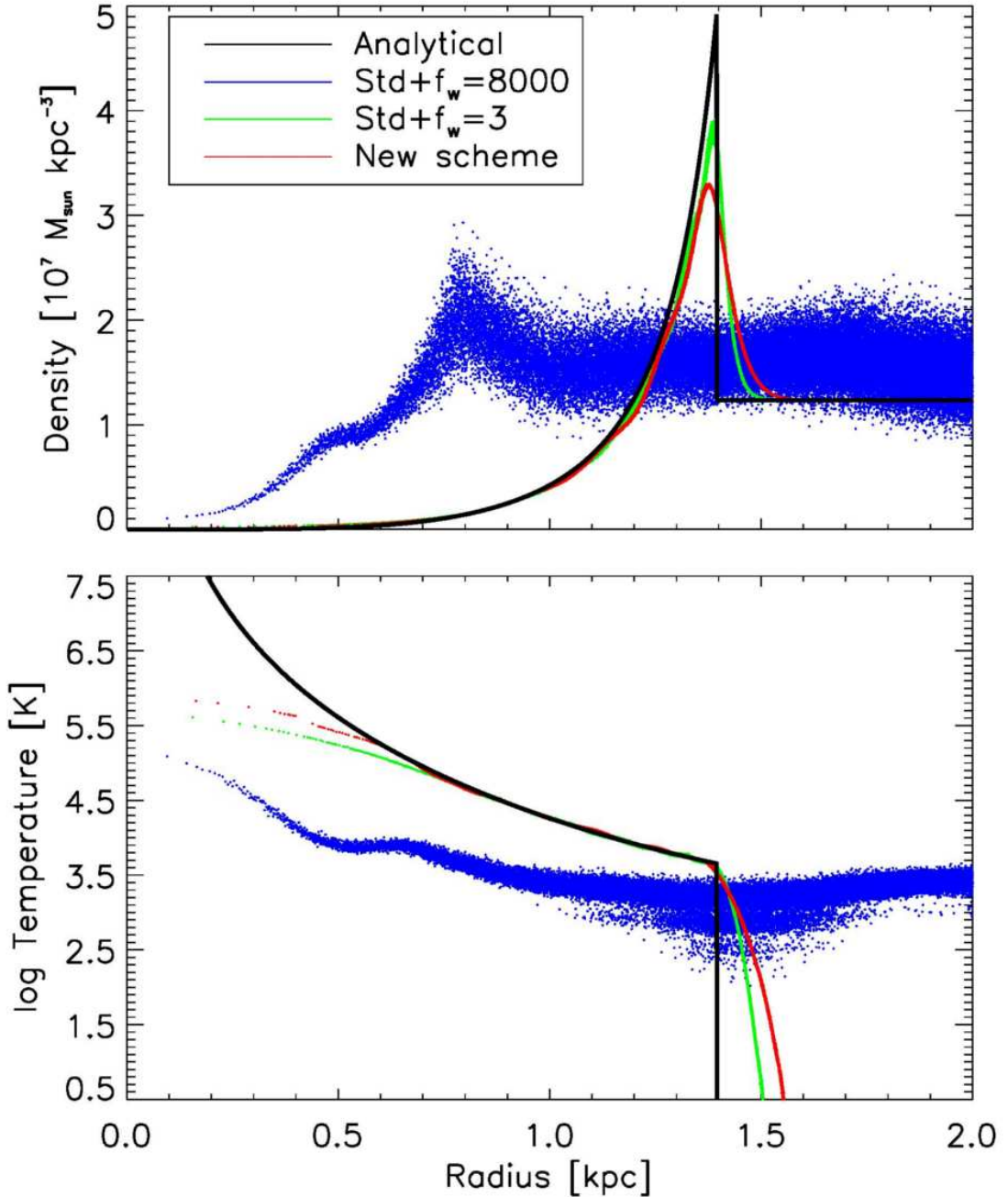


Figure V.5: Sedov blast wave. We show the radial distribution of particles (every 5th particle is plotted) at time $t = 0.03$ with a time-step limiting criterion of $f_w = 3$. We have performed the ‘standard’ run with a time-step limiting criterion of $f_w = 8000$ (green lines, otherwise no meaningful comparison can be performed) and also $f_w = 3$. The classic ‘standard’ scheme (green lines) fails to capture the shock, while the ‘new’ scheme (red lines) captures the position and evolution of the shock front much better compared to the analytical solution (black lines). This test shows the importance of the time-step limiter.

choose the sound speed orders of magnitudes smaller than the orbital velocity to ensure thermal stability of the ring. In contrast to our common set of numerical parameters, we start without a minimal value of AV because it would immediately trigger instability. In the absence of AV the ring should be stable.

Figure V.6 shows the results of the test problem at the times of onset of runaway instability. We perform all test runs with the WC4 kernel in order to exclude possible effects caused by the smoothing scale of kernel sizes and differential estimators. Due to the highly sub-sonic nature and the absence of strong shocks, the impact of AC and the time-step limiter is negligible. The initially stable ring (top left panel) evolves as follows for different implementations of AV. In the ‘standard’ scheme (top right panel), the ring is only stable for about two dynamical times, before the instability has fully developed and the ring breaks up. Also, the Balsara limiter does not succeed in limiting AV because of the insufficient calculation of vorticity. In the ‘M&M’ scheme (bottom left panel) we use the implementation of a low-viscosity scheme initially proposed by [Morris and Monaghan, 1997](#) and implemented into GADGET by [Dolag et al., 2005b](#). Their scheme uses a time-dependent evolution of numerical AV coefficient α_i^v to suppress AV in the absence of shocks and manages to keep the ring stable for about seven dynamical times. However, the M&M scheme requires a minimum value of AV and also uses a low-order estimator for vorticity, which leads to the ring break-up. At last, we show the results of the ‘new’ scheme (bottom right panel), which we used without a minimum value for AV. This scheme uses a high-order estimator of velocity gradient matrix, which results in a very accurate calculation of divergence and vorticity. Therefore, also the computation of the Balsara shear flow limiter is very accurate and suppresses AV completely within the entire ring structure. We do not note an artificially induced transport of angular momentum and orbital changes of test particles. Consequently, the ring remains stable for many dynamical times and the initial Gaussian surface density distribution is preserved until we stopped the simulation.

V-3.4 Cold blob test

We consider the blob test ([Agertz et al., 2007](#); [Read, Hayfield, and Agertz, 2010](#)) set up with publicly available initial conditions¹ to study the SPH behaviour in a test problem with interacting gas phases and surfaces. We initialize 9641651 particles of equal masses using a relaxed glass file in a three-dimensional periodic box with dimensions $\Delta x = 10$, $\Delta y = 10$ and $\Delta z = 30$ in units of the cold cloud radius. A cold cloud is centred at $x, y, z = 5$ and travels at a Mach number of $M = 2.7$. The background medium is set-up ten times less dense and ten times hotter than the cloud. Spherical harmonics are used to seed large-scale perturbations onto the surface of the cloud. Because of the low Mach number shocks we expect the time-step limiter to be only of minor importance.

Figure V.7 shows thin slices through the density structure at various times. In the ‘standard’ scheme, the cold gas cloud is prevented from dissociating by the follow major effect (see also e.g. [Agertz et al., 2007](#)). The presence of artificial surface tension confines the blob of cold gas. This is clearly visible by the numerically induced stretching of the cloud. Cold material, which should have been mixed into the ambient hot medium is confined within an elongated structure.

¹<http://www.astrosim.net/code/doku.php>

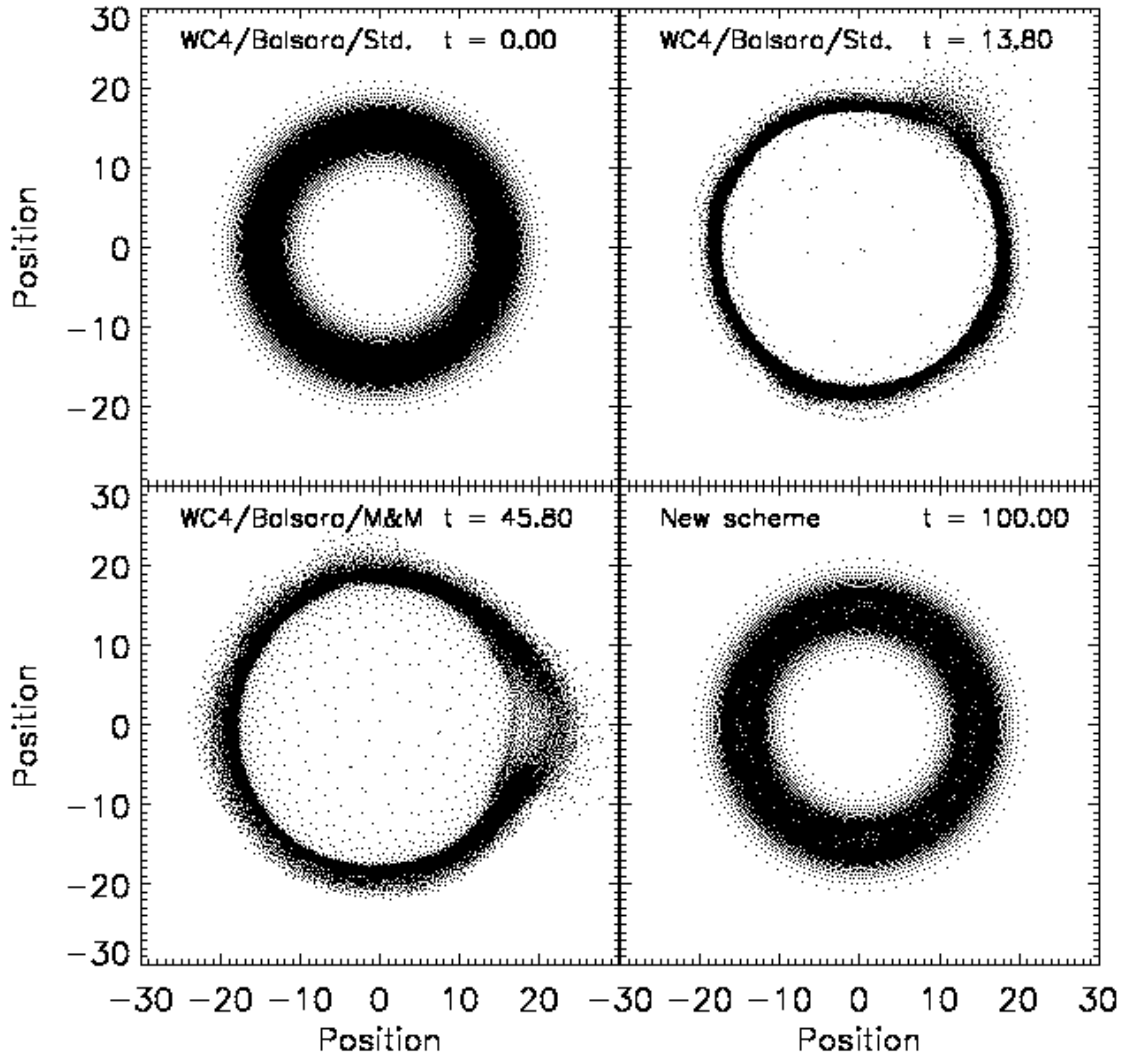


Figure V.6: Keplerian Ring. We show the initial set-up (top left panel) as well as the results of three different AV methods. For a fair comparison we only vary the AV scheme and none of the other SPH modifications. The importance of AV becomes clear as high amounts of viscosity lead to numerical accretion of particles onto the central point mass. Because angular momentum is conserved, the ring breaks up and an instability develops. With a low-order Balsara limiter, neither the standard SPH viscosity (top right panel) nor the M&M viscosity (bottom left panel) are able to preserve the ring. The ‘new’ scheme (bottom right panel), which has a the time-dependent AV coupled with a high-order limiter, is able to preserve the ring to even very late times.

In the ‘new’ scheme, the presence of AC promotes the mixing with external ambient medium. We also note that the ‘new’ scheme resolves different shock structures propagating through the box both more accurately and smoothly.

Figure V.8 illustrates the dissipation of the gas cloud by tracking the time evolution of cold blob mass. We associate (see also [Agertz et al., 2007](#)) particles with the cold cloud with a temperature criterion of $T < 0.9 \cdot T_{\text{ext}}$ (in contrast to the external ambient medium) and a density criterion of $\rho > 0.64 \cdot \rho_{\text{cl}}$ (in contrast to the initial density of the cloud). In the ‘standard’ scheme (blue line), only half of the cold gas mass is mixed into the hot ambient medium over five dynamical times. The effects of the improved AV and WC4 kernel (green line) are negligible. The major impact and contribution to cloud dissociation is made by AC (pink line) and the corresponding introduced mixing process. The results are close to a test run performed with the ENZO ([Bryan et al., 2014](#)) code in a comparable set-up, which we took from [Hopkins, 2013](#). However, some residual surface tension remains.

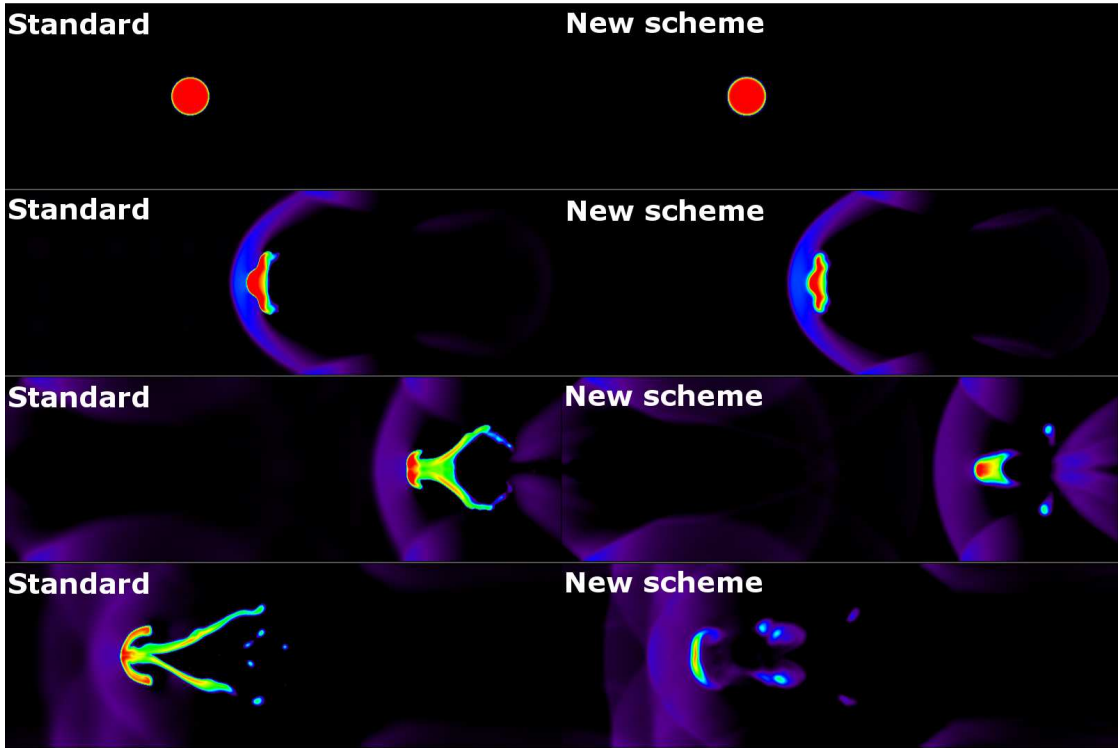


Figure V.7: Blob test. We show thin slices of gas density through the centre of the computational domain at times $t = 0.0, 3.0, 6.0$ and 10.0 . In the ‘standard’ scheme, numerical surface tension prevents mixing between cold and hot phases leading to an artificial stretching of the cloud and an unphysical solution. In the ‘new’ scheme, AC helps to promote cloud dissociation; however, some residual surface tension remains left. Furthermore, the shock structures throughout the box are more defined and better resolved.

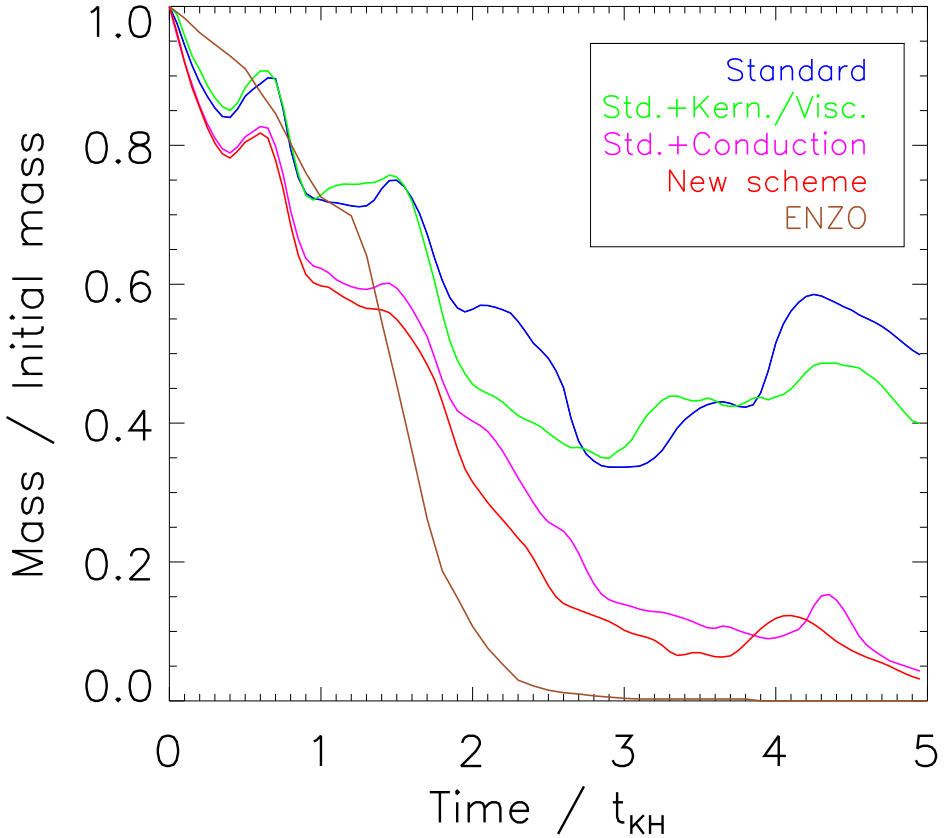


Figure V.8: Blob test. We show the fraction of cold gas as a function of time for four different SPH schemes. In the ‘standard’ scheme, numerical surface tension prevents mixing between the cold and hot phases. The importance of AC becomes clear as it promotes mixing between gas phases, which allows a dissociation of the cloud. Only some residual surface tension is left. Comparing to a run performed with the ENZO grid code, we find our AC scheme to model mixing in a conservative way.

V-3.5 Kelvin-Helmholtz instability

We consider the Kelvin-Helmholtz instability (Agertz et al., 2007; Read, Hayfield, and Agertz, 2010) from publicly available initial conditions¹ to study the SPH behaviour in a simple shearing instability test. We set up 1548288 particles of equal masses using a cubic lattice in a three-dimensional periodic box with dimensions $\Delta x = 256 = \Delta y = 256$ and $\Delta z = 16$ kpc, which is centred around $(0, 0, 0)$. In the central half of the box ($|y| < 64$) we initialize 512000 particles with a density of $\rho_1 = 6.26 \cdot 10^3 \text{ M}_\odot \text{kpc}^{-3}$, temperature of $T_1 = 2.5 \cdot 10^6 \text{ K}$ and a velocity in x -direction of $v_1 = -40 \text{ km/s}$. In the outer half of the box ($|y| > 64$) we initialize 1036288 particles with a density of $\rho_2 = 3.13 \cdot 10^2 \text{ M}_\odot \text{kpc}^{-3}$, temperature of $T_2 = 5.0 \cdot 10^6 \text{ K}$ and a velocity in x -direction of $v_2 = 40 \text{ km/s}$. To trigger the instability, we perturb the velocity in y -direction with a mode of wavelength 128 kpc and amplitude of 4 km/s at the boundary layer that is exponentially damped towards the upper and lower edge of the box.

Figure V.9 shows thin projections through the specific entropy structure of the test problem at various times. In the ‘standard’ scheme, the fluid evolves in a laminar fashion and the growth of perturbations is totally suppressed by the artificial surface tension confining the central gas stream and large amounts of AV damping velocity perturbations (see also e.g. Agertz et al., 2007; Price, 2008). In the ‘new’ scheme, the high-order Balsara shear limiter successfully limits AV and allows large-scale perturbations to develop two prominent roll-ups. Additionally, AC nearly removes the artificial surface tension between the two gas phases and promotes mixing within the roll-ups. The entire test set-up does not evolve completely symmetric because of small secondary perturbations caused by the initial set-up on a cubic lattice. Most importantly, the high-order AV and AC prove crucial for this test problem, while the WC4 kernel and time-step limiter are of less importance. At the late stages, in this set-up the ‘new’ scheme is dominated by diffusion.

V-3.6 Decaying Subsonic Turbulence

Recent comparisons of standard SPH implementations with static and moving mesh grid codes have sparked a debate about the capabilities of SPH to model subsonic turbulences (see e.g. Bauer and Springel, 2012; Price, 2012a; Hopkins, 2013; Hopkins, 2015). We study the behaviour of our ‘new’ scheme in Idealized simulations of decaying subsonic turbulence. In particular, we are interested in the effective viscosity of the two schemes and the behaviour of the ‘SPH noise’ under conditions appropriate to galaxy formation and cluster simulations, i.e. non-isothermal, decaying motions from solenoidal and compressive modes. As most baryons on cosmological scales are in weakly collisional plasmas, numerical models should aim to minimize viscosity where possible (see e.g. Brunetti and Lazarian, 2007).

Grid and particle conversion procedures

We set up 512^3 particles of equal masses within a periodic box of side length 3 Mpc/h using carefully relaxed SPH glass files to minimize spurious initial kinetic energy. Subsequently, we define a velocity field on a grid of the same resolution in k -space by sampling a spectral distribution using the Box-Mueller method. The velocity field is transformed back to real-space

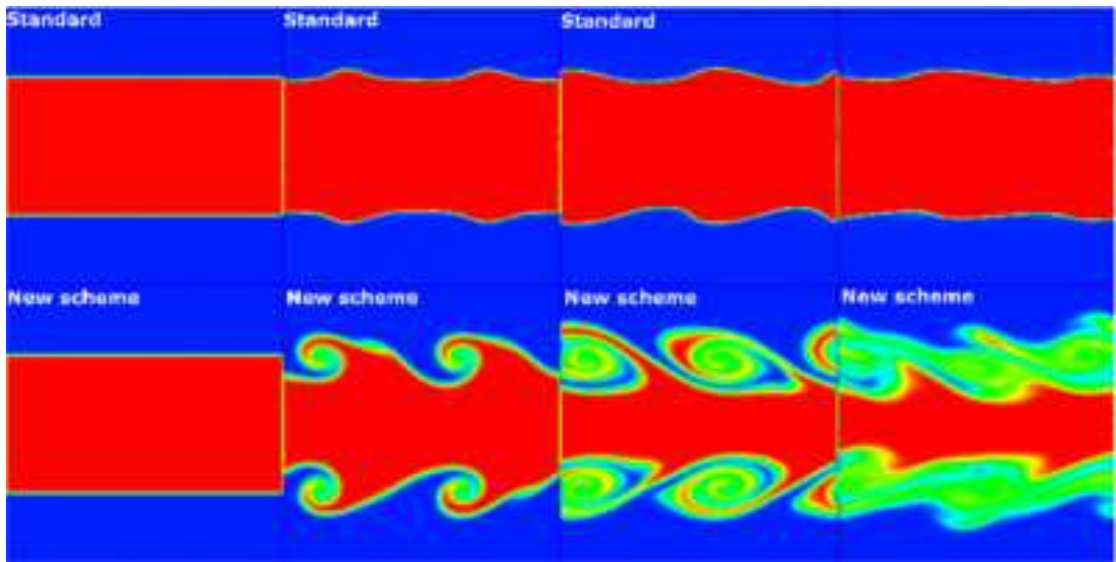


Figure V.9: Kelvin-Helmholtz instability. We show thin projections of specific entropy through the centre of the computational domain at times $t = 3.0$ and 6.0 (dynamical timescale $t_{\text{KH}} \approx 3.4$). In the ‘standard’ scheme, numerical surface tension as well as too much AV prevent the instability to develop and lead to an unphysical laminar behaviour of the fluid. In the ‘new’ scheme, our formulations of AV and AC promote the formation of roll-ups and onset of instability, while at late stages diffusion is dominating.

using a Fast Fourier Transformation (FFT), normalized such that the average velocity is of the desired Mach number. The velocities from the grid are transferred to the particle distribution using the nearest grid point (NGP) sampling kernel.

To assess the impact of random motions near the resolution scale, we need to measure the velocity power spectrum within the SPH kernel. However, the accurate estimation of the velocity power spectrum of a particle distribution close to the Nyquist frequency is non-trivial, because of aliasing of the velocity power by the binning kernel (see discussions in [Jing, 2005](#); [Jasche, Kitaura, and Ensslin, 2009](#); [Cui et al., 2008](#)). This can be compared to a problem in signal processing, where SPH represents an analogue signal and a grid a digital signal representation of it. Aliasing is strongest at the smallest scales/largest modes, where the velocity power on the particles is modified by the shape of the binning kernel in configuration-space. To understand this effect and compare binning kernels, we take initial conditions with a full Kolmogorov power spectrum ($P_k \propto k^{-11/3}$) without performing a simulation and directly bin the velocity back to a grid using different kernels. After a forward fast Fourier transformation we radially average the velocity power in k -space in 32 logarithmic bins.

Figure [V.10](#) shows the resulting power-spectra where the black line represents the original power spectrum. We show the kernels: Nearest Grid Point (NGP, red line), Cloud in Cell (CIC, green line), Triangular Shaped Cloud (TSC, violet line), Daubechies scaling function of 20th order (D20, orange line), and the WC4 SPH kernel with 200 neighbours (SPH, brown line) ([Hockney and Eastwood, 1988](#); [Daubechies, 1992](#); [Dehnen and Aly, 2012](#)). We also show the NGP with two times oversampling (blue line), which was used in [Bauer and Springel, 2012](#). As vertical lines we show the Nyquist frequency $k_{\text{Nyq}} = Nk_{\min}$, the WC4 smoothing scale k_σ and the WC4 kernel compact support $k_{\text{hsm}} = \pi/h_{\text{sml}}$ ([Dehnen and Aly, 2012](#)).

During the binning process, the SPH kernel function conserves density to machine precision but not energy, i.e. binning with the SPH kernel is a diffusive process. The other kernels behave opposite, they conserve mass, scalar velocity and energy to less than one per cent but not SPH density and volume. Figure [V.10](#) clearly shows that the D20 wavelet kernel minimizes aliasing for sufficiently homogeneous particle distributions ([Cui et al., 2008](#)). Our comparison also resolves the differences found in [Bauer and Springel, 2012](#) and [Price, 2012a](#), who use the twice oversampled NGP kernel and the standard SPH kernel, respectively. Prior studies based on the NGP kernel binning over-estimated the SPH noise, while SPH kernel based binning suppressed the real noise by aliasing. We conclude that all kernels except the D20 show substantial aliasing and it seems hard to draw definitive conclusions from simulation results under this condition. Thus we make it our fiducial choice for this study. We note that in the presence of strong gradients in density the SPH kernel remains the only viable choice to obtain binned quantities, because it is the only kernel in our comparison that guarantees a non-negative non-zero density in the entire simulation at all grid resolutions. This works reasonably well for a physical interpretation of velocity power-spectra, because motions below the SPH smoothing scale are caused by numerical effects ([Price, 2012a](#)).

Spectral evolution of turbulence

To compare the ‘standard’ and the ‘new’ schemes we consider decaying turbulence within a periodic box. We seed compressive and solenoidal modes in the range of $k \in [1.6, 3.1]$, to

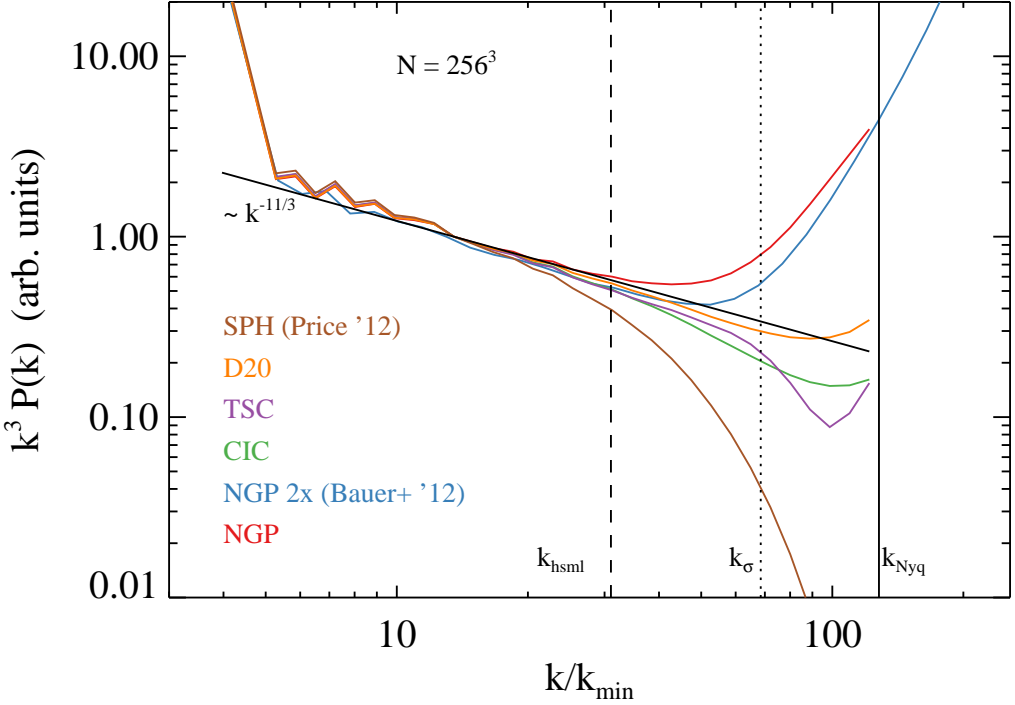


Figure V.10: Comparison of different particle to grid binning methods acting on the same particle distribution sampling a Kolmogorov velocity power spectrum in three dimensions (black line). We show the NGP kernel (red line), the twice oversampled NGP (blue line), the CIC (green line), the TSC (violet line), the D20 (orange line) and the SPH WC4 (brown line). The vertical lines indicate the wave numbers corresponding to the Nyquist frequency (solid line), the WC4 compact support (dashed line) and the WC4 smoothing scale (dotted line).

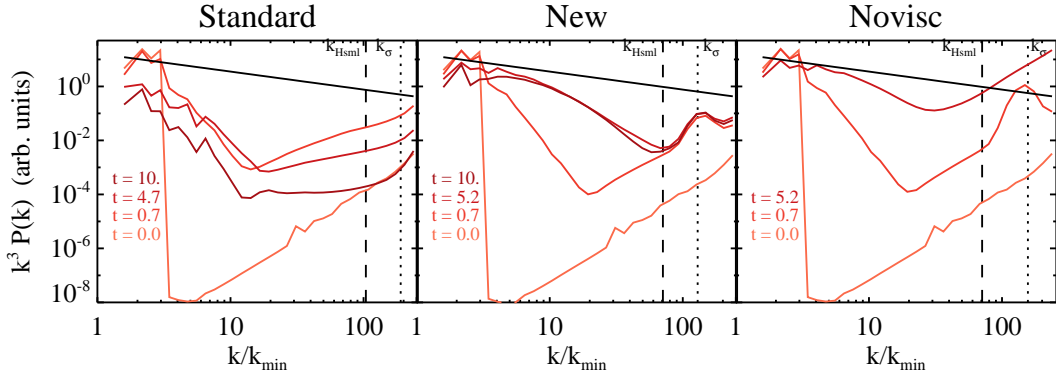


Figure V.11: Decaying subsonic turbulence. We show the build-up and decay of velocity power spectra for different schemes. The colours illustrate the time evolution of the spectra (sound-crossing time of about $t_s = 7.0$). We initially distribute energy on the largest modes, which then develops a spectral distribution. In the ‘standard’ scheme (left panel) turbulent motions are almost completely suppressed by destructive impact of AV. In the ‘new’ scheme (middle panel) turbulent motions develop and a turbulent cascade is built. The diffusive character of AV is significantly changed and the velocity field as well as the kinetic energy are preserved. The spectra are then compared to a simulation without viscosity (right panel).

obtain initial conditions appropriate for the galaxy and cluster environment, where turbulence is injected by merger infall on the scale of the halo core radius. We normalize the velocity fluctuations in the box such that the average velocity equals a Mach number of $M = 0.1$ and we do not time-average spectra.

Figure V.11 (left and middle panels) shows the time evolution of velocity power-spectra for the ‘standard’ scheme (left panel) and the ‘new’ scheme (middle panel). Here we also show the scale of the SPH kernel compact support (black vertical line) and the kernel smoothing scale (dotted vertical line). In-line with previous studies (Bauer and Springel, 2012, their fig. 12), the ‘standard’ scheme does not develop a turbulent cascade and damps kinetic energy very quickly. Our ‘new’ scheme develops a cascade at large scales (small k) but then shows a depression of kinetic energy close to the kernel scale. This, again, is in-line with prior studies (Hopkins, 2013). The damping of the spectrum at the later times appears self-similar, i.e. the shape of the spectrum does not change as energy decreases. Inside the kernel the typical build-up of thermal motions around the smoothing scale k_σ can be observed, but scales outside the kernel are not affected.

In order to understand if the cause of the velocity depression at $k \approx 10$ is caused by the formulation of AV we perform a test-run without any viscosity (figure V.11, right panel). Throughout the whole evolution, the spectrum at the smallest k follows the Kolmogorov scaling, as expected. Once the turbulent cascade is established, the spectrum turns over at increasingly smaller scales, which is equivalent to an isotropisation of kinetic energy inside the kernel and subsequent filling of larger scales with isotropic motions. This follows from the fact that SPH particles are subject to the pair-wise repulsive force (Price, 2012b), and hence behave like a thermal gas below the

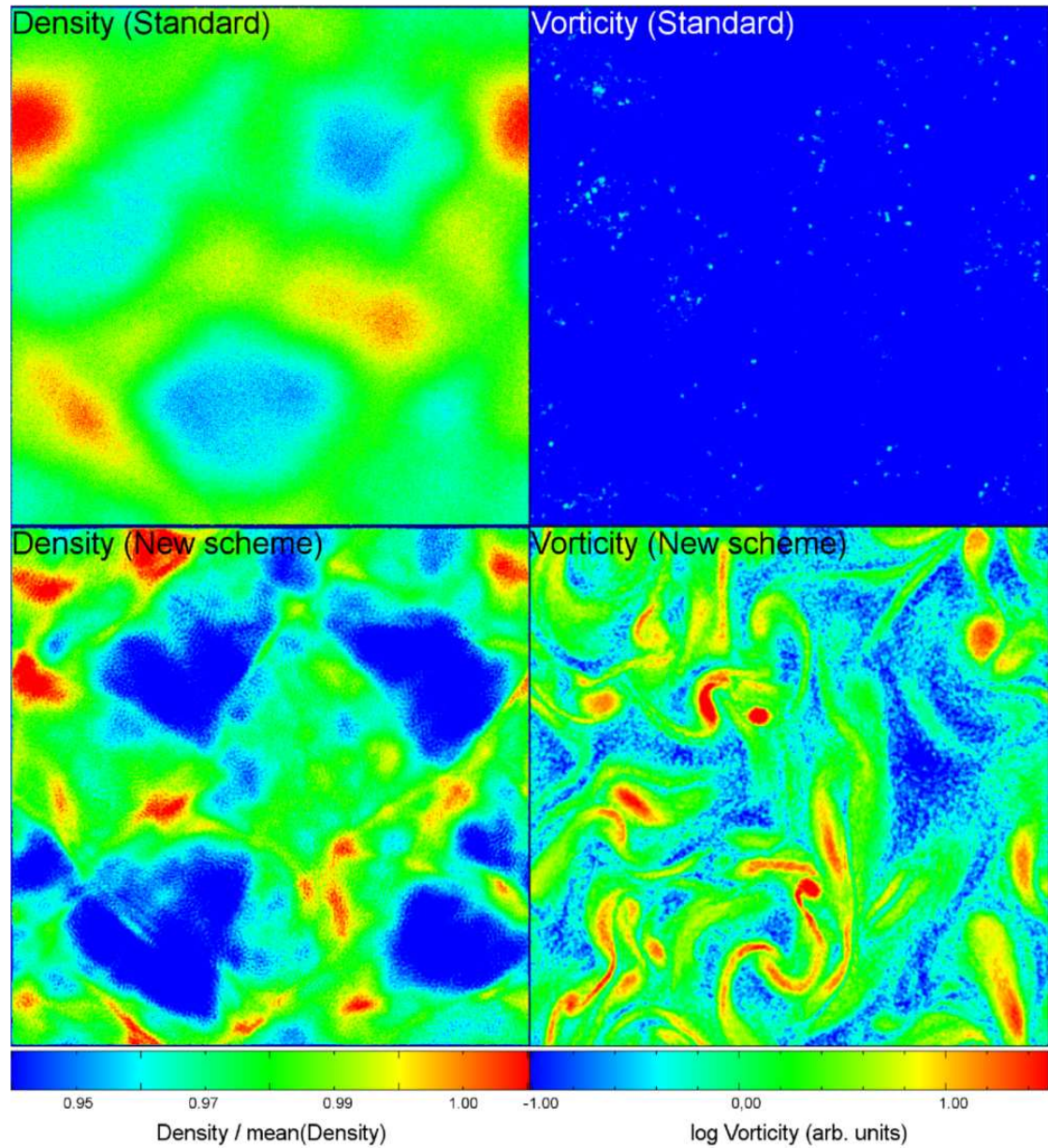


Figure V.12: Decaying subsonic turbulence. We show thin slices through the centre of the simulation box after one sound-crossing time for both schemes. The panels correspond to gas density (left panel) and vorticity (right panel). The velocity field shows well developed turbulence consisting of compressive and shearing motions. The ‘new’ scheme is able to more accurately compute vorticity and suppress AV with the high-order Balsara limiter.

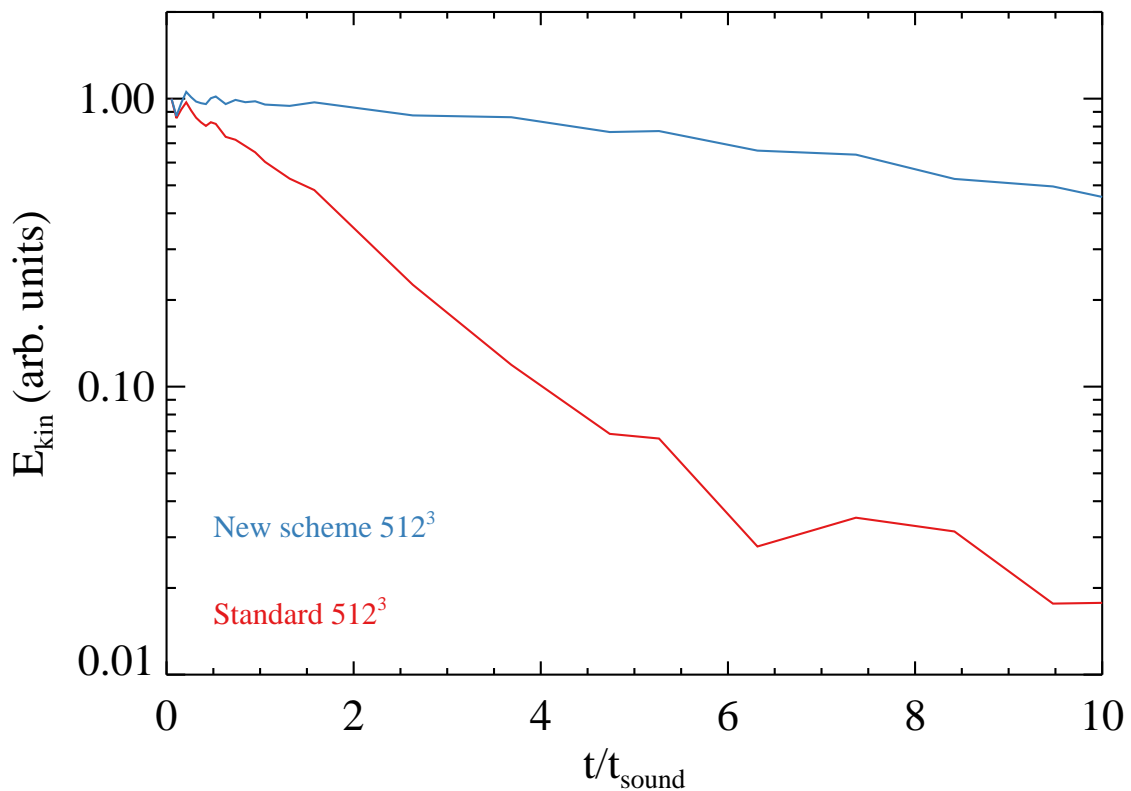


Figure V.13: Decaying subsonic turbulence. We show the total kinetic energy in the simulation box over time.

kernel scale. Eventually, such a system will show a flat power spectrum as expected from the second law of thermodynamics. In our simulation, we also observe the depression outside the smoothing scale, which seems to be an intrinsic feature of SPH related to an energy transfer from outside the kernel to smaller scales, and not related to our formulation of AV.

In our ‘new’ scheme including AV, thermal motions are well controlled inside the kernel scale, commonly referred to as ‘kernel noise’. We argue that these motions are not spurious, because no additional energy is retained in them, as SPH is fully conservative and the spectrum decays roughly in a self-similar manner. If we define the kernel smoothing scale (k_σ) as the dissipation scale intrinsic to SPH, the ‘new’ scheme does not show a bottle-neck effect as found in grid codes at adjacent larger scales but a depression, roughly in the same range in k . This is in line with the results shown by [Hopkins, 2015](#), whose code uses a Riemann solver to formulate noise-free AV on scales of the inter-particle separation to obtain grid-code behaviour. We note that the difference in dissipation scale (d_{\min} versus σ_{kernel}) translates into more resolution elements required by SPH compared to Eulerian methods, i.e. slower convergence.

Figure [V.12](#) shows thin slices through the centre of the simulation box after one sound-crossing time. We visualize gas density (left panel) and vorticity (right panel). It can be clearly seen that our ‘new’ scheme resolves compressive and shearing velocity motions better than the ‘standard’ scheme. The high-order derivatives of velocity lead to a more accurate estimation of vorticity and thus, limit the impact of AV and preserve kinetic energy and turbulent motions. Furthermore, the difference in AV and velocity dissipation between the two schemes becomes strikingly evident in the time evolution of kinetic energy (figure [V.13](#)). The ‘standard’ scheme dissipates 90% of the kinetic energy budget within four sound-crossing times, while the ‘new’ scheme preserves energy better by a factor of 5.

We conclude that our code performs comparably to modern implementations of SPH ([Hopkins, 2013](#); [Price, 2012b](#)), even in the case of non-isothermal compressive and solenoidal decaying turbulence found in cosmological simulations. We show that the disagreement between [Bauer and Springel, 2012](#) and [Price, 2012b](#) is largely caused by technical differences, to solve it we propose a solution based on the D20 binning kernel. We also show that the downturn in the velocity power spectrum is not caused by the AV implementation.

V-4 Hydrodynamical tests with gravity

We continue to evaluate the performance and accuracy of the two different SPH implementations with a second set of standard problems. These second tests include hydrodynamical as well as gravitational forces and also take a cosmological time integration into account.

V-4.1 Hydrostatic sphere

We consider a sphere in hydrostatic equilibrium to study the SPH behaviour in combination with gravity in an ideally stable system. We set up 88088 dark matter particles with individual masses of $2 \cdot 10^9 M_\odot$ and 95156 gas particles with individual masses of $4.75 \cdot 10^8 M_\odot$. The total mass of the sphere is $2.2 \cdot 10^{14} M_\odot$ and we use vacuum boundary conditions and a gravitational softening length of 12 kpc. We set up the initial equilibrium conditions following [Komatsu and Seljak,](#)

2001, as described in [Viola et al., 2008](#). We evolve the sphere adiabatically and do not include cooling or heating mechanisms in this test.

Figure [V.14](#) shows the results of the test problem at various times. At first, the initial set-up (dotted lines) of the sphere is not yet in hydrostatic equilibrium and requires some time to settle. Once hydrostatic equilibrium is reached around time $t = 2.6$ (dashed lines for the ‘new’ scheme) all hydrodynamical schemes must preserve the structure of the sphere and the radial profiles towards the final simulation time $t = 7.6$. Between all schemes, the thermal pressure profiles are indistinguishable balancing the gravitational pressure. However, the composition of the thermal pressure $P = (\gamma - 1)\rho u$ changes and the radial profiles for density ρ and internal energy u change significantly. The ‘standard’ scheme (blue lines) reaches the highest central density and also features lowest central internal energy and entropy. However, the internal energy drops towards the centre and no stable solution is reached at all. We suggest this behaviour to be a joint impact of pairing instability caused by the cubic spline kernel function and lack of internal energy mixing. When introducing only AC, no gravitational limiter and no further SPH developments (green lines), the results marginally improve. Internal energy still drops towards the centre but this time because too much AC was introduced. In principle, AC leads to entropy cores but without the gravitational limiter over-mixing occurs and internal energy is transported from the centre to the outskirts along the pressure gradient. The addition of the gravitational limiter (brown lines) improves the results significantly. The divergence of profiles towards the centre is removed and a stable core of internal energy and entropy is reached. Furthermore, no numerically induced transport of heat takes place. Additionally, we perform a test run with introducing only the WC4 kernel and no further SPH improvements (purple lines). In this run, the central density is lower than in the ‘standard’ scheme, most probably because the clumping of particles in the centre and the occurrence of the pairing instability is suppressed by the WC4 kernel in contrast to the run with the cubic spline. This also leads to a plateau in internal energy in the centre of the sphere. At last, we show the results of the entire ‘new’ scheme (red lines) and find the results to remain stable with all additional modifications to WC4 kernel, AV and time-step limiter. We find this run to give the most stable radial profiles in time. This test confirms the importance of kernel functions immune to pairing instability and a proper implementation of AC and clearly shows the effects of particle clumping and over- and under-mixing in gravitationally virialised systems, which are important in cosmological simulations.

V-4.2 Evrard collapse

We consider the Evrard collapse ([Evrard, 1988](#)) to study the SPH behaviour in the presence of dynamically important gravitational forces and collapse of gas. We initialize a sphere of gas with mass $M = 1$, radius $R = 1$ and density profile of $\rho \sim r$ for $r < R$ and use vacuum boundary conditions and a gravitational softening length of 0.005. We do not use an external gravitational potential, dark matter particles or radiative cooling and thus the cloud only self-gravitates on the free-fall time-scale. The gas is initially at rest and the thermal energy budget is orders of magnitude smaller than the gravitational binding energy.

Figure [V.15](#) shows the results of the test problem at time $t = 0.8$. We compare the SPH results to a reference solution similar to [Steinmetz and Mueller, 1993](#). In density (left panel) as well as in velocity (middle panel) all schemes show similar trends. The general structure of the test is

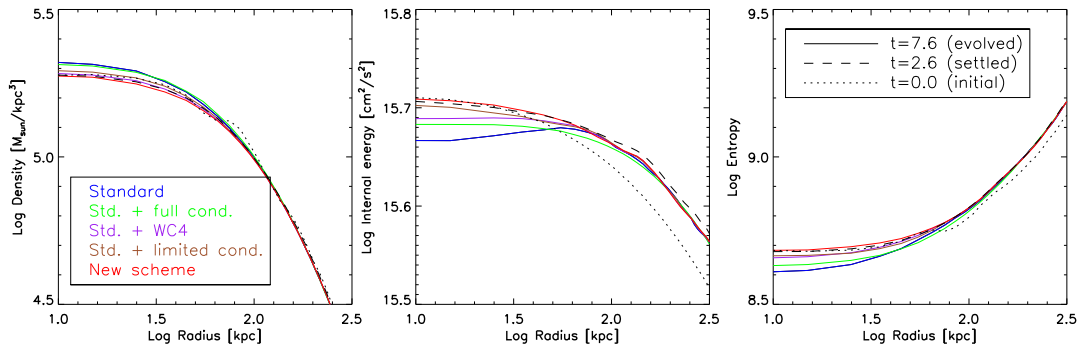


Figure V.14: Sphere in hydrostatic equilibrium. We show radial profiles of density (left panel), internal energy (middle panel) and entropy (right panel) at three different times. At first, the initial conditions (dotted lines) must settle into hydrostatic equilibrium (dashed lines), which then remains stable for an extended period of time (solid lines). The stability of the sphere is determined by the differences occurring between the settled (only shown for the ‘new’ scheme) and the evolved state (shown for all schemes). In the ‘standard’ scheme (blue lines), pairing instability caused by the cubic spline kernel and lack of mixing lead to an incorrect central solution in density (too high) and internal energy (too low). The addition of the WC4 kernel (purple lines) prevents the formation of particle clumps at the centre and AC promotes fluid mixing but full AC without gravity limiter (green lines) leads to a numerical transport of internal energy outwards. The gravity limiter treats this behaviour (brown lines). The ‘new’ scheme (red lines) with WC4 and AC and gravity limiter significantly improves the radial profiles in all physical quantities.

well reproduced; however, the shock front is slightly smoothed and broadened. The solution in density deviates slightly from the reference solution at the centre. The most striking differences can be seen in pre-shock entropy (right panel). The ‘new’ scheme (red line) produces higher levels of entropy compared to the ‘standard’ scheme (blue line). We investigate this trend and perform another test simulation (purple line) with the ‘new’ scheme but the cubic spline kernel. This run is closest to the pre-shock reference solution.

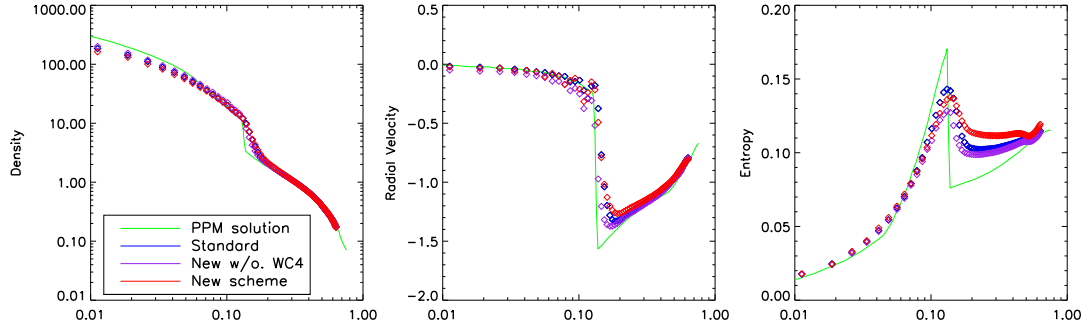


Figure V.15: Evrard collapse. We show radial profiles of density, velocity and entropy at time $t = 0.8$ and compare to a reference piecewise parabolic grid computation (green lines). In principle, all schemes (red, blue and purple lines) show similar characteristics, but they differ as follows. The pre-shock entropy level is significantly higher in the ‘new’ scheme (red lines), which we attribute to the WC4 kernel with a larger smoothing size. A comparison run with the all improvements, but no WC4 kernel (purple lines), shows a lower pre-shock entropy level.

V-4.3 Zel’dovich pancake

We consider the Zel’dovich pancake (Zeldovich, 1970) to study the SPH behaviour for the cosmological time integration with Hubble function $H(t)$ instead of time t . This test describes the evolution of a sinusoidal cosmological perturbation in an expanding Einstein-de-Sitter universe. After an initial linear growth phase, the one-dimensional perturbation collapses and several strong shocks develop. Conveniently, the Zel’dovich pancake has an analytical solution describing the evolution well up to the collapse, which we used to create the initial conditions of the simulation. The comoving position x of an initially unperturbed coordinate q at redshift z is given by

$$x(q, z) = q - \frac{1 + z_c \sin(kq)}{1 + z} \frac{\sin(kq)}{k}, \quad (\text{V-33})$$

where $k = 2\pi/\lambda$ is the wavenumber of the perturbation with a wavelength of λ . We numerically invert equation (V-33) to obtain $q(x)$. The peculiar velocity corresponding to the initial displacement is given by

$$v_{\text{pec}}(x, z) = -H_0 \frac{1 + z_c}{(1 + z)^{1/2}} \frac{\sin(kq)}{k}, \quad (\text{V-34})$$

and the comoving density is given by

$$\rho(x, z) = \frac{\rho_0}{1 - \frac{1+z_c}{1+z} \cos(kq)}, \quad (\text{V-35})$$

where ρ_0 is the critical density, H_0 the present-day Hubble constant and z_c the redshift of collapse. Furthermore, the temperature evolves adiabatically up to the collapse as

$$T(x, z) = T_i \left[\left(\frac{1+z}{1+z_i} \right)^3 \frac{\rho(x, z)}{\rho_0} \right]^{2/3}, \quad (\text{V-36})$$

where z_i is the initial redshift. We follow [Bryan et al., 1995](#), [Trac and Pen, 2004](#) and [Springel, 2010a](#) in our test set-up and choose $\lambda = 64$ Mpc/h, $z_c = 1$, $z_i = 100$ and $T_i = 100$ K. In a fully three-dimensional box, we set up 256^3 dark matter particles of equal masses as well as 256^3 gas particles of equal masses.

Figure V.16 shows the results of the test problem at two redshifts. In the top row we show the evolution of the pancake before the collapse at redshift $z = 3.6$, while it is still in the linear phase. The ‘standard’ (blue lines) and ‘new’ (red lines) schemes give comparable results in density contrast (left column), temperature (middle column) and velocity (right column). The simulated evolution agrees well with the analytical solution (green lines), which describes the linearised evolution of initial sinusoidal perturbation. At this stage of the collapse the test is dominated by gravitational forces and hydrodynamical forces are negligible. Therefore, we do not expect striking differences to arise between both schemes. Both capture the linear growth and adiabatic evolution well.

In the bottom row we show the pancake at the final redshift $z = 0$. Again, we compare to the analytical solution in the regions outside the central shock. In general, both schemes agree but we note the following differences. The peak density contrast is marginally lower in the ‘new’ scheme because of additional smoothing introduced by AC. However, the evolution of density contrast in the low-density regions is described better by the ‘new’ scheme and is resolved with less noise. We recall the Sod shock tube (Section 3.1) and the Sedov blast wave (Section 3.2) problems, where we also find more accurately resolved density fields and lower peak densities. Concerning temperature, we find the central shock to be slightly broader in the ‘new’ scheme, which is caused by two effects. Firstly, the higher amount of viscosity within the shock leads to an earlier heating of particles and thus broadens the shocks. Secondly, the time-step limiting particle wake-up scheme captures highly active particles before they penetrate into inactive regions, which leads to a better fluid sampling and also shock broadening. This can also be noticed in velocity, where the profile is slightly smoothed in the central region. In summary, our ‘new’ scheme gives reasonable results in this cosmological test problem and the differences between both schemes are very small at redshift $z = 0$. Therefore, our new implementation is ready to be applied to Idealized astrophysical problems.

V-5 Astrophysical applications

We complete the evaluation of the performance and accuracy of the two different SPH implementations in idealized simulations of galaxy and galaxy cluster formation.

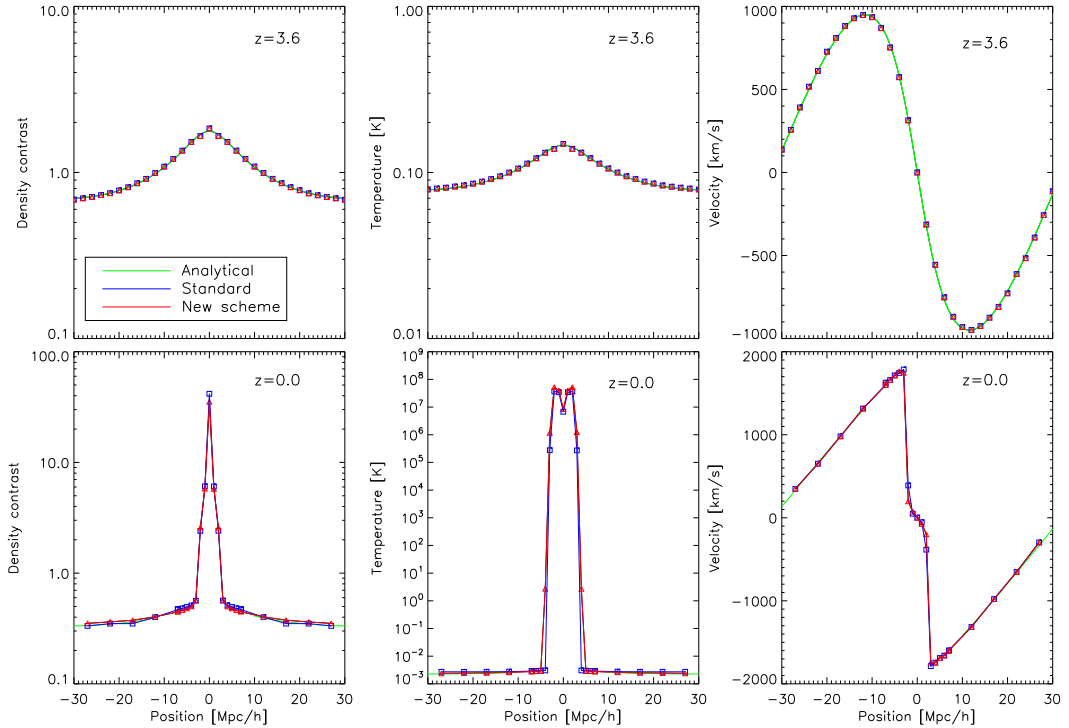


Figure V.16: Zel'dovich pancake. We show the evolution of density contrast (left column), temperature (middle column) and velocity (right column). We show the state of the pancake at an intermediate redshift $z = 3.6$, while it is still in the linear regime before the collapse and at the final redshift $z = 0$, when it is evolved well into the non-linear regime. Both SPH schemes agree well with the analytical solution during the linear growth phase. At the final redshift, the ‘new’ scheme resolves well the density contrast and yields a broader shock and a slightly smoother velocity.

V-5.1 Idealized galaxy formation

In order to check if the ‘new’ scheme is numerically stable when coupled with a simple effective description of the interstellar medium, we consider the formation of an isolated disk from a cooling gas cloud embedded within a rotating dark matter halo. This idealized application also includes a the prescription for cooling, supernova feedback and star formation of (Springel and Hernquist, 2003). We focus on the differences between both hydrodynamical schemes and therefore, we do not consider a cosmological environment or more advanced physical processes such as black holes, stellar evolution or metals. Numerical comparison simulations (see e.g. Scannapieco et al., 2012) are a common tool to study the impact of numerical schemes and physical modules.

Within a computational domain of roughly 1 Mpc³ we set up 4041345 particles resembling a Milky Way-like dark matter halo with a total mass of $1.8 \cdot 10^{12} M_{\odot}$. We include 4466429 gas particles with a total mass of $2.2 \cdot 10^{11} M_{\odot}$, which corresponds to a baryon fraction of approximately 11 per cent. The gravitational softening length is 450 pc. Initially, the distribution of dark matter follows a Navarro-Frenk-White profile (Navarro, Frenk, and White, 1997) and subsequently, we add the gaseous component similar to the set-up of the hydrostatic test (Section 4.1). The only change is that here, we give the gas and dark matter a rotational velocity which peaks at 180 km s⁻¹. Obviously, the initial hydrostatic equilibrium is broken by the onset of the gas cooling and we follow the evolution of the cloud for 10 Gyrs.

Figure V.17 visualizes the spatial distribution of stars, where the colours represent the age of stars (top panels), and the spatial distribution of star forming gas, where the colours represent the star formation rate (bottom panels) at time $t = 7.5$ Gyr. We use the ray-tracing program SPLOTCH (Dolag et al., 2008; Jin et al., 2010) to create the images and choose a linear colour bar for stellar age, where the red end of the colour bar corresponds to stars older than 3 Gyrs and the blue end to recently formed stars. We visualize the star formation rate since it traces the (cold) gas within the disk and use a linear colour bar, which ranges from the minimum to the maximum value of star formation rate. We choose identical plot settings for the ‘standard’ scheme (left panels) and the ‘new’ scheme (right panels), which show striking morphological differences as follows.

In the ‘standard’ scheme, the galaxy shows a prominent bulge containing a large fraction of the stellar population. The entire galaxy appears more spheroidal with a dominant bulge and the stellar disk is not well pronounced. We find similar features in the distribution of star formation. The gas disk is asymmetric and only shows little spiral structure in the face-on view. In the edge-on projection the disk shows a rolling pin morphology. Both disks are dominated by bulges, but in the ‘new’ scheme the bulge is significantly less dominant. The bulge contains a smaller fraction of the stellar population and might eventually be associated with an elliptical bar structure. More as well as younger stars are present within the disk. The gas disk is symmetric and shows a defined spiral structure. At this stage of code testing it is difficult to track down the impact of individual code changes. However, we assume the most significant differences are caused as follows. In the ‘standard’ scheme large amounts of AV might lead to dissipation of kinetic energy, loss of rotational support and numerical angular momentum transport. Additionally, the mixing problem and its associated numerical surface tension tend to confine cold and dense gas blobs. In the ‘new’ scheme, significantly smaller amounts of AV are applied and rotational sup-

port can be provided. Furthermore, the inclusion of AC promotes gas mixing between hot and cold phases.

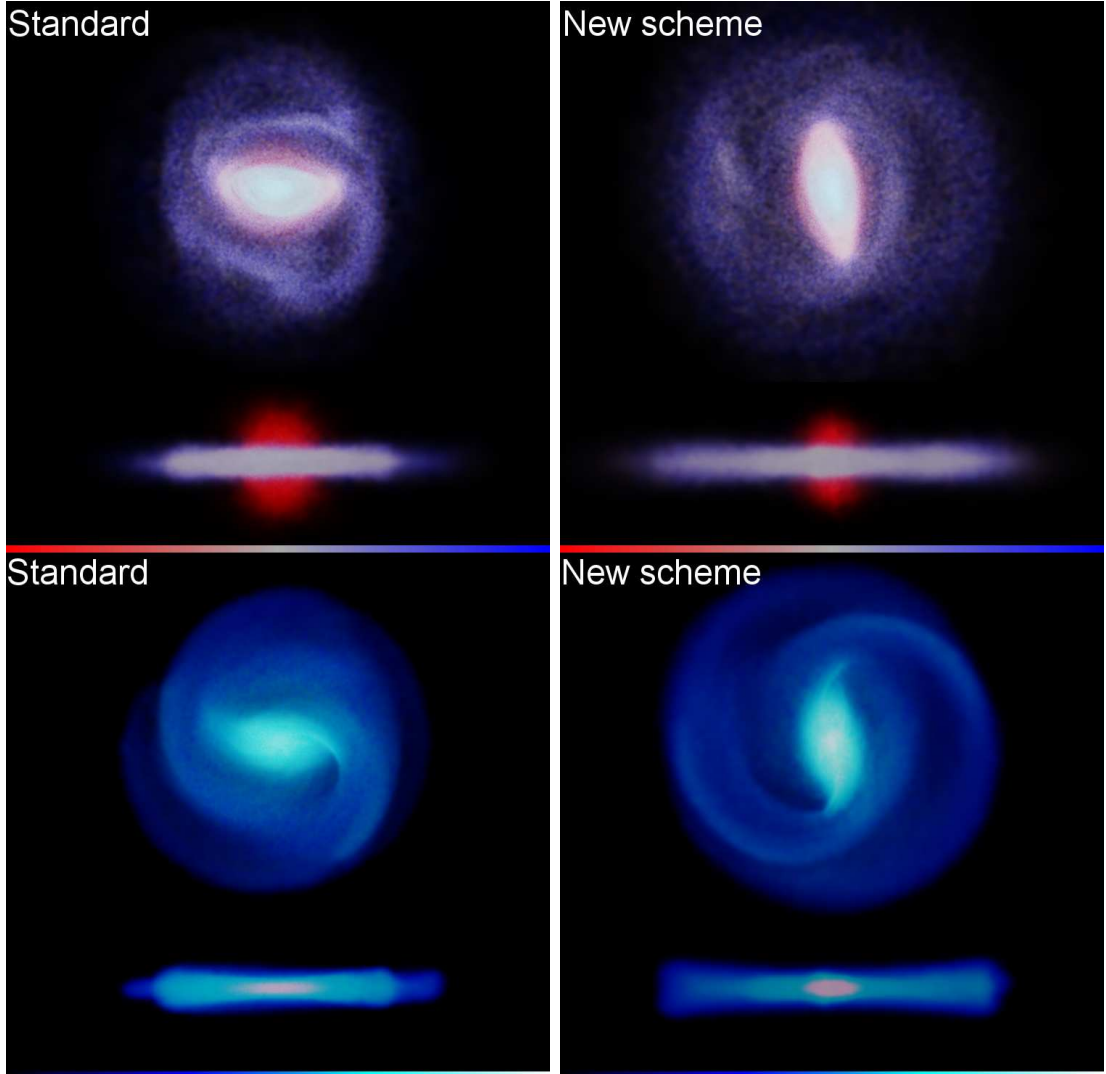


Figure V.17: Idealized galaxy formation. We show the spatial distribution of stars, where the colours visualize the age of stars (top panels) and the spatial distribution of gas, where the colours visualize the star formation rate (bottom panels) at time $t = 7.5$ Gyr. In the ‘standard’ scheme (left panels) the distribution of star formation is clumpy and the object appears bulgy. In the ‘new’ scheme (right panels) the distribution of star formation as well as the stellar component are more extended and pronounced in a disk-like structure. Furthermore, the size of the bulge is smaller and the distribution of young stars is more extended. We show a more quantitative comparison in Figs. V.18 and V.19.

We continue with a more quantitative comparison of both schemes, which confirms our previous findings. Figure V.18 shows density in vertical and radial direction (ρ_z and ρ_r) of the stellar component as well as the associated vertical velocity dispersion (σ_z) at times 2.5 (dashed lines), 5.0 (dotted lines) and 7.5 Gyrs (solid lines). As seen in ρ_z (left panel), the ‘new’ scheme produces a thinner stellar disk and as seen in ρ_r (middle panel) the disk also extends to significantly larger radii. This trend is confirmed by σ_z (right panel), which for the ‘standard’ scheme truncates at smaller radii than for the ‘new’ scheme.

Figure V.19 shows vertical and radial profiles of gas density (ρ_z and ρ_r) as well as the vertical gas velocity dispersion (σ_z) of the cold gas at times 2.5 (dashed lines), 5.0 (dotted lines) and 7.5 Gyrs (solid lines). We employ a temperature criterion of $T < 10^5$ K to distinguish between cold and hot gas. ρ_r decreases towards the centre since the gas within the bulge is hot and exceeds our temperature threshold. In the ‘new’ scheme, the distribution of cold gas is slightly more extended in vertical as well as radial direction. However, σ_z indicates a colder gas disk. Most probably, these features are a result of less numerically induced AV, angular momentum transport and depression of rotational support. Furthermore, the inclusion of AC allows mixing between gas phases and promotes dissociation of cold structures.

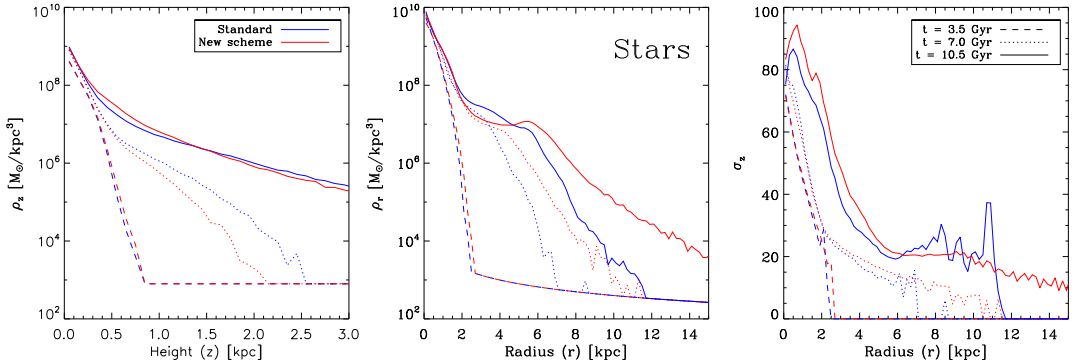


Figure V.18: Idealized galaxy formation. We show the vertical (z) density profile (left panel), the radial density profile (middle panel) and vertical velocity dispersion (right panel) of the stellar component. For the radial plots we use cylindrical bins. In the ‘new’ scheme (red lines), the galactic disk is more defined, extended and colder.

V-5.2 Santa Barbara Cluster

We carried out the Santa Barbara galaxy cluster (Frenk et al., 1999), which is a common reference simulation for cosmological hydrodynamical simulation codes. Although no analytic solutions exists, the cluster has been simulated with a large variety of different codes. The simulation describes the formation of a massive dark matter halo, with virial mass of $1.2 \cdot 10^{15} M_\odot$ and virial radius of 2.8 Mpc. It is evolved in an Einstein-de Sitter cold dark matter cosmology with parameters of $\Omega_M = 1.0$, $\Omega_\Lambda = 0.0$, and $H_0 = 50 \text{ km s}^{-1} \text{ Mpc}^{-1}$. We choose an initial redshift of $z = 20$ with a perturbed distribution of 256^3 dark matter particles and 256^3 gas particles, each of equal masses (see also Frenk et al., 1999, for a detailed description of the initial

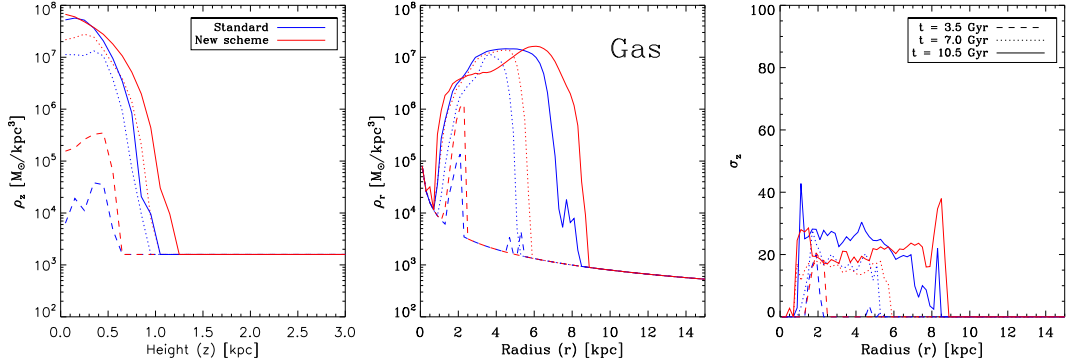


Figure V.19: Idealized galaxy formation. We show the vertical (z) density profile (left panel), the radial density profile (middle panel) and vertical velocity dispersion (right panel) of the cold gas component. For the radial plots we use cylindrical bins. We use a temperature criterion of $T < 10^5 \text{ K}$ to select the cold gas. In the ‘new’ scheme (red lines), the galactic disk is more defined, extended and colder.

conditions), and follow the formation until redshift $z = 0$.

Figure V.20 shows thin slices of gas density (left panels), temperature (middle panels) and entropy (right panels) defining the thermodynamical state of the hot intracluster medium (ICM) at redshift $z = 0$. For the definition of entropy we use $S = T/n_e^{2/3}$, which is commonly used in X-ray studies of the ICM (e.g. Kravtsov and Borgani, 2012). From the maps we note the following interesting features.

The gas density (left panels) tends to be smoother in the ‘new’ scheme, which is mostly due to the effect of AC, which introduces entropy mixing among neighbouring gas particles. In contrast, the ‘standard’ scheme produces a clumpy distribution of gas with gas inhomogeneities associated to stripping from merging haloes and cold blobs. These structures are persistent in the hot ICM mainly due to the lack of mixing. In turn, these ‘features’ of the ‘standard’ scheme prevent an efficient action of hydrodynamical instabilities such as Rayleigh-Taylor and Kelvin-Helmholtz instabilities that are spuriously inhibited. Quite remarkably, the clumps are much less evident in the ‘new’ scheme, which also produces a lower value for the central gas density. In the temperatures slices (middle panels) it becomes clear that gas clumps in the ‘standard’ scheme correspond to objects of low temperature. As expected, the effect of introducing AC is the reduction of the degree of ICM thermal complexity.

However, in the ‘new’ scheme the bow-shock, which is induced by the infall of a large sub-structure onto the main halo is better defined than in the ‘standard’ scheme. The bow-shock is located on the right hand side of the main halo centre (see figure V.20). In fact, the WC4 kernel of the ‘new’ scheme captures the entropy discontinuity associated to the shock better. Most importantly, we note from the entropy maps (right panels) that the entropy level in the innermost region of the clusters increases in the ‘new’ scheme.

Figure V.21 shows radial profiles of gas density, temperature and entropy in the same units as shown in figure V.20 at redshift $z = 0$ for both SPH schemes. Furthermore, for a comparison,

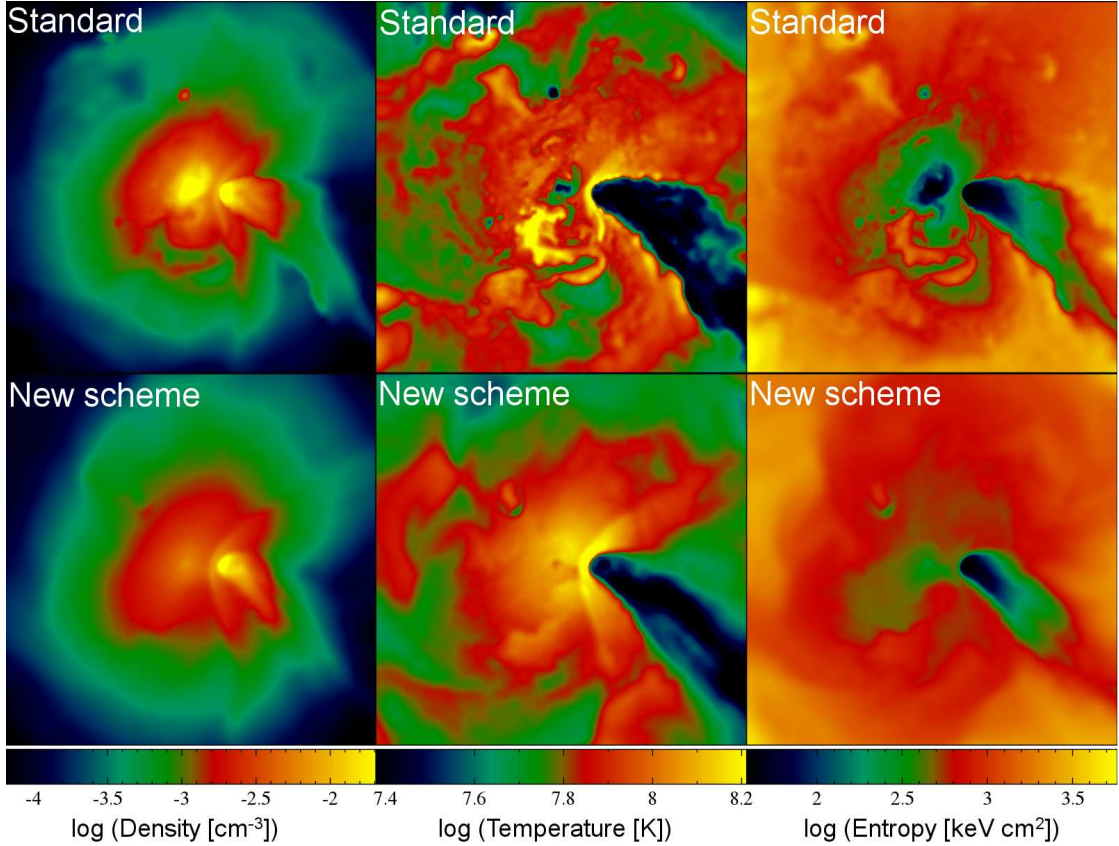


Figure V.20: Santa Barbara Cluster. In boxes with $1 \text{ Mpc}/h$ side length, we show this slices of gas density (left panels), temperature (middle panels) and entropy (right panels) at redshift $z = 0$ for the ‘standard’ scheme (top row) and the ‘new’ scheme (bottom row). In the ‘new’ scheme significantly less dense and cold gas blobs are present, as AC promotes fluid mixing and blob dissociation. This promotes a smoother distribution of higher temperatures and entropies at the halo centre, which reduces the ICM complexity.

we also include results obtained with the MASCLET grid code (see [Quilis, 2004](#)). Both schemes produce quite consistent results at relatively large radii ($> 200\text{kpc}/\text{h}$) but show striking differences in the innermost regions. The ‘new’ scheme predicts a flatter central gas density profile, also with no evidence for the inversion of the temperature gradient produced by the ‘standard’ scheme. Density and temperature profiles for the ‘new’ scheme combine to produce a flat entropy core, which extends out to $\approx 100\text{kpc}/\text{h}$. In the ‘standard’ scheme, the persistence of cold and dense clumps in the cluster atmosphere causes their low-entropy gas to sink to the centre of the cluster, thereby causing the continuous decrease of entropy. In the ‘new’ scheme, AC promotes mixing of gas phases and helps to dissolve low-entropy gas blobs within the hot ICM atmosphere and causes a higher entropy level to be established.

The results for the ‘new’ scheme are remarkably similar to those of the MASCLET code and, more in general, reported by [Frenk et al., 1999](#); [Vazza, 2011](#); [Power, Read, and Hobbs, 2014](#) for Eulerian codes. We point out that such a close agreement has been obtained without any tuning aimed at producing the entropy core predicted by Eulerian codes in cosmological simulations for the formation of galaxy clusters. The choice of parameters for the ‘new’ SPH scheme was only aimed at preventing the limitations of ‘standard’ SPH in terms of the description of discontinuities and efficiency to capture hydrodynamical instabilities. Note also that these results for the Santa Barbara cluster are in qualitative agreement with those obtained in the hydrostatic sphere (see Section 4.1). The behaviour of both schemes are in the same direction, even if they are less evident than in this Santa Barbara cluster test, due to the lack of the hierarchical process of structure formation within a cosmological environment.

Additionally, we analyse the simulation also at redshifts $z > 0$. In general, the profiles of the high-redshift haloes show the same behaviour as their low-redshift counterparts, provided that we choose quiet and virialised objects. Objects, which host dynamically important shocks or undergo merger events show altered radial profiles because the timing of the mergers depends slightly on the simulation scheme. Therefore, a sensible comparison of the entire redshift-evolution and behaviour of both schemes during these violent phases of structure formation is not possible and requires controlled experiments.

V-6 Summary and conclusions

In this paper we presented a novel implementation of the SPH scheme in the GADGET code, which provides improved accuracy for simulations of galaxies and large-scale cosmic structures. Since the first development of SPH great advancements have been made to improve the reliability and stability of this hydrodynamical scheme and, in particular, much effort has been spent in a proper treatment of discontinuities. We implemented and improved several of these modifications of SPH into the developer version of GADGET-3, and tested them against a number of standard hydrodynamical problems, as well as first simple astrophysical applications. The main modifications (see also table V.1) of this ‘new’ scheme, when compared to the ‘standard’ (see e.g. [Price, 2012b](#)) formulation of SPH, can be summarised as follows.

- Artificial viscosity (AV) is introduced for a proper description of shocks. It prevents particle interpenetration into unshocked regions and provides a regularisation of the particle

	AV	AC	WakeUp	Grav.	Cosmo	Radiat.	Main result
Sod shock tube	✓	✓	-	-	-	-	Smooth density field / Sharp shock front / No pressure-blip
Sedov blast wave	✓	✓	✓	-	-	-	Sharp shock front / Central temperature profile
Keplerian ring	✓(imp.)	-	-	-	-	-	Stability of ring / No angular momentum transport
Cold blob test	✓	✓	-	-	-	-	No surface tension / Mixing of gas phases
KH instability	✓(imp.)	✓	-	-	-	-	Growth of perturbation / Mixing of gas phases
Turbulent boxes	✓(imp.)	-	-	-	-	-	Steady-state spectrum / Preservation of kinetic energy
Hydrostatic test	-	✓(imp.)	-	✓	-	-	Stability in radial profiles of density and entropy
Evraud collapse	✓(imp.)	✓(imp.)	✓	✓	-	-	Radial profiles in density and entropy
Zel'dovich pancake	✓	✓(imp.)	✓	✓	✓	-	Smooth density field / Sharp shock front
Idealized galaxy	✓(imp.)	✓(imp.)	-	✓	-	✓	Extended stellar and gas disks
SB cluster	✓(imp.)	✓(imp.)	✓	✓	✓	-	Formation of entropy core / Dissociation of cold blobs

Table V.2: Overview of our test problems. For each test we note the relative importance of a standard method (✓) or an improved method (✓(imp.)) of artificial viscosity (AV), artificial conductivity (AC), time-step limiter (WakeUp) and the physical processes involved beyond pure hydrodynamics such as gravity (Grav.), cosmological time integration (Cosmo), radiative cooling, star formation and supernova feedback (Radiat.).

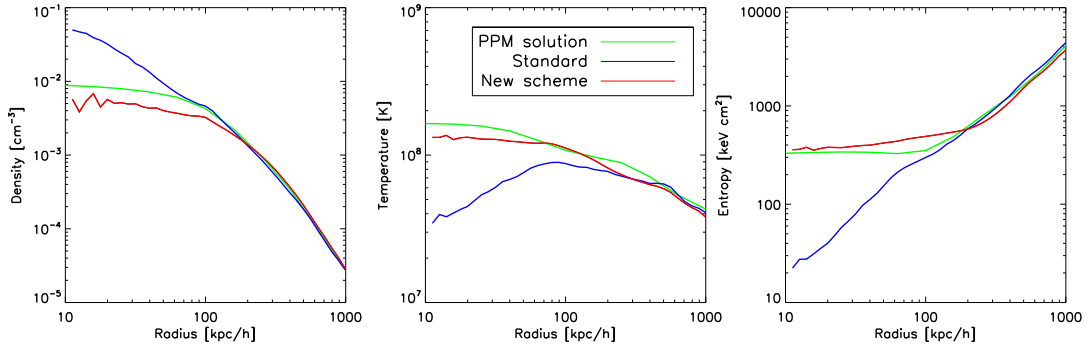


Figure V.21: Santa Barbara Cluster. We show radial profiles of gas density (left panel), temperature (middle panel) and entropy (right panel). In each panel, we compare the results of the ‘standard’ (blue lines) and the ‘new’ (red lines) scheme to a reference solution (black lines) obtained with a piecewise parabolic grid computation with the MASCLET code (see Quilis, 2004). The ‘standard’ scheme does not produce an entropy core but a diverging profile towards the halo centre. In the ‘new’ scheme an entropy core as well as stable temperature and density profiles are reached, which are all in good agreement to the grid code computation.

field, which supports a proper sampling of the fluid. First spatially constant low-order formulations of AV introduce viscosity not only at shocks, but also within unshocked regions and shearing flows, thereby leading to an overly viscous behaviour and a too fast dissipation of kinetic energy. Most commonly, the so called Balsara switch (Introduction, 1995) is used to reduce viscosity in shear flows, while further attempts were made to reduce AV where it is unwanted (Morris and Monaghan, 1997; Dolag et al., 2005b). Recently, modern formulations of AV (Cullen and Dehnen, 2010; Hu et al., 2014) improved greatly on a correct detection of shocks and use high-order gradient estimators to calculate divergence and curl of velocity from the full velocity gradient matrix instead of the classical SPH estimators. This allows shear flow limiters, such as the Balsara one, to work more accurately and suppress AV outside shocks and in shearing flows. In this way, kinetic energy is better preserved, thus helping simulating turbulent flows or hydrodynamical instabilities with higher accuracy. In our ‘new’ scheme, we compute the velocity gradients from the full velocity gradient matrix instead of low-order classic kernel derivatives.

- Artificial conductivity (AC) is introduced to provide a proper fluid description at contact discontinuities. In fact, in the density-entropy formulation a spurious surface tension arises at discontinuities, which also suppresses the formation of instabilities and prevents mixing of different fluid phases. Lately, AC (see e.g. Price, 2008) or pressure-entropy formulations (Hopkins, 2013; Saitoh and Makino, 2013) were proposed to overcome these issues. AC is applied at contact discontinuities and promotes the transport of heat between particles. However, in the presence of gravitationally induced pressure or temperature gradients, common AC schemes might lead to unwanted transport opposite to the gravitational force. Therefore, numerical limiters are necessary to be included in AC.

In our ‘new’ scheme, we include locally adaptive AC to transport heat and treat contact discontinuities in SPH and we limit the amount of AC by correcting for gravitationally induced pressure gradients. While we demonstrated that our AC model is quite efficient at reducing such a surface tension, admittedly a small residual effect is still present, and could potentially impact the long-term stability by over-diffusion.

- As for the choice of the interpolating kernel, the commonly employed cubic spline function has been shown to become easily unstable, which leads to spurious pairs of particles, incorrect gradient estimators and, in general, a poor fluid sampling. Therefore, a change of the kernel function is highly recommended, where commonly the Wendland kernels ([Dehnen and Aly, 2012](#)) are now used. In our ‘new’ scheme, we employ the Wendland C^4 kernel function with 200 neighbours instead of a cubic spline with 64 neighbours. We calculate the density in a classic fashion from the mass distribution of particles and also compute the hydrodynamical forces with the density-entropy formulation.
- At last, within supersonic shocks highly dynamical and computationally active particles can penetrate into regions containing computationally inactive particles causing distortions in the fluid sampling and incorrect hydrodynamical solutions. In our ‘new’ scheme we use a particle wake-up time-step limiting scheme (see [Saitoh and Makino, 2009](#); [Pakmor et al., 2012](#)) as a solution, so as to shorten the time-steps whenever necessary and allow particles to become active earlier.

To highlight the improvements associated to this advanced SPH implementation, we investigate both the new and the original scheme in a variety of hydrodynamical standard tests, with and without gravity. Furthermore, we study the behaviour in the cosmological problem of the formation of galaxy cluster and enable simple prescriptions for radiative cooling, supernova feedback and star formation for a test simulation of an isolated rotating disk galaxy. Table V.2 presents an overview of our test problems and shows if SPH modules are *important* in a standard (✓) or improved (✓(imp.)) with respect to GADGET-SPH without our modifications. Furthermore, we list the probed physical features of each test.

The inclusion of AC in SPH changes the thermodynamical evolution of density, internal energy and pressure. Additionally, physical conduction (see e.g. [Arth et al., 2014](#)) is also sometimes employed in cosmological SPH simulations to promote (an)isotropic heat transport, which also helps to overcome the limitations of ‘standard’ GADGET-SPH. The joint effect of artificial conduction, introduced for purely numerical reasons, and of physical conduction awaits further investigations.

In summary, the ‘new’ GADGET-SPH scheme presented here performs better than the ‘standard’ one in every single of our test simulations. Therefore, it provides a much improved numerical description for weakly collisionless plasmas in cosmological simulations down to galactic scales. We base our future simulations of galaxies and large-scale cosmic structures on this updated formulation of SPH. We will also carry out detailed studies of galactic magnetic fields (see [Beck et al., 2013b](#); [Beck et al., 2016](#)) and the ICM with this advanced method. In view of these applications, it is important to verify how this new SPH implementation performs when compared to other variants of SPH and to Eulerian codes. To this purpose, this SPH implementation participated to the nIFTy cosmology comparison project ([Sembolini et al., 2016a](#)), which compares

the performances of different hydrodynamical codes in cosmological re-simulations of galaxy clusters. In that comparison project, our code is shown to agree very well to both Eulerian codes and modern SPH implementations on the radial profiles of gas density, temperature and entropy. Given the improvements in the description of hydrodynamics provided by the new SPH implementation presented here, we regard it as the core of an efficient code for modern simulations of cosmic structure formation.

Acknowledgements

We thank the anonymous referee for extensive and detailed comments, which helped to improve the quality and presentation of the paper. We thank Volker Springel for always granting access to the developer version of GADGET. We thank Elena Rasia, Veronica Biffi, Milena Valentini, Thorsten Naab, David Hubber and David Schlachtberger for important discussions about numerical topics and SPH. We thank Vicent Quilis for several grid code comparison simulations with MASCLET (Quilis, 2004). We thank Margarita Petkova and the Computational Centre for Particle and Astrophysics (C2PAP) for technical support. AMB thanks the Osservatorio Astronomico di Trieste for its hospitality during several stays. AMB and several authors are part of the MAGNETICUM³ simulation core team. Rendered plots are created using the SPLASH software written by Daniel Price (see Price, 2007). AMB, AA, R-SR, AFT and KD are using SuperMuc of the Leibniz-Rechenzentrum via project 'pr86re'. AMB, AFT and KD are supported by the DFG Research Unit 1254 'Magnetisation of Interstellar and Intergalactic Media' and by the DFG Cluster of Excellence 'Origin and Structure of the Universe'. AFT and KD are supported by the DFG Sonderforschungsbereich TRR 33 'The Dark Universe'. JMFD is supported by the EU FP7 Marie Curie program 'People'. GM, SB and SP are supported by the 'Consorzio per la Fisica di Trieste', the PRIN-INAF12 grant 'The Universe in a Box: Multi-scale Simulations of Cosmic Structures', the PRIN-MIUR 01278X4FL grant 'Evolution of Cosmic Baryons', and the INDARK INFN grant. SP is supported by the 'Spanish Ministerio de Ciencia e Innovación (MICINN) with the grants AYA2010-21322-C03-02 and CONSOLIDER2007-00050.

³<http://www.magneticum.org>

Chapter VI

Understanding SPH data: Transformation to a grid

Fundamental progress has to do with the reinterpretation of basic ideas.

– Alfred North Whitehead

Having outlined the capabilities of our hydrodynamics solver in the last chapter we come now to the topic of proper data analysis. Analogous to chapter IV where we had to translate scalar and vector fields into SPH formalism, we have to perform the inverse transformation in order to analyse a simulation’s data properly. For that we transform our SPH data back onto a regular grid. There are multiple possible methods how to carry out that transformation, which we review in this chapter. We propose a novel modification for a common approach which reduces errors introduced in the transformation and is designed to better conserve the quantities handled like total mass in case of a density field. This chapter is a slight modification of the paper [Roettgers and Arth, 2018](#) which is currently in the submission and reviewing process.

VI-0 Abstract

Analysing data from Smoothed Particle Hydrodynamics (SPH) simulations is about understanding global fluid properties rather than individual fluid elements. Therefore, in order to properly understand the outcome of such simulations it is crucial to transition from a particle to a grid based picture. In this paper we briefly summarise different methods of calculating a representative volume discretisation from SPH data and propose an improved version of commonly used techniques. We present a possibility to generate accurate 2D data directly without the CPU time and memory consuming detour over a 3D grid. We lay out the importance of an accurate algorithm to conserve integral fluid properties and to properly treat small scale structures using a typical galaxy simulation snapshot. For demonstration purposes we additionally calculate velocity power spectra and as expected find the main differences on small scales. Finally we propose two new multi-purpose analysis packages which utilise the new algorithms: Pygad and SPHMapper.

VI-1 Introduction

Since several decades Smoothed Particle Hydrodynamics (SPH), originally formulated by [Lucy, 1977](#) and [Gingold and Monaghan, 1977](#), is a numerical technique particularly widely used in astrophysics as well as for example engineering, geophysics and computer graphics. SPH discretises a medium and also the related equations of hydrodynamics (and potential extensions such as magnetohydrodynamics), formally derived from the fluid Lagrangian by mass (see e.g. [Rosswog and Price, 2007](#)). For a recent review we refer to [Price, 2012b](#).

To the present day many SPH codes have been written and several modifications and improvements have turned up to solve the intrinsic problems that SPH has by construction. These codes include for example Gasoline ([Wadsley, Stadel, and Quinn, 2004](#)), Gadget ([Springel, 2005a](#)), Magma ([Rosswog and Price, 2007](#)), Vine ([Wetzstein et al., 2009](#)), Phantom ([Price and Feder-rath, 2010; Lodato and Price, 2010](#)) and Gandalf ([Hubber, Rosotti, and Booth, 2017](#)). Much work has been put into improvements of the formalism targeting convergence, fluid mixing and related issues. See for example [Hu et al., 2014](#); [Beck et al., 2016](#). While these cover mainly improvements of the simulation codes themselves, amongst others [Beck et al., 2016](#) hint to the importance of a proper SPH to grid transformation scheme, since SPH shows only what happens to one fluid parcel while gridded data shows what happens to a domain. Due to the inherent particle noise it is advisable to carry out some post-processing even at the location of the original SPH particles ([Springel, 2010b](#)). Therefore, this paper targets the question of how to properly understand and analyse the resulting SPH data.

The amount of analysis codes is at least as vast as the number of simulation codes itself. To understand a SPH dataset properly and to translate the fluid variables into a commonly understandable form is far from trivial. Since SPH particles discretise mass and not volume, one can not simply plot, for instance, a column-density map of an astrophysical SPH simulation like of data produced by a grid code. While it is straight forward to think in terms of particles because it resembles a micro-physical point of view, one may never forget that SPH particles are not simply elementary particles of the fluid but rather artificial elements tracing the fluid properties like density or temperature. To visualise fluid properties in a volume related way or to perform further calculations one often needs to generate a scalar or vector field describing the respective quantity as a function of the position at first. Although the applied methods are usually not mentioned in most scientific articles, it is extremely important to conserve as much accuracy as possible within a reasonable amount of computing time since any error made in this process propagates into further analysis. Recent articles about map making and especially visualisation include for example [Dolag et al., 2005a](#); [Navrátil, Johnson, and Bromm, 2007](#); [Fraedrich, Auer, and Westermann, 2010](#); [Forgan and Rice, 2010](#); [Koepferl et al., 2016](#).

In this paper, after revisiting required SPH basics in section VI-2, we review a few of the commonly used techniques how to transform SPH data to gridded data, display issues which arise in certain cases and discuss possibilities to solve these issues (section VI-3). We present a novel formulation we call S-normed SPH binning, hereafter **SNSB**, which approaches typical problems in a clever way while maintaining the resolution of the SPH data as good as possible (section VI-3.2). Furthermore, we show a way to improve the run time requirements of such an algorithm by an intrinsic reduction of dimensions (section VI-3.2). We compare the differ-

ent methods using some astrophysical simulation results in section VI-4 and conclude with a short presentation of two novel multi-purpose analysis tools which incorporate these methods and many more convenient features in section VI-5.

VI-2 SPH principles

We review some SPH basics required. For an extensive review of SPH we refer to the review of [Price, 2012b](#). We start with the definition of the (symmetric) smoothing kernel following [Dehnen and Aly, 2012](#):

$$W(\vec{r}, h) = H(h)^{-\nu} w\left(\frac{|\vec{r}|}{H(h)}\right) \quad (\text{VI-1})$$

with h the smoothing length (a measure for the degree of smoothing, typically direct proportional to H), H the compact kernel support and ν the dimensionality. The smoothing length and the kernel support radius may be, but are not necessarily the same quantity. Therefore, we explicitly distinguish the two. In our tests in section VI-4 we use rather low resolution data with a cubic spline kernel and 32 neighbours to save computing time. We can define the kernel approximation of a physical scalar (or similar vector) field $A(\vec{r})$, i.e. a smoothed version:

$$A(\vec{r}) = \int d^3\vec{r}' A(\vec{r}') \delta(\vec{r} - \vec{r}') \approx \int d^3\vec{r}' A(\vec{r}') W(\vec{r} - \vec{r}', h) \quad (\text{VI-2})$$

This integral is discretised in SPH, historically in terms of mass:

$$A(\vec{r}) = \underbrace{\int \rho(\vec{r}') d^3\vec{r}' \frac{1}{\rho(\vec{r}')} A(\vec{r}') W(\vec{r} - \vec{r}', h)}_{dm} \quad (\text{VI-3})$$

$$\approx \sum_{j=1}^N \frac{m_j}{\rho_j} A_j W(\vec{r} - \vec{r}_j, h) \quad (\text{VI-4})$$

$$= \sum_{j=1}^N \Delta V_j A_j W(\vec{r} - \vec{r}_j, h) =: \langle A(\vec{r}) \rangle_{\text{SPH}}. \quad (\text{VI-5})$$

Generally, it can be discretised with some volume ΔV_j of the particle j , following [Hopkins, 2013](#).

When binning an arbitrary quantity $A(\vec{r})$ onto a grid, one typically seeks to calculate the mean value $A(\vec{k})$ at the centre of each cell \vec{k} (here in the scatter approach):

$$A(\vec{k}) = \frac{1}{\Delta V(\vec{k})} \int_{\Delta V(\vec{k})} d^3\vec{r} A(\vec{r}) \quad (\text{VI-6})$$

$$\stackrel{(\text{VI-5})}{=} \frac{1}{\Delta V(\vec{k})} \sum_{j=1}^N \Delta V_j A_j \int_{\Delta V(\vec{k})} d^3\vec{r} W(\vec{r} - \vec{r}_j, h_j) \quad (\text{VI-7})$$

with $\Delta V(\vec{k})$ being the volume of cell \vec{k} .

VI-3 SPH to Grid: Different Methods

In this section we present some of the commonly used methods for a transition from SPH to gridded data. In order to judge on the quality of these approaches we briefly devote ourselves to the question which requirements they should fulfil in order to reproduce the same meaning as the initial data and to keep the required computation time low:

- Conserving integral properties between SPH and grid data.
- (Which implies:) Taking all particles inside the defined region into account.
- Maintaining the provided resolution of the given SPH data.
- Properly treating boundaries.
- Maintaining balance between a computationally cheap algorithm for post-processing and small resulting errors.

We already mentioned that SPH particles should not be taken as real physically existing particles but as moving fluid elements. Therefore, a transformation involving the actual SPH smoothing kernel most likely gives the best results in contrast to an algorithm which treats the particles directly. In the following subsections we outline several algorithms from a direct particle picture to a smoothed approach.

VI-3.1 Particle-Mesh and Window Functions

[Eastwood and Hockney, 1974](#) and [Cui et al., 2008](#) give a comprehensive overview over several so called window functions. The idea behind this class of algorithms is, to select particles in a certain range from a grid cell's centre and add their contribution to the cell's value multiplied by a certain weight. The main requirements which these are constructed to fulfil are a compact top-hat support in Fourier space and a generic compact support also in real space. While the former helps to minimise sampling effects (i.e. shot noise, for further reference we refer to [Jing, 2005](#)), the latter is useful to restrain computational cost by keeping the number of contributing particles bound.

Technically not a window function but similar nevertheless, [Bauer and Springel, 2012](#) display the simplest approach by always applying the value of the closest particle to a cell without any summation. This requires the use of a grid resolution about half the minimum distance of SPH particles in order to capture all particles and leads to aliasing.

For a generic window function W one can calculate the value of a cell \vec{k} via the sum over all particles i as

$$A^{(\vec{k})} = \frac{1}{\text{Norm}} \cdot \sum_i A_i W(x_i) W(y_i) W(z_i) \quad (\text{VI-8})$$

with $A^{(\vec{k})}$ being the value of the grid cell, A_i the particle's value of property A and x_i, y_i, z_i the particle's coordinates with respect to the cell's centre. Window functions are defined symmetrically along all three coordinate axis and the function W itself is the same for each coordinate direction.

Frequently used window functions are for example the **Nearest Grid Point** method which takes all particles inside a cell into account without weighting them (Hockney, 1966):

$$W(x_i) = \begin{cases} 1 & |x_i| < 0.5 \cdot d \\ 0 & \text{otherwise,} \end{cases} \quad (\text{VI-9})$$

the **Triangular Shaped Cloud** method which takes particles in range of half the neighbouring cells into account using a linear distance weighting (Birdsall and Fuss, 1969; Birdsall, Langdon, and Okuda, 1970):

$$W(x_i) = \begin{cases} 1 - |x_i| & |x_i| < 1.0 \cdot d \\ 0 & \text{otherwise} \end{cases} \quad (\text{VI-10})$$

and finally the **Cloud In Cell** method, which further extends the range and provides a smoother second order weighting, by extending the window function (Buneman, 1973; Hockney and Eastwood, 1981):

$$W(x_i) = \begin{cases} 0.75 - x_i^2 & |x_i| < 0.5 \cdot d \\ \frac{(1.5 - |x_i|)^2}{2} & 0.5 < |x_i| < 1.5 \cdot d \\ 0 & \text{otherwise,} \end{cases} \quad (\text{VI-11})$$

with d denoting the grid cells side length. Furthermore, we refer the interested reader to **Particle In Cell** (Buneman, 1959; Dawson, 1960; Dawson, 1962; Morse, 1969), extensions (Hockney and Eastwood, 1981; Birdsall and Langdon, 1991) and improvements like so called Multipole NGP (Kruer, Dawson, and Rosen, 1973).

Fulfilling the requirement of a compact top hat support in Fourier space leads to a non compact support in real space. Daubechies, 1992 provide a solution approach for mixture of both criteria: so called wavelets. These are base functions similar to those of the Fourier transformation, consisting of sin and cos terms, however, preserving local information better than the latter.

VI-3.2 SPH Kernel Methods

General Idea

Since SPH already comes with a kernel weighting formalism with compact support, one can straightforwardly replace the sum over particles by the typical SPH sum:

$$\tilde{A}^{(\vec{k})} = \sum_{j=1}^N \Delta V_j A_j W(\vec{r}^{(\vec{k})} - \vec{r}_j, h_j) \quad (\text{VI-12})$$

Please note the important difference to window functions which are defined such, that each particle is assigned to at least one cell due to the window being of cubic support, which is (typically) larger than a voxel. However, SPH assumes particles to have a spherical smoothing via the kernel function which can result in particles not being accounted for. We go into more detail about that in the next subsection.

Besides clear differences between window functions and a kernel based approach, the choice of the kernel is equally important especially when it comes to its Fourier properties. For further reading on this we refer for example to [Dehnen and Aly, 2012](#) and [Beck et al., 2016](#) and state that, while our models are valid for all kernels, it is important for consistency to use the same kernel in post-processing as during the SPH simulation itself. In our analysis we use the cubic spline function.

In principal the SPH sum results in a physically more meaningful value, since it mirrors exactly how a simulation treats the respective equations. However, some problems, for which we discuss several solution approaches in the next subsections, can still arise.

Solving Common Issues

Without modifications this approach formally fails all criteria outlined above except being a computationally relatively cheap scheme even though it resembles very closely how SPH works. Over the years several people evaluated improvements on the algorithm in order to fix these shortcomings as best as possible.

Multiple evaluations

So far all mentioned prescriptions assumed that we want to calculate the value in the centre of a grid cell and, therefore, weighted a particles contribution by the distance to this centre. In order to increase accuracy one can average over several points within a voxel.¹ An example is given by [Pakmor, 2006](#) using 9 distinct points in the cell:

$$A^{(\vec{k})} = \frac{1}{9} \cdot \sum_i \frac{m_i \cdot A_i}{\rho_i} \left[W\left(r_i - r^{(\vec{k})}\right) + W\left(r_i + \frac{d}{\sqrt{3}}(\pm 1, \pm 1, \pm 1) - r^{(\vec{k})}\right) \right] \quad (\text{VI-13})$$

Obviously this increases the computational cost by roughly a factor of 9 but captures way more detail in a single grid cell possibly yielding better results for large variations in one cell. It is also useful not to miss certain particles, if they actually reside inside a certain grid cell but their kernels do not overlap with the cell centre. However, the results are still resolution dependent and the same effect might be reachable by simply decreasing the grid cell size, therefore we do not further discuss this approach.

Broadening the kernel

To prevent particles from falling through the grid, [Pakmor, 2006](#) also suggests the possibility to broaden the kernel, i.e. to add a constant to the smoothing length of each particle. Setting this value to $\sqrt{3}/2$ times the cell size guarantees that each particle will contribute to at least one cell in three dimensions while the effect on particles with big smoothing lengths is on average

¹A voxel is the same as a pixel but in three dimensions.

small, since the relative change of the smoothing length is small. However, this approach artificially worsens the acquired resolution of the grid, since small features are increased in size and therefore smoothed out which is a drastic drawback whenever one is interested in the details. Furthermore, an additional error term is introduced, regarding the conservation of properties when integrating over the resulting grid.

Boundaries

A serious problem is posed by the boundaries, since here again particles may easily intersect with a cell but not any point inside it. We briefly discuss this as a special case when outlying our final approach in the next section.

Normalisation of SPH noise

SPH fields have shot noise due to the particle discretisation and the fixed form of the kernels. This means for instance that even if all SPH particles carry the same value for an arbitrary fluid quantity, the total field is not necessarily constant but flawed by particle noise. One can divide the end result by the unity condition I as suggested by [Price, 2007](#):

$$I(\vec{r}^{(\vec{k})}) = \sum_i \frac{m_i}{\rho_i} W(\vec{r}_i - \vec{r}^{(\vec{k})}) \approx 1 \quad (\text{VI-14})$$

This re-normalisation has its biggest effect at locations where only few SPH particles sit, ergo for example at the boundaries of a fluid. Without this additional term one can expect very small values at those locations and a smooth drop off while the re-normalisation increases the resulting values. While this is certainly not always wished for, it brings the benefit of independence from the particle structure. [Price, 2007](#) suggests to use this approach whenever no free surfaces are involved. An additional benefit of this modification is that it allows to generate weighted data in the particles in a very straight forward way by replacing the quantity A_i in the numerator by $A_i \cdot w_i$ and introducing w_i in the denominator. Typically weighting is, however, done in the volume discretised picture.

Conservation of integral properties

Another conservation property we can impose is that the integral over the whole volume in particle and grid picture of some quantity should always be the same. This means for example, that total mass or energy is conserved in the conversion process. We further elaborate on this condition in the next section and formulate the condition quantitatively, which we then call ‘S-normalisation’². Note that this requirement does not conflict with the normalisation of SPH noise.

Resolution

Finally, we want to be able to transport the same resolution we have in SPH data to the grid. This is not an easy task with a fixed grid, since SPH has the advantage of being able to model large density contrasts and therefore inhomogeneities. Mesh refinement techniques come to mind as an option, however these are beyond the scope of this work. For a fixed grid one can start by

²The S in the name stands for sum, as the sum of the kernel values at the grid points times their volume (a discrete integral) shall be equal to one as for the continuous integral over the kernels.

choosing the cells' side length to a value comparable to the average smoothing length. This results in general in regions with plenty particles intersecting with a cell and such where only very few or even no particles lay. While the former leads to a resolution worse than possible, the latter is what really divides the methods for binning. In contrast to an SPH formalism, window functions will drastically fail since they rely heavily on counting of particles. This can lead to the conclusion, that only a SPH-like approach grants the possibility for resolution down to particle level.

S-Normed SPH-Binning

Having outlined several conditions, problems and solution approaches for general SPH binning, we propose a different ansatz in this section which we call the **S-normed SPH binning** (from here on SNSB). The basic idea behind this method is that we calculate the kernel integral discretised to the sum S over the grid and require that it is equal to one as the continuous integral over the kernel:

$$S_j = \sum_{\vec{k}} \Delta V^{(\vec{k})} W(\vec{r}^{(\vec{k})} - \vec{r}_j, h_j) \quad (\text{VI-15})$$

with the sum over all grid cell centres \vec{k} . In the limit of an infinitesimal small cell size, $\Delta V^{(\vec{k})} \rightarrow 0$, we indeed recover the continuous integral:

$$S_j \xrightarrow{\Delta V^{(\vec{k})} \rightarrow 0} \int d^3 \vec{r} W(\vec{r} - \vec{r}_j, h_j) = 1 \quad (\text{VI-16})$$

This normalisation by S implies that each particle j contributes fully and with the correct weight to the grid (neglecting boundaries of the grid here).

For $S_j \neq 0$, we define the cell value $\tilde{A}^{(\vec{k})}$ for cell \vec{k} by modifying equation VI-12:

$$\tilde{A}^{(\vec{k})} \Big|_{S_j \neq 0} := \sum_{j=1}^N \Delta V_j (S_j)^{-1} A_j \Big|_{S_j \neq 0} W(\vec{r}^{(\vec{k})} - \vec{r}_j, h_j). \quad (\text{VI-17})$$

Please note that the formula asymptotically goes to equation VI-5 for small cells since S_j becomes unity. We can easily prove that the integral for an arbitrary property A is conserved using this modification

$$\begin{aligned} \sum_{\vec{k}} \Delta V^{(\vec{k})} \tilde{A}^{(\vec{k})} \Big|_{S_j \neq 0} &= \\ \stackrel{(\text{VI-17})}{=} \sum_{\vec{k}} \Delta V^{(\vec{k})} \sum_{j=1}^N \Delta V_j (S_j)^{-1} A_j \Big|_{S_j \neq 0} W(\vec{r}^{(\vec{k})} - \vec{r}_j, h_j) & \quad (\text{VI-18}) \end{aligned}$$

$$= \sum_{j=1}^N \Delta V_j A_j \Big|_{S_j \neq 0} (S_j)^{-1} \underbrace{\sum_{\vec{k}} \Delta V^{(\vec{k})} W(\vec{r}^{(\vec{k})} - \vec{r}_j, h_j)}_{=S_j} \quad (\text{VI-19})$$

$$= \sum_{j=1}^N \Delta V_j A_j|_{S_j \neq 0}, \quad (\text{VI-20})$$

which is transitioning the sum over all cells to the sum over all particles (restricted to where $S_j \neq 0$).

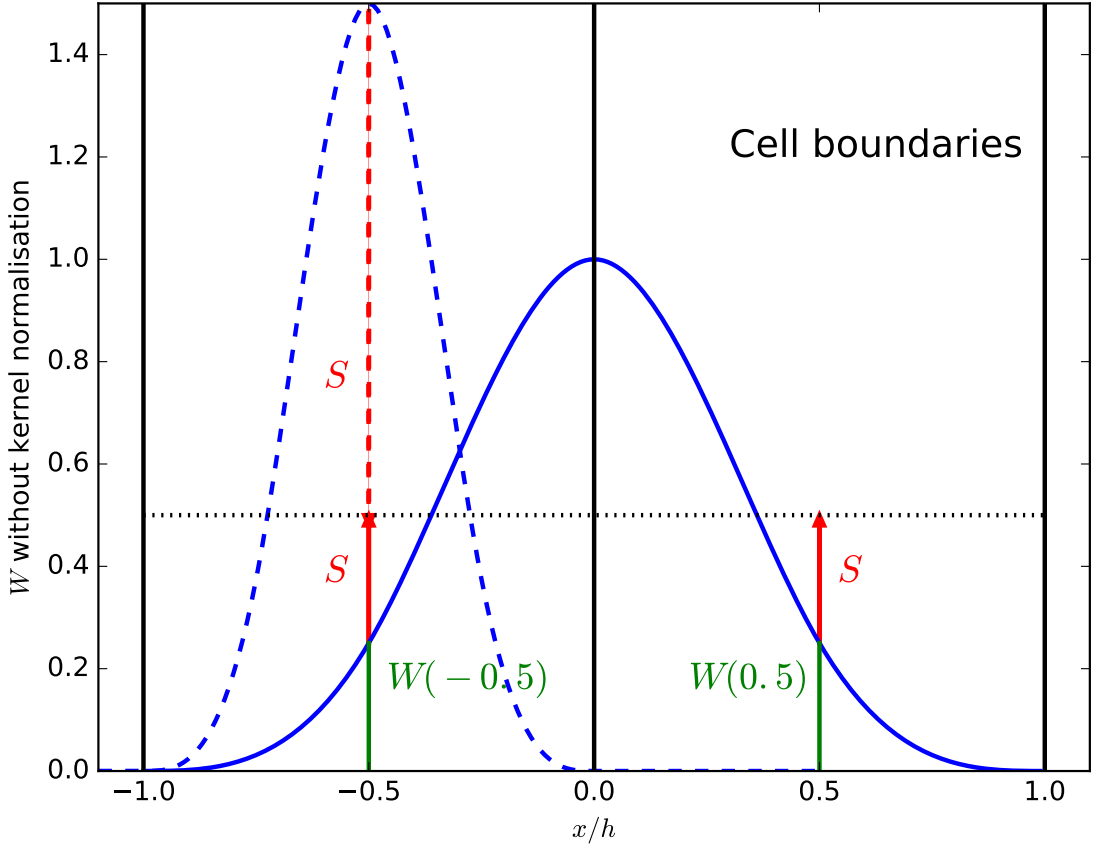


Figure VI.1: A simple example with one particle sitting exactly between two cells (solid blue line indicating its kernel) and one sitting exactly in a cell (dashed blue line) in order to illustrate the meaning of the S-normalisation in equation VI-17.

To illustrate the meaning of S we sketched a dimensional example in figure VI.1. Let a particle sit at the boundary between two cells and overlap only with those two. A traditional SPH binning assigns only small portions of the particle to both cells, so that part of its information is lost ($W(-0.5) + W(0.5) \approx 0.5 \ll 1$). Since equation VI-15 denotes the overlap of a particle with the grid cells, applying this correction increases the impact value of the particle to the desired amount. Furthermore, if a particle sits close to the centre of a cell and does not (or only marginally) contribute to any other cells, its impact is highly dependent on the central kernel value and, hence, its smoothing length due to the integral normalisation property of the SPH kernel. In that case a particle might even contribute too much to this grid cell, because its kernel

function is bigger than unity in the central part, which leads to a reduction by $S > 1$ and equation VI-17.

Since grid cells are of finite size there may be particles for which $S = 0$ as they “fall through the grid” by not having their kernel overlapping with any cell’s centre $\vec{r}^{(\vec{k})}$. We add those particles in a volume weighted way to the nearest cell k :

$$\tilde{A}^{(\vec{k})} \Big|_{S_j=0} := \sum_{\vec{k} \text{ nearest to } \vec{r}_j} \frac{\Delta V_j \ A_j|_{S_j=0}}{\Delta V^{(\vec{k})}} \quad (\text{VI-21})$$

For those it trivially holds again that

$$\sum_{\vec{k}} \Delta V^{(\vec{k})} \tilde{A}^{(\vec{k})} \Big|_{S_j=0} = \sum_{\vec{k} \text{ nearest to } \vec{r}_j} \Delta V_j \ A_j|_{S_j=0}, \quad (\text{VI-22})$$

resulting in overall integral conservation.

Furthermore, there are particles which only partially overlap with the grid, hence, equation VI-16 does not hold any more. Since such a particle’s sphere of influence is cut into a peace contributing to the grid and a residual, we can not judge properly upon conserving the contribution of this particle. In this case we therefore set $S_j := 1$, i.e. we simply evaluate kernels at cell centres. To guarantee numerical stability we also treat small values (for example $S < 10^{-4}$) the same way as particles with $S = 0$. A different approach would be to extend the grid in order to properly calculate S_j . In order to be on the completely save side, this extension would have to cover the largest kernel support radius of all boundary particles. We argue that one typically extends the grid anyway, keeping all interesting features rather central while typically only a few voxels close to the boundaries are actually affected, which renders this safety procedure obsolete. About 5 voxels per side have to be added as an extension, because as soon as the smoothing lengths are much larger than the voxel sizes the discrete integral S is close to one. We see this behaviour later in our test analysis section VI-4.2. We do not concern ourselves much more with this issue here, since one can always extend the grid’s size in any case where this might be desirable, without adding to much computational cost.

The presented normalisation seems somewhat similar to the unity condition by Price, 2007, however one has to keep in mind that the former is calculated per particle while the latter is per grid cell. This unity condition states a fundamental property of SPH (SPH noise) and does not contradict with the integral conservation condition (equation VI-20) enforced by the S-normalisation, as one can easily see by calculation. It may seem that the idea of conservation and this unity condition contradict each other while they are actually compatible, however, using the SNSB method for the numerator as well as the denominator. We present the impact of this additional condition briefly in section VI-4.3.

3D vs. 2D

Another problem is, that the grid’s resolution is strongly restricted by the availability of main memory. Assume a typical use case where we want to generate a 500^2 sized map with a line-of-sight that requires 2000 pixels along. This results already in 4GB of data just for the three

dimensional grid. There are possibilities like out-of-core computing to approach this problem, for example the memory management library Rambrain (Imgrund and Arth, 2017a) which is actually used by the tool SPHMapper presented in section VI-5.2. However, this only allows to the user to create a huge grid and somehow fit it into memory without reducing the resulting requirements of CPU time. We propose a different approach, simplifying the problem algorithmically. Assuming one is not actually interested in the full 3D information but only in 2D data, integrating the 3D grid would be the task at hand anyway. It is actually possible to generate 2D data on the fly in order to minimise the memory footprint as well as runtime. For this approach we embed the projection task already into the formalism by using the projected kernel:

$$W|_{2D,i}(\vec{x}, h) := \int_{-\infty}^{+\infty} dr_i W(\vec{r}, h) \stackrel{(VI-1)}{=} H^{-\nu+1} w|_{2D}(|\vec{x}|/H) \quad (VI-23)$$

where

$$w|_{2D}(b) := \int_{-\sqrt{1-b^2}}^{\sqrt{1-b^2}} d\ell w\left(\sqrt{b^2 + \ell^2}\right) \quad (VI-24)$$

with the impact parameter b . The integral $w|_{2D}$ can be pre-calculated with high precision and tabulated as a function of b . We compare this 2D approach with the standard 3D plus integration approach in section VI-4 and show that it can even lead to better results than the classical 3D method due to the more precise integral along the l.o.s..

Non-Cartesian Grids

A big advantage of the SNSB method, and most SPH based approaches in general, is that it is totally independent of the grid structure. The only property of the grid itself which enters is the volume of each cell, therefore a regular grid is not required for the approach to work out and complexity rises only when the kernel integral over a voxels volume is not computable in a straightforward way. Therefore, it is possible to get even better results with techniques like adaptive mesh refinement (Berger and Oliger, 1984; Berger and Colella, 1989) or perhaps Voronoi grids (Lejeune Dirichlet, 1850; Voronoi, 1908). A typical type of binning which is commonly required is a radial or cylindrical one. While usually computed using adapted window functions, a native SPH binning would be very helpful. However, since the grid cells are not of constant size any more, typical calculations break down and constructing a method to fulfil the stated requirements is very difficult and beyond the scope of this paper.

VI-4 Comparison by Examples

In this section we compare some of the methods we discussed in section VI-3 by analysing a cosmological zoom simulation of a Milky Way-like galaxy at redshift zero. The methods of our choice are listed in table VI.1. We cut out a cubic box with side length of 600 kpc around the

Scheme	Pros	Cons
NGP	easy, fast	SPH particles treated as point-like
SPH	weighting via particle properties	misses small particles, not integral conserving
Broadened SPH	uses all particles	wrong weighting of particles, not integral conserving
SNSB	proper weighting of all particles	computationally slightly more expensive

Table VI.1: The major pros and cons of the different schemes which we compare in this section. These cover the Nearest Grid Point method and SPH binning without and with the S-norm as well as broadened SPH. If applicable, we also compare our direct 2D method to the general 3D grid followed by integration along the line of sight.

main galaxy and run the analysis tool Pygad (see section VI-5.1) with different settings over the SPH data in order to generate projected maps. In order to check the errors depending on grid resolution we remove the effects of boundary particles by considering only particles with their smoothing kernel being totally enclosed by the selected box. In the following subsections we focus on the different issues we discussed in section VI-3 and illuminate how the chosen methods behave in such a common application.

VI-4.1 The dataset

At first we show a qualitative comparison in order to understand what the data at hand contains. In figure VI.2 we plot the column density of the chosen sample for all four methods with an underlying grid of size 120^3 . To ensure robustness of these results we carry out the same analysis also with higher (200 cells) and lower resolution (84 cells) with similar outcome and therefore do not present the additional plots. The left column shows the overall box, while the second and third one present zooms of interesting regions: One of the main galaxy itself and one of a small satellite galaxy. These three cuts contain $3.1 \cdot 10^5$, $4.1 \cdot 10^4$ and $1.4 \cdot 10^3$ particles respectively. Starting with the left column we see that while SNSB and broadened SPH agree very well, the other two methods produce quite different results. The NGP result shows correct density amplitudes but by construction lacks smoothing which leads to a rather grainy image. As outlined before, SPH data is just not interpreted correctly here. On the other hand, the classical SPH binning has a smoothed character but fails to produce proper densities in the central galaxy. Since smoothing lengths are small there compared to the voxel size, many particles just fall through the grid without being taken into account. This is quantitatively analysed later in figure VI.6. This effect is drastically reduced in the zoom onto the central or satellite galaxy proving this to be a resolution effect. Here, the classical SPH binning and SNSB produces a fairly similar result, while the broadened SPH appears to be over-smoothed. It requires a more quantitative analysis to see properly that substructures are more prominently displayed with the SNSB method as outlined in the next subsection.

The smaller the voxels, meaning the bigger the grid resolution is in comparison to the SPH

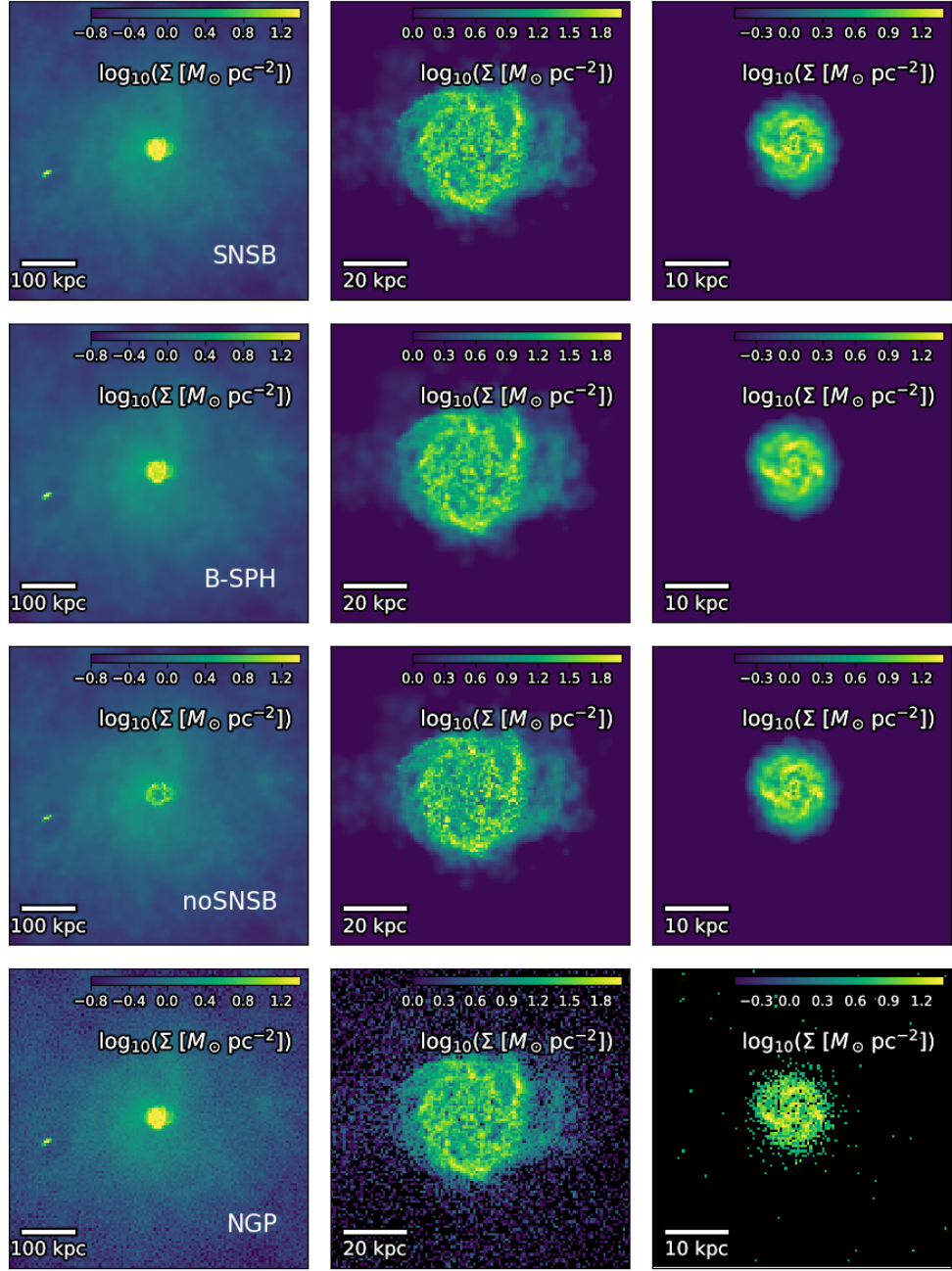


Figure VI.2: Projected 3D gas density maps generated with the different models for three chosen volumes. All grids have $120^3 = 1.7 \times 10^6$ voxels and were integrated along the same axis. The physical sizes of the boxes are $(600 \text{ kpc})^3$, $(100 \text{ kpc})^3$ and $(50 \text{ kpc})^3$. The second column is a zoom onto the central galaxy of the first column; the last column zooms onto some satellite galaxy. The rows from top to bottom use the S-normed SPH, broadened SPH, classical SPH binning, and nearest grid point method.

resolution, the more empty pixels are produced by the NGP method and we transition from a grainy picture to an object which appears to live in a totally gas free environment. However, considering the large smoothing lengths of particles outside of the structures we know that this circumgalactic medium is not empty but just of low density. While it might have been possible to live with NGP as an approximation for the whole box, we get a totally wrong result here by misinterpreting the SPH data.

VI-4.2 Conservation properties

If we want to use the resulting grid data to do further calculations on it, we have to make sure that for example the total mass inside the simulation is still the same after the transformation. For that we use the full 600 kpc^3 box and compare the sum over all SPH particles inside the selected region with the integral over the grid. The result is shown in figure VI.3 with the three dimensional methods in the left column and the two dimensional counterparts on the right. The upper row shows the relative error between the two mass calculations while the lower one displays the calculated masses.

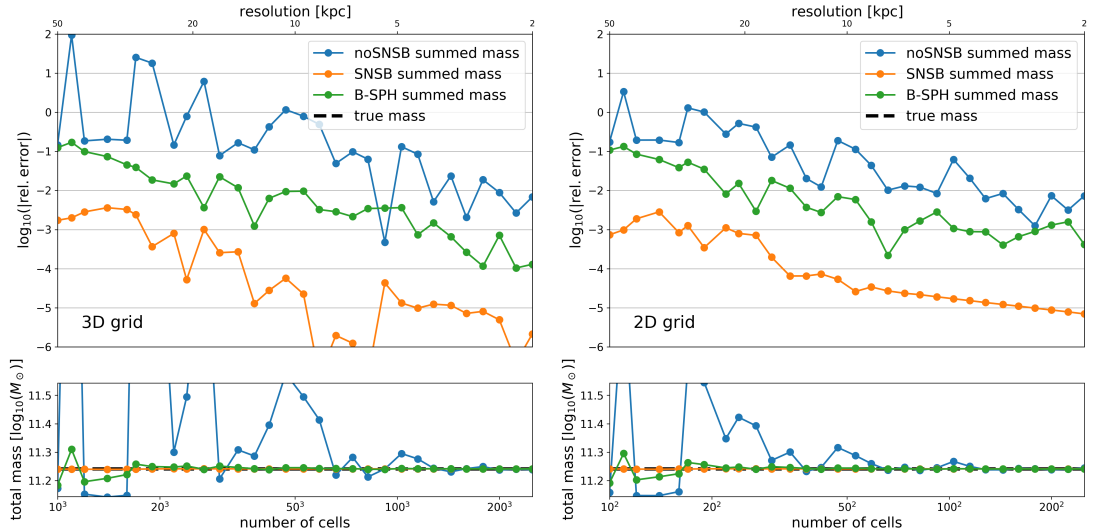


Figure VI.3: This figure shows the relative errors of integrated mass over the resulting grid in comparison to a sum over all particles. We vary the grid resolution from 10 to 250 cells per side. We compare our new method with and without the correction normalisation of equation VI-15 and broadened SPH binning. The left panel displays the result for the 3D grid data while the right panel shows the projected method.

Before we come to the differences of the standard 3D approach to the native 2D version, let us focus on the left panel first. Comparing the standard SPH binning approach with the S-normalised one we can clearly see, that the latter performs much better most of the time. By construction, it is even usable for very small resolutions with only very few grid cells since it accounts for particles which do not actually overlap with any grid cell centre. The resulting relative errors

are always in the sub-percent regime, while the standard SPH approach needs a minimum resolution of about 150 cells per side (which equals roughly $3kpc$ side length of a cell) to achieve even percentage error accuracy. Broadened SPH binning lies about half way between both on a logarithmic scale. Although the methods will converge eventually, changing the amount of grid cells moves all cell centres by a bit so that more resolution can sometimes even result in worse conservation. Our SNSB approach converges slightly smoother, only outperformed by the broadened SPH which is less affected by moving cell boundaries due to the broader kernel. We omit the result for NGP, since here it would just sum up all particle masses and therefore by construction conserve mass perfectly.

As we can see in the lower panel, most errors lead to an overestimation of the mass in the classical SPH case which is a bit counter-intuitive. We stated that the main issue is that particles are not even taken into account and therefore, their mass is lost in the gridding process. However, one has to take an additional effect into account. Especially with a low grid resolution many substructures in the central galaxy may fall through the grid (a more quantitative analysis follows later this section) but, depending on the exact position of grid cell mid-points, some might be very close and therefore being taken into account with a strong weighting ($S \gg 1$). This leads to a grid cell with a very large value originating from only a very small particle volume inside this cell. In total it is very hard to predict, whether the result should over- or underestimate the integrated result.

Now, we compare this to the right panel, where we used the native 2D prescription as presented in section VI-3.2. For classical SPH binning this decreases the error the most for all grid resolutions compared to the 3D approach. This can be easily explained by the reduction of one dimension. While the 3D methods have three space dimensions for the possibility of particles to fall through the grid, here we integrate out one dimension precisely and only two dimensions remain for the distance calculations. One can imagine this as calculating the distance perpendicular to the line of sight and not to several grid midpoints. Since this effect is most prominent in the classical binning, that method is affected the most by the 2D approach. Additionally, the native 2D version even increases the overall smoothness of convergence for all presented methods for the same reason. Since we replace the discretisation along the line of sight by a tabulated, more accurately computed integral we remove the weighting's dependence on this dimension and therefore reduce fluctuations whenever we change the grid resolution.

Furthermore, an interesting effect shows up for the classical SPH binning (i.e. without the S -normalisation), that whenever the 2D version underestimates the mass, the 3D also underestimates it. However, this does not hold other way round. This further supports our reasoning regarding the over- and underestimation. When a particle falls through the grid in the projected plane, it will also do so in all three dimensions. But if it is not taken into account in three dimensions this might be due to the line of sight component and therefore it is accounted for in the 2D method.

In order to understand grid resolutions better in the context of our data set we plot the distribution of smoothing lengths in our full box binned with 120^3 pixels in figure VI.4. To better illustrate the correspondence between grid and SPH resolution, we add the one to one relation as required number of grid cells per side on top of the plot. Since the particle masses vary slightly in our data set we plot the accumulated mass instead of counting particles. Particles in the central

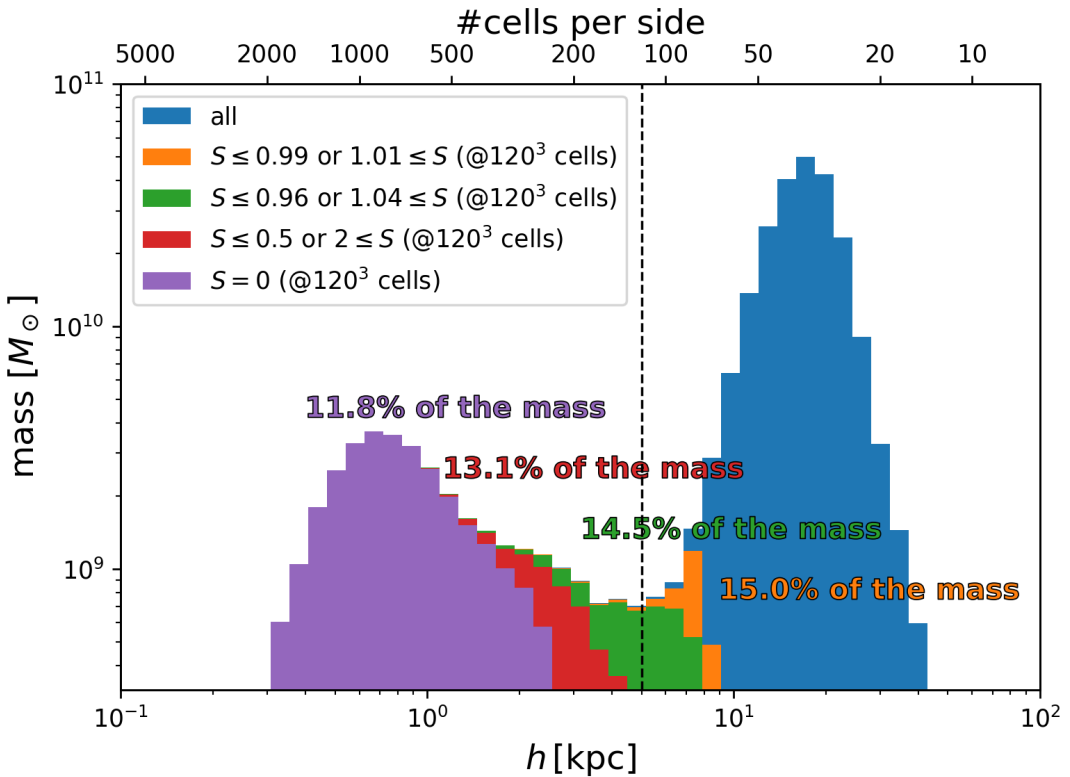


Figure VI.4: This histogram shows the distribution of smoothing lengths of all particles in our large box (left panels of figure VI.2) colour coded with different bins of S -values (which successively include less particles). The dashed line indicates 120 cells per side as used in figure VI.2 and here for determining the S -values. Furthermore, we note down the mass contained in the respective selections for a more quantitative comparison.

galaxy have smoothing lengths in the sub- kpc regime and are therefore much smaller than grid cells even in our high resolution binning, implying that these are the particles which we mostly miss out in the standard SPH approach. This is especially fatal, since most of the time people are strongly interested in the high density regions. In order to fully include all particles in this simulation, an enormous grid of about $3000^3 = 2.7 \cdot 10^{10}$ cells would be required which is not feasible regarding computation time and consumed memory. Even with the native 2D variation this still results in $1.6 \cdot 10^7$ pixels. Since the grid misses out on the adaptivity of SPH this means about a factor of 100 more cells than particles in the original data set in 2D. In 3D this amounts to even 10^5 more cells than particles. With growing SPH resolution smoothing lengths become even smaller and one would need massive computational power to solve this basic post-processing step.

In figure VI.5 we colour code different ranges of S -values to better illustrate the impact of our normalisation. As denoted by the purple region about 11.8% of the mass is completely lost in a classical SPH binning, since the respective particles do not overlap with any line of sight in the given grid and therefore have $S_j = 0$. These particles are added to their respective nearest voxel according to equation VI-21. This exact number is of course extremely dependent on the dataset as well as on the grid resolution and position.

Additionally to these particles which fall through the grid, there is also a significant component of particles of which the contribution to the grid has to be adjusted significantly. About 1.3% of mass consists of particles with $S < 0.5$ or $S > 2$ and 3.2% requires a correction of at least one percent. Of course, this leaves still 85.0% of mass almost unadjusted, but nevertheless the impact is quite significant. Furthermore, we see that particles with S -values deviating from 1 are the main contributors of smoothing lengths below $\approx 8kpc$. The normalisation is therefore less necessary for particles which extend over three grid cells in each dimension. (See also the brief discussion about boundary cells earlier in section VI-3.2.)

Figure VI.5 displays the trend of the mass fractions within certain ranges of S -values in the 3D binning similar to figure VI.4 but as a function of resolution. Again, it becomes clear, that lower resolution leads to higher importance of our S -normalisation. Grid sizes below 100^3 are drastically affected. With this specific data set at $1000^3 = 10^9$ cells about 10% of mass is still at least slightly affected by the normalisation. Since there are no drawbacks except for a slightly increased computational cost we can conclude that it is always worth to include our modification.

Now, we have a closer look at the distribution of S -normalisation values. With the histogram in figure VI.6 we can directly see the amount of contributions we loose without the re-normalisation. We plot a fine binned S against the mass sitting in each bin up to $S = 2$ and note the amount of mass even beyond that. The left plot is for the full box, the middle one for the central galaxy and the right one for the small satellite. Most particles reside in this range, the ones beyond $S = 2$ are the few particles with very narrow kernel functions with a very high central value which just by chance actually intersect closely with a cell centre. These particles might as well just fall through the grid, if we divide the region slightly differently into grid cells. We see, that the distribution of S -values is quite smooth, increasing towards the unaffected particles ($S = 1$; note that this is only about half of the particles of the central galaxy!) from both sides and for the bigger structures also towards the particles falling through ($S = 0$). We have already shown that, as expected, particles with $S = 0$ have very small smoothing lengths (see figure

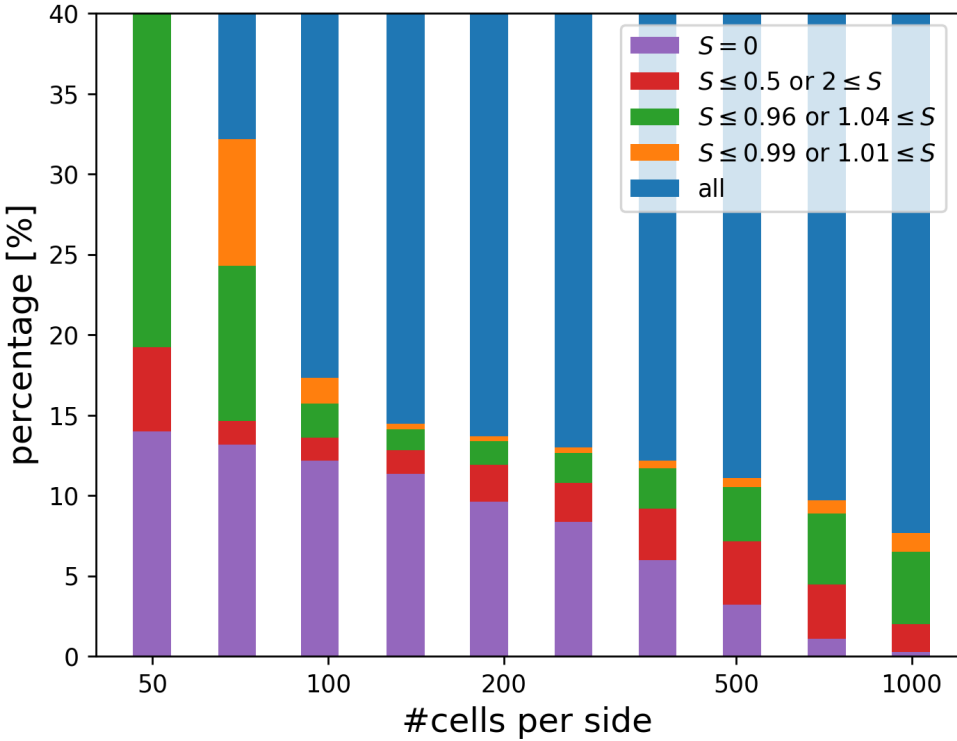


Figure VI.5: Fraction of mass with given S -values as a function of number of cells of the binning. (Cf. also figure VI.4.)

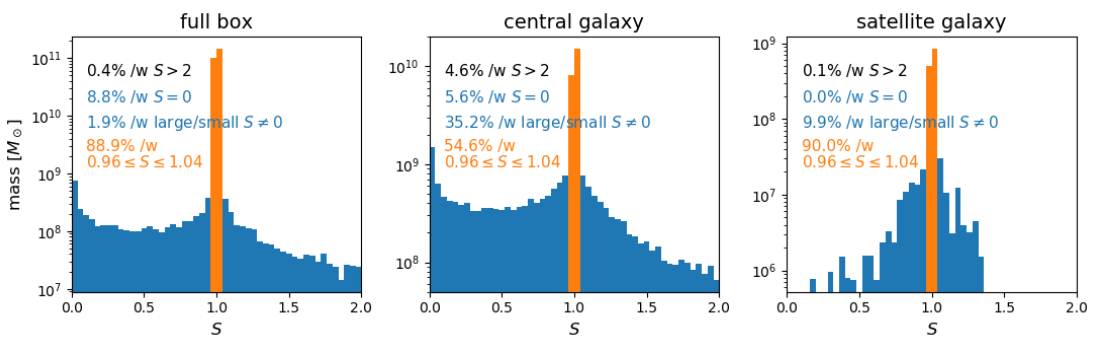


Figure VI.6: The distribution of S -values of the particles contributing to the grids of figure VI.2 (first row, i.e. the fiducial method with 120^3 cells).

VI.4) in comparison to the grid size, which explains why the distribution is much narrower for the satellite galaxy, which is much smaller and therefore the effective resolution is bigger since we keep the number of grid cells fixed. The smoothing lengths of the particles in the satellite range from one to three times the cell size at this resolution.

VI-4.3 Power-spectra

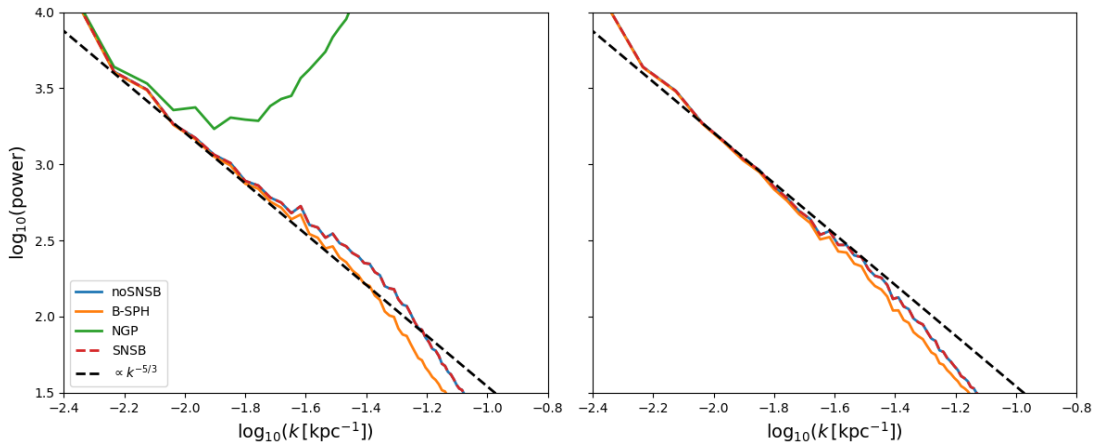


Figure VI.7: Kinetic power spectrum calculated from a 200^3 sized grid for our selected methods (coloured solid lines) including the theoretical Kolmogorov spectrum with a slope of $-5/3$ (black dashed line). The left panel shows spectra from binning as we have presented it until now. The right panel includes an additional normalisation such that a constant field SPH also results in the same constant field on the grid (see section VI-3.2 and Price, 2007).

Finally we use our produced grids for a typical application and calculate the kinetic power spectra for the different methods. The result is shown in figure VI.7. The difference between the left and the right panel is, that on the right we additionally include the unity condition equation VI-14 as presented by Price, 2007. Since the NGP method is not compatible with that, we can only include it in the left plot. We over-plot the theoretical Kolmogorov spectrum with a slope of $-5/3$ to have some indicator on the quality of our results, although we do not expect the simulation data to lie perfectly on top of it. First of all, we see that the NGP method only works on the very large scales (small k) but quickly diverges completely from the relation, showing a great amount of power on the mid range and small scales. This is the effect of the pixelation and graininess we saw in figure VI.2. The classical binning and our modified version produce extremely similar results since both capture features in the structure similarly well. In contrast to them, the approach with broadened kernels is a bit off. The constant broadening plays the biggest role on small scales, where it shows up as an additional smoothing. Thus, small scale variations can vanish and the power on small scales drops. Now, in the left plot the broadened method actually produces a more convincing result but if we include the unity condition normalisation the power on small scales drops for all methods leaving the classical and S -normed binning closer to the expected slope.

VI-5 Analysis packages

In this final section we present two analysis packages which implement most of the discussed mapping methods. Although there exist already some publicly available tools (see for example [Dolag et al., 2005a](#); [Price, 2007](#); [Hummel, 2016](#)), these novel codes include not only our improved map making but also incorporate several features which make them a viable choice for fellow astrophysicists. These cover amongst others typical transformation and selection mechanisms of data, calculating of additional derived SPH quantities, combination with commonly used astrophysical codes like Cloudy ([Ferland et al., 2013](#)) and in situ visualisation. Both tools cover the full range from flexibility and fast visualisation of data to the ability to process huge datasets on a regular desktop computer.

VI-5.1 Pygad

Pygad is a Python module that provides a framework for general analysis of Gadget simulations and the basis for fast and easy development of more specific scripts and programs. It also already provides several specialised sub-modules such as one for generating mock QSO absorption lines. Pygad is publicly available at <https://bitbucket.org/broett/pygad> together with useful data tables and documentation.

The strongest feature of Pygad is that it is designed to put the heavy lifting into the background. Loading a Gadget snapshot regardless the format is a simple call of one function with the file name as single argument. Masking the snapshot to just particles of interest is very straightforward, too, and the resulting sub-snapshot can be used like a regular one in any Pygad function. This masking can be to certain species of particles (e.g. gas and stars only), regions in space (e.g. a friend-of-friend (FoF) halo found by the built-in FoF finder or by Rockstar ([Behroozi, Wechsler, and Wu, 2011](#))), or even a requirement on arbitrary properties using Python syntax (e.g. gas in a certain temperature range and with metallicities larger than solar).

Another handy feature of Pygad we choose to highlight here are the plotting routines. They can plot any quantity, whether it is a regular block in the snapshot or a derived quantity such as stellar luminosities (provided by another module of Pygad) or certain ions (as calculated with Cloudy tables, also provided with the package). These plotting routines build on the mapping procedure presented in this work and automatically print the correct units. The units are carried with all snapshot quantities without noticeable performance penalties.

As any part of Pygad, the plotting routines are kept as general and convenient as possible. And, as with any runtime critical section of Pygad, these routines are written in C++ which are called by the Python frontend in order to ensure a smooth experience. They allow to simply pass a (sub-)snapshot, a region to plot, and the name of a block, or even an Python expression of several blocks that shall be plotted.

All analyses and plots in this work have been done with Pygad as it allows for quick development paired with fast runtime.

VI-5.2 SPHMapper

SPHMapper is an application written in the C++11 standard and basically provides the user with a similar, although currently still more limited usability as does Pygad. With this choice of programming language comes a different approach featuring less interactivity but high applicability to huge data sets and nevertheless high versatility. As computing power grows and simulation data sets become increasingly bigger over time the main requirement for SPHMapper is to be able to handle data sets which cannot be kept in main memory all at once. To approach this issue it features the use of Rambrain (Imgrund and Arth, 2017a), an automatic memory manager which utilises second storage capacity to overextend memory.

SPHMapper is able to do all common Cartesian and radial binning tasks and is straight forward to expand further. Amongst other features, it handles snapshot reading, unit conversions, spatial transformation of the data sets, interaction with Subfind (Springel et al., 2001; Dolag et al., 2009) outputs and selection of particles based on a complete metric in its parameter file. Binning results are visualised and output as preview using hplotlib (<https://github.com/sweetpony/hplotlib>).

SPHMapper is still under development and will be made publicly available under an open source license soon.

VI-6 Conclusion

In this paper we reviewed the importance of a proper understanding of SPH particle data and the difficulties of the transformation into a volume discretised picture. We showed typical approaches to solve these issues and presented a novel modification to the classical SPH binning. Our method calculates the discretised kernel integral on the grid (or a cell-particle volume ratio for particles that fall through the grid) which enables us to bin particles properties such as density in an integral conserving way (in case of density this is mass conserving).

We compared our method with other classically used approaches and analysed the properties of our method using a real simulation data set of a galaxy and its satellite. We find that our method allows us to reduce the relative error in integrated mass down to 10^{-5} even for rather coarse grids where the classical approach is in the percent rage. We proved that our approaches main contribution comes from particles sitting in over-dense regions, where smoothing lengths are small compared to a cell's size. Highly enough resolved grids, however, are often not feasible. In our full data set, particles with a combined mass of a few percent of the total mass are significantly affected by the normalisation and over ten percent of mass is completely lost without the additional treatment of non-intersecting particles. We investigated thoroughly these contributions for different regions of our data and with different grid to particle resolution levels. Furthermore, we presented a technique to handle projection onto 2D maps already before the binning using tabulated integrals, which not only reduces the memory footprint and required computing time drastically but also reduces errors for all methods. Due to one dimension being integrated out more precisely the possibility for particles to jump between hitting a cell centre and not intersecting at all is reduced, granting much smoother convergence with number of cells. As a typical application we calculated the kinetic power spectrum of our data set and explained

the behaviour of the compared techniques. As expected, divergence of the methods' results can be seen best again at small scales. We also included a quick comparison if we further include the unity condition into the analysis, which arises from the requirement that a constant field maps to a constant SPH field.

We further presented two analysis tools, Pygad and SPHMapper, which incorporate the different options for binning and provide many usage features beyond that. We have shown the prowess of the S -normalisation and can strongly suggest to include it into any binning code.

Beyond what we have shown here, improvements can be definitely made by applying adaptive or non regular grids instead of the fixed, Cartesian ones.

Acknowledgements

The authors thank K. Dolag, S. Heigl, C.-Y. Hu, F. Schulze and A. Beck for very useful discussion during the creation of this work.

Chapter VII

Analysing big data: The Rambrain library

A computer would deserve to be called intelligent if it could deceive a human into believing that it was human.

– Alan Turing

In the last chapter we hinted towards upcoming problems with modern simulations: the huge amounts of data that are generated which need to be processed somehow. This does not only affect simulations but also observations of any kind. Computing power has risen to such a great level that it is sometimes easier to redo entire simulations than to store the resulting data somehow. But data need to be also processed and evaluated which requires increasing amounts of memory. We have come to the point where we can not run our analyses on our own computers any more but need to resort to computing centres also for that. In order to tackle the case of data intensive low computing cost operations we have developed the open source C++ library Rambrain, which is featured in this chapter. This chapter is a slightly modified version of the fully referred arxiv version of the corresponding paper ([Imgrund and Arth, 2017b](#)) which has been accepted for publication in the SoftwareX journal in a shortened version ([Imgrund and Arth, 2017a](#)).

VII-0 Abstract

We introduce Rambrain, a user space C++ library that manages memory consumption of data-intense applications. Using Rambrain one can overcommit memory beyond the size of physical memory present in the system. While there exist other more advanced techniques to solve this problem, Rambrain focusses on saving development time by providing a fast, general and easy-to-use solution. Rambrain takes care of temporarily swapping out data to disk and can handle multiples of the physical memory size present. Rambrain is thread-safe, OpenMP and MPI compatible and supports asynchronous I/O. The library is designed to require minimal changes to existing programs and pose only a small overhead.

Nr.	Code metadata description	
C1	Current code version	1.1
C2	Permanent link to code/repository used for this code version	https://github.com/mimgrund/rambrain
C3	Legal Code License	GPL
C4	Code versioning system used	git
C5	Software code languages, tools, and services used	C++, OpenMP, MPI
C6	Compilation requirements, operating environments & dependencies	Linux, libaio
C7	If available Link to developer documentation/manual	http://mimgrund.github.io/rambrain/
C8	Support email for questions	arth@usm.uni-muenchen.de

Table VII.1: Code metadata

VII-1 Introduction

Facing large amounts of data, be it simulations or observation results, many astrophysicists have become part-time software engineers. As the primary target of their work focuses on producing astrophysical results, developing data analysis code is an inevitable obstacle on their way to the actual goal. In the case of the authors this goal is respectively to analyse extensive data sets of pulsar timing information (based on [Imgrund et al., 2015](#)) and to post-process large snapshots of cosmological simulations (see Arth et al. in prep.). While typical software-engineering amounts to serialising given tasks to be executed as quickly as possible, many everyday codes evaluating data or simulation results are written to be run only a few times. In this light, the primary focus of an astrophysicist often lies on saving development time and not execution time.

Writing code that processes large data sets is one of the most time consuming tasks. When developing applications that use large amounts of main memory, a single larger dataset may suffice for the system to run out of memory. The typically chosen solution to this is finding a machine with more main memory. It is obvious that this solution is only temporary when facing growing amounts of data. The sophisticated solution amounts to writing memory management functions in an optimised but specialised way for the problem at hand, so called “out-of-core computing”. This, however, is very (development) time consuming.

Alternatively, one can think of following the typical approach nowadays, which has been made possible by ongoing hardware developments, and solve the memory shortage by parallelising one’s code. In addition to a common computing cluster hardware vendors increase the amount of possibilities by introducing additional components like non-volatile memory (NVRAM) or memory with high bandwidth (MCDRAM). However, the task of parallelising the code remains and is, in general, non trivial to implement since a distributed memory parallelisation, for example using MPI, has to be chosen. Additionally, not every code scales properly. Thus, one might run into the issue of wasting a lot of CPU time, which has to be granted after writing computing proposals, just to fulfil memory requirements.

Therefore, we introduce Rambrain, a library that facilitates quick development of applications in need of large main memory. It is built to easily integrate with existing C++ code on Linux and helps applications to swap out temporarily unneeded data to transparently access multiples of the actual physical memory available on the system.

While there may exist other solutions more specific to the problem at hand showing slightly better performance, we argue that in most situations the flexibility of a fast, reliable and out-of-the-box solution is preferred to a few percent performance gain. In the following, we provide a quick review of other solutions to the problem at hand and discuss in which cases Rambrain might be a superior choice.

VII-2 Common strategies to avoid out-of-memory errors

The most basic strategy to still run an application in a situation of scarce free memory is using native system swapping. Modern operating systems like Linux manage association of physical memory to various processes running at a given moment. As an application developer, you are presented a more or less consecutive virtual memory address space. It is in general not clear whether a chunk of virtual memory, a so called “page”, is residing in a physical main memory location, called a “frame”, at a given time or not. This layer of abstraction facilitates assignment of memory to a process, so that the system can overcommit physical memory and reassign virtual pages to physical frames, when desired. When free frames become scarce, the system writes out currently unused pages to secondary storage (such as hard disks) in order to free frames. When a process tries to access a non-resident page, a page fault is triggered and the page is read in from secondary storage by the memory manager of the system (Ligh et al., 2014, p.20) and if necessary, according frames are freed by writing the occupying pages out beforehand. While this process is efficient under normal operation, the system typically slows down to being unusable when actively consuming nearly all physical memory. Especially when multiple processes compete for the remaining space (a typical situation for a developer working and debugging), the computer is virtually unusable until the memory-intense calculation has finished. How long a system can survive in a usable state might be dependent of the type of secondary storage employed. For example a SSD may keep a system usable for a longer time than a common HDD just because of its higher speed of reading and writing data. Inevitably, the system will be still overwhelmed by the amount of data scheduled for transfer and especially the concurrent requests due to multitasking.

This swapping mechanism is also limited by the available swap space on the secondary storage. While adding more swap space with the system’s on-board mechanisms¹ is possible, it needs super user privileges and reserves the whole swap size on the disk even if it is not used completely. Furthermore, it aggravates the situation when multiple processes are competing for memory, as more and more parts of other programs can be swapped out and need to be swapped in again in order to continue execution.

Using system swapping as a mechanism for overcommitting main memory can also provoke the action of the so called “Out-Of-Memory Killer (OOM-Killer)”. As available memory becomes sparse, the system tries to keep most processes running. In order to free memory for

¹Using the system tools *mkswap/swapon* as root.

other processes, the OOM-Killer will kill one or more processes by assigning a score correlated with importance, memory consumption, execution and idle times of the candidate process. The OOM-Killer thus can abort simulation or analysis at the very last step and protections against it are hard to find (see e.g. [Rodrigues, 2009](#)). The OOM-Killer can by now be controlled a bit finer via the `/proc` file system, but shutting it off for a certain process needs administrator privileges. However, one has to keep in mind that even if one can force the own application to stay alive, the OOM-Killer can simply shut down system processes which may trigger secondary effects on the target process. To the knowledge of the authors, it is not possible to completely turn off the OOM-Killer on every system. This becomes clear when concerning the alternatives in a situation of low RAM. A call to the `sbrk`-family of functions to increase heap size could possibly block indefinitely, locking the process that called for more memory. Unless any other process will free memory or terminate, the next process demanding for more heap memory will block too. The resulting cascade of blocking processes would probably have much worse consequences for system health than killing a specific process based on a reasonable metric.

There exist other global kernel parameters such as kernel 'swappiness' to manipulate kernel swapping behaviour. At first glance, decreasing or increasing the amount of preemptive swap out of idle application's virtual memory to disk sounds like a reasonable strategy to globally keep the system efficiently in function. Tuning this parameter, however, is only useful when the amount of free physical memory is huge compared to the problem at hand. While low values of this parameter will delay starting to swap out considerably, the demand of the main application for more RAM will dominate at some point below the physical memory size.

In addition, such global tweaks have to be applied system wide. While a user space solution like Rambrain can be allied to any system at hand, it requires very good cooperation with system administrators to employ such a behaviour on a managed machine.

The next often mentioned solution to memory and swap management is the `mlock` and `mmap` family of kernel functions.

`mlock` is capable of locking address ranges for kernel swap out and can also advice the kernel to swap in ranges of memory from the swap space. While these functions can be a usable approach for real-time applications that rely on fast memory access, it in no way limits heap growth. Thinking from the perspective of 'freeing physical memory for new calculations', the functions are of very limited use, as one cannot force the operating system to write out data to swap and there is no guarantee that this will affect physical process size at all.

The `mmap`-family of functions is used to seamlessly map disk files to virtual address space. The file can then be manipulated as if it were resident at that virtual address space location. Combined with `mlock` calls, the user is able to finely tune which parts of a file will be resident in physical memory. There even exists an interface that can be used to track which parts of a file currently reside in physical memory. Also, the memory mapped regions are accounted for as cache, thus this memory will be swapped away preferably when system memory becomes low, which reduces the overall memory footprint of the application. However, usage of memory maps for large files effectively can be very complicated, as it may only be reasonable to open certain 'windows' into regions of the file used for swapping and the number of regions is limited by file descriptor limits. Such a more controllable user-space solution is desirable, for example combining the memory mapping system calls with moderate sized swap files on the secondary storage.

Memory mapping techniques are fast because they use the same paging and copy mechanisms such as system swapping, but are subject to stronger limitations than letting the system handle the paging itself.² The consecutive logical address space that is handed over to the process has to be managed by the user. This means that the user has to take care of allocating multiple data structures on top of the space, a mechanism that the new/delete operators deal with in C++, normally. While handling for example a vector of fixed size structures in a memory map is simple, allocating objects of different sizes is highly non-trivial. As the system is responsible for writing out the memory mapped regions to the file on secondary storage, efficient interaction with the kernel when changing the memory-mapped region is challenging when trying to optimise this process for performance. Furthermore, a strategy deciding which contiguous region to swap out is all but clear.

The authors in fact started to write a backend for the actual swapping I/O of Rambrain with memory mapped files. On the long run, it turned out to be much more complicated to synchronize the swapping behaviour of the mapped regions to gain performance without knowing the exact access pattern of the user beforehand and having only a few guarantees from the Linux kernel API. Thus, a perhaps more performant solution to a problem at hand can be implemented using these facilities, but this turns out to be a difficult encounter that will at least lead to complicated memory management code. Rambrain wants to facilitate development of memory-intensive applications and is designed to take the burden of writing exactly such code from the user. In that respect, Rambrain will not beat a custom tailored solution, but coding such a solution is a hard task in its own respect. This renders such a technique possible, but complicates robust implementation and favourable run time behaviour in highly dynamic situations.

Of course, there exist already other solutions to tackle large data structures in memory, such as the STXXL ([Dementiev, Kettner, and Sanders, 2008](#)) that facilitate out-of-core computation providing large standard containers in analogy to the Standard Template Library (STL). While this is a very useful idea, it has still some drawbacks imposed by its specialised approach. Rambrain has built in class support for the full C++ standard in contrast to the limitation to POD-support of the STXXL. Rambrain provides direct access to pointers in memory and thus will pose no overhead over heap allocation once the pointers have been provided. Additionally, objects created with Rambrain can be used in association with normal STL-containers and will be swapped, too. An alternative approach, using parallel virtual file systems is also imaginable (see for example [Tang et al., 2004](#)). However, this kind of approach still leaves the programmer with the burden to write I/O operations himself, even if they may be encapsulated e.g. as a function.

Furthermore, optimising the data flow on this level comes near to developing an out-of-core algorithm for the problem at hand that takes control over all input and output operations manually. Introductory reviews of such algorithms can be found in [Toledo, 1999a](#); [Vitter, 2001](#). Of course one can design a very clever way of handling input and output data to boost performance. This, however, opposes the goal to find a more generic solution that gives the developer moderate control over input and output flow while taking from him the burden of handling the input and output manually. Specialised solutions cover for example n-body codes ([Salmon and Warren, 1997](#)) or linear algebra calculations ([Toledo, 1999b](#); [Reiley and Geijn, 1999](#)).

From the view of the application developer, the situation is very simple: When writing a pro-

²Both the number and size of memory maps are limited by the system.

Listing VII.1: Typical two dimensional field initialisation

```

1 double k_x=1.,k_y=1.;
2 unsigned int x_max=1024, y_max=1024;
3
4 double *arr[x_max];
5 for (int x=0;x<x_max;++x) //allocate rows
6     arr[x] = new double[y_max];
7 for (int x=0;x<x_max;++x){ //initialize field
8     double *line = arr[x];
9     double xx = x / (double) x_max;
10    for (int y=0;y<y_max;++y){
11        double yy = y/(double) y_max;
12        line[y] = sin((xx*k_x+yy*k_y));
13    }
14 }
15 //do something and delete afterwards:
16 for (int x=0;x<x_max;++x)
17     delete arr[x]; //deallocate lines

```

gram the developer knows what data he uses, what he will use next, and what is not needed for longer time. This information is always present directly in the source code. In the next section, we introduce the interface which communicates this information to the library to plan swapping operations.

VII-3 Interfacing Rambrain

In order to manage the storage needs of a C++ application, we are faced with the problem of designing an interface to tell Rambrain, which data is to be managed and when it has to be present. In this chapter we introduce this interface built to require minimal changes of existing code while at the same time providing rich convenience features when possible.

VII-3.1 Basic usage

As a memory manager keeping track of data has some overhead on its own, it is only useful when the data managed is large. Rambrain can manage simple primitives, arrays, whole classes and also supports nesting of managed objects into managed classes. For a start, consider the code in Listing VII.1 that is initialising a two dimensional plane wave field of data type double on heap memory. We allocate an array of pointers to the respective field rows in line 4, allocate the actual rows in line 6, and set up a plane wave over all field values in lines 7 to 14. Some calculations are executed prior to the deallocation of the rows in line 17.

If we assume now that y_{max} and x_{max} take large values, the allocated doubles will consume a non-negligible amount of RAM, passing a gigabyte at roughly 11600^2 elements. Thus, the developer would have to swap out elements if he seeks to avoid system-swapping to occur, to

Listing VII.2: typical two dimensional field initialisation with Rambrain

```

1  double k_x=1.,k_y=1.;
2  unsigned int x_max=1024, y_max=1024;
3
4  managedPtr<double> *arr [x_max];
5  for (int x=0;x<x_max;++x) //allocate rows
6    arr [x] = new managedPtr<double>(y_max);
7  for (int x=0;x<x_max;++x){ //initialize field
8    adhereTo<double> glue(arr [x]);
9    double *line = glue;
10   double xx = x / (double) x_max;
11   for (int y=0;y<y_max;++y){
12     double yy = y/(double) y_max;
13     line [y] = sin ((xx*k_x+yy*k_y));
14   }
15 }
16 //do something and delete afterwards:
17 for (int x=0;x<x_max;++x)
18   delete arr [x]; //deallocate lines

```

ensure that the program does not run out of physical memory. Manual implementation inserts many lines of code when allocating memory and around line 8. Alternatively, the user would write his own memory manager version calling functions to load and unload data. When several objects are needed at once, loading and unloading become the dominant part of the code.

Furthermore the additional lines start to obfuscate algorithmic code structure. The nested `for`-loops as well as the essential initialisation done will be difficult to spot. Minimal changes to this passage of code will allocate the arrays so that Rambrain is aware of them and dynamically loads and unloads the lines if needed, as can be seen in Listing VII.2.

The overall structure is minimally changed. Up to adding line 8 we only wrap data objects. We introduce two template classes here, `managedPtr<>` and `adhereTo<>` to emplace Rambrain. When using Rambrain in a minimal way, these two classes will be the only ones actively referenced by the developer.

The first class, `managedPtr<>`, replaces allocation and deallocation by Rambrain wrappers. This replacement is necessary to hide away the pointer to the actual data in logical memory, as the element may or may not be present when the user dereferences that pointer.

Consequently, we need a way to give back access to the data. This is done by `adhereTo<>` which states its meaning in camel-case: This objects adheres to the data. While the respective `adhereTo<>` object exists according to scoping rules, it is guaranteed that the user can fetch a valid pointer to the data by assigning the `adhereTo<>` object to the pointer, as is done in line 9. In the following, we will also refer to this as “pulling the pointer”.

The scoping relieves the user from the need to explicitly state that the data is no longer used for the moment. While the corresponding `adhereTo<>` object exists, the pointer to the data remains valid. When this “glue” to a `managedPtr<>` is deleted, for example by going out of

scope, the object may be swapped out to disk in order to free space in physical memory for other objects, if needed.

This already concludes what a developer needs to know about Rambrain to write his own code using the library in the most basic fashion.

VII-3.2 Advanced usage

Currently, Rambrain is, amongst others, equipped with the following advanced features that give more detailed control or convenience. The line numbers given refer to the code examples in Listing VII.3. The advanced features show that the interface is both minimalistic and powerful enough to facilitate development with Rambrain.

- **Allocation of simple datatypes.** The user may allocate a single object or multiple objects at once, passing an initial value. Also multidimensional arrays are supported, that will be collapsed to an array of `managedPtr<>`s of the size of the last dimension. (lines 1-4)
- **Class allocation.** Class objects may have nested `managedPtr<>`s which can be swapped out independently of the class object. Rambrain supports parametrised as well as default constructors. Destructors will be called in the correct sequence. Furthermore, the member hierarchy can be tracked. Finally, Rambrain will ensure correct deallocation of the object. As some or all parts of it may have been swapped out, this is a non-trivial task. The code supports array initialisation on classes, too. (lines 6-15)
- **Different kinds of loading stages.** The user may explicitly state whether to load objects immediately or delay actual loading until the first pointer is being pulled from the `adhereTo<>` object. Rambrain can profit from `const`-accessing the data. In case of the object having been swapped out already, the swap file copy is not changed and reused and thus another write-out is not necessary. If the developer requests write access, the object has to be rewritten to the file system for a swap-out. Therefore, when only reading data, using `const`-pointers is highly encouraged as will be seen in section VII-5.4. (lines 17-23)
- **Convenience macros.** When adhering to an object and pulling a pointer should happen in the same slot, we provide convenience macros that create the `adhereTo<>`-object together with pulling a pointer in a single line. For class members this may happen shadowing a parameter. In this case, the resulting code reads as if the class would contain an unmanaged array of the same name. Of course, `const`-versions of these macros exist, too. (lines 25-30)
- **Multithreading options.** When using Rambrain in a single threaded context, Rambrain throws an exception when the user tries to pull pointers referencing more data than the physical memory limit at once. This can be disabled by a function call to enable overcommitment in multithreaded situations. In this case, pulling a pointer that would violate the limits blocks until enough RAM has become available by other threads destroying their `adhereTo<>`s. (line 33). However, this can potentially introduce a deadlock. Take for example a couple of threads that need two pointers each to start their calculation.

Listing VII.3: Advanced features

managedPtr<double> a1; //single element	1
managedPtr<double> a2(5); //array of five elements	2
managedPtr<double> a3(5,1.); //five elements, all set to 1.	3
managedPtr<double,2> a1(5,5,0); //two dim., vals set to 0.	4
	5
class B { public:	6
B(); B(double &a, double &b);	7
~B();	8
void someFunction();	9
managedPtr<double> data; } //Class with ctors/dtor	10
	11
managedPtr b1; //single element, default constructor	12
managedPtr b2(1) //single element, default constructor	13
managedPtr b2(1,a,b); //single element, param. ctor	14
managedPtr b2(5,a,b); //5 elements, parametrised ctor	15
	16
adhereTo<double> glue1(a1); //Load right away	17
adhereTo<double> glue2(a2, false); // Load when used	18
const adhereTo<double> glue3(a3); // Access const	19
	20
double *c1=glue1;	21
double *c2=glue2; //If not present, will be fetched here	22
const double *c3 = glue3;	23
	24
//= adhereTo<double> a1_glue(a1); double* a1data = a1_glue;	25
ADHERETOLOC(double, a1, a1data);	26
	27
void B::someFunction(){	28
ADHERETO(double,data); //shadows member B::data	29
data[0] = 42.; }	30
	31
//MT: Do not fail if too much memory is requested:	32
managedMemory::defaultManager->setOutOfSwapIsFatal(false);	33
//MT: Avoid deadlock when needing multiple data at once:	34
double *c5,*c6;	35
adhereTo<double> c5_glue(a1),c6_glue(a2);	36
{LISTOFINGREDIENTS	37
c5 = c5_glue;	38
c6 = c6_glue; }	39

Assume only half or less of these `managedPtr<>`s fit into RAM. In this case, all or some threads may have requested the first of the needed two pointer in parallel. Since Rambrain cannot free pulled pointers while the respective `adhereTo<>`s in scope exist, it blocks all threads and waits for memory to become available to swap-out. This, however, will never happen, as all threads are waiting and no thread is eventually finishing to unlock data for swapping. To circumvent this situation, the user may use a globally locking scope conveniently provided by Rambrain (lines 37-39). It is however highly encouraged not to over-commit memory also in multi-threaded situations as performance may drop by this forced serialisation.

VII-3.3 Design considerations for user code

Having introduced the basic usage style of the library, let us evaluate the impact of using Rambrain on code design. While the syntax suggests that there would be nothing to keep in mind, a few limits and caveats apply nevertheless.

Maximum problem size

Rambrain's physical memory usage is limited to a certain amount the `managedPtr<>`s may consume.³ As Rambrain cannot use the native OS paging mechanisms, it is bound to the memory limits set by the user. Consequently, the set of currently existing `adhereTo<>`s⁴ marks data as in-use and determines what cannot be swapped out. Additional managed pointers may only consume the remaining free memory. Thus, Rambrain will be unable to manage problems that demand the simultaneous use of more data than this limit. The code has to be written in a way that the maximum simultaneously accessed data amounts to less bytes than the limit. This usually is the case anyway as algorithms are being formulated in a local way on the data.

Data structures

The size of the simultaneously used data structures relates to the way of solving a problem. A matrix operation, for example, can typically be formulated on various matrix representations such as rows, columns, sparse single elements or smaller submatrices. To gain something from managing such a subobject, the user has to take care that the payload per managed pointer is large enough, so that the overhead of managing the data becomes small. We propose allocating smaller structures via traditional mechanisms and leaving the data-intense elements to Rambrain. If however a `managedPtr<>` is chosen, it is vital to keep in mind that this block of data can only be swapped out and in as a whole.

Ideally, all elements of a single requested `managedPtr<>` will be needed in one step of a calculation. If not, Rambrain might end up having to swap in many excess bytes to use just one or two elements. Fortunately enough, the same argument applies for normal CPU cache locality and developers are used to developing for this consecutive, local access scheme. For a review of

³Currently we do not track the overhead imposed by the usage of Rambrain, as well as other heap allocations. This is planned for a future release.

⁴Explicit delayed loading can be emplaced to limit this to the set of `adhereTo<>`s that a pointer was pulled from.

the term locality and further hints please see for example [Denning, 2005](#); [Chellappa, Franchetti, and Püschel, 2008](#). Therefore, existing and highly optimised libraries are perfectly suited to be used together with Rambrain.

VII-4 Architecture and Design

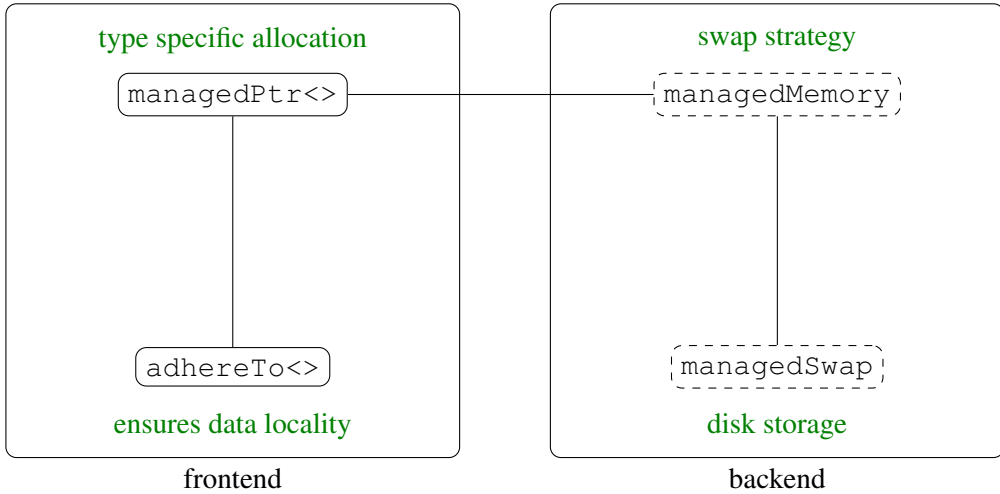


Figure VII.1: **Architecture of Rambrain:** Rambrain is divided into four major classes, each serving a distinct purpose. The classes in dashed boxes are abstract classes.

Having described the interface of Rambrain, let us now describe how Rambrain is internally implemented and what design decisions have been taken to serve the user's data requests. As depicted in figure VII.1, Rambrain is divided into four independent classes. While the user front end is implemented in a standardized way by the two classes `managedPtr<>` and `adhereTo<>`, whose functioning has been described above, the abstract backend classes can be inherited to implement a custom strategy which elements to select for swapping. We currently serve two implementations of these classes each. One amounts to a dummy class that is used for testing purposes. The other implementations, `cyclicManagedMemory` as well as `managedFileSwap`, will be described in the following sections. We provide profound source code documentation for all classes. The documentation can be compiled from source code using doxygen ([Heesch, 2015](#)) or viewed online ([Imgrund and Arth, 2015a](#); [Imgrund and Arth, 2015b](#)) in a daily generated version.

VII-4.1 Swapping Strategy

It is a major design decision which elements to choose for swap-out to secondary storage when facing many currently not used objects. In this section we argue that a generic strategy should be at least capable of handling random access and access in the same order in an efficient way and describe the actual implementation.

When swapping out the same amount of data to media not capable of fast random access, swap-out size and fragmentation factors limit the speed achieved in a practical situation: The throughput per byte to be written/read is reduced when writing small chunks only, as the overhead of managing the transfer both physically and logically will take a greater fraction of execution time of the request. This is especially true when using hard disks as secondary storage: When fragments of the data needed are distributed over larger parts of the disk, the read/write head of the disk has to be positioned differently at every fragment. This process consumes more time than accessing consecutively stored data. While this argument does not apply for modern solid state disks any more, splitting data over multiple locations still poses an overhead as there must exist structures to describe and manage the splitting. Consequently a strategy writing out and reading in larger and consecutive parts at once will in general be faster than a strategy swapping out small chunks.

With no prior knowledge on what access pattern the user will impose on the data we can only

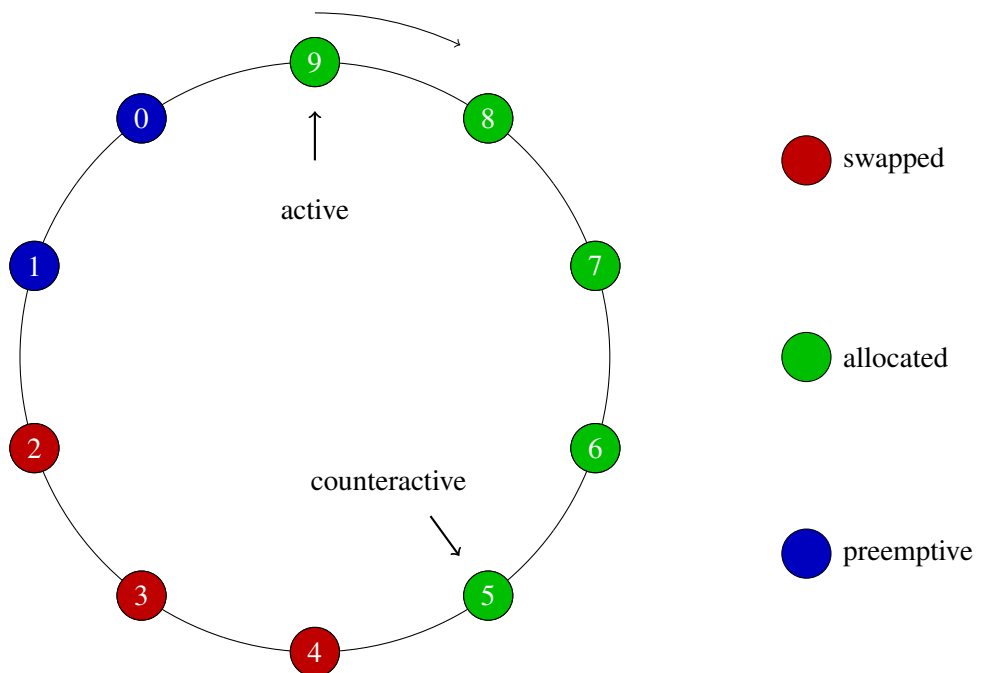


Figure VII.2: **Cyclic managed memory:** Having accessed one element, it is very likely that the former next element will be the next one this time, too. Obeying this ordering, the algorithm will asynchronously pre-fetch “preemptive” elements and swap out allocated but unused elements when necessary.

make general assumptions and search for a strategy which can learn access patterns. The actual pattern encountered will lie somewhere in between the two extremes of a completely ordered and repeated sequence and random access patterns.

The Linux kernel for example tracks ‘page age’ and, when needed, preferably swaps out pages that have not recently been touched by the memory management subsystem. Without further

going into details⁵, this strategy has proven useful to general access patterns encountered on systems which have to swap memory occasionally. In the intended use case of Rambrain, however, the need to swap out data is an all present circumstance. Letting the user state which data is required currently, places Rambrain in a better situation than the kernel memory management is in. Rambrain is being actively told which data is not required any more and there exist hints, which data will be accessed by the application in near future. Thus, Rambrain can much more clearly specify the 'age' and 'ageing' of data in the application's context and also infer what to swap in next.

Thinking of looping over an array of data, which is very common in scientific codes, the most simple strategy is based on the assumption that if one element has been accessed right after the other, it repeatedly may be requested in that sequence in the future. Having accessed all elements, it is most likely that the first element will be accessed again. When there are multiple array objects, this also holds when a subset of objects is under consideration. Even when needing only a subset of all arrays, it is likely that the elements of the array will be accessed in the same order. This assumption suggests a cyclic strategy which we implement in the `cyclicManagedMemory` class and illustrate in figure VII.2. This order is represented as a doubly linked list of element pointers with connected end points.

To organize this as an effective queueing system, the most recently accessed element is marked with a so called "active" pointer and the last still allocated and not swapped out element as "counteractive". The counteractive element is followed by swapped out elements or elements that are in the process of being written to secondary storage. When accessed in an ordered way, we may keep elements in physical memory for as long as possible. The cycle defines a reasonable sequence of swap-out: the elements that have not been accessed for the longest time are the next candidates for swap-out. They are conveniently found by dereferencing the counteractive pointer and moving this pointer backwards as elements are swapped. This will write large chunks of data consecutive into the swap files. When a swapped out element is requested by the user, also the elements that are presumed to be needed next will be loaded preemptively and the elements will be placed in front of the former active element.

In this way, accessing the next element in a local sequence will be very fast as it can have already been loaded and no re-ordering has to be done to the cycle at all. Only the active pointer has to be moved backwards one element to apparently move all active elements one position forward in the cycle. As long as the arrays themselves will be accessed consecutively, local ordering is also preserved by this scheme when interchanging access to various arrays.

VII-4.2 Preemptive element swap-in and decay

It is a non-trivial question to decide the amount of bytes which are to be swapped in preemptively. A preemptively swapped in element will use up free physical space. Thus one has to make sure to not load unneeded elements that would be swapped out again immediately. This could cause major increase of I/O-operations, thereby slowing down the system. It is prevented by tracking the amount of preemptively swapped in bytes. Preemptive swap-in will take place only as long as only a certain number of preemptively loaded bytes or less are present. If a preemptively

⁵The interested reader may consult e.g. [Rusling, 1998](#) or <https://linux-mm.org/>

loaded memory element is accessed by the user, its size will be subtracted from the preemptive budget. If an element has to be swapped in from the swap file, the next elements will be fetched too, until the preemptive budget is filled up again. In this way, random access does not cause additional overhead by swapping in unnecessary bytes as the preemptive budget will always be near its limit and thus no further preemptive elements are swapped in.

This procedure however can lead to a constantly filled up preemptive budget. Imagine that an array A fills the RAM completely before an array B is accessed consecutively. Given that some elements of A have been loaded preemptively, they will never be used while B is accessed. Thus, they effectively block the preemptive budget that would be useful in loading B consecutively. To avoid this situation, Rambrain implements a decay of preemptive elements. The amount of decaying preemptive elements is determined by probabilistic arguments to prevent random access from producing too many useless preemptive bytes in the following way:

The maximum size of the preemptive budget can be used to estimate the probability of hitting a preemptive element at random:⁶

$$P_{\text{preemptive}} \approx L_{\text{preemptive}} / (L_{\text{ram}} + L_{\text{swap}}) \leq L_{\text{preemptive}} / L_{\text{ram}}$$

Where L_{ram} is the maximum physical memory allowed, L_{swap} the amount of occupied swapped out bytes and $L_{\text{preemptive}}$ the size of the preemptive budget. Now, every time an element is not available in RAM, we determine the amount of preemptive elements that have been accessed since the last element had to be swapped in. The probability that these N elements have been accessed randomly consequently can be estimated by $P_{\text{preemptive}}^N$. If this value drops below 1 percent, we let decay twice the amount of the free preemptive budget, but at least one byte. Decaying implies swapping out preemptive elements to make space for new preemptive elements. This typically implies loading at least two elements preemptively, as the preemptive swap-in fraction is by default set to ten percent and this fraction squared equals the significance level assumed above.

VII-4.3 Swap file usage

When loaded into RAM, the data area of a `managedPtr<>` has to be allocated consecutively as pulling a pointer guarantees consecutive layout. On secondary storage devices we may split up the data over various swap file locations. While this is not desirable, it is of use when free swap file location is running out and we want to use smaller left-over chunks from previous deallocations.

Another major difference to managing heap memory, like the memory allocator in the standard libraries that is interfaced by the `new/delete` operator implementations, is that one cannot easily use the free space for the management overhead. This is because the managing structures have to be accessible very fast and would cause considerable latency when resident in secondary storage.

Of course managing the chunks of the swap file in physical memory poses unavoidable overhead. It will limit the amount of managed memory as this overhead grows over the physical size of memory available. At the moment the user has to manage large enough data amounts in one

⁶Assuming equally distributed element sizes which are only a fraction of the preemptive budget.

managedPtr<> to keep this overhead small. While this sounds like reintroducing the problem we sought out to solve, we find a typical memory overhead to be 5 to 10 percent of the amount of allocated structures when the data content is about 1kB. This amounts to being able to manage half a terrabyte of data as if it were in RAM on a 32GB machine. The data would be saved in roughly $5 \cdot 10^8$ managedPtr<>s of this size. It is advisable to switch to higher memory loads per managedPtr<> which reduces the overhead by the according factor, making more space addressable on disk. We plan to pack up objects into larger sets in future versions of the library to further reduce the overhead. It is also planned to monitor the overhead and strictly constrain it to the overall limit in future releases.⁷

Thus, given the task to swap out a managedPtr<>, our standard implementation managedFileSwap checks its list of free chunks of memory in the swap files and tries to find the first free chunk the managedPtr<> fits into. If it fails to find such a chunk, it starts to split the data consecutively over the remaining gaps. If this also fails, it cleans up cached managedPtr<>s produced by const accesses and tries again. If no free space is left, it will simply fail. As this unfortunate case may happen after days of calculation, we also provide a swap policy mechanism that states how the library should react in that case. Policies amount to “fail in case of a full swap”, “ask the user if he wants to assign more swap space” or “automatically extend swap space if free disk space is left to do so”.

VII-4.4 Asynchronous I/O and Direct Memory Access

The main techniques to write out large data sets to secondary storage are Memory Mapping (MM), Direct Memory Access (DMA) and using Asynchronous I/O (AIO) or a mixture of these. We briefly review the different approaches with respect to the task of transferring objects from primary to secondary storage:

- **Memory Mapping:** The memory management unit in control of the virtual address space can be used to seemingly load contents of a whole file into physical memory. The same process used for paging will be utilised to write out or read in missing pieces and let an application use all space at once. When dealing with large files, this technique is very popular, as it is fast (may use DMA internally). However, when files become too big, the memory management unit quickly runs into similar problems to the one encountered with native swapping. A possible fix may be to map only parts of the swap files. In this case, however, one has to control tightly which mappings to close first, as closing will block when the mapped region is not written to disk completely. While there exists kernel hinting, a technique to tell the kernel which pages to write out first, the one-to-one mapping of allocations to the page file poses a bigger obstacle. Optimal decisions where to store certain elements are hard to find in a generic way and one is again limited to consecutive memory allocations. Splitting data would render pulling a pointer to consecutive memory impossible. Furthermore, the advantage of directly mapping allocations to swap file locations quickly can become a problem when the data has to be moved to still use a minimal memory mapped region. We thus quickly deferred using this method. There may be some

⁷This, however, is a non-trivial task as typically the standard memory allocation implementation has the control over the system call extending heap size.

interesting features to it, as automatic pre-fetching might already mimic an early stage of preemptive loading. Cleverly opening and closing such page-file “windows”, however, is hard to handle having no guarantees for future access patterns.

- **Direct Memory Access:** DMA can in principle copy parts of memory directly to secondary storage without routing the data through the CPU. It is fast in both throughput and latency. However, it imposes memory alignment restrictions on both sides and supports only writing chunks of a certain size (typically 512kB for hard disks). Since writing is direct, the action bypasses any buffering by the kernel and thus directly leads to disk access. While this can be advantageous in situations where one writes out many consecutive datasets and implements a write cache on ones own, it typically leads to overhead in our use case. Together with the imposed alignment restrictions, it is not clear how to write an efficient implementation without writing complex scheduling code or having lots of overhead when user objects do not fit into the DMA alignment. DMA, while fast, is very complex to handle in situations where a priori it is not clear what the user requests from Rambrain. Thus the benefits of fast I/O and low CPU impact vanish in light of kernel file system buffering efficiency. There is a long going discussion involving Linus Torvalds who highly discourages the use of DMA by the user (please see [Torvalds, 2002](#)).
- **Asynchronous I/O:** The Linux kernel provides the user with the possibility to asynchronously load and save data to file descriptors. Primary actions are taken only on the file system cache which has gone through a long evolution and is by now a very fast and efficient way to use free physical space without negative effects under high load. Furthermore, DMA or Memory Mapping techniques may be present in the background to bring the cache in sync with the secondary storage. Implementing Asynchronous I/O upon normal buffering implies fast execution and efficient write-out while at the same time being robust to architecture changes. Finally the most efficient way of actually carrying out a certain storage operation may only be found out at system level.

The interested reader may be warned, however, that there currently exist three AIO implementations: kio (Kernel asynchronous I/O), libaio (which is just a C wrapper for the former) and POSIX AIO. The latter is currently implemented as blocking AIO, the former is not guaranteed to be truly asynchronous, as its implementation is file system driver specific. We use a pool of submitting threads using AIO to provide true AIO where possible and simulated AIO otherwise, using the libaio wrapper for the system calls. In this way, I/O operations will be non-blocking and have a low impact on CPU load.

By using asynchronous read and write requests, Rambrain is capable of loading data in the background with small impact on the CPU load. A technique for doing this is to first create the `adhereTo<>-object`, which triggers swapping in of the object. While the asynchronous I/O is swapping in the element, other calculations can be done. When finally pulling the requested pointer, it may already have been copied in in the background. A graphical scheme comparing synchronous and explicit asynchronous requests to Rambrain is available in figure [VII.3](#) and a schematic listing of the code producing this access scheme can be found in Listing [VII.4](#). Putting the highlighted line four after line six would constitute a synchronous version of the code. As the application can already process other

data while fetching in next needed objects, this can effectively hide latency similar to GPU programming techniques or pre-fetching for caches (see e.g. [Callahan, Kennedy, and Porterfield, 1991](#)).

Listing VII.4: Explicit asynchronous access

```

1 managedPtr<double> data(1024),
2           data2(1024);
3 adhereTo<double> glue(data);
4 adhereTo<double> glue2(data2);
5 double* ptr = glue;
6 do_something_on_data(ptr);
7 double* ptr2 = glue2;
8 do_something_on_data2(ptr2);

```

Having chosen AIO for transferring the data to secondary storage, the actual implementation is simple on the interface side but quite demanding on the scheduler side, as the scheduler has to deal with non-complete swap-outs and swap-ins when scheduling further action. As a rule of thumb, it has been found very useful to “double-book” memory in the sense that chunks moving from or to physical memory will demand their size in both budgets. At the same time we also track the amount of memory which will be freed by such actions (and thus can be waited for when needed). When completed, the budget of free memory on the source side will be restored to the correct value and the bytes which were pending before will be subtracted from the pending bytes count. In this way, the scheduler can find the right strategy, given currently pending I/O, and demand a small amount of I/O to satisfy its constraints imposed by user requests.

VII-4.5 Compatibility to multithreading

Multithreading complicates writing the scheduler code a lot since one has to be very careful that the needs of one thread do not interfere with the needs of another thread. Scheduler and swap both are written as one instance shared by all local threads. This design decision was taken as data may be shared among threads and thus needs a common swapping procedure. Copying data between threads however will result in various `managedPtr<>`s for each instance. This does not impose a big memory overhead since only the shallow control structures are possibly present multiple times and not the data themselves. Consequently, passing `managedPtr<>`s and `adhereTo<>`s from one to another thread has to happen thread-safely, as well as access to one `managedPtr<>` from multiple threads. Thread safety in this sense does not mean that one thread has exclusive access to a managed pointer, but that the mechanisms ensuring the availability of the data are written in a way that the object is present if at least one `adhereTo<>` in any thread is present and that the object may be swapped out at destruction of the very last `adhereTo<>` instance.

While reference counting is strongly related to the concept of shared memory parallelisation, a distributed memory setup is much easier described. Since every machine harbours its own memory unit, it instantiates its own management structures, swap and data pointers. Data are then copied between threads via the classical send and receive routines of the employed library, as for example MPI. This poses slightly more overhead than the shared memory case, but also

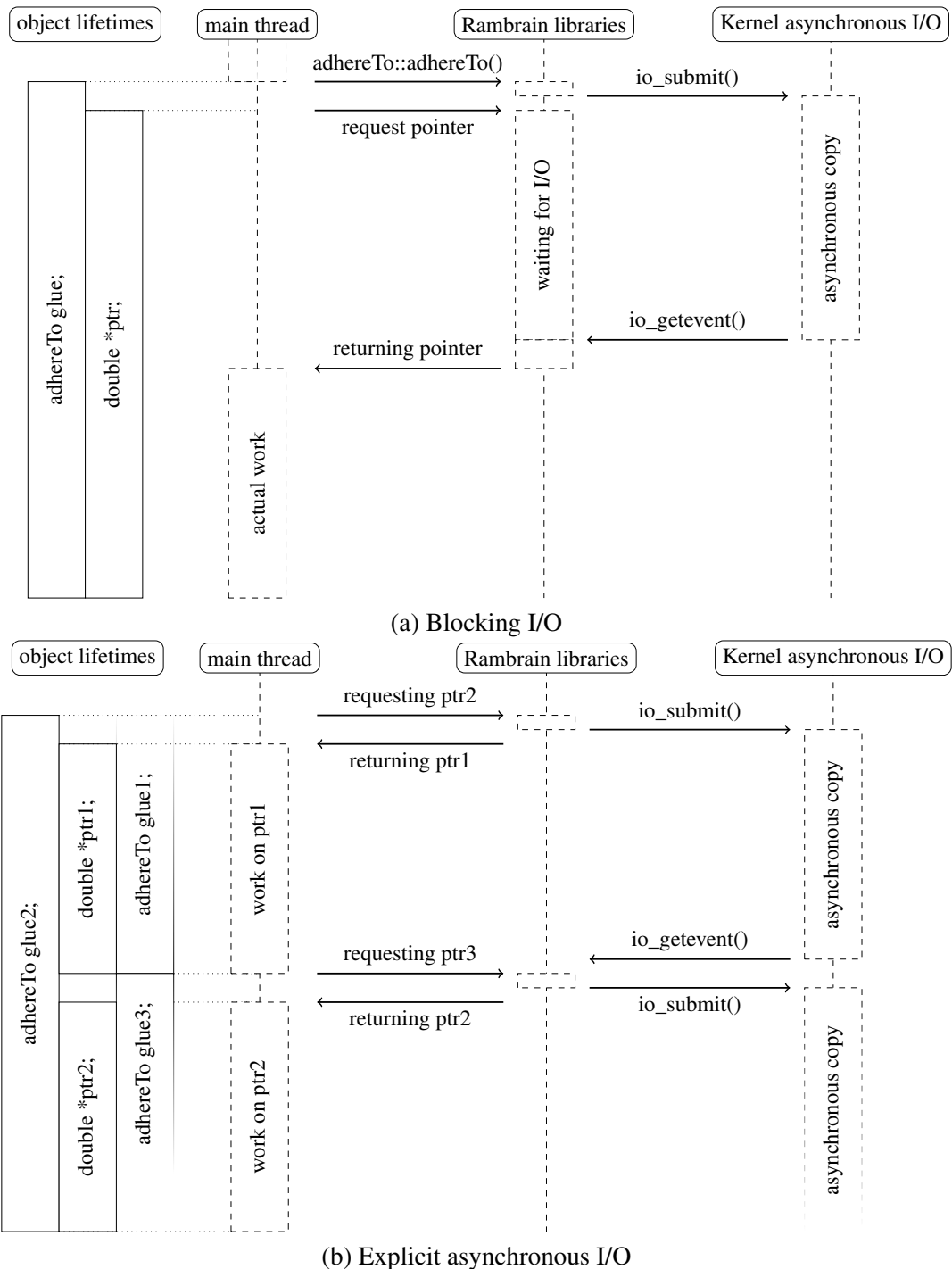


Figure VII.3: **Exemplary interaction of user code with Rambrain library.** Rambrain may be faster when giving clues about upcoming data requirements. While in (a) the time waiting for data to arrive is wasted, the user may use this idle time for calculations on already arrived data, as depicted in (b) and written in Listing VII.4. As preventing idle time is highly desirable, Rambrain tries to behave like case (b) without the user explicitly hardcoding this. In order to do so Rambrain tries to guess the upcoming data demands of the program and automatically pre-fetches elements that will be needed.

provides the ability of a more intelligent access strategy especially if an asynchronous parallelisation model is implemented. One has to keep in mind, however, that if all machines or compute nodes write their swap files to the same disk, they may compete and slow down all I/O, highly dependent on the timing of operations.

In total the amount of memory overhead due to parallelism should be negligible, especially since typical applications are globally memory dominated by the amount of data handled.

VII-5 Results and Discussion

In this section we measure how code which utilises Rambrain compares to a code without Rambrain. Measuring performance is a non-trivial task for technical as well as theoretical reasons. First of all, tests should be reproducible and measure the overhead imposed by Rambrain. However, reaching this goal is non-trivial, as file system operations, kernel Asynchronous I/O or scheduler performance in a multithreaded situation may affect the overall performance as well. Especially the typical use case - a developer seeking to work and debug on the same system - is hard to simulate in a reproducible and meaningful way. Separating library-imposed overhead and I/O performance would be of no use either, as the user is interested in overall performance. Most of the carried out tests however will be highly speeded up by disk caching, which is also found in a productive system. We emphasize that while only RAM-to-RAM copying is done by the OS in these cases, these tests measure best the overhead implied by the workings and logic of the Rambrain library, since once the user is I/O limited, test results will be dominated by hardware performance.

In order to provoke swapping actions we set up a test system finding a PC with the smallest physical RAM module sizes removing all RAM modules up to one. The tests were then carried out using OpenSuse 13.2 (based on kernel 3.16) on an Intel(R) Core(TM)2 Quad CPU Q6700 operating at 2.66GHz on an ASUSTeK P5NT WS mainboard with 32Kb L1 Cache, 4MB L2 Cache and a standard unbranded 2GB memory module. The hard disk used is a Samsung SpinPoint S250.

VII-5.1 Library overhead without swapping

We present the overhead the library imposes on the execution time of a user code in a regime, where actually nothing has to be swapped. This allows to judge whether Rambrain reaches near-native performance and thus can be employed if it is unclear whether it will be needed on the target system. We propose a test in which we perform a rather simple n-body simulation of a fixed set of particles using a Forward-Euler integrator ([Euler, 1768](#)). While each timestep only depends on the last position and velocities of all particles, we save the trajectories and velocities along the way in two dimensional arrays. A typical use case for this is in place visualisation of such a simulation. Therefore, the memory used by the program grows over time, adding two vectors per particle in each iteration. The results of both runs are shown in figure [VII.4](#).

In the beginning of the simulation, when hardly any data is present, we notice quite a big relative overhead of the Rambrain library. However, this only amounts to an absolute difference of only one to two seconds. From a few MB of data on, both curves show the same scaling with

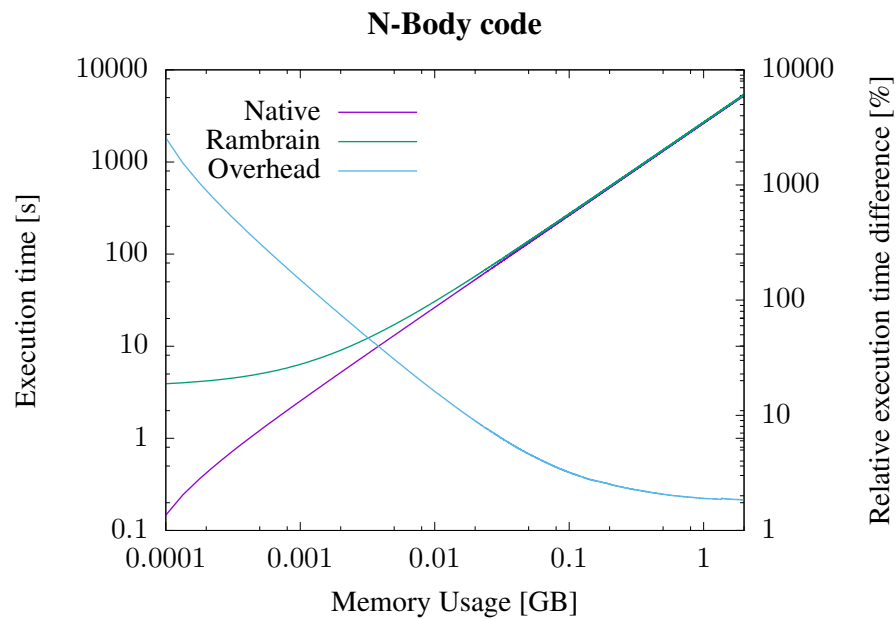


Figure VII.4: **Execution time of a n-body code:** We present timing information from a simple n-body code which accumulates data by saving particle trajectories and velocities. By comparing a version with and without Rambrain we see that the overhead of the library amounts to only a few percent of execution time in the regime of reasonable data sizes.

time, which is given by the algorithm itself. The relative overhead presented by the blue line declines very rapidly and finally converges down to a value between one and two percent close to the two GB mark.

In conclusion, a code utilising Rambrain is always a bit slower in the regime where no data has to be swapped out compared to native code. However, the impact on execution time is not a very big factor and we see no strict need for user to completely switch off Rambrain in this case.

VII-5.2 Matrix operations

In this subsection we demonstrate the internal movement of data for a common problem: Transposing a big matrix which itself does not completely fit in memory. We save matrices block wise, as it is done in many linear algebra libraries (see e.g. [Blackford et al., 2002](#)). This allows for a straight forward migration to a Rambrain version of the algorithm, simply replacing one layer of pointers by a `managedPtr<>` class.

The result is shown in figure VII.5. The left part of the plot shows the data allocation phase.

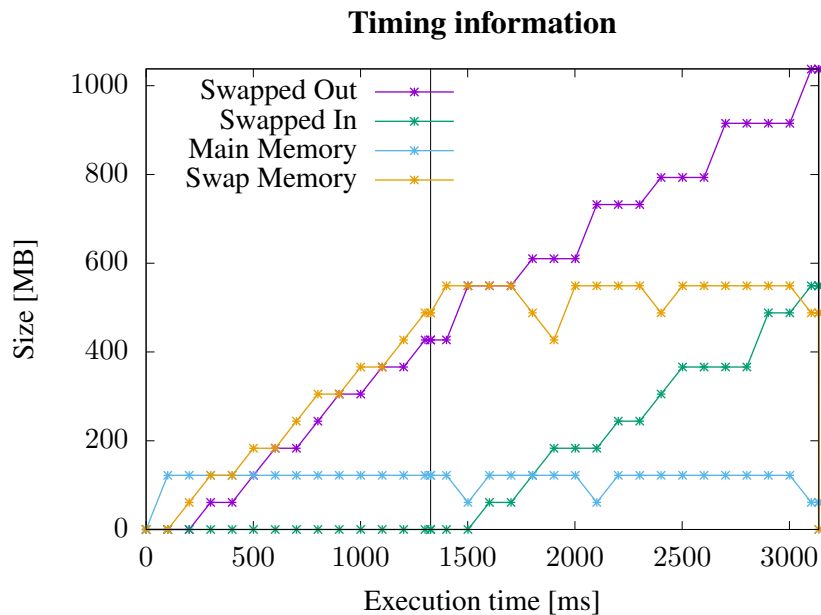


Figure VII.5: **Data movement for one 'Block' algorithm matrix transpose:** We show how data is moved between main memory and swap in one matrix transpose run. The vertical line marks the time point when the execution progresses from data allocation to the actual transposition.

At first the main memory is filled up very quickly with data, then data is consecutively swapped out to make room for more allocations. In the transposition phase afterwards, data is exchanged from swap to memory and back, loading all necessary blocks for the current transposition step. Please note that the asynchronous nature of Rambrain makes it very difficult to measure these values at a few discrete time points, since it is not clear when exactly the AIO events are handled

Listing VII.5: Standard implicitly asynchronous loading

```

1 unsigned int numel = 1024, bytesize;
2 managedPtr<managedPtr<char>> arr ( numel, bytesize );
3 ADHERETOLOC( managedPtr<char>, arr, ptr );
4 float load;
5 float rewritetimes = load / 100.;
6 int iterations = 10230;
7
8 for ( int i = 0; i < iterations; ++i ) {
9     unsigned int use = ( i % numel );
10    //AdhereTo
11    adhereTo<char> glue ( ptr[use] );
12    //Pull the pointer to the object
13    char *loc = glue;
14
15    //Produce some computational load
16    for ( int r = 0; r < rewritetimes * bytesize; r++ ) {
17        loc[r % bytesize] = r * i;
18    }
19 }
```

in the background. Finally, the deletion of data is also plotted in the graph, but happens so fast that it is below the resolution limit of this plot. In total, we see that our design criteria are met and that Rambrain behaves well by constraining the usable memory. Additionally, the approximately linear scaling of the "Swapped Out" curve demonstrates, that the overhead of the library itself is not dependent on the current state of the memory.

The diagnostic output leading to figures like this can be triggered directly in Rambrain, so that the user is able to easily profile the fundamental behaviour of his code.

VII-5.3 Asynchronous I/O and preemptive reading/writing

In this subsection we address the possible speed-up in execution time one can gain by efficiently using the asynchronous nature of Rambrain and the possibility to preemptively load and unload elements automatically.

To measure the performance of this mechanism, we propose the test shown in Listing VII.5. We set up a two dimensional array which is realised by a list of managed pointers. While keeping the first dimension (i.e. the amount of one dimensional arrays) fixed at 1024, we vary the size of the underlying arrays (second dimension, *bytesize*). In order to measure the speed-up by asynchronism and preemptive actions we need to give the library some time to work in the background. Therefore, as in a typical use case, we iterate over the arrays in consecutive order and write the result of a simple integer multiplication into the respective array. We vary the percentage of the array that data is written to (*load*) and data chunk size, simulating an arbitrary computational load that scales with the data. The results of this test are presented in figure VII.6.

It is clearly observable that the execution time decreases due to preemptive strategy. Increasing

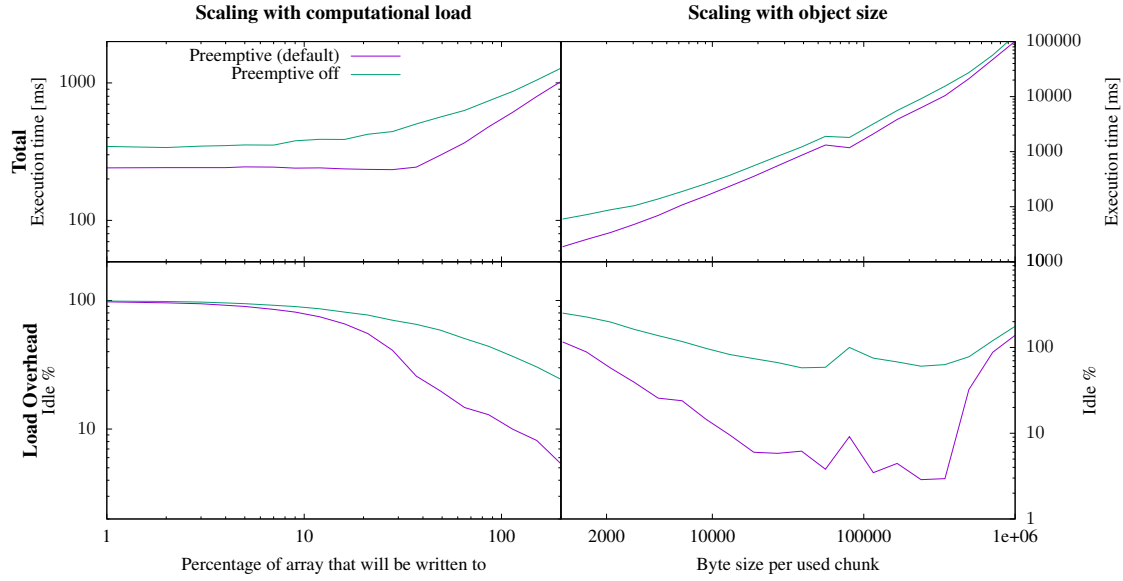


Figure VII.6: **Preemptive loading:** We compare enabled and disabled preemptive mechanism of Rambrain and find that the preemptive behaviour of Rambrain results in a significant performance boost.

the work which is done on the data in the left plot, the library's overhead is already masked at a few tens of percent of touched array elements. Working on the file buffer cache only, this test shows the minimal overhead of the Rambrain libraries. In a real use case scenario, the required computational load to completely mask swapping is increased. This result clearly encourages the user to leave the standard behaviour of preemptive support enabled whenever possible. Even if the data access is completely random, it does not imply a big performance drawback to try to be preemptive. Of course a problem-specific approach pre-fetching exactly the next needed elements without guessing can improve performance here. However, this strongly violates our assumption, that we value development time over execution time. We therefore argue that this optimisation leads towards developing a customized out-of-core algorithm, something no generic memory manager can substitute for. Be aware however, that when disk bandwidth becomes the limiting factor, only part of the swap in/out procedure can be masked by preemptive swap-in. For this reason, the overhead loading the data can become dominant when limited by the disk process and not carrying out enough calculations. While the preemptive strategy is still faster than not using the calculation time for loading in the next needed data in the background, the loading overhead in percent assimilates in the bandwidth-limited case. This can be seen in the lower right panel of the figure, as preemptive and non-preemptive strategies assimilate when disk-caching is not sufficient any more and write-outs to secondary storage dominate the timing.

VII-5.4 Constant vs Non-Constant

Our next test is designed to examine how much time is saved by properly pulling `const` pointers when possible. As outlined in section VII-3.2 it is possible to request a pointer to constant data

from an `adhereTo<>` object instead of a pointer to mutable data. This should be done in general, see e.g. [Meyers, 2012](#), but is of special importance to the case of Rambrain. Not following this best practise will leave Rambrain with no clue on whether the data has been modified and forcing Rambrain to write the data out to the swap again. Hence, if the data has already a representation in the swap and is addressed as constant, this copy is kept as long as the swap has enough free space. When the in-memory copy of the data pointer is later deleted and a swap-out occurs, the data needs not to be written out again, saving expensive writing operations. In order to test this mechanism we allocate two blocks of data consisting of an array of smaller data chunks. The first one we call the real data while the second one is the dummy data which we will adhere to and pull a pointer from to ensure the real data being swapped out due to memory restrictions. Afterwards we access the real data and the dummy data in alternating sequence, once swapping in the data `const` and once non-`const`. We measure the time it takes to swap in the dummy data in both cases, ergo capturing the time it takes to also swap out the real data. We present the resulting behaviour for different sizes of data blocks in figure [VII.7](#).

We notice that the change in execution time by `const`-access obviously scales with the amount of data, since it is highly dependent on the time it takes to complete the swap-out. In the regime of a data block amounting to between one and ten megabytes, we decrease the execution time of the relevant code sections by about 20 to 30 percent. Since these are relatively small data sizes in comparison to the main memory, we can assume that these data swap-outs are completely handled by the disk cache. Therefore we save only the time for cache management and basically a memory copy. When we enter the regime of secondary storage I/O we can expect the difference in execution time to be even larger since the secondary storage itself is much slower than the main memory. For most storage types, storing data takes longer than reading data, thus we expect this mechanism to save even more time in this case. It is strongly advised to use `const`-access whenever possible, also in light of other caches' properties and optimisations being used by the compiler.

VII-5.5 Comparison with native OS swapping

Finally, let us compare the performance of Rambrain and system swapping. In principle, a local administrator can equip a Linux system with more swap space than usual by creating additional swap files or partitions with the system command `mkswap` and enable them for use with the command `swapon`. However, please note that it is not possible to do so as a normal user. Additionally, this approach requires the allocation of the whole swap file space on secondary storage already in the beginning - regardless of how much of it will be actually used. Using this technique we create and enable a 10GB swap file on the described test machine.

We compare a code which uses Rambrain to a non-managed code utilising system swapping. We carry out two different runs: In the first one, data is written consecutively to an 8GB sized matrix. In the second one, the application randomly writes to elements of this matrix. In the latter test we explicitly disabled the preemptive swapping algorithm.

On some attempts to run unmanaged, the native application is killed by the OOM-killer. This probably happens due to the fast growth of heap memory. Also having a swap file which is not at least about 25 percent bigger than the actual swapped size often provokes the OOM-killer to terminate the process. Even if the OOM-killer does not kill the test process, it may be that it

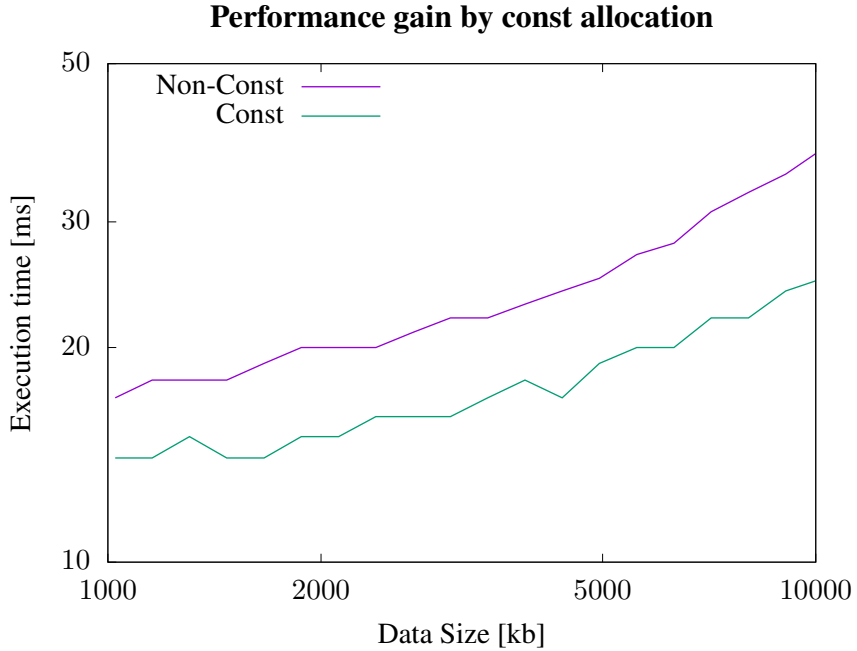


Figure VII.7: **Speed-up by pulling const pointers:** We run a simple test where data is drawn once as constant and once as writeable pointers and compare the time it takes to swap out the data afterwards in a regime where all the data still fits in the disk cache.

may shut down other processes in the background to free memory for the test process. When the attempts succeed, the system is virtually unusable as even opening another shell prompt takes minutes. Furthermore, the interference of the native code with the system does not stop when the application exits, but leaves the system in a slowly reacting state for minutes to hours of usage, as large parts of other applications and system processes have been swapped out to disk. We expect that running other applications such as an integrated development environment in parallel will aggravate the situation when trying to solve the problem using OS swapping. But also the actual execution time of Rambrain-managed code is favouring the use of our library. In the case of consecutive access, the version using Rambrain is about 10 percent faster than the native version. In case of random access, Rambrain is only 2% faster than the native code, if we obey the design limitation that all elements of a single `managedPtr<>` will be accessed. This test result is further confirmed by daily experience of the authors being able to develop code on the same machine their analysis software runs in parallel without being disturbed by the process which uses Rambrain.

VII-5.6 Real world application: Difference imaging

To demonstrate that Rambrain is actually applicable to a real world problem, we choose a memory intensive difference imaging algorithm. The algorithm is designed to find variable light sources by comparison of multiple images. To mitigate errors due to noise these have to be

convolved with a kernel first, before being subtracted from each other. For best accuracy, a variable point-spread function with a high number of free parameters is chosen as a kernel and an optimal version is computed by a minimisation technique. [Alard, 2000](#) show that best results can be achieved by choosing one global kernel for the whole image. While this may seem to be the best approach anyway, we want to emphasize that usually only local kernels can be used because of the vast amount of memory consumption that arises in case of high resolution image material. This applies for example for the difference imaging code presented by [Goessl and Riffeser, 2002](#) into which we embed Rambrain in order to overcome exactly these limitations set by main memory.

High resolution images taken with state of the art instruments (see for example [Lee et al., 2012](#); [Lee et al., 2015](#)) can easily be of about 14000^2 pixels in size, each. Typically kernels with several hundreds of free parameters are used which lead to an exemplary memory consumption by kernel matrices of

$$\text{ImageSize} \cdot \text{KernelSize} \cdot (\text{Values} + \text{Errors}) \cdot \text{float} = 14000^2 \cdot 400 \cdot 2 \cdot 4B \approx 600GB.$$

This exceeds the physical size of main memory of a typical PC while the CPU time needed for such an analysis amounts to only a few hundred CPU hours.

In figure VII.8 we present the results of such an analysis using simulated data. We assess the

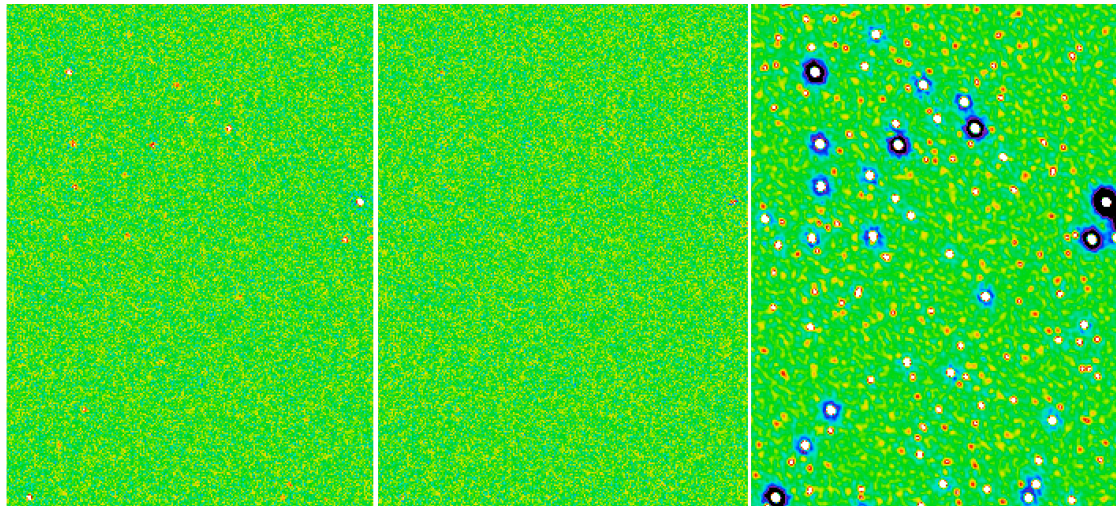


Figure VII.8: **Difference imaging residual:** Left: Multiple local kernels; Middle: Global kernel with Rambrain; Right: Difference of both images.

quality of the achieved fit by folding the reconstructed signal with the kernel and subtracting this from the input. If the kernel that has been constructed by the method reproduces the point spread function very well, the signal should vanish completely and only noise should remain. The left panel presents the result with a local kernel, where the image has been subdivided into several parts in order to fit into memory. The still present starlike features indicate that the kernel does not fit as well as in the middle image. This panel shows the global kernel in combination with Rambrain and the right one displays the differences between those two. One can clearly see, that

it does not only make a difference to use a global kernel, but being able to use this kind of global algorithm on the data leads to a result that contains a larger fraction of the signal of variable light sources in the sky.

With Rambrain's capabilities to extend memory up to disk limitations, even more advanced algorithms can be applied without the typical memory restrictions. [Barris et al., 2005](#) for example propose to use all unique pairs of images of a given set in order to calculate a yet more elaborate kernel. Memory management for this task can be delegated to a library suited, such as Rambrain is. For further scientific analysis of actual observational images we refer to the upcoming paper of Riffeser et al. in prep.

VII-6 Conclusions And Outlook

We introduced the reader to writing code that utilises the Rambrain library. We described in detail why the proposed interface is sufficient to consistently handle data swap-out automatically and leads to satisfactory performance. We have demonstrated that the outlined mechanisms not only work properly, but also outperform naive approaches to mimic their strategy. Of course the library cannot compete with a fully specialized out-of-core algorithm, but can save a lot of development time in providing automatic facilities for large data sets. The library handles asynchronous transfer of data which provides latency hiding of disk I/O operations and reduces idle times to a few percent if computational load allows. Furthermore, we have shown that the memory and CPU overhead of the library are both in the acceptable regime of only several percent. As all of this is provided by minimal user-side interaction, we feel the goal of writing a memory manager that enables the user to transparently access multiples of the physical memory to be fulfilled. As memory management is a short-cut to just stating what data is currently needed, the user can focus on the main goals of his application at the price of only a small overhead.

We demonstrated the actual usage of our library via the example of difference imaging in astrophysics. However, the opportunities where such data intense problems rise to the surface of scientific work are vast and growing in numbers.

The interested reader may find the code released as open source project ([Imgrund and Arth, 2015b](#)) accompanied by extensive further documentation, a list of the small set of prerequisites, notes about the (also system-wide) configuration options, a complete list of features and code examples. Interesting features are planned for future releases, such as direct mapping of file content to `managedPtr<>`'s so that loading the data beforehand is not necessary any more.

While currently the usage of Rambrain is only shown natively in other C++ codes, it is possible to interface and call the relevant functions also from codes written in different programming languages such as Fortran or Python. The library might lose some of its elegance regarding the usage of strict scoping in C++, however we expect it to be fully functional when interfaced correctly. Writing such interfaces in proper manor is also part of future plans. Since the code is open source and available on github, the interested reader is happily invited to collaborate and assist in the development of such future features.

Carrying out over 100 automatic tests partly consisting of random interaction with the library on every development step and keeping track of performance has proven very useful to find bugs which only occur under rare circumstances e.g. in multithreaded situations and improved ro-

bustness of the code a lot.

We feel this library to be ready for use by a more general scientific audience.

VII-7 Acknowledgements

We thank Karsten Wiesner and Christian Storm for helpful comments on presentation of advanced topics in this paper. We thank Arno Riffeser for working together with us on implementing and evaluating Rambrain in his difference imaging code. We thank Susanna Maurer for helping us organising a workshop on Rambrain at LMU. We also thank the anonymous reviewers and our colleague Stefan Heigl, who helped to improve the overall quality of the paper and provided suggestions to complete the argumentation. Additionally we thank all others who helped us to find bugs in the actual implementation.

Chapter VIII

Anisotropic thermal conduction in SPH: Influence of magnetic fields

We can only see a short distance ahead, but we can see plenty there that needs to be done.

– Alan Turing

Having outlined all the important aspects around our code, we can progress into the astrophysical applications. In chapter I we introduced the long going discussions about cooling flows in galaxy clusters and the search for a mechanism to balance cooling losses effectively. The effect we want to investigate in depth in this chapter is thermal conduction in the presence of magnetic fields. As we have shown that the ICM exists in a hot plasma state (see chapter II) and know, that thermal conduction is based on Coulomb collisions of charged particles it is clear, that magnetic fields should play a significant role here. We present a description of the conduction mechanism and an implementation of the discretised SPH equations into GADGET, followed by some standard tests and a discussion of the impact towards the production of (non-) cool-core clusters in simulations (see chapter I). This chapter is strongly based on [Arth et al., 2014](#).

VIII-0 Abstract

We present an implementation of physically motivated thermal conduction including the anisotropic effects of magnetic fields for smoothed particle hydrodynamics (SPH). The diffusion of charged particles and therefore thermal conduction is mainly proceeding parallel to magnetic field lines and suppressed perpendicular to them. We derive an SPH formalism for the anisotropic heat transport and solve the corresponding equations with an implicit conjugate gradient scheme. We discuss several issues of unphysical heat transport in the cases of extreme anisotropies or unmagnetised regions and present possible numerical workarounds.

We implement our algorithm into the GADGET code and study its behaviour in several 3D test cases. In general, we reproduce the analytical solutions of our idealised test problems, and obtain good results in cosmological simulations of galaxy cluster formations. Within galaxy clusters, the anisotropic conduction produces a net heat transport similar to an isotropic Spitzer conduction model with an efficiency of one per cent. Compared to observations, isotropic conduction

with more than 10 per cent of the Spitzer value leads to an oversmoothed temperature distribution within clusters, while the results obtained with anisotropic conduction reproduce observed temperature fluctuations well.

A proper treatment of heat transport is crucial especially in the outskirts of clusters and in high density regions. It's connection to the local dynamical state of the cluster also might contribute to the observed bimodal distribution of (non) cool core clusters. Our new scheme significantly advances the modelling of thermal conduction in numerical simulations and overall gives better results compared to observations.

VIII-1 Introduction

Galaxy clusters are the largest gravitationally bound systems in our Universe. They typically contain hundreds of galaxies and are detected in a broad range of frequencies. In particular, we observe strong X-ray radiation from the hot intra cluster medium (ICM), which is mainly caused by continuous free-free emission of thermal electrons and discrete metal lines. Observations show that clusters contain roughly ten per cent of their total mass in a hot baryonic gas component with temperatures up to several 10^8 K (corresponding to about 15 keV) at typical densities of 10^{-3} cm $^{-3}$.

The state of the ICM and its related physical properties are crucial to investigate and learn about the formation and evolution of galaxy clusters. The gas is partially heated at the virial shock by the gravitational infall and furthermore raised in temperature by shocks within the ICM. Galactic winds driven by the star formation process and feedback of active galactic nuclei (AGN) inject additional kinetic and thermal energy to the hot cluster medium. Radiative processes within the ICM, such as thermal bremsstrahlung or metal lines (Peterson and Fabian, 2006) allow the gas to cool and loose energy. Furthermore, all galaxy cluster are known to host magnetic fields with strengths up to several μ G (Kronberg, 1994; Taylor et al., 2006), which influences the dynamics of the hot plasma. The structure and the amplitude of the cluster magnetic fields guide the propagation of charged particles and contribute to the equation of motion via the Lorentz force. The magnetic field lines are assumed to be highly tangled and twisted on small scales, which then will contribute of the heating of the plasma by magnetic reconnection (e.g. Fabian, 1994). Little is known about the magnetic field structure as its mapping is observationally challenging (Fabian, 2002; Sarazin, 2008; Komarov et al., 2014).

We discuss the influence of the anisotropic magnetic field on plasma transport processes and in particular on thermal conduction. From a microscopic point of view thermal conduction is the heat transport due to collisions of electrons. Therefore, it strongly depends on temperature, which allows us to use probes of the hot ICM to study large-scale transport of heat. From a macroscopic point of view thermal conduction can be modelled as a diffusion process redistributing internal energy. Usually, the so called Spitzer conduction see Spitzer, 1956 is used as a general formulation and multiplied with an efficiency factor, which changes with and depends on the astrophysical environment. This original formulation assumes an isotropic movement of electrons and corresponding distribution of collisions. As galaxy clusters host significantly strong magnetic fields the influence of the magnetic fields onto thermal conduction has to be taken into account. Since particle movement perpendicular to magnetic field lines is restricted,

the assumption of isotropic collisions does not hold any longer and thermal conduction is coupled to the magnetic field topology. This result in different heat transport timescales parallel and perpendicular to the magnetic field. However, the magnetic fields needs to be sufficiently strong to dominate the mean free path (Rechester and Rosenbluth, 1978).

Observational evidence in galaxy clusters of suppressed perpendicular heat transport is found in so called cold fronts, i.e. regions with a rather stable temperature gradient, but no pressure gradient (Owers et al., 2009; Owers, Nulsen, and Couch, 2011). This phenomenon demonstrates the insulation of gas with respect to conduction most probably through magnetic fields (Peterson et al., 2003). Moreover, turbulent magnetic fields also become a very interesting case to study giving rise to different ways to estimate efficiency factors averaging the suppression effect over volume. For example Chandran and Cowley, 1998 proposed that Spitzer conduction should be suppressed by a factor of about 1/300, while Narayan and Medvedev, 2001 claimed that conduction can still be efficient up to 1/5 of the Spitzer value in highly turbulent environments. Recent studies of density and velocity power spectra also suggest a significant amount of conductivity in galaxy clusters. (Gaspari et al., 2014)

Thermal conduction was frequently discussed as a heating source to balance cooling losses in galaxy clusters in order to explain why hot gas is observed despite the cooling times being smaller than the cluster life times. However, the impact of this effect is questioned and even less significant, when the anisotropies of the magnetic field are included. For detailed discussions of this problem we refer to Binney and Cowie, 1981, Bregman and David, 1989, Fabian, 2002, Loeb, 2002, Zakamska and Narayan, 2003, Voigt and Fabian, 2004, Fabian et al., 2006 and Rasia et al., 2015.

In pioneering work, usually a factor of 1/3 is multiplied onto the Spitzer value as a correction for the influence magnetic fields (e.g. Dolag et al. 2004, supported by work presented in Rosner and Tucker 1989). We present a numerical implementation of the anisotropic heat transport equation including the seeding and evolution of magnetic fields applied to cosmological simulations of galaxy clusters.

A solver for anisotropic thermal conduction is already part of several commonly used grid based codes, which solve the equations of magnetohydrodynamics (MHD). For implementation details and cluster simulations see for example Parrish and Stone, 2005, Bogdanović et al., 2009, Avara, Reynolds, and Bogdanović, 2013 (ATHENA code) or Ruszkowski et al., 2011 (FLASH code). Recently Hopkins, 2016 presented the implementation of diffusion equations for the hybrid code GIZMO. However, we present the first implementation of anisotropic thermal conduction into a smoothed particle magnetohydrodynamics (SPMHD) code. In contrast to the Eulerian methods, which discretise the volume, SPH discretises the mass and is commonly used in simulations of structure formation. The Lagrangian nature of SPH ensures the conservation of energy, momentum and angular momentum and allows to resolve large density gradients. For a recent review on the SPH method we refer to Price, 2012b.

In this paper we present simulations performed with the N-body / SPH code GADGET (Springel, Yoshida, and White, 2001; Springel, 2005a) with the non-ideal MHD implementation based on Dolag and Stasyszyn, 2009, Stasyszyn, Dolag, and Beck, 2013 and Bonafede et al., 2011. The SPH code evolves entropy as the thermodynamical variable of choice (Springel and Hernquist, 2002). Additionally, we include several improvements for SPH such as the Wendland kernel

functions (Dehnen and Aly, 2012). More information on some of the SPH improvements can be found in Beck et al., (2016). Our cosmological simulations include sub-grid models for radiative cooling, star formation and supernova feedback as described by Springel and Hernquist, 2003. Furthermore, we employ a supernova seeding scheme for the magnetic field (Beck et al., 2013b) in contrast to previous simulations using uniform initial magnetic fields (e.g. Dolag, Bartelmann, and Lesch, 1999; Beck et al., 2012). Therefore, we start without any initial magnetic field in all of the simulations. Magnetic fields are then frequently seeded (i.e. injected) during the simulation within star-forming regions by supernova events and then further evolved by the MHD equations (Dolag and Stasyszyn, 2009). We use and extend the existing implementation of isotropic thermal conduction by Jubelgas, Springel, and Dolag, 2004 with the conjugate gradient solver described in Petkova and Springel, 2009.

The paper is structured as follows. In section VIII-2 we explain the physics behind (anisotropic) thermal conduction, and describe our SPH implementation in section VIII-3. Section VIII-4 presents several test problems before we analyse simulations of galaxy cluster formation in section VIII-5.

VIII-2 Phenomenology of thermal conduction

We start with a brief introduction in the physical properties and concepts of isotropic as well as anisotropic conduction.

VIII-2.1 Review of isotropic thermal conduction

According to Spitzer, 1956 we can write down a conduction heat flux resulting from a temperature gradient using Fourier's law as

$$\vec{Q} = -\kappa \vec{\nabla} T \quad (\text{VIII-1})$$

with the conduction coefficient κ . For an idealized Lorentz gas we can assume Spitzer conductivity, which equals a coefficient of

$$\kappa_{\text{Sp}} = 20 \left(\frac{2}{\pi} \right)^{3/2} \frac{(k_B T_e)^{5/2} k_B}{m_e^{1/2} e^4 Z \ln \Lambda}, \quad (\text{VIII-2})$$

with Z the average proton number of the plasma, the Coulomb logarithm $\ln \Lambda$ and electron temperature T_e , mass m_e and elementary charge e . Most important is the strong dependence of conductivity on the electron temperature. Therefore, we assume that thermal conduction has an important influence mainly on very hot gas, as for example in the central regions of massive galaxy clusters where the plasma reaches temperatures up to about 10⁸K.

In fact, we need to multiply the idealized Spitzer conductivity by an additional factor δ :

$$\kappa = \delta \cdot \kappa_{\text{Sp}}. \quad (\text{VIII-3})$$

This factor has been calculated by Spitzer and Härm, 1953 and is highly dependent on the average proton number of the plasma. $\delta = 0.225$ for a pure proton electron plasma and rises up close to 1 for large values of Z .

Spitzer and Härm, 1953 describe a way to calculate the average proton number by summation over all ions in the plasma. Applying a primordial hydrogen - helium plasma, they find a value of $Z \approx 1.136$. Using the tabulated values in Spitzer, 1956 we obtain a factor of $\delta \approx 0.3$.

When used for cosmological simulations one often assumes a primordial gas distribution. A typical value for an effective conductivity κ is e.g. given by Sarazin, 1986

$$\kappa = 1.31 \cdot n_e \lambda_e k_B \left(\frac{k_B T_e}{m_e} \right)^{1/2}, \quad (\text{VIII-4})$$

or

$$\kappa = 4.6 \cdot 10^{13} \left(\frac{T_e}{10^8 K} \right)^{5/2} \frac{40}{\ln \Lambda} \frac{\text{erg}}{\text{s cm K}} \quad (\text{VIII-5})$$

with the electron number density n_e and the mean free path of the electrons λ_e . Because of the inverse dependence on mass we infer that electrons give a much stronger contribution to heat conduction than protons. This is reasonable since lighter particles have higher thermal velocities at a fixed temperature and can be accelerated much easier. Therefore, the amount of collisions in a given time span are drastically increased for low mass particles. Consequently, only electrons are considered in the calculation and we omit the index e in our equations hereafter.

We neglect any dependency of the Coulomb logarithm on temperature and electron density and use $\ln \Lambda = 37.8$, which is a fairly good approximation for typical plasmas in our study. More precise calculations for different collision events (e.g. electron-electron or electron-proton) can be found for example in Huba, 2011. What remains is the strong dependence on temperature to the power of 5/2.

Furthermore, we need to apply an important correction. So far we assumed, that the typical length scale of the temperature gradient $l_T = T / |\vec{\nabla} T|$ is always much larger than the mean free path. However, for very low density plasmas one cannot expect a high conductivity even if the temperature rises a lot, since scatterings and therefore energy transfer events happen only at a very low rate. Cowie and McKee, 1977 have calculated the saturated heat flux for this case as

$$Q_{\text{sat}} = 0.4 n_e k_B T \left(\frac{2 k_B T}{\pi m} \right)^{1/2}. \quad (\text{VIII-6})$$

Interpolating between these findings and the common Spitzer conduction coefficient we estimate a corrected heat flux as

$$Q_{\text{tot}} = - \frac{\kappa \cdot T}{l_T + 4.2 \lambda} \frac{\vec{\nabla} T}{|\vec{\nabla} T|}. \quad (\text{VIII-7})$$

Alternatively, we can redefine the conduction coefficient as

$$\kappa = \frac{\kappa_{\text{Sp}}}{1 + 4.2 \lambda / l_T}. \quad (\text{VIII-8})$$

This modified Spitzer conduction is applicable to galaxy clusters and giant elliptical galaxies if magnetic fields are not taken into account. For a detailed discussion we refer to Rosner and Tucker, 1989.

Finally, we can write the effect of thermal conduction as a change of specific internal energy

$$\frac{du}{dt} = -\frac{1}{\rho} \vec{\nabla} \cdot \vec{Q} = \frac{1}{\rho} \vec{\nabla} \cdot (\kappa \vec{\nabla} T), \quad (\text{VIII-9})$$

which depends on the density ρ and on the heat flux directed anti-parallel to the temperature gradient.

VIII-2.2 Description of anisotropic conduction

Next, we add magnetic fields to the picture. As previously mentioned, thermal conduction is based on Coulomb collisions of charged particles. Except these collisions particles are allowed to move freely in the plasma. However, in the presence of magnetic fields the movement perpendicular to the field lines is restricted. The electrons move on spiral trajectories around the field lines. The frequency of the circular motion, which depends on the strength of the magnetic field B , is called Larmor- or gyrofrequency:

$$\omega_g = \frac{eB}{mc}. \quad (\text{VIII-10})$$

To see how this affects the capability of electrons to transport energy, we present some phenomenological ideas and scaling relations on how a general electron diffusion process is affected by magnetic fields, following [Frank-Kamenezki, 1967](#). A detailed derivation and discussion of the plasma physics behind this simplistic approach can be found for example in [Braginskii, 1965](#), who presents three terms of conductive heat flux:

$$Q = -\kappa_{\parallel} \nabla_{\parallel} T - \kappa_{\perp} \nabla_{\perp} T - \kappa_{\Lambda} \hat{B} \times \nabla T \quad (\text{VIII-11})$$

We investigate how the perpendicular term κ_{\perp} scales with the magnetic field strength in the following two subsections and shortly talk about the hall term κ_{Λ} afterwards in section [VIII-2.2](#). Due to the similar microscopic origin we can infer the following relations for diffusion to hold also for thermal conduction. This connection is motivated through some scaling relations starting with the ideal gas law

$$pV = Nk_B T. \quad (\text{VIII-12})$$

Assuming a more or less constant density we infer

$$\vec{\nabla} p \approx nk_B \vec{\nabla} T. \quad (\text{VIII-13})$$

Knowing that the source of a heat flux corresponds to the time evolution of pressure and using equation [VIII-1](#) we obtain

$$\frac{\partial p}{\partial t} \sim \vec{\nabla} \cdot \vec{Q} \rightarrow nk_B \frac{\partial T}{\partial t} \sim \vec{\nabla} \cdot (\kappa \vec{\nabla} T). \quad (\text{VIII-14})$$

Discretising the derivatives by typical length and time scales we get for the conduction coefficient

$$\kappa \sim \frac{l^2}{\tau} \cdot nk_B \sim D \cdot nk_B, \quad (\text{VIII-15})$$

where we can identify the diffusion coefficient D . According to this relation, the two coefficients behave similarly and we can therefore apply the following scaling relations on an implementation of anisotropic thermal conduction.

Coefficient proportional to B^{-2}

At first, we connect the mean free path and collision time via the particle's velocity $\lambda \approx v\tau$. A typical diffusion coefficient of units $cm^2 s^{-1}$ can be defined as

$$D \approx \frac{\lambda^2}{\tau} \approx \lambda v \approx v^2 \tau. \quad (\text{VIII-16})$$

Since particle movement parallel to the magnetic field is not restricted, the diffusion along the field lines should not be affected, which corresponds to $D_{\parallel} = D$.

We assume that motion of particles perpendicular to magnetic field lines is only possible by jumps between cyclotron trajectories, which results in a diffusion coefficient like

$$D_{\perp} \approx \frac{v^2}{\omega_g^2 \tau} \approx \frac{\lambda v}{\omega_g^2 \tau^2}. \quad (\text{VIII-17})$$

Therefore, the relation between the two coefficients is

$$\frac{D_{\perp}}{D_{\parallel}} \approx \frac{1}{\omega_g^2 \tau^2} \propto B^{-2}. \quad (\text{VIII-18})$$

This is however only valid if $\omega_g \tau \gg 1$, ergo if the gyroradius is much smaller than the mean free path. In other words, we need the magnetic field to impose a notable restriction onto the electrons movement. In the regime of $\omega_g \tau \sim 1$ we have to change the relation in order to ensure $D_{\perp} \leq D_{\parallel}$:

$$\frac{D_{\perp}}{D_{\parallel}} \approx \frac{1}{1 + \omega_g^2 \tau^2}. \quad (\text{VIII-19})$$

To evaluate this relation for a given system we require the collision time or the corresponding frequency

$$\frac{1}{\tau} = \nu = \frac{\omega_{pl}}{n \lambda_D^3}, \quad (\text{VIII-20})$$

with the plasma frequency

$$\omega_{pl} = \sqrt{\frac{4\pi n e^2}{m}} \quad (\text{VIII-21})$$

and the Debye length

$$\lambda_D = \sqrt{\frac{k_B T}{4\pi n e^2}}. \quad (\text{VIII-22})$$

Putting these relations together we finally obtain

$$\frac{1}{\omega_g \tau} = \frac{16\pi^2 c e^3 \sqrt{m} n}{(k_B T)^{3/2} B} \approx 10^{-5} \frac{n}{T^{3/2} B} \text{ cm}^3 \text{ K}^{3/2} \text{ G}. \quad (\text{VIII-23})$$

To check the order of magnitude of the fraction of perpendicular and parallel diffusion coefficient, we use typical values for the magnetic field strength, temperature and density in galaxy clusters (see section VIII-1). Equation VIII-19 results in a factor of $D_{\perp}/D_{\parallel} \sim 10^{-28}$ which means that conduction perpendicular to the magnetic field is be typically extremely suppressed in the ICM.

Coefficient proportional to B^{-1}

However, these relations are only phenomenological estimates. Additionally, perpendicular diffusion is overlayed with turbulence transport processes, which are extremely difficult to describe. However, laboratory experiments show, that the scaling with the magnetic field effectively changes from B^{-2} to B^{-1} , which characterises so called Bohm diffusion. ([Guthrie and Wakerling, 1949](#)) According to the calculations above we construct a scaling relation for this kind of behaviour of

$$D_{\perp} \approx \frac{v^2}{\omega_g} \approx \frac{k_B T c}{e B}. \quad (\text{VIII-24})$$

We assume an electrons movement with their thermal speed $v \approx \sqrt{k_B T / m}$ and neglect further influences for example by plasma instabilities. We get in total

$$\frac{D_{\perp}}{D_{\parallel}} \approx \frac{1}{\omega_g \tau}, \quad (\text{VIII-25})$$

which allows a much stronger diffusion orthogonal to the magnetic field lines for typical values. A more detailed analysis with similar results is given for example in [Golant, Zhilinsky, and Sakharov, 1980](#).

For highly tangled magnetic fields [Pistinner and Shaviv, 1996](#) discuss if the coherence length should replace the gyroradius. However, they find that this assumption is wrong. This matches the considerations of [Rosner and Tucker, 1989](#) who present that tangled magnetic fields do not suppress thermal conduction very strongly, despite general believe. Their results state a reduction factor of $\langle \cos \delta\theta \rangle^2$ which is an average over the local angles between magnetic field lines and the temperature gradient. We briefly analyse this behaviour for totally random magnetic field configurations in section [VIII-4.1](#).

Summing up, thermal conduction perpendicular to magnetic fields lines with reasonable field strengths is in general almost totally suppressed. When we come into a regime where we need to apply scaling relations regarding the magnetic fields, the ratio $\kappa_{\perp}/\kappa_{\parallel}$ scales either like B^{-2} or B^{-1} .

Coefficient for the cross product term

Finally we come to the last term of equation [VIII-11](#) which is a bit different then the other two contributions to thermal conduction. So far we have only talked about collisional thermal conduction. As the name states, heat is exchanged microscopically due to collisions of particles. This last term arises however from a different origin, namely the Hall effect. This term handles heat transport in the third spatial direction, perpendicular to both the temperature gradient and the magnetic field. According to [Braginskii, 1965](#) it scales also linear with the magnetic field strength, amounting in a similar description of the coefficient as presented in the previous section. We will not go into further detail here, since we will later show that this term plays no role in our discretisation scheme (see section [VIII-3.3](#)).

VIII-2.3 The anisotropic conduction equation

We finalize our considerations and derive the anisotropic conduction equation. In principle, there are different possible approaches. We briefly repeat the immediate requirements for the resulting scheme:

- Unchanged isotropic conduction if the magnetic field is parallel to the temperature gradient,
- Strong suppression of energy transfer via conduction if the magnetic field is perpendicular to the temperature gradient,
- Scaling of the suppression factor inverse with the magnetic field strength to some power.

A simplistic approach to fulfil the first two requirements, however not the third, can be taken by multiplying the projection of the magnetic field onto the temperature gradient to the conduction coefficient

$$\vec{Q} = -\kappa \frac{\vec{\nabla}T \cdot \vec{B}}{|\vec{\nabla}T \cdot \vec{B}|} \vec{\nabla}T =: -(\kappa \cos \theta) \vec{\nabla}T. \quad (\text{VIII-26})$$

This approach has the advantage that it requires barely any change in the existing numerical scheme presented in [Jubelgas, Springel, and Dolag, 2004](#) and does not cost much additional computation time. It can be regarded as motivation for the 1/3 suppression factor of Spitzer conduction in earlier simulations including only isotropic conduction. However, we have no possibility to introduce a scaling of the suppression dependent on the actual strength of the magnetic field. We therefore would have to assume a sufficiently strong magnetic field, which can not be guaranteed in the whole computational domain at all times. Problems arise especially in combination with a magnetic seeding mechanism when no initial magnetic field is present. Instead we follow a different derivation by splitting up the conduction equation into a part parallel and a part perpendicular to the magnetic field and assign different conduction coefficients to both parts

$$\frac{du}{dt} = \frac{1}{\rho} \vec{\nabla} \cdot \left[\kappa_{\parallel} (\hat{B} \cdot \vec{\nabla}T) \hat{B} + \kappa_{\perp} (\vec{\nabla}T - (\hat{B} \cdot \vec{\nabla}T) \hat{B}) \right]. \quad (\text{VIII-27})$$

With \hat{B} being the normalised magnetic field vector. For the moment we focus only on the collisional terms and come back to the hall term, later.

Please note, that we can easily regain the isotropic equation from this by setting $\kappa_{\parallel} = \kappa_{\perp}$ or $\hat{B} = \vec{0}$. Plugging in the relation between parallel and perpendicular diffusion we derived earlier, it can be seen that all of our requirements are fulfilled.

We reshuffle the terms for better handling.

$$\frac{du}{dt} = \frac{1}{\rho} \vec{\nabla} \cdot \left[(\kappa_{\parallel} - \kappa_{\perp}) (\hat{B} \cdot \vec{\nabla}T) \hat{B} + \kappa_{\perp} \vec{\nabla}T \right] \quad (\text{VIII-28})$$

From section [VIII-2.2](#) we know that within galaxy clusters mainly $\kappa_{\perp} \ll \kappa_{\parallel}$. However, we can not simply neglect the second term along the temperature gradient. Comparing the absolute

values of the two terms we see, that except of $\kappa_{\perp} \ll \kappa_{\parallel}$ the first term contains a $\cos \theta$ which can be arbitrarily small and make both terms comparable in magnitude. If the magnetic field and the energy gradient are almost totally perpendicular, the second term dominates and can not be neglected. For further reference on how exemplary previous work (mostly on galaxy clusters) of the past 15 years has handled the different terms of thermal conduction please see [Ruderman et al., 2000](#); [Dolag et al., 2004](#); [Schekochihin et al., 2008](#); [Rasera and Chandran, 2008](#); [Parrish, Quataert, and Sharma, 2009](#); [Sharma, Parrish, and Quataert, 2010](#); [ZuHone et al., 2013](#); [Suzuki et al., 2013](#); [Komarov et al., 2014](#); [ZuHone et al., 2015](#); [Dubois and Commerçon, 2015](#); [Kannan et al., 2015](#); [Yang and Reynolds, 2015](#).

VIII-3 Numerical implementation

In this section we derive our numerical representation of anisotropic thermal conduction. Before transforming equation [VIII-28](#) into SPH formalism we note that the second term can be handled similar to the isotropic implementation just with a different coefficient. For details we refer to [Jubelgas, Springel, and Dolag, 2004](#). Here we discuss only on the first term.

VIII-3.1 A fully consistent derivation

Initially, the term suggests a split-up of the calculation of temperature gradient and divergence. However, this requires a large amount of additional computation time, since it needs an additional SPH loop, but also leads to further numerical errors due to the effective second kernel derivative introduced (see [Brookshaw 1985](#)). Furthermore, chaining SPH discretisations can introduce strongly growing numerical errors and should be avoided.

Instead, we derive a consistent formulation with only one SPH loop following the example of [Petkova and Springel, 2009](#), who developed an SPH scheme for a similar diffusion equation in radiative transfer. In the following calculations latin indices like i, j and k always denote particles while greek indices like α, β indicate components of tensors.

Before we start discretising the modified conduction equation, we have to find a better estimate for mixed second derivatives. The derivation is at first similar to the one presented by [Jubelgas, Springel, and Dolag, 2004](#), but gets more complicated since we also need mixed derivatives.

Consider an arbitrary quantity Q at x_j which we expand around x_i

$$Q(x_j) \approx Q(x_i) + \vec{\nabla}Q \Big|_{x_i} x_{ij} + \frac{1}{2} \sum_{\alpha\beta} \frac{\partial^2 Q}{\partial x_{\alpha} \partial x_{\beta}} \Big|_{x_i} (x_{ij})_{\alpha} (x_{ij})_{\beta} + \mathcal{O}((x_{ij})^3). \quad (\text{VIII-29})$$

With the distance vector $x_{ij} = x_i - x_j$.

We multiply both sides by $\frac{(x_{ij})_{\gamma}}{|x_{ij}|^2} \frac{\partial W_{ij}}{\partial (x_i)_{\delta}}$ and integrate over $\int d^3 x_j$.

The first order term vanishes due to antisymmetry of the integrand and we solve for the second order term. More detailed calculations are presented in appendix [VIII-A](#). Assuming Q is a second order tensor quantity, we can rewrite the equation to

$$\sum_{\alpha\beta} \frac{\partial^2 (Q_i)_{\alpha\beta}}{\partial x_{\alpha} \partial x_{\beta}} = 2 \int d^3 \vec{x}_j \frac{x_{ij}^{\top} [\tilde{Q}_j - \tilde{Q}_i] \vec{\nabla}_i W_{ij}}{|x_{ij}|^2} \quad (\text{VIII-30})$$

and

$$\sum_{\alpha, \beta} (Q_i)_{\alpha \beta} \frac{\partial^2 T_i}{\partial x_\alpha \partial x_\beta} = 2 \int d^3 \vec{x}_j \frac{x_{ij}^\top \tilde{\mathbf{Q}}_i [T_j - T_i] \vec{\nabla}_i W_{ij}}{|x_{ij}|^2} \quad (\text{VIII-31})$$

with the substituted tensor

$$\tilde{\mathbf{Q}} = \frac{5}{2} \mathbf{Q} - \frac{1}{2} \text{tr}(\mathbf{Q}) \mathbf{1}. \quad (\text{VIII-32})$$

This is a very compact and neat formulation and we use [Jubelgas, Springel, and Dolag, 2004](#) to check this formula for consistency.

Consider $\mathbf{Q} = Q \cdot \mathbf{1}$. Then we get

$$\tilde{\mathbf{Q}} = \frac{5}{2} \cdot Q \cdot \mathbf{1} - \frac{1}{2} \cdot Q \cdot 3 \cdot \mathbf{1} = Q \cdot \mathbf{1} \quad (\text{VIII-33})$$

Putting this into equation [VIII-30](#) or [VIII-31](#) we recover the result which can be obtained for the isotropic implementation, where only non-mixed second derivatives are needed:

$$\sum_{\alpha} \frac{\partial^2 Q_i}{\partial x_\alpha^2} = 2 \int d^3 x_j (Q_j - Q_i) \frac{x_{ij}^\top \cdot \vec{\nabla}_i W_{ij}}{|x_{ij}|^2}. \quad (\text{VIII-34})$$

Before we further analyse the properties of these approximation formulas let us at first review our basic equation.

As previously mentioned we consider only the part of equation [VIII-28](#) parallel to the magnetic field (the first term). The term conducting along the temperature gradient can be handled isotropically, which is described in [Jubelgas, Springel, and Dolag, 2004](#).

We start by writing the equation in component form:

$$\frac{du}{dt} \Big|_{1st} = \frac{1}{\rho} \sum_{\alpha, \beta} \frac{\partial}{\partial x_\alpha} \left[(\kappa_{\parallel} - \kappa_{\perp}) \hat{B}_\alpha \hat{B}_\beta \frac{\partial}{\partial x_\beta} T \right]. \quad (\text{VIII-35})$$

Furthermore, we define the components of a tensor \mathbf{A} as

$$A_{\alpha \beta} := (\kappa_{\parallel} - \kappa_{\perp}) \hat{B}_\alpha \hat{B}_\beta. \quad (\text{VIII-36})$$

Next, we write the equation only in terms of mixed second derivatives:

$$\frac{du}{dt} \Big|_{1st} = \frac{1}{2\rho} \sum_{\alpha, \beta} \left(\frac{\partial^2 A_{\alpha \beta} T}{\partial x_\alpha \partial x_\beta} - T \frac{\partial^2 A_{\alpha \beta}}{\partial x_\alpha \partial x_\beta} + A_{\alpha \beta} \frac{\partial^2 T}{\partial x_\alpha \partial x_\beta} \right). \quad (\text{VIII-37})$$

Now we use equations [VIII-30](#) and [VIII-31](#) to estimate the second derivatives in equation [VIII-37](#). Re-factoring the terms leads to a compact expression for particle i :

$$\frac{du_i}{dt} \Big|_{1st} = \frac{1}{\rho_i} \int d^3 x_j x_{ij}^\top \left[\frac{(\tilde{\mathbf{A}}_j + \tilde{\mathbf{A}}_i) (T_j - T_i)}{|x_{ij}|^2} \right] \vec{\nabla}_i W_{ij}. \quad (\text{VIII-38})$$

Finally, we discretise the integral and rewrite the temperature to specific internal energy:

$$\frac{du_i}{dt} \Big|_{1st} = \frac{\mu(\gamma - 1)}{k_B \cdot \rho_i} \cdot \sum_{j=1}^{N_{ngb}} \frac{m_j}{\rho_j} \cdot x_{ij}^\top \left[\frac{(\tilde{\mathbf{A}}_j + \tilde{\mathbf{A}}_i)(u_j - u_i)}{|x_{ij}|^2} \right] \vec{\nabla}_i W_{ij} \quad (\text{VIII-39})$$

with the mean molecular mass μ and the adiabatic index γ . This equation allows us to calculate the effects of anisotropic conduction without an additional SPH loop.

One convenient property is that we managed to generate the term $(T_j - T_i)$ like in the isotropic conduction case. This ensures only conduction if the temperatures of two particles differ and the sign takes care of the heat flux' direction.

VIII-3.2 Ensuring the 2nd law of thermodynamics

There might still be a problem with this approximative formula. To ensure the correct flow of internal energy from hot to cold (according to the second law of thermodynamics) the tensor $(\tilde{\mathbf{A}}_j + \tilde{\mathbf{A}}_i)$ must be positive definite. However, from the definition of a variable with tilde (equation VIII-32) we see, that this tensor does not necessarily fulfil this condition. For a very anisotropic setup heat flows in the wrong direction. In addition to a violation of classical thermodynamics this can lead to numerical instabilities depending on the solved used (please see section VIII-3.4 for further details). To overcome this problem we have basically three options which are both artificial and therefore might negatively influence onto our discretisation formula in general:

1. Implement a limiter in the code, which checks for non physical heat flows.
2. Check if a configuration leads to wrong flux and prevent anisotropic conduction
3. Change the tensor to a more isotropic version, which is always positive definite.

Flux limiters in a sense that each heat flux is decreased by a certain amount scaling with it's initial amount are hard to judge. There exist several approaches as shown by [Petkova and Springel, 2009](#); [Koerner et al., 2014](#) but usually one has to settle down with an empirically found formulation. It is hard to determine whether a given limiter is the best one for a certain problem. However, we actually already employ a physically motivated limiter in our code: the consideration of a saturated heat flux for low density plasmas given by equation VIII-6. While this does not guarantee us to prevent all non physical heat flux it turns out to do a very good job in our galaxy cluster simulations keeping the convergence of our solver fast and well defined.

The second option seems to be a rather artificial one. We can determine the angle between the temperature gradient and the magnetic field for each SPH particle and clearly detect, whenever heat would flow in the wrong direction. In this case we could either forbid all conduction or simply fall back to the isotropic formulation. Being a mixture of anisotropic and isotropic or even totally suppressed conduction, this kind of algorithm would be extremely hard to control and render any results of cosmological simulations incomprehensible.

[Petkova and Springel, 2009](#) also propose the third option, namely to add an isotropic component to the anisotropic tensor in order to prevent temperature flowing from cold to warm regions. We

already have a pure isotropic component which is however proportional to κ_{\perp} and it is not clear if this is already sufficient.

While the first option is hardly applicable in our tests, we will go on by comparing the *fully anisotropic* formulation with an *isotropised* version in our tests and cluster simulations in the next sections. In order to ensure that option 3 works, we add an artificial isotropic component and replace the tensor $\tilde{\mathbf{A}}$ by

$$\tilde{\mathbf{A}} \rightarrow \alpha \tilde{\mathbf{A}} + \frac{1}{3} (1 - \alpha) \operatorname{tr}(\tilde{\mathbf{A}}) \mathbf{1}. \quad (\text{VIII-40})$$

Calculations carried out by [Petkova and Springel, 2009](#) show that we need to set $\alpha \geq \frac{2}{5}$. We use the minimum value to prevent a large error in the estimate. This leads to $\tilde{\mathbf{A}} \rightarrow \mathbf{A}$, which is computationally very cheap since we have to compute \mathbf{A} for each particle, anyway. We call this formulation the *isotropised* discretisation.

We can check, that \mathbf{A} itself is positive definite by diagonalising it:

$$\operatorname{diag}(\mathbf{A}) \propto \operatorname{diag}(\hat{B} \otimes \hat{B}) = \begin{pmatrix} 0 & 0 & 0 \\ 0 & 0 & 0 \\ 0 & 0 & 1 \end{pmatrix}. \quad (\text{VIII-41})$$

This isotropic term added to the conduction matrix helps to remove non-physical heat flux; however, it does not come straight forward from our derivation of the conduction equation. It is artificially added and presents itself as an offset to the direct derivation. Therefore, we can not expect that this isotropised version of the heat flux equation will still behave exactly as the undiscretised equation dictates. To which degree this adjusted formulation is better or worse than the fully anisotropic description remains to be investigated by the test cases.

Similar problems of non physical heat fluxes arise also in grid code solutions and are not an intrinsic problem of SPH formulations (see e.g. [Sharma and Hammett, 2007](#)).

VIII-3.3 Discretising the hall term

So far we have left out the cross product term of equation [VIII-11](#) in our discretisation. However, this can be easily done in the same fashion as before. By writing the equation component wise we can again define a 3x3 tensor \mathbf{A}_{Λ} :

$$A_{\Lambda \alpha \beta} = \kappa_{\Lambda} \hat{B}_{\gamma} \epsilon_{\alpha \gamma \beta}, \quad (\text{VIII-42})$$

which is then differentiated as equation [VIII-35](#), calculating

$$\frac{\partial}{\partial x_{\alpha}} \left(A_{\Lambda \alpha \beta} \frac{\partial}{\partial x_{\beta}} T \right) \quad (\text{VIII-43})$$

This allows us to follow the same path of the derivation as before.

However, one crucial difference is not to be overlooked: While the matrix \mathbf{A} is symmetric, \mathbf{A}_{Λ} is antisymmetric due to the epsilon tensor in its definition. As we see in equation [VIII-39](#), the matrix is basically multiplied with the position difference vector of two particles from both sides, since the kernel gradient also points in that direction. But, if an antisymmetric matrix is

multiplied by the same vector from both sides, the result is zero. This can be easily shown by changing the order of the terms:

$$\begin{aligned} x_{ij} \mathbf{A}_\Lambda x_{ij} &= x_{ij\alpha} \cdot \kappa_\Lambda \hat{B}_\gamma \epsilon_{\alpha\gamma\beta} \cdot x_{ij\beta} \\ &= -\kappa_\Lambda \cdot x_{ij\alpha} x_{ij\beta} \epsilon_{\alpha\beta\gamma} \cdot \hat{B}_\gamma \\ &= -\kappa_\Lambda (x_{ij} \times x_{ij}) \hat{B} = 0 \end{aligned} \quad (\text{VIII-44})$$

Therefore, the hall term vanishes in our discretisation and in all other discretisations with the same property.

VIII-3.4 Solving the differential equation

Finally, we address the time integration of the resulting equation.

[Jubelgas, Springel, and Dolag, 2004](#) show how to apply a symmetry enforcing finite difference scheme. This is a fairly simple and computationally cheap approach, however, they conclude that a kernel averaging of the temperature is required to suppress the effects of small-scale noise in the temperature distribution. Therefore, an additional SPH loop is required, which greatly increases the computational cost.

In contrast, [Petkova and Springel, 2009](#) considered an implicit integration scheme. That requires again an additional SPH loop but has the advantage of much more accurate results for larger conduction time steps, therefore reducing the computational cost. They chose the so called conjugate gradient (CG) method which we discuss in the following subsection followed by an analysis of a possibly more stable alternative..

The conjugate gradient

The CG solver is basically an algorithm to solve a matrix inversion problem. Instead of fully inverting the matrix, it is also often used as an iterative approximation method with very good convergence properties. In our case such an iterative approach is mandatory, since the matrix we are dealing with is of dimension particle number squared. Inverting this matrix explicitly would consume way to much time to be a viable. Basically the algorithm calculates the direction in which it has to iterate in order to monotonically approach the correct solution with each iteration step being weighted by the residual of the previous one. Such an iterative algorithm requires an initial guess for the solution, for which we plug in the current state of the system. Assuming that thermal conduction only changes energies on small scales within reasonable time steps, this approach results in a fast convergence rate for the algorithm. A detailed discussion of the algorithmic properties is for example given by [Saad, 2003](#).

Due to the advantages in overall computational cost and precision we want to use the conjugate gradient method to solve the anisotropic conduction equation. At first, we need to ensure, that our equation suffices the requirements of the CG solver. To discuss the properties consider the following equation which we want to solve for the vector \vec{x} :

$$\mathbf{C} \cdot \vec{x} = \vec{b}. \quad (\text{VIII-45})$$

For the algorithm to succeed, we place a few constraints on the matrix \mathbf{C} : It needs to be real, symmetric and positive definite. Because the equations do not contain imaginary parts, the first condition is always fulfilled.

Symmetry corresponds to conservation of energy since each matrix entry poses the heat flow between two particles, which should always be fulfilled for an energy transport scheme. If this was not the case self-consistently from the derivation, we would have to symmetrise the result afterwards.¹ We see if this property is fulfilled after writing down the equation explicitly as a matrix inversion problem.

The positive definiteness can be argued as follows: In the continuous limit the matrix becomes diagonal. Positive definite for a symmetric and real matrix means that the eigenvalues are positive. In our case this corresponds to heat being transported only anti-parallel to the temperature gradient following the 2nd law of thermodynamics. We argued about positive definiteness already in section VIII-3.1: The fully anisotropic formulation can violate this condition, which can therefore lead to non-physical heat flows as well as numerical instabilities, since the CG method in principle requires it to be given. The isotropised version is constructed such that it definitely fulfils positive definiteness.

Now we show how to write equation VIII-39 in CG formalism. Discretising the time step using

$$\frac{du_i}{dt} \rightarrow \frac{\Delta u_i}{\Delta t} = \frac{u_i^{n+1} - u_i^n}{\Delta t} \quad (\text{VIII-46})$$

we get for the part along the magnetic field lines

$$u_i^{n+1} = u_i^n + \sum_{j=1}^{N_{ngb}} c_{ij} (u_i^{n+1} - u_j^{n+1}) \quad (\text{VIII-47})$$

with

$$c_{ij} = -\frac{(\gamma-1)\mu}{k_B} \cdot \frac{m_j \Delta t}{\rho_i \rho_j} \cdot \frac{x_{ij}^\top}{|x_{ij}|^2} (\tilde{\mathbf{A}}_i + \tilde{\mathbf{A}}_j) \vec{\nabla}_i W_{ij}. \quad (\text{VIII-48})$$

We can then write this as the matrix equation $\mathbf{C} \cdot \vec{x} = \vec{b}$ with:

- $C_{ij} := \delta_{ij} (1 - \sum_k c_{ik}) + c_{ij}$
- $x_j := u_j^{n+1}$
- $b_i := u_i^n$

Now, we check again if the energy is conserved properly (except for numerical errors). $\tilde{\mathbf{A}}$ and therefore \mathbf{c} and \mathbf{C} are symmetric, which is exactly the property we identified with energy conservation. For the isotropised version we get the same equations just without the tilde above each \mathbf{A} and therefore same argumentation holds.

¹Please note that we would have to consider the real internal energy, hence the equations for u_i derived above have to be multiplied by m_i .

An improved approach: The bi-CGStab

Since it is worrisome that the conjugate gradient solver may be numerically unstable for a non positive definite matrix we also propose a slightly different algorithm: The bi-Conjugate Gradient. Geometrically speaking this solver does not only converge monotonically along one direction given by the gradient as the CG does, but also iterates along a second vector. This ensures that at a saddle point where the gradient can not be determined properly, the algorithm does not simply get stuck before convergence. There exist several flavours of the bi-CG like for example the Conjugate Gradient-Squared ([Sonneveld, 1989](#)) or the bi-Conjugate Gradient Stabilised ([Vorst, 1992](#)).

We propose using the latter algorithm since it poses a very good way around the difficulties with just a few changes required. Since in each iteration two vectors are followed, two matrix-vector multiplications are needed which a priori doubles the computational cost in comparison to the CG. However, the bi-CGStab is supposed to have rather smooth convergence properties (in contrast to other flavours of the biCG) and even uses both operations to increase the convergence rate. In the case of a positive definite matrix it even falls back to the CG, only with two steps in one iteration meaning that bottom line no additional computational cost has been added.

Of course there exist also totally different algorithms to handle the matrix inversion problem, the most popular being probably GMRES ([Saad and Schultz, 1986](#)). However, these are also not guaranteed to perform better with faster convergence and therefore we prefer to use a conjugate gradient style of method in order to maintain the maximum possible backwards compatibility in our code.

Further improvements: preconditioning

Independent of the solver, as long as we treat the problem as a matrix inversion, there exists the possibility to speed up convergence of the iteration by applying a preconditioner to the matrix. Since our matrix contains the particle-particle interaction terms it has a rather sparse pattern, limited by the amount of neighbours. Therefore, we do not save the whole matrix in memory but calculate the elements on demand. Moreover, the sparsity pattern is highly dependent on the particle ordering by the SPH tree. This makes it highly non trivial to find a good preconditioner which always helps to speed up convergence. Since our tests reveal, that convergence is not an issue for us we refrain from implementing a preconditioning matrix here and keep the possibility in mind should the need arise. For more literature on this topic we like to refer to the references given by [Vorst, 1992](#).

VIII-4 Tests for the new code

Next, we carry out several tests for the different implementations. We use rather simple test cases for which we can verify the behaviour analytically, before we apply it to a physically challenging problem like galaxy cluster evolution.

For all of the following tests we use initial conditions with "glass-like" particle distributions. Therefore, we rule out any alignment effects which arise by the definition of a grid. Even if

the test setups could be done in one or two dimensions, we perform all tests in a fully three dimensional set-up.

Furthermore, we run the simulations with gas only and disable any accelerations on the SPH particles which would come from self-gravity or the MHD equations. With this approach, we ensure that hydrodynamical properties like the density and the internal energy are computed correctly in their respective SPH loops, but we evolve only the conduction equation to thoroughly test the behaviour of our implementations. Additionally, we keep the heat flux limiter due off to gain a better understanding of how the code behaves.

We always start by describing a test case and the derivation of an analytic solution. We are only be able to derive an analytic solution for a constant conduction coefficient, which we enforce in our code for the test problems instead of using Spitzer conduction. Afterwards we show the behaviour of the existing code (i.e. isotropic conduction) with a reference run and further present our results with the new anisotropic approaches (fully anisotropic and isotropised).

Finally, we present a more complicated test, where we allow a temperature dependent Spitzer conduction and check the influence of different prescriptions for perpendicular suppression.

VIII-4.1 Temperature step problem

At first, we reproduce the first test of [Jubelgas, Springel, and Dolag, 2004](#) and slightly modify it, so that we can apply it to the new anisotropic conduction implementation. The basic idea is to set-up a temperature step and let the particles exchange heat. We fix the particle positions (and also the magnetic field, which we add later) and therefore only evolve the conduction equation. Also considering a fixed conduction coefficient instead of Spitzer conduction we can pull the κ out of the divergence and get

$$\frac{du}{dt} = \frac{\kappa}{\rho} \Delta T. \quad (\text{VIII-49})$$

This simplified conduction equation can be solved analytically (depending on the initial conditions) and we compare to the simulation results. We assume a gas with constant density and use

$$u = c_v \cdot T. \quad (\text{VIII-50})$$

with the specific heat capacity c_v . We rewrite equation [VIII-49](#) to

$$\frac{du}{dt} = \alpha \cdot \Delta u \quad (\text{VIII-51})$$

with the so called thermal diffusivity $\alpha = \kappa/c_v\rho = \text{const}$, which is simply a diffusion coefficient, as discussed in section [VIII-2.2](#). For this temperature step problem it is sufficient to solve the equation in one dimension. The more general solution can be inferred later and basically differs only in some pre-factors. Following [Jubelgas, Springel, and Dolag, 2004](#) and [Landau and Lifschitz, 2007](#) this equation can be solved through Fourier transformation. For details please see appendix [VIII-B](#).

We describe the initial internal energy distribution with the following step function:

$$u_0(x') = \begin{cases} u_0 - \frac{\Delta u}{2} & \text{for } x' < x_m \\ u_0 + \frac{\Delta u}{2} & \text{for } x' > x_m. \end{cases} \quad (\text{VIII-52})$$

with x_m being the position of the temperature step, Δu the height and u_0 the mean value. We get in total

$$u(t, x) = u_0 + \frac{\Delta u}{2} \cdot \text{erf} \left(\frac{x - x_m}{2\sqrt{\alpha t}} \right). \quad (\text{VIII-53})$$

At first, we cross check our calculations with the existing implementation of isotropic conduction. The result is shown in figure VIII.1. The SPH particles are directly plotted as black points without any binning or additional smoothing. The result matches well with the analytic solution. Therefore, the existing implementation works even for sudden temperature jumps.

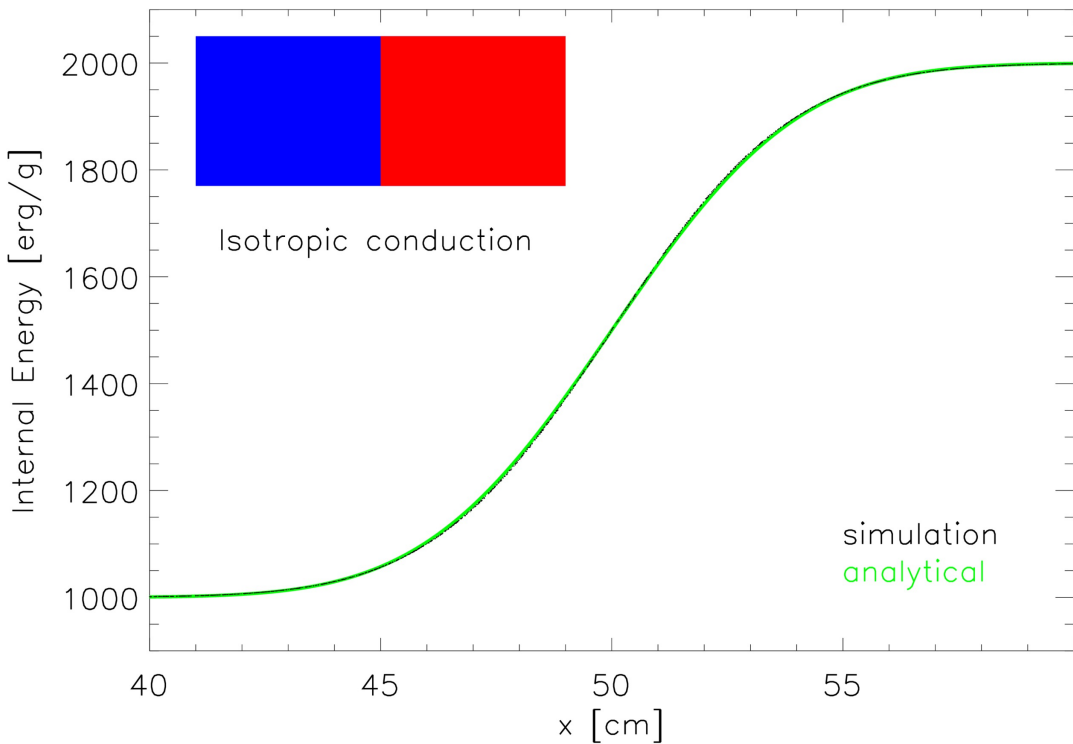


Figure VIII.1: First conduction test: One dimensional temperature step without magnetic field. The green line is the analytical solution (equation VIII-53), the black dots are SPH particles. Both solutions match very well.

Diagonal magnetic field

The next step is to include a magnetic field into the test problem to check the new anisotropic implementation. For simplicity we keep the magnetic field fixed. We introduce a homogeneous field in direction $(x, y, z) = (1/\sqrt{2}, 1/\sqrt{2}, 0)$. Hence, there is an angle of 45° between the \vec{B} -field and the energy gradient, which is in our set-up parallel to the x -axis.

The results of the fully anisotropic conduction version at the same simulation time as before are plotted in figure [VIII.2](#) in the top left box. This implementation reproduces the analytic solution quite well; however, we get more scatter than in the run with isotropic conduction. It is still not yet clear what the origin for this noise exactly is, but for a cosmological simulation this is of less importance, since thermal conduction is not the dominating effect modifying and the scatter is smoothed out. Probably, this formulation does not ensure a positive definite transport matrix, which induces errors into the conjugate gradient solver. However, we see that for a 45° magnetic field we do not need an artificial isotropisation to obtain a stable solution.

The top right panel shows the results using the isotropised formulation. Clearly, we never get the exact analytic result, since the isotropisation is artificially added into the numerics, but our result is close to the real solution. In contrast to the fully anisotropic formulation we get less scatter since the anisotropic part of the equation is mixed with an isotropic component and therefore has a weaker effect. Furthermore, we ensure positive definiteness of the transport matrix which guarantees stability of the algorithm.

Parallel and perpendicular magnetic field

So far we performed all tests with a magnetic field 45° to the temperature gradient. To exclude the arbitrariness of this choice and to study in more detail the different implementations we carry out the tests also with two other setups:

- A magnetic field along the temperature gradient to check if the isotropic case can be recovered with the new code at sufficient accuracy.
- The other extreme case of a magnetic field perpendicular to the temperature gradient to see if the different implementations really recover total suppression of heat flux.

In the middle row of figure [VIII.2](#) we show the results for a parallel magnetic field again for both implementations. The fully anisotropic implementation recovers the analytic solution very well, however, with some noise. The amount of noise is about the same as with a the diagonal magnetic field. Since we have no difference to isotropic conduction in the case of a parallel magnetic field we see, that the noise can not origin from computational instability due to a non positive definite transport matrix. In comparison, we find less scatter but the same expected offset in the isotropised run as before.

In the bottom row we show similar plots for a magnetic field perpendicular to the temperature gradient. From our preconditions we expect no conduction in this case, so the initial conditions should stay constant except for numerical noise.

For the fully anisotropic derivation we find a rather stable solution. However, we encounter the regime, where the anisotropy is strong enough for heat to flow in the wrong direction. What we

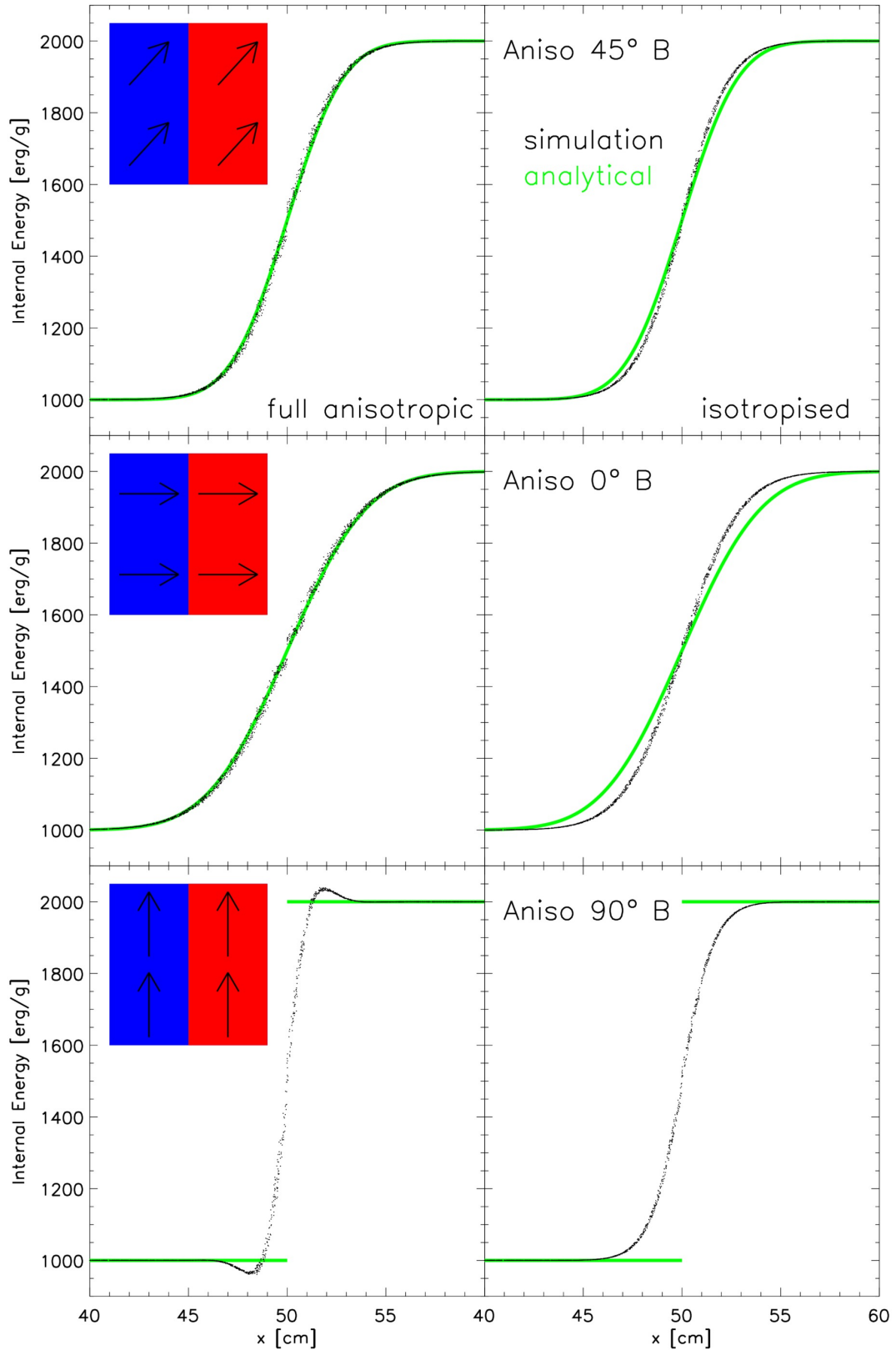


Figure VIII.2: The temperature step problem, simulated with the fully anisotropic implementation left and the isotropised version right for a diagonal (upper row), parallel (middle row) and vertical magnetic field (lower row). All plots are made at the same simulation time.

see here is not a numerical instability, since we eliminated the criterion of positive definiteness by using the advanced bi-CG solver, but rather an effect of the chosen discretisation. We counter that behaviour and implemented the isotropised variation as a possible fix. Please keep in mind that in these tests we did not switch on our saturated heat flux limiter on purpose, to better see the effects of our discretisation on its own. Besides that not being the case in real simulations, we do not expect to see this behaviour in simulations anyway, where other, more dominant, processes are included and immediately damp numerical instabilities. We will further investigate how this error evolves with time in section [VIII-4.1](#).

The isotropised approach can by construction not show a stable solution for this setup: The anisotropic part may be suppressed, but the isotropic part continues to work independently of the magnetic field. We find that while the conduction parallel to magnetic field lines is damped, we gain an increase of the perpendicular component. These violate the initial assumptions of our derivation for the sake of enforcing a physical heat flux. We have to consider different test setups to find out, which formulation gives better results and can be used for cosmological simulations.

\vec{B} direction	$\Delta_{\text{full aniso}} [\%]$	$\Delta_{\text{isotropised}} [\%]$
No	0.15	
45°	0.37	0.84
0°	0.38	2.2
90°	2.2	4.1

Table VIII.1: Mean calculated relative errors of each particle's internal energy with respect to the analytic solution for the temperature step problem.

In table [VIII.1](#) we present a more quantitative analysis of these results. For each particle inside the displayed range of $x \in [40, 60]$ cm we calculate the relative error in internal energy and collect the mean values for each displayed simulation. All shown errors lay at a percent level or below. Additionally, the isotropised version is about a factor two to ten worse than the fully anisotropic approach in all cases. For comparison we included the same calculation also for the reference run without magnetic field, where we reach a slightly smaller error value of about a factor two.

For later simulation times the errors in the isotropised version rise slightly until the temperature profiles start to settle down to the isothermal convergence state, while the fully anisotropic version in general tends to converge stronger to the analytic result.

Random magnetic field

As last configuration, we check whether our implementation reproduces the common idea to approximate anisotropic conduction by an isotropic implementation damped by a factor of 1/3. We imprint a random magnetic field onto our initial problems and fit the analytic solution with fitting parameter κ to it. We find factors of about 0.33 at different times matching our expectations. The fully anisotropic approach usually shows slightly smaller values than the isotropised version, however the difference is very small. We emphasize that besides scatter, the shape of the analytic solution is reproduced very well. We conclude that unphysical errors like in the

bottom left part of figure [VIII.2](#) will probably not arise in simulations with turbulent magnetic fields.

Time evolution

So far we only looked at a single snapshot of the internal energy's time evolution. In order to judge check that our conduction algorithm also behaves over long timescales and especially what happens with a perpendicular magnetic field we let the simulations run for a longer time and plot the result in figure [VIII.3](#).

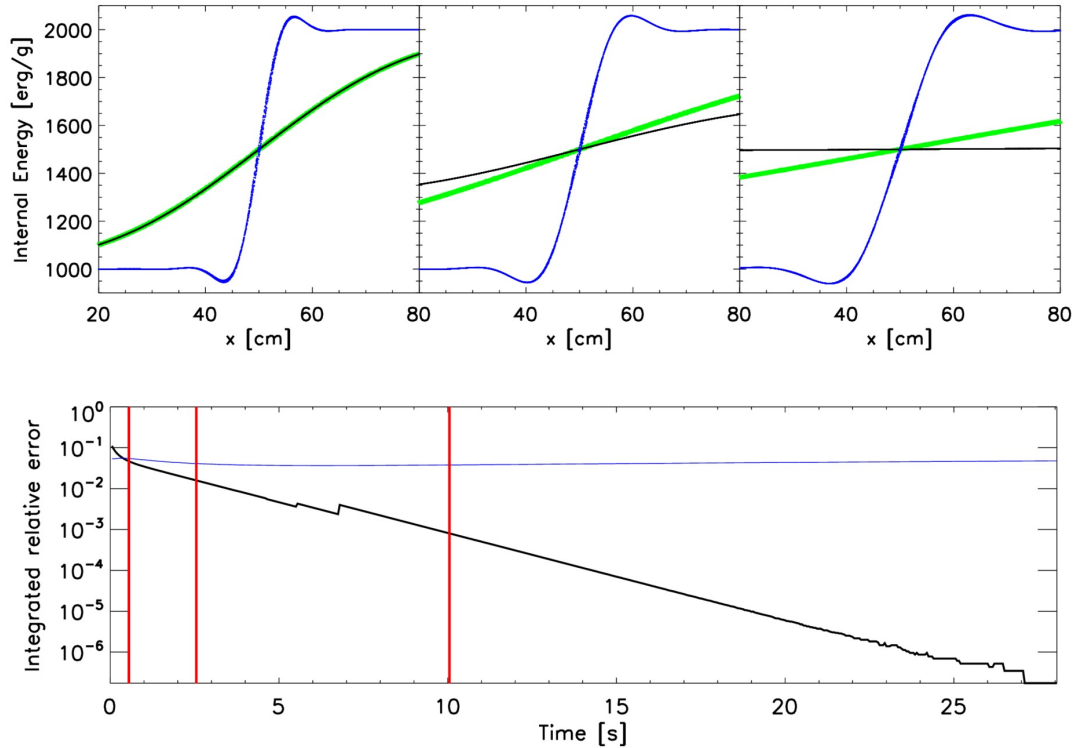


Figure VIII.3: In this plot we show the time evolution of the temperature step test with the fully anisotropic formulation. The green line shows the analytic solution, in case of a diagonal magnetic field, integrated from minus until plus infinity, the black line presents the according simulation (with a finite box x -length of course, see text for further explanation) and the blue line depicts the simulation with a perpendicular magnetic field. The upper panel plots three snapshots in time which are marked by vertical lines in the lower panel, where the integrated relative error of both simulations compared to the solution are plotted.

In the top layer we plot the analytic solution (green) and simulation (black) for the diagonal magnetic field and the simulation for the perpendicular magnetic field (blue) at three points in time, each further evolved than the plots we showed in the last subsections.

The first thing to notice is, that while the shape of the black and green lines is always similar, the simulation seems to evolve much faster and settles for an isothermal state in the third plot while the analytic solution still harbours a significant temperature gradient. This is easily explained by the fact, that the analytic calculation actually does not match the simulation any more at this time. Recalling the derivation in appendix [VIII-B](#) we see that we integrated along the x-axis from $-\infty$ to ∞ in order to receive an easy result. However, the simulation box is of finite length in the x-direction. Namely it ranges between $x \in [0, 100]$. Up until now we plot only a subrange of this total width because of the same reason that the solution starts to become inaccurate at the boundaries. One can basically understand the difference as the solution harbouring an infinite reservoir of heat outside these boundaries, while the simulation has vacuum boundary conditions. In this plot we reached the time where we can see the influence of this reservoir become significant by pumping in more heat into the system from one side and providing a sink on the other one and therefore slowing down the convergence to an isothermal state in an accelerated manner. We elaborate briefly, why the integration boundaries can not be simply changed to account for that in appendix [VIII-C](#).

As we can further see in this panel, while the bumps in the perpendicular configuration run formed quite quickly they present themselves as extremely stable: The magnitude of the error does not change at all over the whole evolution the only effect is that it broadens out a bit. The error is therefore not at all any kind of instability and it's evolution is strongly suppressed on its own. Please note that the timescale on which we judge here is extremely long, since conduction becomes more and more ineffective when approaching the isothermal state.

Finally the lower panel shows the time evolution of the integrated relative error of both simulations w.r.t. their analytic equivalent. We plot the integrated error because this resembles the conservation of energy. In addition we mark the three times at which the top panel plots were taken with vertical lines in this plot. The integrated error for the diagonal magnetic field stays constant over most of evolution after a small acclimatisation period which results from the discontinuity and a slightly asymmetry in sampling around it with SPH particles. For the perpendicular magnetic field the integrated error even declines exponentially. This perfectly displays how well our code is able to preserve the symmetry of the problem even though the particle setup is not based on a grid but on a glass file.

VIII-4.2 Smooth temperature distribution

Since the temperature step test contained an artificial discontinuity we test the code also with a similar setup but taking a smooth temperature distribution. Following [Cleary and Monaghan, 1999](#) we take a sinusoidal temperature distribution at $t = 0$. At first, we derive the analytic solution for the initial conditions:

$$u_0(x') = u_0 \cdot \sin(kx) \quad (\text{VIII-54})$$

with a generic wavenumber k . The result is:

$$u(t, x) = u_0 \sin(kx) e^{-\alpha k^2 t}. \quad (\text{VIII-55})$$

Assuming periodic boundary conditions we need to add an initial offset to prevent negative energies:

$$u(t, x) = u_1 + u_0 \sin\left(2\pi \frac{x}{L}\right) e^{-4\pi^2 \alpha t / L^2}. \quad (\text{VIII-56})$$

We chose the arbitrary values of $u_1 = 1500 \text{ erg/g}$ and $u_0 = 1000 \text{ erg/g}$. Including a magnetic field we expect a reduced conduction with coefficient $\kappa' = \kappa \cdot \cos^2 \angle(\vec{B}, \vec{\nabla}T)$.

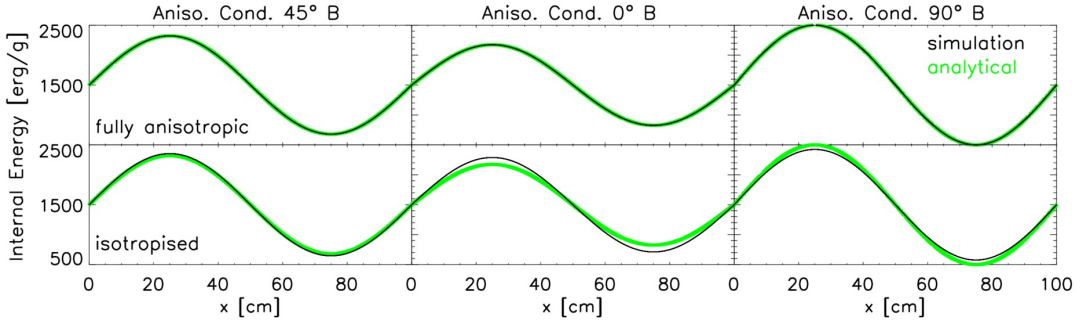


Figure VIII.4: Testing a wave like temperature distribution as initial conditions using both the full anisotropic approach (upper row) and the isotropised version (lower row) with three different magnetic field configurations: 45° to the temperature gradient (left column), parallel (middle column) and perpendicular (right column), all at the same simulation time. Basically, the results are the same as for the temperature step test. However, we see less scatter in our plots for this smooth setup. Even the error which we saw for the perpendicular magnetic field earlier does not appear in this test.

We perform this test with both implementations of anisotropic conduction and three magnetic field configurations with 0° , 45° and 90° to the x -axis. The results are shown in figure VIII.4. Basically, we find a similar behaviour as for the temperature step problem: The isotropised implementation shows always an offset from the analytic solution (weaker conduction parallel and stronger conduction perpendicular to the magnetic field), while the fully anisotropic implementation reproduces the solution very well. We emphasise two main differences to our previous results:

The amount of scatter for the fully anisotropic implementation is similar to what we get for the isotropised run. Since there is no strong discontinuity in this setup the amount of scatter is way lower than for the temperature step test.

Furthermore, we do not get any numerical artefacts in our results and even full suppression of conduction with a perpendicular magnetic field for the fully anisotropic implementation. Therefore, this approach produces the best results as long as there are no sudden temperature jumps.

VIII-4.3 Hot gas sphere

Next, we test how the code behaves for a more complex scenario. Similar to the second test from [Jubelgas, Springel, and Dolag, 2004](#) we set-up a sphere of hot gas. We use spherical symmetric

initial conditions for the internal energy in the form of

$$u_0(r) = u_0 e^{-\beta r}. \quad (\text{VIII-57})$$

For this test case we only show a qualitative comparison of the different runs, to see if the anisotropy is reproduced well.

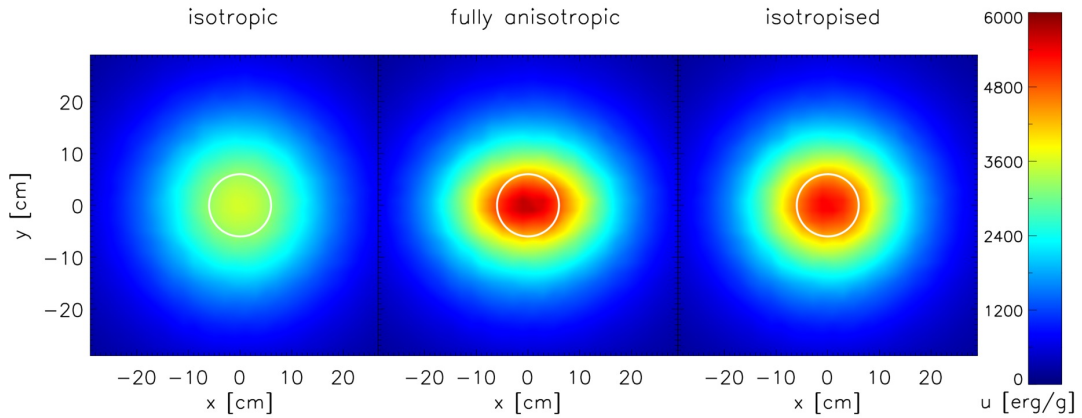


Figure VIII.5: Testing a spherical symmetric temperature distribution with a radial gradient. The left plot shows the reference run with isotropic conduction, while the middle and right plot show the fully anisotropic and isotropised implementations both with a magnetic field in x direction, again all at the same time. One can see, that the overall conduction increases with isotropy of the implementation. The much stronger anisotropic approach in the middle plot can be seen through higher ellipticity of isotherms (illustrated by white circles).

In figure VIII.5 we show our test results using isotropic conduction and both anisotropic approaches for a magnetic field in x direction. The comparison shows well the different overall effect of the three implementations. The more anisotropy the approach contains the lower the temperature decline in the inner region. Additionally, we see the stronger anisotropy in the middle panel compared to the right one through the ellipticity of the resulting profile.

In total, this agrees with our previous findings. Again there are no strange artefacts visible in any of the runs. We conclude that the fully anisotropic approach should be fairly unproblematic to use while it gives us more exact results according to the properties we formulated at the beginning. Therefore, we consider only this formulation.

VIII-4.4 Temperature step with perpendicular Conduction

Finally, we again set up a temperature step problem but now we investigate the behaviour of the suppression mechanism described in section VIII-2.2. We use typical values for temperature and density as they are found in hot regions of galaxy clusters and use a homogeneous magnetic field of the form $\vec{B} = \{B_0, B_0, B_0\}$ with $B_0 \in [10^{-12} \text{G}, 10^{-17} \text{G}]$. The results are shown in figure VIII.6.

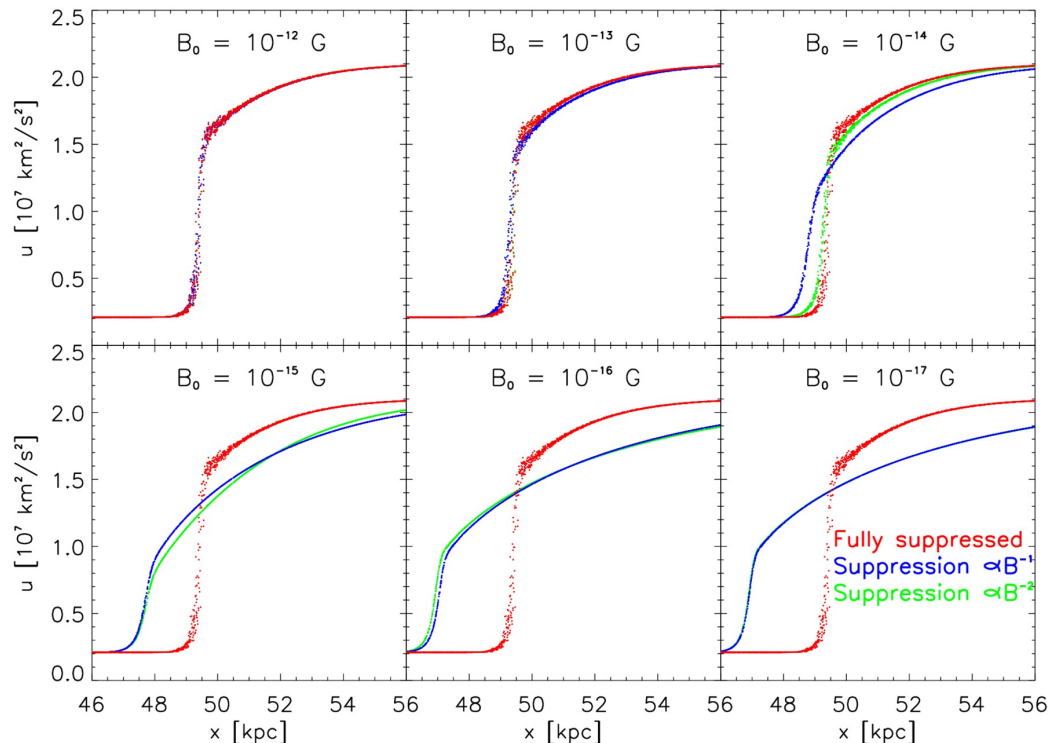


Figure VIII.6: Temperature step problem for different magnetic field strengths and treatments of perpendicular conduction. All plots are made at the same simulation time. One can clearly identify magnetic field strengths where the relation between linear and quadratic suppression flips concerning which prescription results in higher net conduction.

At the beginning we set up the temperature step at $x = 50$ kpc. The generally expected behaviour is, that the discontinuity propagates to the low temperature regime while the two levels close in on the mean temperature. We have run the different set-ups with either totally suppressed conduction perpendicular to the magnetic field and both phenomenologically motivated scaling relations presented in section [VIII-2.2](#).

We can identify the following different behaviours when varying the magnetic field strength:

- $B_0 \geq 10^{-13}$ G: The magnetic field is strong enough to fully suppress perpendicular conduction no matter which prescription we use.
- $B_0 \sim 10^{-14}$ G: The linear scaling relation results in an increased net conduction while the quadratic scaling still suppresses perpendicular conduction strongly.
- $B_0 \sim 10^{-15}$ G: Both prescriptions allow a certain amount of perpendicular conduction however there is no clear relation between both. The denominator of the suppression factor on the higher energy level is larger than one which results in a stronger suppression when the factor is squared. However, it is smaller than one for the low energy level. This is illustrated by figure [VIII.7](#).
- $B_0 \sim 10^{-16}$ G: The relation between linear and quadratic scaling has fully flipped: While both allow for a lot of perpendicular conduction now we get more net conduction with the quadratic formula
- $B_0 \leq 10^{-17}$ G: The magnetic field is so weak that it can not suppress perpendicular conduction any more with either of the discussed scaling relations.

In total, we see that a proper treatment of perpendicular conduction is important mostly for very small magnetic field strengths. We can not judge from this test which prescription is the better, however, it is important to include a prescription if small magnetic fields require proper treatment. Additionally, we note that even if we take into account only hot gas, the suppression is still also dependent on density, which means that also particles with stronger magnetic fields can require this proper description.

VIII-4.5 Summary of test results

After all tests we come to the following conclusions:

- The isotropised formulation for anisotropic conduction ensures that the solving algorithm is stable and does not lead to non-physical heat conduction. However, it violates the prerequisites we used to derive an anisotropic formulation.
- We find that the fully anisotropic formulation behaves sufficiently well for adequately smooth temperature distributions. Since the degree of instability should be small in comparison to hydrodynamical effects and is further suppressed by the application of a heat flux limiter, we only apply this formulation in our cosmological simulations. We made sure that the instability does not grow over time on its own and is furthermore not a numerical one in sense of the solver we apply to the discretisation of the conduction equation.

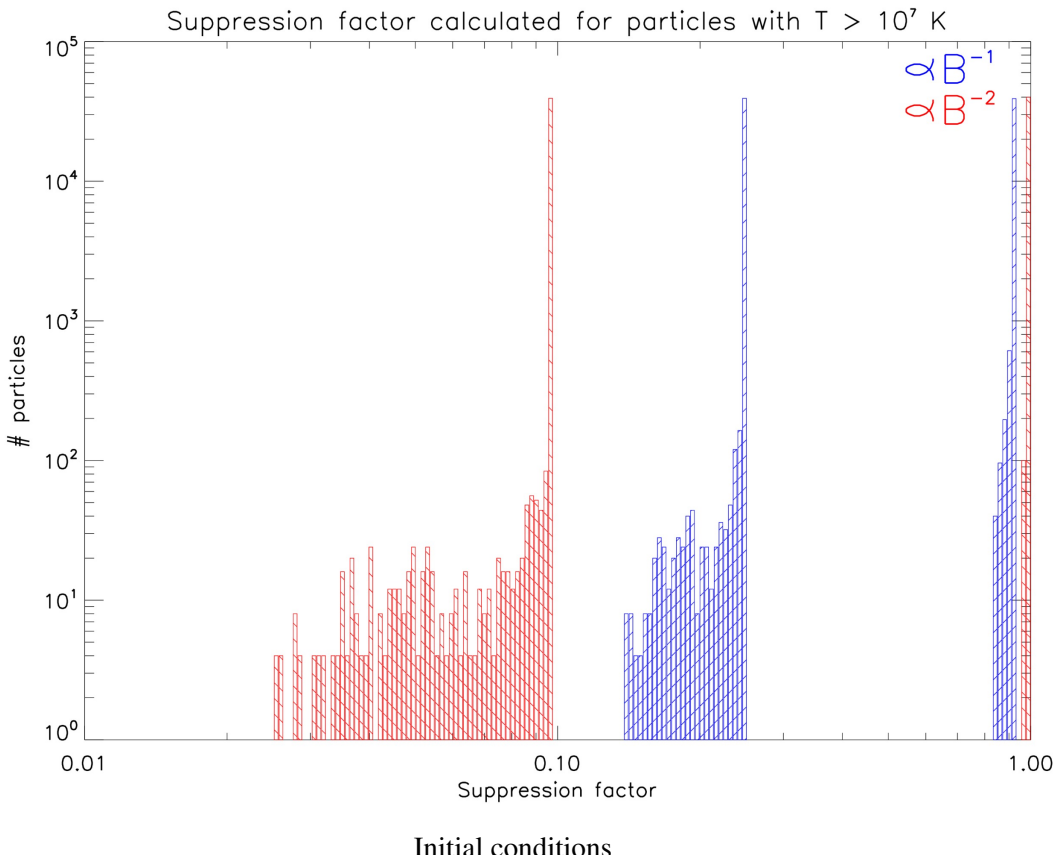


Figure VIII.7: Number of particles per suppression factor bin for the initial conditions with $B_0 = 10^{-15}$ G. Particles at the higher plateau get a stronger suppression for the quadratic formalism while particles at the lower plateau show the opposite behaviour.

- We have briefly investigated the effects of different scalings for perpendicular suppression and further inquire their behaviour in simulations of galaxy clusters.

VIII-5 Application to galaxy clusters

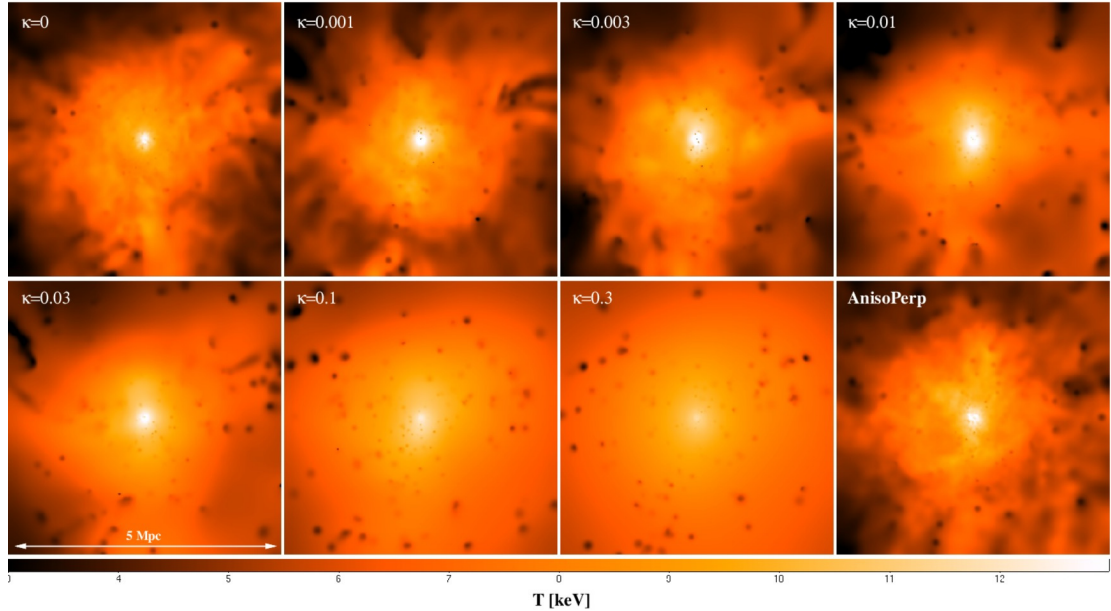


Figure VIII.8: Shown are the mass weighted temperature maps ($5 \text{ Mpc} \times 5 \text{ Mpc}$) of the relaxed cluster $g5699754$ at $z=0$. The upper left panel shows the simulation without any thermal conduction. The other maps (from upper left top lower right) show the sequence for isotropic thermal conduction when changing the suppression factor as indicated in the maps. The lower right one shows the run with anisotropic thermal conduction where the perpendicular term is evaluated proportional to the magnetic field strength.

In this section we present zoomed in re-simulations of massive COMA-like galaxy clusters selected from large Gpc sized cosmological boxes, where the parameters for a Λ CDM cosmology with $\Omega_m = 0.24$, $\Omega_b = 0.04$, $\Omega_\Lambda = 0.76$ and $h = 0.72$. We select five clusters from the original set of simulations presented in [Bonafede et al., 2011](#) to study the effect of thermal conduction within galaxy clusters. These galaxy clusters have virial masses² of $M_{\text{vir}} > 10^{15} M_\odot/h$ corresponding to virial radii of typically $r_{\text{vir}} \sim 2.5 \text{ Mpc}/h$. Calculated virial properties for all runs are listed in table [VIII.2](#). More details about the selection of the galaxy clusters and the generation of the initial conditions can be found in [Bonafede et al., 2011](#).

²Here we define virial properties based on the averaged density as predicted by the top-hat spherical collapse model, corresponding to 95 times the critical density for our chosen cosmology.

VIII-5.1 The effects of different conduction prescriptions

At first, we select one isolated and relaxed looking galaxy cluster (*g5699764*) to perform several simulations testing different settings for the implementation of thermal conduction. Figure [VIII.8](#) displays projected temperature maps of 5 Mpc wide and thick slices through the cluster, demonstrating the effect of thermal conduction on the temperature structure. The upper left panel shows the reference run without any thermal conduction. Then, from left to right and top to bottom the suppression factor is reduced (i.e. the conduction efficiency is increased) for the case of isotropic heat conduction. The last panel bottom right shows the result for anisotropic heat conduction, where we include the linearly scaling perpendicular suppression factor as displayed before (see section [VIII-2.2](#)).

As shown already in [Dolag et al., 2004](#), where similar simulations have been carried out with an earlier version of the implementation of isotropic heat conduction, we see that in such massive (and therefore hot) galaxy clusters, isotropic conduction has a strong effect on the temperature distribution. With less suppression of thermal conduction, more heat gets transported from the central part of the cluster to the outskirts and even more dramatically visible, local temperature fluctuations get smoothed out. In contrast, the simulation with anisotropic heat conduction shows only a very mild smoothing of the temperature fluctuations compared to the control run. This can also be seen in figure [VIII.9](#), where we show the emissivity distributions for all the isotropic and one anisotropic run. The larger the isotropic conduction coefficient the more the distribution is taylored around the mean temperature, (e.g. the cluster gets more isothermal), while the peak increases and shifts to slightly higher temperatures.

To investigate the effect of details in the different treatment of perpendicular conduction for the anisotropic heat conduction, figure [VIII.10](#) shows temperature maps zooming onto the central 2.5 Mpc of our test cluster. Here we compare the isotropic thermal conduction with a suppression factor of $\kappa = 0.01$ with three anisotropic runs with different treatment of the perpendicular component: fully suppressed (*Aniso*), linear (*AnisoPerp*) and quadratic (*AnisoPerpQ*) proportionality to the magnetic field strength. It is clearly visible that the detailed choice of treatment of the perpendicular component has a quite significant effect on the outcome. Still, none of the anisotropic runs show such a strong smoothing of local temperature fluctuations as the isotropic conduction simulation, even if we allow for conduction to become rather isotropic for weak magnetic fields. It also makes a notable difference if we use the linear or the quadratic formula to calculate the perpendicular suppression factor.

This gets again more clear when looking at the emissivity distributions for the different anisotropic runs shown in figure [VIII.11](#). While including a perpendicular suppression coefficient proportional to B^{-1} shrinks the distribution a bit, since it contains overall more conduction, we see clearly a different picture for the case proportional to B^{-2} . We find that this prescription suppresses conduction perpendicular stronger for most particles which results in less conduction compared to the linear case. Therefore, we see the emissivity distribution broadening again, even beyond the case with zero thermal conduction.

A more quantitative analysis is shown in figure [VIII.12](#), where the scaled, radial temperature profiles are presented in the upper panel. Here it can be clearly seen that the stronger we choose the isotropic conduction coefficient, the more internal energy is transported outwards beyond the virial radius. In agreement with previous studies in [\(Dolag et al., 2004\)](#), isotropic thermal

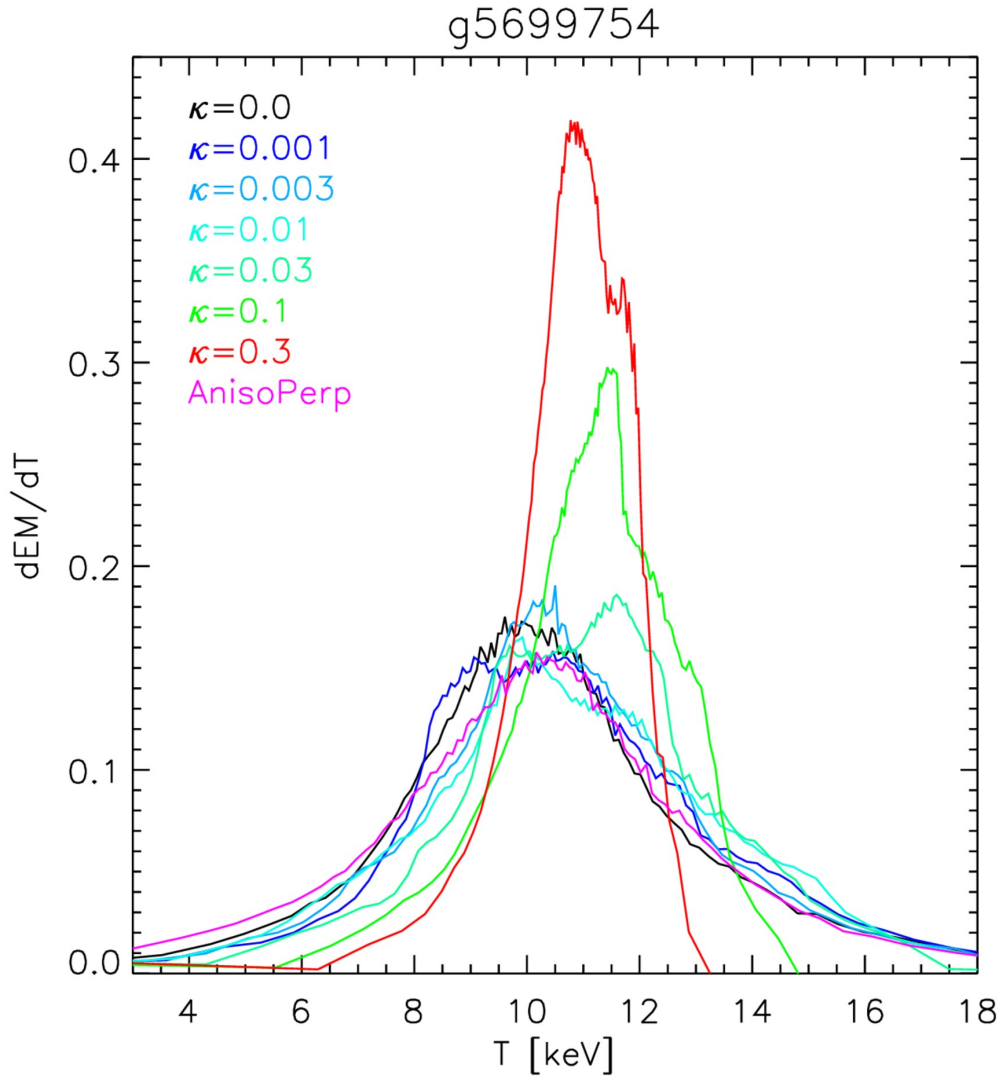


Figure VIII.9: Shown are the emissivity distribution of the ICM within the virial radius as function of the temperature for different treatments of the thermal conduction. Good to see the trend to shrink the distribution around the mean temperature with increasing level of the coefficient.

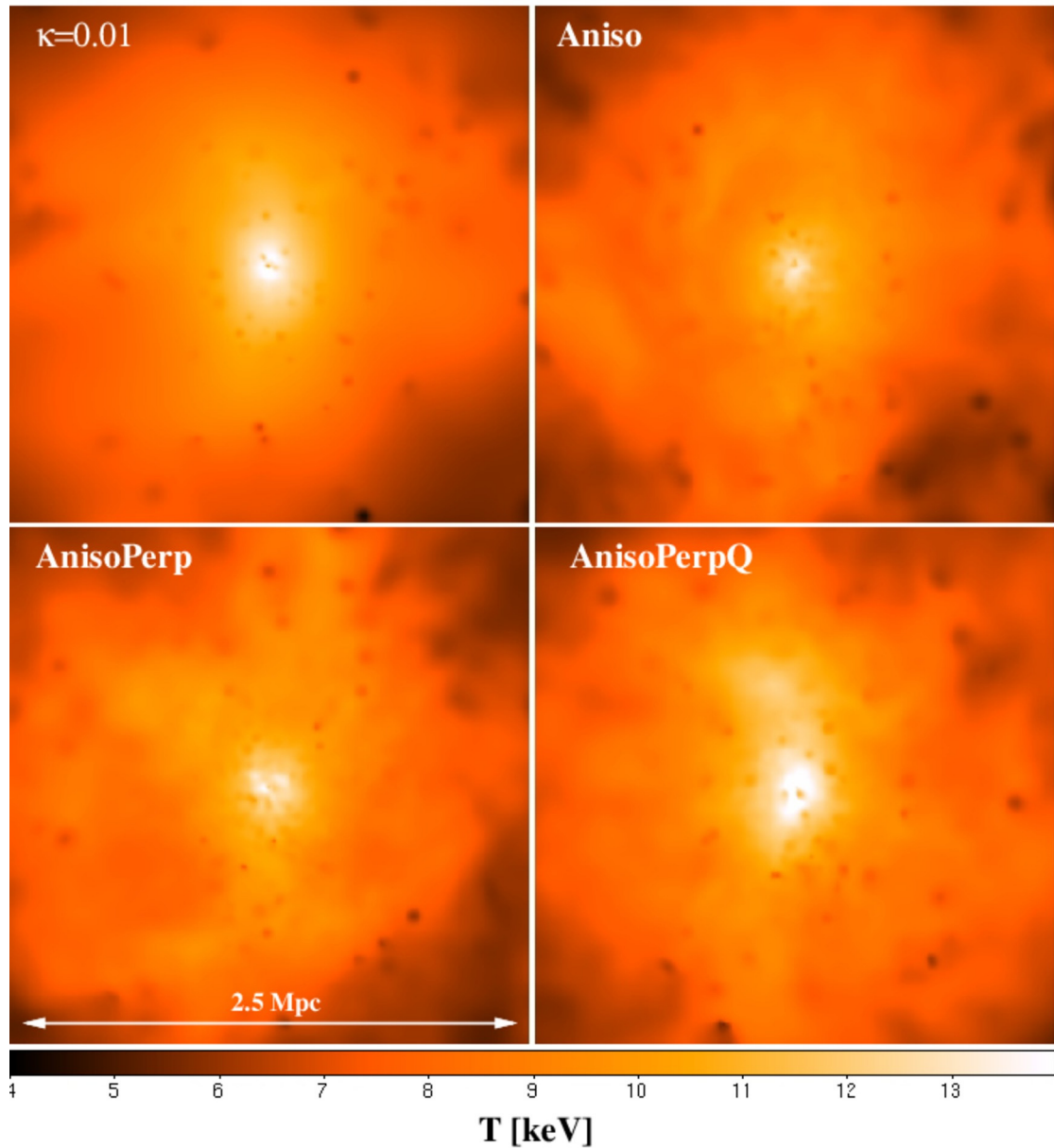


Figure VIII.10: Shown are the mass weighted temperature maps ($2.5 \text{ Mpc} \times 2.5 \text{ Mpc}$) of the inner part of the relaxed cluster at $z = 0$. The upper left panel shows the simulation with isotropic conduction for $\kappa = 0.01$. The other three maps show the runs with anisotropic thermal conduction for different treatment of the perpendicular case (see section- [VIII-2.2](#)).

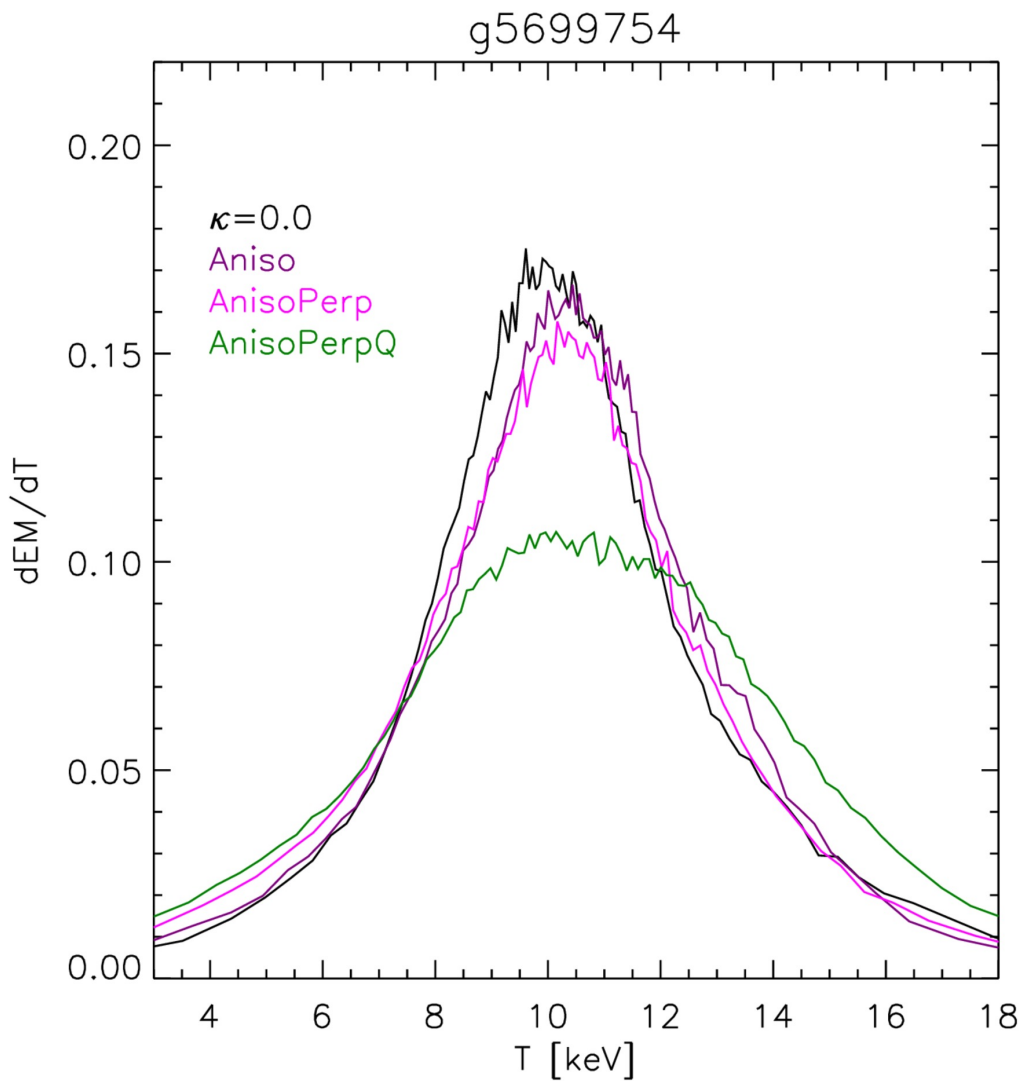


Figure VIII.11: Shown are the emissivity distribution of the ICM within the virial radius as function of the temperature for runs with anisotropic thermal conduction for the different treatments of the perpendicular case (see section VIII-2.2).

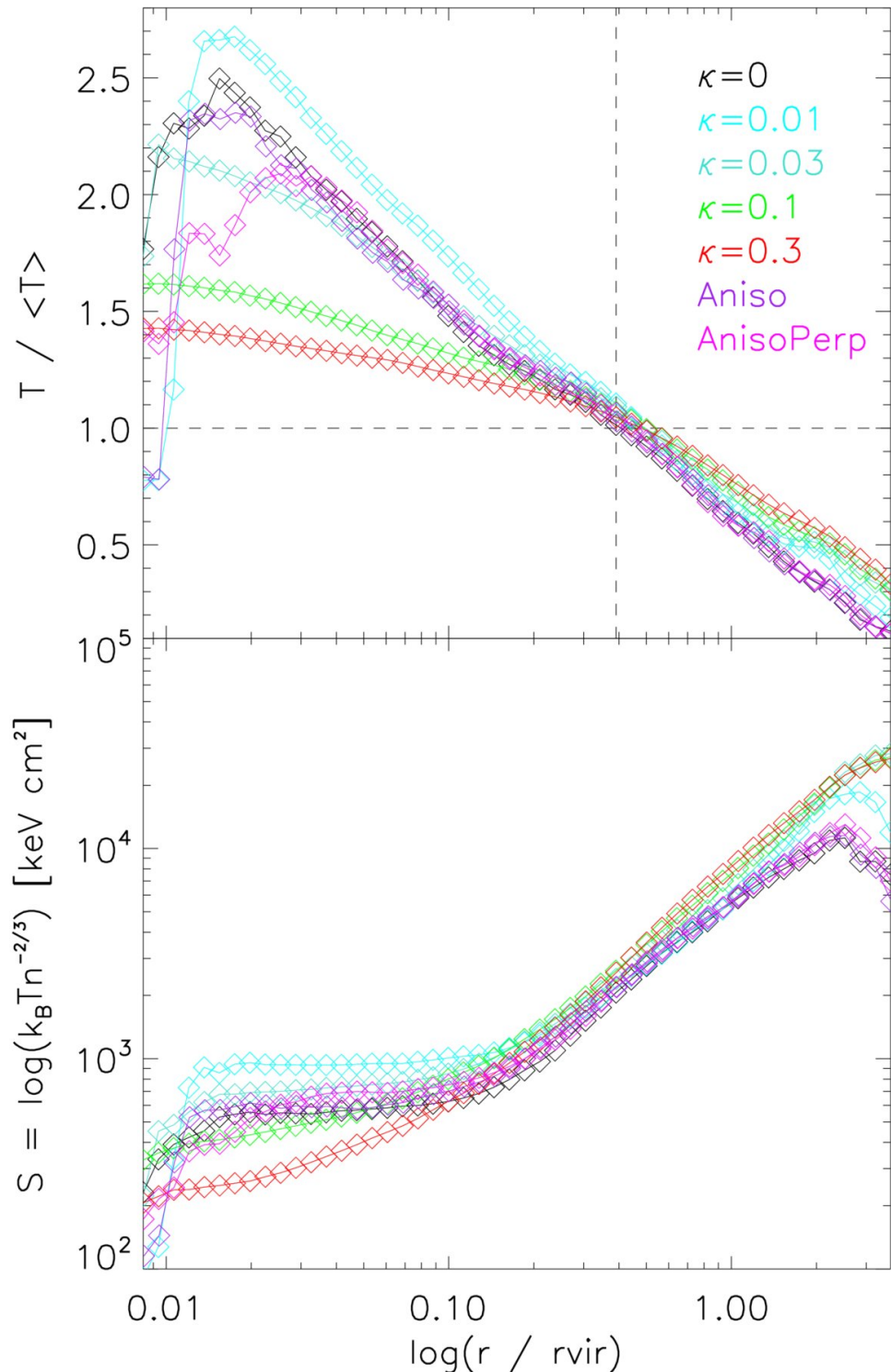


Figure VIII.12: Shown are radial temperature (upper panel) and entropy (lower panel) profiles for $g5699764$ with several different conduction settings at $z = 0$. The temperature profiles are normalized by the mean temperature within the virial radius for each respective run.

conduction at a level of 1/3 of the Spitzer value already leads to an isothermal temperature distribution in the inner part of the galaxy cluster. Regarding anisotropic conduction we include two runs, the one with full suppression perpendicular to magnetic field lines as well as the one using the linearly scaling suppression factor. While the totally suppressed run resembles almost zero level of isotropic thermal conduction, the temperature profile of the latter one lies somewhere between $\kappa \approx 0.01$ and $\kappa \approx 0.03$ for isotropic thermal conduction. The entropy profiles in the lower panel are in general more difficult to interpret. Here, already the reference run builds up a significant entropy core (in line with what was reported for the non ideal MHD simulations in [Bonafede et al., 2011](#)). Their shape is rather similar for all runs and due to combined effects including the different implementations of thermal conduction the trends are not easy to interpret and seem to depend on the local dynamical structures in the core of the galaxy cluster.

Finally, we can compare the simulated cluster to a sample of observations with *XMM-Newton* presented by [Frank et al., 2013](#), where they measured the width of the temperature fluctuations within the central part (e.g. within R_{2500}) of a sample of galaxy clusters. Figure [VIII.13](#) shows these observational data points over plotted with results for our different implementations of thermal conduction within our simulations. Please note that here we not only use the central galaxy cluster but also make use of a smaller galaxy cluster present within our simulation, which has a temperature of roughly 1 keV. For the case of isothermal conduction we see that the high isotropic conduction coefficients (e.g. $\kappa = 0.3$ and $\kappa = 0.1$) produce results which are below the observed temperature fluctuations for the high temperature system, similar to the findings in [Rasia et al., \(2014\)](#). For the low temperatures all implementations are consistent with the observations. In contrast, the anisotropic runs are matching with the simulations without thermal conduction. Interestingly, the simulation with the quadratic dependency of the suppression factors shows the largest temperature fluctuations, in line with the broader temperature distribution shown before.

To enforce the idea of a proper treatment of perpendicular conduction we display the range of suppression factors for all hot particles in one of our simulations in figure [VIII.14](#) at several redshifts. Since conduction scales strongly with the temperature of the plasma, we take into account only the most important contributors to thermal conduction, selecting particles within the hot atmosphere of groups and clusters by requesting their temperatures T to exceed 10^7 K. As the typical formation time of clusters and groups is around $z = 1$, the amount of particles within this hot gas phase increases significantly until the redshift approaches $z = 1$. While either suppression formulation results in fairly low suppression factors for the bulk of particles, there are significant differences in the amount of particles which have moderate suppression factors up to the regime of almost unsuppressed conduction. Furthermore, it seems that the quadratic formula produces in general lower factors and therefore less net conduction than the linear one. As we have already seen in our tests in section [VIII-4.4](#) the two formulations show opposite behaviour in different regimes.

To further investigate the effects of the isotropic and anisotropic treatment of thermal conduction we select the same four, Coma like galaxy clusters ($g0272097$, $g1657050$, $g4606589$ and $g6802296$) as in [Bonafede et al., \(2011\)](#) and simulate them with zero thermal conduction, isotropic conduction at a level of $\kappa = 0.3$ and anisotropic thermal conduction using the lin-

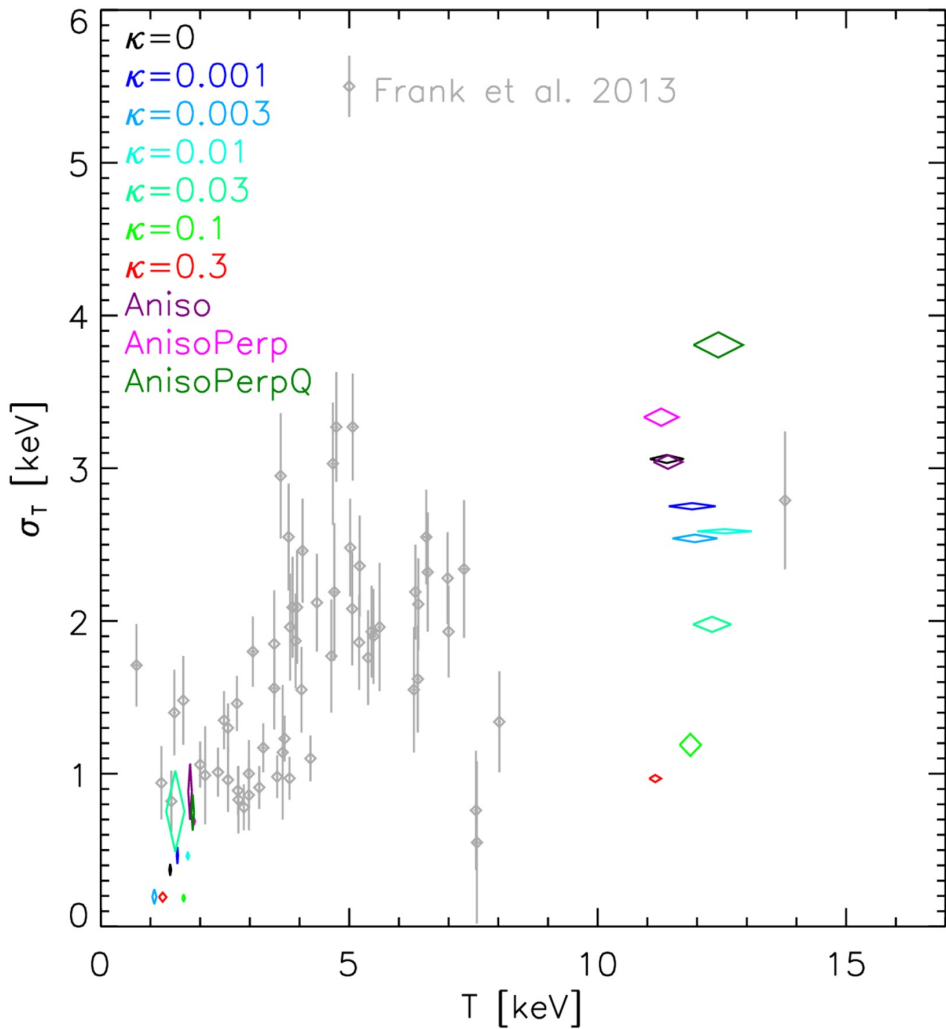


Figure VIII.13: Comparing the temperature fluctuations within R_{2500} as inferred from observations by [Frank et al., 2013](#) with the one predicted for the simulated relaxed cluster with the different treatment of the thermal conduction (as labelled).

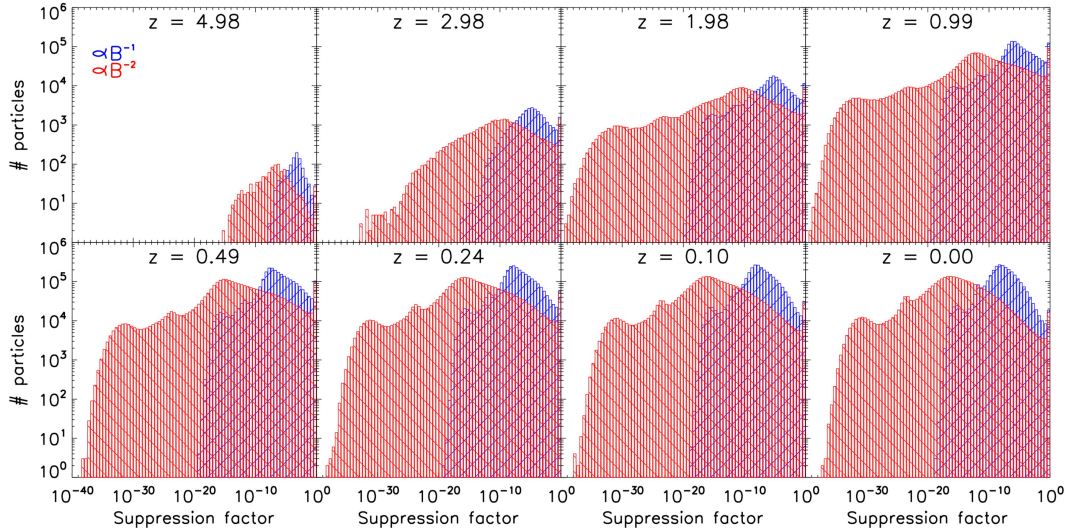


Figure VIII.14: This plot shows distribution of linear and quadratic suppression factors calculated for all particles of the run AnisoPerr with temperatures higher than 10^7 K for several redshifts. (see section VIII-2.2).

ear scaling for the perpendicular case. Table VIII.2 lists the general properties of the resulting galaxy clusters.

While the virial properties of the halo are basically unchanged, the amount of condensed baryons in form of stars and cold gas changes with the treatment of thermal conduction. This fraction slightly grows with increasing net conduction, similar to previous findings (Dolag et al., 2004), again indicating that thermal conduction alone is not able to prevent cooling in the centres of cluster. Although, due to the inclusion of magnetic fields, the fraction of condensed baryons is smaller than in previous numerical studies, it is still larger than previous observations (Balogh et al., 2001; Lin, Mohr, and Stanford, 2003; Andreon, 2010). However, more recent observational studies by Kravtsov, Vikhlinin, and Meshcheryakov, 2014 indicate a significantly larger amount of stars in the central galaxies of clusters than previously thought. Ultimately, including anisotropic thermal conduction seems not to change the amount of cold baryons in the centre of simulated galaxy clusters significantly.

The respective temperature maps for all five clusters with the three settings for thermal conduction are shown in figure VIII.15. The four additional clusters show a very similar behaviour as we saw before in the relaxed one. Temperature is transported outwards with the isotropic conduction using $\kappa = 0.3$, while substructures are strongly smoothed out, whereas the run with anisotropic conduction shows only mild smoothing of temperature fluctuations. One interesting aspect gets clearly visible in figure VIII.16, where we present the corresponding radial temperature profiles for five clusters for the three different runs. Again, we see that isotropic conduction leads to a significant flattening of the temperature profile embedding a cold core with varying size and moderate temperature. The simulations without thermal conduction show a rising temperature profile towards the centre with a much larger drop of temperature within the central

Cluster	Bon.	Cond. κ	r_{vir}	m_{vir}	f_{col}
g5699754	D17	0	2.568	1.739	0.184
		0.001	2.566	1.736	0.183
		0.003	2.569	1.742	0.175
		0.01	2.569	1.742	0.175
		0.03	2.566	1.735	0.181
		0.1	2.569	1.741	0.188
		0.3	2.564	1.732	0.191
		Aniso	2.553	1.710	0.197
		AnisoPerp	2.562	1.727	0.188
		AnisoPerpQ	2.553	1.709	0.183
g0272097	D2	0	2.375	1.3989	0.179
		0.3	2.378	1.393	0.185
		AnisoPerp	2.310	1.280	0.267
g1657050	D5	0	2.397	1.427	0.185
		0.3	2.387	1.410	0.191
		AnisoPerp	2.380	1.398	0.193
g4606589	D13	0	2.145	1.025	0.174
		0.3	2.153	1.037	0.191
		AnisoPerp	2.154	1.038	0.180
g6802296	D20	0	2.062	0.909	0.172
		0.3	2.054	0.899	0.204
		AnisoPerp	0.202	8.566	0.211

Table VIII.2: Calculated virial masses [$10^{15} M_{\odot}/h$], virial radii [Mpc/h] and mass fraction of collapsed baryons (stars + gas with $T < 3 \cdot 10^4$ K) for all runs. Different conduction settings do not alter the global halo properties significantly. The fraction of collapsed baryons seems to grow slightly with increasing net conduction. For further cross reference our initial conditions with the numbering used by [Bonafede et al., 2011](#).

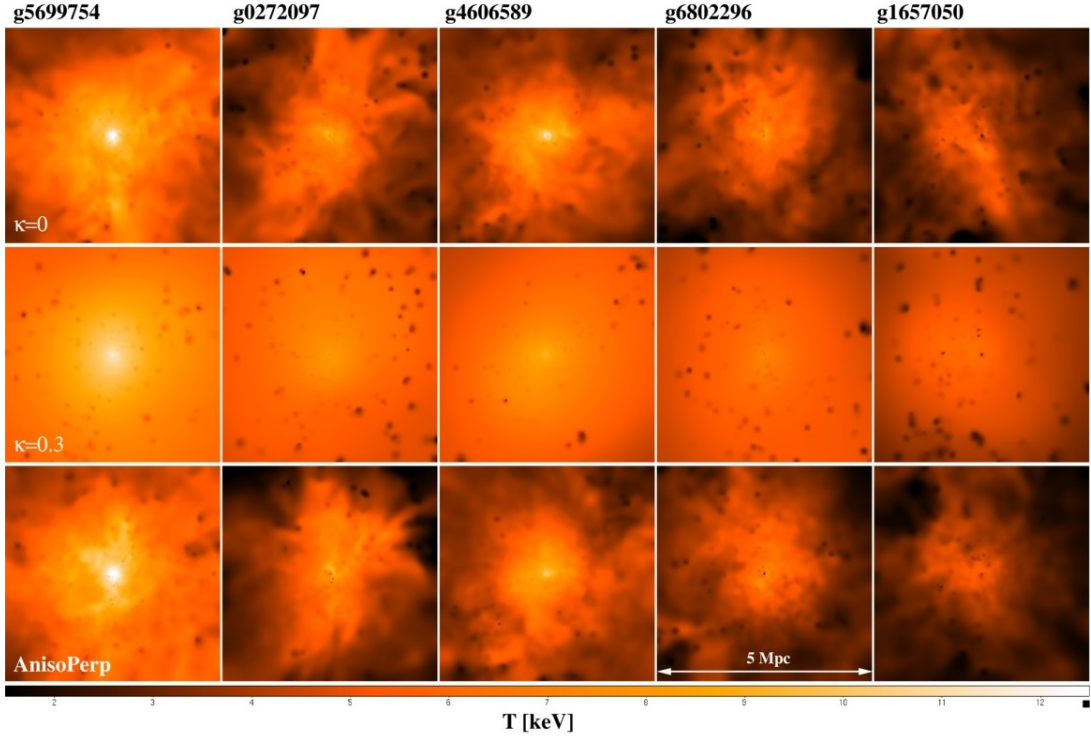


Figure VIII.15: Shown are the mass weighted temperature maps ($5 \text{ Mpc} \times 5 \text{ Mpc}$) of the five simulated clusters at $z=0$. The upper left row shows the simulation without thermal conduction. The middle maps show the simulations with isotropic thermal conduction for $\kappa = 0.3$ and the lower row shows the runs with anisotropic thermal conduction, where the perpendicular term is evaluated with the linear scaling.

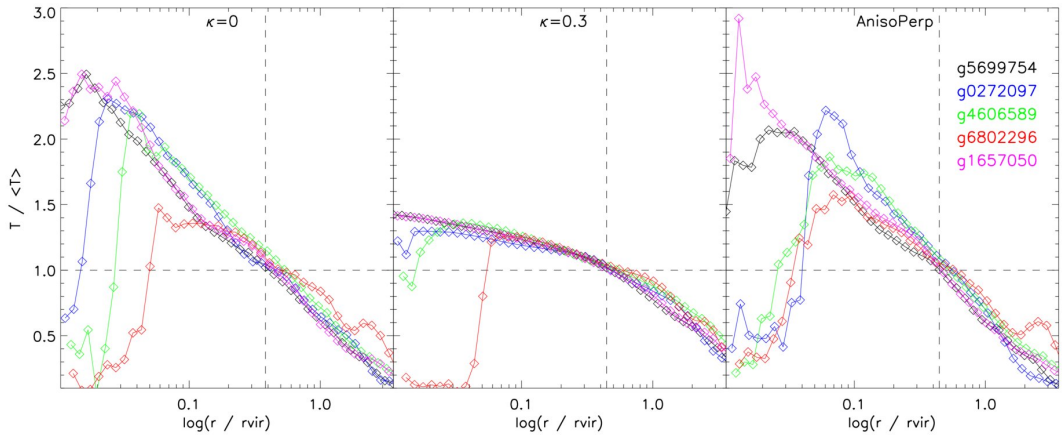


Figure VIII.16: Radial temperature profiles for all five clusters as in figure VIII.15. Dashed lines indicate the first crossing of $T = < T >$.

core. The simulations with anisotropic thermal conduction where we used the linear scaling for the perpendicular component shows a more bimodal temperature profile. Some clusters show very similar temperature profiles compared to the simulations without any thermal conduction, some have a very pronounced cold core. The sample is much to small to draw robust conclusions but this indicates that in the case of anisotropic thermal conduction the amount of heat transport is strongly varying with the current dynamical state of the cluster and therefore might contribute to the observed bimodality of cool core and non cool core clusters. The temperature for all runs drops lower than the specific mean temperature of gas inside the virial radius at about 40 to 45 per cent of the virial radius.

At last, again, we compare the temperature fluctuations to the observational data of [Frank et al., 2013](#). Similar as before, beside the central, massive cluster we also take other clusters found in the high resolution region into account, allowing us to get also some objects with various temperatures, sampling the low temperature region. Figure [VIII.17](#) shows the comparison of the data with our simulations without thermal conduction, with isotropic conduction using $\kappa = 0.3$ and with anisotropic conduction including linear scaling for the perpendicular component. While the simulated clusters with isotropic conduction using $\kappa = 0.3$ fall significantly below the bulk of data points for clusters above 5 keV, the simulations without thermal conduction and with anisotropic thermal conduction seem to represent the observed data points reasonably well. Still a more clearly selected set of simulated galaxy clusters across the whole temperature range as well as observations in the high temperature regime are needed to draw more robust conclusions.

VIII-5.2 The magnetic field structure in the simulated clusters

Since there is a tight connection between thermal conduction and magnetic field evolution, we now investigate the magnetic field in the simulated galaxy clusters. We show in figure [VIII.18](#) thin slices of the magnetic pressure through the cluster centre. In high density regions, in the cores of clusters and groups, almost all particles have magnetic fields at μG levels, while they drop down to nG levels in the outer regions. Since the magnetic fields are introduced by supernova seeding events we see, that the high magnetic fields are strongly localised in our simulations. Transport processes smooth out the magnetic field distribution but a bubbly structure still remains. Particles which are not directly influenced by the supernova seeding have rather low magnetic field values as low as even $B \approx 10^{-20}$ G. These particles are sensitive to the chosen scaling of the conduction mechanism.

Still, also particles sitting in extreme density peaks contribute significantly to this dependency, since equations [VIII-19](#) and [VIII-25](#) are not only dependent on the magnetic field strength but also on density. Therefore this discrimination of scaling is always important and not only an artefact of the magnetic field seeding mechanism.

Since differences in the four maps are only marginally, we also present the radial magnetic field profiles (volume-averaged) for several runs in figure [VIII.19](#). We see that the radial profiles for all different runs are of very similar shape and broadly agree with previous findings in the literature. The more efficient we allow conduction to be, the steeper the profiles become outside the cluster core. The runs with anisotropic conduction resemble again runs with a very low isotropic coefficient.

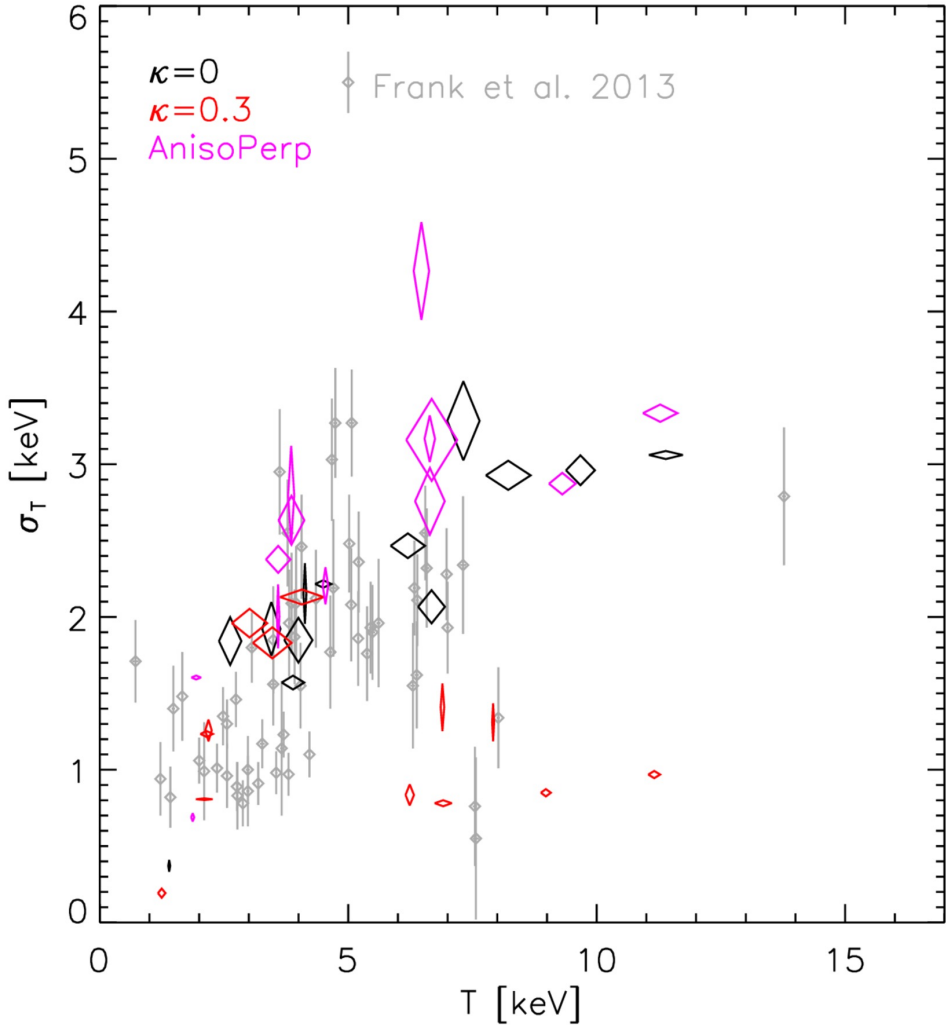


Figure VIII.17: Comparing the temperature fluctuations within R_{2500} as inferred from observations by Frank et al., 2013 with the one predicted for the set of simulated clusters, including also some less massive ones which are found within the high resolution region of the zoomed simulations. The different colours correspond to the simulations without thermal conduction (black), isotropic thermal conduction with $\kappa = 0.3$ (red) and anisotropic thermal conduction, where the perpendicular term is evaluated using the linear scaling (pink).

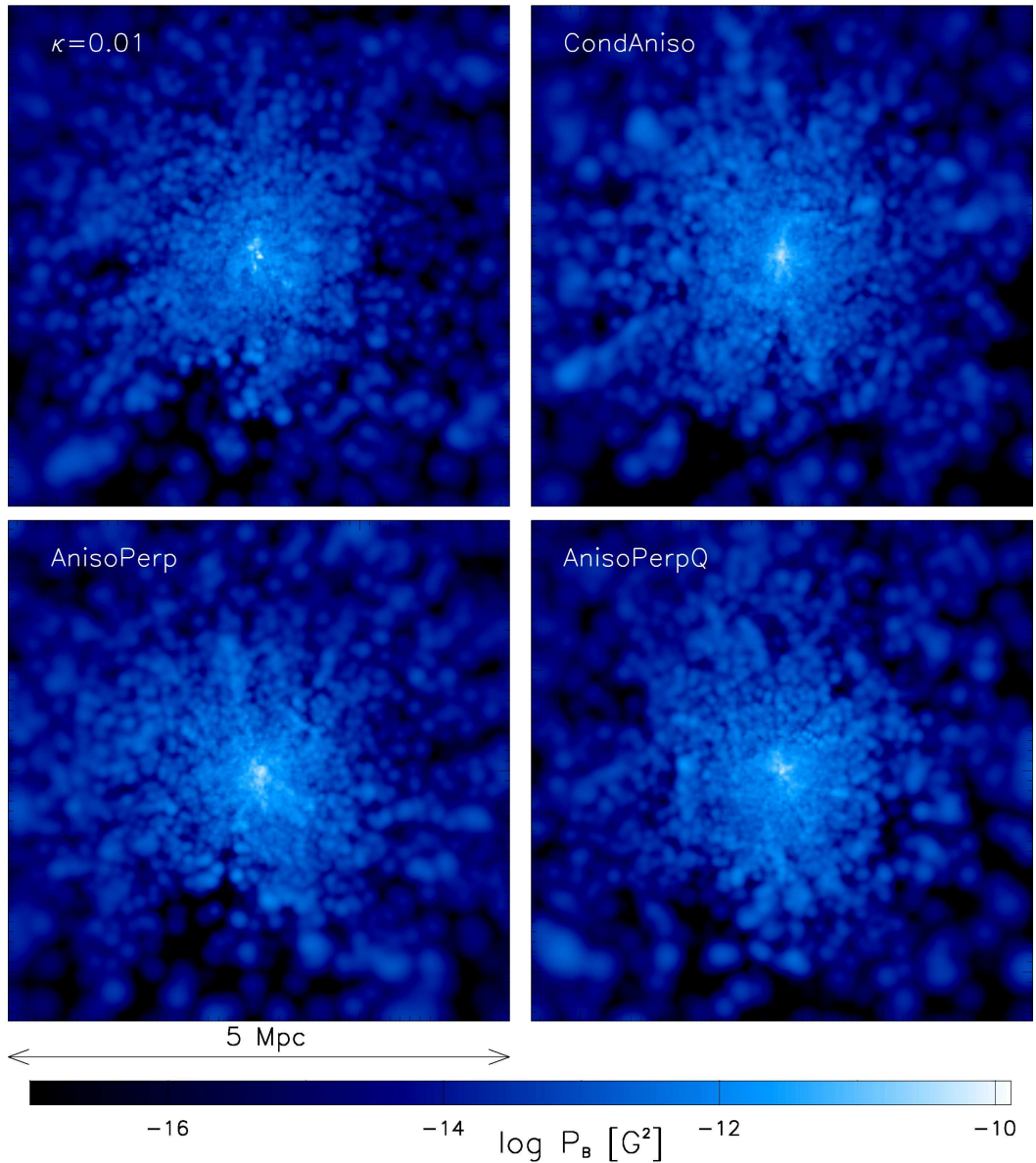


Figure VIII.18: We present maps of the magnetic pressure $P_B = B^2/8\pi$ in a thin slice through the cluster centre. As before we compare four runs with different conduction settings.

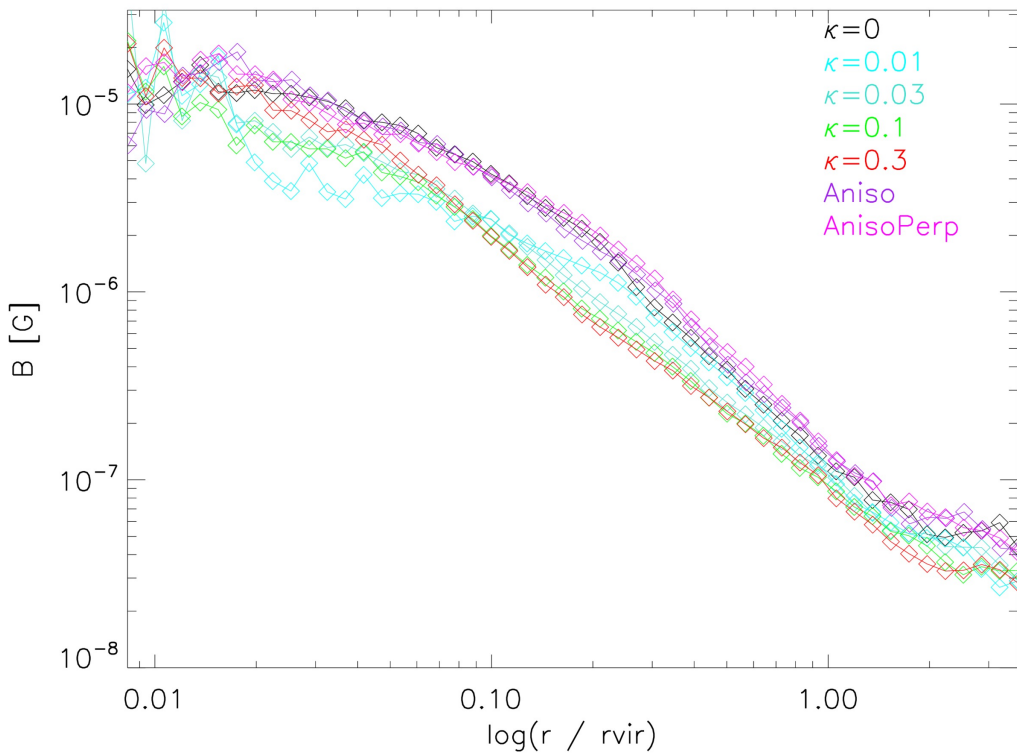


Figure VIII.19: We show the volume-averaged radial magnetic field profiles of the most massive galaxy cluster for different conduction settings. Stronger conduction leads to a steeper profile while the curves of the anisotropic runs are closest to the non-conductive run.

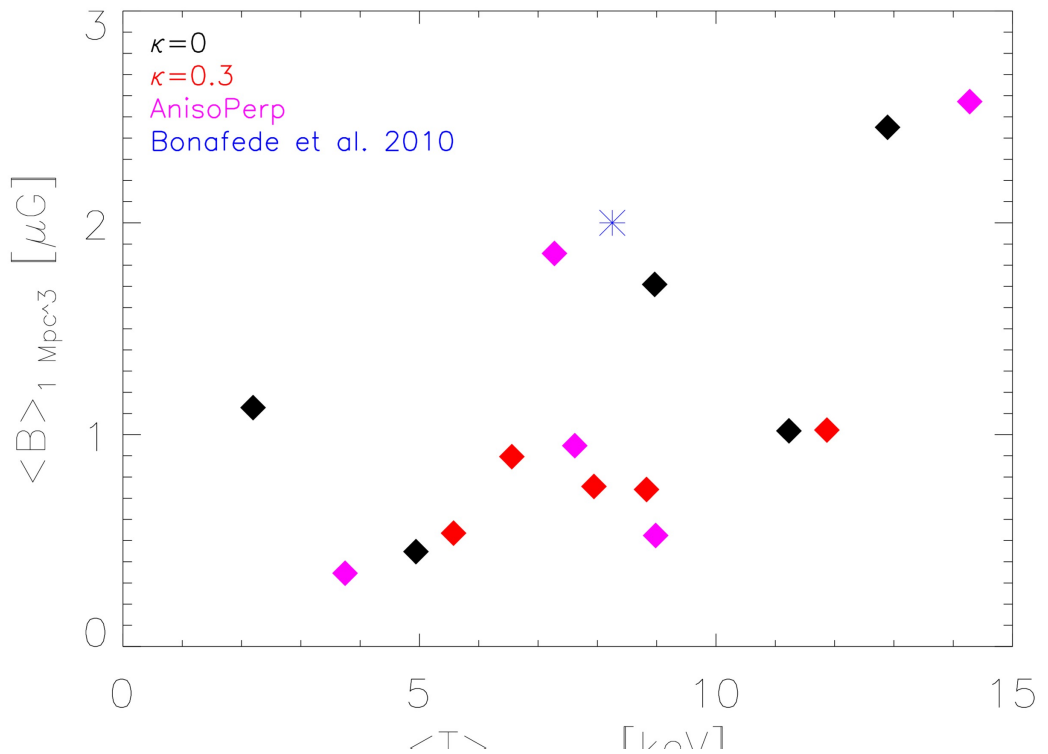


Figure VIII.20: We show the mean volume-averaged temperature against the mean volume-averaged magnetic field strength of the five most massive clusters inside the central one Mpc^3 . Additionally, we overplot an observational data point for the Coma Cluster taken from [Bonafede et al., \(2010\)](#).

To illustrate the resulting magnetic field strengths in the larger cluster sample we plot temperature against magnetic field volume-averaged within a sphere of volume one Mpc^3 around the cluster centres in figure [VIII.20](#). We choose this region in order to compare to an observational result for the Coma cluster presented by [Bonafede et al., \(2010\)](#). Overall, the results obtained with our simulated clusters are in good agreement with the magnetic field observed in the Coma cluster, although there is a trend for some clusters to have slightly lower magnetic fields. The amplitudes are more in the range of mean magnetic fields inferred from the radio halo (e.g. $0.7 - 1.9 \mu\text{G}$ given by [Thierbach, Klein, and Wielebinski, 2003](#)) than from rotation measurements. Compared to previously findings, this is probably related to our seeding mechanism by supernova events.

Comparing the different runs we present, one can clearly see that changes in the conduction prescription pose an overall influence over the presented averaged quantities. The runs without thermal conduction and with our anisotropic prescription produce a larger variance of cluster temperatures and higher magnetic fields on the high temperature end in comparison to runs with rather strong isotropic thermal conduction. This matches well with the conclusions we drew from the radial temperature profiles in the previous subsection.

VIII-6 Summary and Conclusions

We derive and discuss a numerical scheme for anisotropic thermal conduction in the presence of magnetic fields. We present a discretisation for SPH and implement our new method into the cosmological simulation code GADGET. We show a variety of standard tests as well as cosmological simulations of galaxy cluster formation with different choice of conduction parameters, where we combined the new conduction implementation with a supernova seeding scheme for the magnetic field (Beck et al. 2013), leading to a self consistent evolution of magnetic fields within the cosmic structures.

Our numerical scheme for anisotropic conduction in SPH solves the corresponding equations using a conjugate gradient solver, and therefore need only a very small amount of extra computational effort in the MHD version of GADGET. However, the straight forward derivation can violate the second law of thermodynamics in cases of strong anisotropies and large jumps in temperature. Additionally, this can causes an unstable behaviour of the conjugate gradient solver in the presence of extremely sharp jumps of temperature. Typically, this problem is solved by introducing a correction which ensures positive definiteness of the linear equation system by adding an artificial isotropic component. However, this correction can lead to significant, artificial heat flow perpendicular to the magnetic field and it is therefore questionable if such a numerical correction is useful in a realistic environment, where it can hide the effect of anisotropic conduction. In general, for any realistic situation, our anisotropic implementation with fully suppressed perpendicular term is already stable enough so that we do not have to add an artificial, destructive isotropisation term. However, a closer look at the term of the perpendicular conduction coefficient reveals that the amount of suppression of the perpendicular conduction coefficients can scale with either with B^{-1} or with B^{-2} ([Huba, 2011](#)). Depending on other plasma properties, these two scalings can have different relative effect on the amount of perpendicular heat transport. To test them, we perform cosmological simulations of the formation of galaxy clusters

with different implementations of the perpendicular transport coefficients. We also compare the results with a fully isotropic implementation of heat transport for different values of the suppression of thermal conduction with respect to the classical Spitzer value. Our main results can be summarised as follows:

- Temperature maps from simulated galaxy clusters show that isotropic thermal conduction not only transports heat outwards, but also smoothes small-scale features. Anisotropic conduction seems to resemble isotropic transport with coefficients like $\kappa \sim 0.01 \cdot \kappa_{\text{Sp}}$; however, prominent substructures in the temperature distribution survive due to insulation by magnetic field lines.
- Radial temperature profiles change differently when applying anisotropic thermal conduction depending on the dynamical evolution of the cluster. Some profiles are very similar to those without thermal conduction showing a rising profile with a large drop towards the centre while others show a very pronounced cool core. In contrast, isotropic conduction produce flattened, almost isothermal temperature profiles in the central regions.
- We show the relevance of a proper treatment of perpendicular conduction instead of only parallel transport. At all times we find a significant amount of particles with temperatures $T > 10^7$ K for which a non negligible perpendicular component is assigned. These particles sit either in regions with negligible magnetic field or at gas density peaks. The particles with low or no magnetic field are especially important in the simulations, since many particles have not undergone magnetic supernova seeding events.
- We find that different conduction prescriptions also have some influence on the resulting magnetic field of the clusters. Lower conduction leads to steeper radial profiles in the most massive cluster. In the larger sample we see that anisotropic conduction leads to a larger variance of mean cluster temperatures and slightly stronger magnetic fields on the high temperature end.
- We calculate emissivity distributions and compare to observed temperature fluctuations of [Frank et al., 2013](#). We find that simulations with either zero or anisotropic conduction reflect the observational data points best, whereas isotropic conduction with $\kappa > 0.1$ shows a clear lack of temperature fluctuations compared to the observational data points. In comparison, although clearly visible, the differences for the different descriptions for perpendicular conduction show only mild changes in the amount of temperature fluctuations. Here a significant increase of number of simulated galaxy clusters as well as many more observations of high temperature clusters will be needed to discriminate between them.
- We compare the fractions of cold gas and stars in different simulations and find a weak dependence on the conduction parameters. Conduction seems not to play a key role in suppressing cooling in galaxy clusters, but due to the coupling of the suppression factors to the local dynamical state of the cluster, the anisotropic conduction might contribute to the observed bimodality of cool core and non cool core systems.

In conclusion, anisotropic thermal conduction is not a dynamically dominant process within galaxy clusters, but can influence the evolution of small-scale structure. In contrary to isotropic heat conduction, it produces a reasonable amount of temperature fluctuations compared to observations and still allows locally for transport of heat. In general, it comes only with a small amount of computational cost for cosmological SPMHD codes and eliminates the need for a free efficiency parameter. A next step would be to consider also non-collisional thermal conduction and include the cross term mentioned in section VIII-2.2. Since we have seen that a perpendicular conduction component can have quite an impact we expect this term to also play a role in the process.

In the future, a larger sample of cosmological simulations with possibly even higher resolution will allow a better statistical analysis of the detailed temperature and magnetic field structures and the role of anisotropic transport effects in galaxy clusters. This will help to gain further knowledge about the scaling relations of perpendicular conduction or the importance of small-scale plasma instabilities, which is very challenging to resolve.

Acknowledgements

We thank Volker Springel for access to the developer version of GADGET. We thank the anonymous referees for very helpful comments that helped to further improve this work along the way. AA gives special thanks to his colleagues Max Imgrund, Marco Häuser and Carsten Upphoff for very useful discussions during the creation of this work. KD and AMB are supported by the DFG Research Unit 1254 'Magnetisation of interstellar and intergalactic media' and by the DFG Cluster of Excellence 'Origin and Structure of the Universe'. KD is supported by the SFB-Transregio TR33 'The Dark Universe'. We also thank the anonymous referee for very helpful comments to this article. AA, KD, AMB and MP are part of the MAGNETICUM³ simulation project.

VIII-A Solving the Taylor approximation for the second order term

We show the solution of the modified equation VIII-29 solved for the second order term, which we need to compute the mixed second derivatives in the conduction equation. At first, the kernel derivative is expressed as

$$\frac{\partial W_{ij}}{\partial (x_i)_\delta} = -W'_{ij} \frac{(x_{ij})_\delta}{|x_{ij}|}. \quad (\text{VIII-58})$$

Looking at the first order error term of the modified equation VIII-29, we see, that

$$\int d^3 x_j \frac{(x_{ij})_\alpha (x_{ij})_\gamma}{|x_{ij}|^2} \cdot \left(-\frac{(x_{ij})_\delta}{|x_{ij}|} W'_{ij} \right) = 0, \quad (\text{VIII-59})$$

since for all possibilities of α , γ and δ there is always at least one component, where the integral vanishes because of an antisymmetric integrand. All indices range from 1 to 3, so there is always

³<http://www.magneticum.org>

one component with an odd amount of x_{ij} . The denominator and W'_{ij} are even with respect to x_j , so the integral vanishes.

The next step is to calculate the integrals of the second order error term with a substitute as

$$T_{\alpha\beta\gamma\delta} = \int d^3x_j \frac{(x_{ij})_\alpha (x_{ij})_\beta (x_{ij})_\gamma (x_{ij})_\delta}{|x_{ij}|^3} \cdot W'_{ij}. \quad (\text{VIII-60})$$

We distinguish between the following three cases, which we address one after another:

1. At least three indices are unequal
2. All indices are equal
3. The indices form two pairs, e.g. $\alpha = \beta$ and $\gamma = \delta$

1. At least three indices are unequal

If at least three of the four indices are unequal, then there is at least one integration where the integrand contains only a single x_{ij} component. Since the denominator and W'_{ij} are even functions with respect to x_j , the integrand for this component is in total an odd function which vanishes when integrating over the whole (symmetric) domain. Therefore, the integral is zero.

2. All indices are equal

If all indices are equal, we start the calculations with substituting the integration variable $x_j \rightarrow x_{ij}$ without further implications on the integration. Then equation [VIII-60](#) simplifies to

$$T_\alpha = \int d^3x_{ij} \frac{(x_{ij})_\alpha^4}{|x_{ij}|^3} \cdot W'_{ij}, \quad (\text{VIII-61})$$

where we used the short hand notation $T_\alpha := T_{\alpha\alpha\alpha\alpha}$.

Since W'_{ij} is only dependent on $|x_{ij}|$ we choose spherical coordinates for x_{ij} . We can arbitrarily choose the rotation of our coordinate system. For simplicity we let $(x_{ij})_\alpha$ be along the z -axis of the coordinate system. This results in

$$T_\alpha = \int dr \int d\phi \int d\theta r^2 \sin \theta \cdot (r \cos \theta)^4 \cdot \frac{W'(r)}{r^3}. \quad (\text{VIII-62})$$

We can easily perform the ϕ and θ integrations and obtain

$$T_\alpha = \frac{4\pi}{5} \int dr r^3 W'(r). \quad (\text{VIII-63})$$

Next, we perform a partial integration, where the boundary term vanishes, since the kernel is monotonically decreasing towards zero. It remains:

$$T_\alpha = -\frac{12\pi}{5} \int dr r^2 W(r) = -\frac{3}{5}, \quad (\text{VIII-64})$$

because of the kernel normalisation condition.

3. The indices form two pairs

This last case can be calculated pretty similar, except that we have to chose two indices, which have to be unequal. We choose $\alpha = 1$ and $\beta = 3$. Again, written in spherical coordinates we get

$$T_{\alpha\beta} = \int dr \int d\phi \int d\theta \frac{r^2 \sin \theta \cdot (r \sin \theta \cos \phi)^2}{(r \cos \theta)^2 \cdot \frac{W'(r)}{r^3}}. \quad (\text{VIII-65})$$

Using the results from the r -integration before we calculate $T_{\alpha\beta} = -\frac{1}{5}$ and the total result is:

$$T_{\alpha\beta\gamma\delta} = \begin{cases} -\frac{3}{5} & \text{if } \alpha = \beta = \gamma = \delta \\ -\frac{1}{5} & \text{if } \alpha = \beta \neq \gamma = \delta \\ -\frac{1}{5} & \text{if } \alpha = \gamma \neq \beta = \delta \\ -\frac{1}{5} & \text{if } \alpha = \delta \neq \beta = \gamma \\ 0 & \text{else} \end{cases} \quad (\text{VIII-66})$$

So basically T is only non zero, if we have two pairs of indices.

All cases combined

Plugging everything back into the modified equation [VIII-29](#) gives:

$$\begin{aligned} I_{\gamma\delta} &:= 2 \int d^3x_j \frac{Q(x_j) - Q(x_i)}{|x_{ij}|^2} (x_{ij})_{\gamma} \frac{\partial W_{ij}}{\partial (x_i)_{\delta}} \\ &= - \sum_{\alpha\beta} T_{\alpha\beta\gamma\delta} \frac{\partial^2 Q}{\partial x_{\alpha} \partial x_{\beta}} \Big|_{x_i}. \end{aligned} \quad (\text{VIII-67})$$

To infer a general behaviour we take a look at an example with $\gamma = \delta = 0$

$$I_{00} = \frac{3}{5} \frac{\partial^2 Q}{\partial^2 x_0} \Big|_{x_i} + \frac{1}{5} \frac{\partial^2 Q}{\partial^2 x_1} \Big|_{x_i} + \frac{1}{5} \frac{\partial^2 Q}{\partial^2 x_2} \Big|_{x_i}. \quad (\text{VIII-68})$$

Since we want to infer an approximation for second order mixed derivatives of Q , we have to linearly combine terms for different choices of γ and δ . It can be found that,

$$\begin{aligned} \frac{\partial^2 Q}{\partial x_0^2} &= 2 \cdot I_{00} - \frac{1}{2} \cdot I_{11} - \frac{1}{2} \cdot I_{22} \\ &= 2 \cdot \frac{5}{4} \cdot I_{00} - \frac{1}{2} \cdot I_{00} - \frac{1}{2} \cdot I_{11} - \frac{1}{2} \cdot I_{22} \end{aligned} \quad (\text{VIII-69})$$

and cyclic permutation for other second derivatives. A similar formula applies for mixed derivatives. Consider for example

$$I_{01} = \frac{1}{5} \frac{\partial^2 Q}{\partial x_0 \partial x_1} \Big|_{x_i} + \frac{1}{5} \frac{\partial^2 Q}{\partial x_1 \partial x_0} \Big|_{x_i}. \quad (\text{VIII-70})$$

It is better to keep both parts separated to explicitly indicate the symmetry for simplicity in the assembly process.

From this example we get directly

$$\frac{\partial^2 Q}{\partial x_0 \partial x_1} = \frac{5}{4} \cdot I_{01} + \frac{5}{4} \cdot I_{10} \quad (\text{VIII-71})$$

and cyclic permutations.

Combining the equations (VIII-69) and (VIII-71) we see that all $I_{\gamma\delta}$ occur times a factor of 5/2 minus a trace term times 1/2. This finding is represented by the substitution equation VIII-32 in our final result.

VIII-B Analytic solution for the temperature step problem

We show the derivation of the analytic solution of the conduction equation for the temperature step test (section VIII-4.1). We start with the Fourier transformation of the specific internal energy in both directions:

$$u(t, x) = \int_{-\infty}^{\infty} u_k(t) e^{ikx} \frac{dk}{2\pi} \quad (\text{VIII-72})$$

and

$$u_k(t) = \int_{-\infty}^{\infty} u(t, x) e^{-ikx} dx. \quad (\text{VIII-73})$$

The conduction equation expressed in Fourier space is

$$\frac{du_k(t)}{dt} = -\alpha k^2 u_k(t) \quad (\text{VIII-74})$$

with the simple solution

$$u_k(t) = u_{k0} e^{-\alpha k^2 t}. \quad (\text{VIII-75})$$

Using $u(t = 0, x) = u_0(x)$ we express the unknown coefficient in terms of the initial condition in real space

$$u_{k0} = \int_{-\infty}^{\infty} u_0(x') e^{-ikx'} dx'. \quad (\text{VIII-76})$$

We insert this result into the reverse Fourier transformation (equation VIII-72) and obtain

$$u(t, x) = \int_{-\infty}^{\infty} dx' \int_{-\infty}^{\infty} \frac{dk}{2\pi} u_0(x') e^{-\alpha k^2 t} e^{ik(x-x')}. \quad (\text{VIII-77})$$

At first, we perform the integration over dk . For this we rewrite the exponentials completing the square to bring them into Gaussian form, which is a simple integration and get

$$u(t, x) = \frac{1}{2\sqrt{\alpha t}} \int_{-\infty}^{\infty} dx' u_0(x') \exp\left(-\frac{(x - x')^2}{4\alpha t}\right). \quad (\text{VIII-78})$$

At this point we need to use the specific initial conditions of our problem. For the temperature step they are defined as

$$u_0(x') = \begin{cases} u_0 - \frac{\Delta u}{2} & \text{for } x' < x_m \\ u_0 + \frac{\Delta u}{2} & \text{for } x' > x_m, \end{cases} \quad (\text{VIII-79})$$

with x_m being the position of the temperature step.

Inserting this into equation [VIII-78](#) we get two integrals to perform:

$$u(t, x) = \frac{1}{2\sqrt{\alpha \pi t}} \left[\int_{-\infty}^{x_m} dx' \left(u_0 - \frac{\Delta u}{2} \right) e^{-y^2} + \int_{x_m}^{\infty} dx' \left(u_0 + \frac{\Delta u}{2} \right) e^{-y^2} \right], \quad (\text{VIII-80})$$

where we substituted $y \equiv y(x') = \sqrt{\frac{(x - x')^2}{4\alpha t}}$.

We split this expression into two parts: One which is multiplied by u_0 and one which is multiplied by $\Delta u/2$. The u_0 term can be simply integrated, since it is again only a Gaussian integral, which results in $2\sqrt{\alpha \pi t} \cdot u_0$. For a little consistence check consider $\Delta u = 0$ then we get $u(t, x) = u_0$, which is what we would expect for a isothermal region without any other effects than thermal conduction.

To integrate the second term, with Δu , one has to rewrite the integrals to resemble the definition of error functions. The final result reads

$$u(t, x) = u_0 + \frac{\Delta u}{2} \cdot \operatorname{erf}\left(\frac{x - x_m}{2\sqrt{\alpha t}}\right). \quad (\text{VIII-81})$$

VIII-C Temperature step with vacuum boundaries

In section [VIII-4.1](#) we require a similar derivation as shown in appendix [VIII-B](#), however, we need to change the boundaries of the initial conditions given by equation [VIII-79](#) to

$$u_0(x') = \begin{cases} u_0 - \frac{\Delta u}{2} & \text{for } x_0 < x' < x_m \\ u_0 + \frac{\Delta u}{2} & \text{for } x_m < x' < x_1 \\ 0 & \text{otherwise.} \end{cases} \quad (\text{VIII-82})$$

This leads to finite integral boundaries in the x -integration which be written again in terms of the error function

$$u(t, x) = u_0 \cdot [\operatorname{erf}(y(t, x_1)) + \operatorname{erf}(y(t, x_0))] + \frac{\Delta u}{4} \cdot [-\operatorname{erf}(y(t, x_1)) + 2 \cdot \operatorname{erf}(y(t, x_m)) - \operatorname{erf}(y(t, x_2))] \quad (\text{VIII-83})$$

, which behaves perfectly fine for $x_0 \rightarrow -\infty$, $x_1 \rightarrow \infty$. However, if we let $t \rightarrow \infty$ then $y \rightarrow 0$ and therefore $u \rightarrow 0 \neq u_0$. Mathematically the difference lies in two integrals of infinite integration length with integrand zero. Physically this can be understood as heat dissipating into the boundaries given by x_0 and x_1 . Therefore, it is not possible in a straight forward way to extract an analytic solution for these modified, finite initial temperature step.

Chapter IX

Galaxy cluster code comparison: The 300

Machines take me by surprise with great frequency.

– Alan Turing

This chapter describes the ongoing work of a galaxy cluster code comparison project which started with [Sembolini et al., 2016a](#) as the *nIFTy* galaxy clusters simulations and is now going on as *The Three Hundred*. The basic idea behind this study is to simulate identical initial conditions for galaxy clusters with different numerical codes in order to learn about which aspects result from certain physics modules or maybe are purely of a numerical origin. This is where the code diversity discussed in chapter [III](#) can really pay off.

This chapter is subdivided into four main parts: At first we describe the parent cosmological simulation box and elaborate on the process of making zoom simulations. Then we briefly present the projects that have been carried out and published already and finish with a description of the ongoing project and a list of the current science goals. We have to keep this description very brief as the new projects are just kicking off.

IX-1 The MultiDark parent simulation

The whole project builds upon the MultiDark cosmological box¹ which was first introduced by [Prada et al., 2011](#). The box used in MultiDark run 1 has a side length of $1h^{-1}Gpc$ and contains 2048^3 dark matter particles which leads to a particle mass of $8.63 \cdot 10^9 h^{-1} M_\odot$ and a gravitational softening of $7h^{-1}kpc$ (see section [III-5.1](#)).² The simulation was carried out with a Λ CDM cosmology with parameters based on *WMAP-5*. [Klypin et al., 2014](#) present a similar cosmological simulation but following the cosmological parameters given by *PLANCK* (see chapter [I](#)) and with a significantly higher resolution of 3840^3 particles. Figure [IX.1](#) shows slices of the resulting density distributions of both runs respectively at redshifts $z = 0.53$ and $z = 0.51$. Both beautifully illustrate the cosmic web which is generated by initial density

¹Also called BigBolshoi due to being the successor of the Bolshoi simulation

² h is the dimensionless Hubble parameter $h = H_0/100 sMpc/km$.

fluctuations and evolving gravity for collision-less cold dark matter. Besides effects from the increased resolution, which makes the right image look much more finely grained, the effect of the slightly different cosmological parameters employed can hardly be seen by the naked eye.

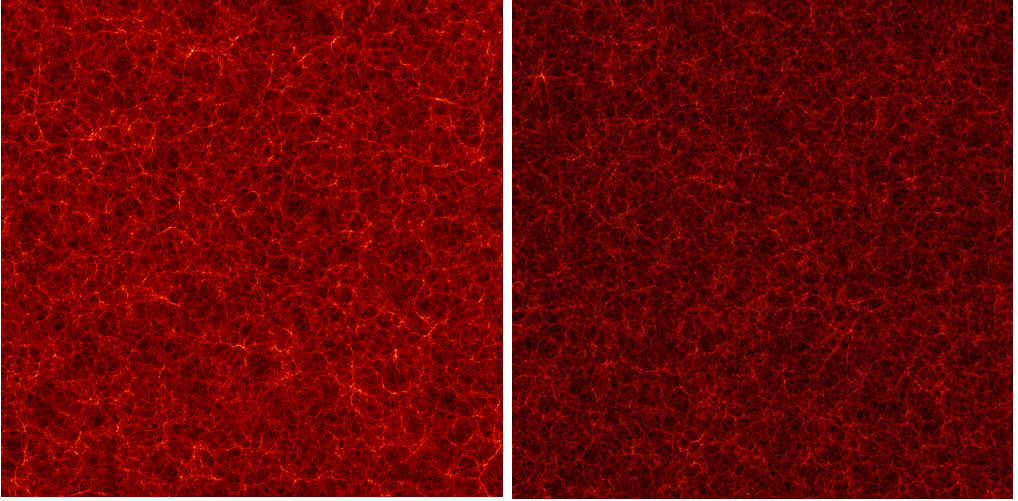


Figure IX.1: Left: Density structure of the MultiDark box run 1 at redshift $z = 0.53$. Right: Density structure of the higher resolution box with *PLANCK* cosmology at $z = 0.51$. Note the slightly different redshifts due to different output strategies.

IX-2 Zoom simulations

As initial conditions for the code comparison project, the technique described in [Klypin et al., 2001](#) has been used to extract regions out of the big cosmological boxes and to improve the resolution simultaneously. The basic process is as follows. First one selects all particles inside a sphere of a sensible radius around the object to re-simulate. In this case a sphere with radius $6h^{-1}Mpc$ around a galaxy cluster centre at redshift $z = 0$ was taken. This set of particles is then tracked back to the initial conditions to identify a Lagrangian region which is responsible for the formation of this cluster. This region is then taken and it's dark matter particles are split up to improve the resolution. The same is done to achieve initial conditions with gas particles. Typically each dark matter particle is split into two particles of similar mass, one being dark matter and the other gas. Proper placement of the resulting particles ensures that the resulting gravitational potential is not altered.

This process is further enhanced by including several resolution steps with different amounts of dark matter particles. The GADGET code typically assumes three levels. These can be subdivided into high resolution dark matter particles, which actually form the cluster halo and two steps of lower resolution which do not actually collide with the cluster material but pose as a sample points for a realistic environment in order to keep the large scale evolution intact without wasting computing time on these regions. A typical configuration is shown in figure IX.2.

[Sembolini et al., 2016a](#) started with the MUSIC-2 sample extracted from the MultiDark run 1.

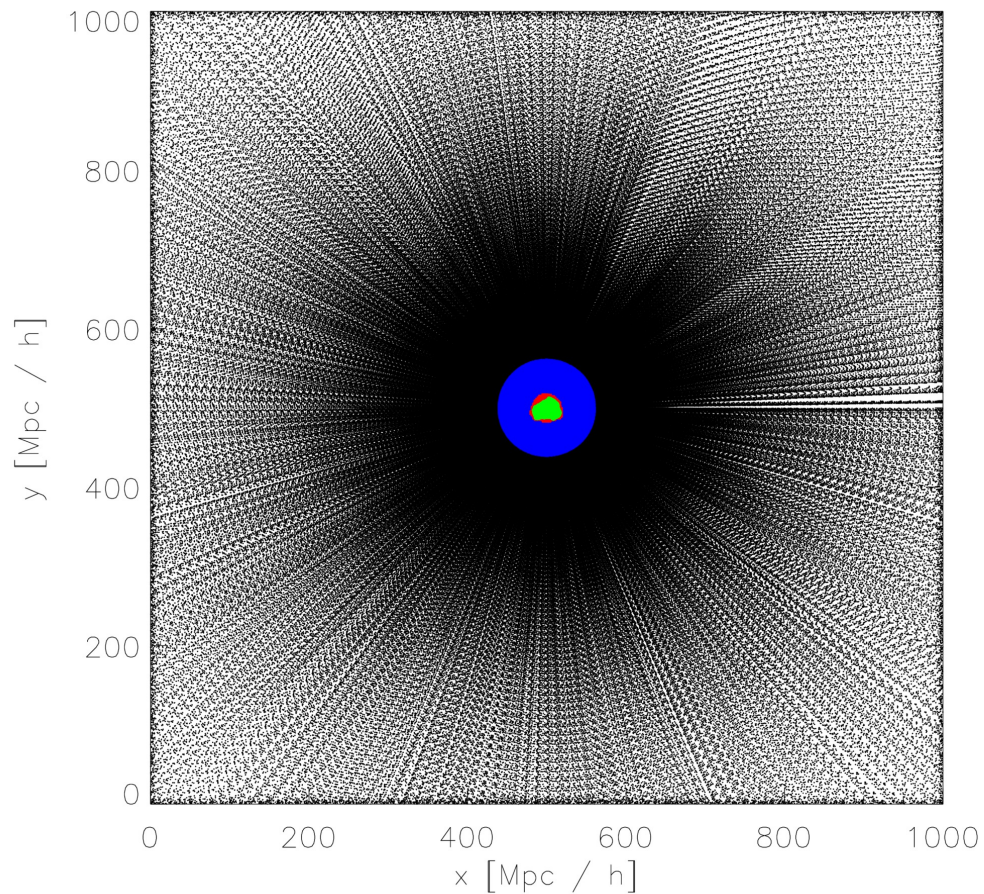


Figure IX.2: Typical particle configuration of zoomed initial conditions with three different resolution steps of dark matter particles in black, blue and red and gas particles in green.

The abbreviation term *MUSIC* stands for **M**ULTidark **S**Imulations of galaxy **C**lusters. The MUSIC-2 sample contains a total of 545 zoom initial conditions of central objects in a mass range of $5 \cdot 10^{13} h^{-1} M_{\odot} < m < 10^{15} h^{-1} M_{\odot}$ at redshift $z = 0$. For the ongoing projects over 300 new initial conditions from the MultiDark Planck box have been produced in different resolution stages. The corresponding data can be accessed online.

The evolution of one of the new clusters is shown in figure IX.3. These plots have been generated using the SPLOTCH ray-tracing program (Dolag et al., 2008) using the specific internal energy as colour scale and the gas density as intensity.

IX-3 nIFTy: What has been achieved so far

The nIFTy project spawned eight papers so far of which we describe some briefly. Before the galaxy cluster comparisons began, Knebe et al., 2015 actually started by comparing different galaxy formation models on top of a $62.5 h^{-1} Mpc$ side length box, exploring 14 different semi-analytic and halo-occupancy distribution models. So far we have not mentioned these techniques in this thesis so a brief explanation is of order. Basically a dark matter only simulation is taken. In there a halo finder is used to identify gravitationally bound structures. The growth history of these structures is investigated creating a so called merger tree. Then a model is applied, which assigns several properties to each halo depending on the collected data, like the baryon fraction, metallicity or star formation rate. These are not simulated directly, but calculated from a stochastical model using various assumptions.

As mentioned earlier, the first nIFTy paper regarding galaxy cluster comparisons was Sembolini et al., 2016a presenting a comparison of dark matter only runs and simulations including non-radiative gas physics.³ The comparison includes classical AMR (see section III-2.1), moving mesh (see section III-4.1) and several different SPH codes (mostly GADGET2 or GADGET3 based), including our modernised code there called G3-X (see chapter V) and the very similar one used for the MAGNETICUM simulations G3-Magneticum (see chapter XI). The outcome of the dark matter comparison is unsurprisingly similar as the gravity solver is actually the same in most of the employed codes. Nevertheless, differences of the order of a few percent, which might be at least partially of numerical origin, remain in the resulting density profiles. Including gas physics increases the deviations by a lot, especially regarding the central concentration of gas and the radial temperature profiles. The latter, as shown in figure IX.4, reveals very drastic differences regarding the central temperature of the resulting cluster depending on the chosen numerical method, as we have hinted towards already in chapter I. Even in the midst of different flavours of GADGET there is hardly any agreement if the core in that cluster should be cool or not. This can serve as eye opener, why the diversity of different numerical methods and codes is important, as to learn about how large the effects of for example bad mixing can become globally (see also chapter III). Luckily some sort of consensus seems to emerge, as some of the more modern code choices tend to agree with each other: AREPO, G3-X and G3-SPHS.

The next logical step was to include radiative physics as presented by Sembolini et al., 2016b. Now the different codes do not only represent various numerical techniques but also incorporate different subgrid models to handle cooling, star formation, chemistry and stellar and AGN feed-

³Meaning no radiative cooling, feedback or such processes.

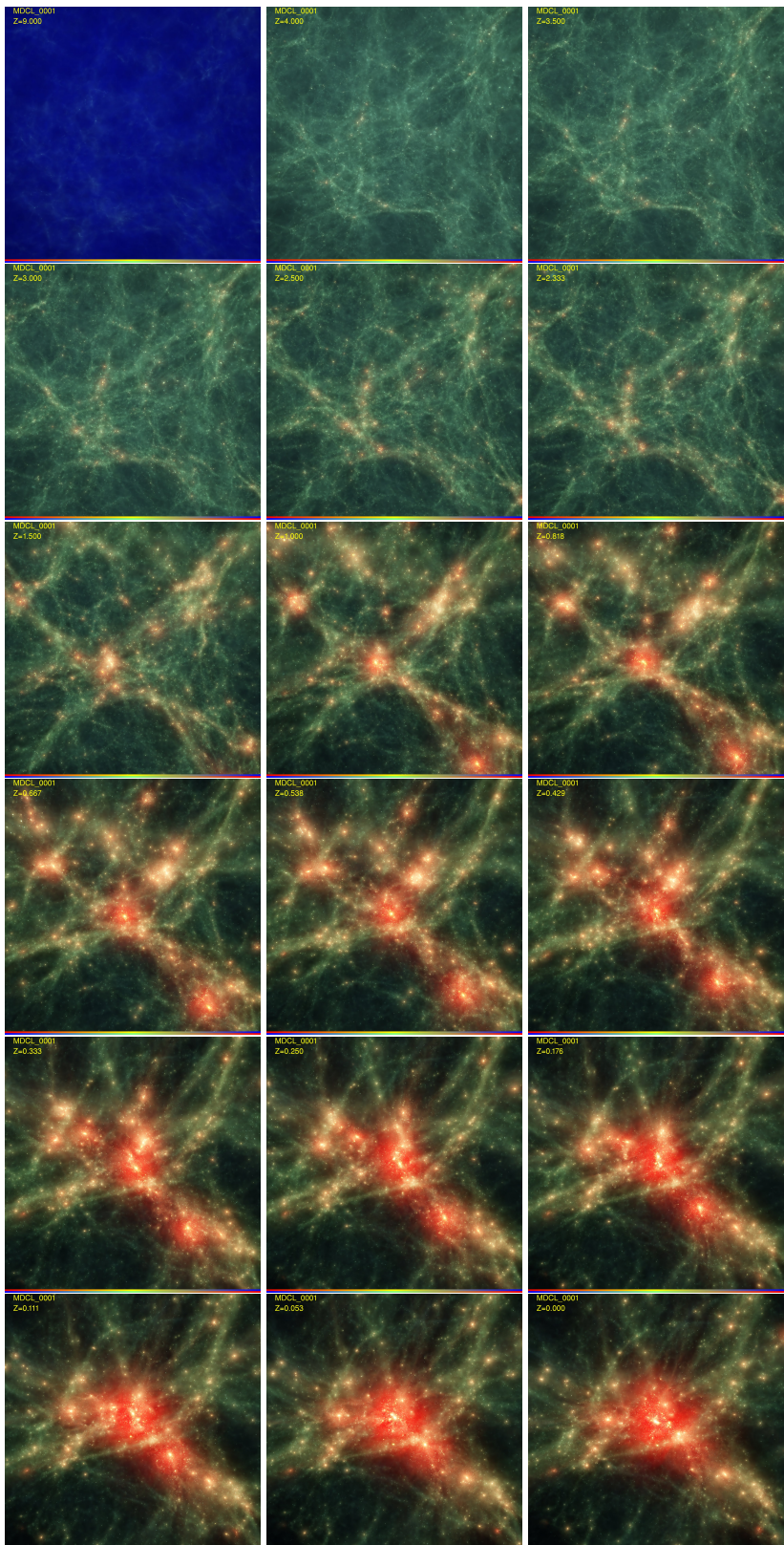


Figure IX.3: Evolution of a zoomed galaxy cluster simulation taken from the MUSIC web page <http://music.ft.uam.es/2012-06-20-09-53-16/radiative/2015-05-06-01-02-28>.

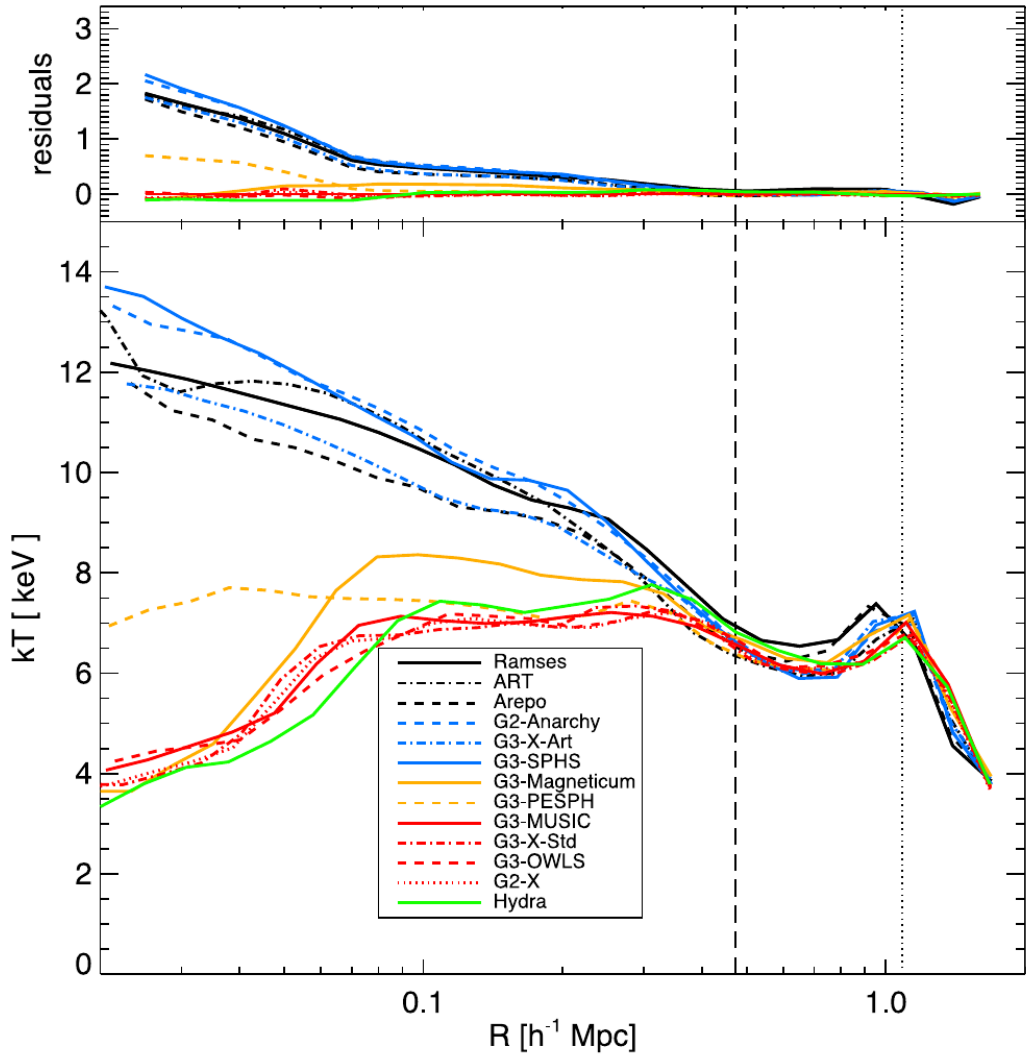


Figure IX.4: Comparison of radial temperature profiles of the same galaxy cluster simulated with different codes without radiative physics included. Taken from [Sembolini et al., 2016a](#).

back. Radial temperature distributions are much less clear to distinguish now but come actually into better agreement than before while density distributions show a degree of scatter which removes any clear distinguishing between older and modernised or grid and SPH codes.

After these very general comparisons, more detailed analyses could be carried out, including a more in depth look into galaxies and small subhaloes (Elahi et al., 2016), investigations towards the actual impact of baryonic physics (Cui et al., 2016), studies of infalling galaxies (Arthur et al., 2016) and again a comparison of galaxy formation models on top of the dark matter simulation (Pujol et al., 2017).

IX-4 The Three Hundred

The nIFTy comparison papers only considered one single galaxy cluster simulated with different codes. The next step “The Three Hundred” goes a step further, extending this comparison to a large variety of galaxy cluster initial conditions, allowing to make better statistically driven statements. Since the first code comparisons revealed already some insight into the effects of different numerical techniques this project is carried out with a reduced amount of numerical codes. These are GADGETMUSIC (which was used initially for all the simulations; for the first data release see Knebe et al., 2018), GADGETX (as representative of the different GADGET flavour which produced excellent results so far), GIZMO (a new addition to get meshless techniques on board; for a description see section III-4.1) and RAMSES (a classical grid code). Additionally, three different semi analytic models participate in the comparison project: Galacticus (Benson, 2011; Benson et al., 2012; Benson, 2012), SAG (Cora et al., 2018a; Cora et al., 2018b) and SAGE (Croton et al., 2016a; Croton et al., 2016b). The sample of initial conditions is divided up into two: The “Enomotia”⁴, which contains a selected sub-sample of 36 diverse clusters (a reference one, relaxed and non-relaxed ones, different sizes and mass assembly histories and some resembling observations of the Hubble frontier fields), and the “Lochos”⁵, which contains all 324 different initial conditions. Some of the regions selected even contain only structures not bigger than galaxy groups: $M < 10^{13} M_{\odot}$. For a spread sheet covering some basic properties of all these we refer to https://docs.google.com/spreadsheets/d/1TSvNpkQEsIjgTylIM1SsDsIi2s-Ly-QaXQqpE_XfG2c/edit#gid=0.

Although the project has been kicked off already in 2016, the most time so far has been spent in actually running all simulations, verifying the outputs and reducing the data. For example one GADGETX snapshot took up originally about 1.8GB of storage, which could be reduced to about 700MB. For each simulation 130 snapshots were generated, which in total comes down to about 30TB just for the runs with this one code. The most time was actually not even spent with the simulations themselves but with copying, reducing and archiving all the data. The Enomotia runs are done for all codes, but all codes besides the two GADGET ones are still running part of the Lochos.

Additionally, some of the Enomotia initial conditions were re-generated with 8 times higher resolution, to also allow resolution studies. This amounts to a rather small dark matter particle mass of $1.6 \cdot 10^8 h^{-1} M_{\odot}$, which is equivalent to a $1h^{-1} Gpc$ box with 7680^3 particles.

⁴Named after the smallest unit of the ancient Spartan army.

⁵Named after a big unit of the ancient Greece army.

To validate the data and make comparable analyses especially with semi analytic models possible, the next step was the evaluation of different halo finder results. Now the Amiga Halo Finder (AHF, see [Gill, Knebe, and Gibson, 2004](#); [Knollmann and Knebe, 2009](#)) and VELOCIraptor ([Elahi, Thacker, and Widrow, 2011](#); [Elahi et al., 2013](#), <https://github.com/pelahi/VELOCIraptor-STF>) are used to generate information about structure and structure growth. At this point we can only give very short insight into the projects currently spawning from these data, as not even all data have been generated yet. First, some very general comparisons like the previous papers will have to be of order, just to validate and improve the previous results. These can be extended by the comparison with the semi-analytic models, looking for example at stellar mass functions. The vastness of data provides us with the possibility for proper comparison to observations by looking at statistics of cluster morphology and X-ray mock observations. Other applications are for example to look into galaxy properties depending on their environment, investigate gas stripping and flows of cold gas. This list can go on and on and we will have to see what happens next. But one thing is clear, the opportunities to make statements about physical models rather independent of a numerical setting provided by these data are very promising.

Chapter X

Magnetic driven winds: Break up of a galaxy

Science is nothing but perception.

– Plato

In this chapter we investigate the effects of a realistic circumgalactic medium (CGM) and the presence of magnetic fields onto the evolution of a disk galaxy. We describe in detail the process used to create the required initial conditions, which could now be done easier by using our tool described in chapter IV. We simulate differently sized galaxies and compare the outcome due a primordial magnetic field to those of a magnetic seeding models based on supernovae. This chapter is based on a modified version of the paper draft of Steinwandel, Beck, Arth, Dolag, Moster, Nielaba in prep. whose publication will be pursued in the near future.

X-0 Abstract

We present simulations of isolated disk galaxies in a realistic environment performed with the highly parallelised Tree-SPMHD-Code GADGET-3. Our simulations include a spherical circumgalactic medium (CGM) surrounding the galactic disk, which is represented by a hot gas halo. The CGM is motivated by observations and cosmological simulations. We present three galactic models with different halo masses and two different seeding models for the magnetic field. For each halo mass we perform a simulation without magnetic field and one run for each magnetic field model. Thus, we get in total nine simulations with various spatial resolutions and a wide range of halo masses. We are interested in the interaction between the CGM of our galaxies, the inter stellar medium (ISM) of the galactic disk and the influence of the CGM on the star formation rate of the galactic disk. In addition we show the structure and evolution of the magnetic field in both, the galactic disk and the CGM and present results which underpin the presence of a biconal magnetic driven outflow in our simulations.

X-1 Introduction

Magnetic fields are a very important component of the Universe and are essential for describing many processes in theoretical astrophysics correctly. The relevance of magnetic fields range from the small scales in star formation and in the interstellar medium (ISM) over galaxies and their circumgalactic medium (CGM) to galaxy-clusters and the large scale structure of the Universe. While there is a large amount of observational data when it comes to magnetic fields, especially in the field of galaxy formation and evolution (i.e. [Hummel, 1986](#); [Chyzy et al., 2003](#); [Chyzy et al., 2007](#); [Beck, 2007](#)) there are just a few simulations in the field of numerical astrophysics which include detailed studies about the behaviour of magnetic fields, like [Kotarba et al., 2011](#), [Pakmor and Springel, 2013](#), [Beck et al., 2016](#) or [Rieder and Teyssier, 2016](#).

In the case of galaxies the magnetic field becomes important for several reasons. On the one hand the magnetic field acts as an additional pressure component, and thus it is required as a correction of the equations of hydrodynamics, resulting in the well known equations of ideal magneto-hydrodynamic. This means that if the magnetic field is large enough to reach a value where it introduces a pressure which is comparable to the thermal pressure and therefore has a non negligible effect on the dynamical evolution, it is necessary to include it in simulations. Often this is not the case and pure hydrodynamical simulations are used to study the dynamics of galactic disks arguing that magnetic fields are not that important for the galaxies dynamical evolution ([Beck, 2009](#)).

Additionally, magnetic fields can be very important for star formation and the regularization of cosmic rays and should not be excluded when these processes are taken into account.

Observationally there are a few methods to measure the magnetic field in galaxies. [Brown et al., 2007](#) investigate the magnetic field of the inner Milky Way using rotation measurements of 148 objects behind the galactic disk. Furthermore, magnetic fields of nearby galaxies can be determined using the radio synchrotron emission of these objects. In this case the unpolarized component of the magnetic field is important because it is needed to explain galactic dynamics and magnetic driven outflows ([Beck et al., 2016](#)). Radio synchrotron emission is also used to calculate the magnetic field strengths in nearby galaxies which leads to $20 - 30 \mu\text{G}$ in the spiral arms and to $50 - 100 \mu\text{G}$ in the galactic centre, as shown in [Beck et al., 2016](#). [Robishaw, 2008](#) presented measurements of magnetic fields due to Zeeman-splitting emission in OH-Megamasers of five ultra luminous infrared galaxies leading to magnetic field strengths along the line of sight between 0.5 and 18 mG. Beyond the observations of the magnetic fields in galactic disks there are also observations of the magnetic fields of the CGM of galactic disks. [Carretti et al., 2013](#) present measurements of magnetized outflows towards the CGM of the Milky Way in two giant lobes located in the north and south of the galactic centre with a magnetic field strength of around $15 \mu\text{G}$.

However, when it comes to simulations of isolated disk galaxies the CGM of the observed system is typically neglected. Therefore, we present a new set of simulations of isolated disk galaxies explicitly including the CGM of these galaxies. Recent observations of the Milky Way's CGM ([Miller and Bregman, 2013](#)) indicate that the Milky-Ways CGM can be described using a β -powerlaw ([Cavaliere and Fusco-Femiano, 1978](#)) for its density distribution. The β -powerlaw is quite popular in studies of globular clusters ([Plummer, 1911](#)) and cosmological simulations of

galaxy-clusters (i.e [Donnert, 2014](#)). The CGM is typically neglected in simulations of isolated disk galaxies to reduce the number of particles and save the computational effort in this simulations. Furthermore, when it comes to pure dynamics the CGM is merely irrelevant. However, an obvious reason for including the CGM is that it can be found in observations and it helps to get a more realistic model for an isolated disk galaxy. Furthermore, by including the CGM it is possible to fix some severe problems in this kind of simulation. Typically, simulations of isolated disk galaxies are performed by centring the galactic disk in a box and let the system evolve with time. This results in unrealistic boundary conditions at the edge of the disk, where the density lowers from a typical density value in a galactic disk to zero in an instant. The presence of the CGM in such a simulation leads to a more realistic scenario and we are able to study the interaction between the galactic disk and its CGM directly from the simulation. In the SPMHD formalism the magnetic field is a property of the gas particles only. Therefore, one needs a carrier for the magnetic field, which gives further justification for the presence of the CGM in our simulations. As mentioned above there are not many simulations of disk galaxies in isolation. [Wang and Abel, 2009](#) investigate the magnetic field in isolated disk galaxies without star formation using the grid Code ENZO ([Bryan and Norman, 1997](#), [O’Shea et al., 2004](#)). [Dubois and Teyssier, 2010](#) studied the magnetic field of dwarf galaxies with a closer look on winds driven by stars using the grid Code RAMSES ([Teyssier, 2002](#)). [Pakmor and Springel, 2013](#) and [Rieder and Teyssier, 2016](#) present studies of magnetic fields for isolated galaxy formation by collapsing a giant gas halo in a dark matter potential. While [Pakmor and Springel, 2013](#) investigates general properties of the magnetic field, [Rieder and Teyssier, 2016](#) points out the importance of feedback. Another detailed study of magnetic fields in isolated disks is presented in [Butsky et al., 2017](#) where they find a small scale turbulent dynamo of the magnetic field. The same behaviour can be found in cosmological zoom simulations presented in [Pakmor et al., 2017](#).

There are also studies of the magnetic field evolution using particle methods. [Kotarba et al., 2009](#) investigates the magnetic field in an isolated disk galaxy using GADGET-3. In [Kotarba et al., 2010](#), [Kotarba et al., 2011](#) as well as in [Geng et al., 2012a](#), [Geng et al., 2012b](#) GADGET-3 is used to study the magnetic field in galaxy-mergers. [Beck et al., 2016](#) is looking to the magnetic field structure of the Milky Way in more detail.

In this paper we aim to put the simulations of isolated disk galaxies to the edge in terms of resolution with the appropriate star formation models of GADGET-3 and investigate the behaviour if we include a well shaped CGM in our simulations. Furthermore, we can look into the structure of the magnetic field in the disk and the CGM as well as the interaction of the CGM and the galactic disk. On top of that we will investigate the ability of the magnetic field to drive an effective wind in our simulations.

X-2 Simulation Method

The simulations we present in this paper were performed using the highly parallelised Tree-SPH-Code GADGET-3, the developer version of the public available GADGET-2 code ([Springel, 2005a](#)). In our simulations we use a modern implementation of SPH, as presented in [Beck et al., 2016](#). This SPH formulation includes various improvements like higher order SPH-Kernels described by [Dehnen and Aly, 2012](#), a time step limiter, time dependent artificial viscosity and

a new model for time dependent artificial conduction. GADGET-3 further includes magnetic fields and magnetic dissipation (Dolag and Stasyszyn, 2009). We also include star formation, cooling, supernova-feedback and metals following Springel and Hernquist, 2003. Furthermore, one of our models for the magnetic field couples the seed rate of the magnetic field directly to the supernova rate within the ISM, which is the model presented in Beck et al., 2013a. In this section we summarize the used SPH formalism in a very compact way and introduce the physical models we use.

X-2.1 Kernel function and density estimate

We use the density-entropy formulation of SPH, which means, that we smooth the density distribution in the way

$$\rho_i = \sum_j m_j W_{ij}(x_{ij}, h_i), \quad (\text{X-1})$$

where h_i is the smoothing-length. The sum in equation X-1 is performed over the neighbouring particles. $W_{ij}(x_{ij}, h_i)$ is the smoothing kernel with the property

$$W_{ij}(x_{ij}, h_i) = \frac{1}{h^3} w(q), \quad (\text{X-2})$$

with $q = |x_{ij}| / h_i$. In our simulations we use the Wendland C4 function for $w(q)$, with 200 neighbouring particles. The function $w(q)$ is given by

$$w(q) = \frac{495}{32\pi} (1 - q)^6 (1 + 6q + \frac{35}{3}q^2), \quad (\text{X-3})$$

for $0 < q < 1$. For $q > 1$ we set $w(q)$ to zero. We are aware that the Wendland C6 Kernel as presented by Dehnen and Aly, 2012 gives an even better density estimate as the C4 Kernel. However, the C6 Kernel needs around 300 particles to work at its optimum. This results in a higher computational effort for the SPH loop. Because our simulations are performed with very high particle numbers, compared to other simulations of isolated disk galaxies, we suggest that the Wendland C4 is sufficient enough when it comes to the estimation of the SPH-density. The overage of CPU-time can then be used to increase the mass resolution of our simulations.

X-2.2 SPH and SPMHD formulation

It is possible to derive the equation of motion in both, the hydrodynamical and the magnetohydrodynamical case from a discrete Lagrangian, via the principle of least action. This has been presented in Price, 2012b, resulting in the SPH or SPMHD formulation. Because we need both formulations in our simulations, we shortly present the equation of motion in both cases. The SPH-formulation of the equation of motion (EOM) is given by

$$\frac{d\mathbf{v}_i}{dt} = - \sum_j m_j \left[f_j^{\text{co}} \frac{P_j}{\rho_j^2} \frac{\partial W_{ij}(h_i)}{\partial \mathbf{r}_i} + f_j^{\text{co}} \frac{P_j}{\rho_j^2} \frac{\partial W_{ij}(h_j)}{\partial \mathbf{r}_i} \right]. \quad (\text{X-4})$$

with

$$f_j^{\text{co}} = \left[1 + \frac{h_j}{3\rho_j} \frac{\partial \rho_j}{\partial h_j} \right]^{-1}. \quad (\text{X-5})$$

The formulation of equation X-4 conserves energy, momentum and angular momentum per construction. For SPMHD, the EOM takes the form

$$\begin{aligned} \frac{d\mathbf{v}_i}{dt} = & - \sum_j \left[\frac{P_i + \frac{1}{2\mu_0} B_i^2}{\Omega_i \rho_i^2} \nabla_i W_{ij}(h_i) + \frac{P_j + \frac{1}{2\mu_0} B_j^2}{\Omega_j \rho_j^2} \nabla_i W_{ij}(h_j) \right] \\ & + \frac{1}{\mu_0} \sum_j m_j \left[\frac{\mathbf{B}_i (\mathbf{B}_i \cdot \nabla_i W_{ij}(h_i))}{\Omega_i \rho_i^2} + \frac{\mathbf{B}_j (\mathbf{B}_j \cdot \nabla_i W_{ij}(h_j))}{\Omega_j \rho_j^2} \right]. \end{aligned} \quad (\text{X-6})$$

We note, that the magnetic field influences the EOM in two ways. At first the presence of the magnetic field generates a pressure alongside the thermal pressure of the fluid, which scales with \mathbf{B}^2 . We note further, that there is a second term which is introduced for numerical stability of the SPMHD formulation. In general, the second term is needed to fulfil the $\nabla \cdot \mathbf{B} = 0$ constraint. For SPMHD energy and linear momentum are conserved down to machine precision. However, angular momentum is violated due to the fact that the second term in equation X-6 is anisotropic and therefore not invariant under rotation of the system.

X-2.3 Advanced SPH Methods

We use time dependent artificial viscosity and time dependent artificial conductivity as described in detail in [Beck et al., 2016](#) to control discontinuities and density jumps much better. We note that in the case of artificial conduction we need a gravity limiter, because the rate of change of the artificial conductivity is determined using the gradient of the internal energy. In our case the pressure gradient is dominated by gravity which leads to unwanted conduction. The details of this procedure are described in [Beck et al., 2016](#). Furthermore, we use a particle wake-up scheme, which we need because of the adaptive time-stepping-algorithm in GADGET-3. In this algorithm particles are split into active and inactive particles. We integrate the hydrodynamical quantities of the fluid for the active particles, while the inactive particles sleep and wait for their larger individual time step. If a particle is moving with high velocity, it may happen, that it penetrates the region of inactive particles. These particles need to wake up and interact with the high velocity particle. This procedure is similar to the time-step-limiter of [Dalla Vecchia and Schaye, 2012](#). Furthermore, we need to mention, that artificial-viscosity and artificial-conductivity fix the above mentioned problems in terms of shock capturing and fluid mixing, but violate the conservation of angular momentum. We conserve angular momentum up to the artificial viscosity and conductivity terms.

X-2.4 Cooling, Star formation and Supernova Seeding

We briefly describe the cooling, star formation and the supernova-seeding approach that is used in a subset of our simulations. We include cooling as described in [Katz, Weinberg, and Hernquist, 1996](#). In this framework, cooling is mainly driven due to collisional excitation of H^0 and He^+ , collisional ionization of H^0 , He^0 and He^+ , recombination of H^+ , He^+ and He^{++} , Di-electronic recombination of He^+ and free-free emission (thermal Bremsstrahlung emission). The cooling rates are then calculated via the assumption of ionization equilibrium and optically thin gas.

We use the stochastical star formation approach, presented in [Springel and Hernquist, 2003](#). In this model stars are formed in a way that they resemble the Kennicutt-Schmidt law of star formation-density. In the simulations where we calculate the magnetic field but don't use a primordial constant magnetic field, we use the supernova seeding presented in [Beck et al., 2013b](#).

X-3 Initial conditions

At first we want to discuss the initial conditions that represent our setup. Our setup contains an isolated disk galaxy, surrounded by a spherical CGM.

For the setup of the disk, we use the method described in [Hernquist, 1993](#). A more detailed documentation can be found in [Springel and White, 1999](#), [Springel, 2000](#) and [Springel, Di Matteo, and Hernquist, 2005](#).

In this method we construct a model for a spiral disk galaxy, consisting out of a dark matter halo, a bulge, a stellar and a gas disk. The dark matter halo and the bulge are spherical and follow the density shape of a Hernquist-profile. The stellar and the gas disk follow surface-density-profiles known from observations. The surrounding CGM is a spherical gas halo, constructed using a β -model ([Cavaliere and Fusco-Femiano, 1978](#)) for the density distribution. In this paper we prepare the initial conditions for three galaxies with $10^{10} M_\odot$, $10^{11} M_\odot$ and $10^{12} M_\odot$. These represent a dwarf galaxy, a middle size shaped galaxy and a Milky Way-like galaxy. We introduce the abbreviations *LWM* for the $10^{10} M_\odot$ galaxy, *MWM* for the $10^{11} M_\odot$ galaxy and *HWM* for the $10^{12} M_\odot$ galaxy without magnetic fields. Furthermore, we perform runs with two different magnetic field models. The first model uses a constant magnetic seed field in the x-direction. For this magnetic field model we introduce the abbreviations *LBX*, *MBX* and *HBX* respectively. The second magnetic field model is the supernova-seeding model presented in [Beck et al., 2013a](#). For this model we introduce the abbreviations *LBS*, *MBS* and *HBS* respectively. The models with the same mass are totally equal in terms of the general physical properties, but they are divided by the implementation of the magnetic field.

In table [X.1](#) we present the particle numbers used in our models and list the mass resolution as well as the gravitational softening lengths, which we calculated via the recursive formula:

$$\epsilon_{\text{new}} = \epsilon_{\text{old}} \cdot \left[(N^{\text{old}}/N^{\text{new}}) \cdot M_{200}^{\text{new}}/M_{200}^{\text{old}} \right]^{1/3} \quad (\text{X-7})$$

Particle Numbers				
		LMG	MMG	HMG
Gas disk	$N_{\text{gd}} [10^6]$	0.8	1.0	1.2
Gas halo	$N_{\text{gh}} [10^6]$	5.0	6.0	7.0
Stellar disk	$N_{\text{sd}} [10^6]$	3.2	4.0	4.8
Stellar bulge	$N_{\text{b}} [10^6]$	1.3	1.6	2.0
Dark matter	$N_{\text{dm}} [10^6]$	4.6	5.7	6.9
Mass resolution				
		LMG	MMG	HMG
Gas particles	$m_{\text{gas}} [M_{\odot}]$	72	510	4800
Star particles	$m_{\text{star}} [M_{\odot}]$	72	510	4800
Dark matter	$m_{\text{dm}} [M_{\odot}]$	1440	10200	96000
Gravitational softening				
		LMG	MMG	HMG
Gas particles	$\epsilon_{\text{gas}} [\text{pc}]$	20	20	20
Star particles	$\epsilon_{\text{star}} [\text{pc}]$	20	20	20
Dark matter	$\epsilon_{\text{dm}} [\text{pc}]$	83	83	83

Table X.1: Number of particles mass resolution and gravitational softening lengths.

X-3.1 Dark matter halo

The dark matter halo is described using a Hernquist-profile for its density distribution (Hernquist, 1993). The radial density profile $\rho_{\text{dm}}(r)$ of the halo then follows:

$$\rho_{\text{dm}}(r) = \frac{M_{\text{dm}}}{2\pi} \frac{a}{r(r+a)^3}, \quad (\text{X-8})$$

where M_{dm} is the mass of the dark matter halo. The parameter a describes the relation between the halo concentration CC and the scale length r_s of the well known Navarro-Frenk-White-profile (NFW-profile, see Navarro, Frenk, and White, 1997). We use the Hernquist-profile because it declines faster in its outer regions than the NFW profile, which makes any artificial truncation unnecessary (Springel, Di Matteo, and Hernquist, 2005).

X-3.2 Bulge, stellar and gaseous disk

The stellar disk and the stellar bulge of the galaxy is modelled by collision less N -body particles with an exponential stellar disk and a stellar bulge following a Hernquist-profile (Springel, Di Matteo, and Hernquist, 2005). Additionally, a gaseous disk is modelled by SPH particles. The density of the stellar bulge is then given by:

$$\rho_b(r) = \frac{M_b}{2\pi} \frac{l_b}{r(r+l_b)^3}, \quad (\text{X-9})$$

using the scale length l_b of the bulge as free parameter.

The mass of the bulge is given by $M_b = m_b M_{200}$, where m_b is the dimensionless bulge mass fraction.

The exponential surface densities of the stellar and the gaseous disk are given by Σ_\star and Σ_{gas} :

$$\Sigma_\star = \frac{M_\star}{2\pi l_d^2} \cdot \exp\left(-\frac{r}{l_d}\right), \quad (\text{X-10})$$

$$\Sigma_{\text{gas}} = \frac{M_{\text{gas}}}{2\pi l_d^2} \cdot \exp\left(-\frac{r}{l_d}\right), \quad (\text{X-11})$$

using the scale length l_d of the disk. The mass of the disk is given by $M_d = (M_\star + M_{\text{gas}}) = m_d M_{200}$, with the dimensionless disk mass fraction m_d . We take a fraction f of the disks mass to compose the gaseous disk, which consists of SPH-particles. The remaining particles of the disk are collision less N-body particles of stellar type. The mass which does not belong to the bulge or to the disk can be assigned to the dark matter halo. So the mass of the dark matter halo is given by $M_{\text{dm}} = M_{200} - (m_b + m_d) \cdot M_{200}$. Finally, the system is given an angular momentum through the spin parameter λ . From this spin parameter it is possible to calculate the total angular momentum as described in [Mo, Mao, and White, 1998](#) via:

$$J_{200} = \lambda \cdot G^{\frac{1}{2}} M_{200}^{\frac{3}{2}} \cdot r_{200}^{\frac{1}{2}} \left(\frac{2}{f_{\text{CC}}} \right) \quad (\text{X-12})$$

We can now calculate the angular momentum of the galactic disk, using the disk spin fraction, which is typically set to exactly the same value, we adopt for the disk mass fraction. In this case one could calculate the angular momentum of the galactic disk, by multiplying the total angular momentum of the system given by J_{200} with the disk spin fraction j_d , thus the equation $J_d = j_d \cdot J_{200}$ holds. The factor f_{CC} can be calculated following [Mo, Mao, and White, 1998](#) with:

$$f_{\text{CC}} = \frac{CC}{2} \frac{1 - 1/(1 + CC)^2 - 2\ln(1 + CC)/(1 + CC)}{[CC/(1 + CC) - \ln(1 + CC)]^2} \quad (\text{X-13})$$

All parameters we discussed so far are listed in table [X.2](#). These parameters characterize our galactic system completely.

X-3.3 Initial values for the multi phase model of star formation

In our simulations we use the initial values for the multi phase model of star formation, given in table [X.3](#). The model itself is shortly described in section [X-2.4](#). For a closer look into the model we recommend [Springel and Hernquist, 2003](#) where the details of the model are explained in more details. We calibrate the star formation model using a Schmidt-Kennicut-plot for each galactic system we present and obtain the values presented in table [X.3](#) which are in accordance with [Springel and Hernquist, 2003](#).

Disk Parameters				
		HMG	MMG	LMG
Total mass in $[10^{10} M_{\odot}]$	M_{200}	100	10	1
Virial velocity in [km/s]	v_{200}	145	67	31
Virial radius in [kpc/h]	r_{200}	145	67	31
Halo concentration	CC	12	12	12
Spin parameter	λ	0.033	0.033	0.033
Disk mass fraction	m_d	0.041	0.2	0.067
Bulge mass fraction	m_b	0.014	0.1	0.034
Disk spin fraction	j_d	0.041	0.2	0.067
Gas fraction	f	0.2	0.2	0.2
Disk scale length in [kpc/h]	l_d	2.1	2.1	2.1
Disk height	z_0	0.2	0.2	0.2
Bulge size	l_b	0.2	0.2	0.2

Table X.2: Parameters for the simulated disk galaxies.

Multiphase model parameters		
Gas consumption time-scale in [Gyr]	t_{MP}	2.1
Mass fraction of massive stars	β_{MP}	0.1
Evaporation parameter	A_0	1000
Effective supernova temperature in [K]	T_{SN}	$1 \cdot 10^8$
Temperature of cold clouds in [K]	T_{CC}	1000

Table X.3: Parameters for the multiphase model.

X-3.4 Circumgalactic medium

We assume a radial symmetric density distribution for the medium surrounding the galaxy. We use the well known beta-model (Cavaliere and Fusco-Femiano, 1978) as density distribution. This choice is motivated by observations (see e.g. Croston et al., 2008). The density distribution in the beta-model takes the form:

$$\rho_{\text{gas}} = \rho_0 \left(1 + \frac{r^2}{r_c^2} \right)^{-\frac{3}{2}\beta} \quad (\text{X-14})$$

For reasons of simplification we set $\beta = \frac{2}{3}$ (Mastropietro and Burkert, 2008) which is underpinned by observations (Miller and Bregman, 2013), where a value for β has been found, close to $\frac{2}{3}$. We choose the central gas density ρ_0 to be $5 \cdot 10^{-26} \text{ g/cm}^3$, motivated by the electron density found through cosmological simulations (Dolag et al., 2015), as well as in observations of milky way's hot gas halo (Miller and Bregman, 2013). r_c is called the core radius of our gas halo which is chosen to be $r_c = 0.3 \text{ kpc}$, also motivated by both observations (Miller and Bregman, 2013) and simulations (Donnert, 2014). The value of r_c conforms quite well with $\frac{1}{40} r_s$ where r_s is again the scale length of the corresponding NFW-halo, set by $r_s = r_{200}/CC$. The setting for β makes it very easy to affiliate the mass distribution for our gas halo in a analytic model. Through integration over the density distribution, given by equation X-14 one finds the following form for the mass distribution in the presented analytic model inside radius r .

$$M_{\text{gas}}(< r) = 4\pi r_c^3 \rho_0 \left[\frac{r}{r_c} - \arctan \left(\frac{r}{r_c} \right) \right]. \quad (\text{X-15})$$

At first we want to sample the gas density for our CGM. Note, that we want the density distribution as close as possible to equilibrium. Therefore, we have decided to sample the particle positions of the CGM using a normalized glass distribution. For the construction of the glass distribution we use the Wendland C4 kernel to be consistent with our simulations of the disk galaxies. Therefore, we introduce the variable q as follows

$$q_{\text{gas}} = \frac{M_{\text{gas}}(< r_{\text{new}})}{M_{\text{gas}}} \quad (\text{X-16})$$

This means, that we take the mass distribution and normalize it by the total gas mass we want to have in the CGM. This leads to a value of q between zero and one. Therefore, we need to solve the following equation to sample the particle distribution.

$$\frac{4\pi r_c^3 \rho_0}{M_{\text{gas}}} \left[\frac{r}{r_c} - \arctan \left(\frac{r}{r_c} \right) \right] - q = 0. \quad (\text{X-17})$$

As stated above we want q to be connected to a normalized glass distribution. Now, we take this glass distribution and transform its components to spherical coordinates r', θ, ϕ . As we can see from equation X-15, the mass distribution of the β -profile depends only on the radius coordinate. Thus we identify the component r' with q and solve equation X-17 with the Newton-Raphson-Method for finding roots i.e. we search $r(q)$ which full fills equation X-17. Doing this we get a

new radius component, with a slightly different value as r' , representing the density distribution of equation X-14. Of course this procedure damages the glassiness of our particle distribution, but the error turns out to be quite small within our simulations. The angular coordinates stay unchanged and we can perform the transformation from spherical coordinates back to Cartesian coordinates with the new radius coordinate.

Alternatively q could be rather chosen as a random number or from a cubic or hexagonal lattice. In case of random numbers, we are dependent of the random number generator we use. However, in SPH simulations random numbers lead to a noisy density distribution. Furthermore, the particles do not have any correlation apart from the random number algorithm we plug in and we do not have any chance to be close to an equilibrium condition. While we could fix the equilibrium condition by choosing q as a component of a regular grid, we can not fix the noise in the density distribution at the same quality as in a (kernel dependent) glass distribution. Therefore, we choose the glass distribution to be the optimal choice for our purpose.

In the end, we have a particle distribution for the CGM which is balanced quite well by gravity (because of the glass) and by taking hydrodynamics into account for the glass we reduced the noise of the particle distribution. But we have not balanced the gas halo in the present dark matter profile of the galactic disk. The condition for hydrostatic equilibrium between the dark matter halo of the galaxy and the CGM holds as follows

$$\frac{1}{\rho_{\text{gas}}} \frac{dP_{\text{gas}}}{dr} = -G \frac{M_{\text{total}}(< r)}{r^2} \quad (\text{X-18})$$

Therefore, we can calculate the temperature profile of the CGM by integrating the equilibrium condition using the ideal equation of state for a one atomic gas.

$$T(r) = \frac{\mu m_p}{k_B} \frac{G}{\rho_{\text{gas}}} \int_r^{R_{\text{max}}} \frac{\rho_{\text{gas}}(t)}{t^2} M_{200}(< t) dt \quad (\text{X-19})$$

which leads to:

$$T(r) = G \frac{\mu m_p}{k_B} \left(1 + \frac{r^2}{r_c^2} \right) [M_{\text{dm}} F_0(r) + 4\pi r_c^3 \rho_0 F_1(r)]. \quad (\text{X-20})$$

The temperature profile consists of two parts. The first part comes from the dark matter halo and the second part is the influence of the CGM itself. The functions $F_0(r)$ and $F_1(r)$ are given via

$$F_0(r) = \frac{r_c}{a^2 + r_c^2} \left[\frac{\pi}{2} (a^2 - r_c^2) + r_c \frac{a^2 + r_c^2}{a + r} - (a^2 - r_c^2) \arctan \left(\frac{r}{r_c} \right) - r_c a \ln \left(\frac{(a + r)^2}{r^2 + r_c^2} \right) \right] \quad (\text{X-21})$$

and

$$F_1(r) = \frac{\pi^2}{8r_c} - \frac{\arctan^2(r/r_c)}{2r_c} - \frac{\arctan(r/r_c)}{r}. \quad (\text{X-22})$$

The implementation of the gas halo is in principle the same as shown in [Donnert, 2014](#) for simulations of the cluster collision in El-Gordo.

From the observational side it is useful to calculate a virial temperature for the gas halo $T_c = T(r_c)$. Which we can write it down as:

$$T_c = \frac{2G\mu m_p}{k_B} \left[M_{\text{dm}} \frac{r_c^2}{(a^2 + r_c^2)} \cdot \left(\frac{\pi}{4r_c^2} (a^2 - r_c^2) + \frac{a^2 + r_c^2}{a + r_c} \right. \right. \\ \left. \left. - a \ln \left(\frac{(a + r_c)^2}{2r_c^2} \right) \right) + \pi^2 r_c^2 \rho_0 \left(\frac{3\pi}{8} - 1 \right) \right] \quad (\text{X-23})$$

In table X.4 we summarize the values which are most important to construct a realistic gas halo for a Milky Way-like galaxy as we recommend them. These values are chosen by using observational data from [Miller and Bregman, 2013](#).

Furthermore, the gas halo has to be constructed in a way to ensure that we have a baryon-fraction between 12 and 17 percent in the whole galaxy.

Gas halo parameters			
	LMG	MMG	HMG
Mass in $[10^{10} M_\odot]$	M_{gashalo}	3.8	3.8
Temperature in [K]	T_{vir}	10^6	10^5
Settings for the β -model			
Density in $[\text{g/cm}^3]$	ρ_0	$5 \cdot 10^{-26}$	$5 \cdot 10^{-26}$
Core radius in [kpc]	r_c	0.6	0.6
Exponent	β	$\frac{2}{3}$	$\frac{2}{3}$

Table X.4: Parameters for the gas halo.

X-3.5 Combination of the galactic disk with the CGM

So far, we have the initial conditions for the galactic disk and the CGM separately. Now we combine them in a way, that keeps the initial conditions as close to equilibrium as possible. Furthermore, we do not want any overlap between the particles of the galactic disk and the CGM to prevent numerical instability and a flawed density estimate. Therefore, we implement a procedure to cut out the central part of the CGM and place the disk in the resulting gap. An obvious choice would be to cut out a cylinder, with the radius of the disk and the height of the disk height. This procedure has the advantage, that it is very simple. However, this method results in a relatively large gap between the disk and the CGM. Luckily, the density profile of the galactic disk and the CGM are slightly different and we can use this for selecting the the part of the CGM we want to take out, by introducing a quality condition for the density in the overlap region of galactic disk and CGM. To do so, we bring the SPH data of the galactic disk on a grid and compare the density of the each grid cell to the density of the CGM. To minimise the gap between disk and gas halo, we remove the particles of the CGM if their density is ten percent different from the grid cell they are related to. The grid we use for this purpose has a spatial resolution of $20^3 = 8000$ grid cells. Further note, that we can cut out the CGMs particles better, if we use a higher grid resolution (higher computational cost) or if we choose a lower deviation

from the CGM densities to the grid densities, which means that we increase the sensitivity of the method. The values for the grid and the quality condition are motivated by closing the gap between galactic disk and CGM. But we do not want the gap to be too small to ensure not to have an overlap between galactic disk and CGM which could destabilize the whole system.

X-4 Results

In this section we present and discuss the results of our various simulations, evolved without magnetic field, the supernova seeding introduced in section X-2 and an idealized aligned magnetic field in x-direction. We present studies of the disk morphology, the star formation rate, the growth rate of the magnetic fields, the magnetic field structure and the interaction between the galactic disk and the CGM. Furthermore, we test the ability of the magnetic field to be the perpetrator of a galactic wind within our simulations.

X-4.1 Morphology of the galactic disk and the magnetic field

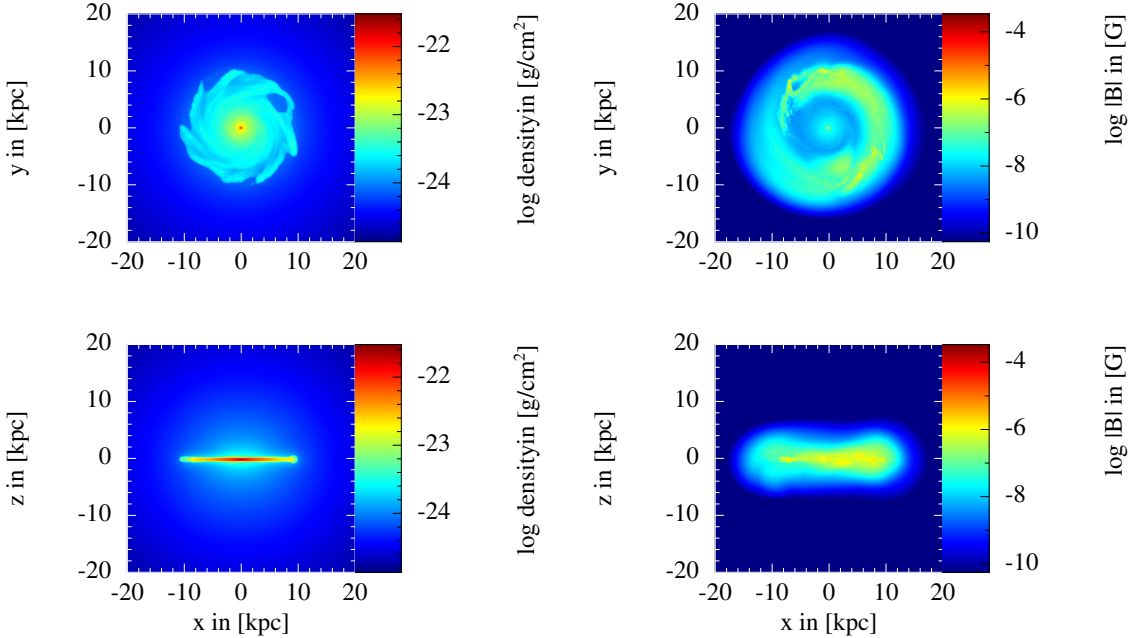


Figure X.1: The face on view of the projected gas density (top left) and the projected magnetic field (top right) for the model HBS. The bottom row shows the projected gas density (bottom left) and the projected magnetic field strength (bottom right) for the edge on view on the galactic disk. The plot is snapshot for $t = 1Gyr$.

We start with a closer look onto the morphology of our galactic model, regarding the morphology of the gas density, as well as the morphology of the magnetic field strength. We present both of our magnetic field models and show differences and similarities, especially in terms of

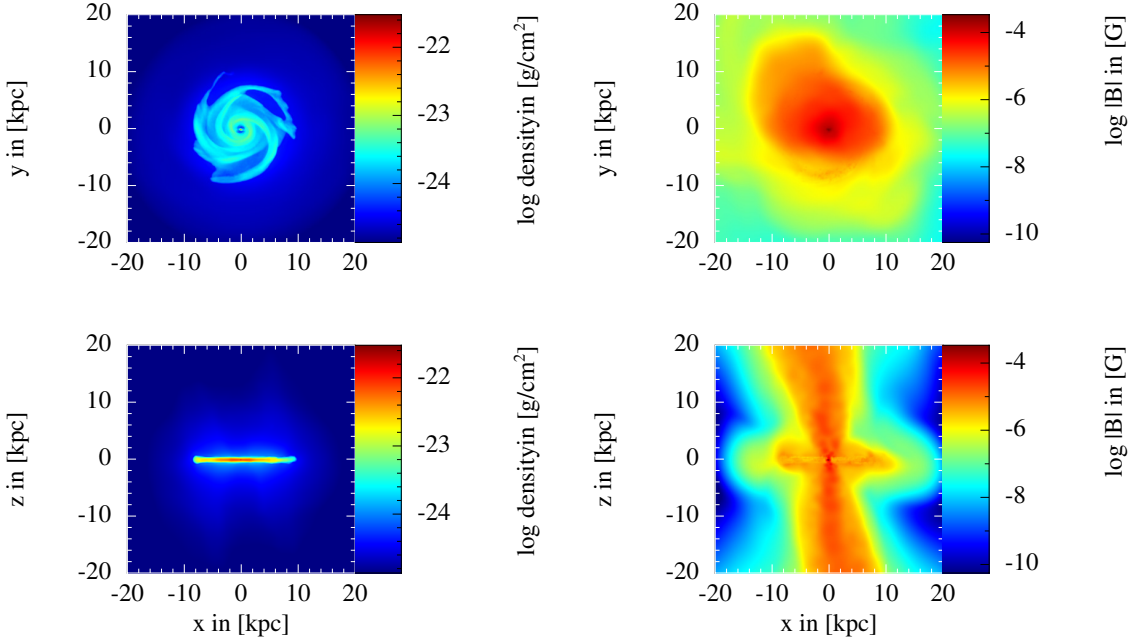


Figure X.2: Same as figure X.1 but for $t = 2\text{Gyr}$.

the magnetic field morphology within the different approaches. Figure X.1 and figure X.2 show the projected gas density and the projected magnetic field strength for the model HBS, for two different points in time. All maps, except otherwise mentioned are produced using SPLASH [Price, 2007](#). In the top left panel of figure X.1 we can see the face on view of the model HBS to an early point of our simulation ($t = 1\text{ Gyr}$). Up to this point of time we can present a nice spiral structure within the projected gas density. Taking a closer look to the bottom left panel we see that the system evolved to a thin disk. Furthermore, we can see the presence of the CGM which surrounds the galactic disk very well in the bottom left panel. On the right hand side of figure X.1 we present the projected magnetic field strength face on (top right of figure X.1) and edge on (bottom right of figure X.1). So far we seeded a certain amount of magnetic dipoles through the supernova-seeding model we use. Looking to the top right panel we see that there are two areas with a large magnetic field strength. The first one is in the centre of our galactic disk. In this case the magnetic field amplifies due to the large star formation rate in the centre of the galaxy. The gas density there is larger (top left of figure X.1) which results in a large star formation rate which then leads to an increased amount of supernova events in the centre of the galaxy. However, the amplification process of the magnetic field in the centre of the galaxy is relatively weak, because the galactic rotation curve in the centre is close to zero and the amplification of the magnetic field is proportional to the rotation speed of the galaxy in the first place. In contrast, at the edge of the galactic disk we find a very large rotation speed due to the differential rotation of the disk. This explains, the strong magnetic field in the outer parts of the galaxy, although the star formation rate is very low in this region.

In the edge on view of the gas density and the magnetic field we can see the thin disk. In case of

the magnetic field (right bottom panel of figure X.1) we can see a thicker disk than in the case of the gas density (bottom left of figure X.1)

figure X.2 presents the same density and magnetic field strength maps as figure X.1, but for a later point in time ($t = 2$ Gyr). While the differences in the projected gas density in both the face on view and the edge on view are relatively small, the changes in the morphology of the magnetic field are stunning. At first we notice in the face on view of the magnetic field strength (top right of figure X.2), that any spiral structure the disk evolves in the magnetic field is hidden by projection effects and will be investigated later. We find a nice structure at the edge on view of the galactic disk (bottom right panel of figure X.2): an impressive biconal magnetic tube. While the magnetic field is brought into the ISM by the dipole seeding of the supernovae, the magnetic field is amplified due to the rotation of the disk. This leads to a larger magnetic pressure within the disk. At a certain point of time the magnetic pressure in the disk becomes strong enough to let the field break up perpendicularly to the disk in z -direction.

Another interesting fact that we find is shown in the bottom left panel of figure X.2. While the edge on view of the disk itself has not changed much, the structure of the surrounding CGM looks completely different. We can see the indication of a X-shaped or H-shaped structure of the CGM, which is known from investigations of biconal winds in galactic disks, driven by AGN or star burst feedback, both features we did not include in our simulations. This becomes even more clear in the density slices we present in figure X.5, where we can see the X-shape of the surrounding halo gas much better than in projection. We note that we find a biconal outflow of the magnetic field. We discuss the ability of the magnetic field as a perpetrator of a galactic wind in more detail in section X-4.5. Note that we can so far reproduce all indicators, known from AGN and starburst driven winds just with the magnetic field within our simulations.

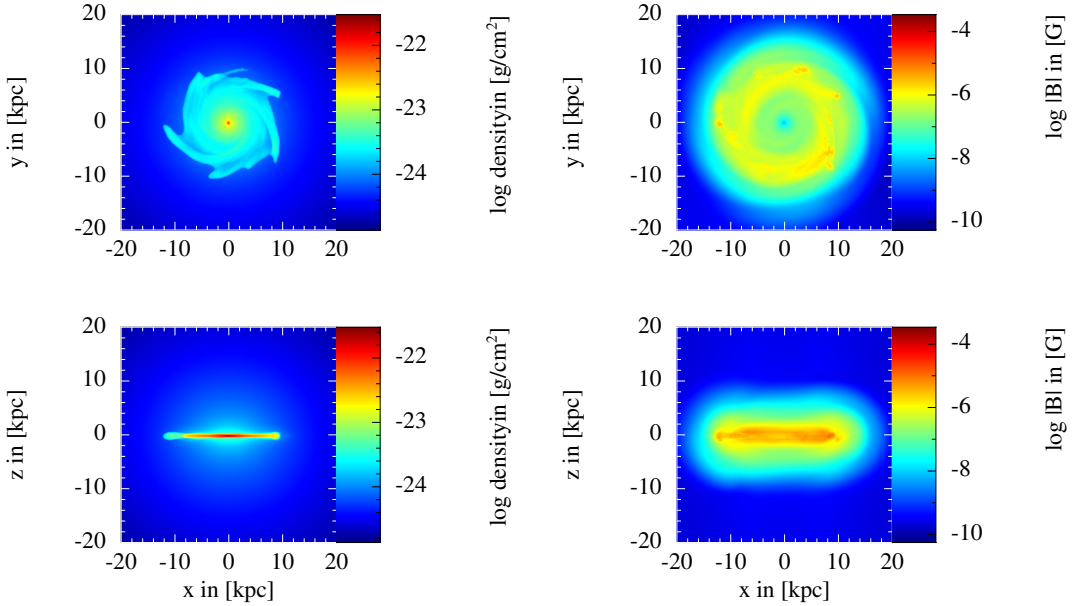


Figure X.3: Same as figure X.1 but with constant initial magnetic field.

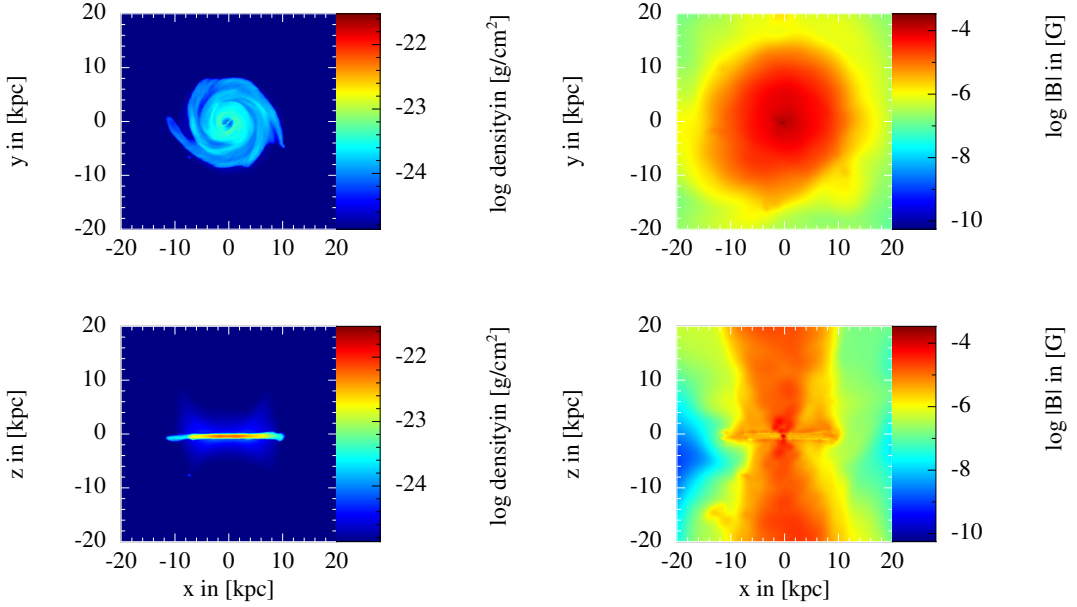


Figure X.4: Same as figure X.3 but for $t = 2Gyr$.

In figure X.3 and figure X.4 we present the exact same properties at the same points in time and the findings are quite the similar to the HBS case using the model HBX with an idealized initial magnetic field uniformly aligned in x-direction. At first we see that the galactic disk evolves a nice spiral structure in the gas density. The magnetic field is in this case amplified in a ring structure, because of the high rotation speed at the disks edge. In this case the magnetic field in the centre of the disk is weaker because there is nearly no rotation and in this model we do not seed magnetic dipoles with supernovae, thus we see not such a high correlation between the star formation rate and the magnetic field in the first place.

Finally, we note that such strong magnetic fields which are consistent with observations are not unproblematic in terms of the disks stability and the structure of magnetic field in the galactic disk. We need to be careful in this regime and need to proof that they do not destroy the morphological structure of the galactic disk. From the projected gas densities in figure X.1 to figure X.4, we can assume that the spiral disk in the gas density is relatively weakly affected by the strong magnetic fields. But we also want to keep the morphological structure of the magnetic field itself alive. Therefore, we will check in section X-4.6 if there is any structure left in the magnetic field in the disk or if the disks magnetic field is dominated by turbulence in the presence of a strong magnetic field.

X-4.2 Star formation rate within the different models

Now, we discuss the star formation rate for our galaxies as shown in figure X.6 for various galactic models as a function of time. The left panel of figure X.6 represents the models HWM, HBS and HBX. The centred panel shows the star formation rate for the models MWM, MBS

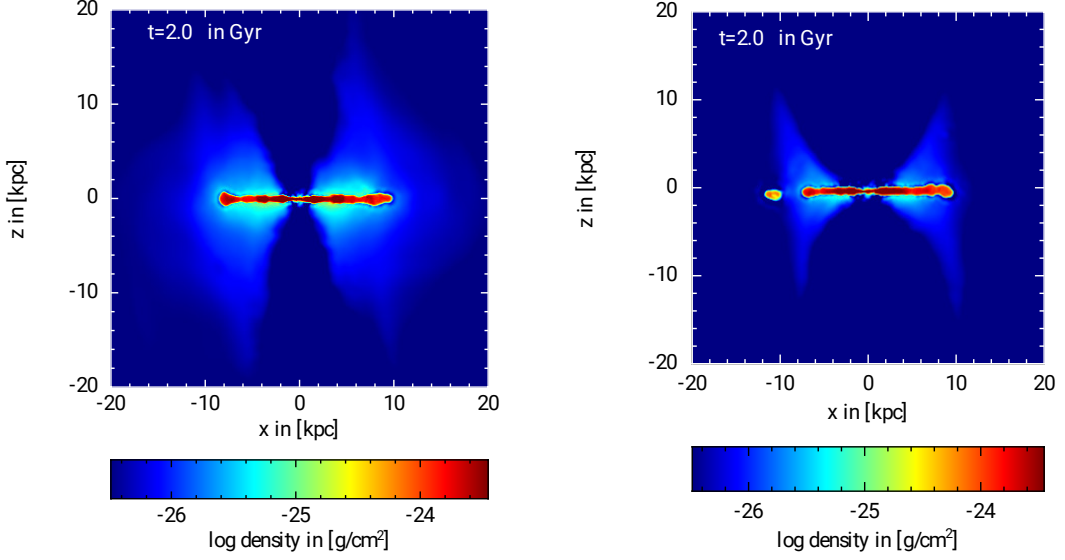


Figure X.5: Density cross section slice for the models HBS (left) and HBX (right). We show one of the most beautiful features within our simulations the observed X-shape in both of our magnetic field models.

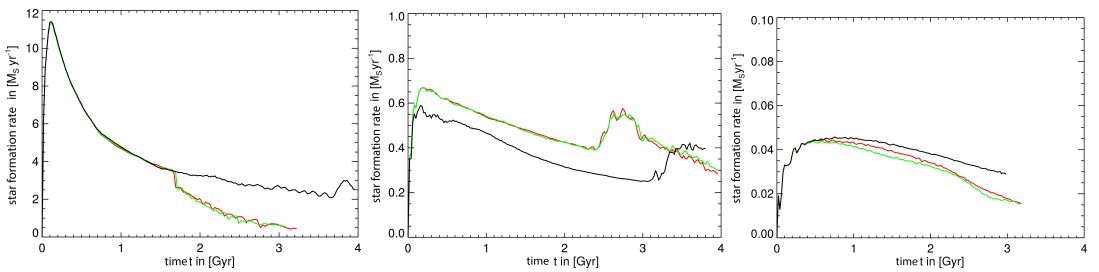


Figure X.6: Star formation rate for all models we prepared for our study. The figure on the left presents the star formation rate for the models HWM (black line), HBS (red line) and HBX (green line). The centre one presents the star formation rate for the models HWM (black line), HBS (red line) and MBX (green line). The right one presents the star formation rate for the models LWM (black line), LBS (red line) and LBX (green line).

and MBX. In the right panel we present the star formation rate for the models LWM, LBS, LBX. In each simulation the star formation peaks shortly after the start of the simulation. Every simulation of an isolated disk galaxy suffers from this behaviour. This is due to the fact, that in such simulations star formation starts out of a non-equilibrium state. There are no supernovae which could heat the gas. This means cooling dominates until the first supernovas explode. After that the star formation can relax into an equilibrium with the heating rate of the supernovae. After the peak, we notice that star formation drops and we can see from the simulations without magnetic field (black lines in figure X.6), that the star formation drops to an almost constant value. This is an expected behaviour, because it seems that the gas disks of the galaxies are feeding on gas out of the CGM, to compensate the mass loss due to the star formation in the disk, which actually keeps the star formation rate constant.

Furthermore, one can see by looking to the star formation rates of the models with magnetic field, that star formation is quenched at a certain point in time. Because this appears only in the simulations with magnetic field, we can assume that drop of star formation is caused by the additional magnetic pressure component. Due to the rotation of the galactic disk, the magnetic pressure rises until the pressure is high enough to move a certain amount of gas out of the disk. Therefore, we have a lower total gas reservoir in the disk and for that reason star formation is turned off. Further we note, that this behaviour is also a strong indicator for a magnetic driven outflow within our set of simulations.

X-4.3 Amplification of the magnetic field

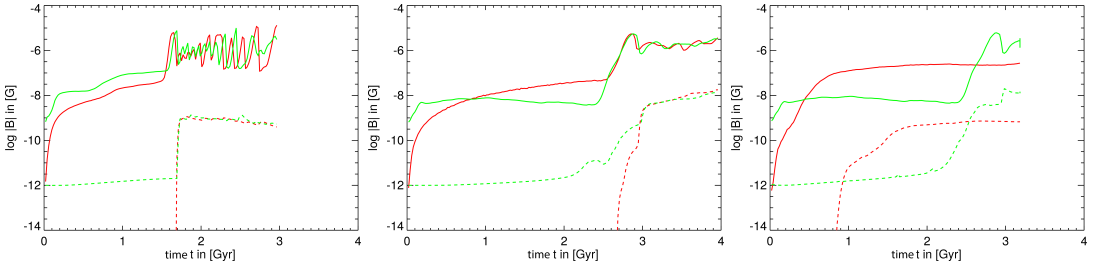


Figure X.7: Magnetic field strength for the models including magnetic fields. The figure on the left presents the magnetic field strength for the models HBS (red line) and HBX (green line). The centre one presents the magnetic field strength of the models HBS (red line) and MBX (green line). The right one shows the magnetic field strength for the models LBS (red line) and LBX (green line). We split up the contribution from the disk (solid lines) and the CGM (dashed lines).

A very important part when it comes to the simulations of disk galaxies in SPMHD, is to reproduce the correct magnetic field strengths in the disk, known from observations. There are many observations of magnetic fields in galactic disks (see e.g. Beck, 2008). These show magnetic fields in the disks ranges from $10\mu G$ between the spiral arms up to $50\mu G$ in the spiral arms. We present the growth rate of the magnetic field within our models in figure X.7. The red and green solid lines represent the magnetic field strength in the galactic disk, in the models with

supernova-seeding (red) and a constant magnetic seed-field (green). The dashed lines represent the magnetic field strength in the CGM respectively. The left panel of figure X.7 shows the magnetic field strengths for the models *HBS* and *HBX*. While the initial magnetic field in the models *HBS* is equal to zero over the whole simulation domain, we set the initial magnetic field for *HBX* to $10^{-9}G$ in the disk and to $10^{-12}G$ in the CGM. A drop of the magnetic field at the edge of the disk from a finite value to zero would be non-physical. Thus, we decided to give the CGM an initial magnetic field. Of course this also has an edge but any effects from that travel slowly enough towards the galaxy that we do not need to concern us with them. Regarding the left panel of figure X.7 we notice, that in the beginning of the simulation the magnetic field in the disk grows exponentially in both models. This is expected from dynamo-theory. In galaxies there operate in general two amplification processes. On the one hand there is the turbulent small scale dynamo and on the other hand there is the mean-field α - ω -dynamo. In the following argumentation we point out which dynamo is dominating in which regime. Both dynamos can lead to either exponential or linear growth of the magnetic field. In case of the turbulent small scale dynamo the amplification of the magnetic field comes from the turbulent motion in the ISM as long as we can neglect the pressure caused by the magnetic field itself. Thus the dynamo operates in the kinetic regime, as stated by [Pakmor et al., 2017](#). The magnetic energy density rises exponentially until equilibrium with the kinetic energy density is reached. At this point the magnetic energy can be transported to the large scales due to an inverse energy cascade. In this regime the small scale dynamo is only able to follow linear amplification as stated in [Federrath, 2016](#). In case of the α - ω -dynamo we argue using the differential rotation and the α -effect (small scale vertical motion) in the galactic disk itself. This effect can lead to both exponential and linear growth of the magnetic field. At this point it is unclear which amplification process is favoured in our simulations.

In the CGM there is nearly no growth of the magnetic field visible. In the case of model *HBX* for small times there is a small amplification of the magnetic field in the beginning, because of the none zero magnetic field in the CGM in this model. But the amplification in this case is minimal and as expected from dynamo-theory, we can see a small exponential growth. Note, that there is no relevant magnetic field in the CGM in the first 1.6 Gyr of the simulation in case of the high mass galaxy. However, at the time of around 1.7 Gyr we see a jump of the magnetic field strength in the CGM in both magnetic field models about several orders of magnitude followed by an oscillatory pattern hinting maybe towards periodic outbursts. In case of the middle mass galaxy (middle panel) the outflow and therefore magnetisation of the halo sets in later at around 2.7 Gyr while the low mass galaxies (right panel) shows drastically different behaviour for the two magnetic field models. Magnetisation of the halo happens at different points in time and also the magnetic field strength in the disk evolves quite differently. In contrast, there is no observable difference in the behaviour of the magnetic field strength in the CGM within the two models for the magnetic field for the high and middle mass galaxy. This underpins the fact, that the observed magnetic field within our simulations depends mainly on the dynamical structure of the galaxy and is not dominated by the initial conditions we use for the magnetic field.

To judge on the dominance of magnetic field amplification processes we take a look at the powerspectrum of the magnetic field, which is shown for both magnetic field models in figure X.8. We obtain these powerspectrum using an appropriate binning for SPH-data on a regular grid

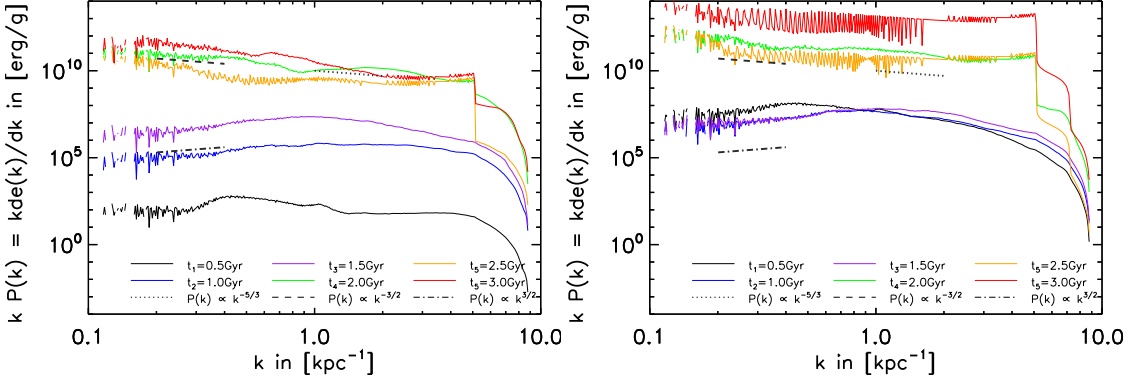


Figure X.8: Magnetic powerspectra for the models HBS (left) and HBX (right). Both power-spectra indicate, that the power of the magnetic field follows a similar structure, independent of the magnetic field model we favour in our simulations. The magnetic field is amplified by turbulent motion on small scales and is transported to large scales over a inverse cascade. This behaviour is known as Kazantsev spectrum (Kazantsev, Ruzmaikin, and Solokov D. D., 1985) and is an indicator for a small scale turbulent dynamo, resulting in an increase of the power $P(k) \propto k^{3/2}$ on large scales. The small scale dynamo stops for larger times due to the large magnetic field and then we have an Iroshnikov spectrum (Iroshnikov, 1963) with $P(k) \propto k^{-3/2}$.

with the same kernel we used within our simulations using the tool SPHMapper (Roettgers and Arth, 2018). Because the binning and the following calculation of the powerspectra are quite expensive when it comes to computational power, we just show the powerspectra for the models *HBS* and *HBX*.

The top panel of figure X.8 shows the powerspectrum for five different points in time in the case of the model HBS. The lower panel of figure X.8 presents the powerspectra of the same points in time for the models HBS field. We can see that the power of the magnetic field is much more smooth in the case of the model HBS, than in the case of the model HBX. Regardless, we find strong evidence for a small scale turbulent dynamo for both magnetic field models. From dynamo-theory we expect a powerspectrum $P(k) \propto k^{3/2}$ in that case which we can see in both plots very clearly. Especially in the beginning of the simulation, when the equilibrium state between the magnetic and the kinetic energy is not reached yet. The magnetic field is amplified by turbulent motion on the small scales and is transported to the large scales by an inverse energy cascade, as predicted by dynamo-theory. We note, that the powerspectrum on the large scales is fully consistent with a Kazantsev spectrum (Kazantsev, Ruzmaikin, and Solokov D. D., 1985) on the large scales, known from a turbulent small scale dynamo. This is also consistent with the findings of other simulations of isolated disk galaxies (Butsky et al., 2017; Rieder and Teyssier, 2016; Rieder and Teyssier, 2017a), as well as cosmological zoom-in simulations (Pakmor et al., 2017; Rieder and Teyssier, 2017b). Interestingly, at later times we do not see the Kazantsev spectrum on the large scales any more. This is an indicator, that the amplification process is not dominated by the small scale dynamo at later times any more. We state, that the magnetic powerspectrum then rather follows an Iroshnikov spectrum for strong magnetic fields (Iroshnikov, 1963). Examining this behaviour, we think, that the small scale dynamo is turned off for

the later times due to the strong, dominating magnetic field in the galaxy. This is in agreement with the behaviour observed in figure X.7 where we see an exponential growth in the beginning, which becomes linear for the later times. The combination of the Iroshnikov spectrum and the linear growth of the magnetic field in the regime of larger times leads to the statement, that the amplification process of the magnetic field in this regime is driven by the α - ω -dynamo instead of the small scale turbulent dynamo, which seems to be inactive for larger times.

X-4.4 Interaction between the galactic disk and the CGM

A very important part of our simulations is the CGM we include, compared to simulations of isolated disk galaxies like [Kotarba et al., 2011](#) or [Pakmor and Springel, 2013](#). This gives us the advantage to observe the interaction of an isolated disk galaxies with its CGM in detail. We discussed this already in section X-4.3, due to the fact that the CGM is heavily magnetized because of outflows in the magnetic field. These outflows are quite strong and transport the magnetic field which is amplified in the galactic disk via the small scale turbulent dynamo and the mean field α - ω dynamo to the outer parts of the CGM. We observe an impressive tube with a radius of approximately 2 kpc close to the disk which opens up to 5 kpc in its outer parts with a magnetic field strength about 10^{-6} G. Further, we observe that the tube is quite long and moves about 80 kpc into the CGM. It transports gas out of the disk into the CGM in positive and negative z-direction at the same rate with a velocity of a few 100 km/s. After leaving the disk the gas is moving outwards the magnetized tube and falls back to the disk outside of the magnetic tube. This means that there is an active exchange of the disks gas with the hot gas of the CGM. Because the CGM consists of hot gas we can observe an other important process. There is not just gas which has been initially located in the disk moving to the CGM and falling back. We also observe a cooling flow of hot gas out of the CGM towards the disk. This stabilizes the star formation rate in the disk, because the CGM acts as an immense reservoir of gas which supports the star formation rate.

X-4.5 Magnetic driven outflows

A central part of the presented study here is the strong magnetized outflow from the galactic centre in the deep regions of the CGM. Thus we study this outflow in more detail. We start the study about the magnetic outflow by taking a closer look to the cooling flows from the CGM towards the disk we mentioned in section X-4.4. We investigate this mainly for our high mass models HWM (black), HBS (red) and HBX (green). In figure X.9 we show the total mass of the baryonic disk for these three models over time. This result is remarkable for two reasons. The first one is that we can observe a cooling flow from the CGM to the disk. This alone is not very surprising, because we have radiative cooling processes included in our simulations. Interesting is the cooling rate of hot gas to the disk. It is in the same order of magnitude as the star formation rate turns gas into star particles. This indicates that the disk can compensate the loss of gas mass due to star formation by accreting hot gas from the CGM.

The second thing we notice is that the accretion of hot gas is constant for larger times and without the magnetic field the disk keeps accreting more mass from the CGM. In case of the models HBS

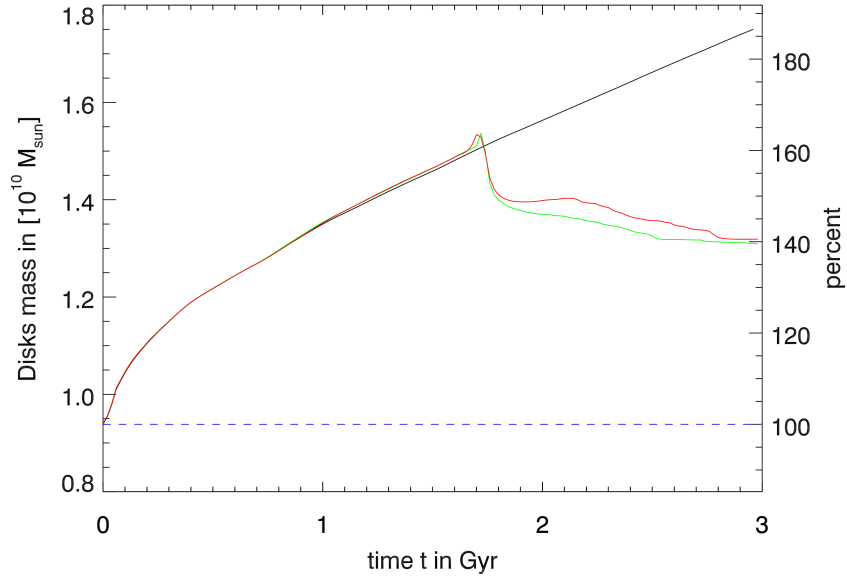


Figure X.9: Total mass of the disk for the models HWM (black), HBS (red) and HBX (green). While the disk is accreting a large amount of gas in the model HWM, the inflow of gas is suppressed in the models HBS and HBX when the magnetic outflow sets in at 1.7 Gyr.

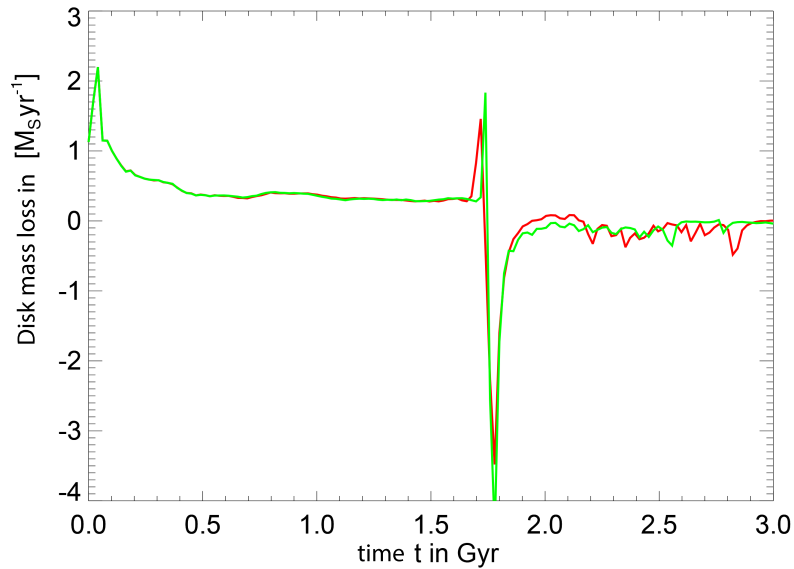


Figure X.10: Rate of change of the mass of the galactic disk in the case of the models HBS (red) and HBX (green) which drive an outflow. We can identify that the disk loses a certain amount of gas when that magnetic outflow sets in.

and HBX were we included magnetic fields we see that the disk mass is dropping around $t = 1.7$ Gyr significantly. This becomes even more clear by taking figure X.10 into account where we plot the change of mass of the galactic disk. We can observe a strong magnetic driven wind with a peak value of around $-4M_{\odot}/\text{yr}$. After that the change of mass of the disk drops to a value about $-0.3M_{\odot}$, but it is still slightly negative, which means that the mass of the disk is still decreasing. For larger times the rate of change of the disks mass slowly approaches zero. This indicates that the system reaches an equilibrium between the magnetic driven outflow and the cooling flow towards the disk.

X-4.6 Magnetic field structure

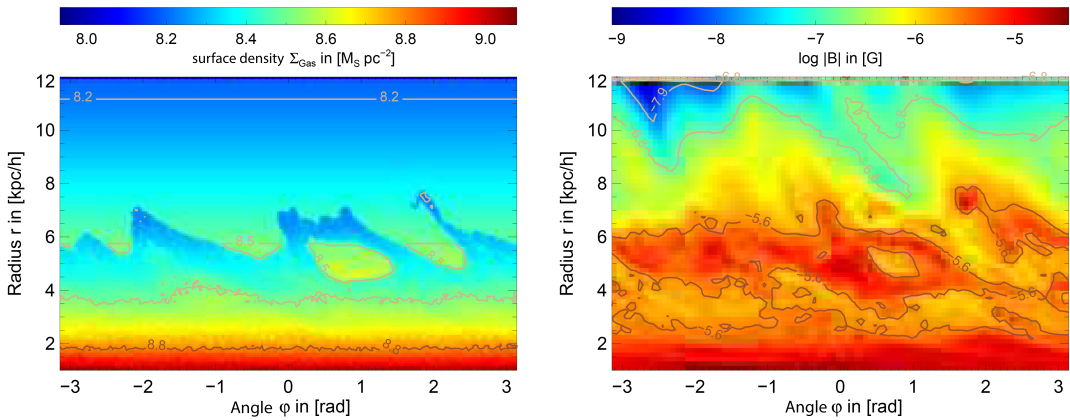


Figure X.11: Structure of the gas density (left) and of the magnetic field (right) both for the model HBS both colour coded and indicated with contours. The spiral structure of the magnetic field follows the spiral structure of the gas density.

We already discussed the general morphological properties of the magnetic field in section X-4.1. In this section we investigate the structure of the magnetic field and point out whether the magnetic field is dominated by turbulence or not. At first we show a more detailed comparison between the structure of the gas density and the magnetic field strength. Therefore, we compare the surface density of the gas with the magnetic field strength in the case of the model HBS. As shown in figure X.11 we plot the radius over the azimuthal angle φ . In the left panel we show the surface density, in the right one we show the magnetic field strength in colours. This kind of plotting is prominent when it comes to the investigation of spiral galaxies in observations, as shown for example in Bitner et al., 2017. Therefore, figure X.11 is not only useful for the comparison of the gas density and the magnetic field in our simulations. It makes our simulations comparable to the surface densities observed in various spiral galaxies. We obtain both plots using the similar technique. Therefore, we explain it for the case of the gas density in more detail. We use a two dimensional grid of the size $100 \cdot 66 = 6600$. One pixel corresponds to a certain pair of r and φ . For each pixel we calculate the gas density (or the magnetic field) using the triangular shaped cloud (TSC) method for calculating densities on a regular grid. The plot is then a density slice for a fixed r for one circulation over the whole galaxy.

The left panel of figure X.11 shows the spiral structure of the galaxy HBS in great detail. We can see clearly four peaks within the gas density, where it is larger than in the surrounding regions of the galaxy. This means that we can observe at least four spiral arms in the model HBS which equals to two spiral modes. This is somewhat expected from a Milky Way-like type of galaxy. If we compare our findings of the left panel of figure X.11 to the panel on the right we see that the same peaks we notable in the gas density are also visible in the magnetic field. This means, that the magnetic field in this model directly follow the distribution of the gas surface density. This is something which is also expected from literature (i.e. [Beck et al., 2013b](#)), which states that in gas rich galaxies the spiral structure of the magnetic field follows exactly the spiral structure of the cold gas.¹ Because the model HBS represents a Milky Way-like disk galaxy with an extended gas rich CGM we can state that this argument matches the presented case. Although we come up with an explanation for the connection between the gas density and the magnetic field density we need to mention that our implementation follows the equations of ideal MHD which in the limit of small magnetic fields leads to a direct correlation between large densities and strong magnetic fields. Thus from theory it is not surprising that we have a strong magnetic field where the gas density is high. But the same fact holds for observations as well. The limit of ideal MHD is allowed in this case, because our magnetic fields are expected to not significantly reach values above $100\mu\text{G}$ and we expect effects of non ideal MHD at the cut off around $1000\mu\text{G}$.

Furthermore, we present two ways to evaluate the detailed structure of the magnetic field. The first one is presented in figure X.12. This method is based on the evaluation of the quantity ζ_1 given via

$$\zeta_1 = \frac{|\mathbf{B} - \mathbf{B}_{\text{sm}}|}{|\mathbf{B}_{\text{sm}}|}, \quad (\text{X-24})$$

where \mathbf{B} is the magnetic field and \mathbf{B}_{sm} is the Gauss-smoothed magnetic field.

This quantity is helpful when it comes to the detailed structure of the magnetic field. Because our simulations were done with a SPH-Code, it is more difficult to obtain ζ_1 out of our data, because we need to bring the SPH-data on a regular grid. This would be of course no problem in a grid code because it already works perfect on a regular grid by definition. However for SPH data the case is more difficult. In the first place one could use for example the TSC method we used in figure X.11 to obtain the density and the magnetic field. Although this works well to make the point whether the magnetic field follows the gas density, the TSC method is based on a triangular kernel and thus not accurate enough to point out the detailed structure of the magnetic field in an SPMHD simulation. Therefore, we decided to work out a proper SPH-binning. We use a two dimensional grid with a very high resolution with 512^2 grid points and calculate the magnetic field for each grid point by using the Wendland C4 Kernel and taking the neighbouring (roughly 200) particles into account. Thus we have used exactly the same configuration as our underlying SPH-formalism to bin the data properly. This is the most proper way to work with SPH-data on a regular grid, because we make sure that the magnetic field on the grid is strongly affiliated with the SPMHD magnetic field in our simulations. The data binning has been performed using the SPHMAPPER presented in [Roettgers and Arth, 2018](#).

ζ_1 describes the deviation of the magnetic field in our simulations from the smoothed magnetic

¹Which is the main contributor to the density here.

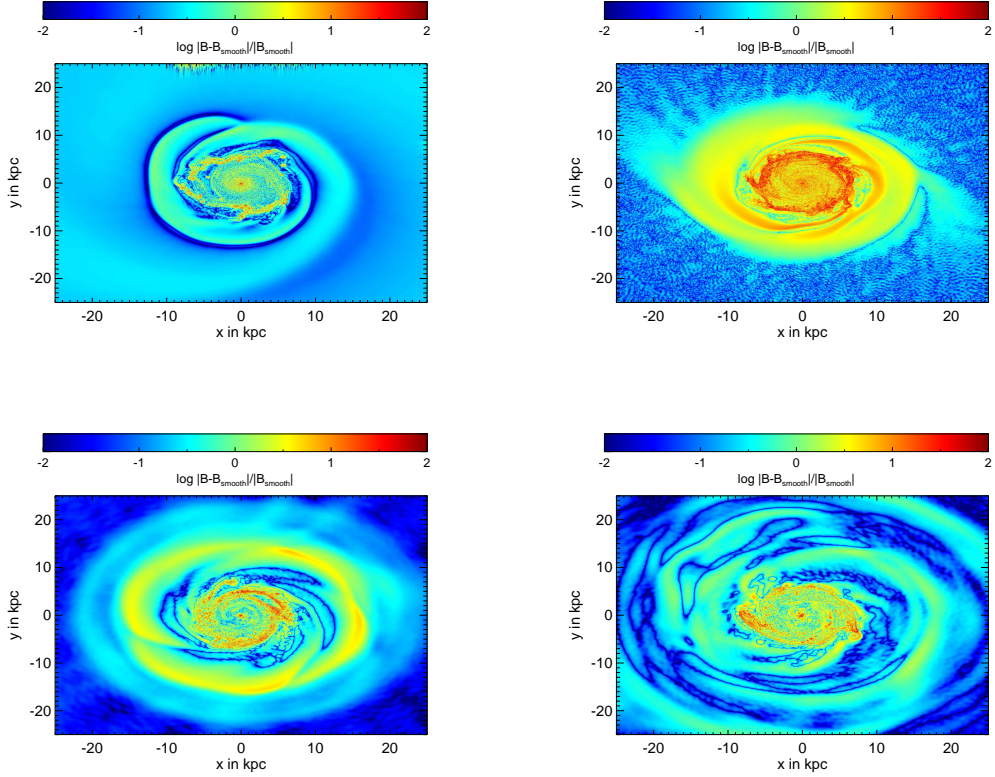


Figure X.12: Structure of the magnetic field in our simulations. The figure shows the normalized relative deviation of the magnetic field towards the magnetic field smoothed using a Gaussian shaped kernel using equation X-24. From this figure one can obtain information about the order in the magnetic field. Blue indicates that turbulence is dominating while red implicates high order of the magnetic field. The top row is at $t = 1.5 \text{ Gyr}$, the bottom row at $t = 2 \text{ Gyr}$. Left is the seeding model, right the constant initial field.

field. The smoothing is performed with a Gaussian shaped Kernel. This method is quite popular in image editing and is called unsharp masking. With this method we can achieve a strong contrast between the smoothed and un-smoothed magnetic field. Therefore, it is easy to find detailed structure using this method. A large value of ζ_1 indicates a large difference between the smoothed magnetic field and the original one. This is an indicator for a strong ordering of the magnetic field. Otherwise a small value of ζ_1 shows little deviation between the smoothed magnetic field and the original one. Therefore, low values indicate a region of strong turbulence. The upper left panel presents ζ_1 for the model HBS at $t = 1.5$ Gyr. This panel shows the structure of the magnetic field in the galactic disk shortly before the outflow sets in. We can observe many structure lines which underline the magnetic fields spiral structure and point out the more complex structure of the magnetic field beside the spiral arms. The complex structure lines can be interpreted as higher order terms of the underlying spiral structure of the magnetic field. Furthermore, we recognise that the turbulent structures are mostly placed in the centre of the galactic plane. This is interesting for several reasons. The first one is that in section X-4.3 we argued that the magnetic field is amplified via a small scale dynamo. The upper left panel shows this beautifully. On the small scales (in the galactic centre) the turbulent character of the magnetic field dominates. Comparing the upper left panel of figure X.12 to the right panel of figure X.2 we further notice that the turbulent region of the galactic plane is the region where the origin of the magnetic outflow is centred. The upper right panel of figure X.12 shows ζ_1 for the model HBX. In this case we can also observe the spiral structure of the magnetic field but we see that the disk is more dominated by turbulence than in the model HBS. Nevertheless, the previous statement that the turbulent magnetic field is the origin of the magnetized outflow seems to be valid. If we compare the upper left panel of figure X.12 to the right panel of figure X.4 we can see that the magnetic outflow is much wider than in the case of the model HBS.

In the panels on the bottom of figure X.12 we show ζ_1 in the x-y-plane for $t = 2$ Gyr. These plots are interesting to prove that the structure of the magnetic field is not destroyed by the magnetic outflow which sets in around $t = 1.7$ Gyr. And indeed we find that much of the magnetic structure is left in the galactic disk even if a large amount of magnetic energy leaves the disk.

ζ_1 evaluates the total magnetic field. By doing this we may ignore some spatial behaviour of each magnetic field component. Thus, we present a second method to evaluate the structure of the magnetic field introducing the variable ζ_2 :

$$\zeta_2 = \sqrt{\left(\frac{B_x - B_{x/sm}}{B_{x/sm}}\right)^2 + \left(\frac{B_y - B_{y/sm}}{B_{y/sm}}\right)^2 + \left(\frac{B_z - B_{z/sm}}{B_{z/sm}}\right)^2}. \quad (\text{X-25})$$

The main point of this quantity compared to ζ_1 is that it takes the structure of the magnetic field in each spatial direction into account. This means we need in total three maps, one for each component of the magnetic field, smooth the magnetic field of each direction, calculate the absolute value of $B_i - B_{i/sm}$ with $i = (x, y, z)$ and normalise it by the smoothed map for the magnetic field component i . Following this procedure we get figure X.13. While figure X.12 clearly shows the underlying magnetic structure of the magnetic field of the disk in the x-y-plane, this method is not able exploit structure in the z-direction of the magnetic field. Or even worse some of the structure seen in figure X.12 could just be an artefact of the not visible z-direction. In figure X.13 on the other hand we normalized each component separately and

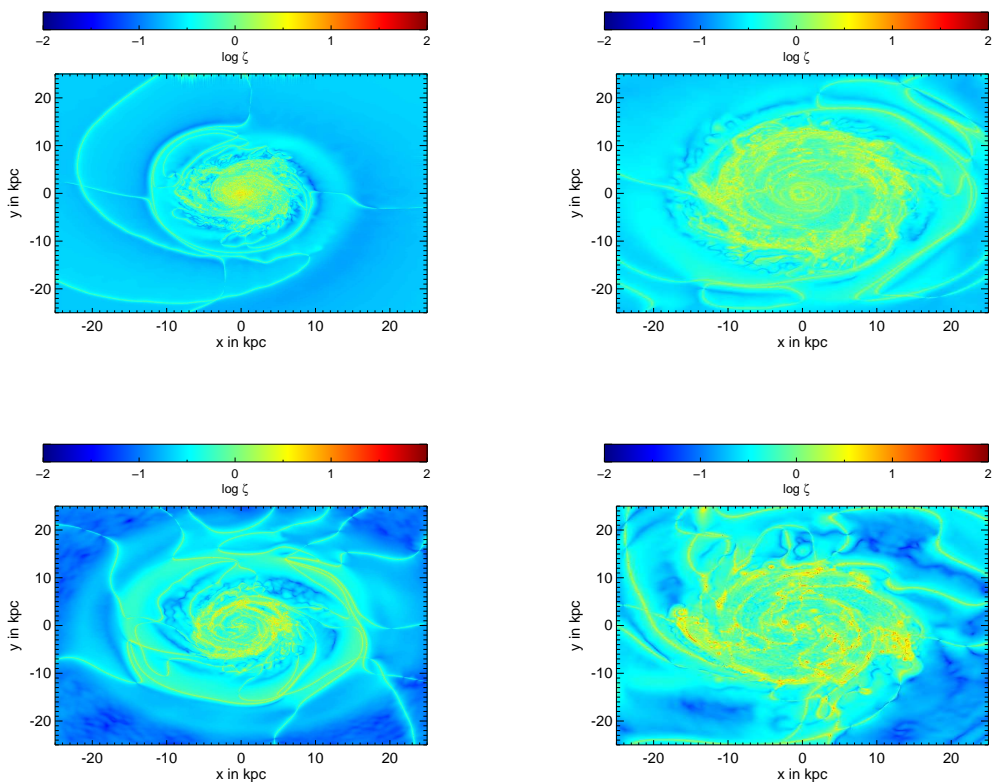


Figure X.13: Same as figure X.12 but using the unsharp masking component-wise according to equation X-25.

calculated the absolute value of the magnetic field divergence after the normalisation of each direction. This prevents an overestimation of the strong magnetized outflows in z-direction we observed for example in figure X.1 when we are mainly interested in the magnetic structure of the galactic disk.

Regarding figure X.13 we can also see the beautiful structure lines we already know from figure X.12. We also notice the magnetic fields spiral structure and can point out that the magnetic field becomes much more turbulent when the magnetic outflow sets in.

X-4.7 Divergence Cleaning

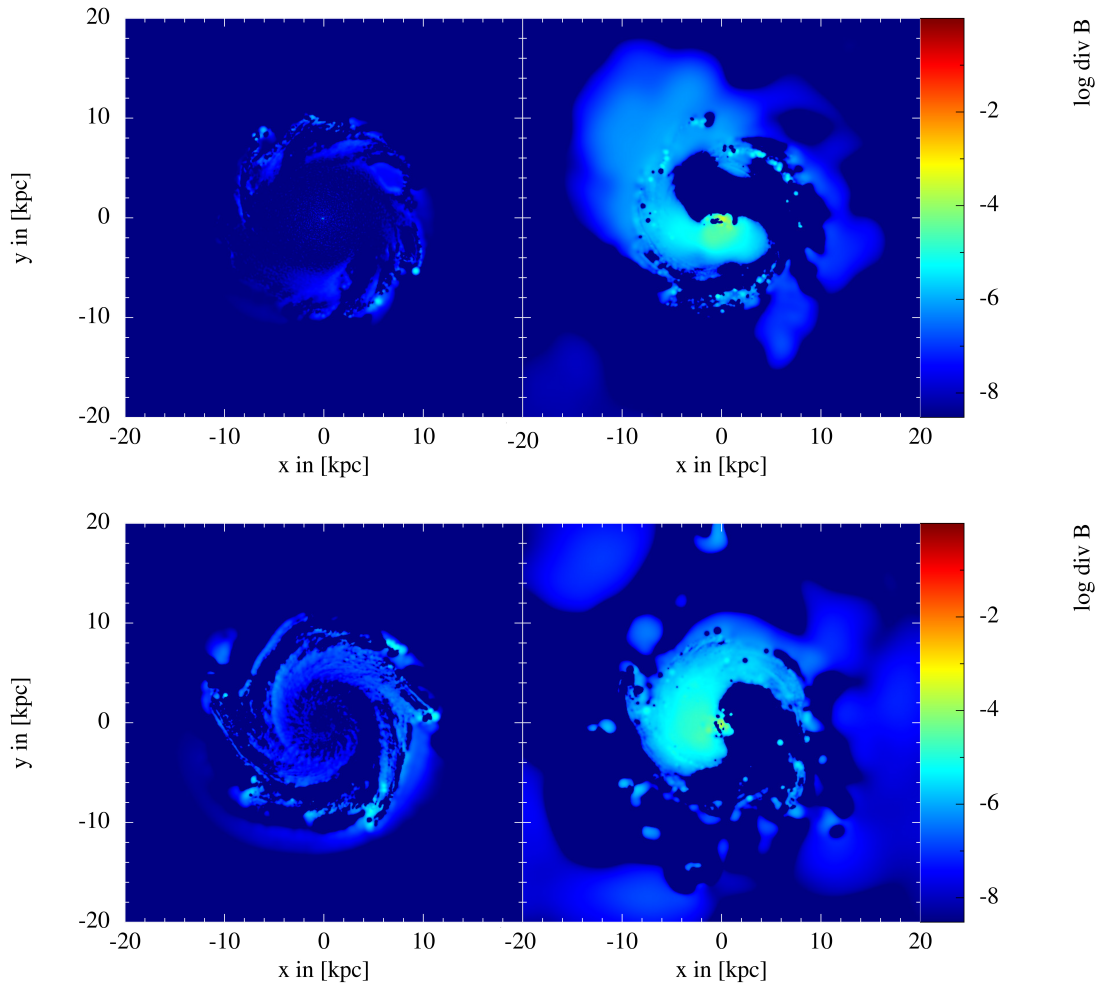


Figure X.14: Absolute divergence errors obtained in our simulations for the model HBS (top) and HBX (bottom). We show the divergence cleaning behaviour within our simulations for $t = 1$ Gyr (left) and $t = 2$ Gyr (right).

Since every numerical simulation has to deal with the $\nabla \cdot \mathbf{B} = 0$ constraint we need to prove

that in our simulations we do not seed a large amount of magnetic monopoles. Thus we present the total $\nabla \cdot \mathbf{B}$ in our simulations for the models HBS and HBX in figure X.14 for two points in time. In each case the left figure represents the time $t = 1.0$ Gyr and the right figure shows the time $t = 2.0$ Gyr. We choose a point of time before the strong magnetic outflow and one after the outflow sets in. The fact that we can observe a more turbulent structure after the outflow sets in leads to an increase of the divergence of the magnetic field due to the sharper gradients we have in this case. In figure X.14 we can see that the maximum value of the magnetic field divergence is around 10^{-3} in the turbulent state. This is acceptable when we compare it to other simulations. Most values of $\nabla \cdot \mathbf{B}$ are around 10^{-8} or below, which is very good for a SPMHD-Code. We note that there are methods in grid Codes like RAMSES which can keep $\nabla \cdot \mathbf{B}$ at zero down to machine precision. However [Pakmor and Springel, 2013](#) use a cleaning scheme ([Powell et al., 1999](#)) similar to ours and their findings are that this cleaning scheme is sufficient, because it is much more complicated to control $\nabla \cdot \mathbf{B}$ using a particle method or a moving mesh because of the irregularity of the particle distribution (for SPH) or the Voronoi-Grid (in case of a moving mesh).

In figure X.14 we can further observe that the higher values of $\nabla \cdot \mathbf{B}$ appear in a spiral structure following the spiral arms of our disk galaxy. This is an expected behaviour, because the magnetic field undergoes strong gradients at the edge of the spiral arms to the surrounding galactic medium. This behaviour improves with better resolution, because the gradients become better resolved.

We further notice, that the divergence of \mathbf{B} seems to be better resolved in the case of supernova seeding. This is due to the mechanism how the magnetic field is brought into the ISM. In case of the supernova seeding we place magnetic dipoles into the ISM. This leads by construction to the effect that the divergence of \mathbf{B} is kept closer to zero, because we force its dipole structure to appear with the supernova explosions. This leads locally to a smoother distribution of the magnetic field and therefore to a smaller divergence error.

X-5 Conclusions

In this study we presented a modified idealised model for isolated disk galaxies including a realistic CGM for galaxies with three different halo masses. The masses of the investigated systems are equivalent to $10^{10} M_{\odot}$, $10^{11} M_{\odot}$ and $10^{12} M_{\odot}$. Thus the aim of our study is to present the general properties of those systems which are describing a dwarf, a middle sized mass galaxy and a Milky Way-like galaxy. Apart from investigating the general properties of those systems we present a detailed study of the morphological structure of both, the gas density, as well as the magnetic field. Furthermore, we present interesting results of the star formation rate where we noticed a drop of the star formation rate in the simulations we performed using our two magnetic field models. A promising result in the context of the behaviour of the magnetic field in our simulations is the small scale dynamo we find in the powerspectra of our galaxies. We also find a major difference to other simulations of this kind that were performed recently. Our powerspectra for both magnetic field models indicate, that the small scale dynamo is turned off for very strong magnetic field in our simulations. This behaviour is interesting because we enter a regime where we are not in a kinetic framework any more and the magnetic field dominates.

Furthermore we find realistic magnetic field strengths within our simulations when it comes to a comparison with observations. A more detailed study of the interaction of galactic disk and CGM shows that a certain amount of magnetic energy is released in the outer regions of the CGM having its origin in the centre of the galactic disk. Our study of turbulence in the magnetic field leads to the assumption that this highly magnetized outflows are mainly driven by the turbulent magnetic field in the centre of the galactic disk. Moreover the structure analysis of the magnetic field indicates that the magnetic field follows a complex structure beside the spiral structure which is obviously following the spiral structure of the gas density.

Acknowledgements

We thank Andreas Burkert, Thorsten Naab and Ruediger Pakmor for useful discussions and their insights on magnetic fields. The authors gratefully acknowledge the computing time granted by the John von Neumann Institute for Computing (NIC) provided on the supercomputer JURECA at Jülich Supercomputing Centre (JSC) and the computing time provided by the Leibniz Rechenzentrum (LRZ) of the Bayrische Akademie der Wissenschaften on the SuperMuc in Garching. UPS and BPM acknowledge an Emmy Noether grant funded by the Deutsche Forschungsgemeinschaft (DFG, German Research Foundation) with the project number MO 2979/1-1.

Chapter XI

Rotation curves of galaxies in Magneticum: Supporting Λ CDM

Everything is self-evident.

— Rene Descartes

Finally we pick up on some recent discussions regarding the Λ CDM model and alternatives to dark matter. As discussed briefly in the introductory section I-1, one of the key observations which lead to the introduction of dark matter was that rotation curves of disk galaxies extended way beyond the visible disks. Consequently the galaxies are believed to be surrounded by some form of invisible dark matter which drives this additional rotation. For a review see e.g. [Sofue and Rubin, 2001](#). Due to limited resolution originally detailed rotation curves have been mainly observed for galaxies pretty close by, ergo at low redshift. However, now [Genzel et al., 2017](#) have published some results for a galaxy sample at redshift $z \sim 2$ with puzzling results in rotation curves showing a strong decline outwards the half-light radius.¹ This is associated with a very small dark matter fraction and obviously fuelled the heated discussion if dark matter is really the correct answer.

In this chapter we present a slightly modified version of our paper “Declining Rotation Curves at $z = 2$ in Λ CDM Galaxy Formation Simulations” which has been just accepted in ApJ Letters ([Teklu et al., 2017a](#)) which approaches these findings from a simulation point of view.

XI-0 Abstract

Selecting disk galaxies from the cosmological, hydrodynamical simulation *Magneticum Pathfinder* we show that almost half of our poster child disk galaxies at $z = 2$ show significantly declining rotation curves and low dark matter fractions, very similar to recently reported observations. These galaxies do not show any anomalous behaviour, reside in standard dark matter halos and typically grow significantly in mass until $z = 0$, where they span all morphological classes, including disk galaxies matching present day rotation curves and observed dark matter fractions. Our findings demonstrate that declining rotation curves and low dark matter fractions

¹The radius in which half of the total luminosity is contained.

in rotation dominated galaxies at $z = 2$ appear naturally within the Λ CDM paradigm and reflect the complex baryonic physics, which plays a role at the peak epoch of star-formation. In addition, we find some dispersion dominated galaxies at $z = 2$ which host a significant gas disk and exhibit similar shaped rotation curves as the disk galaxy population, rendering it difficult to differentiate between these two populations with currently available observation techniques.

XI-1 Introduction

Since the postulation of dark matter (DM) by Zwicky, (1933), many observational studies analysing rotation curves of galaxies (e.g. Rubin, Ford, and Thonnard, 1978) have supported this picture: While rotational velocities (V^{rot}) deduced from the visible matter should decrease proportional to $r^{-1/2}$ in the outer parts of galaxies, they were found to remain flat. The knowledge of this discrepancy in the mass content and thus the need for an explanation for this missing mass lead to the acceptance of dark matter as the dominant mass component of galaxies (see Naab and Ostriker, (2017) for a detailed review).

Recently, Genzel et al., (2017) (see also Lang et al., 2017) presented measurements of rotation curves at redshift $z \approx 2$ that do not stay flat but decrease with increasing radius, opening a debate about the importance and even presence of DM in the outer disks and inner halos of these massive systems (and generally at higher redshift). In this letter we investigate whether the existence of decreasing rotation curves at high redshifts contradicts or actually is a natural outcome of the Λ CDM paradigm, using the state-of-the-art cosmological simulation Magneticum Pathfinder² (K. Dolag et al., in preparation).

XI-2 The Simulations

The *Magneticum Pathfinder* simulations are a set of state-of-the-art, cosmological, hydrodynamical simulations (see Beck et al., 2016, for details on the numerical scheme) of different cosmological volumes with different resolutions. They follow a standard Λ CDM cosmology with parameters (h , Ω_M , Ω_Λ , Ω_b , σ_8) set to (0.704, 0.272, 0.728, 0.0451, 0.809), adopting a WMAP 7 cosmology (Komatsu et al., 2011).

These simulations follow a wide range of physical processes (see Hirschmann et al., 2014; Teklu et al., 2015, for details) which are important for studying the formation of active galactic nuclei (AGN), galaxies, and galaxy cluster. The simulation set covers a huge dynamical range with a detailed treatment of key physical processes that are known to control galaxy evolution, thereby allowing to reproduce the properties of the large-scale, intra-galactic, and intra-cluster medium (see e.g. Dolag, Komatsu, and Sunyaev, 2016; Gupta et al., 2017; Remus, Dolag, and Hoffmann, 2017) as well as the distribution of different chemical species within galaxies and galaxy clusters (Dolag, Mevius, and Remus, 2017), and the properties of the AGN population (Hirschmann et al., 2014; Steinborn et al., 2016). Especially, detailed properties of galaxies of different morphologies can be recovered and studied, for example their angular momentum properties and the evolution of the stellar mass-angular momentum relation (Teklu et al., 2015;

²www.magneticum.org

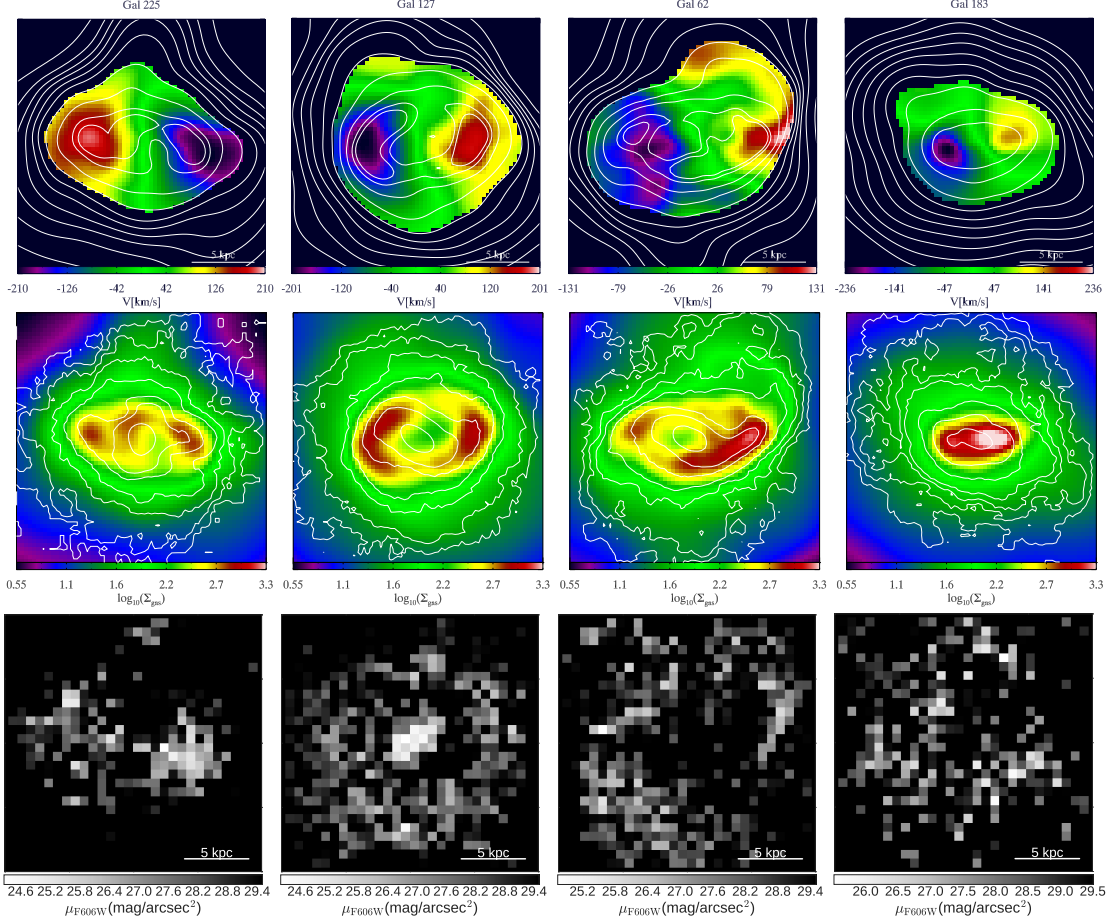


Figure XI.1: Example galaxies from the $z = 2$ sample with declining rotation curves (see figure XI.2), from left to right the three disk galaxies *gal 225*, *gal 127*, and *gal 62*, and the gas-rich spheroidal system *gal 183*, rotated to inclinations (e.g. $i = 60$, $i = 45$, $i = 25$ and $i = 75$, respectively) similar to those of the galaxies presented in Genzel et al., (2017). *Upper row*: Velocity maps of the cold gas component for each galaxy, with contours of the cold gas column density overlaid. *Middle row*: Cold gas column density maps with overlaid stellar column density contours. *Lower row*: Simulated HST broadband F606W images using *GRASIL-3D*.

Teklu, Remus, and Dolag, 2016), the mass-size relations and their evolution (see e.g. Remus and Dolag, 2016; Remus et al., 2016), global properties like the fundamental plane (Remus and Dolag, 2016) or dark matter fractions (Remus et al., 2016), the baryon conversion efficiency (see e.g. Steinborn et al., 2015; Teklu et al., 2017b), as well as the dynamical properties of early type galaxies (Schulze et al., 2018).

For this study we use the simulation *Box4/uhr*, which covers a volume of $(68 \text{ Mpc})^3$, initially sampled with $2 \cdot 576^3$ particles (dark matter and gas), leading to a mass resolution of $m_{\text{gas}} = 7.3 \cdot 10^6 M_{\odot}$ for the gas and $m_{\text{stars}} = 1.8 \cdot 10^6 M_{\odot}$ for stellar particles, with a Plummer equivalent gravitational softening corresponding to 0.33kpc at $z = 2$ for the star particles and twice this value for the gas particles.

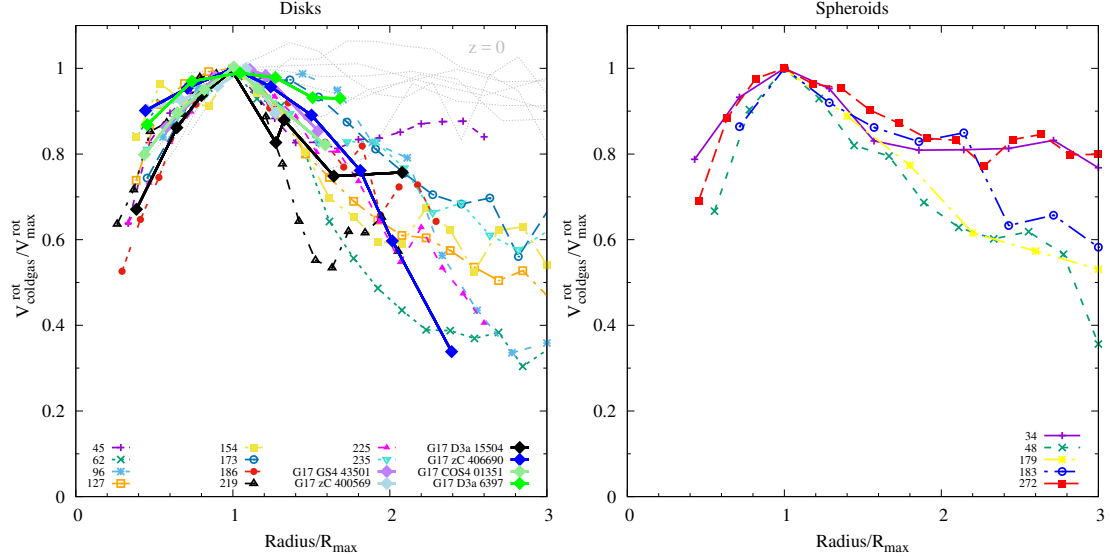


Figure XI.2: Rotation curves obtained from the cold gas for 10 out of the 26 poster child disk galaxies which show clearly declining rotation curves (left panel) and for the 5 gas-rich spheroidal galaxies (right panel) at $z = 2$, normalized by $V_{\text{coldgas}}^{\text{rot}}$ at the radius of maximum velocity R_{max} . The thick coloured lines in the left panel show the 6 declining rotation curves presented in Genzel et al., (2017), while the grey lines show 7 poster child disk galaxies at $z = 0$, using $\approx 1.4 \cdot R_{1/2}$ as R_{max} .

XI-3 Sample of Galaxies

To ensure proper resolution of the inner structure, we only select halos with virial masses above $5 \cdot 10^{11} M_{\odot}$ hosting galaxies with stellar masses above $5 \cdot 10^{10} M_{\odot}$ for this study. These mass ranges are consistent with the observed properties of the high- z galaxy sample of Genzel et al., (2017). This leads to a sample of 212 and 275 halos at $z = 2$ and $z = 0$, respectively. Furthermore, we classify the galaxies based on the distribution of the circularity parameter $\varepsilon = j_z/r\sqrt{GM(r)/r}$ of the stars within the galaxies, where j_z is the z -component of the stars' specific angular momentum (see also Abadi et al., 2002; Scannapieco et al., 2008). Thus,

dispersion-dominated systems represent observed early-type galaxies and are characterized by a broad peak in the distribution at $\varepsilon \simeq 0$, while rotation-supported systems have properties that are characteristic of late-type galaxies and show a broad peak at $\varepsilon \simeq 1$. We define poster child disk galaxies as systems which, in addition to a characteristic peak at $\varepsilon \simeq 1$, have a significant cold gas fraction ($f_{\text{cold}} > 0.5$ at $z = 2$ and $f_{\text{cold}} > 0.2$ at $z = 0$) with respect to their stellar mass, to distinguish them from transition type systems or ongoing merger events (for details see [Teklu et al., 2015](#)). For our simulations it has been shown that, following this classification scheme, galaxies of these two populations reproduce accordingly the observed stellar-mass–angular-momentum–relation ([Teklu et al., 2015](#)) and its evolution ([Teklu, Remus, and Dolag, 2016](#)), the mass-size relation and its evolution ([Remus et al., 2016](#)), as well as the fundamental plane distributions ([Remus and Dolag, 2016](#)).

We then rotate the galaxies such that the minor axis of the gas³ is aligned with the z -axis, so that we can extract the rotation curve without any further modifications.

From the total of 212 (275) galaxies at $z = 2$ ($z = 0$) we classify 26 (15) as poster child disks, which we consider for further analysis. In addition, among our 27 poster child spheroidal galaxies at $z = 2$ we find 5 systems with a large cold gas fraction ($f_{\text{cold}} > 0.5$).

Figure [XI.1](#) shows a 20 kpc region for 4 gas-rich example galaxies at $z = 2$, where the upper row displays the line-of-sight velocity maps of the cold gas component, restricted to regions with $\Sigma_{\text{gas}} > 50 \frac{M_{\odot}}{\text{pc}^2}$, with overlayed cold gas column density contours. The gridded data was created using SPHMapper (Arth & Roettgers, in prep.). The middle row shows the cold gas column density maps with overlayed stellar surface density contours. Inclinations and colours were chosen according to the observations presented in [Genzel et al., \(2017\)](#). Each column represents one galaxy, where *gal 225*, *gal 127*, and *gal 62* (from left to right) resemble disk galaxies, while *gal 183* is a gas-rich spheroidal galaxy. Interestingly, all galaxies, even the spheroidal one, show a similar, regular rotation pattern for the cold gas component. This is due to the fact that the gas is in a flattened, centrifugally supported disk, even in the systems where the stars form a spheroid.

The lower panels show mock images of the four galaxies in the HST broadband F606W (4750A–7000A), which corresponds to rest-frame mid-UV. The images have been generated with the radiative transfer code *GRASIL-3D* ([Domínguez-Tenreiro et al., 2014](#)). This wavelength range traces the regions of very recent star formation, and the spheroidal galaxy shows a very similar mock image as the disks, hiding the real stellar morphology.

XI-4 Rotation Curves at $z = 2$

The rotation curves for our galaxy sample are directly obtained from the averaged velocities (i.e. the circular velocities) of the individual cold gas particles. In order to ensure that only gas within the disk contributes to the rotation curve, only particles within the z -range of $\pm 3\text{kpc}$ are used. While the $z = 0$ disk galaxies show normal rotation curves, 12 out of the 26 poster child disk galaxies at $z = 2$ show a significantly declining rotation profile for their gas disk. However, we

³Note that this is different from the computation for the classification, where the galaxies are rotated into the frame where the angular momentum vector of the stars is aligned with the z -axis.

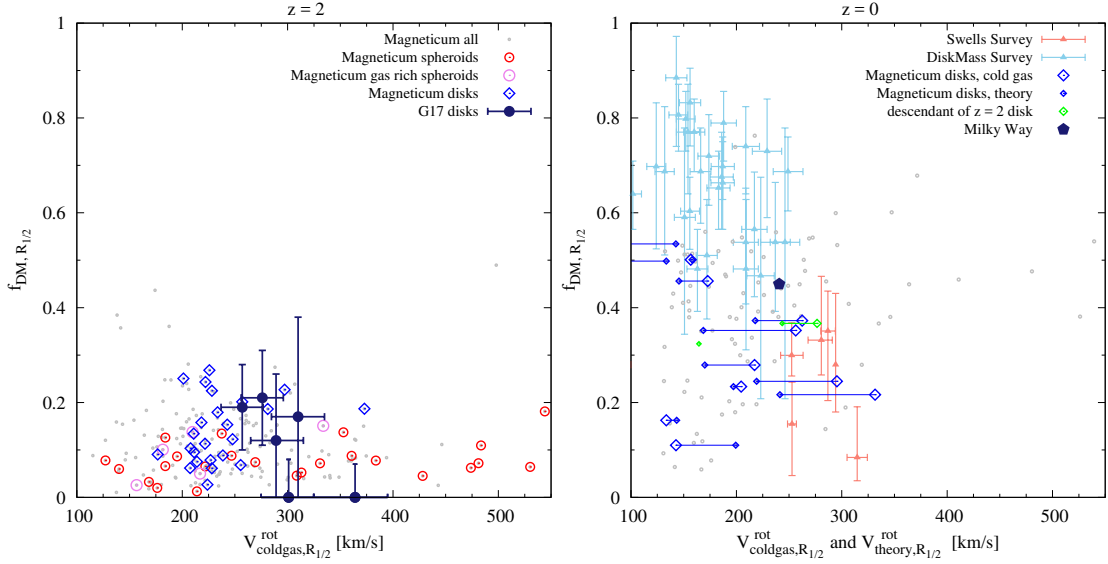


Figure XI.3: The DM fraction f_{DM} within the half-mass radius $R_{1/2}$ versus the rotational velocity $V_{\text{coldgas}}^{\text{rot}}$ at $R_{1/2}$ at redshifts $z = 2$ (left) and $z = 0$ (right). At $z = 2$ (left panel), the simulated disks (blue diamonds) and gas-rich spheroidals (pink open circles) are shown together with the gas-poor spheroidals (red open circles). The observations from [Genzel et al., \(2017\)](#) are included as dark-blue points. At $z = 0$ (right panel), we only show the simulated disk galaxies, together with observations as presented in [Courteau and Dutton, \(2015\)](#) from the Swells Survey ([Barnabe et al., 2012](#); [Dutton et al., 2013](#)) and the DiskMass Survey ([Martinsson et al., 2013](#)). The dark-blue filled pentagon shows the Milky Way according to [Bland-Hawthorn and Gerhard, \(2016\)](#). To indicate uncertainties involved in inferring $V_{\text{coldgas}, R_{1/2}}^{\text{rot}}$ we include for the simulated galaxies both the measured rotational gas velocity at $R_{1/2}$ as well as the theoretical value obtained from the total mass within $R_{1/2}$ and connect both points by lines. We explicitly highlight the data points for those descendants of our $z = 2$ disk galaxies which are still disk galaxies at $z = 0$ (green diamonds).

further remove 2 of the 12 examples from our detailed analysis, as they show remnants of recent merger activity.

The left panel of figure XI.2 shows the rotation curves for these 10 poster child disk galaxies at $z = 2$, which exhibit a decline in the rotation curve similar to the observed high- z disk galaxies presented in [Genzel et al., \(2017\)](#) (thick solid lines). Following the observations, we scaled the individual rotation curves by R_{\max} and V_{\max}^{rot} , where R_{\max} is the radius at which the rotational velocity ($V_{\text{coldgas}}^{\text{rot}}$) has its maximum. We only plot radii larger than two times the gravitational softening of the gas particles, which corresponds to $\simeq 1.33\text{kpc}$ at $z = 2$. As can clearly be seen, the simulated galaxies show the same behaviour as the observed ones, with some having an even steeper decline in the rotation curves as the observed galaxies. For comparison, the rotation curves of 7 disk galaxies at $z = 0$ are shown as grey lines. The difference in profile shapes between high- z and present-day galaxies is clearly visible.

Since at high redshift galaxies are in general more gas-rich, we also plot the same curves for the 5 gas-rich spheroidal galaxies from our $z = 2$ sample in the right panel of figure XI.2. As for the disks, the gas shows a clear rotational pattern (see also example in figure XI.1), and all of our gas-rich spheroidal galaxies show a declining rotation curve similar to the observed disk galaxies. The only difference here is that the gas disks in the spheroidals are much smaller than the stellar spheroidal bodies, while the sizes are similar in the disk galaxy cases (see figure XI.1). The high redshift HST images mainly show young stars, which morphologically closely resemble the gas disks even in the spheroidals (see lower panel of figure XI.1). This indicates a potential difficulty in distinguishing disk galaxies from gas-rich spheroidals at $z = 2$ observationally. However, this uncertainty should be resolved using the next generation of telescopes which will be able to probe the old stellar component in high redshift systems as well.

XI-5 DM Fractions

For spheroidal galaxies it is well known that the DM fraction within the half-mass radius is decreasing at higher redshift, which is commonly interpreted as indication for late growth by dry mergers of such systems. While this trend is qualitatively supported by cosmological simulations independent of the details in the implemented feedback models, the AGN feedback used in our simulation has been shown to produce DM fractions which quantitatively agree well with observations (see [Remus et al., 2016](#)).

The left panel of figure XI.3 shows the DM fractions within the stellar half-mass radius $R_{1/2}$ for our full galaxy sample (grey dots) compared to observations at $z = 2$. Generally, our galaxies have a tendency for higher average DM fractions with decreasing $V_{\text{coldgas}}^{\text{rot}}$, however, nearly all fractions are well below 30%. Our disk galaxies (blue diamonds) cover the same range of small DM fractions as the observations presented in [Genzel et al., \(2017\)](#) (dark-blue filled circles with error bars)⁴. Interestingly, the DM fractions of the disk systems are almost as small as those of the spheroidal systems. Furthermore, the gas-rich spheroidals cover the same range in DM fractions as the observed and simulated disk galaxies, again highlighting the similarities between the gas-rich systems at $z = 2$ independent of their morphologies and demonstrating the

⁴Note that especially at $z = 2$ the unavoidable differences when inferring the half-mass radius in simulations and observations could lead to noticeable differences.

difficulty in distinguishing pure rotation-dominated systems from dispersion-dominated systems which host a significant gas disk.

At $z = 0$ the disk galaxies in the simulations show much larger DM fractions which decrease with rotational velocity and agree well with the different measurements for disk galaxies (see right panel of figure XI.3). To indicate uncertainties involved in inferring $V_{\text{coldgas}, R_{1/2}}^{\text{rot}}$ we used both, the measured rotational gas velocity at $R_{1/2}$ as well as the theoretical values obtained by adopting centrifugal equilibrium and taking the total mass within $R_{1/2}$.

XI-6 Surface Density, Dispersion and Theoretical Rotation Curve

A detailed look at the four examples from figure XI.1 shows that the surface density profiles $\Sigma(r)$ of the cold gas disks in the three poster child disk galaxies and the gas-rich spheroidal galaxy follow the expected exponential decline, as shown in the upper panel of figure XI.4. While the theoretical rotation curves as obtained by the total matter distribution within these halos are flat, as expected, the real measured rotation of the cold gas disk shows a significant decline, as can be seen in the middle panel of figure XI.4. This decline is a result of the kinetic pressure effect which partly compensates the gravitational force as proposed by [Burkert et al., \(2010\)](#). As expected for a self-gravitating, exponential disk, the maximum of the real rotation curve for the three disk galaxies in the central part, where the baryons dominate over the dark matter halo, is slightly ($\approx 10\text{-}20\%$) above the maximum value for a spherically averaged mass distribution ([Binney and Tremaine, 2008](#)). Furthermore, at large distances the real rotational velocity is conspiratorially close to the expected rotational velocity if considering only the cold gas mass. For the gas-rich spheroidal galaxy *gal 183*, the latter holds even across almost all radii, due to its even lower DM fraction and the small size of the disk compared to the stellar body of the galaxy. As a result, the gaseous disk of the spheroidal galaxy *gal 183* is strongly self-gravitating, more compact and shows an even stronger decline. None of our systems with a falling rotation curve shows any significant feature or change in the radial component of the velocity dispersion measured for the cold gas disk which is related to the position at which the rotation curve declines, as shown in the σ_r profiles in the lower panel of figure XI.4.

XI-7 Discussion and Conclusions

Selecting disk galaxies with M_{vir} above $5 \cdot 10^{11} M_{\odot}$ and M_{*} above $5 \cdot 10^{10} M_{\odot}$ from the cosmological, hydrodynamical simulation *Magneticum Pathfinder* we investigated the rotation curves of disk galaxies at $z = 2$. We find that almost half of our poster child disk galaxies (10 out of 26) show significantly declining rotation curves, very similar to the observations reported in [Genzel et al., \(2017\)](#). Interestingly, the peak of the rotation curve is a fairly good approximation ($\approx 10\%$ larger) of the theoretical value, based on the total mass of the galaxies.

These disk galaxies do not show any significant dynamical features except that the radial dispersion has generally significantly larger values compared to $z = 0$ disks, as expected for dynamically young systems in their assembly phase. [Forbes, Krumholz, and Burkert, 2011](#) already presented a model description to explain this temporal evolution, which also quantitatively agrees well with the results of the much higher resolution hydrodynamical simulations *Eris* ([Bird et al.,](#)

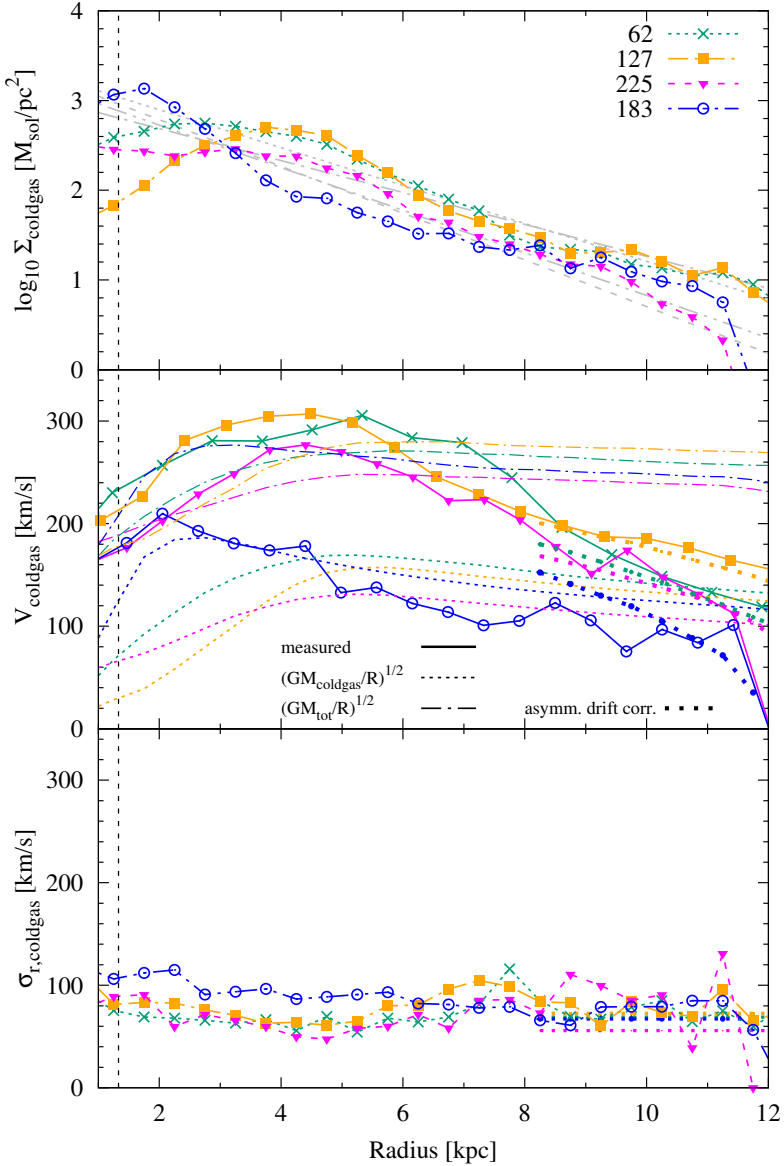


Figure XI.4: For the three poster child disks (*gal 62*, *gal 127*, and *gal 225*), and the gas-rich spheroidal galaxy (*gal 183*): *Upper panel*: Surface density Σ of the cold gas. The vertical dashed line indicates four/two times the gravitational softening of the stellar/gas particles at this redshift. The grey lines are fits for an exponential surface density profile for $\Sigma(x) = a \cdot \exp(-x/b)$ with $b \approx 2$ kpc. *Middle panel*: Rotation curves of the cold gas (solid lines) compared to the rotation curves expected from the spherically averaged total mass distribution (dash-dotted lines). Dotted lines show the corresponding cold gas contribution. The thick dotted lines at large radii show the expected theoretical rotation curves when corrected for the asymmetric drift. *Bottom panel*: Radial velocity dispersion σ_r of the cold gas. Thin dotted lines indicate the σ used for the asymmetric drift correction in the middle panel.

2013), finding ratios of $3 - 4$ between v_{rot} and σ_{gas} for galaxies at $z = 0$ and much smaller σ_{gas} for galaxies at $z = 0$. Furthermore, this is also in line with the observational findings of [Simons et al., \(2017\)](#), who showed that observed galaxies at $z \sim 2$, independently of their stellar mass, typically have $\sigma_{\text{gas}} \sim 60$ km/s, similar to our galaxies shown in figure [XI.4](#). Applying a simple correction

$$v_{\text{rot}}^2 = v_{\text{circ}}^2 + 2\sigma^2 \times (d\ln\Sigma/d\ln R) = v_{\text{circ}}^2 - 2\sigma^2 \times (R/R_d)$$

for the asymmetric drift ([Burkert et al., 2010](#)) based on our measured dispersion profiles onto the theoretical rotation curve results in reduced rotation curves, which qualitatively agree well with our measured ones. Therefore, we conclude that the declining rotation curves of the high redshift galaxies are caused by a relatively thick, turbulent disk, as already discussed in [Genzel et al., \(2017\)](#). We also find that these galaxies show similarly low DM fractions as reported for the observations. The DM halos of these disk galaxies have a mean concentration parameter $c_{\text{vir}} \approx 8$ (as expected for these halo masses at $z = 2$) and therefore we can exclude that the low dark matter fractions are caused by especially low concentrations of the underlying halos.

Tracing these galaxies in the simulations until $z = 0$ allows us to infer the present-day appearances of these galaxies. We find that, on average, these galaxies still grow by a factor of ≈ 3.5 both in virial as well as in stellar mass. Two of them resemble present-day disk galaxies with small remaining gas disks, and one ends as a central galaxy of a small group. Three of them become satellite galaxies of small groups, while the rest is mostly classified as transition types. Therefore, we can exclude that the low DM fractions at $z = 2$ imply that these systems have to be the progenitors of today's elliptical galaxies with similar stellar mass and low dark matter fractions.

Interestingly, in our simulations we also find several spheroidal galaxies at $z = 2$ which host a massive cold gas disk with similarly declining rotation curves as the disk galaxies. These gas disks are typically more compact, but as star formation is dominated by the gas disks, these spheroidals appear indistinguishable from the disk galaxies in our mock HST images, highlighting the need for observational instruments that detect the old stellar component even at high redshifts.

In general, we conclude that high-redshift disk galaxies with declining rotation curves and low DM fractions appear naturally within the Λ CDM paradigm, reflecting the complex baryonic physics which plays a role at $z = 2$ and can be found commonly in state-of-the-art, Λ CDM cosmological hydrodynamical simulations.

Acknowledgements

We thank Tadziu Hoffmann for useful discussions. AFT and KD are supported by the DFG Transregio TR33, AB is supported by the DFG Priority Programme 1573. AO has been funded by the Deutsche Forschungsgemeinschaft (DFG, German Research Foundation) – MO 2979/1-1. This research is supported by the DFG Cluster of Excellence “Origin and Structure of the Universe.” We are especially grateful for the support by M. Petkova through the Computational Center for Particle and Astrophysics (C2PAP). Computations have been performed at the ‘Leibniz-Rechenzentrum’ with CPU time assigned to the Project “pr86re.”

Chapter XII

Conclusions and Outlook: The Answer to the ultimate question of life, the universe and everything?

The only true wisdom is in knowing you know nothing.

– Socrates

In this thesis we gave an overview of how we improved our numerical tool set for simulations of galaxies and galaxy clusters during the last few years. We presented our modernised SPH code and showed how well we can circumvent the typical flaws of any SPH discretisation. We discussed this in the context of other numerical approaches people take and which, according to some, will at some point completely overtake classical grid and SPH codes. However, we aspired to give a glance of the importance of different numerical schemes and the potential the huge variety of codes actually inhibits. In order to gain knowledge about what we simulate we always need to divide numerical from physical reason as best as we can which can be done ideally by comparing results from different numerical approaches with each having it's own biases and flaws as we aspire in the ongoing comparison project “The Three Hundred”. So maybe it is not even the question if and when SPH will vanish in favour of e.g. MFM (meshless finite mass) but rather an important point that this should not even happen.

Besides improving the basic numerics of our code we reported our effort to improve everything else we need to successfully keep researching with upcoming simulations. These include the easier creation of better initial conditions, the ability to process huge amounts of data and post processing codes which can analyse SPH data properly and transform them into a grid picture without introducing large errors. A lot of time has been spent on these topics and sometimes it might seem to others almost like a waste of time which could be spent on actually performing and analysing simulations. Nevertheless, these kind of efforts are necessary to keep the ball running on the long run. We have reached a point where our simulation codes have grown to such an extent that developing them further and especially optimising them to scale properly on huge computing clusters is a full time job and can hardly been done any more just in ones free time between astrophysical projects. In the future it will become increasingly important to manage this kind of development properly most probably through collaborations with computer

scientists which devote all their time on these development and optimisation tasks. There is a lot to learn in how to improve the processes which take place. For example automatic testing of code, not in a sense of real physical scenarios but rather on the basis of abstract code unit tests, is something which is successfully adapted in the development of software on the free market but has hardly found its way into our community yet. This again requires a lot of time on the short run but saves so much more in long term. There are efforts to drive this, like a new open source version of our code called OPENGADGET, for which automatic testing is indeed in development right now.

All the technical works presented in this thesis were born out of direct requirement coming from another project. For example, to look further into the performance of our thermal conduction model we wanted to simulate a small patch of a cluster atmosphere with a shallow density and temperature gradient in hydrostatic equilibrium in order to see whether our code would successfully develop the HBI (heat flux buoyancy instability) and MTI (magneto thermal instability) plasma instabilities. However, with the methods we had at hand the quality of initial conditions was never sufficiently well and the relevant gradients were too much hidden by particle noise to develop the instabilities. This and the experience how much time setting up the standard tests for our code took lead to the efforts regarding a generic initial conditions generator as we presented it in this thesis.

On the astrophysical side of this thesis we presented said model for thermal conduction in the presence of magnetic fields and investigated the impact changing the model and the efficiency of conduction onto the development of several galaxy clusters. The anisotropic formulation produces results similar to highly suppressed net conduction (about 1%) due to entanglement of magnetic fields and is sufficient to let a sample of clusters show a bi-modality of cool-core and non cool-core temperature profiles, a topic highly discussed as simulations typically fail to reproduce the bi-modality properly as we observe it.

The importance of magnetic fields got further investigated on the level of disk galaxies where we looked into the question how magnetic fields can break up when a critical pressure is reached and drive outflows perpendicular to the plane of a disk galaxy. We studied that question for galaxies of different mass and with both a primordial magnetic field and fields seeded into the surrounding medium from supernova explosions. We can nicely follow the build up of magnetic fields due to a small scale dynamo which stops after a certain growth phase.

Furthermore, due to recent observations of declining rotation curves at high redshift disk galaxies, we investigated and found similar behaviour in the Magneticum simulations, showing that this is indeed consistent with the standard Λ CDM model and not a reason to drop it in favour of modified gravity.

There are multiple next possible steps building upon this work. As we have improved our hydrodynamical backbone of the SPH code this has to be further tested in the context of magnetohydrodynamics as for example the signal velocity may change from the speed of sound to the Alfvén velocity. Also the diffusion of magnetic fields might be subject to improvements. Some of the parts of this thesis are based on paper drafts which have to be finished obviously and along go improvements of the actual work described, including the initial conditions generation code which is far from perfect. The cluster comparison project with a multitude of simulations is obviously just kicking off and can be the source of many studies. Regarding models in our

code, magnetic fields are still somewhat disconnected from other parts like star formation and AGNs, which is already worked on improving. Wherever a hydrodynamical pressure comes into play, the magnetic pressure might also be of importance. Studying MHD turbulence with the improved code is certainly an interesting although difficult topic, due to the nature of SPH. Finally regarding magnetic fields, including for example a prescription of cosmic rays into the simulations can improve not only results but also provide more possibilities for comparison with observations. As always, exciting times lie ahead.

Bibliography

Aarseth, Sverre J. (2003). *Gravitational N-body simulations*. Cambridge University Press, p. 413. ISBN: 0521432723. URL: <http://adsabs.harvard.edu/abs/2003gnbs.book.....A>.

Abadi, Mario G. et al. (2002). “Simulations of Galaxy Formation in a Lambda CDM Universe II: The Fine Structure of Simulated Galactic Disks”. In: *Astrophys. J.* 597.1, pp. 21–34. ISSN: 0004-637X. DOI: [10.1086/378316](https://doi.org/10.1086/378316). arXiv: [0212282 \[astro-ph\]](https://arxiv.org/abs/astro-ph/0212282). URL: <http://arxiv.org/abs/astro-ph/0212282> [http://dx.doi.org/10.1086/378316](https://dx.doi.org/10.1086/378316).

Abel, Tom (2011). “rpSPH: A novel smoothed particle hydrodynamics algorithm”. In: *Mon. Not. R. Astron. Soc.* 413.1, pp. 271–285. ISSN: 00358711. DOI: [10.1111/j.1365-2966.2010.18133.x](https://doi.org/10.1111/j.1365-2966.2010.18133.x). arXiv: [1003.0937 \[astro-ph.CO\]](https://arxiv.org/abs/1003.0937).

Agertz, Oscar et al. (2007). “Fundamental differences between SPH and grid methods”. In: *Mon. Not. R. Astron. Soc.* 380.3, pp. 963–978. ISSN: 00358711. DOI: [10.1111/j.1365-2966.2007.12183.x](https://doi.org/10.1111/j.1365-2966.2007.12183.x). arXiv: [0610051 \[astro-ph\]](https://arxiv.org/abs/0610051).

Alard, C. (2000). “Image subtraction using a space-varying kernel”. In: *Astron. Astrophys. Suppl. Ser.* 144.2, pp. 363–370. DOI: [10.1051/aas:2000214](https://doi.org/10.1051/aas:2000214). URL: <http://aas.aanda.org/10.1051/aas:2000214>.

Alfvén, Hannes (1937). “Versuch zu einer Theorie über die Entstehung der kosmischen Strahlung”. In: *Zeitschrift für Phys.* 105.5-6, pp. 319–333. DOI: [10.1007/BF01330603](https://doi.org/10.1007/BF01330603). URL: <http://link.springer.com/10.1007/BF01330603>.

Andreon, S. (2010). “The stellar mass fraction and baryon content of galaxy clusters and groups”. In: *Mon. Not. R. Astron. Soc.* 407.1, pp. 263–276. ISSN: 00358711. DOI: [10.1111/j.1365-2966.2010.16856.x](https://doi.org/10.1111/j.1365-2966.2010.16856.x). arXiv: [1004.2785](https://arxiv.org/abs/1004.2785). URL: <http://mnras.oxfordjournals.org/cgi/doi/10.1111/j.1365-2966.2010.16856.x>.

Antuono, M., A. Colagrossi, and S. Marrone (2012). “Numerical diffusive terms in weakly-compressible SPH schemes”. In: *Comput. Phys. Commun.* 183.12, pp. 2570–2580. DOI: [10.1016/J.CPC.2012.07.006](https://doi.org/10.1016/J.CPC.2012.07.006). URL: <http://www.sciencedirect.com/science/article/pii/S0010465512002342?via%3Dihub>.

Arth, Alexander et al. (2014). “Anisotropic thermal conduction in galaxy clusters with MHD in Gadget”. In: arXiv: [1412.6533](https://arxiv.org/abs/1412.6533). URL: <http://arxiv.org/abs/1412.6533>.

Arthur, Jake et al. (2016). “nIFTy galaxy cluster simulations V: Investigation of the Cluster Infall Region”. In: *Mon. Not. R. Astron. Soc.* 464.2, pp. 2027–2038. DOI: [10.1093/mnras/stw2424](https://doi.org/10.1093/mnras/stw2424). arXiv: [1609.07311](https://arxiv.org/abs/1609.07311). URL: <http://arxiv.org/abs/1609.07311>.

Avara, Mark J., Christopher S. Reynolds, and Tamara Bogdanović (2013). “Role of magnetic field strength and numerical resolution in simulations of the heat-flux-driven buoyancy instability”. In: *Astrophys. J.* 773.2. ISSN: 15384357. DOI: [10.1088/0004-637X/773/2/171](https://doi.org/10.1088/0004-637X/773/2/171). arXiv: [1305.0281](https://arxiv.org/abs/1305.0281).

Bagla, J. S. (2002). “TreePM: A code for Cosmological N-Body Simulations”. In: *J. Astrophys. Astron.* 23, pp. 185–196. DOI: [10.1007/BF02702282](https://doi.org/10.1007/BF02702282). arXiv: [9911025 \[astro-ph\]](https://arxiv.org/abs/astro-ph/9911025). URL: <http://arxiv.org/abs/astro-ph/9911025>.

Bagla, J. S. and Suryadeep Ray (2003). “Performance Characteristics of TreePM codes”. In: *New Astron.* 8.7, pp. 665–677. DOI: [10.1016/S1384-1076\(03\)00056-3](https://doi.org/10.1016/S1384-1076(03)00056-3). arXiv: [0212129 \[astro-ph\]](https://arxiv.org/abs/astro-ph/0212129). URL: <http://arxiv.org/abs/astro-ph/0212129>.

Balbus, Steven A and Pierre Henri (2008). “On the Magnetic Prandtl Number Behavior of Accretion Disks”. In: *Astrophys. J.* 674.1, pp. 408–414. ISSN: 0004-637X. DOI: [10.1086/524838](https://doi.org/10.1086/524838). arXiv: [0706.0828](https://arxiv.org/abs/0706.0828). URL: [http://stacks.iop.org/0004-637X/674/i=1/a=408](https://stacks.iop.org/0004-637X/674/i=1/a=408).

Balogh, Michael L. et al. (2001). “Revisiting the cosmic cooling crisis”. In: *Mon. Not. R. Astron. Soc.* 326.4, pp. 1228–1234. ISSN: 00358711. DOI: [10.1111/j.1365-2966.2001.04667.x](https://doi.org/10.1111/j.1365-2966.2001.04667.x). arXiv: [0104041v1 \[arXiv:astro-ph\]](https://arxiv.org/abs/0104041v1). URL: <https://academic.oup.com/mnras/article-lookup/doi/10.1111/j.1365-2966.2001.04667.x>.

Balsara, Dinshaw S. and Daniel S Spicer (1999). “A Staggered Mesh Algorithm Using High Order Godunov Fluxes to Ensure Solenoidal Magnetic Fields in Magnetohydrodynamic Simulations”. In: *J. Comput. Phys.* 149.2, pp. 270–292. ISSN: 00219991. DOI: [10.1006/jcph.1998.6153](https://doi.org/10.1006/jcph.1998.6153). URL: <http://linkinghub.elsevier.com/retrieve/pii/S0021999198961538>.

Barai, Paramita et al. (2016). “Kinetic AGN feedback effects on cluster cool cores simulated using SPH”. In: *Mon. Not. R. Astron. Soc.* 461.2, pp. 1548–1567. ISSN: 13652966. DOI: [10.1093/mnras/stw1389](https://doi.org/10.1093/mnras/stw1389). arXiv: [1605.08051](https://arxiv.org/abs/1605.08051). URL: <http://adsabs.harvard.edu/abs/2016arXiv160508051B>.

Barnabe, Matteo et al. (2012). “The SWELLS survey – IV. Precision measurements of the stellar and dark matter distributions in a spiral lens galaxy”. In: *Mon. Not. R. Astron. Soc.* 423, pp. 1073–1088. DOI: [10.1111/j.1365-2966.2012.20934.x](https://doi.org/10.1111/j.1365-2966.2012.20934.x). URL: https://watermark.silverchair.com/mnras0423-1073.pdf?token=AQECAHi208BE49Ooan9kkhW{\}_Ercy7Dm3ZL{\}_9Cf3qfKAc485ysgAAAb0wgG5BqkqhkiG9w0BBwagggGqMIIBpgIBADCAZ8GCSqGSIB3DQEHTAeBglghkgBZQMEAS4wEQQMTXMvCG4cYcl1LvRbAgEQgIIBcPsvPjKMYEiUz39e{\}_3U2pC8dyKS9QZgI5P8z-1Q.

Barnes, Josh and Piet Hut (1986). “A hierarchical O(N log N) force-calculation algorithm”. In: *Nature* 324.6096, pp. 446–449. DOI: [10.1038/324446a0](https://doi.org/10.1038/324446a0). URL: <http://www.nature.com/articles/324446a0>.

Barris, Brian J. et al. (2005). “The NN2 Flux Difference Method for Constructing Variable Object Light Curves”. In: *Astron. J.* 130, pp. 2272–2277. DOI: [10.1086/491583](https://doi.org/10.1086/491583). arXiv: [0507584 \[astro-ph\]](https://arxiv.org/abs/0507584). URL: <http://arxiv.org/abs/astro-ph/0507584>.

Bate, Matthew R., Terrence S. Tricco, and Daniel J. Price (2013). “Collapse of a molecular cloud core to stellar densities: Stellar-core and outflow formation in radiation magnetohydrodynamic simulations”. In: *Mon. Not. R. Astron. Soc.* 437.1, pp. 77–95. ISSN: 00358711. DOI: [10.1093/mnras/stt1865](https://doi.org/10.1093/mnras/stt1865). arXiv: [1310.1092](https://arxiv.org/abs/1310.1092).

Batra, R. C. and G. M. Zhang (2007). “SSPH basis functions for meshless methods, and comparison of solutions with strong and weak formulations”. In: *Comput. Mech.* 41.4, pp. 527–545. DOI: [10.1007/s00466-007-0209-3](https://doi.org/10.1007/s00466-007-0209-3). URL: <http://link.springer.com/10.1007/s00466-007-0209-3>.

Bauer, Andreas and Volker Springel (2012). “Subsonic turbulence in smoothed particle hydrodynamics and moving-mesh simulations”. In: *Mon. Not. R. Astron. Soc.* 423.3, pp. 2558–2578. ISSN: 00358711. DOI: [10.1111/j.1365-2966.2012.21058.x](https://doi.org/10.1111/j.1365-2966.2012.21058.x). arXiv: [1109.4413](https://arxiv.org/abs/1109.4413).

Beck, Alexander M. et al. (2012). “Origin of strong magnetic fields in Milky Way-like galactic haloes”. In: *Mon. Not. R. Astron. Soc.* 422, pp. 2152–2163. ISSN: 00358711. DOI: [10.1111/j.1365-2966.2012.20759.x](https://doi.org/10.1111/j.1365-2966.2012.20759.x). arXiv: [1202.3349](https://arxiv.org/abs/1202.3349).

Beck, Alexander M. et al. (2013a). “On the magnetic fields in voids”. In: *Mon. Not. R. Astron. Soc.* 429.1, pp. L60–L64. DOI: [10.1093/mnrasl/sls026](https://doi.org/10.1093/mnrasl/sls026). arXiv: [1210.8360](https://arxiv.org/abs/1210.8360). URL: <http://arxiv.org/abs/1210.8360>.

Beck, Alexander M. et al. (2013b). “Strong magnetic fields and large rotation measures in protogalaxies from supernova seeding”. In: *Mon. Not. R. Astron. Soc.* 435.4, pp. 3575–3586. ISSN: 0035-8711. DOI: [10.1093/mnras/stt1549](https://doi.org/10.1093/mnras/stt1549). URL: <http://mnras.oxfordjournals.org/cgi/doi/10.1093/mnras/stt1549>.

Beck, Alexander M. et al. (2016). “An improved SPH scheme for cosmological simulations”. In: *Mon. Not. R. Astron. Soc.* 455, pp. 2110–2130. DOI: [10.1093/mnras/stv2443](https://doi.org/10.1093/mnras/stv2443). arXiv: [1502.0735](https://arxiv.org/abs/1502.0735). URL: <http://arxiv.org/abs/1502.0735>.

Beck, R. (2009). “Galactic and extragalactic magnetic fields – a concise review”. In: *Astrophys. Sp. Sci. Trans.* 5.1, pp. 43–47. DOI: [10.5194/astra-5-43-2009](https://doi.org/10.5194/astra-5-43-2009). URL: <http://www.astrophys-space-sci-trans.net/5/43/2009/>.

Beck, Rainer (2000). “Magnetic fields in normal galaxies”. In: *Philos. Trans. R. Soc. A Math. Phys. Eng. Sci.* 358.1767, pp. 777–796. DOI: [10.1098/rsta.2000.0558](https://doi.org/10.1098/rsta.2000.0558). URL: <http://rsta.royalsocietypublishing.org/cgi/doi/10.1098/rsta.2000.0558>.

— (2001). “Galactic and extragalactic magnetic fields”. In: *Space Sci. Rev.* 99.1/4, pp. 243–260. arXiv: [0012402 \[astro-ph\]](https://arxiv.org/abs/0012402). URL: <http://arxiv.org/abs/astro-ph/0012402>.

— (2007). “Magnetism in the spiral galaxy NGC 6946: magnetic arms, depolarization rings, dynamo modes and helical fields”. In: *Astron. Astrophys.* 470.2, pp. 539–556. DOI: [10.1051/0004-6361:20066988](https://doi.org/10.1051/0004-6361:20066988). arXiv: [0705.4163](https://arxiv.org/abs/0705.4163). URL: <http://arxiv.org/abs/0705.4163>.

— (2008). “Galactic and Extragalactic Magnetic Fields”. In: *HIGH ENERGY GAMMA-RAY Astron. Proc. 4th Int. Meet. High Energy Gamma-Ray Astron.* Vol. 1085. Potsdam: AIP, pp. 83–96. DOI: [10.1063/1.3076806](https://doi.org/10.1063/1.3076806). arXiv: [0810.2923](https://arxiv.org/abs/0810.2923). URL: <http://arxiv.org/abs/0810.2923>.

Beck, Rainer (2016). “Magnetic fields in spiral galaxies”. In: *Astron. Astrophys. Rev.* 24.4. DOI: [10.1007/s00159-015-0084-4](https://doi.org/10.1007/s00159-015-0084-4). URL: <https://link.springer.com/content/pdf/10.1007%2Fs00159-015-0084-4.pdf>.

Beck, Rainer et al. (1996). “Galactic Magnetism: Recent Developments and Perspectives”. In: *Annu. Rev. Astron. Astrophys.* 34.1, pp. 155–206. DOI: [10.1146/annurev.astro.34.1.155](https://doi.org/10.1146/annurev.astro.34.1.155). URL: <http://www.annualreviews.org/doi/10.1146/annurev.astro.34.1.155>.

Beck, Rainer et al. (2003). “Systematic bias in interstellar magnetic field estimates”. In: *Astron. Astrophys.* 411, pp. 99–107. DOI: [10.1051/0004-6361:20031101](https://doi.org/10.1051/0004-6361:20031101). arXiv: [0307330 \[astro-ph\]](https://arxiv.org/abs/astro-ph/0307330). URL: <http://arxiv.org/abs/astro-ph/0307330>.

Behroozi, Peter S., Risa H. Wechsler, and Hao-Yi Wu (2011). “The Rockstar Phase-Space Temporal Halo Finder and the Velocity Offsets of Cluster Cores”. In: *Astrophys. J.* 762.2. DOI: [10.1088/0004-637X/762/2/109](https://doi.org/10.1088/0004-637X/762/2/109). arXiv: [1110.4372](https://arxiv.org/abs/1110.4372). URL: <http://arxiv.org/abs/1110.4372>.

Benson, Andrew (2011). “Galacticus: A Semi-Analytic Model of Galaxy Formation”. In: *Astrophys. Source Code Libr.* URL: <http://adsabs.harvard.edu/abs/2011ascl.soft08004B>.

Benson, Andrew J. (2012). “Galacticus: A Semi-Analytic Model of Galaxy Formation”. In: *New Astron.* 17.2, pp. 175–197. DOI: [10.1016/j.newast.2011.07.004](https://doi.org/10.1016/j.newast.2011.07.004). arXiv: [1008.1786](https://arxiv.org/abs/1008.1786). URL: <http://arxiv.org/abs/1008.1786>.

Benson, Andrew J. et al. (2012). “Convergence of Galaxy Properties with Merger Tree Temporal Resolution”. In: *Mon. Not. R. Astron. Soc.* 419.4, pp. 3590–3603. DOI: [10.1111/j.1365-2966.2011.20002.x](https://doi.org/10.1111/j.1365-2966.2011.20002.x). arXiv: [1107.4098](https://arxiv.org/abs/1107.4098). URL: <http://arxiv.org/abs/1107.4098>.

Beresnyak, A, Alex Lazarian, and J Cho (2005). “Density Scaling and Anisotropy in Supersonic Magnetohydrodynamic Turbulence”. In: *Astrophys. J.* 624, pp. 93–96. URL: <http://iopscience.iop.org/article/10.1086/430702/pdf>.

Berger, M. J. and P. Colella (1989). “Local adaptive mesh refinement for shock hydrodynamics”. In: *J. Comput. Phys.* 82.1, pp. 64–84. ISSN: 10902716. DOI: [10.1016/0021-9991\(89\)90035-1](https://doi.org/10.1016/0021-9991(89)90035-1).

Berger, Marsha J. and Joseph Oliger (1984). “Adaptive mesh refinement for hyperbolic partial differential equations”. In: *J. Comput. Phys.* 53.3, pp. 484–512. ISSN: 10902716. DOI: [10.1016/0021-9991\(84\)90073-1](https://doi.org/10.1016/0021-9991(84)90073-1). URL: <http://linkinghub.elsevier.com/retrieve/pii/0021999184900731>.

Bertone, Gianfranco and Dan Hooper (2016). *A History of Dark Matter*. Tech. rep. Fermilab. arXiv: [1605.04909](https://arxiv.org/abs/1605.04909). URL: <http://arxiv.org/abs/1605.04909>.

Betti, Sarah et al. (2017). “VLA Observations of the Magnetic Field of the Smith High Velocity Cloud”. In: *Am. Astron. Soc. AAS Meet. #229, id.340.35*. Vol. 229. URL: <http://adsabs.harvard.edu/abs/2017AAS...22934035B>.

Biffi, Veronica and Riccardo Valdarnini (2015). “The role of the artificial conductivity in SPH simulations of galaxy clusters: effects on the ICM properties”. In: *Mon. Not. R. Astron. Soc.* 446.3, pp. 2802–2822. ISSN: 13652966. DOI: [10.1093/mnras/stu2278](https://doi.org/10.1093/mnras/stu2278). arXiv: [1410.8529](https://arxiv.org/abs/1410.8529). URL: <http://arxiv.org/abs/1410.8529>.

Biffi, Veronica et al. (2016). “On the nature of hydrostatic equilibrium in galaxy clusters”. In: 4. arXiv: 1606.02293. URL: <http://arxiv.org/abs/1606.02293>.

Binney, James and Lennox L Cowie (1981). “X-Ray Emission from M87: A Pressure Confined Cooling Atmosphere Surrounding a Low Mass Galaxy”. In: *Astrophys. J.* 247.1, pp. 464–472.

Binney, James and Scott Tremaine (2008). *Galactic dynamics*. 2nd. Princeton: Princeton University Press, p. 885. ISBN: 9780691130262. URL: <http://adsabs.harvard.edu/abs/2008gady.book.....B>.

Bird, Jonathan C. et al. (2013). “Inside Out and Upside Down: Tracing the Assembly of a Simulated Disk Galaxy Using Mono-Age Stellar Populations”. In: *Astrophys. J.* 773.1. DOI: 10.1088/0004-637X/773/1/43. arXiv: 1301.0620. URL: <http://arxiv.org/abs/1301.0620>.

Birdsall, C K and Dieter Fuss (1969). “Clouds-in-Clouds, Clouds-in-Cells Physics for Many-Body Plasma Simulation”. In: *J. Comput. Phys.* 3, pp. 494–511.

Birdsall, C. K. and A. B. Langdon (1991). *Plasma Physics via Computer Simulation*.

Birdsall, C K, A B Langdon, and H Okuda (1970). “Finite-Size Particle Physics applied to Plasma Simulation”. In: *Methods Comput. Phys.* 9.

Bittner, Adrian et al. (2017). “How do spiral arm contrasts relate to bars, disc breaks and other fundamental galaxy properties?” In: *Mon. Not. R. Astron. Soc.* 471.1, pp. 1070–1087. DOI: 10.1093/mnras/stx1646. arXiv: 1706.09904. URL: <http://arxiv.org/abs/1706.09904>.

Blackford, L S et al. (2002). “An Updated Set of Basic Linear Algebra Subprograms (BLAS)”. In: *ACM Trans. Math. Softw.* 28.2, pp. 135–151. ISSN: 0098-3500. DOI: 10.1145/567806.567807. URL: <http://doi.acm.org/10.1145/567806.567807>.

Bland-Hawthorn, Joss and Ortwin Gerhard (2016). “The Galaxy in Context: Structural, Kinematic and Integrated Properties”. In: *Annu. Rev. Astron. Astrophys.* 54, pp. 529–596. ISSN: 0066-4146. DOI: 10.1146/annurev-astro-081915-023441. arXiv: 1602.07702. URL: <http://arxiv.org/abs/1602.07702> <http://dx.doi.org/10.1146/annurev-astro-081915-023441>.

Bode, Paul, Jeremiah P. Ostriker, and Guohong Xu (2000). “The Tree-Particle-Mesh N-body Gravity Solver”. In: *Astrophys. J. Suppl. Ser.* 128, pp. 561–569. DOI: 10.1086/313398. arXiv: 9912541 [astro-ph]. URL: <http://arxiv.org/abs/astro-ph/9912541>.

Bogdanović, Tamara et al. (2009). “Simulations of Magnetohydrodynamics Instabilities in Intracluster Medium Including Anisotropic Thermal Conduction”. In: *Astrophys. J.* 704.1, pp. 211–225. ISSN: 0004-637X. DOI: 10.1088/0004-637X/704/1/211. URL: <http://stacks.iop.org/0004-637X/704/i=1/a=211?key=crossref.60d2fc18982bac354ad357b9799ce2d1>.

Bonafede, Annalisa et al. (2010). “The Coma cluster magnetic field from Faraday rotation measures”. In: *Astron. Astrophys.* 513, A30. ISSN: 0004-6361. DOI: 10.1051/0004-6361/200913696. URL: <http://www.aanda.org/10.1051/0004-6361/200913696>.

Bonafede, Annalisa et al. (2011). “A non-ideal magnetohydrodynamic gadget: simulating massive galaxy clusters”. In: *Mon. Not. R. Astron. Soc.* 418.4, pp. 2234–2250. ISSN: 00358711. DOI: [10.1111/j.1365-2966.2011.19523.x](https://doi.org/10.1111/j.1365-2966.2011.19523.x). arXiv: [1107.0968](https://arxiv.org/abs/1107.0968). URL: <http://mnras.oxfordjournals.org/cgi/doi/10.1111/j.1365-2966.2011.19523.x>.

Borgani, Stefano and Andrey Kravtsov (2009). “Cosmological simulations of galaxy clusters”. In: arXiv: [arXiv:0906.4370v1](https://arxiv.org/abs/0906.4370v1).

Boss, A. P. and P. Bodenheimer (1979). “Fragmentation in a rotating protostar - A comparison of two three-dimensional computer codes”. In: *ApJ* 234, p. 289. ISSN: 0004-637X. DOI: [10.1086/157497](https://doi.org/10.1086/157497). URL: <http://adsabs.harvard.edu/abs/1979ApJ...234..289B>.

Bowyer, A. (1981). “Computing Dirichlet tessellations”. In: *Comput. J.* 24.2, pp. 162–166. DOI: [10.1093/comjnl/24.2.162](https://doi.org/10.1093/comjnl/24.2.162). URL: <https://academic.oup.com/comjnl/article-lookup/doi/10.1093/comjnl/24.2.162>.

Brackbill, J.U and D.C Barnes (1980). “The Effect of Nonzero $\cdot B$ on the numerical solution of the magnetohydrodynamic equations”. In: *J. Comput. Phys.* 35.3, pp. 426–430. ISSN: 00219991. DOI: [10.1016/0021-9991\(80\)90079-0](https://doi.org/10.1016/0021-9991(80)90079-0). URL: <http://linkinghub.elsevier.com/retrieve/pii/0021999180900790>.

Braginskii, S. I. (1965). “Transport Processes in a Plasma”. In: *Rev. Plasma Phys.* P. 205.

Bregman, Joel N. and Laurence P. David (1989). “Alternative Models of Cooling Flows”. In: *Astrophys. J.* 341, pp. 49–53.

Brookshaw, L. (1985). “A method of calculating radiative heat diffusion in particle simulations”. In: *Astron. Soc. Aust. Proceeding*. Vol. 6. 2, pp. 207–210.

Brown, J. C. et al. (2007). “Rotation Measures of Extragalactic Sources Behind the Southern Galactic Plane: New Insights into the Large-Scale Magnetic Field of the Inner Milky Way”. In: *Astrophys. J.* 663.1, pp. 258–266. DOI: [10.1086/518499](https://doi.org/10.1086/518499). arXiv: [0704.0458](https://arxiv.org/abs/0704.0458). URL: [http://arxiv.org/abs/0704.0458](https://arxiv.org/abs/0704.0458).

Brown, Shea and Lawrence Rudnick (2011). “Diffuse Radio Emission in/around the Coma Cluster: Beyond Simple Accretion”. In: *Mon. Not. R. Astron. Soc.* 412.1, pp. 2–12. arXiv: [arXiv:1009.4258v2](https://arxiv.org/abs/1009.4258v2). URL: <https://arxiv.org/pdf/1009.4258.pdf> <http://adsabs.harvard.edu/abs/2011MNRAS.412....2B>.

Brunetti, Gianfranco and Alex Lazarian (2007). “Compressible turbulence in galaxy clusters: Physics and stochastic particle re-acceleration”. In: *Mon. Not. R. Astron. Soc.* 378.1, pp. 245–275. ISSN: 00358711. DOI: [10.1111/j.1365-2966.2007.11771.x](https://doi.org/10.1111/j.1365-2966.2007.11771.x). arXiv: [0703591 \[astro-ph\]](https://arxiv.org/abs/0703591).

— (2011). “Particle reacceleration by compressible turbulence in galaxy clusters: Effects of a reduced mean free path”. In: *Mon. Not. R. Astron. Soc.* 412.2, pp. 817–824. ISSN: 00358711. DOI: [10.1111/j.1365-2966.2010.17937.x](https://doi.org/10.1111/j.1365-2966.2010.17937.x). arXiv: [1011.1198 \[astro-ph.CO\]](https://arxiv.org/abs/1011.1198).

Bryan, G. L. and M. L. Norman (1997). “Simulating X-ray Clusters with Adaptive Mesh Refinement”. In: *Comput. Astrophys. 12th Kingst. Meet. Theor. Astrophys.* Ed. by D.A. Clarke and

M.J. West. Vol. 123. Halifax; Nova Scotia: ASP Conference Series, p. 363. arXiv: 9710186 [astro-ph]. URL: <http://arxiv.org/abs/astro-ph/9710186>.

Bryan, Greg L. et al. (1995). “A piecewise parabolic method for cosmological hydrodynamics”. In: *Comput. Phys. Commun.* 89, pp. 149–168. ISSN: 00104655. DOI: [10.1016/0010-4655\(94\)00191-4](https://doi.org/10.1016/0010-4655(94)00191-4).

Bryan, Greg L. et al. (2014). “Enzo: An Adaptive Mesh Refinement Code for Astrophysics”. In: *Astrophys. J. Suppl. Ser.* 19. ISSN: 0067-0049. DOI: [10.1088/0067-0049/211/2/19](https://doi.org/10.1088/0067-0049/211/2/19). arXiv: 1307.2265. URL: <http://arxiv.org/abs/1307.2265> <http://dx.doi.org/10.1088/0067-0049/211/2/19>.

Buneman, O. (1959). “Dissipation of currents in ionized media”. In: *Phys. Rev.* 115.3, pp. 503–517. ISSN: 0031899X. DOI: [10.1103/PhysRev.115.503](https://doi.org/10.1103/PhysRev.115.503).

— (1973). “Subgrid resolution of flows and force fields”. In: *J. Comput. \ Phys.* 11, pp. 250–268.

Burkert, A et al. (2010). “High-redshift Star-forming Galaxies: Angular Momentum and Baryon Fraction, Turbulent Pressure Effects, and the Origin of Turbulence”. In: *Astrophys. J.* 725, pp. 2324–2332. DOI: [10.1088/0004-637X/725/2/2324](https://doi.org/10.1088/0004-637X/725/2/2324). URL: <http://iopscience.iop.org/article/10.1088/0004-637X/725/2/2324/pdf>.

Burkert, Andreas and Peter Bodenheimer (1993). “Multiple fragmentation in collapsing protostars”. In: *Mon. Not. R. Astron. Soc.* 264.

Butsky, Iryna et al. (2017). “Ab initio Simulations of a Supernova Driven Galactic Dynamo in an Isolated Disk Galaxy”. In: *Astrophys. J.* 843.2. DOI: [10.3847/1538-4357/aa799f](https://doi.org/10.3847/1538-4357/aa799f). arXiv: 1610.08528. URL: <http://arxiv.org/abs/1610.08528>.

Calhoun, Donna and Randall J. LeVeque (2000). “A Cartesian Grid Finite-Volume Method for the Advection-Diffusion Equation in Irregular Geometries”. In: *J. Comput. Phys.* 157.1, pp. 143–180. ISSN: 00219991. DOI: [10.1006/jcph.1999.6369](https://doi.org/10.1006/jcph.1999.6369). URL: <http://linkinghub.elsevier.com/retrieve/pii/S0021999199963696>.

Callahan, David, Ken Kennedy, and Allan Porterfield (1991). “Software Prefetching”. In: *Proc. Fourth Int. Conf. Archit. Support Program. Lang. Oper. Syst.* ASPLOS IV. New York, NY, USA: ACM, pp. 40–52. ISBN: 0-89791-380-9. DOI: [10.1145/106972.106979](https://doi.org/10.1145/106972.106979). URL: <http://doi.acm.org/10.1145/106972.106979>.

Carretti, E. et al. (2013). “Giant Magnetized Outflows from the Centre of the Milky Way”. In: *Nature* 493.7430, pp. 66–69. DOI: [10.1038/nature11734](https://doi.org/10.1038/nature11734). arXiv: 1301.0512. URL: <http://arxiv.org/abs/1301.0512>.

Cartwright, Annabel, Dimitris Stamatellos, and Anthony P. Whitworth (2009). “The effect of Poisson noise on SPH calculations”. In: *Mon. Not. R. Astron. Soc.* 395.4, pp. 2373–2380. ISSN: 00358711. DOI: [10.1111/j.1365-2966.2009.14720.x](https://doi.org/10.1111/j.1365-2966.2009.14720.x). URL: <http://mnras.oxfordjournals.org/cgi/doi/10.1111/j.1365-2966.2009.14720.x>.

Caswell, J. L. et al. (2010). “The 6-GHz methanol multibeam maser catalogue I: Galactic Centre region, longitudes 345 to 6”. In: *Mon. Not. R. Astron. Soc.* 404, pp. 1029–1060. ISSN: 0035-8711. DOI: [10.1111/j.1365-2966.2010.16339.x](https://doi.org/10.1111/j.1365-2966.2010.16339.x). arXiv: 1002.2475. URL: <http://arxiv.org/abs/1002.2475> <http://dx.doi.org/10.1111/j.1365-2966.2010.16339.x>.

Caswell, J. L. et al. (2011). “The 6-GHz methanol multibeam maser catalogue - III. Galactic longitudes 330 to 345”. In: *Mon. Not. R. Astron. Soc.* 417.3, pp. 1964–1995. ISSN: 00358711. DOI: [10.1111/j.1365-2966.2011.19383.x](https://doi.org/10.1111/j.1365-2966.2011.19383.x). URL: <https://academic.oup.com/mnras/article-lookup/doi/10.1111/j.1365-2966.2011.19383.x>.

Cavaliere, A. and R. Fusco-Femiano (1978). “The Distribution of Hot Gas in Clusters of Galaxies”. In: *Astron. Astrophys.* 70, p. 677. ISSN: 1432-0756. URL: <http://adsabs.harvard.edu/abs/1978A&A...70..677C>.

Cha, Seung-Hoon, Shu-Ichiro Inutsuka, and Sergei Nayakshin (2010). “Kelvin-Helmholtz instabilities with Godunov smoothed particle hydrodynamics”. In: *Mon. Not. R. Astron. Soc.* 403.3, pp. 1165–1174. ISSN: 00358711. DOI: [10.1111/j.1365-2966.2010.16200.x](https://doi.org/10.1111/j.1365-2966.2010.16200.x). URL: <http://mnras.oxfordjournals.org/cgi/doi/10.1111/j.1365-2966.2010.16200.x>.

Chandran, Benjamin and Steven Cowley (1998). “Thermal Conduction in a Tangled Magnetic Field”. In: *Phys. Rev. Lett.* 80.14, pp. 3077–3080. ISSN: 0031-9007. DOI: [10.1103/PhysRevLett.80.3077](https://doi.org/10.1103/PhysRevLett.80.3077). URL: <http://link.aps.org/doi/10.1103/PhysRevLett.80.3077>.

Chandrasekhar, S. and E. Fermi (1953). “Magnetic Fields in Spiral Arms.” In: *Astrophys. J.* 118, p. 113. ISSN: 0004-637X. DOI: [10.1086/145731](https://doi.org/10.1086/145731). URL: <http://adsabs.harvard.edu/doi/10.1086/145731>.

Chapman, Nicholas L. et al. (2011). “The Magnetic Field in Taurus Probed by Infrared Polarization”. In: *Astrophys. J.* 741.1. DOI: [10.1088/0004-637X/741/1/21](https://doi.org/10.1088/0004-637X/741/1/21). arXiv: [1108.0410](https://arxiv.org/abs/1108.0410). URL: <http://arxiv.org/abs/1108.0410>.

Chellappa, Srinivas, Franz Franchetti, and Markus Püschel (2008). “Generative and Transformational Techniques in Software Engineering II: International Summer School, GTTSE 2007, Braga, Portugal, July 2-7, 2007. Revised Papers”. In: ed. by Ralf Lämmel, Joost Visser, and João Saraiva. Berlin, Heidelberg: Springer Berlin Heidelberg. Chap. How to Wri, pp. 196–259. ISBN: 978-3-540-88643-3. DOI: [10.1007/978-3-540-88643-3_5](https://doi.org/10.1007/978-3-540-88643-3_5). URL: http://dx.doi.org/10.1007/978-3-540-88643-3__5.

Chen, Wei and Tong Qiu (2013). “Simulation of earthquake-induced slope deformation using SPH method”. In: *Int. J. Numer. Anal. Methods Geomech.* 38.3, pp. 297–330. DOI: [10.1002/nag.2218](https://doi.org/10.1002/nag.2218). URL: <http://doi.wiley.com/10.1002/nag.2218>.

Cheng, H., L. Greengard, and V. Rokhlin (1999). “A Fast Adaptive Multipole Algorithm in Three Dimensions”. In: *J. Comput. Phys.* 155.2, pp. 468–498. DOI: [10.1006/jcph.1999.6355](https://doi.org/10.1006/jcph.1999.6355). URL: <http://linkinghub.elsevier.com/retrieve/pii/S0021999199963556>.

Chisari, Nora Elisa and Matias Zaldarriaga (2011). “Connection between Newtonian simulations and general relativity”. In: *Phys. Rev. D* 83.12. DOI: [10.1103/PhysRevD.83.123505](https://doi.org/10.1103/PhysRevD.83.123505). arXiv: [1101.3555](https://arxiv.org/abs/1101.3555). URL: <http://arxiv.org/abs/1101.3555>.

Cho, Jungyeon, Alex Lazarian, and Ethan T Vishniac (2002). “New Regime of Magnetohydrodynamic Turbulence: Cascade below the Viscous Cutoff”. In: *Astrophys. J.* 566, pp. 49–52. URL: <http://iopscience.iop.org/article/10.1086/339453/pdf>.

Cho, Jungyeon and Ethan T Vishniac (2000). “The Anisotropy of Magnetohydrodynamic Alfvénic Turbulence”. In: *Astrophys. J.* 539, pp. 273–282. URL: <http://iopscience.iop.org/article/10.1086/309213/pdf>.

Cho, Jungyeon and Hyunju Yoo (2016). “A Technique for Constraining the Driving Scale of Turbulence and a Modified Chandrasekhar-Fermi Method”. In: *Astrophys. J.* 821, p. 000000. DOI: <10.3847/0004-637X/821/1/21>. URL: <http://iopscience.iop.org/article/10.3847/0004-637X/821/1/21/pdf>.

Chyzy, K. T. et al. (2003). “Magnetic Fields and Ionized Gas in the Local Group Irregular Galaxies IC10 and NGC6822”. In: *Astron. Astrophys.* 405, pp. 513–524. DOI: <10.1051/0004-6361:20030628>. arXiv: [0308500 \[astro-ph\]](0308500). URL: <http://arxiv.org/abs/astro-ph/0308500>.

Chyzy, K. T. et al. (2007). “Magnetic fields and ionized gas in nearby late type galaxies”. In: *Astron. Astrophys.* 462.3, pp. 933–941. DOI: <10.1051/0004-6361:20065932>. arXiv: [0611316 \[astro-ph\]](0611316). URL: <http://arxiv.org/abs/astro-ph/0611316>.

Clark, S E, J E G Peek, and M E Putman (2014). “Magnetically Aligned H I Fibers and the Rolling Hough Transform”. In: *Astrophys. J.* 789.13pp. DOI: <10.1088/0004-637X/789/1/82>. URL: <http://iopscience.iop.org/article/10.1088/0004-637X/789/1/82/pdf>.

Clarke, Tracy E (2004). “Faraday Rotation Observations of Magnetic Fields in Galaxy Clusters”. In: *J. Korean Astron. Soc.* 37, pp. 337–342. URL: http://articles.adsabs.harvard.edu/cgi-bin/nph-iarticle{_}query?2004JKAS...37..337C{\&}data{_}type=PDF{_}HIGH{\&}whole{_}paper=YES{\&}type=PRINTER{\&}filetype=.pdf.

Cleary, Paul W and Joseph J Monaghan (1999). “Conduction Modelling Using Smoothed Particle Hydrodynamics”. In: *J. Comput. Phys.* 148.1, pp. 227–264. ISSN: 00219991. DOI: <10.1006/jcph.1998.6118>. URL: <http://linkinghub.elsevier.com/retrieve/pii/S0021999198961186>.

Cockburn, Bernardo and Chi-Wang Shu (1998). “The Runge–Kutta Discontinuous Galerkin Method for Conservation Laws V”. In: *J. Comput. Phys.* 141.2, pp. 199–224. ISSN: 00219991. DOI: <10.1006/jcph.1998.5892>. URL: <http://linkinghub.elsevier.com/retrieve/pii/S0021999198958922>.

Conlon, Joseph P. et al. (2017). “Consistency of Hitomi, XMM-Newton and Chandra 3.5 keV data from Perseus”. In: *Phys. Rev. D* 96.12. DOI: <10.1103/PhysRevD.96.123009>. arXiv: <1608.01684>. URL: <http://arxiv.org/abs/1608.01684>.

Coombes, David (2011). *Fluid Simulation in Alice: Madness Returns* | NVIDIA Developer. URL: <https://developer.nvidia.com/content/fluid-simulation-alice-madness-returns> (visited on 01/19/2018).

Cora, Sofía A. et al. (2018a). “Semi-Analytic Galaxies - I. Synthesis of environmental and star-forming regulation mechanisms”. In: *eprint arXiv:1801.03883*. arXiv: <1801.03883>. URL: <http://arxiv.org/abs/1801.03883>.

Cora, Sofía A. et al. (2018b). “Semi-Analytic Galaxies - II. Revealing the role of environmental and mass quenching in galaxy formation”. In: *eprint arXiv:1801.03884*. arXiv: <1801.03884>. URL: <http://arxiv.org/abs/1801.03884>.

Courteau, Stéphane and Aaron A Dutton (2015). “On the Global Mass Distribution in Disk Galaxies”. In: *Astrophys. J. Lett.* 801.2. DOI: [10.1088/2041-8205/801/2/L20](https://doi.org/10.1088/2041-8205/801/2/L20). URL: <http://iopscience.iop.org/article/10.1088/2041-8205/801/2/L20/pdf>.

Cowie, Lennox L and Christopher F. McKee (1977). “The Evaporation of Spherical Clouds in a Hot Gas. I. Classical and Saturated Mass Loss Rates”. In: *Astrophys. J.* 211, pp. 135–146.

Crespo, A.J.C. et al. (2015). “DualSPHysics: Open-source parallel CFD solver based on Smoothed Particle Hydrodynamics (SPH)”. In: *Comput. Phys. Commun.* 187, pp. 204–216. DOI: [10.1016/j.cpc.2014.10.004](https://doi.org/10.1016/j.cpc.2014.10.004). URL: [http://www.sciencedirect.com/science/article/pii/S0010465514003397{\#}](http://www.sciencedirect.com/science/article/pii/S0010465514003397).

Crockett, R. K. et al. (2005). “An Unsplit, Cell-Centered Godunov Method for Ideal MHD”. In: *J. Comput. Physics*, Vol. 203, Issue 2, p. 422-448. 203, pp. 422–448. ISSN: 0021-9991. DOI: [10.1016/j.jcp.2004.12.002](https://doi.org/10.1016/j.jcp.2004.12.002). arXiv: [0309307 \[astro-ph\]](https://arxiv.org/abs/astro-ph/0309307). URL: <http://arxiv.org/abs/astro-ph/0309307> [http://dx.doi.org/10.1016/j.jcp.2004.12.002](https://doi.org/10.1016/j.jcp.2004.12.002).

Croston, J. H. et al. (2008). “Galaxy-cluster gas-density distributions of the Representative XMM-Newton Cluster Structure Survey (RECESS)”. In: *Astron. Astrophys.* 487.2, pp. 431–443. DOI: [10.1051/0004-6361:20079154](https://doi.org/10.1051/0004-6361:20079154). arXiv: [0801.3430](https://arxiv.org/abs/0801.3430). URL: <http://arxiv.org/abs/0801.3430>.

Croton, Darren J. et al. (2016a). “SAGE: Semi-Analytic Galaxy Evolution”. In: *Astrophys. Source Code Libr.* URL: <http://adsabs.harvard.edu/abs/2016ascl.soft01006C>.

— (2016b). “Semi-Analytic Galaxy Evolution (SAGE): Model Calibration and Basic Results”. In: *Astrophys. J. Suppl. Ser.* 222.2. DOI: [10.3847/0067-0049/222/2/22](https://doi.org/10.3847/0067-0049/222/2/22). arXiv: [1601.04709](https://arxiv.org/abs/1601.04709). URL: <http://arxiv.org/abs/1601.04709>.

Crutcher, R. M. and I. Kazes (1983). “The magnetic field of the NGC 2024 molecular cloud - Detection of OH line Zeeman splitting”. In: *Astron. Astrophys.* 125.2, pp. L23–L26. URL: <http://adsabs.harvard.edu/abs/1983A{\%}26A...125L..23C>.

Crutcher, R. M. et al. (1993). “OH Zeeman observations of dark clouds”. In: *Astrophys. J.* 407, p. 175. DOI: [10.1086/172503](https://doi.org/10.1086/172503). URL: <http://adsabs.harvard.edu/doi/10.1086/172503>.

Crutcher, Richard M. (2012). “Magnetic Fields in Molecular Clouds”. In: *Annu. Rev. Astron. Astrophys.* 50.1, pp. 29–63. ISSN: 0066-4146. DOI: [10.1146/annurev-astro-081811-125514](https://doi.org/10.1146/annurev-astro-081811-125514). URL: <http://www.annualreviews.org/doi/10.1146/annurev-astro-081811-125514>.

Crutcher, Richard M. and Richard M. (1999). “Magnetic Fields in Molecular Clouds: Observations Confront Theory”. In: *Astrophys. J.* 520.2, pp. 706–713. ISSN: 0004-637X. DOI: [10.1086/307483](https://doi.org/10.1086/307483). URL: <http://stacks.iop.org/0004-637X/520/i=2/a=706>.

Cudlip, W. et al. (1982). “Far infrared polarimetry of W51A and M42”. In: *Mon. Not. R. Astron. Soc.* 200.4, pp. 1169–1173. DOI: [10.1093/mnras/200.4.1169](https://doi.org/10.1093/mnras/200.4.1169). URL: <https://academic.oup.com/mnras/article-lookup/doi/10.1093/mnras/200.4.1169>.

Cueto-Felgueroso, L. et al. (2004). “On the Galerkin formulation of the smoothed particle hydrodynamics method”. In: *Int. J. Numer. Methods Eng.* 60.9, pp. 1475–1512. DOI: [10.1002/nme.1011](https://doi.org/10.1002/nme.1011). URL: <http://doi.wiley.com/10.1002/nme.1011>.

Cui, Weiguang et al. (2008). “An Ideal Mass Assignment Scheme for Measuring the Power Spectrum with Fast Fourier Transforms”. In: *Astrophys. J.* 687.2, pp. 738–744. ISSN: 0004-637X. DOI: [10.1086/592079](https://doi.org/10.1086/592079). arXiv: 0804.0070. URL: <http://arxiv.org/abs/0804.0070> { \& } 5Cnhttp://stacks.iop.org/0004-637X/687/i=2/a=738.

Cui, Weiguang et al. (2016). “nIFTy Galaxy Cluster simulations IV: Quantifying the Influence of Baryons on Halo Properties”. In: *Mon. Not. R. Astron. Soc.* 458.4, pp. 4052–4073. DOI: [10.1093/mnras/stw603](https://doi.org/10.1093/mnras/stw603). arXiv: 1602.06668. URL: <http://arxiv.org/abs/1602.06668>.

Cullen, Lee and Walter Dehnen (2010). “Inviscid smoothed particle hydrodynamics”. In: *Mon. Not. R. Astron. Soc.* 408.2, pp. 669–683. ISSN: 00358711. DOI: [10.1111/j.1365-2966.2010.17158.x](https://doi.org/10.1111/j.1365-2966.2010.17158.x). URL: <http://mnras.oxfordjournals.org/cgi/doi/10.1111/j.1365-2966.2010.17158.x>.

Dalla Vecchia, Claudio and Joop Schaye (2012). “Simulating galactic outflows with thermal supernova feedback”. In: *Mon. Not. R. Astron. Soc.* 426.1, pp. 140–158. DOI: [10.1111/j.1365-2966.2012.21704.x](https://doi.org/10.1111/j.1365-2966.2012.21704.x). arXiv: 1203.5667. URL: <http://arxiv.org/abs/1203.5667>.

Daubechies, Ingrid (1992). “Ten lectures on wavelets”. In: *CBMS-NSF Reg. Conf. Ser. Appl. Math. Lect. Deliv. CBMS Conf. wavelets*. Ed. by Ingrid Daubechies. DOI: <http://dx.doi.org/10.1137/1.9781611970104>.

Dauch, T. F. et al. (2017). “Preprocessing Workflow for the Initialization of SPH Predictions based on Arbitrary CAD Models”. In: *Proc. SPHERIC 2017 – 12th Int. SPHERIC Work.* Ourense.

Dawson, John (1962). “One-Dimensional Plasma Model”. In: *Phys. Fluids* 5.4, pp. 445–459. ISSN: 00319171. DOI: [10.1063/1.1706638](https://doi.org/10.1063/1.1706638). URL: <http://link.aip.org/link/PFLDAS/v5/i4/p445/s1&Agg=doi> { \& } 5Cnhttp://scitation.aip.org/content/aip/journal/pof1/5/4/10.1063/1.1706638.

Dawson, John M. (1960). “Plasma Oscillations of a Large Number of Electron Beams”. In: *Phys. Rev.* 118.2, pp. 381–389. ISSN: 0031-899X. DOI: [10.1103/PhysRev.118.381](https://doi.org/10.1103/PhysRev.118.381). URL: <https://link.aps.org/doi/10.1103/PhysRev.118.381>.

Deguchi, S. and W. D. Watson (1984). “Linear polarization of molecular lines at radio frequencies”. In: *Astrophys. J.* 285, p. 126. ISSN: 0004-637X. DOI: [10.1086/162483](https://doi.org/10.1086/162483). URL: <http://adsabs.harvard.edu/doi/10.1086/162483>.

Dehnen, Walter (2000). “A Very Fast and Momentum-conserving Tree Code”. In: *Astrophys. J.* 536.1, pp. L39–L42. DOI: [10.1086/312724](https://doi.org/10.1086/312724). URL: <http://stacks.iop.org/1538-4357/536/i=1/a=L39>.

— (2002). “A Hierarchical (N) Force Calculation Algorithm”. In: *J. Comput. Phys.* 179.1, pp. 27–42. DOI: [10.1006/jcph.2002.7026](https://doi.org/10.1006/jcph.2002.7026). URL: <http://linkinghub.elsevier.com/retrieve/pii/S0021999102970269>.

Dehnen, Walter and Hossam Aly (2012). “Improving convergence in smoothed particle hydrodynamics simulations without pairing instability”. In: *Mon. Not. R. Astron. Soc.* 1082. ISSN: 00358711. DOI: [10.1111/j.1365-2966.2012.21439.x](https://doi.org/10.1111/j.1365-2966.2012.21439.x). URL: <http://doi.wiley.com/10.1111/j.1365-2966.2012.21439.x>.

Dementiev, R, L Kettner, and P Sanders (2008). “STXXL: standard template library for XXL data sets”. In: *Softw. Pract. Exp.* 38.6, pp. 589–637. ISSN: 1097-024X. DOI: [10.1002/spe.844](https://doi.org/10.1002/spe.844). URL: <http://dx.doi.org/10.1002/spe.844>.

Denning, Peter J (2005). “The Locality Principle”. In: *Commun. ACM* 48.7, pp. 19–24. ISSN: 0001-0782. DOI: [10.1145/1070838.1070856](https://doi.org/10.1145/1070838.1070856). URL: <http://doi.acm.org/10.1145/1070838.1070856>.

Dickey, J. M. et al. (2013). “GASKAP – The Galactic ASKAP Survey”. In: *Publ. Astron. Soc. Aust.* 30. DOI: [10.1017/pasa.2012.003](https://doi.org/10.1017/pasa.2012.003). arXiv: [1207.0891](https://arxiv.org/abs/1207.0891). URL: <http://arxiv.org/abs/1207.0891>.

Diehl, Steven et al. (2012). “Generating Optimal Initial Conditions for Smooth Particle Hydrodynamics Simulations”. In: *Mon. Rev.* 000.November, p. 30. arXiv: [1211.0525](https://arxiv.org/abs/1211.0525). URL: <http://arxiv.org/abs/1211.0525>.

Dilts, Gary A. (2000). “Moving least-squares particle hydrodynamics II: conservation and boundaries”. In: *Int. J. Numer. Methods Eng.* 48.10, pp. 1503–1524. DOI: [10.1002/1097-0207\(20000810\)48:10<1503::AID-NME832>3.0.CO;2-D](https://doi.org/10.1002/1097-0207(20000810)48:10<1503::AID-NME832>3.0.CO;2-D). URL: <http://doi.wiley.com/10.1002/1097-0207{\%}2820000810{\%}2948{\%}3A10{\%}3C1503{\%}3A{\%}3AAID-NME832{\%}3E3.0.CO{\%}3B2-D>.

Dolag, Klaus, Matthias Bartelmann, and Harald Lesch (1999). “SPH simulations of magnetic fields in galaxy clusters (proceedings)”. In: *Astron. Astrophys.* 363, p. 4. ISSN: 0004-6361. arXiv: [9907199 \[astro-ph\]](https://arxiv.org/abs/9907199). URL: <http://arxiv.org/abs/astro-ph/9907199>.

Dolag, Klaus, Eiichiro Komatsu, and Rashid Sunyaev (2016). “SZ effects in the Magneticum Pathfinder Simulation: Comparison with the Planck, SPT, and ACT results”. In: *Mon. Not. R. Astron. Soc.* 463.2, pp. 1797–1811. ISSN: 0035-8711. DOI: [10.1093/mnras/stw2035](https://doi.org/10.1093/mnras/stw2035). arXiv: [1509.05134](https://arxiv.org/abs/1509.05134). URL: <http://arxiv.org/abs/1509.05134> <http://dx.doi.org/10.1093/mnras/stw2035>.

Dolag, Klaus, Emilio Mevius, and Rhea-Silvia Remus (2017). “Distribution and Evolution of Metals in the Magneticum simulations”. In: *Galaxies* 5, p. 35. DOI: [10.3390/galaxies5030035](https://doi.org/10.3390/galaxies5030035). arXiv: [1708.00027](https://arxiv.org/abs/1708.00027). URL: <http://arxiv.org/abs/1708.00027>.

Dolag, Klaus and Federico Stasyszyn (2009). “An MHD gadget for cosmological simulations”. In: *Mon. Not. R. Astron. Soc.* 398.4, pp. 1678–1697. ISSN: 00358711. DOI: [10.1111/j.1365-2966.2009.15181.x](https://doi.org/10.1111/j.1365-2966.2009.15181.x). URL: <http://doi.wiley.com/10.1111/j.1365-2966.2009.15181.x>.

Dolag, Klaus et al. (2004). “Thermal Conduction in Simulated Galaxy Clusters”. In: *Astrophys. J.* 606.2, pp. 2000–2003.

Dolag, Klaus et al. (2005a). “The imprints of local superclusters on the Sunyaev-Zel’dovich signals and their detectability with PLANCK”. In: *Mon. Not. R. Astron. Soc.* 363.1, pp. 29–39.

Dolag, Klaus et al. (2005b). “Turbulent gas motions in galaxy cluster simulations: The role of smoothed particle hydrodynamics viscosity”. In: *Mon. Not. R. Astron. Soc.* 364.3, pp. 753–772. ISSN: 00358711. DOI: [10.1111/j.1365-2966.2005.09630.x](https://doi.org/10.1111/j.1365-2966.2005.09630.x). arXiv: [0507480 \[astro-ph\]](https://arxiv.org/abs/0507480).

Dolag, Klaus et al. (2008). “Splotch: visualizing cosmological simulations”. In: *New J. Phys.* 10.12, p. 125006. ISSN: 1367-2630. DOI: [10.1088/1367-2630/10/12/125006](https://doi.org/10.1088/1367-2630/10/12/125006). URL: <http://stacks.iop.org/1367-2630/10/i=12/a=125006?key=crossref.64abf987af382f22c02df5219a6d0e5d>.

Dolag, Klaus et al. (2009). “Substructures in hydrodynamical cluster simulations”. In: *Mon. Not. R. Astron. Soc.* 399.2, pp. 497–514. ISSN: 00358711. DOI: [10.1111/j.1365-2966.2009.15034.x](https://doi.org/10.1111/j.1365-2966.2009.15034.x). URL: <http://mnras.oxfordjournals.org/cgi/doi/10.1111/j.1365-2966.2009.15034.x>.

Dolag, Klaus et al. (2015). “Constraints on the distribution and energetics of fast radio bursts using cosmological hydrodynamic simulations”. In: *Mon. Not. R. Astron. Soc.* 451.4, pp. 4277–4289. DOI: [10.1093/mnras/stv1190](https://doi.org/10.1093/mnras/stv1190). arXiv: [1412.4829](https://arxiv.org/abs/1412.4829). URL: <http://arxiv.org/abs/1412.4829>.

Domínguez-Tenreiro, R et al. (2014). “GRASIL-3D: an implementation of dust effects in the SEDs of simulated galaxies”. In: *Mon. Not. R. Astron. Soc.* 439, pp. 3868–3889. DOI: [10.1093/mnras/stu240](https://doi.org/10.1093/mnras/stu240). URL: https://watermark.silverchair.com/stu240.pdf?token=AQECAHi208BE49Ooan9kjhW{_}Ercy7Dm3ZL{_}9Cf3qfKAc485ysgAAAaowggGmBqkqhkiG9w0BBwagggGXMTIBkwIBADCCAYwGCSqGSIB3DQEhATAeBglghkgBZQMEAS4wEQQMaImv6KUpgh27W5TrAgEQgIIBXWIdR6aglhFo97g{_}oYqqgQi-gNAjYGje0Jn01XfHW4KKoOpR.

Donnert, Julius M. F. (2014). “Initial conditions for idealized clusters mergers, simulating ‘El Gordo’”. In: *Mon. Not. R. Astron. Soc.* 438.3, pp. 1971–1984. ISSN: 00358711. DOI: [10.1093/mnras/stt2291](https://doi.org/10.1093/mnras/stt2291). arXiv: [1311.7066](https://arxiv.org/abs/1311.7066).

Donnert, Julius M. F. et al. (2017a). *Glithub repository for WVTICs*. URL: <https://github.com/jdonnert/WVTICs/>.

Donnert, Julius M. F. et al. (2017b). “Simulations of the Galaxy Cluster CIZA J2242.8+5301 I: Thermal Model and Shock Properties”. In: 19.March, pp. 1–19. arXiv: [1703.05682](https://arxiv.org/abs/1703.05682). URL: [http://arxiv.org/abs/1703.05682](https://arxiv.org/abs/1703.05682).

Dormy, Emmanuel. and Andrew M. Soward (2007). *Mathematical aspects of natural dynamos*. CRC Press/Taylor & Francis, p. 504. ISBN: 1420055267. URL: https://books.google.de/books?id=E1bvBQAAQBAJ{\&}dq=Mathematical+Aspects+of+Natural+Dynamos{\&}hl=de{\&}source=gbss{_}navlinks{_}s.

Dubois, Yohan and Benoît Commerçon (2015). “An implicit scheme for solving the anisotropic diffusion of heat and cosmic rays in the RAMSES code”. In: *ArXiv e-prints*. arXiv: [arXiv:1509.07037v3](https://arxiv.org/abs/1509.07037v3).

Dubois, Yohan and Romain Teyssier (2010). “Magnetised winds in dwarf galaxies”. In: *Astron. Astrophys.* 523. DOI: [10.1051/0004-6361/200913014](https://doi.org/10.1051/0004-6361/200913014). arXiv: [0908.3862](https://arxiv.org/abs/0908.3862). URL: [http://arxiv.org/abs/0908.3862](https://arxiv.org/abs/0908.3862).

Durier, Fabrice and Claudio Dalla Vecchia (2012). “Implementation of feedback in smoothed particle hydrodynamics: Towards concordance of methods”. In: *Mon. Not. R. Astron. Soc.*

419.1, pp. 465–478. ISSN: 00358711. DOI: [10.1111/j.1365-2966.2011.19712.x](https://doi.org/10.1111/j.1365-2966.2011.19712.x). arXiv: [1105.3729](https://arxiv.org/abs/1105.3729).

Dutton, Aaron A et al. (2013). “The SWELLS survey – V. A Salpeter stellar initial mass function in the bulges of massive spiral galaxies”. In: *Mon. Not. R. Astron. Soc.* 428, pp. 3183–3195. DOI: [10.1093/mnras/sts262](https://doi.org/10.1093/mnras/sts262). URL: <https://doi.org/10.1093/mnras/sts262.pdf> ? token = AQECAHi208BE49Ooan9khhW{_}Ercy7Dm3ZL{_}9Cf3qfKAc485yssgAAAakwggGlBqkqhkiG9w0BBwagggGWMIIIBkgIBADCCAYsGCSqGSIB3DQEHAeBglghkgBZQMEAS4wEQQMWeMTBUnej-OrgsydAgEQgIIBXDvZvqjYwyenjVD75ZftRjXWZGpcnGUbjxk88cfEq9b{_}hrAN.

Eastwood, J. W. and R. W. Hockney (1974). “Shaping the force law in two-dimensional particle-mesh models”. In: *J. Comput. Phys.* 16.4, pp. 342–359. ISSN: 10902716. DOI: [10.1016/0021-9991\(74\)90044-8](https://doi.org/10.1016/0021-9991(74)90044-8).

Eckart, Carl (1960). “Variation Principles of Hydrodynamics”. In: *Phys. Fluids* 3.3, p. 421. DOI: [10.1063/1.1706053](https://doi.org/10.1063/1.1706053). URL: [http://scitation.aip.org/content/aip/journal/pof1/3/3/10.1063/1.1706053](https://doi.org/10.1063/1.1706053).

Efstathiou, G. and J. W. Eastwood (1981). “On the clustering of particles in an expanding Universe”. In: *Mon. Not. R. Astron. Soc.* 194.3, pp. 503–525. DOI: [10.1093/mnras/194.3.503](https://doi.org/10.1093/mnras/194.3.503). URL: [https://academic.oup.com/mnras/article-lookup/doi/10.1093/mnras/194.3.503](https://doi.org/10.1093/mnras/194.3.503).

Elahi, Pascal J., Robert J. Thacker, and Lawrence M. Widrow (2011). “Peaks above the Maxwellian Sea: A New Approach to Finding Substructure in N-Body Haloes”. In: *Mon. Not. R. Astron. Soc.* 418.1, pp. 320–335. DOI: [10.1111/j.1365-2966.2011.19485.x](https://doi.org/10.1111/j.1365-2966.2011.19485.x). arXiv: [1107.4289](https://arxiv.org/abs/1107.4289). URL: [http://arxiv.org/abs/1107.4289](https://arxiv.org/abs/1107.4289).

Elahi, Pascal J. et al. (2013). “Streams Going Notts: The tidal debris finder comparison project”. In: *Mon. Not. R. Astron. Soc.* 433.2, pp. 1537–1555. DOI: [10.1093/mnras/stt825](https://doi.org/10.1093/mnras/stt825). arXiv: [1305.2448](https://arxiv.org/abs/1305.2448). URL: [http://arxiv.org/abs/1305.2448](https://arxiv.org/abs/1305.2448).

Elahi, Pascal J. et al. (2016). “nIFTY galaxy cluster simulations III: The Similarity & Diversity of Galaxies & Subhaloes”. In: *Mon. Not. R. Astron. Soc.* 458.1, pp. 1096–1116. DOI: [10.1093/mnras/stw338](https://doi.org/10.1093/mnras/stw338). arXiv: [1511.08255](https://arxiv.org/abs/1511.08255). URL: [http://arxiv.org/abs/1511.08255](https://arxiv.org/abs/1511.08255).

Euler, L (1768). *Institutionum calculi integralis*. Institutionum calculi integralis Bd. 1. imp. Acad. imp. Saënt. URL: <https://books.google.de/books?id=Vg8OAAAAQAAJ>.

Evans, Charles R. and John F. Hawley (1988). “Simulation of magnetohydrodynamic flows - A constrained transport method”. In: *Astrophys. J.* 332, p. 659. DOI: [10.1086/166684](https://doi.org/10.1086/166684). URL: [http://adsabs.harvard.edu/doi/10.1086/166684](https://adsabs.harvard.edu/doi/10.1086/166684).

Evrard, August E. (1988). “Beyond N-body: 3D cosmological gas dynamics”. In: *Mon. Not. R. Astron. Soc.* 235.3, pp. 911–934. DOI: [10.1093/mnras/235.3.911](https://doi.org/10.1093/mnras/235.3.911). URL: <https://doi.org/10.1093/mnras/235.3.911>.

Fabian, A. C. (1994). “Cooling Flows in Clusters of Galaxies”. In: *Annu. Rev. Astron. Astrophys.* 32.1, pp. 277–318. ISSN: 00664146. DOI: [10.1146/annurev.astro.32.1.277](https://doi.org/10.1146/annurev.astro.32.1.277).

URL: <http://astro.annualreviews.org/cgi/doi/10.1146/annurev.astro.32.1.277>.

— (2002). “Cooling flows in Clusters of Galaxies”. In: *Light. Universe Most Lumin. Celest. Objects Their Use Cosmol.* DOI: [10.1007/10856495_3](https://doi.org/10.1007/10856495_3). arXiv: [0201386v1](https://arxiv.org/abs/0201386v1) [arXiv:astro-ph].

Fabian, A. C. et al. (2006). “A very deep Chandra observation of the Perseus cluster: shocks, ripples and conduction”. In: *Mon. Not. R. Astron. Soc.* 366.2, pp. 417–428. ISSN: 0035-8711. DOI: [10.1111/j.1365-2966.2005.09896.x](https://doi.org/10.1111/j.1365-2966.2005.09896.x). URL: <http://mnras.oxfordjournals.org/cgi/doi/10.1111/j.1365-2966.2005.09896.x>.

Falceta-Gonçalves, Diego, Alex Lazarian, and Grzegorz Kowal (2008). “Studies of Regular and Random Magnetic Fields in the ISM: Statistics of Polarization Vectors and the Chandrasekhar-Fermi Technique”. In: *Astrophys. J.* 679, pp. 537–551. URL: <http://iopscience.iop.org/article/10.1086/587479/pdf>.

Fang, Le et al. (2017). “A high-order SPH method by introducing inverse kernels”. In: *Chinese J. Aeronaut.* 30.1, pp. 1–14. DOI: [10.1016/j.cja.2016.09.014](https://doi.org/10.1016/j.cja.2016.09.014). URL: <https://www.sciencedirect.com/science/article/pii/S1000936116302187>.

Federrath, Christoph (2016). “On the universality of interstellar filaments: theory meets simulations and observations”. In: *Mon. Not. R. Astron. Soc.* 457.1, pp. 375–388. DOI: [10.1093/mnras/stv2880](https://doi.org/10.1093/mnras/stv2880). arXiv: [1510.05654](https://arxiv.org/abs/1510.05654). URL: <http://arxiv.org/abs/1510.05654>.

Felten, James E and Philip Morrison (1966). “Omnidirectional Inverse Compton and Synchrotron Radiation from Cosmic Distributions of Fast Electrons and Thermal Photons”. In: *Astrophys. J.* 146, p. 686. DOI: [10.1086/148946](https://doi.org/10.1086/148946). URL: http://articles.adsabs.harvard.edu/cgi-bin/nph-iarticle{_}query?1966ApJ..146..686F{_}&data{_}type=PDF{_}HIGH{_}&whole{_}paper=YES{_}&type=PRINTER{_}&filetype=.pdf.

Feretti, Luigina et al. (2012). “Clusters of galaxies: observational properties of the diffuse radio emission”. In: *Astron. Astrophys. Rev.* 20. DOI: [10.1007/s00159-012-0054-z](https://doi.org/10.1007/s00159-012-0054-z). URL: https://link.springer.com/content/pdf/10.1007{_}2Fs00159-012-0054-z.pdf.

Ferland, G J et al. (2013). “Review The 2013 Release of Cloudy”. In: *Rev. Mex. Astron. y Astrofísica* 49, pp. 137–163.

Fermi, Enrico (1949). “On the Origin of the Cosmic Radiation”. In: *Phys. Rev.* 75.8, pp. 1169–1174. DOI: [10.1103/PhysRev.75.1169](https://doi.org/10.1103/PhysRev.75.1169). URL: <https://link.aps.org/doi/10.1103/PhysRev.75.1169>.

Fernández-Méndez, Sonia, Javier Bonet, and Antonio Huerta (2005). “Continuous blending of SPH with finite elements”. In: *Comput. Struct.* 83.17-18, pp. 1448–1458. DOI: [10.1016/j.COMPSTRUC.2004.10.019](https://doi.org/10.1016/j.COMPSTRUC.2004.10.019). URL: <https://www.sciencedirect.com/science/article/pii/S004579490500074X>.

Fließbach, Thorsten (2006). *Allgemeine Relativitätstheorie*. 5th ed. München: Elsevier. ISBN: 978-3-8274-1685-8.

Forbes, John, Mark R. Krumholz, and Andreas Burkert (2011). “Evolving Gravitationally Unstable Disks Over Cosmic Time: Implications For Thick Disk Formation”. In: *Astrophys. J.*

754.1. DOI: [10.1088/0004-637X/754/1/48](https://doi.org/10.1088/0004-637X/754/1/48). arXiv: [1112.1410](https://arxiv.org/abs/1112.1410). URL: <http://arxiv.org/abs/1112.1410>.

Forgan, Duncan and Ken Rice (2010). “Native synthetic imaging of smoothed particle hydrodynamics density fields using gridless Monte Carlo radiative transfer”. In: *Mon. Not. R. Astron. Soc.* 406.4, pp. 2549–2558. ISSN: 00358711. DOI: [10.1111/j.1365-2966.2010.16842.x](https://doi.org/10.1111/j.1365-2966.2010.16842.x). arXiv: [1004.2846](https://arxiv.org/abs/1004.2846).

Fortin, P, E Athanassoula, and J.-C Lambert (2011). “Astrophysics Comparisons of different codes for galactic N-body simulations”. In: *Astron. Astrophys.* 531. DOI: [10.1051/0004-6361/201015933](https://doi.org/10.1051/0004-6361/201015933). URL: <https://www.aanda.org/articles/aa/pdf/2011/07/aa15933-10.pdf>.

Fraedrich, Roland, Stefan Auer, and Rüdiger Westermann (2010). “Efficient high-quality volume rendering of SPH data”. In: *IEEE Trans. Vis. Comput. Graph.* 16.6, pp. 1533–1540. ISSN: 10772626. DOI: [10.1109/TVCG.2010.148](https://doi.org/10.1109/TVCG.2010.148).

Frank, K. a. et al. (2013). “Characterization of Intracluster Medium Temperature Distributions of 62 Galaxy Clusters With Xmm-Newton”. In: *Astrophys. J.* 764.1, p. 46. ISSN: 0004-637X. DOI: [10.1088/0004-637X/764/1/46](https://doi.org/10.1088/0004-637X/764/1/46). URL: <http://stacks.iop.org/0004-637X/764/i=1/a=46?key=crossref.4ac274f9a48c4b6fd1aea366a813120>.

Frank-Kamenezki, D. A. (1967). *Vorlesungen über Plasmaphysik*. VEB Deutscher Verlag der Wissenschaften.

Frenk, C. S. et al. (1999). “The Santa Barbara Cluster Comparison Project: A Comparison of Cosmological Hydrodynamics Solutions”. In: *Astrophys. J.* 525.2, pp. 554–582. ISSN: 0004-637X. DOI: [10.1086/307908](https://doi.org/10.1086/307908). arXiv: [9906160 \[astro-ph\]](https://arxiv.org/abs/9906160). URL: <http://stacks.iop.org/0004-637X/525/i=2/a=554>.

Frenk, Carlos S. and Simon D. M. White (2012). “Dark matter and cosmic structure”. In: *Ann. Phys.* 524.9-10, pp. 507–534. DOI: [10.1002/andp.201200212](https://doi.org/10.1002/andp.201200212). arXiv: [1210.0544](https://arxiv.org/abs/1210.0544). URL: <http://arxiv.org/abs/1210.0544>.

Frenkel, D and B Smit (2001). *Understanding Molecular Simulation: From Algorithms to Applications*. Computational science series. Elsevier Science. ISBN: 9780080519982. URL: <https://books.google.de/books?id=5qTzldS9ROIC>.

Fromang, S, P Hennebelle, and R Teyssier (2006). “Astrophysics A high order Godunov scheme with constrained transport and adaptive mesh refinement for astrophysical magnetohydrodynamics”. In: *Astron. Astrophys.* 457, pp. 371–384. DOI: [10.1051/0004-6361:20065371](https://doi.org/10.1051/0004-6361:20065371). URL: <https://www.aanda.org/articles/aa/pdf/2006/38/aa5371-06.pdf>.

Fryxell, B. et al. (2000). “FLASH: An Adaptive Mesh Hydrodynamics Code for Modeling Astrophysical Thermonuclear Flashes”. In: *Astrophys. J. Suppl. Ser.* 131.1, pp. 273–334. URL: [http://iopscience.iop.org/article/10.1086/317361/pdf](https://iopscience.iop.org/article/10.1086/317361/pdf).

Gaburov, Evgenii and Keigo Nitadori (2011). “Astrophysical weighted particle magnetohydrodynamics”. In: *Mon. Not. R. Astron. Soc.* 414.1, pp. 129–154. ISSN: 00358711. DOI: [10.1111/j.1365-2966.2011.18313.x](https://doi.org/10.1111/j.1365-2966.2011.18313.x). arXiv: [1006.4159 \[astro-ph.IM\]](https://arxiv.org/abs/1006.4159).

Galt, J. A., C. H. Slater, and W. L. H. Shuter (1960). “An Attempt to Detect the Galactic Magnetic Field, Using Zeeman Splitting of the Hydrogen Line”. In: *Mon. Not. R. Astron. Soc.*

120.2, pp. 187–192. ISSN: 0035-8711. DOI: [10.1093/mnras/120.2.187](https://doi.org/10.1093/mnras/120.2.187). URL: <https://academic.oup.com/mnras/article-lookup/doi/10.1093/mnras/120.2.187>.

Gaspari, M et al. (2014). “The relation between gas density and velocity power spectra in galaxy clusters : High-resolution hydrodynamic simulations”. In: *Astron. Astrophys.* 67, pp. 1–15.

Geng, Annette Monika et al. (2012a). “Magnetic field amplification and X-ray emission in galaxy minor mergers”. In: *Mon. Not. R. Astron. Soc.* 419, pp. 3571–3589. ISSN: 00358711. DOI: [10.1111/j.1365-2966.2011.20001.x](https://doi.org/10.1111/j.1365-2966.2011.20001.x). arXiv: [1108.4006](https://arxiv.org/abs/1108.4006).

Geng, Annette Monika et al. (2012b). “Synthetic X-ray and radio maps for two different models of Stephan’s Quintet”. In: *Mon. Not. R. Astron. Soc.* 426.4, pp. 3160–3177. ISSN: 00358711. DOI: [10.1111/j.1365-2966.2012.21902.x](https://doi.org/10.1111/j.1365-2966.2012.21902.x). arXiv: [1206.1234](https://arxiv.org/abs/1206.1234).

Genzel, R. et al. (2017). “Strongly baryon-dominated disk galaxies at the peak of galaxy formation ten billion years ago”. In: *Nature* 543.7645, pp. 397–401. DOI: [10.1038/nature21685](https://doi.org/10.1038/nature21685). arXiv: [1703.04310](https://arxiv.org/abs/1703.04310). URL: <http://arxiv.org/abs/1703.04310>.

Ghisellini, Gabriele (2013). *Radiative Processes in High Energy Astrophysics*. 1st ed. Vol. 873. Lecture Notes in Physics. Heidelberg: Springer International Publishing, pp. X, 147. ISBN: 978-3-319-00611-6. DOI: [10.1007/978-3-319-00612-3](https://doi.org/10.1007/978-3-319-00612-3). URL: <http://link.springer.com/10.1007/978-3-319-00612-3>.

Gill, Stuart P. D., Alexander Knebe, and Brad K. Gibson (2004). “The evolution substructure I: a new identification method”. In: *Mon. Not. R. Astron. Soc.* 351.2, pp. 399–409. DOI: [10.1111/j.1365-2966.2004.07786.x](https://doi.org/10.1111/j.1365-2966.2004.07786.x). arXiv: [0404258 \[astro-ph\]](https://arxiv.org/abs/astro-ph/0404258). URL: <http://arxiv.org/abs/astro-ph/0404258>.

Gingold, R. a. and Joseph J Monaghan (1977). “Smoothed particle hydrodynamics-theory and application to non-spherical stars”. In: *Mon. Not. R. Astron. Soc.* 181, pp. 375–389. ISSN: 0035-8711. DOI: [10.1093/mnras/181.3.375](https://doi.org/10.1093/mnras/181.3.375). URL: <http://adsabs.harvard.edu/abs/1977MNRAS.181..375G> <http://adsabs.harvard.edu/full/1977MNRAS.181..375G>.

Glenn, Jason et al. (1997). “Millimeter-Wave Spectropolarimetry of Evolved Stars: Evidence for Polarized Molecular Line Emission”. In: *Astrophys. J.* 487.1, pp. L89–L92. ISSN: 0004637X. DOI: [10.1086/310863](https://doi.org/10.1086/310863). URL: <http://stacks.iop.org/1538-4357/487/i=1/a=L89>.

Gnedin, Nickolay Y (1995). “Softened Lagrangian hydrodynamics for cosmology”. In: *Astrophys. J. Suppl. Ser.* 97.2, pp. 231–257. URL: http://articles.adsabs.harvard.edu/cgi-bin/nph-iarticle{_}query?1995ApJS...97..231G{_}&data{_}type=PDF{_}HIGH{_}&whole{_}paper=YES{_}&type=PRINTER{_}&filetype=.pdf.

Godunov, S. K. (1959). “A difference method for numerical calculation of discontinuous solutions of the equations of hydrodynamics”. In: *Mat. Sb.* 47.3, pp. 271–306.

Goessl, Claus A. and Arno Riffeser (2002). “Image reduction pipeline for the detection of variable sources in highly crowded fields”. In: *Astron. Astrophys.* 381, pp. 1095–1109. DOI: [10.1051/0004-6361:20011522](https://doi.org/10.1051/0004-6361:20011522). arXiv: [0110704 \[astro-ph\]](https://arxiv.org/abs/0110704). URL: <http://arxiv.org/abs/astro-ph/0110704>.

Golant, V. E., A. P. Zhilinsky, and I. E. Sakharov (1980). *Fundamentals of Plasma Physics*. John Wiley & Sons Inc.

Goldreich, P. and N. D. Kylafis (1981). “On mapping the magnetic field direction in molecular clouds by polarization measurements”. In: *Astrophys. J.* 243, p. L75. ISSN: 0004-637X. DOI: 10.1086/183446. URL: <http://adsabs.harvard.edu/doi/10.1086/183446>.

Goldreich, P. and S. Srigar (1995). “Toward a Theory of Interstellar Turbulence. II., Strong Alfvénic Turbulence”. In: *Astrophys. J.* 438.2, pp. 763–775. URL: http://articles.adsabs.harvard.edu/cgi-bin/nph-iarticle{_}query?1995ApJ..438..763G{\&}data{_}type=PDF{_}HIGH{\&}whole{_}paper=YES{\&}type=PRINTER{\&}filetype=.pdf.

Gonnet, Pedro et al. (2013). “SWIFT: Fast algorithms for multi-resolution SPH on multi-core architectures”. In: *8th Int. SPHERIC Work*. Trondheim, Norway, This paper describes a novel approach to neighbour. URL: <http://arxiv.org/abs/1309.3783>.

González-Casanova, Diego F and Alex Lazarian (2017). “Velocity Gradients As a Tracer for Magnetic Fields”. In: *Astrophys. J.* 835.1, pp. 1–11. ISSN: 1538-4357. DOI: 10.3847/1538-4357/835/1/41. arXiv: 1608.06867. URL: <http://dx.doi.org/10.3847/1538-4357/835/1/41>.

Gourlay, Michael J. (2013). *Fluid Simulation for Video Games (part 15) | Intel® Software*. URL: <https://software.intel.com/en-us/articles/fluid-simulation-for-video-games-part-15> (visited on 01/19/2018).

Greaves, J. S. et al. (1999). “Polarized CO emission from molecular clouds”. In: *Astrophys. J.* 512.2, pp. L139–L142. DOI: 10.1086/311888. arXiv: 9812428 [astro-ph]. URL: <http://arxiv.org/abs/astro-ph/9812428>.

Green, J. A. et al. (2010). “The 6-GHz methanol multibeam maser catalogue II: Galactic longitudes 6 to 20”. In: *Mon. Not. R. Astron. Soc.* 409, pp. 913–935. DOI: 10.1111/j.1365-2966.2010.17376.x. arXiv: 1007.3050. URL: <http://arxiv.org/abs/1007.3050>.

Green, J. A. et al. (2012). “The 6-GHz methanol multibeam maser catalogue IV: Galactic longitudes 186 to 330 including the Orion-Monoceros region”. In: *Mon. Not. R. Astron. Soc.* 420, pp. 3108–3125. DOI: 10.1111/j.1365-2966.2011.20229.x. arXiv: 1201.0787. URL: <http://arxiv.org/abs/1201.0787>.

Gresho, Philip M. and Stevens T. Chan (1990). “On the theory of semiimplicit projection methods for viscous incompressible flow and its implementation via a finite element method that also introduces a nearly consistent mass matrix. Part 2: Implementation”. In: *Int. J. Numer. Methods Fluids* 11.5, pp. 621–659. ISSN: 10970363. DOI: 10.1002/fld.1650110510.

Gressel, Oliver et al. (2015). “Global Simulations of Protoplanetary Disks With Ohmic Resistivity and Ambipolar Diffusion”. In: *Astrophys. J.* 801.2, p. 84. DOI: 10.1088/0004-637X/801/2/84. URL: <http://iopscience.iop.org/article/10.1088/0004-637X/801/2/84/pdf>.

Gupta, Nikhel et al. (2017). “SZE Observables, Pressure Profiles and Center Offsets in Magneticum Simulation Galaxy Clusters”. In: *Mon. Not. R. Astron. Soc.* 469.3, pp. 3069–3087. ISSN: 0035-8711. DOI: 10.1093/mnras/stx715. arXiv: 1612.05266. URL: <http://arxiv.org/abs/1612.05266>.

//arxiv.org/abs/1612.05266http://dx.doi.org/10.1093/mnras/stx715.

Guthrie, Andrew and Raymond Kornelious Wakerling (1949). *The Characteristics of Electrical Discharges in Magnetic Fields*. National nuclear energy series: Electromagnetic Separation Project. McGraw-Hill, p. 376.

Hairer, Ernst, Gerhard Wanner, and Christian Lubich (2002). “Symplectic Integration of Hamiltonian Systems”. In: *Springer Ser. Comput. Math. vol. 31*. Berlin, Heidelberg: Springer, Berlin, Heidelberg. Chap. VI, pp. 167–208. ISBN: 978-3-662-05018-7. DOI: 10.1007/978-3-662-05018-7_6. URL: http://link.springer.com/10.1007/978-3-662-05018-7{_}6.

Hall, John S. (1949). “Observations of the Polarized Light From Stars”. In: *Science (80-.).* 109.2825, pp. 166–167. DOI: 10.1126/science.109.2825.166. URL: <http://www.sciencemag.org/cgi/doi/10.1126/science.109.2825.166>.

Hansen, Jean-Pierre and Loup Verlet (1969). “Phase Transitions of the Lennard-Jones System”. In: *Phys. Rev.* 184.1, pp. 151–161. DOI: 10.1103/PhysRev.184.151. URL: <https://link.aps.org/doi/10.1103/PhysRev.184.151>.

Harten, Amiram, Peter D. Lax, and Bram van Leer (1983). “On Upstream Differencing and Godunov-Type Schemes for Hyperbolic Conservation Laws”. In: *SIAM Rev.* 25.1, pp. 35–61. ISSN: 0036-1445. DOI: 10.1137/1025002. URL: <http://epubs.siam.org/doi/10.1137/1025002>.

Heesch, Dimitri van (2015). *Doxxygen project webpage*. <http://www.stack.nl/~dimitri/doxygen/index.html>.

Heitmann, Katrin et al. (2008). “The Cosmic Code Comparison Project”. In: *Comput. Sci. Discov.* 1.1. DOI: 10.1088/1749-4699/1/1/015003. arXiv: 0706.1270. URL: <http://arxiv.org/abs/0706.1270>.

Hennebelle, Patrick et al. (2016). “Magnetically Self-regulated Formation of Early Protoplanetary Disks”. In: *Astrophys. J. Lett.* 830.1. DOI: 10.3847/2041-8205/830/1/L8. URL: <http://iopscience.iop.org/article/10.3847/2041-8205/830/1/L8/pdf>.

Hernquist, Lars (1993). “N-body realizations of compound galaxies”. In: *Astrophys. J. Suppl. Ser.* 86.2, p. 389. DOI: 10.1086/191784. URL: <http://adsabs.harvard.edu/doi/10.1086/191784>.

Hernquist, Lars and Neal Katz (1989). “TREESPH: A Unification of SPH with the Hierarchical Tree Method”. In: *Astrophys. J. Suppl. Ser.* 70, pp. 419–446. DOI: 10.1086/191344. URL: <http://adsabs.harvard.edu/doi/10.1086/191344>.

Herrmann, Joachim, Harald Bukor, and Ruth Bukor (1973). *dtv-Atlas Astronomie*. 10th ed. Munich: Deutscher Taschenbuch Verlag BmbH & Co. KG.

Hess, S. et al. (2010). “Particle hydrodynamics with tessellation techniques”. In: *Mon. Not. R. Astron. Soc.* 406.4, pp. 2289–2311. ISSN: 00358711. DOI: 10.1111/j.1365-2966.2010.16892.x. arXiv: 0912.0629. URL: <http://arxiv.org/abs/0912.0629>.

Hirschmann, Michaela et al. (2014). “Cosmological simulations of black hole growth: AGN luminosities and downsizing”. In: *Mon. Not. R. Astron. Soc.* 442.3, pp. 2304–2324. ISSN: 13652966. DOI: [10.1093/mnras/stu1023](https://doi.org/10.1093/mnras/stu1023). arXiv: [1308.0333](https://arxiv.org/abs/1308.0333).

Hoang, Thiem and Alex Lazarian (2008). “Radiative torque alignment: Essential Physical Processes”. In: *Mon. Not. R. Astron. Soc.* 388.1, pp. 117–143. DOI: [10.1111/j.1365-2966.2008.13249.x](https://doi.org/10.1111/j.1365-2966.2008.13249.x). arXiv: [0707.3645](https://arxiv.org/abs/0707.3645). URL: <http://arxiv.org/abs/0707.3645>.

Hockney, R. W. (1966). “Computer Experiment of Anomalous Diffusion”. In: *Phys. Fluids* 9.9, p. 1826. ISSN: 00319171. DOI: [10.1063/1.1761939](https://doi.org/10.1063/1.1761939). URL: <http://link.aip.org/link/PFLDAS/v9/i9/p1826/s1{\&}Agg=doi>.

Hockney, R. W. and J. W. Eastwood (1988). “Computer simulation using particles”. In: Hockney, R. W. and J. W. Eastwood (1981). *Computer Simulation Using Particles*.

Holmberg, Erik (1941). “On the Clustering Tendencies among the Nebulae. II. a Study of Encounters Between Laboratory Models of Stellar Systems by a New Integration Procedure”. In: *Astrophys. J.* 94, p. 385. DOI: [10.1086/144344](https://doi.org/10.1086/144344). URL: http://articles.adsabs.harvard.edu/cgi-bin/nph-iarticle{_}query?1941ApJ...94..385H{\&}data{_}type=PDF{_}HIGH{\&}whole{_}paper=YES{\&}type=PRINTER{\&}filetype=.pdf.

Hopkins, Philip F. (2013). “A general class of Lagrangian smoothed particle hydrodynamics methods and implications for fluid mixing problems”. In: *Mon. Not. R. Astron. Soc.* 428.4, pp. 2840–2856. ISSN: 00319171. DOI: [10.1093/mnras/sts210](https://doi.org/10.1093/mnras/sts210). arXiv: [1206.5006](https://arxiv.org/abs/1206.5006).

— (2015). “A new class of accurate, mesh-free hydrodynamic simulation methods”. In: *Mon. Not. R. Astron. Soc.* 450, pp. 53–110. ISSN: 13652966. DOI: [10.1093/mnras/stv195](https://doi.org/10.1093/mnras/stv195). arXiv: [1409.7395](https://arxiv.org/abs/1409.7395).

— (2016). “Anisotropic Diffusion in Mesh-Free Numerical Magnetohydrodynamics”. In: *ArXiv e-prints* 000.February. arXiv: [1602.07703](https://arxiv.org/abs/1602.07703). URL: <http://arxiv.org/abs/1602.07703>.

— (2017). “A New Public Release of the GIZMO Code”. In: *ArXiv e-prints*. arXiv: [1712.01294](https://arxiv.org/abs/1712.01294). URL: <http://arxiv.org/abs/1712.01294>.

Hopkins, Philip F. and Matthias J. Raives (2016). “Accurate, meshless methods for magnetohydrodynamics”. In: *Mon. Not. R. Astron. Soc.* 455.1, pp. 51–88. ISSN: 13652966. DOI: [10.1093/mnras/stv2180](https://doi.org/10.1093/mnras/stv2180). arXiv: [1505.02783v1](https://arxiv.org/abs/1505.02783v1).

Houde, Martin et al. (2000). “Probing the Magnetic Field with Molecular Ion Spectra”. In: *Astrophys. J.* 536.2, pp. 857–864. DOI: [10.1086/308980](https://doi.org/10.1086/308980). arXiv: [0311335 \[astro-ph\]](https://arxiv.org/abs/astro-ph/0311335). URL: <http://arxiv.org/abs/astro-ph/0311335>.

Houde, Martin et al. (2009). “Dispersion of Magnetic Fields in Molecular Clouds. II.” In: *Astrophys. J.* 706, pp. 1504–1516. DOI: [10.1088/0004-637X/706/2/1504](https://doi.org/10.1088/0004-637X/706/2/1504). URL: <http://iopscience.iop.org/article/10.1088/0004-637X/706/2/1504/pdf>.

Hough V and Paul C. (1962). *Method and means for recognizing complex patterns*. URL: <http://www.freepatentsonline.com/3069654.html>.

Hu, Chia-Yu et al. (2014). “SPHGal : Smoothed Particle Hydrodynamics with improved accuracy for galaxy simulations”. In: arXiv: [arXiv:1402.1788v1](https://arxiv.org/abs/1402.1788v1).

Hu, Chia-yu et al. (2016). “Star formation and molecular hydrogen in dwarf galaxies: a non-equilibrium view”. In: *Mon. Not. R. Astron. Soc.* 458.4, pp. 3528–3553. ISSN: 0035-8711. DOI: 10.1093/mnras/stw544. arXiv: 1510.0564. URL: <http://arxiv.org/abs/1510.0564>{\%}5Cnhttp://dx.doi.org/10.1093/mnras/stw544{\%}5Cnhttp://adsabs.harvard.edu/abs/2016MNRAS.458.3528H.

Huba, J D (2011). “NRL PLASMA FORMULARY Supported by The Office of Naval Research”.

Hubbard, M.E. (1999). “Multidimensional Slope Limiters for MUSCL-Type Finite Volume Schemes on Unstructured Grids”. In: *J. Comput. Phys.* 155.1, pp. 54–74. ISSN: 00219991. DOI: 10.1006/jcph.1999.6329. URL: <http://linkinghub.elsevier.com/retrieve/pii/S0021999199963295>.

Hubber, D. A. et al. (2011). “SEREN - A new SPH code for star and planet formation simulations”. In: *Astron. Astrophys.* 529. DOI: 10.1051/0004-6361/201014949. arXiv: 1102.0721. URL: <http://arxiv.org/abs/1102.0721>.

Hubber, David A. and Rosotti (2016). *GANDALF: Graphical Astrophysics code for N-body Dynamics And Lagrangian Fluids*. URL: <http://ascl.net/1602.015>.

Hubber, David A., Giovanni P. Rosotti, and Richard A. Booth (2017). “GANDALF - Graphical Astrophysics code for N-body Dynamics And Lagrangian Fluids”. In: 33.September, pp. 1–33. arXiv: 1709.04488. URL: <http://arxiv.org/abs/1709.04488>.

Hummel, E. (1986). “Astronomy and Astrophysics.” In: *Astron. Astrophys.* 160.1, pp. L4–L6. URL: <http://adsabs.harvard.edu/abs/1986A{\%}26A...160L...4H{\%}7D>.

Hummel, Jacob (2016). “gadfly: A pandas-based Framework for Analyzing GADGET Simulation Data”. In: arXiv: 1603.05190. URL: <http://arxiv.org/abs/1603.05190>.

Illingworth, J. and J. Kittler (1988). “A survey of the hough transform”. In: *Comput. Vision, Graph. Image Process.* 44.1, pp. 87–116. DOI: 10.1016/S0734-189X(88)80033-1. URL: <http://www.sciencedirect.com/science/article/pii/S0734189X88800331>.

Imgrund, Maximilian and A Arth (2015a). *Daily auto-generated documentation for Rambrain*. <http://mimgrund.github.io/rambrain/>.

— (2015b). *Github repository for Rambrain*. <https://github.com/mimgrund/rambrain/>.

Imgrund, Maximilian and Alexander Arth (2017b). “Rambrain - a library for virtually extending physical memory”. In: arXiv: 1510.06358. ISSN: 23527110. DOI: 10.1016/j.softx.2017.07.004. arXiv: 1510.06358.

— (2017a). “Rambrain - a library for virtually extending physical memory”. In: *SoftwareX* 6, pp. 179–184. ISSN: 23527110. DOI: 10.1016/j.softx.2017.07.004. arXiv: 1510.06358. URL: <http://dx.doi.org/10.1016/j.softx.2017.07.004>.

Imgrund, Maximilian et al. (2015). “A Bayesian method for pulsar template generation”. In: *\mnras* 449, pp. 4162–4183. DOI: 10.1093/mnras/stv449. arXiv: 1501.03497 [astro-ph.IM].

Imin, Rahmatjan, Ahmatjan Iminjan, and Azhar Halik (2017). “A New Revised Scheme for SPH”. In: *Int. J. Comput. Methods*. DOI: 10.1142/S0219876218500354. URL: <http://www.worldscientific.com/doi/abs/10.1142/S0219876218500354>.

Introduction, I (1995). “von Neumann Stability Analysis of Smoothed Particle Hydrodynamics Suggestions for Optimal Algorithms”. In: *J. Comput. Phys.* 372.2, pp. 357–372.

Inutsuka, S. (1994). “Godunov-type SPH”. In: *Mem. della Soc. Astron. Ital.* 65, p. 1027. URL: http://articles.adsabs.harvard.edu/cgi-bin/nph-iarticle{_}query?1994MmSAI..65.1027I{_}data{_}type=PDF{_}HIGH{_}&whole{_}paper=YES{_}type=PRINTER{_}filetype=.pdf.

Iroshnikov, P. S. (1963). “Turbulence of Conducting Fluid in a Strong Magnetic Field”. In: *Astron. Zhurnal* 40, p. 742. URL: <http://adsabs.harvard.edu/abs/1963AZh...40..742I{\%}7D>.

Jasche, J, F S Kitaura, and T A Ensslin (2009). “Digital Signal Processing in Cosmology”. In: *eprint arXiv* 0901.January, p. 3043. arXiv: 0901.3043. URL: http://adsabs.harvard.edu/cgi-bin/nph-data{_}query?bibcode=2009arXiv0901.3043J{_}link{_}type=ABSTRACT{\%}5Cnpapers://ee00755c-a478-4d4e-a50b-ef01ee7b9957/Paper/p9266.

Jernigan, J. Garrett and David H. Porter (1989). “A tree code with logarithmic reduction of force terms, hierarchical regularization of all variables, and explicit accuracy controls”. In: *Astrophys. J. Suppl. Ser.* 71, p. 871. DOI: 10.1086/191400. URL: <http://adsabs.harvard.edu/doi/10.1086/191400>.

Jin, Zhefan et al. (2010). “High-performance astrophysical visualization using Splotch”. In: *Procedia Comput. Sci.* 1.1, pp. 1775–1784. ISSN: 18770509. DOI: 10.1016/j.procs.2010.04.199. arXiv: 1004.1302.

Jing, Y. P. (2005). “Correcting for the Alias Effect When Measuring the Power Spectrum Using a Fast Fourier Transform”. In: *Astrophys. J.* 620.2, pp. 559–563. ISSN: 0004-637X. DOI: 10.1086/427087. arXiv: 0409240 [astro-ph]. URL: <http://adsabs.harvard.edu/abs/2005ApJ...620..559J>.

Jubelgas, Martin, Volker Springel, and Klaus Dolag (2004). “Thermal conduction in cosmological SPH simulations”. In: *Mon. Not. R. Astron. Soc.* 351.2, pp. 423–435. ISSN: 0035-8711. DOI: 10.1111/j.1365-2966.2004.07801.x. URL: <http://doi.wiley.com/10.1111/j.1365-2966.2004.07801.x>.

Junk, Veronika et al. (2010). “Modelling shear flows with smoothed particle hydrodynamics and grid-based methods”. In: *Mon. Not. R. Astron. Soc.* 407.3, pp. 1933–1945. ISSN: 00358711. DOI: 10.1111/j.1365-2966.2010.17039.x. arXiv: 1004.1957 [astro-ph.GA].

Kale, R et al. (2013). “The Extended GMRT Radio Halo Survey I: New Upper Limits on Radio Halos and Mini-Halos”. In: *Astron. Astrophys.* 557, A99. ISSN: 0004-6361. DOI: 10.1051/0004-6361/201321515. arXiv: 1306.3102. URL: <http://www.aanda.org/10.1051/0004-6361/201321515>.

Kale, R et al. (2015). “The Extended GMRT Radio Halo Survey II: Further results and analysis of the full sample”. In: arXiv: arXiv:1503.02415v1.

Kannan, Rahul et al. (2015). “Accurately simulating anisotropic thermal conduction on a moving mesh”. In: *ArXiv e-prints* 17, pp. 1–17. arXiv: 1512.03053. URL: <http://arxiv.org/abs/1512.03053>.

Katz, Neal, David H. Weinberg, and Lars Hernquist (1996). “Cosmological Simulations with TreeSPH”. In: *Astrophys. J. Suppl.* 105, p. 19. DOI: [10.1086/192305](https://doi.org/10.1086/192305). arXiv: [9509107](https://arxiv.org/abs/astro-ph/9509107) [astro-ph]. URL: <http://arxiv.org/abs/astro-ph/9509107>.

Kazantsev, A. P., A. A. Ruzmaikin, and Solokov D. D. (1985). “Magnetic field transport by an acoustic turbulence-type flow”. In: *Zhurnal Eksp. i Teor. Fiz.* 88, pp. 487–494. URL: [http://adsabs.harvard.edu/abs/1985ZhETF..88..487K{\%}7D](http://adsabs.harvard.edu/abs/1985ZhETF..88..487K).

Klein, Richard I., Christopher F. McKee, and Philip Colella (1994). “On the hydrodynamic interaction of shock waves with interstellar clouds. 1: Nonradiative shocks in small clouds”. In: *Astrophys. J.* 420.1, pp. 213–236. URL: http://articles.adsabs.harvard.edu/cgi-bin/nph-iarticle{_}query?1994ApJ...420..213K{\&}data{_}type=PDF{_}HIGH{\&}whole{_}paper=YES{\&}type=PRINTER{\&}filetype=.pdf.

Kleiner, Steven C and Robert L Dickman (1985). “Large-scale structure of the Taurus molecular complex. II - Analysis of velocity fluctuations and turbulence. III - Methods for turbulence”. In: *Astrophys. J.* 295, pp. 466–478. URL: http://articles.adsabs.harvard.edu/cgi-bin/nph-iarticle{_}query?1985ApJ...295..466K{\&}data{_}type=PDF{_}HIGH{\&}whole{_}paper=YES{\&}type=PRINTER{\&}filetype=.pdf.

Klypin, Anatoly et al. (2001). “Resolving the Structure of Cold Dark Matter Halos”. In: *Astrophys. J.* 554.2, pp. 903–915. ISSN: 0004-637X. DOI: [10.1086/321400](https://doi.org/10.1086/321400). URL: <http://stacks.iop.org/0004-637X/554/i=2/a=903>.

Klypin, Anatoly et al. (2014). “MultiDark simulations: the story of dark matter halo concentrations and density profiles”. In: *Mon. Not. R. Astron. Soc.* Vol. 457, Issue 4, p.4340-4359 457, pp. 4340–4359. ISSN: 0035-8711. DOI: [10.1093/mnras/stw248](https://doi.org/10.1093/mnras/stw248). arXiv: [1411.4001](https://arxiv.org/abs/1411.4001). URL: <http://arxiv.org/abs/1411.4001>[http://dx.doi.org/10.1093/mnras/stw248](https://doi.org/10.1093/mnras/stw248).

Knebe, Alexander et al. (2015). “nIFTy Cosmology: Comparison of Galaxy Formation Models”. In: *Mon. Not. R. Astron. Soc.* 451, pp. 4029–4059. DOI: [10.1093/mnras/stv1149](https://doi.org/10.1093/mnras/stv1149). arXiv: [1505.04607](https://arxiv.org/abs/1505.04607). URL: <http://arxiv.org/abs/1505.04607>.

Knebe, Alexander et al. (2018). “MultiDark-Galaxies: data release and first results”. In: *Mon. Not. R. Astron. Soc.* 474.4, pp. 5206–5231. DOI: [10.1093/mnras/stx2662](https://doi.org/10.1093/mnras/stx2662). arXiv: [1710.08150](https://arxiv.org/abs/1710.08150). URL: <http://arxiv.org/abs/1710.08150>.

Knollmann, Steffen R. and Alexander Knebe (2009). “Ahf: Amiga’s Halo Finder”. In: *Astrophys. J. Suppl.* 182.2, pp. 608–624. DOI: [10.1088/0067-0049/182/2/608](https://doi.org/10.1088/0067-0049/182/2/608). arXiv: [0904.3662](https://arxiv.org/abs/0904.3662). URL: <http://arxiv.org/abs/0904.3662>.

Koepferl, Christine M et al. (2016). “Insights from synthetic star-forming regions: i. reliable mock observations from sph simulations”. In: 2004. arXiv: [arXiv:1603.02270v1](https://arxiv.org/abs/1603.02270v1).

Koerner, D. et al. (2014). “Flux-limited diffusion for multiple scattering in participating media”. In: *Comput. Graph. Forum* 33.6, pp. 178–189. ISSN: 14678659. DOI: [10.1111/cgf.12342](https://doi.org/10.1111/cgf.12342). arXiv: [1403.8105](https://arxiv.org/abs/1403.8105).

Komarov, S. V. et al. (2014). “Suppression of local heat flux in a turbulent magnetized intracluster medium”. In: *Mon. Not. R. Astron. Soc.* 440.2, p. 1153. ISSN: 0035-8711. DOI:

10.1093/mnras/stu281. arXiv: 1304.1857. URL: <http://arxiv.org/abs/1304.1857> <http://adsabs.harvard.edu/abs/2014MNRAS.440.1153K>.

Komatsu, E. and U. Seljak (2001). “Universal gas density and temperature profile”. In: *Mon. Not. R. ...* 336.4, pp. 1353–1366. ISSN: 0035-8711. DOI: 10.1046/j.1365-8711.2001.04838.x. arXiv: 0106151v2 [arXiv:astro-ph]. URL: [\%5Cn<http://mnras.oxfordjournals.org/cgi/doi/10.1046/j.1365-8711.2001.04838.x>](http://onlinelibrary.wiley.com/doi/10.1046/j.1365-8711.2001.04838.x/full).

Komatsu, E et al. (2011). “Seven-year Wilkinson Microwave Anisotropy Probe (WMAP) Observations: Cosmological Interpretation”. In: *Astrophys. J. Suppl. Ser.* 192.47pp. DOI: 10.1088/0067-0049/192/2/18. URL: <http://iopscience.iop.org/article/10.1088/0067-0049/192/2/18/pdf>.

Kotarba, H. et al. (2009). “Magnetic field structure due to the global velocity field in spiral galaxies”. In: *Mon. Not. R. Astron. Soc.* 397.2, pp. 733–747. DOI: 10.1111/j.1365-2966.2009.15030.x. arXiv: 0905.0351. URL: <http://arxiv.org/abs/0905.0351>.

Kotarba, H. et al. (2010). “Simulating magnetic fields in the Antennae galaxies”. In: *Astrophys. J.* 716.2, pp. 1438–1452. DOI: 10.1088/0004-637X/716/2/1438. arXiv: 0911.3327. URL: <http://arxiv.org/abs/0911.3327>.

Kotarba, Hanna et al. (2011). “Galactic ménage à trois: Simulating magnetic fields in colliding galaxies”. In: *Mon. Not. R. Astron. Soc.* 415.4, pp. 3189–3218. ISSN: 00358711. DOI: 10.1111/j.1365-2966.2011.18932.x. arXiv: 1011.5735.

Kowal, G, Alex Lazarian, and A Beresnyak (2007). “Density Fluctuations in MHD Turbulence: Spectra, Intermittency, and Topology”. In: *Astrophys. J.* 658, pp. 423–445. URL: <http://iopscience.iop.org/article/10.1086/511515/pdf>.

Kravtsov, Andrey and Stefano Borgani (2012). “Formation of Galaxy Clusters”. In: ISSN: 0066-4146. DOI: 10.1146/annurev-astro-081811-125502. arXiv: 1205.5556. URL: <http://arxiv.org/abs/1205.5556> <http://dx.doi.org/10.1146/annurev-astro-081811-125502>.

Kravtsov, Andrey, Alexey Vikhlinin, and Alexander Meshcheryakov (2014). “Stellar mass – halo mass relation and star formation efficiency in high-mass halos”. In: *ArXiv e-prints*, p. 21. arXiv: 1401.7329. URL: <http://arxiv.org/abs/1401.7329>.

Kravtsov, Andrey V, Anatoly A Klypin, and Alexei M Khokhlov (1997). “Adaptive Refinement Tree: A New High-Resolution N-Body Code for Cosmological Simulations”. In: *Astrophys. J. Suppl. Ser.* 111, pp. 73–94. URL: <http://iopscience.iop.org/article/10.1086/313015/pdf>.

Kronberg, Philipp P. (1994). “Extragalactic magnetic fields”. In: *Reports Prog. Phys.* 57.4, pp. 325–382.

Krueer, W. L., J. M. Dawson, and B. Rosen (1973). “The dipole expansion method for plasma simulation”. In: *J. Comput. Phys.* 13.1, pp. 114–129. ISSN: 10902716. DOI: 10.1016/0021-9991(73)90129-0.

Kumar, D. et al. (2013). “Parallel Godunov smoothed particle hydrodynamics (SPH) with improved treatment of Boundary Conditions and an application to granular flows”. In:

Comput. Phys. Commun. 184.10, pp. 2277–2286. DOI: <https://doi.org/10.1016/j.cpc.2013.05.014>. URL: https://ac.els-cdn.com/S0010465513001744/1-s2.0-S0010465513001744-main.pdf?{_}tid=da647f32-f6c5-11e7-8229-00000aab0f27{\&}acdnat=1515671709{_}80b8313b6be5d454bf9ba32f36f854e6.

Kylafis, N. D. and N. D. (1983). “Linear polarization of interstellar radio-frequency absorption lines and magnetic field direction”. In: *Astrophys. J.* 275, p. 135. ISSN: 0004-637X. DOI: [10.1086/161520](https://doi.org/10.1086/161520). URL: <http://adsabs.harvard.edu/doi/10.1086/161520>.

Landau, L. D. and E. M. Lifschitz (2007). *Lehrbuch der theoretischen Physik VI Hydrodynamik*. Ed. by Wolfgang Weller and A. Kühnel. 5th. Moskau: Harri Deutsch GmbH. ISBN: 978-3-8171-1331-6.

Lang, P. et al. (2017). “Falling outer rotation curves of star-forming galaxies at $0.6 < z < 2.6$ probed with KMOS^3D and SINS/ZC-SINF”. In: *Astrophys. J.* 840.2. ISSN: 0004-637X. DOI: [10.3847/1538-4357/aa6d82](https://doi.org/10.3847/1538-4357/aa6d82). arXiv: [1703.05491](https://arxiv.org/abs/1703.05491). URL: <http://arxiv.org/abs/1703.05491> <http://dx.doi.org/10.3847/1538-4357/aa6d82>.

Lanson, Nathalie and Jean-Paul Vila (2008a). “Renormalized Meshfree Schemes I: Consistency, Stability, and Hybrid Methods for Conservation Laws”. In: *SIAM J. Numer. Anal.* 46.4, pp. 1912–1934. DOI: [10.1137/S0036142903427718](https://doi.org/10.1137/S0036142903427718). URL: <http://pubs.siam.org/doi/10.1137/S0036142903427718>.

— (2008b). “Renormalized Meshfree Schemes II: Convergence for Scalar Conservation Laws”. In: *SIAM J. Numer. Anal.* 46.4, pp. 1935–1964. DOI: [10.1137/S003614290444739X](https://doi.org/10.1137/S003614290444739X). URL: <http://pubs.siam.org/doi/10.1137/S003614290444739X>.

Lazarian, A and A Beresnyak (2006). “Cosmic ray scattering in compressible turbulence”. In: *Mon. Not. R. Astron. Soc.* 373.3, pp. 1195–1202. DOI: [10.1111/j.1365-2966.2006.11093.x](https://doi.org/10.1111/j.1365-2966.2006.11093.x). URL: https://watermark.silverchair.com/mnras0373-1195.pdf?token=AQECAHi208BE49Ooan9khw{_}Ercy7Dm3ZL{_}9Cf3qfKAc485ysgAAAb4wggG6BgkqhkiG9w0BBwagggGrMIIBpwIBADCCAAAGCSqGSIB3DQEHTAeBglghkgBZQMEAS4wEQQMkaQhfXXTsCYeGthUAgEQgIIBcfGv21WDZEBLKrCgognj-prtiaCTpvjJa8Zh7Lf6.

Lazarian, A and P Desiati (2010). “Magnetic Reconnection as the Cause of Cosmic Ray Excess from the Heliospheric Tail”. In: *Astrophys. J.* 722.1, pp. 188–196. DOI: [10.1088/0004-637X/722/1/188](https://doi.org/10.1088/0004-637X/722/1/188). URL: <http://iopscience.iop.org/article/10.1088/0004-637X/722/1/188/pdf>.

Lazarian, Alex and Ethan T Vishniac (1999). “Reconnection in a Weakly Stochastic Field”. In: *Astrophys. J.* 517, pp. 700–718. URL: <http://iopscience.iop.org/article/10.1086/307233/pdf>.

Lee, C. H. et al. (2012). “PAndromeda - first results from the high-cadence monitoring of M31 with Pan-STARRS 1”. In: *Astron. Journal*, 143. DOI: [10.1088/0004-6256/143/4/89](https://doi.org/10.1088/0004-6256/143/4/89). arXiv: [1109.6320](https://arxiv.org/abs/1109.6320). URL: [http://arxiv.org/abs/1109.6320](https://arxiv.org/abs/1109.6320).

Lee, C. H. et al. (2015). “Microlensing events from the 11-year observations of the Wendelstein Calar Alto Pixellensing Project”. In: *Astrophys. J.* 806. DOI: [10.1088/0004-637X/806/2/161](https://doi.org/10.1088/0004-637X/806/2/161). arXiv: [1504.07246](https://arxiv.org/abs/1504.07246). URL: [http://arxiv.org/abs/1504.07246](https://arxiv.org/abs/1504.07246).

Leer, Bram van (1984). “On the Relation Between the Upwind-Differencing Schemes of Godunov, Engquist–Osher and Roe”. In: *SIAM J. Sci. Stat. Comput.* 5.1, pp. 1–20. DOI: [10.1137/0905001](https://doi.org/10.1137/0905001). URL: <http://pubs.siam.org/doi/10.1137/0905001>.

Lejeune Dirichlet, G. (1850). “Über die Reduction der positiven quadratischen Formen mit drei unbestimmten ganzen Zahlen”. In: *J. für die reine und Angew. Math.* 40, pp. 209–227. URL: <http://eudml.org/doc/147457>.

Leonardis, Aleš, Horst Bischof, and Axel Pinz, eds. (2006). *Computer Vision – ECCV 2006*. Vol. 3951. Lecture Notes in Computer Science. Berlin, Heidelberg: Springer Berlin Heidelberg. ISBN: 978-3-540-33832-1. DOI: [10.1007/11744023](https://doi.org/10.1007/11744023). URL: <http://link.springer.com/10.1007/11744023>.

LeVeque, Randall J. (1992). *Numerical Methods for Conservation Laws*. Basel: Birkhäuser Basel. ISBN: 978-3-7643-2723-1. DOI: [10.1007/978-3-0348-8629-1](https://doi.org/10.1007/978-3-0348-8629-1). URL: <http://link.springer.com/10.1007/978-3-0348-8629-1>.

Li, Hua-bai and Martin Houde (2008). “Probing the Turbulence Dissipation Range and Magnetic Field Strengths in Molecular Clouds”. In: *Astrophys. J.* 677.2, pp. 1151–1156. DOI: [10.1086/529581](https://doi.org/10.1086/529581). arXiv: [0801.2757](https://arxiv.org/abs/0801.2757). URL: <http://arxiv.org/abs/0801.2757>.

Libersky, Larry D. et al. (1993). “High Strain Lagrangian Hydrodynamics: A Three-Dimensional SPH Code for Dynamic Material Response”. In: *J. Comput. Phys.* 109.1, pp. 67–75. DOI: [10.1006/JCPH.1993.1199](https://doi.org/10.1006/JCPH.1993.1199). URL: <https://www.sciencedirect.com/science/article/pii/S002199918371199X>.

Ligh, M H et al. (2014). *The Art Of Memory Forensics*. Wiley.

Lin, Yen-Ting, Joseph J. Mohr, and S. Adam Stanford (2003). “Near-Infrared Properties of Galaxy Clusters: Luminosity as a Binding Mass Predictor and the State of Cluster Baryons”. In: *Astrophys. J.* 591.2, pp. 749–763.

Liu, G. R. and M. B. Liu (2003). *Smoothed Particle Hydrodynamics - A Meshfree Particle Method*. World Scientific, p. 449. ISBN: 978-981-238-456-0. DOI: [10.1142/5340](https://doi.org/10.1142/5340). URL: https://books.google.de/books/about/Smoothed{_}Particle{_}Hydrodynamics.html?id={_}cwFMmEQvZQC{\&}redir{_}esc=yhttp://www.worldscientific.com/worldscibooks/10.1142/5340.

Liu, Wing Kam et al. (1995). “Reproducing kernel particle methods for structural dynamics”. In: *Int. J. Numer. Methods Eng.* 38.10, pp. 1655–1679. DOI: [10.1002/nme.1620381005](https://doi.org/10.1002/nme.1620381005). URL: <http://doi.wiley.com/10.1002/nme.1620381005>.

Lloyd, S. (1982). “Least squares quantization in PCM”. In: *IEEE Trans. Inf. Theory* 28.2, pp. 129–137. DOI: [10.1109/TIT.1982.1056489](https://doi.org/10.1109/TIT.1982.1056489). URL: <http://ieeexplore.ieee.org/document/1056489/>.

Lodato, Giuseppe and Daniel J. Price (2010). “On the diffusive propagation of warps in thin accretion discs”. In: *Mon. Not. R. Astron. Soc.* 405.2, pp. 1212–1226. ISSN: 13652966. DOI: [10.1111/j.1365-2966.2010.16526.x](https://doi.org/10.1111/j.1365-2966.2010.16526.x). arXiv: [1002.2973](https://arxiv.org/abs/1002.2973).

Loeb, Abraham (2002). “Are X-ray clusters cooled by heat conduction to the surrounding intergalactic medium?” In: *New Astron.* 7.6, pp. 279–282.

Lopez-Honorez, Laura et al. (2017). “Constraints on warm dark matter from the ionization history of the Universe”. In: *Phys. Rev. D* 96.10. DOI: [10.1103/PhysRevD.96.103539](https://doi.org/10.1103/PhysRevD.96.103539). arXiv: [1703.02302](https://arxiv.org/abs/1703.02302). URL: <http://arxiv.org/abs/1703.02302>.

Lucy, L.B. (1977). "A numerical approach to the testing of the fission hypothesis". In: *Astron. J.* 82.12, pp. 1013–1024.

Maddison, Sarah T., James R. Murray, and Joseph J Monaghan (1996). "SPH Simulations of Accretion Disks and Narrow Rings". In: *Publ. Astron. Soc. Aust.* 13.

Marongiu, J. C. and E. Parkinson (2006). "SPH Modelling of the flow in a Pelton turbine". In: *Proc. SPHERIC 2006*. Rome, Italy.

Martinsson, Thomas P K et al. (2013). "VII. The distribution of luminous and dark matter in spiral galaxies". In: *Astron. Astrophys.* 557. DOI: [10.1051/0004-6361/201321390](https://doi.org/10.1051/0004-6361/201321390). URL: <https://www.aanda.org/articles/aa/pdf/2013/09/aa21390-13.pdf>.

Mastropietro, Chiara and Andreas Burkert (2008). "Simulating the Bullet Cluster". In: *Mon. Not. R. Astron. Soc.* 389.2, pp. 967–988. DOI: [10.1111/j.1365-2966.2008.13626.x](https://doi.org/10.1111/j.1365-2966.2008.13626.x). arXiv: [0711.0967](https://arxiv.org/abs/0711.0967). URL: [http://arxiv.org/abs/0711.0967](https://arxiv.org/abs/0711.0967).

McClure-Griffiths, N. M. et al. (2009). "GASS: The Parkes Galactic All-Sky Survey. I. Survey Description, Goals, and Initial Data Release". In: *Astrophys. J. Suppl.* 181, pp. 398–412. DOI: [10.1088/0067-0049/181/2/398](https://doi.org/10.1088/0067-0049/181/2/398). arXiv: [0901.1159](https://arxiv.org/abs/0901.1159). URL: [http://arxiv.org/abs/0901.1159](https://arxiv.org/abs/0901.1159).

McNally, Colin P, Wladimir Lyra, and Jean-claude Passy (2012). "a Well-Posed Kelvin – Helmholtz Instability Test and Comparison". In: 18. ISSN: 0067-0049. DOI: [10.1088/0067-0049/201/2/18](https://doi.org/10.1088/0067-0049/201/2/18).

Mestel, L. and L. Spitzer (1956). "Star Formation in Magnetic Dust Clouds". In: *Mon. Not. R. Astron. Soc.* 116.5, pp. 503–514. DOI: [10.1093/mnras/116.5.503](https://doi.org/10.1093/mnras/116.5.503). URL: <https://academic.oup.com/mnras/article-lookup/doi/10.1093/mnras/116.5.503>.

Metropolis, Nicholas et al. (1953). "Equation of state calculations by fast computing machines". In: *J. Chem. Phys.* 21.6, pp. 1087–1092. ISSN: 00219606. DOI: [http://dx.doi.org/10.1063/1.1699114](https://doi.org/10.1063/1.1699114). arXiv: [5744249209](https://arxiv.org/abs/5744249209). URL: [http://jcp.aip.org/resource/1/jcpa6/v21/i6/p1087{_}s1?bypassSSO=1](https://jcp.aip.org/resource/1/jcpa6/v21/i6/p1087{_}s1?bypassSSO=1).

Meyers, S (2012). *Effective C++ Digital Collection: 140 Ways to Improve Your Programming*. Pearson Education. ISBN: 9780132979184. URL: <https://books.google.de/books?id=U71TySXdFk0C>.

Miesch, Mark S, John Scalo, and John Bally (1999). "Velocity Field Statistics in Star-forming Regions. I. Centroid Velocity Observations". In: *Astrophys. J.* 524, pp. 895–922. URL: [http://iopscience.iop.org/article/10.1086/307824/pdf](https://iopscience.iop.org/article/10.1086/307824/pdf).

Mignone, A et al. (2007). "PLUTO: A Numerical Code for Computational Astrophysics". In: *Astrophys. J. Suppl. Ser.* 170, pp. 228–242. URL: [http://iopscience.iop.org/article/10.1086/513316/pdf](https://iopscience.iop.org/article/10.1086/513316/pdf).

Miller, Matthew and Joel Bregman (2013). "The Structure of the Milky Way's Hot Gas Halo". In: *Astrophys. J.* 770.2. DOI: [10.1088/0004-637X/770/2/118](https://doi.org/10.1088/0004-637X/770/2/118). arXiv: [1305.2430](https://arxiv.org/abs/1305.2430). URL: [http://arxiv.org/abs/1305.2430](https://arxiv.org/abs/1305.2430).

Mitchell, N. L. et al. (2009). "On the Origin of Cores in Simulated Galaxy Clusters". In: *Mon. Not. R. Astron. Soc.* 395, pp. 180–196. DOI: [10.1111/j.1365-2966.2009.14550.x](https://doi.org/10.1111/j.1365-2966.2009.14550.x). arXiv: [0812.1750](https://arxiv.org/abs/0812.1750). URL: [http://arxiv.org/abs/0812.1750](https://arxiv.org/abs/0812.1750).

Monaghan, Joseph J and Daniel J. Price (2006). “Toy Stars in two dimensions”. In: *Mon. Not. R. Astron. Soc.* 365.3, pp. 991–1006. ISSN: 00358711. DOI: [10.1111/j.1365-2966.2005.09783.x](https://doi.org/10.1111/j.1365-2966.2005.09783.x). arXiv: [0510713 \[astro-ph\]](https://arxiv.org/abs/0510713).

Morris, J. P. and Joseph J Monaghan (1997). “A Switch to Reduce SPH Viscosity”. In: *J. Comput. Phys.* 136.1, pp. 41–50.

Morse, R. L. (1969). “Numerical Simulation of Warm Two-Beam Plasma”. In: *Phys. Fluids* 12.11, p. 2418. ISSN: 00319171. DOI: [10.1063/1.1692361](https://doi.org/10.1063/1.1692361). URL: <http://scitation.aip.org/content/aip/journal/pof1/12/11/10.1063/1.1692361>.

Muder, D. J. (1988). “Putting the Best Face of a Voronoi Polyhedron”. In: *Proc. London Math. Soc.* Vol. 56, pp. 329–348.

Mueller, Ewald and Matthias Steinmetz (1995). “Simulating Self-gravitating Hydrodynamic Flows”. In: *Comput. Phys. Commun. vol. 89, Issue 1-3, pp.45-58* 89, pp. 45–58. DOI: [10.1016/0010-4655\(94\)00185-5](https://doi.org/10.1016/0010-4655(94)00185-5). arXiv: [9402070 \[astro-ph\]](https://arxiv.org/abs/astro-ph/9402070). URL: <http://arxiv.org/abs/astro-ph/9402070>.

Murante, G. et al. (2011). “Hydrodynamic simulations with the Godunov smoothed particle hydrodynamics”. In: *Mon. Not. R. Astron. Soc.* 417.1, pp. 136–153. ISSN: 00358711. DOI: [10.1111/j.1365-2966.2011.19021.x](https://doi.org/10.1111/j.1365-2966.2011.19021.x). arXiv: [1105.1344](https://arxiv.org/abs/1105.1344). URL: <http://mnras.oxfordjournals.org/cgi/doi/10.1111/j.1365-2966.2011.19021.x?https://doi.org/10.1111/j.1365-2966.2011.19021.x&token=AQECAHi208BE490oan9khW{Ercy7Dm3ZL}9Cf3qfKAc485ysgAAAbswggG3Bqkqhkig9w0BBwagggGoMIIpAIBADCCAZ0GCSqGSib3DQEHAeBglghkgBZQM>.

Munch, G. and Albert D. Wheeler (1958). “Space-Time Correlations in Stationary Isotropic Turbulence”. In: *Phys. Fluids* 1.6, p. 462. ISSN: 00319171. DOI: [10.1063/1.1724368](https://doi.org/10.1063/1.1724368). URL: <http://scitation.aip.org/content/aip/journal/pof1/1/6/10.1063/1.1724368>.

Naab, Thorsten and Jeremiah P. Ostriker (2017). “Theoretical Challenges in Galaxy Formation”. In: *Annu. Rev. Astron. Astrophys.* 55.1, pp. 59–109. ISSN: 0066-4146. DOI: [10.1146/annurev-astro-081913-040019](https://doi.org/10.1146/annurev-astro-081913-040019). arXiv: [1612.06891](https://arxiv.org/abs/1612.06891). URL: <http://adsabs.harvard.edu/abs/2017ARA&A...55...59N>.

Nabors, K. et al. (1994). “Preconditioned, Adaptive, Multipole-Accelerated Iterative Methods for Three-Dimensional First-Kind Integral Equations of Potential Theory”. In: *SIAM J. Sci. Comput.* 15.3, pp. 713–735. DOI: [10.1137/0915046](https://doi.org/10.1137/0915046). URL: <http://epubs.siam.org/doi/10.1137/0915046>.

Narayan, Ramesh and Mikhail V. Medvedev (2001). “Thermal Conduction in Clusters of Galaxies”. In: *Astrophys. J.* 562, pp. 129–132. DOI: [10.1086/338325](https://doi.org/10.1086/338325).

Navarro, Julio F., Carlos S. Frenk, and Simon D. M. White (1997). “A Universal Density Profile from Hierarchical Clustering”. In: *1.1*, pp. 493–508. ISSN: 0004-637X. DOI: [10.1086/304888](https://doi.org/10.1086/304888). arXiv: [9611107 \[astro-ph\]](https://arxiv.org/abs/astro-ph/9611107). URL: <http://arxiv.org/abs/astro-ph/9611107> <https://doi.org/10.1086/304888>.

Navrátil, Paul Arthur, Jarrett L. Johnson, and Volker Bromm (2007). “Visualization of cosmological particle-based datasets”. In: *IEEE Trans. Vis. Comput. Graph.* 13.6, pp. 1712–1718. ISSN: 10772626. DOI: [10.1109/TVCG.2007.70526](https://doi.org/10.1109/TVCG.2007.70526). arXiv: [0708.0961](https://arxiv.org/abs/0708.0961).

Newton, Isaac (1687). *Philosophiae Naturalis Principia Mathematica*.

Novak, G, J L Dotson, and H Li (2009). “Dispersion of Observed Position Angles of Submillimeter Polarization in Molecular Clouds”. In: *Astrophys. J.* 695, pp. 1362–1369. DOI: [10.1088/0004-637X/695/2/1362](https://doi.org/10.1088/0004-637X/695/2/1362). URL: <http://iopscience.iop.org/article/10.1088/0004-637X/695/2/1362/pdf>.

O ’dell, C R and Hector O Castañeda (1987). “Evidence for turbulence in H II regions”. In: *Astrophys. J.* 317, pp. 686–692. URL: http://articles.adsabs.harvard.edu/cgi-bin/nph-iarticle{_}query?1987ApJ...317..686O{\&}data{_}type=PDF{_}HIGH{\&}whole{_}paper=YES{\&}type=PRINTER{\&}filetype=.pdf.

Oort, J. H. (1932). “The force exerted by the stellar system in the direction perpendicular to the galactic plane and some related problems”. In: *Bull. Astron. Institutes Netherlands* 6, p. 249. URL: http://adsabs.harvard.edu/cgi-bin/bib{_}query?1932BAN...6..249O.

O’Shea, Brian W. et al. (2004). “Introducing Enzo, an AMR Cosmology Application”. In: *eprint arXiv:astro-ph/0403044*. arXiv: [0403044 \[astro-ph\]](https://arxiv.org/abs/astro-ph/0403044). URL: <http://arxiv.org/abs/astro-ph/0403044>.

O’Shea, Brian W. et al. (2005). “Comparing AMR and SPH Cosmological Simulations: I. Dark Matter & Adiabatic Simulations”. In: *Astrophys. J. Suppl. Ser.* 160.1, pp. 1–27. DOI: [10.1086/432645](https://doi.org/10.1086/432645). arXiv: [0312651 \[astro-ph\]](https://arxiv.org/abs/astro-ph/0312651). URL: <http://arxiv.org/abs/astro-ph/0312651>.

Ostriker, Eve C. (2002). “Developing Diagnostics of Molecular Clouds Using Numerical MHD Simulations”. In: *Turbul. Magn. Fields Astrophys. Ed. by E. Falgarone, T. Passot., Lect. Notes Physics*, vol. 614, p.252-270 614, pp. 252–270. ISSN: 0075-8450. URL: <https://arxiv.org/pdf/astro-ph/0204463.pdf><https://arxiv.org/abs/astro-ph/0204463>.

Ostriker, Eve C, James M Stone, and Charles F Gammie (2001). “Density, Velocity, and Magnetic Field Structure in Turbulent Molecular Cloud Models”. In: *Astrophys. J.* 546, pp. 980–1005. URL: <http://iopscience.iop.org/article/10.1086/318290/pdf>.

Owen, J. Michael et al. (1998). “Adaptive Smoothed Particle Hydrodynamics: Methodology. II.” In: *Astrophys. J. Suppl. Ser.* 116.2, pp. 155–209. DOI: [10.1086/313100](https://doi.org/10.1086/313100). URL: <http://iopscience.iop.org/article/10.1086/313100/pdf>.

Owers, Matt S., Paul E. J. Nulsen, and Warrick J. Couch (2011). “Minor Merger-Induced Cold Fronts in Abell 2142 and RxJ1720.1+2638”. In: *Astrophys. J.* 741.2, p. 122. ISSN: 0004-637X. DOI: [10.1088/0004-637X/741/2/122](https://doi.org/10.1088/0004-637X/741/2/122). URL: <http://stacks.iop.org/0004-637X/741/i=2/a=122?key=crossref.5c7ebe7681462d21a940cd581e6f2460>.

Owers, Matt S. et al. (2009). “A High Fidelity Sample of Cold Front Clusters From the Chandra Archive”. In: *Astrophys. J.* 704.2, pp. 1349–1370. ISSN: 0004-637X. DOI: [10.1088/0004-637X/704/2/1349](https://doi.org/10.1088/0004-637X/704/2/1349).

0004-637X/704/2/1349. URL: <http://stacks.iop.org/0004-637X/704/i=2/a=1349?key=crossref.b688b86ed012baf2135cd143744af770>.

Padoan, Paolo et al. (2001). “Theoretical Models of Polarized Dust Emission from Protostellar Cores”. In: *Astrophys. J.* 559, pp. 1005–1018. URL: <http://iopscience.iop.org/article/10.1086/322504/pdf>.

Pakmor, Rüdiger (2006). “The imprint of the dynamical state on the structure of magnetic fields in simulated galaxy clusters”. Diploma thesis. Technische Universitaet Muenchen.

— (2010). “Progenitor systems of Type Ia Supernovae: mergers of white dwarfs and constraints on hydrogen-accreting white dwarfs”. In:

Pakmor, Rüdiger and Volker Springel (2013). “Simulations of magnetic fields in isolated disc galaxies”. In: *Mon. Not. R. Astron. Soc.* 432.1, pp. 176–193. ISSN: 00358711. DOI: <10.1093/mnras/stt428>. arXiv: <1212.1452>.

Pakmor, Rüdiger et al. (2012). “Stellar gadget: A smoothed particle hydrodynamics code for stellar astrophysics and its application to Type Ia supernovae from white dwarf mergers”. In: *Mon. Not. R. Astron. Soc.* 424.3, pp. 2222–2231. ISSN: 00358711. DOI: <10.1111/j.1365-2966.2012.21383.x>. arXiv: <1205.5806>.

Pakmor, Rüdiger et al. (2017). “Magnetic field formation in the Milky Way like disc galaxies of the Auriga project”. In: *Mon. Not. R. Astron. Soc.* 469.3, pp. 3185–3199. DOI: <10.1093/mnras/stx1074>. URL: <https://academic.oup.com/mnras/article-lookup/doi/10.1093/mnras/stx1074>.

Parrish, Ian J., Eliot Quataert, and Prateek Sharma (2009). “Anisotropic Thermal Conduction and the Cooling Flow Problem in Galaxy Clusters”. In: *Astrophys. J.* P. 14. ISSN: 15384357. DOI: <10.1088/0004-637X/703/1/96>. arXiv: <0905.4500>. URL: <http://arxiv.org/abs/0905.4500>.

Parrish, Ian J. and James M. Stone (2005). “Nonlinear Evolution of the Magnetothermal Instability in Two Dimensions”. In: *Astrophys. J.* 633.1, pp. 334–348. ISSN: 0004-637X. DOI: <10.1086/444589>. URL: <http://stacks.iop.org/0004-637X/633/i=1/a=334>.

Peano, G (1890). “Sur une courbe, qui remplit toute une aire plane”. In: *Math. Ann.* 36.1, pp. 157–160. ISSN: 1432-1807. DOI: <10.1007/BF01199438>. URL: <https://doi.org/10.1007/BF01199438>.

Peek, J. E. G. et al. (2011). “The GALFA-HI Survey: Data Release 1”. In: *Astrophys. J. Suppl.* 194. DOI: <10.1088/0067-0049/194/2/20>. arXiv: <1101.1879>. URL: <http://arxiv.org/abs/1101.1879>.

Pen, U.L. (1998). “A High-Resolution Adaptive Moving Mesh Hydrodynamic Algorithm”. In: *Astrophys. J. Suppl. Ser.* 115.1, pp. 19–34. URL: <http://iopscience.iop.org/article/10.1086/313074/pdf>.

Peterson, J. R. and A. C. Fabian (2006). “X-ray spectroscopy of cooling clusters”. In: *Phys. Rep.* 427.1, pp. 1–39. ISSN: 03701573. DOI: <10.1016/j.physrep.2005.12.007>. URL: <http://linkinghub.elsevier.com/retrieve/pii/S0370157306000020>.

Peterson, J. R. et al. (2003). “High-Resolution X-Ray Spectroscopic Constraints on Cooling-Flow Models for Clusters of Galaxies”. In: *Astrophys. J.* 590.1, pp. 207–224. arXiv: <0210662>.

Petkova, Margarita and Volker Springel (2009). “An implementation of radiative transfer in the cosmological simulation code gadget”. In: *Mon. Not. R. Astron. Soc.* 396.3, pp. 1383–1403. ISSN: 00358711. DOI: [10.1111/j.1365-2966.2009.14843.x](https://doi.org/10.1111/j.1365-2966.2009.14843.x). URL: <http://mnras.oxfordjournals.org/cgi/doi/10.1111/j.1365-2966.2009.14843.x>.

Phillips, G. J. and J. J. Monaghan (1985). “A numerical method for three-dimensional simulations of collapsing, isothermal, magnetic gas clouds”. In: *Mon. Not. R. Astron. Soc.* 216.4, pp. 883–895. DOI: [10.1093/mnras/216.4.883](https://doi.org/10.1093/mnras/216.4.883). URL: <https://academic.oup.com/mnras/article-lookup/doi/10.1093/mnras/216.4.883>.

Pistinner, Shlomi and Giora Shaviv (1996). “Can tangled magnetic fields suppress thermal conduction in cluster cooling flows?” In: *Astrophys. J.* 459, pp. 147–155.

Planck, Collaboration (2016a). “Planck 2015 results. I. Overview of products and scientific results”. In: *Astron. Astrophys.* 571, A1. ISSN: 0004-6361. DOI: [10.1051/0004-6361/201321529](https://doi.org/10.1051/0004-6361/201321529). arXiv: [1303.5062](https://arxiv.org/abs/1303.5062). URL: <http://link.aps.org/doi/10.1103/Physics.6.107> <http://arxiv.org/abs/1303.5062> <http://www.aanda.org/10.1051/0004-6361/201321529>.

— (2016b). “Planck 2015 results. XIII. Cosmological parameters”. In: *Astron. Astrophys.* 594. DOI: [10.1051/0004-6361/201525830](https://doi.org/10.1051/0004-6361/201525830). URL: [https://www.aanda.org/articles/aa/pdf/2016/10/aa25830-15.pdf](http://www.aanda.org/articles/aa/pdf/2016/10/aa25830-15.pdf).

— (2016c). “Planck 2015 results. XIX. Constraints on primordial magnetic fields”. In: *Astron. Astrophys.* 594. DOI: [10.1051/0004-6361/201525821](https://doi.org/10.1051/0004-6361/201525821). URL: [https://www.aanda.org/articles/aa/pdf/2016/10/aa25821-15.pdf](http://www.aanda.org/articles/aa/pdf/2016/10/aa25821-15.pdf).

Planelles, Susana and Vicent Quilis (2009). “Galaxy cluster mergers”. In: *Mon. Not. R. Astron. Soc.* 399.1, pp. 410–424. ISSN: 00358711. DOI: [10.1111/j.1365-2966.2009.15290.x](https://doi.org/10.1111/j.1365-2966.2009.15290.x). arXiv: [0906.4024 \[astro-ph.CO\]](https://arxiv.org/abs/0906.4024).

Plummer, H. C. (1911). “On the Problem of Distribution in Globular Star Clusters”. In: *Mon. Not. R. Astron. Soc.* 71, pp. 460–470. DOI: [10.1093/mnras/71.5.460](https://doi.org/10.1093/mnras/71.5.460). URL: <https://academic.oup.com/mnras/article-lookup/doi/10.1093/mnras/71.5.460>.

Portegies Zwart, Simon F. et al. (2001). “Star cluster ecology - IV. Dissection of an open star cluster: photometry”. In: *Mon. Not. R. Astron. Soc.* 321.2, pp. 199–226. DOI: [10.1046/j.1365-8711.2001.03976.x](https://doi.org/10.1046/j.1365-8711.2001.03976.x). arXiv: [0005248 \[astro-ph\]](https://arxiv.org/abs/0005248). URL: [http://arxiv.org/abs/astro-ph/0005248](https://arxiv.org/abs/astro-ph/0005248).

Powell, Kenneth G. et al. (1999). “A Solution-Adaptive Upwind Scheme for Ideal Magnetohydrodynamics”. In: *J. Comput. Phys.* 154.2, pp. 284–309. ISSN: 00219991. DOI: [10.1006/jcph.1999.6299](https://doi.org/10.1006/jcph.1999.6299). URL: [http://linkinghub.elsevier.com/retrieve/pii/S002199919996299X](https://linkinghub.elsevier.com/retrieve/pii/S002199919996299X).

Power, Chris, Justin I. Read, and A Hobbs (2014). “The formation of entropy cores in non-radiative galaxy cluster simulations: SPH versus AMR”. In: *Mon. Not. R. Astron. Soc.* 440, pp. 3243–3256. ISSN: 00358711. DOI: [10.1093/mnras/stu418](https://doi.org/10.1093/mnras/stu418). arXiv: [1307.0668](https://arxiv.org/abs/1307.0668). URL: [http://arxiv.org/abs/1307.0668](https://arxiv.org/abs/1307.0668).

Prada, Francisco et al. (2011). “Halo concentrations in the standard LCDM cosmology”. In: *Mon. Not. R. Astron. Soc. Vol. 423, Issue 4, pp. 3018-3030.* 423, pp. 3018–3030. ISSN:

0035-8711. DOI: [10.1111/j.1365-2966.2012.21007.x](https://doi.org/10.1111/j.1365-2966.2012.21007.x). arXiv: [1104.5130](https://arxiv.org/abs/1104.5130). URL: <http://arxiv.org/abs/1104.5130><http://dx.doi.org/10.1111/j.1365-2966.2012.21007.x>.

Price, Daniel J. (2007). “SPLASH: An Interactive Visualisation Tool for Smoothed Particle Hydrodynamics Simulations”. In: *Publ. Astron. Soc. Aust.* 24.03, pp. 159–173. ISSN: 1323-3580. DOI: [10.1071/AS07022](https://doi.org/10.1071/AS07022). URL: http://www.journals.cambridge.org/abstract_S1323358000003672.

— (2008). “Modelling discontinuities and Kelvin–Helmholtz instabilities in SPH”. In: *J. Comput. Phys.* 227.24, pp. 10040–10057. ISSN: 00219991. DOI: [10.1016/j.jcp.2008.08.011](https://doi.org/10.1016/j.jcp.2008.08.011). URL: <http://linkinghub.elsevier.com/retrieve/pii/S0021999108004270>.

— (2012a). “Resolving high reynolds numbers in smoothed particle hydrodynamics simulations of subsonic turbulence”. In: *Mon. Not. R. Astron. Soc. Lett.* 420.1, pp. 33–37. ISSN: 17453933. DOI: [10.1111/j.1745-3933.2011.01187.x](https://doi.org/10.1111/j.1745-3933.2011.01187.x). arXiv: [1111.1255](https://arxiv.org/abs/1111.1255) [astro-ph.CO].

— (2012b). “Smoothed particle hydrodynamics and magnetohydrodynamics”. In: *J. Comput. Phys.* 231.3, pp. 759–794. ISSN: 00219991. DOI: [10.1016/j.jcp.2010.12.011](https://doi.org/10.1016/j.jcp.2010.12.011). URL: <http://linkinghub.elsevier.com/retrieve/pii/S0021999110006753>.

Price, Daniel J. and Christoph Federrath (2010). “Smoothed Particle Hydrodynamics: Turbulence and MHD”. In: *ASP Conf. Ser.* 429, p. 7. ISSN: 1050-3390. arXiv: [0910.0285](https://arxiv.org/abs/0910.0285). URL: <http://arxiv.org/abs/0910.0285>.

Price, Daniel J. and J. J. Monaghan (2007). “An energy-conserving formalism for adaptive gravitational force softening in SPH and N-body codes”. In: *Mon. Not. R. Astron. Soc.* 374, pp. 1347–1358. DOI: [10.1111/j.1365-2966.2006.11241.x](https://doi.org/10.1111/j.1365-2966.2006.11241.x). arXiv: [0610872](https://arxiv.org/abs/0610872) [astro-ph]. URL: <http://arxiv.org/abs/astro-ph/0610872>.

Price, Daniel J. and Joseph J Monaghan (2005). “Smoothed particle magnetohydrodynamics - III. Multidimensional tests and the $\text{div } \mathbf{B} = 0$ constraint”. In: *Mon. Not. R. Astron. Soc.* 364.2, pp. 384–406. ISSN: 00358711. DOI: [10.1111/j.1365-2966.2005.09576.x](https://doi.org/10.1111/j.1365-2966.2005.09576.x). arXiv: [0509083](https://arxiv.org/abs/0509083) [astro-ph].

Price, Daniel J. et al. (2017). “PHANTOM: A smoothed particle hydrodynamics and magnetohydrodynamics code for astrophysics”. In: *Publ. Astron. Soc. Aust.* arXiv: [arXiv:1702.03930v1](https://arxiv.org/abs/1702.03930v1).

Pujol, Arnau et al. (2017). “nIFTy Cosmology: the clustering consistency of galaxy formation models”. In: *Mon. Not. R. Astron. Soc.* 469.1, pp. 749–762. DOI: [10.1093/mnras/stx913](https://doi.org/10.1093/mnras/stx913). arXiv: [1702.02620](https://arxiv.org/abs/1702.02620). URL: <http://arxiv.org/abs/1702.02620>.

Puri, Kunal and Prabhu Ramachandran (2013). “SPH Entropy Errors and the Pressure Blip”. In: pp. 1–22. arXiv: [arXiv:1311.2167v2](https://arxiv.org/abs/1311.2167v2).

Quilis, Vicent (2004). “A new multidimensional adaptive mesh refinement hydro + gravity cosmological code”. In: *Mon. Not. R. Astron. Soc.* 352.4, pp. 1426–1438. ISSN: 00358711. DOI: [10.1111/j.1365-2966.2004.08040.x](https://doi.org/10.1111/j.1365-2966.2004.08040.x). arXiv: [0405389](https://arxiv.org/abs/0405389) [astro-ph].

Randles, P.W. and L.D. Libersky (1996). “Smoothed Particle Hydrodynamics: Some recent improvements and applications”. In: *Comput. Methods Appl. Mech. Eng.* 139.1-4, pp. 375–

408. DOI: [10.1016/S0045-7825\(96\)01090-0](https://doi.org/10.1016/S0045-7825(96)01090-0). URL: <https://www.sciencedirect.com/science/article/pii/S0045782596010900>.

Rasera, Yann and Benjamin Chandran (2008). “Numerical simulations of buoyancy instabilities in galaxy cluster plasmas with cosmic rays and anisotropic thermal conduction”. In: *Astrophys. J.* P. 40. ISSN: 0004-637X. DOI: [10.1086/591012](https://doi.org/10.1086/591012). arXiv: [0809.0354](https://arxiv.org/abs/0809.0354). URL: [http://arxiv.org/abs/0809.0354](https://arxiv.org/abs/0809.0354).

Rasia, Elena et al. (2014). “Temperature Structure of the Intracluster Medium From Smoothed-Particle Hydrodynamics and Adaptive-Mesh Refinement Simulations”. In: *Astrophys. J.* 791.2012, p. 96. ISSN: 1538-4357. DOI: [10.1088/0004-637X/791/2/96](https://doi.org/10.1088/0004-637X/791/2/96). URL: [http://stacks.iop.org/0004-637X/791/i=2/a=96?key=crossref.efb81fef60755dd5781a9c7c6f8397db](https://stacks.iop.org/0004-637X/791/i=2/a=96?key=crossref.efb81fef60755dd5781a9c7c6f8397db).

Rasia, Elena et al. (2015). “Cool Core Clusters from Cosmological Simulations”. In: *Astrophys. J. Lett.* 813. arXiv: [1509.04247](https://arxiv.org/abs/1509.04247). URL: [http://arxiv.org/abs/1509.04247](https://arxiv.org/abs/1509.04247).

Read, Justin I. and T. Hayfield (2012). “SPHS: Smoothed particle hydrodynamics with a higher order dissipation switch”. In: *Mon. Not. R. Astron. Soc.* 422.4, pp. 3037–3055. ISSN: 00358711. DOI: [10.1111/j.1365-2966.2012.20819.x](https://doi.org/10.1111/j.1365-2966.2012.20819.x). arXiv: [1111.6985](https://arxiv.org/abs/1111.6985).

Read, Justin I., T. Hayfield, and Oscar Agertz (2010). “Resolving mixing in smoothed particle hydrodynamics”. In: *Mon. Not. R. Astron. Soc.* 405.3, pp. 1513–1530. ISSN: 00358711. DOI: [10.1111/j.1365-2966.2010.16577.x](https://doi.org/10.1111/j.1365-2966.2010.16577.x). arXiv: [arXiv:0906.0774v1](https://arxiv.org/abs/0906.0774v1).

Rechester, A. B. and M.N. Rosenbluth (1978). “Electron heat transport in a Tokamak with destroyed magnetic surfaces”. In: *Phys. Rev. Lett.* 40.1, pp. 38–41.

Reid, M J and E M Silverstein (1990). “OH masers and the Galactic magnetic field”. In: *Astrophys. J.* 361, pp. 483–486. URL: http://articles.adsabs.harvard.edu/cgi-bin/nph-iarticle{_}query?1990ApJ...361..483R{_}data{_}type=PDF{_}HIGH{_}whole{_}paper=YES{_}type=PRINTER{_}&filetype=.pdf.

Reiley, Wesley C and Robert A van de Geijn (1999). *POOCLAPACK: Parallel Out-of-Core Linear Algebra Package*. Tech. rep. Austin, TX, USA.

Remus, Rhea-Silvia and Klaus Dolag (2016). “Connecting Small and Large Scales: The Role of Feedback in Establishing Global Galaxy Properties over Cosmic Times”. In: *Interplay between Local Glob. Process. Galaxies*. Ed. by C. Morisset S. F. Sanchez and G. Delgado-Ingla. Cozumel. URL: <http://adsabs.harvard.edu/abs/2016ilgp.conf..43R>.

Remus, Rhea-Silvia, Klaus Dolag, and Tadziu L. Hoffmann (2017). “The Outer Halos of Very Massive Galaxies: BCGs and their DSC in the Magneticum Simulations”. In: *Galaxies* 5.3, p. 49. DOI: [10.3390/galaxies5030049](https://doi.org/10.3390/galaxies5030049). arXiv: [1709.02393](https://arxiv.org/abs/1709.02393). URL: [http://arxiv.org/abs/1709.02393](https://arxiv.org/abs/1709.02393).

Remus, Rhea-Silvia et al. (2016). “The Co-Evolution of Total Density Profiles and Central Dark Matter Fractions in Simulated Early-Type Galaxies”. In: *Mon. Not. R. Astron. Soc.* 464.3, pp. 3742–3756. DOI: [10.1093/mnras/stw2594](https://doi.org/10.1093/mnras/stw2594). arXiv: [1603.01619](https://arxiv.org/abs/1603.01619). URL: [http://arxiv.org/abs/1603.01619](https://arxiv.org/abs/1603.01619).

Rieder, Michael and Romain Teyssier (2016). “A small-scale dynamo in feedback-dominated galaxies as the origin of cosmic magnetic fields - I. The kinematic phase”. In: *Mon. Not. R.*

Astron. Soc. 457.2, pp. 1722–1738. DOI: [10.1093/mnras/stv2985](https://doi.org/10.1093/mnras/stv2985). arXiv: [1506.00849](https://arxiv.org/abs/1506.00849). URL: <http://arxiv.org/abs/1506.00849>.

— (2017a). “A small-scale dynamo in feedback-dominated galaxies - II. The saturation phase and the final magnetic configuration”. In: *Mon. Not. R. Astron. Soc.* 471.3, pp. 2674–2686. DOI: [10.1093/mnras/stx1670](https://doi.org/10.1093/mnras/stx1670). arXiv: [1704.05845](https://arxiv.org/abs/1704.05845). URL: <http://arxiv.org/abs/1704.05845>.

— (2017b). “A small-scale dynamo in feedback-dominated galaxies - III. Cosmological simulations”. In: *Mon. Not. R. Astron. Soc.* 472.4, pp. 4368–4373. DOI: [10.1093/mnras/stx2276](https://doi.org/10.1093/mnras/stx2276). arXiv: [1708.01486](https://arxiv.org/abs/1708.01486). URL: <http://arxiv.org/abs/1708.01486>.

Ritchie, Benedict W and Peter A Thomas (2001). “Multiphase smoothed-particle hydrodynamics”. In: 756.September.

Robishaw, Timothy (2008). “Magnetic Fields Near and Far: Galactic and Extragalactic Single-Dish Radio Observations of the Zeeman Effect”. PhD thesis. University of California, Berkeley, p. 158. URL: <https://search.proquest.com/docview/304696225>.

Rodrigues, G (2009). “Taming the OOM killer”. In: *LWN.net*.

Roettgers, Bernhard and Alexander Arth (2018). “SPH to Grid: a new integral conserving method”. In: *ArXiv e-prints* 1803.03652. arXiv: [1803.03652](https://arxiv.org/abs/1803.03652). URL: <https://arxiv.org/abs/1803.03652>.

Roettiger, Kurt, James M. Stone, and Jack O Burns (1999). “Magnetic Field Evolution in Merging Clusters of Galaxies”. In: *Astrophys. J.* 518, pp. 594–602. DOI: [10.1086/307298](https://doi.org/10.1086/307298).

Rosner, R. and W. H. Tucker (1989). “On Magnetic Fields, Heating And Thermal Conduction In Halos, And The Suppression Of Cooling Flows”. In: *Astrophys. J.* 338, pp. 761–769. DOI: [10.1086/167234](https://doi.org/10.1086/167234).

Rosswog, S. et al. (2014). “The long-term evolution of neutron star merger remnants-I. The impact of r-process nucleosynthesis”. In: *Mon. Not. R. Astron. Soc.* 439.1, pp. 744–756. ISSN: 00358711. DOI: [10.1093/mnras/stt2502](https://doi.org/10.1093/mnras/stt2502). arXiv: [arXiv:1307.2939v2](https://arxiv.org/abs/1307.2939v2).

Rosswog, Stephan (2009). “Astrophysical smooth particle hydrodynamics”. In: *New Astron. Rev.* 53.4-6, pp. 78–104. ISSN: 1387-6473. DOI: [10.1016/j.newar.2009.08.007](https://doi.org/10.1016/j.newar.2009.08.007). URL: <http://www.sciencedirect.com/science/article/pii/S1387647309000487?via%20Dihub>.

Rosswog, Stephan and Daniel J. Price (2007). “Magma: A three-dimensional, Lagrangian magnetohydrodynamics code for merger applications”. In: *Mon. Not. R. Astron. Soc.* 379.3, pp. 915–931. ISSN: 00358711. DOI: [10.1111/j.1365-2966.2007.11984.x](https://doi.org/10.1111/j.1365-2966.2007.11984.x). arXiv: [0705.1441](https://arxiv.org/abs/0705.1441).

Rubin, Vera C, W Kent Ford, and Norbert Thonnard (1978). “Extended rotation curves of high-luminosity spiral galaxies. IV - Systematic dynamical properties, SA through SC”. In: *Astrophys. J.* 225, pp. 107–111. URL: http://articles.adsabs.harvard.edu/cgi-bin/nph-iarticle{_}query?1978ApJ...225L.107R{_}&data{_}&type=PDF{_}HIGH{_}&whole{_}&paper=YES{_}&type=PRINTER{_}&filetype=.pdf.

Ruderman, M.S. et al. (2000). “Slow surface wave damping in plasmas with anisotropic viscosity and thermal conductivity”. In: *Astron. Astrophys.* 276, pp. 261–276. ISSN: 00046361. URL: <http://aa.springer.de/bibs/0354001/2300261/small.htm>.

Rusling, David A (1998). *The Linux Kernel*.

Ruszkowski, Mateusz et al. (2011). “Cosmological Magnetohydrodynamic Simulations of Cluster Formation With Anisotropic Thermal Conduction”. In: *Astrophys. J.* 740.2, p. 81. ISSN: 0004-637X. DOI: 10.1088/0004-637X/740/2/81. URL: <http://stacks.iop.org/0004-637X/740/i=2/a=81?key=crossref.852b48fb9b2031414ce731361289c452>.

Ruzmaikin, Alexander, A. M. Shukurov, and D. D. Sokoloff (1988). *Magnetic Fields of Galaxies*. Vol. 133. Astrophysics and Space Science Library. Dordrecht: Springer Netherlands. ISBN: 978-94-010-7776-7. DOI: 10.1007/978-94-009-2835-0. URL: <http://link.springer.com/10.1007/978-94-009-2835-0>.

Ryu, D et al. (2012). “Magnetic Fields in the Large-Scale Structure of the Universe”. In: *Space Sci. Rev.* 166.1-4, pp. 1–35. DOI: 10.1007/s11214-011-9839-z. arXiv: arXiv:1109.4055. URL: <https://link.springer.com/content/pdf/10.1007/s11214-011-9839-z.pdf> <https://arxiv.org/abs/1109.4055>.

Ryu, Dongsu, T. W. Jones, and Adam Frank (1995). “Numerical Magnetohydrodynamics in Astrophysics: Algorithm and Tests for Multidimensional Flow”. In: *Astrophys. J.* 452, pp. 758–796. URL: http://esoads.eso.org/cgi-bin/nph-data/_query?bibcode=1995ApJ...442..228R&link_type=ARTICLE&db=_key=AST&high=1.

Ryu, Dongsu et al. (1993). “A cosmological hydrodynamic code based on the total variation diminishing scheme”. In: *Astrophys. J.* 414, p. 1. DOI: 10.1086/173051. URL: <http://adsabs.harvard.edu/doi/10.1086/173051>.

Saad, Yousef (2003). *Iterative Methods for Sparse Linear Systems*. 2nd. Society for Industrial and Applied Mathematics. URL: <http://www-users.cs.umn.edu/~saad/books.html>.

Saad, Yousef and Martin H Schultz (1986). “GMRES: a Generalized Minimal Residual Algorithm for Solving Nonsymmetric Linear Systems”. In: *SIAM J. Sci. STAT. Comput.* Vol 7.3, pp. 856–869.

Saitoh, Takayuki R. and Junichiro Makino (2009). “A Necessary Condition for Individual Time Steps in Sph Simulations”. In: *Astrophys. J.* 697.2, pp. L99–L102. ISSN: 0004-637X. DOI: 10.1088/0004-637X/697/2/L99. URL: <http://stacks.iop.org/1538-4357/697/i=2/a=L99?key=crossref.4fd4070c93c18733b320c931b78c1bb9>.

— (2013). “A Density Independent Formulation of Smoothed Particle Hydrodynamics”. In: 44.2001. ISSN: 0004-637X. DOI: 10.1088/0004-637X/768/1/44. arXiv: 1202.4277. URL: <http://arxiv.org/abs/1202.4277> <http://dx.doi.org/10.1088/0004-637X/768/1/44>.

Salmon, John K and Michael S Warren (1997). “Parallel, Out-of-Core Methods for N-body Simulation.” In: *PPSC*. SIAM. ISBN: 0-89871-395-1. URL: <http://dblp.uni-trier.de/db/conf/psc/psc1997.html#SalmonW97>.

Sarazin, Craig (1986). “X-ray emission from clusters of galaxies”. In: *Rev. Mod. Phys.* 58.1, pp. 1–115. ISSN: 0034-6861. DOI: [10.1103/RevModPhys.58.1](https://doi.org/10.1103/RevModPhys.58.1). URL: <http://link.aps.org/doi/10.1103/RevModPhys.58.1>.

— (2008). “Gas Dynamics in Clusters of Galaxies”. Dordrecht. URL: <http://www.springerlink.com/index/10.1007/978-1-4020-6941-3>.

Scannapieco, C. et al. (2012). “The Aquila comparison project: The effects of feedback and numerical methods on simulations of galaxy formation”. In: *Mon. Not. R. Astron. Soc.* 423.2, pp. 1726–1749. ISSN: 00358711. DOI: [10.1111/j.1365-2966.2012.20993.x](https://doi.org/10.1111/j.1365-2966.2012.20993.x). arXiv: [arXiv:1112.0315v3](https://arxiv.org/abs/1112.0315v3).

Scannapieco, Cecilia et al. (2008). “Effects of supernova feedback on the formation of galaxy discs”. In: *Mon. Not. R. Astron. Soc.* 389.3, pp. 1137–1149. ISSN: 00358711. DOI: [10.1111/j.1365-2966.2008.13678.x](https://doi.org/10.1111/j.1365-2966.2008.13678.x). URL: <http://mnras.oxfordjournals.org/cgi/doi/10.1111/j.1365-2966.2008.13678.x> https://watermark.silverchair.com/mnras0389-1137.pdf?token=AQECAHi208BE49Ooan9khW{_}Ercy7Dm3ZI{_}9Cf3qfKAc485ysgAAAb4wggG6BqkqhkiG9w0BBwagggGrMII BpwIBADCCAaAGCSqGSIB3DQE HATAeBglghkgBZQM.

Schaye, Joop et al. (2015). “The EAGLE project: Simulating the evolution and assembly of galaxies and their environments”. In: *Mon. Not. R. Astron. Soc.* 446.1, pp. 521–554. ISSN: 13652966. DOI: [10.1093/mnras/stu2058](https://doi.org/10.1093/mnras/stu2058). arXiv: [1407.7040](https://arxiv.org/abs/1407.7040).

Schekochihin, A A and S C Cowley (2006). “Turbulence, magnetic fields and plasma physics in clusters of galaxies”. In: *Phys. Plasmas* 13.5, pp. 24–28. arXiv: [0601246v2 \[arXiv:astro-ph\]](https://arxiv.org/pdf/astro-ph/0601246.pdf). URL: <https://arxiv.org/pdf/astro-ph/0601246.pdf>.

Schekochihin, A. A. et al. (2008). “Nonlinear growth of firehose and mirror fluctuations in astrophysical plasmas”. In: *Phys. Rev. Lett.* 100.8, pp. 1–4. ISSN: 00319007. DOI: [10.1103/PhysRevLett.100.081301](https://doi.org/10.1103/PhysRevLett.100.081301). arXiv: [0709.3828](https://arxiv.org/abs/0709.3828).

Schlickeiser, R., A. Sievers, and H. Thiermann (1987). “The diffuse radio emission from the Coma cluster”. In: *Astron. Astrophys.* 182, pp. 21–35.

Schoenberg, I. J. (1973). “Cardinal spline interpolation”. In: *CBMS-NSF Reg. Conf. Ser. Appl. Math.* Society for Industrial and Applied Mathematics (SIAM 3600 Market Street Floor 6 Philadelphia PA 19104), p. 119. ISBN: 9781611970555.

Schulze, Felix et al. (2018). “Kinematics of Simulated Galaxies I: Connecting Dynamical and Morphological Properties of Early-Type Galaxies at Different Redshifts”. In: *eprint arXiv:1802.01583*. arXiv: [1802.01583](https://arxiv.org/abs/1802.01583). URL: <http://arxiv.org/abs/1802.01583>.

Schüssler, M. and D. Schmitt (1981). “Comments on Smoothed Particle Hydrodynamics”. In: *Astron. Astrophys.* 97.

Sedov, L. I. (1959). “Similarity and Dimensional Methods in Mechanics”. In:

Sembolini, Federico et al. (2016a). “nIFTy galaxy cluster simulations - I. Dark matter and non-radiative models”. In: *Mon. Not. R. Astron. Soc.* 457.4, pp. 4063–4080. ISSN: 13652966. DOI: [10.1093/mnras/stw250](https://doi.org/10.1093/mnras/stw250). arXiv: [1503.06065](https://arxiv.org/abs/1503.06065).

Sembolini, Federico et al. (2016b). “nIFTy galaxy cluster simulations II: radiative models”. In: *Mon. Not. R. Astron. Soc.* 459.3, pp. 2973–2991. DOI: [10.1093/mnras/stw800](https://doi.org/10.1093/mnras/stw800). arXiv: [1511.03731](https://arxiv.org/abs/1511.03731). URL: <http://arxiv.org/abs/1511.03731>.

Shapiro, Paul R. et al. (1996). “Adaptive Smoothed Particle Hydrodynamics, with Application to Cosmology: Methodology”. In: *Astrophys. J. Suppl. Ser.* 103, p. 269. DOI: [10.1086/192279](https://doi.org/10.1086/192279). URL: <http://adsabs.harvard.edu/doi/10.1086/192279>.

Sharma, Prateek and Gregory W. Hammett (2007). “Preserving monotonicity in anisotropic diffusion”. In: *J. Comput. Phys.* 227.1, pp. 123–142. ISSN: 00219991. DOI: [10.1016/j.jcp.2007.07.026](https://doi.org/10.1016/j.jcp.2007.07.026). URL: <http://linkinghub.elsevier.com/retrieve/pii/S0021999107003233>.

Sharma, Prateek, Ian J. Parrish, and Eliot Quataert (2010). “Thermal Instability with Anisotropic Thermal Conduction and Adiabatic Cosmic Rays: Implications for Cold Filaments in Galaxy Clusters”. In: *Astrophys. J.* P. 31. ISSN: 0004-637X. DOI: [10.1088/0004-637X/720/1/652](https://doi.org/10.1088/0004-637X/720/1/652). arXiv: [1003.5546](https://arxiv.org/abs/1003.5546). URL: <http://arxiv.org/abs/1003.5546>.

Shen, Sijing, James Wadsley, and G S Stinson (2010). “The enrichment of the intergalactic medium with adiabatic feedback - I. Metal cooling and metal diffusion”. In: *Mon. Not. R. Astron. Soc.* 407.3, pp. 1581–1596. ISSN: 00358711. DOI: [10.1111/j.1365-2966.2010.17047.x](https://doi.org/10.1111/j.1365-2966.2010.17047.x). URL: <http://mnras.oxfordjournals.org/cgi/doi/10.1111/j.1365-2966.2010.17047.x>.

Shu, Frank H. (1991). *The Physics of Astrophysics Volume II: Gas Dynamics*. University Science Books. ISBN: 0935702652. URL: <https://books.google.de/books?id=50VYSc56URUC&dq=the+physics+of+astrophysics+volume+II+gas+dynamics&source=gbs%20navlinks%20s>.

Silverman, B. W. (1986). *Density estimation for statistics and data analysis*. London. URL: <http://adsabs.harvard.edu/abs/1986desd.book.....s>.

Simons, Raymond C. et al. (2017). “z~2: An Epoch of Disk Assembly”. In: *Astrophys. J.* 843.1. DOI: [10.3847/1538-4357/aa740c](https://doi.org/10.3847/1538-4357/aa740c). arXiv: [1705.03474](https://arxiv.org/abs/1705.03474). URL: <http://arxiv.org/abs/1705.03474>.

Sod, Gary A. (1978). “A survey of several finite difference methods for systems of nonlinear hyperbolic conservation laws”. In: *J. Comput. Phys.* 27.1, pp. 1–31. ISSN: 10902716. DOI: [10.1016/0021-9991\(78\)90023-2](https://doi.org/10.1016/0021-9991(78)90023-2).

Sofue, Yoshiaki and Vera Rubin (2001). “Rotation Curves of Spiral Galaxies”. In: *Annu. Rev. Astron. Astrophys.* 39, pp. 137–174. DOI: [10.1146/annurev.astro.39.1.137](https://doi.org/10.1146/annurev.astro.39.1.137). arXiv: [0010594 \[astro-ph\]](https://arxiv.org/abs/0010594). URL: <http://arxiv.org/abs/astro-ph/0010594>.

Soler, J D et al. (2013). “An Imprint of Molecular Cloud Magnetization in the Morphology of the Dust Polarized Emission”. In: *Astrophys. J.* 774.16pp. DOI: [10.1088/0004-637X/774/2/128](https://doi.org/10.1088/0004-637X/774/2/128). URL: <http://iopscience.iop.org/article/10.1088/0004-637X/774/2/128/pdf>.

Somerville, Rachel S. and Romeel Davé (2015). “Physical Models of Galaxy Formation in a Cosmological Framework”. In: *Annu. Rev. Astron. Astrophys.* 53, pp. 51–113. DOI: [10.1146/annurev-astro-082812-140951](https://doi.org/10.1146/annurev-astro-082812-140951). arXiv: [1412.2712](https://arxiv.org/abs/1412.2712). URL: <http://arxiv.org/abs/1412.2712>.

Sonneveld, P (1989). “CGS, a fast Lanczos-type solver for nonsymmetric linear systems”. In: *SIAM J. Sci. Stat. Comput.* 10.1, pp. 35–62.

Spitzer, L. (1962). *Physics of Fully Ionized Gases*. 2nd ed. New York: Interscience. URL: <http://adsabs.harvard.edu/abs/1962pfig.book.....S>.

Spitzer, Lyman Jr (1956). *Physics of fully ionized gas*. Interscience Publishers. URL: <http://books.google.de/books?id=CilRAAAAMAAJ>.

Spitzer, Lyman Jr and Richard Härm (1953). “Transport Phenomena in a Completely Ionized Gas”. In: *Phys. Rev. Lett.* 89.5, pp. 977–981. DOI: [10.1103/PhysRev.89.977](https://doi.org/10.1103/PhysRev.89.977).

Spreng, Fabian et al. (2017). “An Adaptivity Criterion for Smoothed Particle Hydrodynamics Fluid Simulations Based on Spatial Discretization Error”. In: *Proc. 12th Int. Smoothed Part. Hydrodyn. Eur. Res. Interes. Community SPH Work. (SPHERIC 2017)*. Ourense, Spain.

Springel, Volker (2000). “Modelling star formation and feedback in simulations of interacting galaxies”. In: *Mon. Not. R. Astron. Soc.* 312.4, pp. 859–879. DOI: [10.1046/j.1365-8711.2000.03187.x](https://doi.org/10.1046/j.1365-8711.2000.03187.x). URL: <https://academic.oup.com/mnras/article-lookup/doi/10.1046/j.1365-8711.2000.03187.x>.

— (2005a). “The cosmological simulation code GADGET-2”. In: *Mon. Not. R. Astron. Soc.* 364.4, pp. 1105–1134. DOI: [10.1111/j.1365-2966.2005.09655.x](https://doi.org/10.1111/j.1365-2966.2005.09655.x).

— (2005b). “User guide for GADGET-2”. In: pp. 1–46.

— (2010a). “E pur si muove: Galilean-invariant cosmological hydrodynamical simulations on a moving mesh”. In: *Mon. Not. R. Astron. Soc.* 401.2, pp. 791–851. ISSN: 00358711. DOI: [10.1111/j.1365-2966.2009.15715.x](https://doi.org/10.1111/j.1365-2966.2009.15715.x). arXiv: [0901.4107](https://arxiv.org/abs/0901.4107).

— (2010b). “Smoothed Particle Hydrodynamics in Astrophysics”. In: *Annu. Rev. Astron. Astrophys.* 48.1, pp. 391–430. ISSN: 0066-4146. DOI: [10.1146/annurev-astro-081309-130914](https://doi.org/10.1146/annurev-astro-081309-130914). URL: [http://www.annualreviews.org/doi/abs/10.1146/annurev-astro-081309-130914](https://www.annualreviews.org/doi/abs/10.1146/annurev-astro-081309-130914).

Springel, Volker, Tiziana Di Matteo, and Lars Hernquist (2005). “Modeling feedback from stars and black holes in galaxy mergers”. In: *Mon. Not. R. Astron. Soc.* 361.3, pp. 776–794. DOI: [10.1111/j.1365-2966.2005.09238.x](https://doi.org/10.1111/j.1365-2966.2005.09238.x). arXiv: [0411108 \[astro-ph\]](https://arxiv.org/abs/0411108). URL: [http://arxiv.org/abs/astro-ph/0411108](https://arxiv.org/abs/astro-ph/0411108).

Springel, Volker and Lars Hernquist (2002). “Cosmological smoothed particle hydrodynamics simulations: the entropy equation”. In: *Mon. Not. R. Astron. Soc.* 333.3, pp. 649–664.

— (2003). “Cosmological smoothed particle hydrodynamics simulations: a hybrid multiphase model for star formation”. In: *Mon. Not. R. Astron. Soc.* 339.2, pp. 289–311. ISSN: 0035-8711. DOI: [10.1046/j.1365-8711.2003.06206.x](https://doi.org/10.1046/j.1365-8711.2003.06206.x). URL: [http://mnras.oxfordjournals.org/cgi/doi/10.1046/j.1365-8711.2003.06206.x](https://mnras.oxfordjournals.org/cgi/doi/10.1046/j.1365-8711.2003.06206.x).

Springel, Volker and Simon D. M. White (1999). “Tidal tails in CDM cosmologies”. In: *Mon. Not. R. Astron. Soc.* 307.1, pp. 162–178. DOI: [10.1046/j.1365-8711.1999.02613.x](https://doi.org/10.1046/j.1365-8711.1999.02613.x). arXiv: [9807320 \[astro-ph\]](https://arxiv.org/abs/9807320). URL: [http://arxiv.org/abs/astro-ph/9807320](https://arxiv.org/abs/astro-ph/9807320).

Springel, Volker, Naoki Yoshida, and Simon D.M. White (2001). “GADGET: a code for collisionless and gasdynamical cosmological simulations”. In: *New Astron.* 6.2, pp. 79–117. ISSN: 13841076. DOI: [10.1016/S1384-1076\(01\)00042-2](https://doi.org/10.1016/S1384-1076(01)00042-2). URL: [http://linkinghub.elsevier.com/retrieve/pii/S1384107601000422](https://linkinghub.elsevier.com/retrieve/pii/S1384107601000422).

Springel, Volker et al. (2001). “Populating a cluster of galaxies – I . Results at $z = 0$ ”. In: *Mon. Not. R. Astron. Soc.* 328.3, pp. 726–750.

Springel, Volker et al. (2005). “Simulating the joint evolution of quasars, galaxies and their large-scale distribution”. In: *Nature* 435.7042, pp. 629–636. DOI: [10.1038/nature03597](https://doi.org/10.1038/nature03597). arXiv: [0504097 \[astro-ph\]](https://arxiv.org/abs/0504097). URL: [http://arxiv.org/abs/astro-ph/0504097](https://arxiv.org/abs/astro-ph/0504097).

Stadel, Joachim Gerhard (2001). “Cosmological N-body simulations and their analysis”. PhD thesis. University of Washington, p. 141. URL: [http://adsabs.harvard.edu/abs/2001PhDT.....21S](https://adsabs.harvard.edu/abs/2001PhDT.....21S).

Stasyszyn, Federico, Klaus Dolag, and Alexander M. Beck (2013). “A divergence-cleaning scheme for cosmological SPMHD simulations”. In: *Mon. Not. R. Astron. Soc.* 428. arXiv: [arXiv:1205.4169v1](https://arxiv.org/abs/1205.4169v1).

Steinborn, Lisa K. et al. (2015). “A refined sub-grid model for black hole accretion and AGN feedback in large cosmological simulations”. In: *Mon. Not. R. Astron. Soc.* 448.2, pp. 1504–1525. DOI: [10.1093/mnras/stv072](https://doi.org/10.1093/mnras/stv072). arXiv: [1409.3221](https://arxiv.org/abs/1409.3221). URL: [http://arxiv.org/abs/1409.3221](https://arxiv.org/abs/1409.3221).

Steinborn, Lisa K. et al. (2016). “Origin and properties of dual and offset active galactic nuclei in a cosmological simulation at $z=2$ ”. In: *Mon. Not. R. Astron. Soc.* 458.1, pp. 1013–1028. ISSN: 0035-8711. DOI: [10.1093/mnras/stw316](https://doi.org/10.1093/mnras/stw316). arXiv: [1510.08465](https://arxiv.org/abs/1510.08465). URL: [http://arxiv.org/abs/1510.08465](https://arxiv.org/abs/1510.08465)[http://dx.doi.org/10.1093/mnras/stw316](https://dx.doi.org/10.1093/mnras/stw316).

Steinmetz, M and E Mueller (1993). “On the capabilities and limits of smoothed particle hydrodynamics”. In: *Astron. Astrophys.* 268.1, pp. 391–410. ISSN: 0004-6361. URL: [http://adsabs.harvard.edu/full/1993A&A...268..391S](https://adsabs.harvard.edu/full/1993A&A...268..391S).

Steinmetz, Matthias (1996). “GRAPESPH: Cosmological SPH simulations with the special purpose hardware GRAPE”. In: *Mon. Not. R. Astron. Soc.* 278.4, pp. 1005–1017. DOI: [10.1093/mnras/278.4.1005](https://doi.org/10.1093/mnras/278.4.1005). arXiv: [9504050 \[astro-ph\]](https://arxiv.org/abs/9504050). URL: [http://arxiv.org/abs/astro-ph/9504050](https://arxiv.org/abs/astro-ph/9504050).

Stone, James M and Michael L Norman (1992a). “ZEUS-2D: A radiation magnetohydrodynamics code for astrophysical flows in two space dimensions. I - The hydrodynamic algorithms and tests.” In: *Astrophys. J. Suppl. Ser.* 80, pp. 753–790. URL: [http://articles.adsabs.harvard.edu/cgi-bin/nph-iarticle{_}query?1992ApJS...80..753S{\&}data{_}type=PDF{_}HIGH{\&}whole{_}paper=YES{\&}type=PRINTER{\&}filetype=.pdf](https://articles.adsabs.harvard.edu/cgi-bin/nph-iarticle{_}query?1992ApJS...80..753S{\&}data{_}type=PDF{_}HIGH{\&}whole{_}paper=YES{\&}type=PRINTER{\&}filetype=.pdf).

— (1992b). “ZEUS-2D: A Radiation Magnetohydrodynamics Code for Astrophysical Flows in Two Space Dimensions. II. The Magnetohydrodynamic Algorithms and Tests”. In: *Astrophys. J. Suppl. Ser.* 80, pp. 791–818. URL: [http://articles.adsabs.harvard.edu/cgi-bin/nph-iarticle{_}query?1992ApJS...80..791S{\&}data{_}type=PDF{_}HIGH{\&}whole{_}paper=YES{\&}type=PRINTER{\&}filetype=.pdf](https://articles.adsabs.harvard.edu/cgi-bin/nph-iarticle{_}query?1992ApJS...80..791S{\&}data{_}type=PDF{_}HIGH{\&}whole{_}paper=YES{\&}type=PRINTER{\&}filetype=.pdf).

Stone, James M. et al. (2008). “Athena: A New Code for Astrophysical MHD”. In: *Astrophys. J. Suppl. Ser.* 178.1, pp. 137–177. ISSN: 0067-0049. DOI: [10.1086/588755](https://doi.org/10.1086/588755). URL: [http://stacks.iop.org/0067-0049/178/i=1/a=137](https://stacks.iop.org/0067-0049/178/i=1/a=137).

Strong, A. W., C. Dickinson, and E. J. Murphy (2014). “Synchrotron radiation from molecular clouds”. In: arXiv: 1412.4500. URL: <http://arxiv.org/abs/1412.4500>.

Suresh, A. and H.T. Huynh (1997). “Accurate Monotonicity-Preserving Schemes with Runge–Kutta Time Stepping”. In: *J. Comput. Phys.* 136.1, pp. 83–99. ISSN: 00219991. DOI: 10.1006/jcph.1997.5745. URL: <http://linkinghub.elsevier.com/retrieve/pii/S0021999197957454>.

Suzuki, Kentaro et al. (2013). “Magnetohydrodynamic Simulations of the Formation of Cold Fronts in Clusters of Galaxies: Effects of Anisotropic Viscosity”. In: *Astrophys. J.* 768.2, p. 175. ISSN: 0004-637X. DOI: 10.1088/0004-637X/768/2/175. URL: <http://stacks.iop.org/0004-637X/768/i=2/a=175?key=crossref.76faa2f08caad379ce41d3d314ea9635>.

Swegle, J.W., D.L. Hicks, and S.W. Attaway (1995). “Smoothed Particle Hydrodynamics Stability Analysis”. In: *J. Comput. Phys.* 116.1, pp. 123–134. DOI: 10.1006/jcph.1995.1010. URL: <http://linkinghub.elsevier.com/retrieve/pii/S0021999185710108>.

Tang, Jianqi et al. (2004). “A Parallel Out-of-core Computing System Using PVFS for Linux Clusters”. In: *Proc. Int. Work. Storage Netw. Archit. Parallel I/Os.* SNAPI ’04. New York, NY, USA: ACM, pp. 33–39. DOI: 10.1145/1162628.1162633. URL: <http://doi.acm.org/10.1145/1162628.1162633>.

Tasker, Elizabeth J. et al. (2008). “A test suite for quantitative comparison of hydrodynamics codes in astrophysics”. In: *Mon. Not. R. Astron. Soc.* 390, pp. 1267–1281. DOI: 10.1111/j.1365-2966.2008.13836.x. arXiv: 0808.1844. URL: <http://arxiv.org/abs/0808.1844>.

Taylor, G. B. et al. (2006). “Magnetic fields in the centre of the Perseus cluster”. In: *Mon. Not. R. Astron. Soc.* 368.4, pp. 1500–1506. ISSN: 0035-8711. DOI: 10.1111/j.1365-2966.2006.10244.x. URL: <http://mnras.oxfordjournals.org/cgi/doi/10.1111/j.1365-2966.2006.10244.x>.

Teklu, A. F., Rhea-Silvia Remus, and Klaus Dolag (2016). “Dynamical Properties of Galaxies with Different Morphological Types at $z=0$ and $z=2$ ”. In: *Interplay between Local Glob. Process. Galaxies*. Ed. by C. Morisset S. F. Sanchez and G. Delgado-Ingla. Cozumel. URL: <http://adsabs.harvard.edu/abs/2016ilgp.confE..41T>.

Teklu, Adelheid F. et al. (2015). “Connecting Angular Momentum and Galactic Dynamics: The Complex Interplay between Spin, Mass, and Morphology”. In: *Astrophys. J.* 812, p. 29. DOI: 10.1088/0004-637X/812/1/29. URL: <http://iopscience.iop.org/article/10.1088/0004-637X/812/1/29/pdf>.

Teklu, Adelheid F. et al. (2017a). “Declining rotation curves at $z=2$: A natural phenomenon in Λ CDM cosmology”. In: arXiv: 1711.07985. URL: <http://arxiv.org/abs/1711.07985>.

Teklu, Adelheid F. et al. (2017b). “The Morphology-Density-Relation: Impact on the Satellite Fraction”. In: *Mon. Not. R. Astron. Soc.* 472.4, pp. 4769–4785. ISSN: 0035-8711. DOI: 10.1093/mnras/stx2303. arXiv: 1702.06546. URL: <http://arxiv.org/abs/1702.06546> <http://dx.doi.org/10.1093/mnras/stx2303>.

Teyssier, R (2002). “Cosmological hydrodynamics with adaptive mesh refinement A new high resolution code called RAMSES”. In: *Astron. Astrophys.* 385, pp. 337–364. DOI: [10.1051/0004-6361:20011817](https://doi.org/10.1051/0004-6361:20011817). URL: <https://www.aanda.org/articles/aa/pdf/2002/13/aa1593.pdf>.

Teyssier, Romain (2015). “Grid-Based Hydrodynamics in Astrophysical Fluid Flows”. In: *Annu. Rev. Astron. Astrophys.* 53.1, pp. 325–364. ISSN: 0066-4146. DOI: [10.1146/annurev-astro-082214-122309](https://doi.org/10.1146/annurev-astro-082214-122309). URL: <http://www.annualreviews.org/doi/10.1146/annurev-astro-082214-122309>.

Thierbach, M, U Klein, and R Wielebinski (2003). “Astrophysics The diffuse radio emission from the Coma cluster at 2 . 675 GHz and 4 . 85 GHz”. In: *Astron. Astrophys.* 61, pp. 53–61. ISSN: 0004-6361. DOI: [10.1051/0004-6361](https://doi.org/10.1051/0004-6361).

Titarev, V. A. and E. F. Toro (2002). “ADER: Arbitrary High Order Godunov Approach”. In: *J. Sci. Comput.* 17.1/4, pp. 609–618. ISSN: 08857474. DOI: [10.1023/A:1015126814947](https://doi.org/10.1023/A:1015126814947). URL: <http://link.springer.com/10.1023/A:1015126814947>.

Toledo, Sivan (1999a). “A survey of out-of-core algorithms in numerical linear algebra”. In: *Extern. Mem. Algorithms*. Ed. by James M Abello and Jeffrey Scott Vitter. DIMACS Series in Discrete Mathematics and Theoretical Computer Science. American Mathematical Society, pp. 161–179.

— (1999b). “External Memory Algorithms”. In: ed. by James M Abello and Jeffrey Scott Vitter. Boston, MA, USA: American Mathematical Society. Chap. A Survey o, pp. 161–179. ISBN: 0-8218-1184-3. URL: <http://dl.acm.org/citation.cfm?id=327766.327789>.

Tornatore, Luca et al. (2007). “Chemical enrichment of galaxy clusters from hydrodynamical simulations”. In: *Mon. Not. R. Astron. Soc.* 382.3, pp. 1050–1072. ISSN: 00358711. DOI: [10.1111/j.1365-2966.2007.12070.x](https://doi.org/10.1111/j.1365-2966.2007.12070.x). arXiv: [0705.1921](https://arxiv.org/abs/0705.1921).

Toro, Eleuterio F. (2009). *Riemann Solvers and Numerical Methods for Fluid Dynamics*. Berlin, Heidelberg: Springer Berlin Heidelberg. ISBN: 978-3-540-25202-3. DOI: [10.1007/b79761](https://doi.org/10.1007/b79761). URL: <http://link.springer.com/10.1007/b79761>.

Torvalds, L (2002). “O_DIRECT performance impact on 2.4.18”. In: *Newsgr. fa.linux.kernel*.

Tóth, Gábor and Gábor (2000). “The ·B=0 Constraint in Shock-Capturing Magnetohydrodynamics Codes”. In: *J. Comput. Phys.* 161.2, pp. 605–652. ISSN: 00219991. DOI: [10.1006/jcph.2000.6519](https://doi.org/10.1006/jcph.2000.6519). URL: <http://linkinghub.elsevier.com/retrieve/pii/S0021999100965197>.

Trac, H. and U.L. Pen (2004). “A moving frame algorithm for high Mach number hydrodynamics”. In: *New Astron.* 9.6, pp. 443–465. ISSN: 1384-1076. DOI: [10.1016/j.newast.2004.02.002](https://doi.org/10.1016/j.newast.2004.02.002). URL: <http://www.sciencedirect.com/science/article/pii/S1384107604000326?via%2525Dihub>.

Tricco, Terrence and Daniel J. Price (2013). “A Switch for Artificial Resistivity and Other Dissipation Terms”. In: *8th Int. SPHERIC Work.* 3, p. 8. arXiv: [1310.4260](https://arxiv.org/abs/1310.4260). URL: <http://arxiv.org/abs/1310.4260>.

Valcke, S. et al. (2010). “Kelvin-Helmholtz instabilities in smoothed particle hydrodynamics”. In: *Mon. Not. R. Astron. Soc.* 408.1, pp. 71–86. ISSN: 00358711. DOI: [10.1111/j.1365-2966.2010.17127.x](https://doi.org/10.1111/j.1365-2966.2010.17127.x). arXiv: [1006.1767](https://arxiv.org/abs/1006.1767).

Valdarnini, R. (2012). “Hydrodynamic capabilities of an SPH code incorporating an artificial conductivity term with a gravity-based signal velocity”. In: *Astron. Astrophys.* 546, A45. ISSN: 0004-6361. DOI: [10.1051/0004-6361/201219715](https://doi.org/10.1051/0004-6361/201219715). arXiv: [arXiv:1207.6980v1](https://arxiv.org/abs/1207.6980v1). URL: <http://www.aanda.org/10.1051/0004-6361/201219715>.

Vazza, F. (2011). “The entropy core in galaxy clusters: Numerical and physical effects in cosmological grid simulations”. In: *Mon. Not. R. Astron. Soc.* 410.1, pp. 461–483. ISSN: 00358711. DOI: [10.1111/j.1365-2966.2010.17455.x](https://doi.org/10.1111/j.1365-2966.2010.17455.x). arXiv: [1008.0191](https://arxiv.org/abs/1008.0191).

Verschuur, G. L. (1968). “Positive Determination of an Interstellar Magnetic Field by Measurement of the Zeeman Splitting of the 21-cm Hydrogen Line”. In: *Phys. Rev. Lett.* 21.11, pp. 775–778. DOI: [10.1103/PhysRevLett.21.775](https://doi.org/10.1103/PhysRevLett.21.775). URL: <https://link.aps.org/doi/10.1103/PhysRevLett.21.775>.

Vila, J. P. (1999). “On Particle Weighted Methods and Smooth Particle Hydrodynamics”. In: *Math. Model. Methods Appl. Sci.* 09.02, pp. 161–209. DOI: [10.1142/S0218202599000117](https://doi.org/10.1142/S0218202599000117). URL: <http://www.worldscientific.com/doi/abs/10.1142/S0218202599000117>.

Vilar, François, Pierre-Henri Maire, and Rémi Abgrall (2014). “A discontinuous Galerkin discretization for solving the two-dimensional gas dynamics equations written under total Lagrangian formulation on general unstructured grids”. In: *J. Comput. Phys.* 276, pp. 188–234. ISSN: 00219991. DOI: [10.1016/j.jcp.2014.07.030](https://doi.org/10.1016/j.jcp.2014.07.030). URL: <http://linkinghub.elsevier.com/retrieve/pii/S0021999114005233>.

Viola, M. et al. (2008). “How does gas cool in dark matter haloes?” In: *Mon. Not. R. Astron. Soc.* 383.2, pp. 777–790. ISSN: 00358711. DOI: [10.1111/j.1365-2966.2007.12598.x](https://doi.org/10.1111/j.1365-2966.2007.12598.x). arXiv: [0710.2473](https://arxiv.org/abs/0710.2473).

Vitter, Jeffrey Scott (2001). “External Memory Algorithms and Data Structures: Dealing with Massive Data”. In: *ACM Comput. Surv.* 33.2, pp. 209–271. ISSN: 0360-0300. DOI: [10.1145/384192.384193](https://doi.org/10.1145/384192.384193). URL: <http://doi.acm.org/10.1145/384192.384193>.

Vogelsberger, Mark et al. (2014). “Introducing the *Illustris* project: Simulating the coevolution of dark and visible matter in the universe”. In: *Mon. Not. R. Astron. Soc.* 444.2, pp. 1518–1547. ISSN: 13652966. DOI: [10.1093/mnras/stu1536](https://doi.org/10.1093/mnras/stu1536). arXiv: [1405.2921](https://arxiv.org/abs/1405.2921).

Voigt, L. M. and A. C. Fabian (2004). “Thermal conduction and reduced cooling flows in galaxy clusters”. In: *Mon. Not. R. Astron. Soc.* 347.4, pp. 1130–1149. ISSN: 0035-8711. DOI: [10.1111/j.1365-2966.2004.07285.x](https://doi.org/10.1111/j.1365-2966.2004.07285.x). URL: <http://doi.wiley.com/10.1111/j.1365-2966.2004.07285.x>.

Von Neumann, J. (1951). “Various techniques used in connection with random digits. Monte Carlo methods”. In: *Natl. Bur. Stand.* 12, pp. 36–38.

Voronoi, Georges (1908). “Nouvelles applications des paramètres continus à la théorie des formes quadratiques. Deuxième mémoire. Recherches sur les paralléloèdres primitifs.” In: *J. für die reine und Angew. Math.* 134, pp. 198–287. URL: <http://eudml.org/doc/149291>.

Vorst, H.A. Van Der (1992). “BI-CGSTAB: A Fast and Smoothly Converging Variant of BI-CG for the Solution of Nonsymmetric Linear Systems”. In: *SIAM J. Sci. Stat. Comput.* 13.2, pp. 631–644.

Wadsley, J. W., G. Veeravalli, and H. M P Couchman (2008). “On the treatment of entropy mixing in numerical cosmology”. In: *Mon. Not. R. Astron. Soc.* 387.1, pp. 427–438. ISSN: 00358711. DOI: [10.1111/j.1365-2966.2008.13260.x](https://doi.org/10.1111/j.1365-2966.2008.13260.x).

Wadsley, James, J. Stadel, and T. Quinn (2004). “Gasoline: An adaptable implementation of TreeSPH”. In: *New Astron.* 9.2, pp. 137–158. ISSN: 13841076. DOI: [10.1016/j.newast.2003.08.004](https://doi.org/10.1016/j.newast.2003.08.004). arXiv: [0303521 \[astro-ph\]](https://arxiv.org/abs/astro-ph/0303521). URL: <http://arxiv.org/abs/astro-ph/0303521v1>.

Wang, Peng and Tom Abel (2009). “Magnetohydrodynamic Simulations of Disk Galaxy Formation: the Magnetization of The Cold and Warm Medium”. In: *Astrophys. J.* 696.1, pp. 96–109. DOI: [10.1088/0004-637X/696/1/96](https://doi.org/10.1088/0004-637X/696/1/96). arXiv: [0712.0872](https://arxiv.org/abs/0712.0872). URL: <http://arxiv.org/abs/0712.0872>.

Wang, XiaoKun et al. (2016). “Efficient extracting surfaces approach employing anisotropic kernels for SPH fluids”. In: *J. Vis.* 19.2, pp. 301–317. ISSN: 1343-8875. DOI: [10.1007/s12650-015-0317-7](https://doi.org/10.1007/s12650-015-0317-7). URL: <http://link.springer.com/10.1007/s12650-015-0317-7>.

Wannier, P. G., N. Z. Scoville, and R. Barvainis (1983). “The polarization of millimeter-wave emission lines in dense interstellar clouds”. In: *Astrophys. J.* 267, p. 126. ISSN: 0004-637X. DOI: [10.1086/160850](https://doi.org/10.1086/160850). URL: <http://adsabs.harvard.edu/doi/10.1086/160850>.

Wardle, Mark and Mark (2007). “Magnetic fields in protoplanetary disks”. In: *Astrophys. Space Sci.* 311.1-3, pp. 35–45. DOI: [10.1007/s10509-007-9575-8](https://doi.org/10.1007/s10509-007-9575-8). arXiv: [0704.0970](https://arxiv.org/abs/0704.0970). URL: <http://arxiv.org/abs/0704.0970>.

Watson, D. F. (1981). “Computing the n-dimensional Delaunay tessellation with application to Voronoi polytopes”. In: *Comput. J.* 24.2, pp. 167–172. DOI: [10.1093/comjnl/24.2.167](https://doi.org/10.1093/comjnl/24.2.167). URL: <https://academic.oup.com/comjnl/article-lookup/doi/10.1093/comjnl/24.2.167>.

Wei, Zhangping et al. (2015). “SPH modeling of dynamic impact of tsunami bore on bridge piers”. In: *Coast. Eng.* 104, pp. 26–42. DOI: [10.1016/J.COASTALENG.2015.06.008](https://doi.org/10.1016/J.COASTALENG.2015.06.008). URL: <https://www.sciencedirect.com/science/article/pii/S0378383915001143>.

Wendland, Holger (2017). *Kernels and Convergence*. Ourense, Spain.

Wetzstein, M. et al. (2009). “Vine—a Numerical Code for Simulating Astrophysical Systems Using Particles. I. Description of the Physics and the Numerical Methods”. In: *Astrophys. J. Suppl. Ser.* 184.2, pp. 298–325. ISSN: 0067-0049. DOI: [10.1088/0067-0049/184/2/298](https://doi.org/10.1088/0067-0049/184/2/298). URL: <http://stacks.iop.org/0067-0049/184/i=2/a=298?key=crossref.131eb36407b70a987090b502ab963b20>.

Weyl, H. (1926). *Modern conceptions of universe*.

White, S. D. M., C. S. Frenk, and M. Davis (1983). “Clustering in a neutrino-dominated universe”. In: *Astrophys. J.* 274. DOI: [10.1086/184139](https://doi.org/10.1086/184139). URL: <http://adsabs.harvard.edu/doi/10.1086/184139>.

White, Simon D. M. et al. (1996). “Cosmology and Large Scale Structure”. In:

White, Simon D.M. (1994). *Formation and Evolution of Galaxies: Les Houches Lectures*. arXiv: [9410043 \[astro-ph\]](https://arxiv.org/abs/astro-ph/9410043). URL: <http://arxiv.org/abs/astro-ph/9410043>.

Whitehurst, Robert (1995). “A free Lagrange method for gas dynamics”. In: *Mon. Not. R. Astron. Soc.* 277.2, pp. 655–680. DOI: [10.1093/mnras/277.2.655](https://doi.org/10.1093/mnras/277.2.655). URL: <https://academic.oup.com/mnras/article-lookup/doi/10.1093/mnras/277.2.655>.

Whitworth, A.P. (1995). “Estimating Density in Smoothed Particle Hydrodynamics”. In: *Astron. Astrophys.* Pp. 929–932.

Widrow, Lawrence M et al. (2012). “The First Magnetic Fields”. In: *Space Sci. Rev.* 166.1-4, pp. 37–70. DOI: [10.1007/s11214-011-9833-5](https://doi.org/10.1007/s11214-011-9833-5). arXiv: [arXiv:1109.4052](https://arxiv.org/abs/1109.4052). URL: <https://link.springer.com/content/pdf/10.1007{\%}2Fs11214-011-9833-5.pdf><https://arxiv.org/abs/1109.4052>.

Wilson, Warwick E. et al. (2011). “The Australia Telescope Compact Array Broadband Backend (CABB)”. In: *Mon. Not. R. Astron. Soc.* 416, pp. 832–856. DOI: [10.1111/j.1365-2966.2011.19054.x](https://doi.org/10.1111/j.1365-2966.2011.19054.x). arXiv: [1105.3532](https://arxiv.org/abs/1105.3532). URL: [http://arxiv.org/abs/1105.3532](https://arxiv.org/abs/1105.3532).

Wright, E. L. et al. (1992). “Interpretation of the cosmic microwave background radiation anisotropy detected by the COBE Differential Microwave Radiometer”. In: *Astrophys. J.* 396.1. DOI: [10.1086/186506](https://doi.org/10.1086/186506). URL: [http://adsabs.harvard.edu/doi/10.1086/186506](https://adsabs.harvard.edu/doi/10.1086/186506).

Wurster, James, Daniel J. Price, and Matthew R. Bate (2016). “Can non-ideal magnetohydrodynamics solve the magnetic braking catastrophe?” In: *Mon. Not. R. Astron. Soc.* 457.1, pp. 1037–1061. ISSN: 0035-8711. DOI: [10.1093/mnras/stw013](https://doi.org/10.1093/mnras/stw013). arXiv: [1512.01597](https://arxiv.org/abs/1512.01597). URL: [http://arxiv.org/abs/1512.01597](https://arxiv.org/abs/1512.01597).

Xu, Guohong (1995). “A New Parallel N-body Gravity Solver: TPM”. In: *Astrophys. J. Suppl. Ser.* 98, p. 355. DOI: [10.1086/192166](https://doi.org/10.1086/192166). arXiv: [9409021 \[astro-ph\]](https://arxiv.org/abs/9409021). URL: [http://arxiv.org/abs/astro-ph/9409021](https://arxiv.org/abs/astro-ph/9409021).

Xu, Xiaoyang (2016). “An improved SPH approach for simulating 3D dam-break flows with breaking waves”. In: *Comput. Methods Appl. Mech. Eng.* 311, pp. 723–742. DOI: [10.1016/j.cma.2016.09.002](https://doi.org/10.1016/j.cma.2016.09.002). URL: <https://www.sciencedirect.com/science/article/pii/S0045782516311033>.

Yang, H. Y. K. and C. S. Reynolds (2015). “Interplay among Cooling, AGN Feedback and Anisotropic Conduction in the Cool Cores of Galaxy Clusters”. In: *ArXiv e-prints*. arXiv: [1512.05796](https://arxiv.org/abs/1512.05796). URL: [http://arxiv.org/abs/1512.05796](https://arxiv.org/abs/1512.05796).

Yu, Jihun and Greg Turk (2013). “Reconstructing surfaces of particle-based fluids using anisotropic kernels”. In: *ACM Trans. Graph.* 32.1, pp. 1–12. DOI: [10.1145/2421636.2421641](https://doi.org/10.1145/2421636.2421641). URL: [http://dl.acm.org/citation.cfm?doid=2421636.2421641](https://dl.acm.org/citation.cfm?doid=2421636.2421641).

Yuen, Ka Ho and Alex Lazarian (2017). “Tracing interstellar magnetic field using velocity gradient technique: Application to Atomic Hydrogen data”. In: *Astrophys. J. Lett.* 837.2, pp. 1–7. ISSN: 20418213. DOI: [10.3847/2041-8213/aa6255](https://doi.org/10.3847/2041-8213/aa6255). arXiv: [1701.07944](https://arxiv.org/abs/1701.07944). URL: [http://arxiv.org/abs/1701.07944](https://arxiv.org/abs/1701.07944).

Zakamska, Nadia L. and Ramesh Narayan (2003). “Models of Galaxy Clusters with Thermal Conduction”. In: *Astrophys. J.* 582, pp. 162–169. URL: [http://iopscience.iop.org/0004-637X/582/1/162/pdf/56383.web.pdf](https://iopscience.iop.org/0004-637X/582/1/162/pdf/56383.web.pdf).

Zeeman, P. (1897). "On the Influence of Magnetism on the Nature of the Light Emitted by a Substance". In: *Astrophys. J.* 5, p. 332. DOI: [10.1086/140355](https://doi.org/10.1086/140355). URL: http://articles.adsabs.harvard.edu/cgi-bin/nph-iarticle{_}query?1897ApJ.....5..332Z{\&}data{_}type=PDF{_}HIGH{\&}whole{_}paper=YES{\&}type=PRINTER{\&}filetype=.pdf.

Zeldovich, Ya. B. (1970). "Gravitational Instability: An Approximate Theory for Large Density Perturbations". In: *Astron. Astrophys.* 5, pp. 84–89.

Zhang, G M and R C Batra (2009). "Symmetric smoothed particle hydrodynamics (SSPH) method and its application to elastic problems". In: *Comput. Mech.* 43.3, pp. 321–340. DOI: [10.1007/s00466-008-0308-9](https://doi.org/10.1007/s00466-008-0308-9). URL: <https://link.springer.com/content/pdf/10.1007{\%}2Fs00466-008-0308-9.pdf>.

Ziegler, U (2005). "Astrophysics Self-gravitational adaptive mesh magnetohydrodynamics with the NIRVANA code". In: *Astron. Astrophys.* 435, pp. 385–395. DOI: [10.1051/0004-6361:20042451](https://doi.org/10.1051/0004-6361:20042451). URL: <https://www.aanda.org/articles/aa/pdf/2005/20/aa2451.pdf>.

Ziegler, Udo and Udo (1998). "NIRVANA+: An adaptive mesh refinement code for gas dynamics and MHD". In: *Comput. Phys. Commun.* 109.2-3, pp. 111–134. ISSN: 00104655. DOI: [10.1016/S0010-4655\(98\)00022-8](https://doi.org/10.1016/S0010-4655(98)00022-8). URL: <http://linkinghub.elsevier.com/retrieve/pii/S0010465598000228>.

Zienkiewicz, O C (1971). *The finite element method in engineering science*. McGraw-Hill. URL: https://books.google.de/books?id={_}d1RAAAAMAAJ.

ZuHone, J. a. et al. (2013). "Cold Fronts and Gas Sloshing in Galaxy Clusters With Anisotropic Thermal Conduction". In: *Astrophys. J.* 762.2, p. 69. ISSN: 0004-637X. DOI: [10.1088/0004-637X/762/2/69](https://doi.org/10.1088/0004-637X/762/2/69). URL: <http://stacks.iop.org/0004-637X/762/i=2/a=69?key=crossref.acb624c34469bc64548a84934c485d77>.

ZuHone, J. a. et al. (2015). "Todehe Effect of Anisotropic Viscosity on Cold Fronts in Galaxy Clusters". In: *Astrophys. J.* 798.2, p. 90. ISSN: 1538-4357. DOI: [10.1088/0004-637X/798/2/90](https://doi.org/10.1088/0004-637X/798/2/90). URL: <http://adsabs.harvard.edu/abs/2015ApJ...798...90Z>.

Zwicky, Fritz (1933). *Die Rotverschiebung von extragalaktischen Nebeln*. Vol. 6, pp. 110–127. URL: <http://adsabs.harvard.edu/abs/1933AcHPh...6..110Z>.

List of Figures

I.1	Energy density evolution over time.	4
I.2	Current energy budget of the universe.	5
I.3	CMB temperature deviations and spectrum.	5
I.4	Different stages of the universe’s evolution.	6
I.5	Bottom-up evolution resulting in an elliptical galaxy.	7
I.6	Some of the recent observatories tied to the wavelength regime they observe in.	8
I.7	Collage of different observations from star forming regions to galaxy clusters.	10
I.8	M51 observed in multiple wavelengths.	13
I.9	Polarized radio emission and B-vectors of M 51.	14
I.10	Synchrotron and dust emission observed by Planck.	14
I.11	Polarized radio emission in the Coma galaxy cluster.	15
II.1	Illustration for the importance of magnetic fields.	18
II.2	Illustration of relativistic beaming.	20
II.3	Synchrotron spectrum of a single electron.	21
II.4	Illustration of the detection process of the Faraday rotation measure.	24
II.5	Faraday rotation map of Hydra A overlayed over total intensity in colours.	25
II.6	Dust polarisation measurements in the Taurus dark-cloud complex.	27
II.7	Observational results of diffuse and molecular cloud Zeeman measurements.	29
II.8	Schematic illustrating the calculation of velocity gradients	33
II.9	Magnetic field directions obtained via the velocity gradient technique.	34
II.10	Number of scatterings compared to a straight fly outwards a galaxy cluster.	36
II.11	Ionisation fraction due to the Saha equation.	44
II.12	Paper statistics.	45
II.13	Paper statistics with “numeric” in the abstract.	47
III.1	Illustration of the one dimensional Riemann problem.	52
III.2	Illustration of three approaches to calculate the density from mass elements.	56
III.3	Illustration of the kernel bias.	59
III.4	Illustration of a 2D Voronoi grid and Delaunay triangulation.	66
III.5	Illustration of the point insertion algorithm.	67
III.6	Illustration of different cell/particle volumes.	69
III.7	Moore’s law as number of resolution elements over time.	80

IV.1	2D particle placement for a constant density model.	86
IV.2	Density evolution of a 3D constant density model.	92
IV.3	Histogram of nearest neighbour distances for a 3D constant density model.	93
IV.4	Auto correlation function for a 3D constant density model.	95
IV.5	Evolution of a plateau density function with gradients.	96
IV.6	Evolution of a sine wave density function.	98
IV.7	Evolution of a sawtooth density function.	99
IV.8	Auto correlation function for a sine wave density model.	100
IV.9	Comparison w/ and w/o redistribution in the plateau test.	101
IV.10	Statistics for plateau test.	102
IV.11	Zoom of the plateau test with varying particle number.	104
IV.12	L1 error evolution.	105
IV.13	Zel'dovich pancake initial conditions.	107
IV.14	Integrated density of the Boss-Bodenheimer test case.	109
IV.15	Beta profile for an isolated galaxy cluster.	110
IV.16	Example for initial conditions sampled according to a read image.	111
V.1	Sod shock tube.	131
V.2	Sod shock tube zoom on pressure blip.	132
V.3	Sod shock tube zoom on velocity noise.	132
V.4	Sedov blast wave density and temperature map.	133
V.5	Sedov blast wave radial distribution.	134
V.6	Keplerian Ring.	136
V.7	Blob test density slices.	137
V.8	Blob test cold gas fraction evolution.	138
V.9	Kelvin-Helmholtz instability.	140
V.10	Comparison of binning methods.	142
V.11	Decaying turbulence in velocity power spectra.	143
V.12	Decaying turbulence maps.	144
V.13	Decaying turbulence kinetic energy evolution.	145
V.14	Sphere in hydrostatic equilibrium.	148
V.15	Evrard collapse.	149
V.16	Zel'dovich pancake.	151
V.17	Disk galaxies maps.	153
V.18	Disk galaxy density and velocity dispersion profiles of stars.	154
V.19	Disk galaxy density and velocity dispersion profiles of cold gas.	155
V.20	Santa Barbara Cluster slices.	156
V.21	Santa Barbara Cluster radial profiles.	159
VI.1	Sketch to illustrate S norm.	171
VI.2	Gas density maps with different methods for different regions.	175
VI.3	Relative errors of integrated mass.	176
VI.4	Distribution of smoothing lengths.	178
VI.5	Mass fractions in S -value bins.	180

LIST OF FIGURES	365	
VI.6	Distribution of S -values.	180
VI.7	Kinetic power spectra calculated with different methods.	181
VII.1	Architecture of Rambrain.	195
VII.2	Cyclic managed memory.	196
VII.3	Exemplary interaction of user code with Rambrain library.	202
VII.4	Execution time of a n-body code.	204
VII.5	Data movement for one 'Block' algorithm matrix transpose.	205
VII.6	Preemptive loading.	207
VII.7	Speed-up by pulling const pointers.	209
VII.8	Difference imaging residual.	210
VIII.1	One dimensional temperature step test without magnetic field.	230
VIII.2	Temperature step test with magnetic field.	232
VIII.3	Time evolution of temperature step test.	234
VIII.4	Wave like temperature distribution test.	236
VIII.5	Spherical temperature distribution test.	237
VIII.6	Temperature step test with different magnetic field strengths.	238
VIII.7	Suppression factor distribution.	240
VIII.8	Temperature maps of galaxy cluster with different conduction.	241
VIII.9	Emissivity distribution with different conduction.	243
VIII.10	Temperature maps for central cluster part for different perpendicular conduction.	244
VIII.11	Emissivity distribution for different perpendicular conduction.	245
VIII.12	Radial temperature and entropy distributions.	246
VIII.13	Temperature fluctuations compared to observations.	248
VIII.14	Distribution of suppression factors.	249
VIII.15	Temperature maps of different clusters with different conduction.	251
VIII.16	Radial temperature profiles of different clusters.	251
VIII.17	Temperature fluctuations of different clusters.	253
VIII.18	Magnetic pressure maps with different conduction.	254
VIII.19	Radial magnetic field profiles for different conduction.	255
VIII.20	Temperature against magnetic field strength of different clusters.	256
IX.1	Density structures of cosmological boxes.	266
IX.2	Typical particle configuration of zoomed initial conditions.	267
IX.3	Evolution of a zoomed galaxy cluster simulation.	269
IX.4	Comparison of radial temperature profiles of one galaxy cluster.	270
X.1	Projections with magnetic seeding at $t = 1Gyr$	285
X.2	Projections with magnetic seeding at $t = 2Gyr$	286
X.3	Projections with constant magnetic field at $t = 1Gyr$	287
X.4	Projections with constant magnetic field at $t = 2Gyr$	288
X.5	Density cross sections of magnetic field strengths.	289
X.6	Star formation rate over time.	289
X.7	Evolution of magnetic field strengths over time.	290

X.8	Magnetic powerspectra for both models.	292
X.9	Evolution of total disk mass over time.	294
X.10	Rate of change of mass in the disk.	294
X.11	Gas density and magnetic field structure.	295
X.12	Structure of the magnetic field using unsharp masking.	297
X.13	Structure of the magnetic field using unsharp masking in each component.	299
X.14	Magnetic divergence errors.	300
XI.1	Example galaxies with declining rotation curves.	305
XI.2	Rotation curves obtained from cold gas.	306
XI.3	DM fraction versus rotational velocity.	308
XI.4	Surface density, rotation curves and radial velocity dispersion.	311

List of Tables

II.1	Prandtl numbers estimated for different astrophysical systems.	43
III.1	List of popular astrophysical hydrodynamics codes	73
IV.1	Hydrodynamic and magneto-hydrodynamics test cases, implemented in the code.	108
IV.2	Compilation options with default values and description.	112
IV.3	Runtime parameters with example values and descriptions.	113
V.1	List of SPH improvements.	121
V.2	Overview of test problems.	158
VI.1	Major pros and cons of different binning schemes.	174
VII.1	Code metadata	186
VIII.1	Relative errors of internal energy for temperature step test.	233
VIII.2	General cluster properties.	250
X.1	Number of particles mass resolution and gravitational softening lengths. . .	279
X.2	Parameters for the simulated disk galaxies.	281
X.3	Parameters for the multiphase model.	281
X.4	Parameters for the gas halo.	284

Acknowledgements

Lieber Harald, lieber Klaus, allen voran möchte ich euch beiden vielen Dank sagen für die viele Unterstützung fachlicher und menschlicher Art. Ihr habt mich aufgefangen als ich nicht mehr wusste wie es weitergehen soll und mir dabei geholfen, die letzten Jahre zu einem einmaligen Erlebnis zu machen. Harald, du hast mich durch mein ganzes Studium geleitet und erst zur Astrophysik gebracht und ich würde sagen, das hat sich doch mal gelohnt! Auch wenn nicht immer alles so geklappt hat, wie wir es uns vorgestellt haben hat doch alles ganz funktioniert. Ich hatte viel Spaß und denke so kann es durchaus auch noch weitergehen.

Mein Dank gilt auch Ralf Bender und dem MPE, ohne die es nicht die nötige Finanzierung gegeben hätte, um mir das Anfertigen dieser Doktorarbeit zu ermöglichen.

Vielen Dank an meine Eltern und Großeltern, die mir mein Studium bis zu diesem Punkt und darüber hinaus in vielerlei Hinsicht ermöglicht haben. Ich habe mein Ziel erreicht, aber vermutlich war auch das nur eine Etappe auf einem langen Weg.

Auch meine guten Freunde und Kollegen sollen nicht unerwähnt bleiben, auch wenn ihr inzwischen zu zahlreich seid um alle namentlich zu erwähnen. Ihr habt euch jahrein, jahraus anhören müssen was ich von mir gegeben habe und mich dabei unterstützt soweit zu kommen ohne zwischendurch durchzudrehen. Und wer hätte gedacht, dass jemand, der keinen Kaffee trinkt so einen Spaß an Kaffeepausen haben könnte. Einige von euch haben es vor mir geschafft fertig zu werden, manche habe ich letztendlich doch noch geschlagen und insbesondere euch wünsche ich alles Gute.

Mein besonderer Dank gilt Alex, dass er mich so gut angelernt hat und Max für die schöne Zeit, ausgezeichnete Zusammenarbeit und fortwährende Unterstützung. Das Ende unserer gemeinsamen Projekte ist noch nicht gekommen! Danken möchte ich auch allen bei TNG, die mich immer wieder eingeladen haben und mir so viel beigebracht haben, was mir bei meiner Arbeit unersetzliche Dienste geleistet hat. Abschließend noch ein besonderer Dank an Moritz und vor allem Ralle, die es sich angetan haben trotz Umfang und Zeitdruck Teile dieser Arbeit zu lesen.